ORISE--99-0164-Vol.1
CONF-960536--PROC.-Vol.1

SIXTH INTERNATIONAL RADIOPHARMACEUTICAL DOSIMETRY SYMPOSIUM

Proceedings of a Conference
Held in Gatlinburg, Tennessee

May 7-10, 1996

Edited by

Audrey T. S.-Stelson
Michael G. Stabin
Richard B. Sparks

Compilers
Fanny B. Smith
Audrey T. S.-Stelson

SPONSORS

Oak Ridge Associated Universities
U.S. Food and Drug Administration
U.S. Department of Energy

January 1999

This report was prepared under contract number DE-AC05-76OR00033 between the U.S. Department of Energy and Oak Ridge Asssociated Universities

DISCLAIMER

DEDICATION

The Radiopharmaceutical Internal Dosimetry Information Center was established in 1971 at Oak Ridge Associated Universities, formally the Oak Ridge Institute for Nuclear Studies, to assist the nuclear medicine community and government agencies in the evaluation of absorbed radiation doses from clinical uses of radioactive materials. The Center's goals were to improve the accuracy of radiation dose estimates and to increase communication and exchange of information among those who perform dose estimates and those who need such information for clinical purposes.

For twenty-eight years the Center, now the Radiation Internal Dose Information Center (RIDIC), has met these goals by developing sophisticated dosimetry models, including mathematical models of the pregnant woman at three stages of gestation; by producing software for dose estimation using the MIRD technique; by maintaining a bibliographic data base of internal dosimetry information; and by organizing six international radiopharmaceutical dosimetry symposia. The Center has also collaborated with other research groups and worked on committees for the ICRP and the NCRP.

Roger Cloutier and Evelyn Watson were the motivating force behind RIDIC at its inception. Both have been Director of the Center and both have been Chair of the MIRD Committee (Evelyn continues to serve in that capacity in her retirement). Under their leadership RIDIC achieved an international reputation for excellence in dosimetry. They were organizers of the first five symposia and have approximately two hundred publications between them on dosimetry-related topics. Their paper entitled *Radiation Dose from Radioisotopes in the Blood*, published in the 1969 symposium proceedings, is one of the most cited references in the dosimetry literature. The dosimetry community is indebted to Evelyn and Roger for their dedication and their contributions to the field of internal dosimetry.

The editors and RIDIC staff respectfully dedicate these proceedings to these two remarkable scientists and their work in internal dosimetry.

ACKNOWLEDGMENTS

The editors gratefully acknowledge those who assisted in the preparation of this publication. The authors of the manuscripts deserve our special gratitude for making these proceedings possible. We regret that some of the authors were unable to submit their papers. The U.S. Department of Energy provided necessary publication funds. The Information Services Department at Oak Ridge Associated Universities advised and helped coordinate the tasks associated with printing and binding.

We also want to acknowledge and thank the companies that provided travel funds for invited speakers at the meeting: BRACCO RESEARCH USA, Princeton, NJ; DUPONT PHARMA, North Billerica, MA; MALLINCKRODT MEDICAL, INC., St. Louis, MO; RADIATION DOSIMETRY SYSTEMS OF OAK RIDGE, Knoxville, TN; SYNCOR INTERNATIONAL CORPORATION, Chatsworth, CA; and TRI-MED SPECIALTIES, INC., Lenexa, KS.

Special thanks go to David Foster for the Thursday evening SAAM II demonstration and workshop. We also appreciate the help with logistics and the technical aspects of the meeting, as well as administrative assistance from the Glenwood Lodge staff, Dick Toohey, Sue Holloway, Jeff Evans, Fanny Smith and Bendi Lowery.

In conclusion, we express our utmost appreciation to Fanny Smith for her word-processing skills. We had a difficult time with the translation of some of the graphics and equations from one software package to another. Some figures and equations may not be placed in the most appropriate location because they were anchored and could not be moved in the text.

Audrey T. S.-Stelson
Michael G. Stabin
Richard B. Sparks

CONTENTS

VOLUME 1

QUANTITATIVE ANALYSIS AND TREATMENT PLANNING (CONTINUED)

Session Chairmen: A. Bertrand Brill and Terry Smith

CELLULAR AND SMALL-SCALE DOSIMETRY

Session Chairman: Claude Brihaye and James Stubbs

CELLULAR AND SMALL SCALE DOSIMETRY (CONTINUED)

Session Chairmen: Robert Atcher and Darrell Fisher

POSTERS

VOLUME 2

POSTERS (CONTINUED)

DOSIMETRIC MODELS

Session Chairmen: Peter Roberson and Michael Stabin

MEDICAL INTERNAL DOSIMETRY: WHERE ARE WE GOING?

Mattsson S and Johansson L
Departments of Radiation Physics
Malmö University Hospital/Lund University, S-205 02 Malmö and
Umeå University Hospital/University of Umeå, S-901 85 Umeå, Sweden

ABSTRACT

Risk estimates and optimal use of various radiodiagnostic techniques necessitate accurate dosimetry for representative groups of patients. The small, but increasing, use of radiopharmaceuticals for therapy requires even more detailed and patient-specific dosimetry, for both tumor and normal tissue. This paper summarizes developments in internal dosimetry with reference to radiopharmaceuticals.

During recent years, considerable improvements have been made in physical methods and computer simulation of radiation transport and absorption. It has also become easier to get detailed information about the localization of organs and tissues and their volumes using CT and MR. Such measurements will be the base for patient-specific dosimetry and for construction of a series of representative human-like phantoms.

Serial quantitative gamma-camera images of patients and normal volunteers will continue to be the base for biokinetic information. The kinetics of many radiopharmaceuticals and their associated labeled decomposition products is still not always well enough described to facilitate reliable dose estimates. Variations in anatomy and biokinetics between individuals and changes due to disease should be considered.

The driving force for patient-specific dosimetry is the need to optimize radionuclide therapy. In diagnostic nuclear medicine there is normally no reason to use patient-specific dosimetry. However, the experiences gained in radionuclide therapy will be of great importance in helping to enlighten and explain variations and relations in diagnostic nuclear medicine.

Information on the distribution of the radionuclide within organs and tissues, and even within cells, in combination with knowledge about the relevant biological structures, is of importance both for therapeutic use of the radionuclide and for risk estimates in connection with diagnostic procedures.

Efforts have to be made to investigate biokinetics and dosimetry for new products such as receptor-substances and monoclonal antibodies as well as for older products for which the current dose estimates may be uncertain, e.g. pure β-emitters.

General biokinetic models such as the ICRP models for GI-tract, bone, respiratory tract, kidney and bladder, gallbladder and circulating blood must be developed also for children of various ages. We also hope to see more practical computer programs for organ dose calculations and further use of

information on effective dose to characterize radiation detriment. Increasing importance should be placed on providing data for the embryo/fetus. Absorbed doses received from breast feeding should continuously be under review. The influence on risk estimations of the large difference in dose rate between nuclear medicine procedures and procedures used in diagnostic radiology is still unknown and should be studied.

INTRODUCTION

Together with judgement of the diagnostic image quality, a dose estimate is an essential parameter in the optimization of diagnostic procedures for various groups of patients and investigations. Careful dose estimates are also needed for a correct comparison of different diagnostic methods in terms of radiation risk. They are essential for the estimation of the risk of developing radiation-induced cancer later in life and also facilitate calculation of population dose estimates. Absorbed dose estimates from radiopharmaceuticals require knowledge of biokinetic data (e.g. cumulated activities in organs and tissues) as well as physical data (e.g. decay properties of the radionuclide, emitted radiation and source-target geometry).

Radiotherapy with radiopharmaceuticals requires individual dose estimates for the tumor as well as for normal tissues (bone marrow, liver, kidneys, etc.) to predict tumor effect and normal tissue acute and late reactions. Even if the therapeutic use of radiopharmaceuticals is limited today, developments in internal dosimetry are being pushed forward by an interest in improving the dosimetry in connection with therapy. The result of this development is also of interest for the dosimetry in diagnostic nuclear medicine.

The developments in internal dosimetry during the last decades are summarized roughly in Figure 1. The time axis shows the years in which International Symposia on Radiopharmaceutical Dosimetry have taken place in Oak Ridge, and presently in Gatlinburg. The "curve" indicates the path of internal dosimetry, now splitting up into alternative and complementary routes for macrodosimetry (model-specific or patient-specific), millidosimetry (or small-scale dosimetry) and microdosimetry. The history of medical internal dosimetry goes further back in time than 1969, having its origin at the end of World War II, as described in detail in a recent paper by Stelson et al. (1).

CURRENT PHYSICAL METHODS USED FOR INTERNAL DOSIMETRY

Over the last 30 years, the Medical Internal Dose Committee (MIRD) of the Society of Nuclear Medicine in the USA has developed methods for estimating organ absorbed doses (2). The cumulated activity in the various source organs must be known, as must the Monte Carlo calculated absorbed fractions of energy or the mean absorbed dose in the target organ per unit cumulated activity in the source organ (the so called S factor) (3). During recent years, revised data for adults as well as new pediatric mathematical phantoms representing children of five different ages, 0, 1, 5, 10 and 15 years, have been developed (4). Using these phantoms, absorbed fractions have been calculated. Today organ doses can be calculated easily from cumulated activities using the MIRDOSE3 program (5), which uses these new absorbed fractions. The published data on absorbed fractions have been used in various dose calculation programs. Results from such calculations have been published in the MIRD Dose Estimate Reports (2) and in ICRP Publications 53 (6) and 62 (7). There are also other dose calculation programs based on the Monte Carlo technique and simplified or more human-like geometries, primarily intended for dosimetry in connection with radiopharmaceutical therapy (e.g. 8, 9).

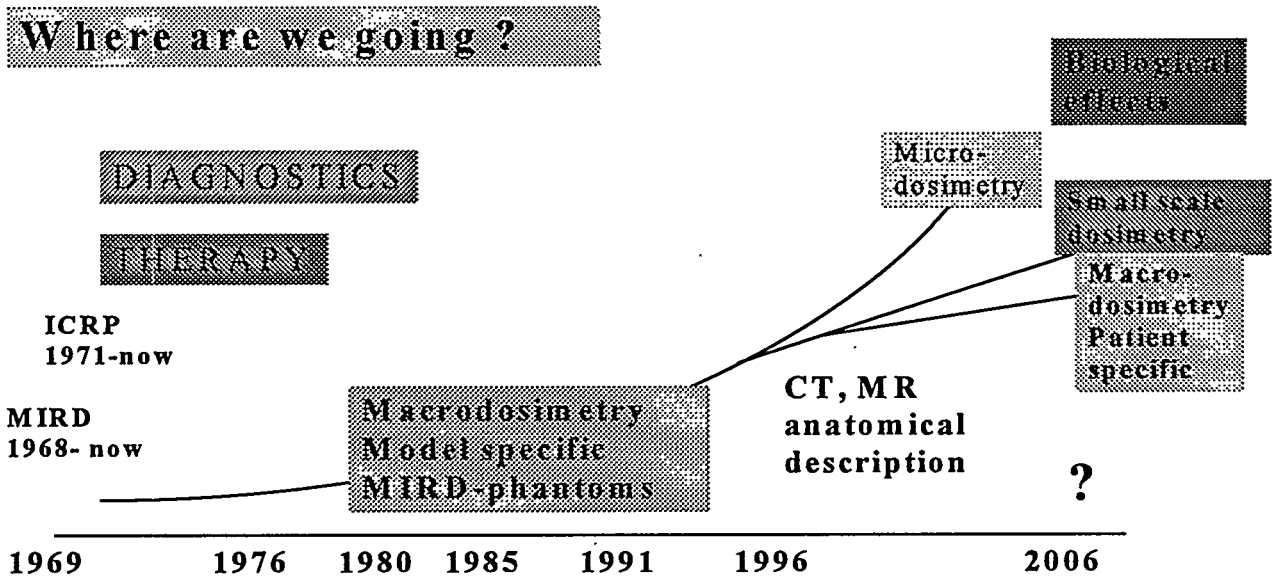

Figure 1. Illustration of main developments and milestones in medical internal dosimetry.

Phantoms for the pregnant woman at 3, 6 and 9 months of gestation has also recently been developed from the 15 year-old phantom and absorbed fractions including those for the fetus, fetal skeleton and soft tissue are given (10). These data are included in the MIRDOSE3 program (5) and used for the calculation of S values.

ASSESSMENT OF BIOKINETIC DATA

Estimates of cumulated activity should be made for all organs and tissues with a significant uptake as well as for the total body, and the routes of excretion should be identified. Cumulated activities for tissues through which the radionuclide is excreted should also be estimated. Basic biokinetic information is normally collected from patients and from normal volunteers using ordinary nuclear medicine imaging techniques such as serial quantitative planar gamma-camera and emission tomographic imaging (SPECT, PET) following the administration. Usually the cumulated activity is estimated from a series of anterior and/or posterior gamma-camera planar images starting immediately after administration and progressing until the biokinetics are suitably established. The available information is used to construct biokinetic models, which are not generally patient-specific. Such models, representing normal adults, are now used by ICRP (6).

As there are very few biokinetic data for children, the same data as for adults are normally used with pediatric phantoms for the estimation of absorbed dose to children of various ages.

In the absence of data to describe human placental transfer and fetal uptake of radiopharmaceuticals, estimates of absorbed dose to the mother and the fetus during pregnancy are still mainly based on biokinetic data for the nonpregnant woman.

For therapy, patient-specific models and data are necessary for the calculation of absorbed dose to the tumors and radiosensitive tissues. For a patient-specific dose calculation, volumes of organs and tumor also should be known. Such data can in principle be computed from CT, MR, SPECT or PET images.

GENERAL BIOKINETIC AND DOSIMETRIC MODELS FOR USE IN DIAGNOSTIC NUCLEAR MEDICINE

For dosimetry, there are some processes, physiological or nonphysiological, which are common to all radiopharmaceuticals. Therefore, for the purpose of dosimetry, the ICRP has described general biokinetic models for certain organ systems. These models are often primarily developed for occupational exposure, but are also used for radiopharmaceutical dosimetry. Two important examples of such models are the gastrointestinal tract model (11) and the respiratory tract model (11, 12).

There are also a number of dosimetric models developed to facilitate dosimetry and to make the different dose calculation methods more consistent. As examples of such dosimetric models the blood flow model introduced in ICRP Publication 53 (6), and the bone model, as described in ICRP 30 (11), may be mentioned.

Gastrointestinal Tract

There is an increasing need for accurate dosimetry for the gastrointestinal tract, since several of the new substances frequently used in nuclear medicine are excreted through this pathway (e.g. MIBI and HM-PAO). The model used by ICRP is essentially that proposed by Dolphin and Eve in 1966 (13). It is based on four catenary compartments (stomach, small intestine, upper large intestine and lower large intestine) where the transfers between the compartments are assumed to follow first order kinetics. This model has been considered to be sufficient for the purpose of dosimetry. The "unphysiological" use of first-order kinetics in this context is justified by the large individual variations in transit times of material in the intestine that can be observed. The error introduced by using such kinetics is less significant in comparison with these differences. Another reason for using first order kinetics in the model is that the mean residence time for the different parts of the GI tract can easily be calculated analytically.

Several individuals and groups have pointed out the need for a new physiologically-based gastrointestinal tract model. Stubbs (14) presented a new model using a combination of zero- and first-order kinetics to describe the movement of material. This model takes variations due to age, sex, phase of menstrual cycle, meal composition etc. into account. Simkó and Nosske (15) recently discussed the basis for a revision of the gastrointestinal tract model, and ICRP has now a task group for developing a new model.

Kidneys - Urinary Bladder

Substances used in nuclear medicine are often excreted through the kidneys and urinary bladder. For a number of substances, the effective dose to the patient will be dominated by the absorbed dose to the wall of the urinary bladder. The cumulated activity in the bladder is influenced by length of voiding interval, time between administration and first voiding etc. (16). The absorbed fraction in the bladder wall with a source in the content depends on the volume of the content; it is thus time-dependent. The traditional absorbed fractions for calculation of absorbed dose to the bladder are based, however, on a constant volume of 200 ml for adults (3). In ICRP Publications 53 (6) a standard voiding interval of 3.5 hours is used for adults. ICRP Publications 67 (17) and 69 (18), dealing with occupational or environmental exposure, use first order kinetics to represent bladder voiding with an elimination rate corresponding to a voiding interval of 4 hours (18). An age-dependent voiding interval is applied in ICRP 62 (7). The published "dynamic bladder" model (19) uses time-dependent absorbed fractions. However, a number of input parameters are required in this model, which are not easily determined and standardized, and it is therefore less practical for more general use.

Gallbladder

In the ICRP Publication 53 (6), a model for the liver and biliary excretion was introduced. This model also describes the emptying of the gallbladder, which is assumed to be identical for all substances. The model describes the pathways of the activity from the liver, either via temporal storage in the gallbladder, or directly into the intestine. The model does not include rates or fractional distribution between the two pathways.

Bone

Bone is a highly complex and heterogeneous tissue with cellular and mineral components arranged in a varied and irregular pattern. The absorbed dose to the radiosensitive parts of the skeleton, the bone surfaces and the red marrow depends strongly on the site of deposition and the structure of the bone at that point. In ICRP 30 (11), a dosimetric model for the bone is presented, which includes absorbed fractions of energy in the red marrow and the endosteal bone surfaces for non-penetrating radiation. In this model, the source may be found in trabecular or cortical bone, and the absorbed fraction depends on whether the source should be considered as deposited on the surface or in the volume of the mineral bone. For penetrating radiation, the absorbed fractions to bone tissues have been estimated using Monte Carlo calculations in a similar way as for other organs and tissues. For an adult, the ICRP assumes that the mass of the trabecular bone is 20 % of the total bone volume, but contains 50% of the bone surface cells (11). For children under 5 years of age, there are few data on distribution between cortical and trabecular bone. For dosimetric purposes, the ICRP Task Group on Dose to Patients from Radiopharmaceuticals has found it reasonable to assume that trabecular bone comprises 40 % of the total bone mass and 60 % of the bone surface (6). These assumptions are rather critical for the result of the dose estimation, since the dose to the radiation sensitive parts of the bone, i.e. red marrow and bone surfaces, is much higher from a source in the trabecular than in the cortical bone.

There are other problems related to bone dosimetry. In children bones are still growing, and therefore a bone-seeking substance or radionuclide will concentrate in the epiphyseal growth plates. This alters the activity distribution, and thus also the configuration of the source, affecting not only the absorbed fractions for the skeleton, but also for other organs. The cells of the growing regions are also probably more radiosensitive than other parts of the skeleton, and the absorbed dose to these parts should therefore be estimated separately. At present, however, this is usually not done, primarily due to lack of both information and a standardized technique for the calculation.

Circulating Blood

For radionuclides in circulating blood one of two alternative distribution models may be used; distribution according to blood volume, or distribution determined by the fraction of cardiac output. The first model may be used for radionuclides present in circulating blood during a longer period. For ultra-short-lived radionuclides, with physical half-time of a few minutes or less, the second model is used. Leggett and Williams (20) recently proposed a blood circulation model for reference man. The result of their work is highly relevant for application in radiopharmaceutical dosimetry. Their model is a more general biokinetic model which replaces both the blood flow model and the blood volume model.

ICRP DOSE ESTIMATES

As early as 1968, the ICRP initiated a report on the protection of patients in radionuclide investigations. It was adopted in 1969 and first published in 1971 (21). An appendix to the publication contains absorbed dose estimates and literature references for 92 compounds. In 1987 ICRP Publication 53 was published (6) containing dose estimates for 174 substances. In 1991, data for 6 additional substances were published (7) and data for another six substances are under preparation.

The biokinetic models, which are intended for dosimetry and described above, are often derived from very limited data for normal subjects. The models are therefore not necessarily representative for the individual patient, as data are assumed to vary between normal subjects and patients and also according to age and sex, and to be influenced by diet and drug therapy. There are also agents specifically designed to reduce uptake and retention (diuretics, laxatives) which greatly influence the kinetics.

It has been estimated that the calculation of organ doses will agree with actual patient doses within a factor of three; somewhat less for short-lived radionuclides. The factor may have a value of around two for estimation of effective dose (22).

EFFECTIVE DOSE FOR PATIENTS

The absorbed dose, as well as the risk per unit absorbed dose, varies between different organs and tissues in the body. In order to compare various irradiation situations, various tissue risk weighting factors may be applied to the organ absorbed doses. Theoretically, the weighted sum of all organ doses thus obtained is proportional to the total risk from the irradiation and defines the effective dose (23). This quantity can be used to compare the exposure from various irradiation situations using a single figure which is proportional to the risk from the irradiation. Using weighting factors from ICRP Publication 60 (23), ICRP provides effective dose values for reference adults, and for 15-, 10-, 5- and 1-year old children (6,7). The risk is, however, age-dependent and is two to three times higher for a young child than for the general public. For an age of exposure of about 60 years, the relative radiation detriment would be lower, perhaps by a factor of 3 (23). The risk for an individual is also dependent on a variety of other, less well known parameters. It must therefore be emphasized that data on the effective dose should primarily be used as a crude indicator of the average risk for a group of persons and not as a risk estimate for an individual. Figure 2 gives typical effective dose values for adult patients undergoing different investigations in nuclear medicine and diagnostic radiology.

HETEROGENEITY OF ABSORBED DOSE AND ENERGY ABSORPTION

The activity as well as the absorbed dose is not uniformly distributed in the body. The activity may not be uniformly distributed in a specific organ or tissue, or even within a cell. The dosimetric consequences may be illustrated by the now classical example from Adelstein (24) about ^{99m}Tc-MAA particles in the lungs. The majority of the lung cells receive about 25% of the mean organ dose, while a small minority (8%) receive higher doses ranging from 3 to almost 10 000 times the mean absorbed dose. Similar heterogeneities are assumed to be found in bone marrow and in tumors. This creates a need for what could be described as "millidosimetry".

The effects of a heterogeneous energy absorption may be even more pronounced if a radionuclide emitting low-energy Auger electrons binds to the DNA molecule. In this situation the biological effect

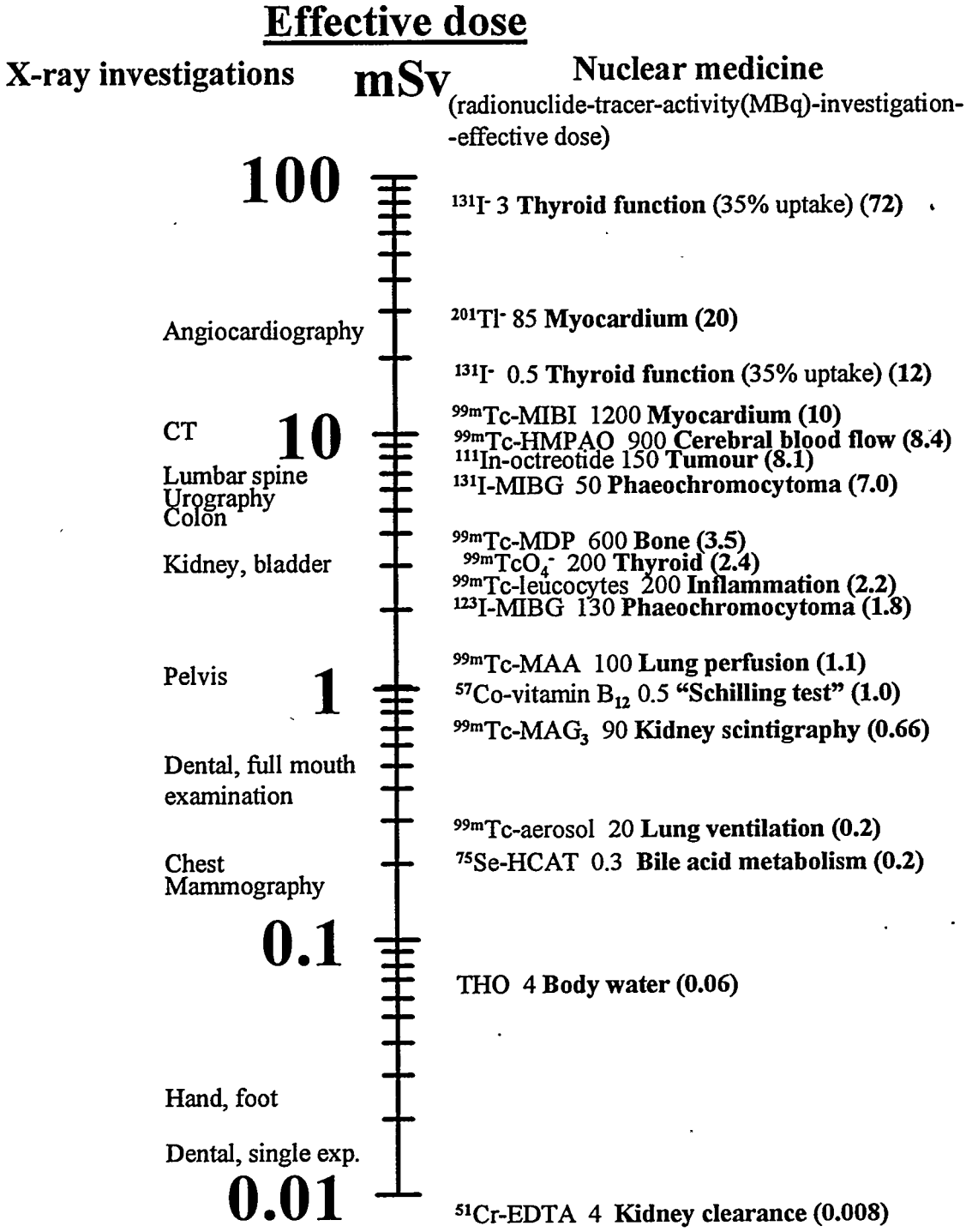

Figure 2. Effective dose values for adult patients undergoing nuclear medicine investigations. Data for a limited number of x-ray investigations are given for comparison.

can be comparable to that from high LET-radiation. To handle the problem with Auger electron emitters from a radiation protection point of view, a Task Group of the American Association of Physicists in Medicine has proposed that the fraction of absorbed dose which comes from the Auger electrons from radionuclides bound to DNA should be given a radiation weighting factor of 20 for stochastic effects and 10 for deterministic effects (25, 26). In the future, dose calculations for Auger electron emitters should therefore be accompanied by determinations of the subcellular distribution of the radionuclide. This creates a need for what is described as microdosimetry.

OTHER SPECIAL DOSIMETRIC PROBLEMS

Pediatric Nuclear Medicine

For dose estimations in children, absorbed fractions valid for children of specified ages (masses) are now available (4). There are also differences in biokinetic parameters. However, as the biokinetics for most nuclear medicine substances for children is little known, the same biokinetic data as for adults are normally used for dose estimations.

Embryo/Fetus

In general, pregnancy is a contraindication to most nuclear medicine investigations. The absorbed dose to an embryo or fetus is very different from investigation to investigation and varies also with time of gestation. The irradiation of an embryo or fetus consists of contributions from various organs and tissues in the mother. There is also a varying degree of uptake of the radionuclide in the fetus depending on the ability of the different compounds to cross the placental barrier. The amount of placental crossover is not well known and difficult to determine (27). The limited human data available and extrapolations from animal data have recently been compiled and used for dose estimates for some radiopharmaceuticals (28).

Breast Milk

Today there are reliable data concerning the transfer of a number of the most commonly used radiopharmaceuticals (29, 30, 31). There is a need for complementary data for new substances.

PATIENT-SPECIFIC BIOKINETIC AND DOSIMETRIC DATA NEEDED FOR THERAPY WITH RADIOPHARMACEUTICALS

The therapeutic use of radionuclides is today very small compared with their use in diagnostic procedures, and is dominated by the treatment of thyroid diseases with ^{131}I, together with ^{89}Sr chloride and other radiopharmaceuticals for bone metastatic pain palliation and ^{32}P phosphate for treatment of polycytaemia vera. There is, however, an increasing number of new substances introduced that are of potential interest for therapy, especially receptor-specific substances and monoclonal antibodies, which can be used for therapy if labeled with a suitable radionuclide.

Appropriate radionuclide therapy for tumors requires accurate individual dosimetry. For this purpose patient-specific biokinetic data are needed together with anatomical and morphological data for the tissues of interest. The activity distribution of a test administration can be obtained by whole-body planar gamma-camera imaging using the conjugate view method with attenuation correction. The use of quantitative SPECT or PET with proper photon attenuation and scatter correction may improve the determination of the activity distribution. Based on CT, MR or other tomographic techniques, a "voxel" phantom may be defined for the individual patient. This phantom can then be used in Monte Carlo calculations of absorbed fractions for organs, parts of organs and tissues (9). As

a complement CT or MR images may be used, but if these are used alone the configuration of the radionuclide distribution within the various organs and in the tumor tissue cannot be visualized.

THE FUTURE

Nuclear medicine will continue its role in clinical medicine and it will keep its potential in medical research as a method to image physiological processes or the distribution of specific receptors. Some traditional clinical investigations will be taken over by MR and CT while other new investigations, using specific receptor binding substances, will be employed. A continued rise in the number of functional imaging procedures and a decrease in morphological imaging and nonimaging procedures is expected. The greater availability of CT, MR and ultrasound has already resulted in less frequent use of radionuclides for brain and liver investigations, whereas bone, lung, renal and cardiac nuclear medicine studies are all increasing in importance. Tumor imaging using receptor-specific substances or antibodies is one of the most important lines of development and has a unique potential. Receptor scintigraphy may also be used for diagnosis of inflammations etc.

It is assumed that investigations with positron emitters will increase slowly. More rapid introduction has been hampered by the cost and availability of radiopharmaceuticals. The method has, however, a great potential in pharmaceutical research.

No immediate breakthrough is anticipated in nuclear medicine instrumentation, but a continuous development of two- and three-headed gamma-camera SPECT and 3D reconstruction is foreseen. There will also be important innovations and improvements, such as the revival of coincidence counting for positron emitters using two ordinary gamma cameras, and wider use of multimodality image combination (SPECT and CT/MR).

Among the priorities for future work in radiopharmaceutical dosimetry and the radiological protection of the patient is the continuation of work towards more detailed and individual dosimetry. Better access to CT, MR and ultrasound, together with improved nuclear medicine technology, will make it easier to get detailed information about the anatomy of a patient, facilitating patient-specific dosimetry. Determination of absolute organ uptake and organ volume is still crucial for the accuracy of the absorbed dose calculations. Improved uptake measurements necessitate improved estimates of absorbed fractions for photons as well as for electrons. For therapy, individual biokinetic data are needed. For diagnostic nuclear medicine, improved knowledge about variations in biokinetics between patient groups is needed. It is especially important to provide more accurate dose estimates for patient groups who differ considerably from the 70 kg adult standard man, e.g. children. The dosimetry for the embryo and fetus needs to be improved. To handle the new methods and data, practical and reliable computer programs for dose calculations should be developed and made available.

Many of the problems in dosimetry for diagnostic nuclear medicine are similar to those in internal dosimetry for occupationally exposed workers as well as for members of the general public, and all three fields should benefit from a closer cooperation related to radiation transport models, mathematical as well as anthropomorphic, and voxel phantoms, general biokinetic models, fetal dosimetry, etc.

In the near future we will also have to discuss biological dosimetry to understand dose rate effects, adaptive response etc. We must learn from cell biologists and molecular geneticists about chromosome aberrations, apoptosis, various types of DNA damage, etc. This will be done in conjunction with the development of small-scale- and microdosimetry. It is of special relevance to study the radiobiological importance of the low dose rate in nuclear medicine compared to high dose rates in x-ray investigations and external radiotherapy.

ACKNOWLEDGMENT

The author expresses his appreciation and thanks to Professor Bertil Nosslin for reviewing this manuscript.

REFERENCES

1. Stelson AT, Watson EE and Cloutier RJ. A history of medical internal dosimetry. Health Phys 69(5):766-782, 1995.
2. Loevinger R, Budinger TF and Watson EE. MIRD primer for Absorbed Dose Calculations, Revised Edition, Society of Nuclear Medicine, New York, USA, 1991.
3. Snyder WS, Ford MR, Warner GG and Watson SB. "S", Absorbed Dose per Unit Cumulated Activity for Selected Radionuclides and Organs. MIRD Pamphlet No 11, Society of Nuclear Medicine, New York, USA, 1975.
4. Cristy M and Eckerman KF. Specific Absorbed Fractions of Energy at Various Ages from Internal Photon Sources. Report ORNL/TM-8381/V1 - V7, Oak Ridge National Laboratory, Oak Ridge, Tenn., USA, 1987.
5. Stabin M. MIRDOSE: Personal computer software for internal dose assessment in nuclear medicine. J Nucl Med 37(3):538-546, 1996.
6. International Commission of Radiological Protection. Radiation dose to patients from radiopharmaceuticals. ICRP Publication 53, Annals of the ICRP 18 (1-4), 1987, Pergamon Press, Oxford.
7. International Commission of Radiological Protection. Addendum to Publication 53. Radiological Protection in Biomedical Research. ICRP Publication 62. Annals of the ICRP 22(3), 1993, Pergamon Press, Oxford.
8. Johnson TK, McClure DL, McCourt SL, Andl GJ and Berman BD. MABDOSE: A computer program for the calculation of dose. This publication, pp: 425-439, 1999.
9. Tagesson M, Ljungberg M and Strand S-E. The SIMDOS Monte Carlo code for the conversion of activity distributions to absorbed dose and dose rate distributions. This publication, pp: 416-424, 1999.
10. Stabin MG, Watson EE, Cristy M, Ryman JC, Eckerman KF, Davis JL, Marshall D and Gehlen MK. Mathematical Models and Specific Absorbed Fractions of Photon Energy in the Nonpregnant Adult Female and at the End of Each Trimester of Pregnancy. Report ORNL/TM-12907, Oak Ridge National Laboratory, Oak Ridge, Tenn., USA, 1995
11. International Commission of Radiological Protection. Limits for Intakes of Radionuclides by Workers. ICRP Publication 30, Part 1. Annals of the ICRP 2 (3-4), 1979, Pergamon Press, Oxford
12. International Commission of Radiological Protection. Human Respiratory Tract Model for Radiological Protection. ICRP Publication 66. Annals of the ICRP 24 (1-3), 1994, Pergamon Press, Oxford.
13. Dolphin GW and Eve IS. Dosimetry of the gastrointestinal tract. Health Phys 12(2):163-172, 1966.
14. Stubbs JB. Results from a new mathematical model of gastrointestinal transit that incorporate age- and gender-dependent physiological parameters. Rad Prot Dosim 41(2-4):63-69, 1992.
15. Simkó M and Nosske D. Basis for a revision of the gastrointestinal tract model. Rad Prot Dosim 63(1):29-36, 1996.

16. Smith T, Veall N, and Wotton R. Bladder wall dose from administered radiopharmaceuticals: The effect of variations in urine flow rate, voiding interval and initial bladder content. Rad Prot Dosim 2 :183-189, 1982.
17. International Commission of Radiological Protection. Age-dependent Doses to Members of the Public from Intake of Radionuclides: Part 2 Ingestion Dose Coefficients. ICRP Publication 67. Annals of the ICRP 23(3-4), 1994, Pergamon Press, Oxford.
18. International Commission of Radiological Protection. Age-dependent Doses to Members of the Public from Intake of Radionuclides: Part 3 Ingestion Dose Coefficients. ICRP Publication 69. Annals of the ICRP 25(1), 1995, Pergamon Press, Oxford.
19. Thomas SR, Stabin MG, Chen CT and Samaratunga RC. MIRD Pamphlet No. 14: A dynamic urinary bladder model for radiation dose calculations. J Nucl Med 33(5):783-802, 1992.
20. Leggett RW and Williams LR. A proposed blood circulation model for reference man. Health Phys 69(2):187-201, 1995.
21. International Commission on Radiological Protection. Protection of the Patient in Radionuclide Investigations. ICRP Publication 17. Pergamon Press, Oxford, 1971.
22. Roedler HD. Accuracy of internal dose calculations with special consideration of radiopharmaceutical biokinetics. In: Third International Radiopharmaceutical Dosimetry Symposium, Proceedings of a Conference held at Oak Ridge 1980 (Ed. by EE Watson, AT Schlafke-Stelson, JL Coffey, RJ Cloutier), pp. 1-20. HHS Publ. FDA 81-8166, 1981.
23. International Commission of Radiological Protection. 1990 Recommendations of the International Commission on Radiological Protection. ICRP Publication 60. Annals of the ICRP, 21 (1-3), 1991, Pergamon Press, Oxford.
24. Makrigiorgos GM, Adelstein SJ, Kassis AI. Cellular radiation dosimetry and its implications for estimation of radiation risks. Illustrative results with technetium 99m-labeled microspheres and macroaggregates. JAMA 264(5):592-595, 1990.
25. Humm JL, Howell RV and Rao DV. Dosimetry of Auger-electron emitting radionuclides. Report No.3 of AAPM Nuclear Medicine Task Group No. 6. Med Phys 21(12):1901-1915, 1994.
26. Persson L. Radiation protection issues of Auger electron emitters. Rad Prot Dosim 64(3):189-191, 1996.
27. Mattsson S. Exposure of the embryo and fetus. In: Radiation Research 1895-1995, Volume 2. (Ed by U Hagen, H Jung and C Streffer), 10th ICRR Society, Würzburg, 1995, Published 1996.
28. Russell J and Stabin M. Placental transfer of radiopharmaceuticals and dosimetry in pregnancy. Health Phys 73(5):747-755, 1997.
29. Mattsson S, Johansson L, Nosslin B and Ahlgren L. Excretion of radionuclides in human breast milk following administration of ^{125}I-fibrinogen, ^{99m}Tc-MAA and ^{51}Cr-EDTA. In: Third International Radiopharmaceutical Dosimetry Symposium, Proceedings held at a conference in Oak Ridge, 1980 (Ed by Watson EE, Schlafke-Stelson AT, Coffey JL and Cloutier RJ.), HHS Publication FDA 81-8166, pp 102-110, 1981.
30. Ahlgren L, Ivarsson S, Johansson L, Mattsson S and Nosslin B. Excretion of radionuclides in human breast milk after the administration of radiopharmaceuticals. J Nucl Med 26 (9): 1085-1090, 1985.
31. Mountford PJ, Coakley AJ. A review of the secretion of radioactivity in human breast milk: data, quantitative analysis and recommendations. Nucl Med Commun 10(1):15-27, 1989.

QUESTIONS

Brihaye: In your opinion, what is the maximum ED value for volunteers?

Mattsson: ICRP Publication 62 gives guidance regarding radiological protection in biomedical research and describes categories of risk and the corresponding levels of benefit to the public. There is no maximum effective dose value.

Srivastava: In the preparation of the 1997 ICRP working document is there any effort being made to include therapeutic isotopes? If not, why? Your listing showed only diagnostic procedures?

Mattsson: For the moment there are no plans to include radionuclides which are solely used for radiotherapy. Therapy with radiopharmaceuticals always needs individual patient-specific absorbed dose estimates, and general biokinetic and dosimetric information can only serve as a rough guide for estimating absorbed doses to organs and tissues other than tumor tissue and therapy limiting normal tissue.

TREATMENT PLANNING FOR INTERNAL EMITTER THERAPY: METHODS, APPLICATIONS AND CLINICAL IMPLICATIONS

Sgouros G
Memorial Sloan-Kettering Cancer Center
New York NY 10021

ABSTRACT

Treatment planning involves three basic steps: 1) a procedure must be devised that will provide the most relevant information, 2) the procedure must be applied and 3) the resulting information must be translated into a definition of the optimum implementation. There are varying degrees of treatment planning that may be implemented in internal emitter therapy. As in chemotherapy, the information from a Phase I study may be used to treat patients based upon body surface area. If treatment planning is included on a patient-specific basis, a pretherapy, trace-labeled, administration of the radiopharmaceutical is generally required. The data collected following the tracer dose may range from time-activity curves of blood and whole-body for use in blood, marrow or total body absorbed dose estimation to patient imaging for three-dimensional internal emitter dosimetry. The most ambitious approach requires a three-dimensional set of images representing radionuclide distribution (SPECT or PET) and a corresponding set of images representing anatomy (CT or MRI). The absorbed dose (or dose-rate) distribution may be obtained by convolution of a point kernel with the radioactivity distribution or by direct Monte Carlo calculation. A critical requirement for both techniques is the development of an overall structure that makes it possible, in a routine manner, to input the images, to identify the structures of interest and to display the results of the dose calculations in a clinically relevant manner. One approach to the representation of absorbed dose, the dose-volume histogram, has already demonstrated that a tumoricidal mean absorbed dose does not necessarily predict tumor eradication since a portion of the tumor volume may have received a dose below that required for tumor cell kill. Three-dimensional, patient-specific dosimetry may provide the most comprehensive information regarding tumor and normal tissue dose. The additional cost and potential patient discomfort required for its implementation must, however, be weighed against anticipated patient benefits. Such an approach is also fundamentally limited by the requirement of radionuclide imaging. To insure that the development of new agents is not unduly burdened, only those techniques that have been rigorously proven to yield an improvement in patient treatment should be adopted. Treatment planning for internal emitter therapy remains an active area of research.

INTRODUCTION

The essence of treatment planning is to devise and apply a procedure which will yield information for defining the best possible implementation of a specific therapy. This involves three basic steps: 1) a procedure must be devised that will provide the most relevant information, 2) the procedure must be applied and 3) the resulting information must be translated into a definition of the optimum

implementation. Each of these steps requires consideration of a number of fundamental issues and each step is also constrained by cost and by the level of patient discomfort. In most new therapeutic approaches, the information required for treatment planning is obtained from Phase I and II trials (1). In chemotherapy, a Phase I trial is used to determine the maximum amount of drug that may be administered without resulting in an unacceptable level of morbidity. There are varying degrees of treatment planning that may be implemented in internal emitter therapy (2). As in chemotherapy, the information from a Phase I study may be used to treat patients up to a previously defined maximum tolerated dose. A moderate enhancement to this involves the analysis of blood or whole-body clearance data, obtained during the Phase I study. These data may be used to arrive at an optimum overall protocol that is then implemented in subsequent phases without obtaining such information for individual patients. This approach may be used, for example, to determine the optimal mg. amount of antibody that should be administered during therapy. If treatment planning is included on a patient-specific basis, this generally requires a pre-therapy, trace-labeled, administration of the radiopharmaceutical so that patient-specific pharmacokinetic data may be collected and used to define the therapeutic administration. Inclusion of a pre-therapy study increases the range of treatment planning approaches considerably. Such approaches may range from the collection of blood and whole-body clearance data to the use of patient imaging for three-dimensional internal emitter dosimetry. The former approach has been used for more than 30 years in the treatment of thyroid cancer with radioiodine (3). The latter approach is just becoming feasible (4-19). Improvements in patient imaging, combined with the ever-increasing power of computer processors and the development of pharmacokinetic models, are beginning to make it possible to obtain absorbed dose estimates that account for anatomy and activity distribution on a patient-specific basis.

TREATMENT PLANNING PARADIGM

The different steps in evaluating a new agent's clinical effectiveness are summarized below. Each step in the process is categorized as being either an element of data collection or of treatment planning.

Data Collection	Treatment Planning
1) Biodistribution and toxicity studies in a relevant animal model (if available).	
	2) Data from (1) are used to determine starting dose level and dose increments for a Phase I study.
3) Maximum tolerated dose is assessed in a Phase I study. Additional data collection is included in the study design in anticipation of treatment planning for a Phase II study.	
	4) Data from (3) are used to assess the importance of patient-specific planning and to evaluate alternative dosing schedules and treatment protocols.
5) The results of (4) and (3) are used to define one or more Phase II studies. Based upon the results obtained in (4), the study design may include a patient-specific treatment planning component.	

As may be observed in the outline, a broad definition of treatment planning is chosen. If an agent meets the efficacy criteria upon completion of step 5, subsequent, treatment planning-related, steps should be oriented primarily towards minimizing the effort required to plan treatment. For example, the tradeoffs associated with replacing whole-body imaging with whole-body probe measurements may be examined. In general, the simplest treatment planning approach should be adopted as long as the sacrifice in potential therapeutic gain is acceptable. A strong rationale should be established for any measurements or calculations that are incorporated into a treatment plan, since additional procedures are likely to increase cost and patient discomfort.

Radioiodine therapy of thyroid cancer is probably the oldest example of internal emitter therapy that includes a treatment planning procedure. Based upon a very large database of patient data (3), a relationship between the absorbed dose to blood, the amount of activity remaining in the patient's lungs, and hematologic or respiratory organ toxicity was established. The guidelines developed by this relationship then formed a rationale for patient-specific treatment planning. In radioiodine therapy, the therapeutic administration is preceded by a tracer administration of I-131. The latter is used to measure patient kinetics, which are then used to calculate the absorbed dose to blood and the activity in lungs per unit administered activity. This information is used to constrain the therapeutic administration.

If a radiolabeled antibody or other targeting protein is being investigated, the data-collection/treatment-planning outline described above includes more steps since the toxicity associated with the protein itself and the toxicity associated with the radiolabeled protein must be independently assessed in Phase I studies. A protein (mg) escalation trial is first conducted. In such a trial, the antibody is usually radiolabeled with a tracer amount of activity to enable imaging and pharmacokinetic measurements (step 3). The measurements performed during this trial are then used to decide upon the mg. amount of antibody that should be administered for the Phase I activity-escalation trial. The data obtained from the mg.-escalation trial and the activity-escalation trial are used in step 4 to assist in designing protocols for phase II trials. In radioimmunotherapy, therefore, two different approaches may be adopted in treatment planning. These are illustrated in Figure 1.

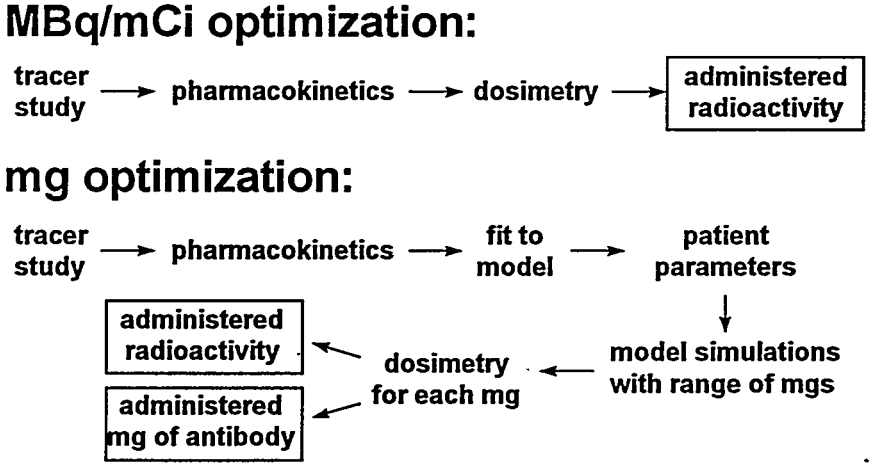

Figure 1. Treatment planning for antibody therapy.

Planning may be used to determine the optimum amount of radioactivity that should be administered to a patient while the mg amount is fixed at a preselected value (top half of Figure 1), or, alternatively, both the mg amount and the administered activity may be allowed to vary and are selected according to treatment planning criteria (bottom half of Figure 1).

TREATMENT PLANNING METHODS - MODELING

In the context of treatment planning, modeling may also be broadly defined. The assumptions that are made in performing red marrow dosimetry using blood data, for example, may be thought of as a simple model relating the concentration of radiolabeled antibody in blood to that in the red marrow (20-23). Alternatively, conventional models may be made of several compartments describing the pharmacokinetics of a particular agent throughout the body and in different chemical states or biological compartments (24-26). Mathematical models may be categorized as phenomenological or mechanistic. Phenomenological models are intended to fit to as wide a variety of relevant data as possible but need not contain information regarding the mechanisms involved in the processes that are being modeled. The exponential equations used to fit blood or whole-body clearance data, for example, describe a phenomenological model that can accurately represent a wide range of clearance curves, but does not provide information regarding the mechanisms involved in the clearance (discounting physical decay of the radionuclide). Mechanistic models endeavor to provide an understanding and a mathematical representation of the processes involved. The same clearance data, for example, may be fit to a mathematical model that simulates rapid dilution of an intravenously administered agent, followed by binding to target cells, followed by excretion. Such a model may be used to determine the degree to which the rapid component of a two-component exponential clearance curve in blood, for example, is the result of dilution within a distribution volume or is due to binding to rapidly accessible target cells (25). The understanding obtained by fitting data to a mechanistic model may be used to extend the measured data and obtain information in tissues or compartments that were not directly sampled. In the mechanistic model described above, for example, knowledge of the degree to which the rapid clearance component is due to target-cell binding as opposed to dilution provides information that may be used to estimate the extent of target-cell binding (25,27).

Mechanistic models may also be categorized as lumped or distributed parameter models. In lumped parameter models, for example, factors such as vascular permeability, surface-area-to-volume-ratio, and vascular or interstitial osmotic pressure that are specifically included in distributed parameter models (28,29) are lumped together into a single parameter that represents transfer of material from one compartment to another. Due to limitations on the amount and type of data that may be collected in patients participating in a Phase I or II trial, most mathematical models that are derived from clinical trial data are compartmental or lumped parameter models.

If a mathematical model of the agent's biodistribution and kinetics has been established, modeling may be used as indicated in Figure 1. The optimum amount of an agent may be estimated by simulating different administration levels and schedules. The resulting absorbed dose to normal and target tissues may be calculated from the model-derived biodistribution data to assess the therapeutic potential associated with a particular administration level or schedule. This approach may be implemented on several levels. In a nonpatient-specific manner, modeling may be used to guide the design of treatment protocols. As humanized antibodies become available and as fractionated-infusion protocols are implemented, modeling may become critical in helping design optimum infusion schedules. Such nonpatient-specific modeling may be implemented using model parameters that are representative of a patient population as a whole. Patient-specific modeling requires a set of measurements that may be used to establish model parameters for the given patient. These measurements, typically obtained from a tracer study, are performed immediately prior to the therapy administration.

Two models, depicted in Figures 2 and 3, are used to illustrate some of the principles associated with pharmacokinetic modeling of radiolabeled antibodies.

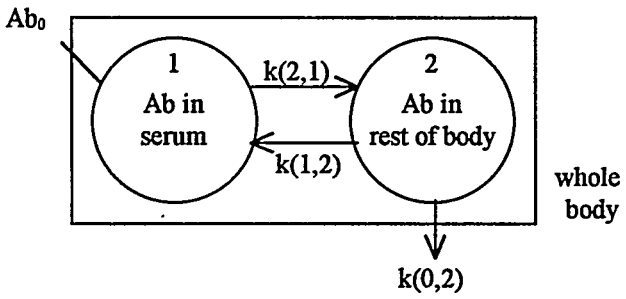

Figure 2. Simplified two-compartment model of Ab kinetics in solid disease. Ab_0 = amount of I.V.-administered antibody, k(2,1) = transfer rate from initial distribution volume of Ab (V_d) to rest-of-body, k(1,2) = transfer rate from rest-of-body to V_d and k(0,2) = excretion rate.

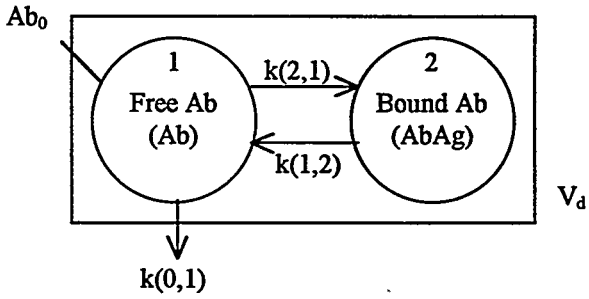

Figure 3. Simplified two-compartment model of Ab kinetics in leukemia. Ab_0 = amount of I.V.-administered antibody, k(2,1) = free to bound Ab transfer rate, k(1,2) = bound to free Ab transfer rate, k(0,1) = excretion rate, k+ = Ab - Ag association rate and k_- = Ab - Ag dissociation rate.

$$\frac{dAb_1}{dt} = -k(2,1)\cdot Ab_1 + k(1,2)\cdot Ab_2$$

$$\frac{dAb_2}{dt} = k(2,1)\cdot Ab_1 - k(1,2)\cdot Ab_2 - k(0,2)\cdot Ab_2$$

$$Ab_1 = \left[Ab_1\right]\cdot V_d$$

$$\frac{dAb}{dt} = -k(2,1)\cdot Ab + k(1,2)\cdot AbAg - k(0,1)\cdot Ab$$

$$\frac{dAbAg}{dt} = k(2,1)\cdot Ab - k(1,2)\cdot AbAg$$

$$Ab = [Ab]\cdot V_d$$

$$k(2,1) = \frac{k_+}{V_d}\cdot\left(Ag_0 - AbAg\right)$$

$$k(1,2) = k_-$$

The equations governing these models are provided below each model. The first model simulates antibody kinetics in radioimmunotherapy of solid disease, the second of leukemia. Both models describe the fate of radiolabeled antibody that is administered intravenously. Compartment 1 of the first model is the central pool within which intravenously administered antibody distributes. The volume associated with this compartment is the total initial distribution volume, V_d, of the radiolabeled antibody. For a 150,000 molecular weight protein, this is usually the volume of plasma plus that of the extracellular fluid space of the reticuloendothelial system (25,30). Assuming that the radiolabel remains attached to the antibody throughout the measurement period, the concentration of radioactivity in plasma over time may be used as input data to compartment 1. If blood activity concentration is measured, then a volume adjustment is necessary to obtain the concentration of radioactivity in plasma; this requires an estimate of the hematocrit (23). If the total activity in each organ is provided as input to the model, the activity concentration in plasma must be converted to total activity in the central pool. This requires an estimate of the initial distribution volume of the antibody. Standard values for the plasma volume and the extracellular fluid volume of liver, spleen and red marrow may be scaled by patient height and weight to provide initial estimates of distribution volume (25,31). The second compartment in this model represents the remainder of the body. The sum of activity in compartments 1 and 2 may be equated to a whole-body clearance curve. If detailed pharmacokinetic data are available for individual organs or for tumor, the second

compartment may be resolved into separate individual compartments, each representing an organ, organ system or tumor (30,32).

Since antibody binding to antigen sites is not specifically included in model 1, the equations governing the model are linear. The second model represents antibody targeting to rapidly accessible leukemia cells (25). In this model, the assumption is made that antigen-positive cells are within the initial distribution volume of the antibody. Compartment 1 represents free antibody and compartment 2 represents antigen-bound antibody. Both compartments are within a single space - the distribution volume, V_d, of the antibody. Both compartments of model 2 would therefore correspond to the first compartment of model 1. In this case, the model is nonlinear since there are presumed to be a fixed number of tumor cells and therefore total antigen sites (Ag_0). After antibody has bound these sites (i.e., compartment 2 has been saturated), the addition of antibody into compartment 1 will not increase the content of compartment 2. The antibody-antigen binding reaction is characterized by an association rate, k_+, and a dissociation rate, k_-. It is important to note that this model for antibody-antigen binding is a simplification in that internalization and the potential for irreversible binding are not specifically considered (33).

In some cases, a nonlinear model may be necessary even when binding to tumor is not specifically included in the model. This may occur if the antibody cross-reacts with saturable sites on normal tissues (32). In tracer-based pharmacokinetic modeling, the issue of tracer vs tracee behavior should be addressed. In each of the models described above, the assumption is made that the radionuclide remains with the antibody. Measurements of radioactivity may, therefore, be directly translated to antibody content. This assumption may not apply as antibody is catabolized or as the radiolabel dissociates from the antibody. In blood, the tracer vs tracee assumption may be examined by measuring the concentration of protein in each sample as well as the concentration of radioactivity. If the radionuclide-antibody bond is verified to remain intact, measurements of radioactivity concentration may be directly translated to antibody concentration by decay correcting and by adjusting for the specific activity. These data may then be directly used for compartmental modeling. It is important to note that this applies even if the model is non-linear. Physical decay does not depend upon the nature of the model used to describe the pharmacokinetics of the tracee. Decay-corrected data may be used for modeling regardless of the nature of the model.

TREATMENT PLANNING METHODS - DOSIMETRY

The standard formalism for patient dosimetry was developed by the Medical Internal Radiation Dose (MIRD) Committee and is described in references (34-38). The following are required in calculating absorbed doses: 1) an estimate of the total number of radionuclide disintegrations occurring in a source region, 2) the emission type and energy per disintegration, 3) the fraction of energy absorbed in a target region for each emission originating in the source region, and 4) the mass of the target region. Item 1 is dependent on the radionuclide half-life and on the agent's pharmacokinetics. It may be obtained by integrating the activity-vs-time curve, for the chosen source region. As indicated in the previous section, pharmacokinetics may be obtained by direct measurement or by modeling. Items 2, 3 and 4 are radionuclide- and geometry-specific. To simplify absorbed dose calculations, the MIRD Committee developed a formalism by which these three items are lumped into a single radionuclide- and source-target-region-specific value called an S value (34). To generate tables of S values for different radionuclides and source-target organ combinations, a standard model of human anatomy was adopted in which organ position, dimensions, and composition were mathematically defined. The radioactivity was assumed to be uniformly distributed throughout each source organ, and the S values were defined as the mean absorbed dose to a target organ per unit cumulated activity in a source organ.

As the position and size of tumors may vary within the body and since a standard model of human anatomy was adopted for generating the S-value tables, tumors are not included in the published tables. A number of approaches have been developed for estimating the absorbed dose to tumors and the dose

contribution from tumors to normal organs (39). The simplest approximation is made by assuming that all electrons are deposited locally and that the relative contribution to the tumor absorbed dose from photons is negligible. Using tables of photon absorbed fraction to spheres or ellipsoids (40-42), the photon self-dose may be added by assuming that the tumor is a sphere or ellipsoid. If this assumption is made, the photon dose to and from normal organs may also be calculated by placing the idealized tumor geometry in a defined position relative to the standard geometry used for the S value calculations (43,44). If a point-kernel convolution technique is used in estimating absorbed dose, the true tumor and normal tissue geometry as well as the activity distribution may be taken into account to yield a spatial absorbed dose or dose-rate distribution (4,7). Tissue composition and density variations are not easily accounted for using point-kernel techniques. To account for these, Monte Carlo techniques are needed to estimate absorbed doses (19).

The spatial distribution of absorbed dose that is provided by a patient-specific point-kernel or Monte Carlo technique may be represented in a number of different ways. A set of images may be generated in which intensity represents absorbed dose; alternatively isodose contours may be superimposed upon CT images and dose-volume histograms may be generated. The latter provide information regarding the fraction of a tissue or tumor volume that receives a particular absorbed dose or dose range (12). In external beam radiotherapy, dose-volume histograms are routinely used to compare different treatment plans and to determine the extent to which a tumor volume receives the prescribed absorbed dose. Such dose-volume histograms plot the fraction of volume receiving an absorbed dose that is greater than or equal to a specified dose as a function of dose. This information may be combined with radiobiological models of tumor and normal tissue response to yield tumor control probability or normal tissue complication probability. In internal emitter therapy, dose-volume histograms have made it possible to quantitate the degree of absorbed dose nonuniformity (17).

The logistics associated with performing fully patient-specific 3D-dosimetry are considerable. To define the anatomy and to provide tissue density information, a CT scan over the region of interest is required. To provide the activity distribution, a PET or SPECT scan is required. If absorbed dose rather than absorbed dose rate is desired, then kinetic information is required. In conventional dosimetry, kinetic information that is averaged over the whole source organ volume suffices; in 3D-dosimetry, variations in pharmacokinetics within an organ must be taken into account. Ideally kinetic information on a voxel-by-voxel basis should be used. This would require multiple SPECT or PET studies taken over time, each registered to each other, and also registered to the CT study. Assuming such data are available, a voxel-by-voxel based integration of the activity would need to be performed to yield a 3-D representation of residence time or cumulated activity. To achieve this type of comprehensive 3-D dosimetry calculation, a number of logistical, technical, and fundamental hurdles must be overcome. The logistical difficulties arise because it may not be feasible to perform PET or SPECT imaging of a particular patient multiple times. The time required for such imaging is considerably greater than planar imaging. This may lead to difficulties with patient compliance and camera availability. The technical difficulties include registration of PET or SPECT images to each other and to a CT study. Although this step is independent of the dosimetry algorithm itself, the fidelity of the registration impacts the quality of the input which, in turn, will determine the reliability of the dose estimates. Registration accuracy will depend upon the anatomical region-of-interest, the agent being imaged, and the technique that is used for registration (45-48). Since it is likely that the total number of counts associated with any given voxel will be low, yielding a high standard deviation, the voxel-by-voxel based integration outlined above may be fundamentally limited by the error associated with each voxel value. Integration on a voxel-by-voxel basis may yield unreliable values for residence time or cumulated activity due to these errors. A number of techniques and approximations may be adopted to overcome some of these difficulties. It is possible to derive a residence time or cumulated activity image, for example, by using planar imaging to obtain kinetics and SPECT or PET imaging to obtain the spatial distribution. A residence time or cumulated activity image may be

obtained by assuming that all points making up the spatial distribution of activity follow the same kinetics (7).

Most of the effort in patient-specific 3-D dosimetry has been made in the development of algorithms and computational techniques. Application of such techniques, however, requires a system that translates CT and PET or SPECT studies into a common data format, provides the tools needed to draw contours around regions of interest for identifying source regions or generating dose-volume histograms, and outputs the absorbed dose calculations as images, isodose contours or dose-volume histograms (17). Each of these steps requires considerable user interaction and is input/output-intensive. As computational techniques develop, the structure needed to implement such techniques may limit their usage.

APPLICATIONS AND CLINICAL IMPLICATIONS

Initial calculations using 3-D dosimetry techniques have been performed primarily for phantom or standard organ geometries. The standard anatomy used in the S value and absorbed fraction calculations has been used to independently derive S values and absorbed fractions for validation and benchmarking. Table 1 shows S values obtained by Monte Carlo and by the point-kernel method compared with MIRD Pamphlet 11 and MIRDOSE 3 values.

Table 1

^{131}I S Values (Gy/MBq-s)				
	MIRD-11	MIRDOSE 3	Point-Kernel	Monte Carlo
liver→spleen	2.0×10^{-10}	2.2×10^{-10}	2.7×10^{-10}	2.2×10^{-10}
spleen→liver	2.3×10^{-10}	2.2×10^{-10}	2.7×10^{-10}	2.3×10^{-10}
pancreas↔spleen[1]	4.1×10^{-9}	3.6×10^{-9}	4.3×10^{-9}	4.1×10^{-9}

[1]Spleen→pancreas and pancreas→spleen S values were identical.

The difference in S values for MIRDOSE 3 vs MIRD-11 for pancreas ↔ spleen arises, in part, because the weight that is assumed for pancreas in the Cristy-Eckerman phantom (49), which is used in MIRDOSE 3, is different from that assumed in the Pamphlet 11 phantom (34). The differences observed for liver→spleen and spleen→liver using the point-kernel method compared to the other values are likely due to the assumptions inherent in using a point-kernel method. The point-kernel is obtained assuming an isotropic, infinite medium. The absence of backscatter in organs near the periphery of the body is therefore not accounted for in a point-kernel calculation. This would cause a slight overestimate in the absorbed dose to such organs.

Dose-volume histograms for liver and two tumors within the liver, obtained from reference (17), are shown in Figure 4. The two tumor curves are shown by the dark dashed lines. The two vertical dotted lines indicate values of the mean absorbed doses obtained for these two tumors. It is important to note that both tumor volumes receive a significant range of absorbed doses. The minimum dose delivered to a volume subfraction of tumor one, indicated by the 100% dose value, is approximately .54 mG/MBq (2 rad/mCi); the maximum dose is 2.16 mG/MBq (8 rad/mCi). Although the mean dose calculated for either of these tumors may be above the dose required for tumor cell kill, the dose distributions shown in the histogram allow for the possibility that a significant fraction of the tumor volume may receive a dose below that needed for tumor cell kill.

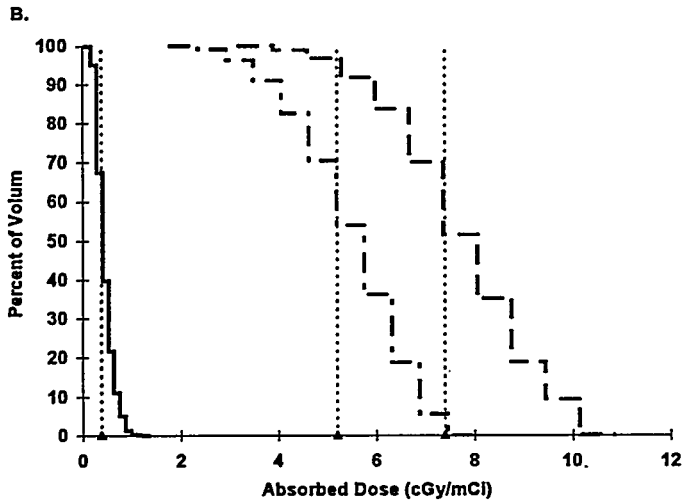

Figure 4. Dose-volume histogram for liver (solid) and two tumor (dash) within the liver (from reference 17). Dotted lines depictthe mean absorbed dose values for each tumor.

In radioimmunotherapy, 3-D dosimetry is primarily useful in evaluating the absorbed dose to tumor and to adjacent normal tissue. In terms of treatment planning, however, such dose estimates are generally less important than the absorbed dose to the limiting tissue. Red marrow toxicity has been dose-limiting in most radioimmunotherapy trials. Since marrow is a distributed organ that is not easily resolved by imaging, the patient-specific 3-D dosimetry techniques described above do not easily apply. Such techniques may become important for treatment planning protocols that combine radiotherapy with radioimmunotherapy (50-52). Estimation of the absorbed dose from radioimmunotherapy to tissues containing, or adjacent to, the tumor will be important in prescribing the appropriate dose for external beam radiotherapy.

DISCUSSION

Treatment planning, as broadly defined, is an integral part of the process used to evaluate a new agent's clinical effectiveness. At the earliest level, treatment planning may be used to define the best patient population and disease characteristics for evaluating a new agent. Planning may also occur at a number of other levels to obtain a dosing schedule for Phase I studies, to optimize treatment for a patient population, and to optimize treatment for a particular patient. A strong rationale should be established for any measurements or calculations that are incorporated into a treatment plan since additional procedures are likely to increase cost and patient discomfort. In particular, the need for patient-specific planning must be rigorously justified. If deemed necessary, treatment planning design should be oriented towards minimizing the measurements and effort required to plan treatment without sacrificing planning objectives.

By providing a better spatial representation of the absorbed dose distribution, three-dimensional internal emitter dosimetry has the potential of providing valuable information regarding treatment failure and tissue toxicity. This methodology will become particularly important if radioimmunotherapy is combined with external radiotherapy. The additional cost and potential patient discomfort required for its implementation, however, must be weighed against anticipated patient benefits. Such an approach is also fundamentally limited by the requirement of radionuclide imaging.

It is important in treatment planning design that the costs and additional requirements for the implementation of various approaches be assessed against patient benefit. To ensure that the development of new agents is not unduly burdened, only those techniques that have been rigorously proven to yield an improvement in patient treatment should be adopted.

ACKNOWLEDGMENTS

This work was supported, in part, by NIH grants. R01 CA62444 and U01 CA58260 and DOE grant DE-FG02-86ER-60407

REFERENCES

1. DeVita VT, Hellman S and Rosenberg SA. Cancer Principles and Practices of Oncology, 4th edition, pp:276-292, J.B. Lippincott Co., New York, 1993.
2. DeNardo GL, Raventos A, Hines HH et al. Requirements for a treatment planning system for radioimmunotherapy. Int J Radiat Oncol Biol Phys 11:335-348, 1985.
3. Benua RS, Cicale NR, Sonenberg M et al. The relation of radioiodine dosimetry to results and complications in the treatment of metastatic thyroid cancer. Am J Roentgenol 87:171-182, 1962.
4. Sgouros G, Barest G, Thekkumthala J, et al. Treatment planning for internal radionuclide therapy: Three-dimensional dosimetry for nonuniformly distributed radionuclides. J Nucl Med 31:1884-1891, 1990.
5. Roberson PL, Buchsbaum DJ, Heidorn DB, Ten and Haken RK. Three-dimensional tumor dosimetry for radioimmunotherapy using serial autoradiography. Int J Radiation Oncology Biol Phys 24:329-334, 1992.
6. van Dieren EB, van Lingen A, Roos JC and Teule GJJ. Validation of the distance histogram technique for three-dimensional and two-dimensional dosimetric calculations. Appl Rad Isot 43(10):1211-1221, 1992.
7. Sgouros G, Chiu S, Pentlow KS, Brewster LJ, Kalaigian H, Baldwin B, Daghighian F, Graham MC, Larson SM and Mohan R. Three-dimensional dosimetry for radioimmunotherapy treatment planning. J Nucl Med 34:1595-1601, 1993.
8. Strand SE, Jonsson BA, Ljungberg M and Tennvall J. Radioimmunotherapy dosimetry - a review. Acta Oncologica 32:807-817, 1993.
9. Leichner PK, Koral KF, Jaszczak RJ et al. An overview of imaging techniques and physical aspects of treatment planning in radioimmunotherapy. Med Phys 20:569-577, 1993.
10. Koral KF, Zasadny KR, Kessler ML, Luo JQ, Buchbinder SF, Kaminsky MS, Francis I and Wahl RL. CT-SPECT fusion plus conjugate views for determining dosimetry in iodine-131-monoclonal antibody therapy of lymphoma patients. J Nucl Med 35:1714-1720, 1994.
11. Tagesson M, Ljungberg M and Strand SE. Transformation of activity distribution in quantitative SPECT to absorbed dose distribution in a radionuclide treatment planning system. J Nucl Med 123P, 1994.
12. Kolbert KS, Sgouros G, Scott AM, Baldwin B, Zhang J, Kalaigian H, Macapinlac HA, Graham MC and Larson SM. Dose-volume histogram representation of patient dose distribution in three-dimensional internal dosimetry. J Nucl Med 35:123P, 1994.
13. Fisher DR. Radiation dosimetry for radioimmunotherapy. An overview of current capabilities and limitations. Cancer 73:905-911, 1994.
14. Erdi AK, Wessels BW, DeJager R, Erdi YE, Atkins FB, Yorke ED, Smith L, Huang E, Smiddy M, Murray J, Varma VM, McCabe R, McNellis R, John C, Ney A, Nochomovitz L and Hanna MG Jr. Tumor activity confirmation and isodose curve display for patients receiving iodine-131-labeled 16.88 human monoclonal antibody. Cancer 73:932-944, 1994.
15. Giap HB, Macey DJ and Podoloff DA. Development of a SPECT-based three-dimensional treatment planning system for radioimmunotherapy. J Nucl Med 36(10):1885-1894, 1995.

16. Akabani G, Hawkins WG, Eckblade MB and Leichner PK. Patient specific dosimetry based on quantitative SPECT imaging and 3D-DFT convolution: A comparison with Monte Carlo transport calculations. J Nucl Med 37:89P, 1996.
17. Kolbert KS, Sgouros G, Scott AM, Bronstein JE, Malane RA, Zhang J, Kalaigian H, Stephen M, Schwartz L and Larson SM. Implementation and evaluation of patient-specific three-dimensional internal dosimetry. J Nucl Med (In Press).
18. Erdi AK, Erdi YE, Yorke ED and Wessels BW. Treatment planning in radio-immunotherapy. Phys Med Biol 41: (In Press).
19. Furhang EE, Chui C-S and Sgouros G. A Monte Carlo approach to patient-specific dosimetry. Med Phys 23: (In Press).
20. Siegel JA, Wessels BW, Watson EE et al. Bone marrow dosimetry and toxicity for radioimmunotherapy. Antibody Immunocon Radiopharm 3:213-233, 1990.
21. Johnson TK, Gonzalez R, Kasliwal RK et al. Distribution of a breast-directed I-131-radiolabeled monoclonal antibody in blood and bone marrow: Implications for radiation immunotherapy. Radiology 182:107-114, 1992.
22. Kwok CS, Firnau G, Reynolds G, Kotzeff A, Lee S and Dobson H. Uptake kinetics of Cu-64-labeled IgG in the bone marrow of adult dogs: A preliminary study. Med Phys 20:874, 1993.
23. Sgouros G. Bone marrow dosimetry for radioimmunotherapy: Theoretical considerations. J Nucl Med 34:689-694, 1993.
24. Sgouros G. Plasmapheresis in radioimmunotherapy of micrometastases: A mathematical modeling and dosimetrical analysis. J Nucl Med 33:2167-2179, 1992.
25. Sgouros G, Graham MC, Divgi CR, Larson SM and Scheinberg DA. Modeling and dosimetry of monoclonal antibody M195 (anti-CD33) in acute myelogenous leukemia. J Nucl Med 34:422-430, 1993.
26. Strand SE, Zanzonico PB and Johnson TK. Pharmacokinetic modeling. Med Phys 20:515-527, 1993.
27. Daghighian F, Pentlow KS, Larson SM, Graham MC, DiResta GR, Yeh SDJ, Macapinlac H, Finn RD, Arbit E and Cheung NV. Development of a method to measure kinetics of radiolabelled monoclonal antibody in human tumor with applications to microdosimetry: Positron emission tomography studies of iodine-124 labeled 3F8 monoclonal antibody in glioma. Eur J Nucl Med 20:402-409, 1993.
28. McFadden R and Kwok CS. Mathematical model of simultaneous diffusion and binding of antitumor antibodies in multicellular human tumor spheroids. Cancer Res 48:4032-4037, 1988.
29. Jain RK. Physiological barriers to delivery of monoclonal antibodies and other macromolecules in tumors. Cancer Res 50:814s-819s, 1990.
30. Zanzonico PB, Bigler RE, Primus FJ et al. A compartmental modeling approach to the radiation dosimetry of radiolabeled antibody. in Proceedings of the Fourth International Dosimetry Symposium, edited by AT Schlafke-Stelson, and EE Watson, pp. 421-445, Oak Ridge, TN: CONF-851113-(DE86010102), 1986.
31. International Commission on Radiological Protection. Report of the task group on reference man. ICRP Publication 23, New York: Pergamon Press, 1975.
32. Koizumi K, DeNardo GL, DeNardo SJ, et al. Multicompartmental analysis of the kinetics of radioiodinated monoclonal antibody in patients with cancer. J Nucl Med 27:1243-1254, 1986.
33. Shih LB, Thorpe SR, Griffiths GL, Diril H, Ong GL, Hansen HJ, Goldenberg DM, Mattes MJ. The processing and fate of antibodies and their radiolabels bound to the surface of tumor cells in vitro: a comparison of nine radiolabels. J Nucl Med 25:899-908, 1994.
34. Snyder WS, Ford MR, Warner GG, Watson SB. "S," absorbed dose per unit cumulated activity for selected radionuclides and organs. MIRD Pamphlet No. 11, Revised. New York: Society of Nuclear Medicine, 1975.

35. Loevinger R, Berman M. A revised schema for calculating the absorbed dose from biologically distributed radionuclides. MIRD Pamphlet No. 1, Revised. New York: Society of Nuclear Medicine, 1976.
36. Snyder WS, Ford MR, Warner GG. Estimates of specific absorbed fractions for photon sources uniformly distributed in various organs of a heterogeneous phantom. MIRD Pamphlet No. 5, Revised. New York: Society of Nuclear Medicine, 1978.
37. Loevinger R, Budinger TF, Watson EE. MIRD Primer for Absorbed Dose Calculations. New York:The Society of Nuclear Medicine, 1991.
38. Watson EE, Stabin MG, Siegel JA. MIRD formulation. Med Phys 20:511-514, 1993.
39. Meredith RF, Johnson TK, Plott G, Macey DJ, Vessella RL, Wilson LA, Breitz HB, Williams LE. Dosimetry of solid tumors. Med Phys 20:583-592, 1993.
40. Brownell GL, Ellett WH, Reddy AR. MIRD Pamphlet No. 3: Absorbed fractions for photon dosimetry. J Nucl Med 9(Suppl 1):28-39, 1968.
41. Ellett WH, Humes RM. Absorbed fractions for small volumes containing photon-emitting radioactivity. MIRD Pamphlet No. 8, New York: Society of Nuclear Medicine, 1971.
42. Stabin MG. MIRDOSE-the personal computer software for internal dose assessment in nuclear medicine. J Nucl Med 37:538-546, 1996
43. Johnson TK. MABDOS: A generalized program for internal radionuclide dosimetry. Computer Methods Programs Biomed 27:159-167, 1988.
44. Johnson TK, Vessella RL. On the possibility of 'real-time' Monte Carlo calculations for the estimation of absorbed dose in radioimmunotherapy. Computer Methods Programs Biomed 29:205-210, 1989.
45. Pelizzari CA., Chen GTY. Registration of multiple diagnostic imaging scans using surface fitting. Use of Comput in Radiat Ther:437-440, 1987.
46. Kramer EL., Noz ME., Sanger SJ., Megibow AJ., Maguire GQ. CT-SPECT fusion to correlate radiolabeled monoclonal antibody uptake with abdominal CT findings. Radiology 172:861-865, 1989.
47. Scott AM, Macapinlac H, Zhang JJ, Kalaigian H, Graham MC, Divgi CR, Sgouros G, Goldsmith SJ, Larson SM. Clinical applications of fusion imaging in oncology. Nucl Med Biol 21(5):775-784, 1994.
48. Turkington TG, Jaszczak RJ, Pelizzari CA, Harris CC, MacFall JR, Hoffman JM, Coleman RE. Accuracy of registration of PET, SPECT and MR images of a brain phantom. J Nucl Med 34:1587-1594, 1993.
49. Cristy M, Eckerman KF. Specific Absorbed Fractions of Energy at Various Ages from Internal Photon Sources. Department of Energy, Oak Ridge National Laboratory, Oak Ridge TN, Document No. ORNL/TM-8381/V1, 1987.
50. Kalofonos H, Rowlinson G, Epenetos AA. Enhancement of monoclonal antibody uptake in human colon tumor xenografts following irradiation. Cancer Res 50:159-163, 1990.
51. Maraveyas A, Meyers M, Stafford N, Rowlinson-Busza G, Stewart JSW, Epenetos AA. Radiolabeled antibody combined with external radiotherapy for the treatment of head and neck cancer: Reconstruction of a theoretical phantom of the larynx for radiation dose calculation to local tissues. Cancer Res 55:1020-1027, 1995.
52. Buchegger F, Rojas A, Bischof-Delaloye A, Vogel C, Mirimanoff R, Coucke P, Sun L, Raimondi S, Denekamp J, Pelegrin A, Delaloye B, Mach J. Combined radioimmunotherapy and radiotherapy of human colon carcinoma grafted in nude mice. Cancer Res 55:83-89, 1995.

QUESTIONS

Muller: Please explain the higher dose in lung tissue. If the tumor is emitting most of the radiation, the situation is comparable to external radiotherapy where this effect is never observed.

Sgouros: The difference is caused by the relatively uniform uptake in both liver and lung tissue. Therefore, the relative uptake in the low density tissue is much higher.

T. Johnson: Your Monte Carlo selection scheme is based on perfect precision in the activity assigned to each voxel. This is not true in nuclear medicine. How does this affect the dosimetry results?

Sgouros: The Monte Carlo method is independent of the precision in the activity assigned to each voxel. If voxel activity is known with a high precision (e.g. high-activity or large voxels or PET) the results of the calculation will be more precise; if the activity is known to a low precision the dose will be estimates will be imprecise.

Kwok: Which computer code did you use for the Monte Carlo calculations and how much computational time was required for a typical patient study?

Sgouros: The EGS Monte Carlo Code is used for the Monte Carlo dosimetry calculations. The time required for the calculation is a function of the radionuclide and the activity distribution. The time ranged from less than 1 hour to overnight for the set of sample calculations that I presented. More detailed information will be coming out in *Medical Physics*.

PARAMETERS TO CONSIDER FOR RADIONUCLIDE THERAPY TREATMENT PLANNING WITH SPECT

Ljungberg M, Tagesson M, Sjögreen K and Strand S-E.
Department of Radiation Physics,
Lund University,
S-221 85 Lund, SWEDEN

ABSTRACT

The use of SPECT is preferable to planar imaging when quantitative activity distributions for dose planning in internal radionuclide dosimetry are needed. The main reason is the ability to provide 3D activity distribution and segmented activity volumes for absorbed dose calculation. Several important difficulties should be considered before reaching this goal, for example, photon attenuation, scatter contribution, partial volume effects, limited system resolution and alignment problems with other imaging modalities. This overview discusses some of these parameters and give examples of the effects using Monte Carlo simulated data.

INTRODUCTION

A large portion of cancer patients are at present not curatively treated because of the disseminated nature of the disease. Efforts should therefore be undertaken to guide more patients into curative treatments. In recent years, several methods to target cancer cells have evolved. Tumor-seeking molecules developed are, for example, monoclonal antibodies, hormone analogues etc. These tumor-specific agents have raised expectations in use for radionuclide therapy and several are today in clinical use. Many therapies today are based on some crude estimates of the therapeutic activity to be administered to the patient. The numbers are not individually calculated for each patient and can be based on mean tolerable effects to normal tissues obtained in escalation studies in cohorts, or in some cases, on simple algorithms to calculate a mean absorbed dose.

When the area of radionuclide therapy expands with newer therapeutic radiopharmaceuticals, more patients will be eligible for such therapy. Regardless if the therapy is to be used alone or in combination with other modalities, a prerequisite should be to have as accurate an absorbed dose calculation as possible. These calculations should form the basis for correlation of the therapeutic effect to absorbed dose and, preferably, for individual dose planning before therapy. Such a treatment planning scheme must be based on the most accurate methods available, using both image quantitation techniques and precise calculation methods. If such a scheme should be available, individual treatment plans would be possible, helping both the individual patient to receive a more accurate therapy, but also to exclude those patients not eligible for that particular therapy.

In this overview, we discuss the different components in a treatment planning system, outlining possible approaches to obtaining an accurate scheme for clinical radionuclide therapy.

MATERIALS AND METHODS

Data have been generated using the Monte Carlo program, SIMIND, (1), instead of using real measurements because of the ability to separate scatter from primary events. Two fictitious tumors located inside the liver and close to the spleen have been simulated using the anthropomorphic voxel phantom developed by Zubal et al. (2) The complete decay scheme of I-131 was simulated. The SPECT camera system was a Siemens DIACAM system with a high-energy collimator and an energy resolution of 10.4% FWHM at 140 keV. Sixty-four x 64 projections for 64 views were simulated. For clarity, the linear black-and-white color table has been modified in such a way that a grey-level of white has been defined for all pixel values with a zero content.

Image Acquisition

The image acquisition and a proper selection of parameters is fundamental for an accurate quantitative measurement. Imaging parameters such as matrix size, angular sampling and center-of-rotation should be carefully selected to receive a high spatial resolution and to introduce no artifacts. However, a trade-off between the sensitivity (cps/MBq) and the spatial resolution is often needed when selecting parameters, e.g. a collimator for a particular study. Regular quality control to ensure proper uniformity correction, correct pixel size units, and minimal misalignment between mechanical and electronical center-of-rotation (COR) are fundamental (3).

Image Reconstruction

An essential element is the accuracy of the image reconstruction software. By far the most common method is the filtered backprojection algorithm (FBP), where measured projection data are backprojected into an image matrix. If applied directly without filtering, serious streak-artifacts appear, since data are projected also onto areas where no activity is present. When filtering the data, a certain fraction of counts will still appear as streak-artifacts outside the patient outline, because of limited sampling density and noise contribution. If one assumes a 1:1 linearity between total measured counts and total counts in the reconstructed images, the number of events inside the patient outline will be underestimated.

The iterative reconstruction methods, e.g. the ML/EM (maximum likelihood expectation maximization) algorithm (4), compare calculated projections, forward projected from an initial SPECT image with the measured projections and change the count density distribution in the SPECT image until the difference between the calculated and measured projections is less than some predefined value. This algorithm does not have the drawback of streak-artifacts as FBP method does. Presently, algorithms have been optimized for speed, allowing them to be potential candidates for clinical routine evaluation.

As an example, consider Figure 1 where the same data have been reconstructed with FBP (2D Butterworth prefiltering, cutoff=0.2 cm^{-1}, order=5) and with an ML/EM method (30 iterations)(4). For the FBP image, 94% of the total number of counts in the image are inside the body outline, as compared to the ML/EM image where 99.3% of the counts remain inside. Thus, if one uses the measured sensitivity (cps/MBq) in air as a calibration factor to obtain the activity in a region then this 'loss' of events when using FBP needs to be considered.

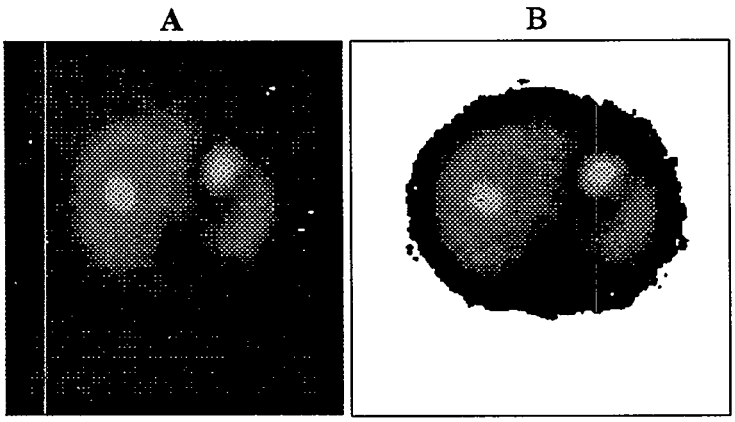

Figure 1. Left image (A) shows a reconstructed SPECT image with FBP. Right image (B) show same data reconstructed with ML/EM 30 iterations. Note the grey shade outside the phantom in the FBP image which is not the case in the ML/EM image.

Iterative reconstruction methods can also include modeling of scatter, attenuation (nonhomogeneous, by an attenuation map), and detector blur when calculating the projection data from the initial image.

Scatter Correction

Scatter in the image is caused by limited energy resolution in the NaI(Tl) crystal (9-12% FWHM at 140 keV). Small-angle scattered photons cannot be rejected by the energy window discriminator, leading to registration of mispositioned data. If no correction is applied, loss of image contrast and a quantitatively inaccurate image results.

The magnitude of the scatter contribution generally depends on the photon energy, the energy resolution, energy window settings, the object shape and the activity distribution inside the object. Several of these parameters are nonstationary, implying a potential difficulty when developing proper scatter and attenuation correction techniques.

The majority of scatter correction techniques fall into two categories; 1) the spatial domain methods, where the scatter distribution is estimated by a convolution-subtraction procedure with predefined scatter response functions and 2) energy domain methods, where scatter is estimated from multiple energy window acquisitions in different locations of the energy pulse-height distribution (Figure 2).

An early approach for the convolution subtraction method was developed by Axelsson et al. (5), where 1D monoexponential scatter functions were used to model the scatter in projection data. The limitation in this method was the assumption of invariant scatter. The method was extended to 2D by Msaki et al. (6). A 2D convolution-subtraction with invariant scatter functions was developed by Ljungberg et al. for both homogeneous (7) and nonhomogeneous objects (8).

If the acquisition hardware allow multiple acquisitions into separate data files, the energy domain scatter correction methods becomes feasible, because of the relative simple processing. Jaszczak et al. (9) suggested the use of a secondary lower scatter window in combination with a constant multiplier, k, to estimate of the scatter in the photopeak window for ^{99m}Tc. Limitations in this method include the fact that k in reality is not a constant, and that the spatial distribution of scatter in the lower Compton regions are different compared to the photopeak window events. This is due to the large-angle scattering events. Nevertheless, this method has been widely adopted and has been shown in many situations to give sufficient accuracy. Other approaches, based on multiple energy window

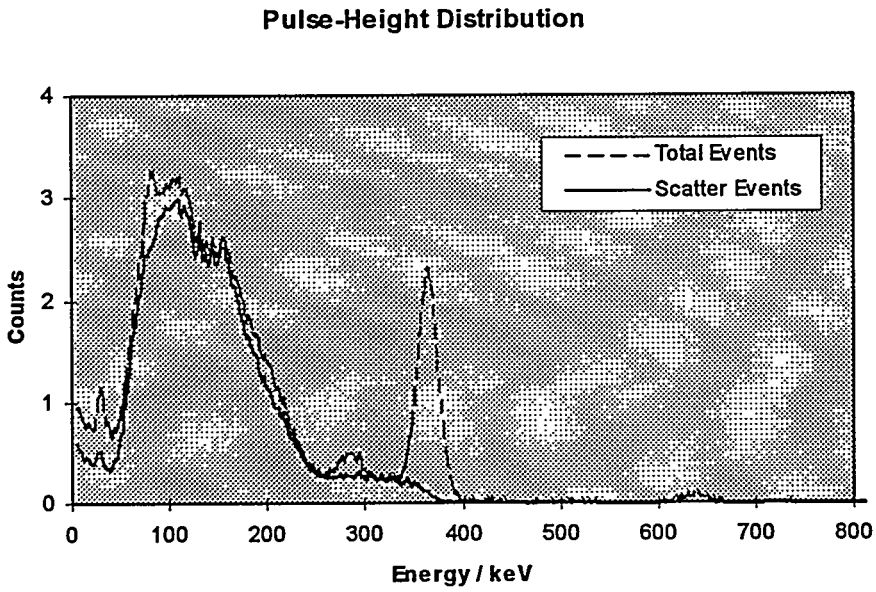

Figure 2. Energy pulse-heigh distribution of I-131, displayed as total number of events and scattered events only.

acquisitions, are the Dual-Window Method (10), the Triple Energy Window (11), and correction by local energy spectra analysis (12).

In many situations in oncological nuclear medicine imaging, the radionuclide employed emits photons of multiple energies, e.g. I-131, I-123 and Re-186 (13,14). The high-energy photon emissions contribute negatively to the images in three ways: 1) they generate scattered photons in the patient that appear in the photopeak window; 2) they scatter in the collimator and appear in the photopeak; or 3) they penetrate through the collimator septa to subsequently appear in the photopeak window by a Compton scattering interaction in the crystal followed by escape of the scattered photon (15). The latter produce the characteristic star-artifacts in the planar images. Combinations of 1-3 may also occur.

The Triple Energy Window method, described by Ogawa et al. (11,16), corrects for scatter from high-energy photons. This method use two narrow energy windows at each side of the photopeak. The scatter in the photopeak windows is estimated (on a pixel by pixel basis) by scaling the average of the counts in the lower and the upper secondary energy window by the ratio of the sizes of the photopeak energy windows, W_{peak}, and the secondary windows, W_{lower} and W_{upper}

$$P_{scatt}^{TEW}(\theta,r) = \left[\frac{P_{lower}(\theta,r)}{W_{lower}} + \frac{P_{upper}(\theta,r)}{W_{upper}}\right] \cdot \frac{W_{peak}}{2}.$$

The estimated scatter, P_{scatt} is subtracted from the original projection data. Figure 3A shows a reconstructed image of the scatter contribution in the photopeak window. The scatter events originate from narrow-angle scattered photons, due to the high energy of the emitted primary photon, which means that the distribution of scatter events in the image is close to the primary distribution, shown in Figure 1. Figure 3B shows a reconstructed image of the true scatter within the photopeak.

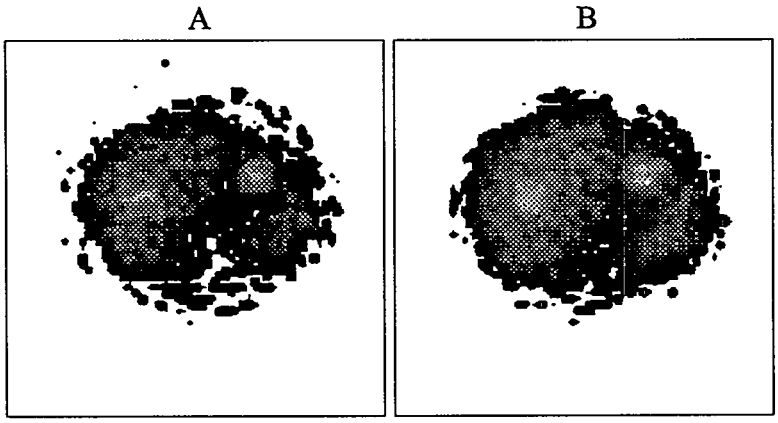

Figure 3. Left image (A) shows scatter distribution, estimated by the TEW method. Right image (B) shows the true scatter distribution within the photopeak window.

Attenuation Correction

Photon attenuation decreases the number of photons detected by photoabsorption or scattering in the object. The attenuation leads to a decrease in registered events down to about 20-30%. Significant attenuation also introduces artifacts when projections for some views are significantly attenuated compared to other views. If no correction for attenuation is made, the reconstruction algorithm will produce a false distribution of the activity. Thus, even for 'qualitative SPECT', attenuation correction becomes important. This is especially important in nonhomogeneous regions, such as the heart region.

The correction for attenuation is performed after the scatter estimate has been subtracted. Uniform attenuation may be assigned to certain parts of the body (abdomen, brain), although a more accurate distribution of attenuating tissue is preferable. Nonhomogeneous attenuation correction requires a correlated attenuation map that can be obtained by several methods, described below.

1) **Preprocessing methods** - Correction factors are applied directly to projection data (17,18). The basis for such calculations is the derivation of the arithmetic (or geometric) mean of opposing views. These methods are fast, but in most cases inaccurate, as several approximations, such as uniform attenuation and uniform source distribution, are required.

2) **Postprocessing methods** - A correction matrix is calculated from a reconstructed SPECT image, a body outline and, in some cases, a nonhomogeneous attenuation map (19). The method of Chang (20) is the most used and is today a standard method in many commercial software systems. The Chang correction can be improved by an iterative procedure where an error image is obtained by calculating new projections from the corrected image and then comparing with measured data. A variation of the post-processing method is the method, described by Larsson, where attenuation factors are calculated from a reconstructed SPECT image, but applied on the measured projection data (21). This method can also be iterative and include nonhomogeneous attenuation maps.

3) **Intrinsic methods** - Attenuation correction is carried out within the iterative reconstruction algorithm (22,23). These types of reconstruction methods have generated interest because of the development of both faster computers and more efficient reconstruction algorithms. The

attenuation correction method used in this overview, is such a method, and is part of the ML/EM iterative reconstruction method.

Detector Blur

Limited spatial resolution in SPECT is caused by 1) intrinsic spatial resolution of the crystal, 2) collimator resolution and, in some cases, 3) additional blur by photon scattering in the patient. The major contribution to the system resolution is, however, from the collimator, due to its inherent construction of parallel holes that allows detection within a fixed solid angle that is a function of the hole diameter and the collimator thickness. Thus, the spatial resolution varies with distance for a parallel hole collimator. Figure 4A shows an image from a 'hypothetical' SPECT system with perfect collimation, and Figure 4B shows an image where the radius of rotation is not optimal defined. From the images, it is clear that a careful preparation for a SPECT study is very important.

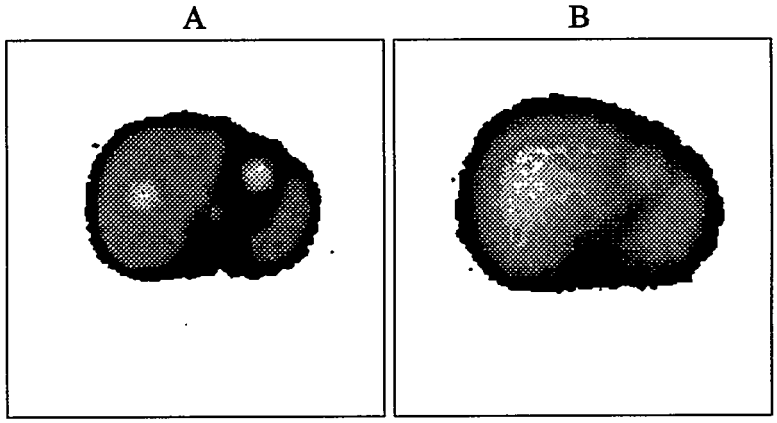

Figure 4. Left image (A) shows a simulation with perfect collimation. Right image (B) shows a corresponding simulation where the radius or rotation has not been optimally set (30 cm).

Several approaches have been suggested to correct for the blurring effect (24). In theory, it is possible to deconvolve the data with the known response function to obtain an unblurred image. However, the main drawback with this method is the required invariant detector blurring model, which is often not available. Also, noise tends to be greatly enhanced and cause problem. Glick et al., (25) have developed a distance-dependent method to compensate for the detector blur, based on the Fourier transform of the sinogram, which has been shown to be useful. Spatial-variant detector blur can also be incorporated in the iterative reconstruction methods to produce more accurate transversal SPECT images (26).

Attenuation Map

The accuracy of the attenuation correction strongly depends on the accuracy in the patient outline, as the attenuation is a function of the product of μ and x where μ is the linear attenuation coefficient and x is the distance to the body surface. Attenuation maps can be obtained by:

1) **Point source measurements** - An early and simple method to define an attenuation map is the definition of the body contour as an ellipse calculated from measured point sources that defines the major and minor axis of the patient. Uniform attenuation is assigned to the pixels inside the ellipse. The drawback is the inaccuracy in the elliptical outline, and the fact that one outline is

used in all slices.

3) **X-ray computed tomography** - X-ray computed tomography (CT) can produce attenuation maps that have very high spatial resolution and high signal-to-noise ratio. In radionuclide therapy, where CT most probably is performed as a routine investigation, these images can be used for both attenuation correction and for patient-specific absorbed dose calculations (described later). For a SPECT study, where the exact activity location inside the patient can be difficult to determine, a coregistration procedure between CT and SPECT might also be of great value (27) .

4) **Transmission SPECT (T-SPECT)** - Multiple-detector head SPECT systems allow simultaneous SPECT/T-SPECT measurements, as one detector head can be assigned for the T-SPECT without significant loss in sensitivity. Several methods have been developed, based on fan-beam collimation (28), slant-hole collimation (29) and scanning line-sources (30). Fan-beam collimation has potentially the easiest setup, but truncation of data (31) when imaging large patients can be a serious problem, and much research is focused on this issue.

Transmission measurements with SPECT has an advantage over CT in that the SPECT and T-SPECT are made simultaneously, and attenuation maps are correctly matched to the SPECT data. Spatial resolution is, however, poor compared to CT, making the modality less important, e.g. coregistration of functional and anatomical data.

Figure 5 shows a comparison of the resolution between a transmission SPECT of the Zubal voxel phantom and the actual voxel slice, obtained from CT. It should be noted that in the Zubal phantom only three densities have been used (lung, soft tissue and bone). This means that some details do not appear that otherwise are shown in conventional CT.

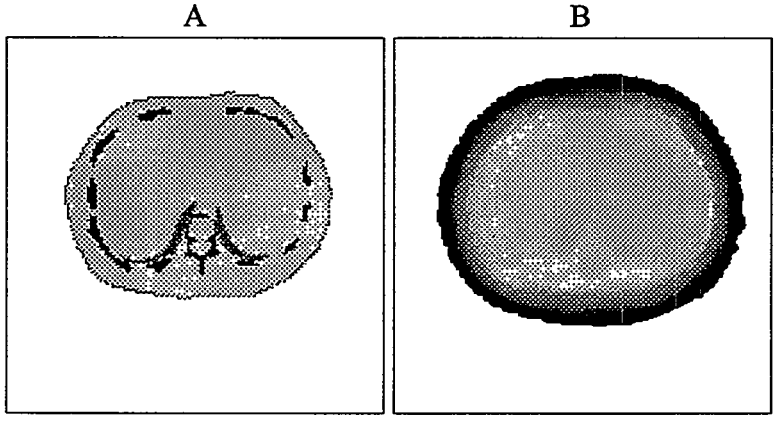

Figure 5. Left image (A) shows an example of the resolution obtained by CT. Right image (B) shows the corresponding slice obtained by simulated transmission SPECT.

Compton Scatter Acquisition

The information in the Compton region can in some cases be used to outline the patient. This is because the events, registered in the lower Compton region, are caused by large-angle scattered photons that 'distribute' the apparent activity within the whole patient outline. By reconstructing these data and applying thresholding techniques, the outline can be determined. However, the accuracy of this method strongly depends on the activity distribution (as this is the source for the

Compton scatter events) and on the photon energy.

An estimate of convex surface boundaries can be obtained by using the methodology originally described by Bergström et al. (32) for PET brain images. Object boundaries are estimated from scatter projection data. Coordinates of contours are determined for example, by a thresholding algorithm in projection matrixes. Binary projections containing a true Boolean at the contour positions only are produced and then reconstructed by backprojection. Practically, the outlining of the contours is performed in a slice-by-slice manner using scatter sinograms. An example of a scatter sinogram is shown in Figure 6A, in which contours are created. The binary sinogram is reconstructed giving the image shown in Figure 6B. The pixels within the boundary region can then be used as an estimate of the patient extension.

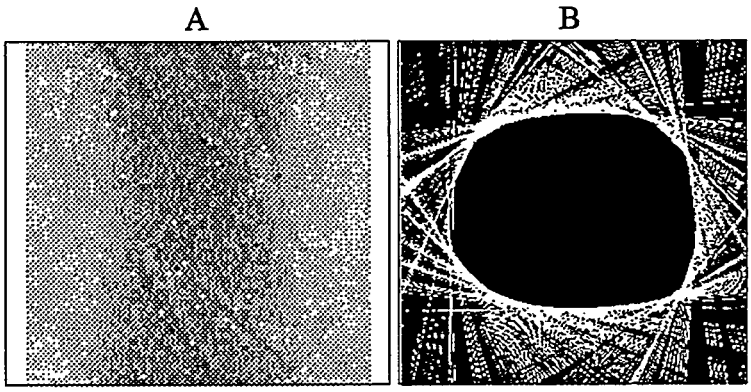

Figure 6. Left image shows the scatter sinogram in which contours can be delineated. Right image shows the reconstructed binary slice that may serve as estimate of patient boundary.

The reconstruction of Compton scattered data can also include internal major structures, such as the lung regions (33). The approach here is to segment the lung contours and assign a known attenuation coefficient to these regions. It is assumed that the major contribution to nonuniform attenuation is from the lungs, and that the differences in attenuation within the lung regions do not make a large contribution as compared to using a single average attenuation coefficient. The advantage would then be the ability to obtain a nonhomogeneous attenuation map without additional transmission SPECT.

Volume Segmentation

Absorbed dose and imparted energy calculations from a voxel-based input (such as SPECT data) give the deposited energy per unit voxel mass. However, it may be necessary to determine the absorbed dose in larger volumes, e.g. tumor volume and/or dose-limiting organs. An accurate segmentation of the activity volume is then needed to determine the total activity and the tumor/tissue mass. Image segmentation of small volumes in SPECT is, however, limited by the spatial resolution.

A variety of segmentation methods have been proposed. In brief, they may be divided into 1) operator delineation of activity regions, 2) count-based methods and 3) techniques based on edge detection. The use of operator-drawn regions-of-interests (ROI) is probably one of the most widespread methods. The technique is, however, time consuming and may suffer from subjectivity and lack of reproducibility. Among the count-based methods, the pixel count criterion groups pixels together. It is common to use a fixed threshold value that has been determined for the actual object

size and shape . Search for similar intensity levels can also be conducted among pixels surrounding an operator-defined starting point (so called region growing). The selection of threshold may be automated by evaluating a grey-level histogram of a rough ROI covering the organ/lesion.

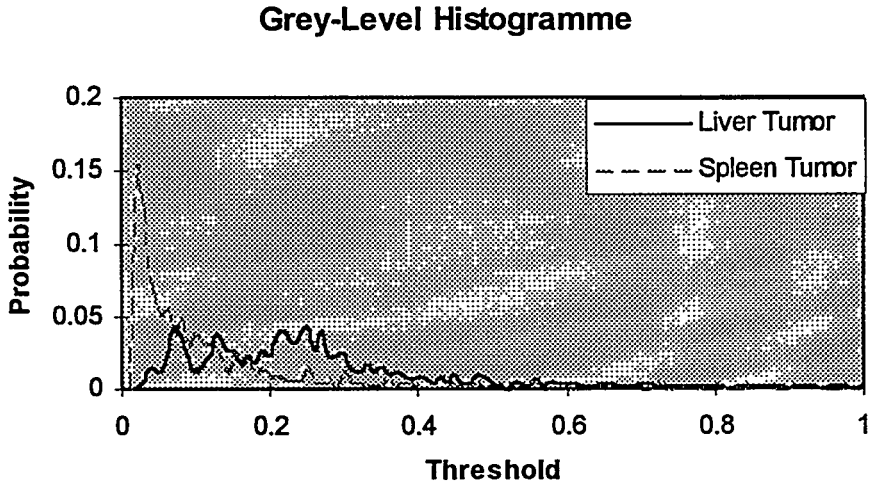

Figure 7. Grey-level histogram for the two different tumor locations in Figure 1. From this information, a threshold value can be calculated.

In either case, careful calibration is required to account for limited spatial resolution and filter effects. Problems in the count-based methods may arise if e.g.,the activity in the background is not homogenous. Edge detection utilizes the derivative of the pixel intensity, in two or three dimensions, to obtain edge information from the image. Since edges occur in all directions, searching for both the direction and the magnitude of the gradient is required. Further, selection among the pixels of high derivative intensity must be performed to obtain a closed surface. A comparison of several methods has been performed by Long et al. (34).

In some segmentation algorithms (35), a calibration function is needed to determine the true volume from the measured volume to correct for the spatial resolution. It should be remembered that extensive low-pass filtering will detoriate the spatial resolution and hence make such a calibration procedure inaccurate. It is therefore important to use a calibration function that has been developed to be as close to the true imaging situation as possible.

Activity Calculation

To calculate the absorbed dose, both the activty and the tissue volume it represents must be calculated. The tissue volume, calculated by one of the segmentation methods described above, may not always be the same as the volume needed to integrate counts for the activity calculation. This is due to the limited spatial resolution of SPECT systems that may spread counts outside the actual volume. In volume segmentation, these residual counts are not important because the segmentation methods often seach for maximum gradients. However, for calculation of the counts (i.e. the activity), these counts need to be included in the calculations. A solution may be to add a 'shell' to the segmentated volume and include the counts in this subvolume to the activity calculation (36). The thickness of the shell depends on the spatial resolution of the system. This method has several limitations in situations in which significant background counts occur that give significant errors when counted as part of the activity volume.

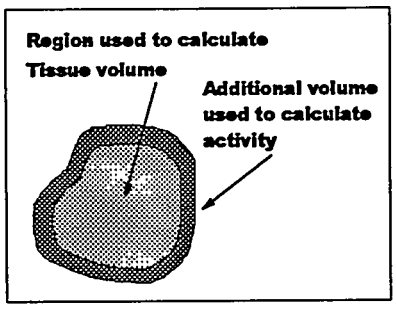

Figure 8. A sketch describing the additional shell added for the activity calculation.

Imaging Parameters

Several parameters that cannot be controlled influence the accuracy and precision in the quantitative information that can be obtained from SPECT images, e.g. the object contrast, the object size and shape, signal-to-noise ratio, and organ and patient movement (37,38). To obtain optimal quality, acquisition parameters such as image size, angular sampling and energy window width must be optimized for the actual situation. To account for noisy images, filtering may be applied. These processes influence the distribution of counts and the position of edges and must therefore be considered and, if possible, accounted for during evaluation. Figure 9 shows an example of how the choice of cut-off frequency affects the ratio of true and determined volume and also the activity and contrast of a 20 ml sphere (diameter 3.4 cm in comparison to 2.2 cm FWHM spatial resolution of the measuring system).

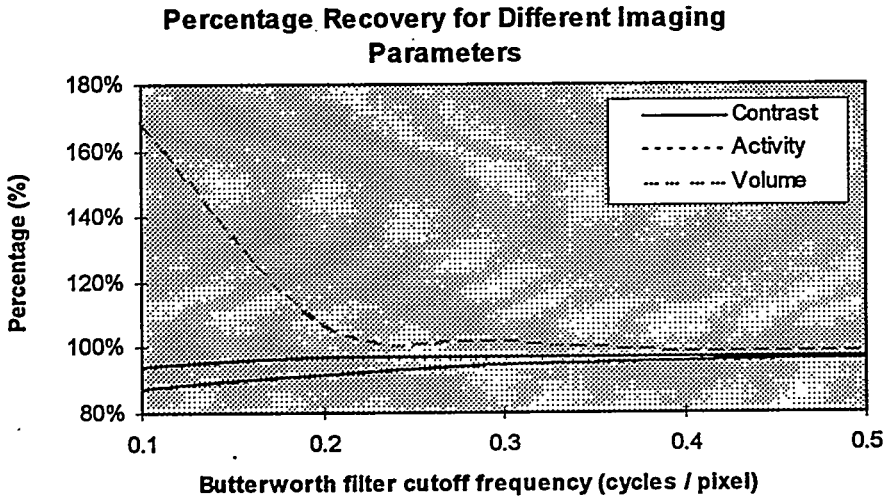

Figure 9. The change in calculated volume as function of different filtering parameters.

As can be seen for a smooth filter, the redistribution of counts causes the volume to be overestimated while both the activity and the image contrast underestimates the true situation. Careful optimization and evaluation must thus be performed to properly use the quantitative information provided by the images.

Absorbed Dose Calculations

When quantitative SPECT images have been obtained, the absorbed dose distribition within the patient can be calculated, in principle, by three different ways.

1) Assuming that all emitted energy from particles is locally absorbed. The knowledge of the decay scheme (39) is then sufficient.
2) Calculate the absorbed dose distribution in 3D by the use of photon- (40) and electron (41) point dose kernels. These kernels are derived by calculating the radial distribution of imparted energy per unit activity from a point source in an infinite medium of water or some other material of interest. The activity, corresponding to a particular pixel location is convolved with the point dose kernel and the distribution is integrated over all pixels (42,43). The drawback to this method is inaccuracies in boundaries between different materials and densities, such as soft tissue/bone tissue or tissue/lung tissue.
3) The emitted particles can be followed by explicit Monte Carlo simulation of photon- and electron emission in a patient specific 3D computer phantom. Decays are simulated according to the pixel contents in the quantitative SPECT images.

At our laboratory, we have adopted the Monte Carlo technique and developed a code, called SIMDOS, that converts activity distributions to absorbed dose distributions (44). The code can take into account patient-specific inhomogeneities, like lung and bone surfaces, giving a better estimate of the absorbed dose near interfaces. The SIMDOS code and its applications are described in detail elsewhere in these proceedings.

DISCUSSION

Quantitative SPECT can be used to calculate absorbed dose distribution for dose planning in radionuclide therapy. Several important parameters must be considered, as described above. A major limitation with SPECT is the limited spatial resolution of the SPECT system, which affects the determination of small activity volumes and tissue volumes. Information on tissue volume can be obtained by other modalities, such as CT and MRI, but it is important to recognize that these modalities in general show morphological information rather than functional information. For a heterogeneously activity distribution, the tissue volume obtained from CT or MRI may result in an overestimate of the volume/mass, which then affects the accuracy of the absorbed dose calculation.

This overview shows the possibilities of using quantitative SPECT, different correction methods, and image processing in combination with Monte Carlo technique to develop a treatment planning system for radionuclide therapy. When obtaining the activity concentration, body outline and volume segmentation should be paid special attention. The absorbed dose calculations should preferably be done with a Monte Carlo technique.

With the scheme outlined in this paper, absorbed dose calculations in radionuclide therapy should be able to be performed with high accuracy. Such absorbed dose distributions are a prerequisite for appropriate evaluation of clinical trails and for accurate dose planning for an individual patient.

ACKNOWLEDGMENT

This work, has been supported by grants from the Swedish Cancer Foundation, grant 2353-B94-08XAB, 3559-B95-02XBB, the Swedish Radiation Protection Institute #893.95, the Nilsson Foundation, the Medical Faculty of Lund University, the Royal Physiographic Society, the J&A

Persson Foundation, the Kamprad Foundation and the Swedish Foundation for Medicine.

REFERENCES

1. Ljungberg M and Strand S-E. A Monte Carlo program simulating scintillation camera imaging. Comp. Meth. Progr. Biomed 29:257-272, 1989.
2. Zubal IG and Harrell CR. Computerized three-dimensional segmented human anatomy. Med Phys 21:299-302, 1994.
3. Murphy PH, Acceptance testing and quality control of gamma cameras, including SPECT. J Nucl Med 28:1221-1227, 1987.
4. Pan T-S, Luo D-S and King MA. Design of an efficient 3D projector and backprojector for SPECT. Proceedings of the 1995 International Meeting on Fully 3D Image Reconstruction in Radiology and Nuclear Medicine, 181-185, 1995.
5. Axelsson B, Msaki P and Israelsson A. Subtraction of Compton-scattered photons in single-photon emission computed tomography. J Nucl Med 25:490-494, 1984.
6. Msaki P, Axelsson B and Dahl CM. Generalized scatter correction in SPECT using point scatter distribution functions. J Nucl Med 28:1861-1869, 1987.
7. Ljungberg M and Strand S-E. Scatter and attenuation correction in SPECT using density maps and Monte Carlo simulated scatter functions. J Nucl Med 31:1559-1567, 1990.
8. Ljungberg M and Strand S-E. Attenuation and scatter correction in SPECT for sources in a nonhomogeneous object: A Monte Carlo study. J Nucl Med 32:1278-1284, 1991.
9. Jaszczak RJ, Greer KL, Floyd CE, Harris CC and Coleman RE: Improved SPECT quantification using compensation for scattered photons. J Nucl Med 25:893-900, 1984.
10. King MA, Hademenos GJ and Glick SJ. A dual photopeak window method for scatter correction. J Nucl Med 33:605-613, 1992.
11. Ogawa K, Harata H, Ichihara T, Kubo A and Hashimoto S. A practical method for position dependent compton-scatter correction in single photon emission CT. IEEE Trans Med Imag 10:408-412, 1991.
12. Koral KF, Wang XQ, Rogers WL, Clinthorne NH and Wang XH. SPECT Compton-scattering correction by analysis of energy spectra. J Nucl Med 29:195-202, 1988.
13. McKeighen RE, Muehllehner G and Mayer RA. Gamma camera collimator considerations for imaging ^{123}I. J Nucl Med 15:328-331, 1974.
14. Clarke LP, Saw CB, Leong LK and Serafini AN. SPECT imaging of 131-I (364 keV): importance of collimation. Nucl Med Comm 6:41-47, 1985.
15. Muehllehner G and Luig H. Septal penetration in scintillation camera collimators. Phys Med Biol 18:855-862, 1973.
16. Ogawa K, Chugo A, Ichihara T, Kubo A and Hashimoto S. Quantitative image reconstruction using position-dependent scatter correction in single photon emission CT. In: Conference Record of the 1992 Nuclear Science Symposium and the Medical Imaging Conference, Orlando, 1993, 1011-1013.
17. Larsson SA. Gamma camera emission tomography: Development and properties of a multi-sectional emission computed tomography system. Acta Radiol Suppl 363:1-75, 1980.
18. Sorenson JA. Methods for quantitating radioactivity in vivo by external counting measurements. University of Wisconsin, Madison.[Doctoral Thesis]
19. Manglos SH, Jaszczak RJ, Floyd CE, Hahn LJ, Greer KL and Coleman RE. Nonisotropic attenuation in SPECT: Phantom tests of quantitative effects and compensation techniques. J Nucl Med 28:1584-1591, 1987.

20. Chang LT. A method for attenuation correction in radionuclide computed tomography. IEEE Trans Nucl Sci 25:638-643, 1978.
21. Axelsson B. Studies of a techniques for attenuation correction in single photon emission computed tomography. Phys Med Biol 32:737-749, 1987.
22. Gilland DR, Jaszczak RJ, Wang HL, Turkington TG, Greer KL and Coleman RE. A 3D model of non-uniform attenuation and detector response for efficient iterative reconstruction in SPECT. Phys Med Biol 39:547-561, 1994.
23. Gullberg GT, Huesman RH, Malko JA, Pelc NJ and Budinger TF. An attenuated projector-backprojector for iterative SPECT reconstruction. Phys Med Biol 30:799-816, 1985.
24. Floyd CE, Jaszczak RJ, Manglos SH and Coleman RE. Compensation for collimator divergence in SPECT using inverse Monte Carlo reconstruction. IEEE Trans Nucl Sci 35:784-787, 1988.
25. Glick SJ, Penney BC, King MA and Byrne CL. Non-iterative compensation for the distance-dependent detector response and photon attenuation in SPECT imaging. IEEE Trans Med Imag 1:1, 1993.
26. Liang Z, Turkington TG, Gillard DR, Jaszczak RJ and Coleman RE. Simultaneous compensation for attenuation, scatter and detector response for SPECT reconstruction in three dimensions. Phys Med Biol 37:587-603, 1992.
27. Kramer EL and Noz ME. CT-SPECT fusion for analysis of radiolabeled antibodies: Applications in gastrointestinal and lung carcinoma. Nucl Med Biol 18:27-42, 1991.
28. Jaszczak RJ, Gilland DR, Hanson MW, Jang S, Greer KL and Coleman RE. Fast transmission CT for determining attenuation maps using a collimated line source, rotatable air-copper-lead attenuator and fan-beam collimation. J Nucl Med 34:1577-1586, 1993.
29. King MA, Luo D, Dahlberg ST, Villegas BJ, Penney BC and Morgan HT. Transmission imaging of large attenuators using a slant hole collimator on a three-headed spect system. Med Phys 23(2):263-272, 1996.
30. Tan P, Bailey DL, Meikle SR, Eberl S, Fultun RR and Hutton BF. A scanning line source for simultaneous emission and transmission measurements in SPECT. J Nucl Med 34:1752-1761, 1993.
31. Kadrmas DJ, Jaszczak RJ, Mccormick JW, Coleman RE and Lim CB. Truncation artifact reduction in transmission CT for improved SPECT attenuation compensation. Phys Med Biol 40:1085-1104, 1995.
32. Bergstrom M, Litton J, Eriksson L, Bohm C and Blomqvist G. Determination of object contour from projections for attenuation correction in cranial positron emission tomography. J Comp Assist Tomogr 6:365-372, 1982.
33. Pan T-S, Ljungberg M, King MA and DeVries DJ. Attenuation correction of cardiac perfusion images in SPECT using compton scatter data: A Monte Carlo investigation. IEEE Trans Med Imag 15:13-24, 1996.
34. Long DT, King MA and Sheehan J. Comparative evaluation of image segmentation methods for volume quantitation in SPECT. Med Phys 19:483-489, 1992.
35. Mortelmans L, Nuyts J, Van Pamel G, Van den Maegdenburgh V, De Roo M and Suetens P. A new thresholding method for volume determination by SPECT. Eur J Nucl Med 12:284-290, 1986.
36. Ljungberg M, King MA and Strand S-E. Quantitative SPECT: Verification for sources in an elliptical water phantom. Eur J Nucl Med 19:838-844, 1992.
37. King MA, Long DT and Brill BA. SPECT volume quantitation: Influence of spatial resolution, source size and shape, and voxel size. Med Phys 18:1016-1024, 1991.
38. Sjögreen K, Ljungberg M and Strand S-E. Parameters influencing volume and activity

quantitation in SPECT. Acta Onc 35(3):323-330, 1996.
39. Dillman LT, Radionuclide Decay Schemes and Nuclear Parameters for Use in Radiation Dose Estimation. Part 2: MIRD Pamphlet No. 6. J Nucl Med 11:5-32, 1970.
40. Berger MJ. Energy Deposition in Water by Photons from Point Isotropic Sources: MIRD Pamphlet No. 2. J Nucl Med 9:15-25, 1968.
41. Berger MJ. Distribution of Absorbed Dose Around Point Sources of Electrons and Beta Particles in Water and other Media: MIRD Pamphlet No. 7. J Nucl Med 12:5-23, 1971.
42. Sgouros G, Barest G, Thekkumthala J, Chui C, Mohan R, Bigler RE and Zanzonico PB. Treatment planning for internal radionuclide therapy: Three-dimensional dosimetry for nonuniform distributed radionuclides. J Nucl Med 31:1884-1891, 1990.
43. Sgouros G, Chiu S, Pentlow KS, Brewster LJ, Kalaigian H, Baldwin B, Daghighian F, Graham MC, Larson SM and Mohan R. Three-dimensional dosimetry for radioimmunotherapy treatment plannning. J Nucl Med 34:1595-1602, 1993.
44. Tagesson M, Ljungberg M and Strand S-E. A photon-electron Monte Carlo program converting arbitrary activity distributions to absorbed dose distributions in a treatment planning system. Acta Onc 35(3):367-372, 1996.

A SPECT-BASED ACTIVITY QUANTITATION METHOD FOR DOSIMETRY

Dunn RM[1], Juweid M[1], Behr TM[1,2], Siegel JA[1], Sharkey RM[1], and Goldenberg DM[1]
[1]Garden State Cancer Center at the Center for Molecular Medicine and Immunology
Newark, New Jersey 07103
[2]Department of Nuclear Medicine
University of Göttingen, Germany

ABSTRACT

The clinical use of radiolabeled antibodies for the treatment of cancer necessitates quantitative analysis of their biodistribution for dose estimates. Most current methods rely on serial conjugate planar view images. Planar imaging suffers from a number of factors that complicate time-activity determinations (e.g., attenuation, overlying/underlying activity from nearby structures, necessity of background correction). We developed a SPECT-based method for ^{131}I in order to establish a more reliable dosimetry method. This methodology uses processed high-count SPECT images acquired on at least three time points, a calibration factor, attenuation correction using Chang's technique, and a computer algorithm to determine the regional counts based on the threshold method. The calibration factor is determined by imaging a point source that contains in the range of 8-11 MBq of ^{131}I; data are processed, and the counts/second/MBq are determined. Patient SPECT images are reconstructed and attenuation corrected. The counts per second in the organ or tumor are determined using a threshold algorithm. The threshold method allows for activity quantitation in tissues, based on pixel counts in a region of interest, which includes only those pixels with counts above an experimentally determined value. These counts, in collaboration with the calibration factor, yield the activity (MBq) at the respective time point. Resultant time-activity data are integrated to determine the cumulated activity using a least-squares fitting technique to an exponential function. These data are then incorporated into the standard MIRD formalism to calculate dose estimates. The resultant organ/tumor dose estimates are within ± 20% of those obtained with planar-based techniques. More importantly, this method allows for dose estimates to be calculated for tissues obscured by vessels or organs (e.g., tumors), which is difficult with planar techniques, and with minor modifications can be used to derive volumes (e.g., for tumors) from SPECT. Also, a three-dimensional profile of the activity distribution is possible based on a counts-per-voxel examination of the region of interest.

INTRODUCTION

With the advent of radiolabeled antibodies for the detection and treatment of cancer (1-4), the necessity of accurate biodistribution data for pharmacokinetic analysis and dose estimation has become more demanding. Several methods of activity quantitation based on conjugate view planar imaging techniques have been developed by several investigators, along with a number of complex

SPECT (Single Photon Emission Computed Tomography) based methods (5-6). As the Focus Committee of the Society of Nuclear Medicine Computer and Instrumentation Council points out in their assessment of quantitative SPECT, attempts at accurate quantitation need to be based on a given facility's ability and resources (7) . To make SPECT quantitation attractive and practical in a routine Nuclear Medicine setting, a methodology which would not require a great deal of sophistication, modification to equipment, or place unnecessary strain on patients would be an invaluable asset.

Planar imaging is subject to several mitigating factors that complicate the accurate delineation of regional activity quantitation, which are not encountered in SPECT imaging, making SPECT a viable alternative for activity quantitation. Some of the complicating factors in planar imaging include overlying/underlying activity from nearby structures, difficulty in determining depth of a structure, need for attenuation determination, and choice of a suitable background region of interest. While SPECT imaging has inherent limitations, these can be accounted for to a reasonable extent with conventional methods.

Inherent in SPECT imaging is the ability to resolve the superposition of activities, removing the need for background correction. The result is the ability to determine a more accurate distribution of activity, and with dose convolution techniques, to devise a three-dimensional dose distribution profile in an organ/tumor. Photon attenuation and scatter are the primary limiting characteristics; however, several methods have been proposed to offset these factors (7-12). Nevertheless, in SPECT, septal penetration, poor counting statistics, and finite energy resolution are of concern. Each of these factors can be overcome, or compensated for, with a calibration factor that is determined under the same conditions that patient imaging is performed, allowing quantitation by a technique which is easy to implement and does not require sophisticated modifications to existing systems, or complicated algorithms, to correct for the limitations of SPECT.

Once activity determination is performed, time-activity data are generated from serial imaging sessions and the cumulated activity in an organ/tumor can be derived through integration. Cumulated activity is the activity accumulated over time and is equal to the sum of all nuclear transitions (i.e., the cumulated activity is the product of the nuclear transition rate and the time the activity is within the region).

MATERIALS AND METHODS

Phantom Studies

All imaging studies were performed using a single-headed gamma camera (Sophy DS-X , SMV America, Twinsburg, Ohio) interfaced to a conventional nuclear medicine computer system, with a modification for performing threshold analysis of reconstructed SPECT data. In order to determine the calibration factor, a SPECT acquisition was performed in air, using a point source containing approximately 8-11 MBq of ^{131}I. The acquisition was performed using a 64 x 64 word mode matrix, 360^0 circular rotation over 64 projections, at 40 seconds per frame. The raw data from the point source acquisition were then processed and reconstructed using a Hamming-Hann filter, which was experimentally determined to provide the best reconstruction , without enhancing noise, or significantly altering the reconstructed image data-sets. All the slices of the reconstructed data set were then summed and a region of interest was drawn around the point source, based on a threshold method, in order to decrease the influence of the star-effect on the processed data, and the total counts contained in the region were derived. The resultant total counts over time, divided by the known activity in the point source, yielded the appropriate calibration factor in counts per unit time per unit activity (cpm/kBq).

A phantom study was performed in order to calibrate the threshold method used to

experimentally determine the appropriate threshold cutoff value for activity determination. Approximately 80 MBq of ^{131}I was placed into a 2cc sphere, then placed into a 10,000cc Alderson body phantom filled with water to simulate patient scattering conditions, and was imaged in the same manner as the point source used for the calibration factor. The processing of the raw acquisition data was the same as for the point source, with the exception that attenuation correction was performed based on Chang's algorithm (8). To perform this operation, it is necessary that the pixel dimensions of the imaging system and the linear attenuation coefficient of the radionuclide used be determined. To arrive at the pixel value, two line sources were prepared, spaced by a known distance (in this case, 10cm), and a SPECT acquisition was performed. The line sources were processed and reconstructed, and the number of pixels from the center of one line source to the other was determined from the reconstructed data. The number of pixels was then divided by the known distance, yielding the pixel size. As for the linear attenuation coefficient (μ), we used a value of 0.088 cm^{-1}, based on a half-value layer (HVL) of 7.9 cm in tissue for ^{131}I (HVL = 0.693/μ). Ideally, it is desirable to measure patient-specific attenuation coefficients through transmission imaging rather than incorporating a broad beam measurement. However, a number of the patients examined in this trial were imaged prior to attempting SPECT quantification, necessitating the use of a calculated attenuation coefficient. For this trial, a threshold value of 18% was found to be optimal to arrive at the known amount of activity in the sphere.

Patient Studies

All patient SPECT imaging was acquired using a 64 x 64 word mode matrix, 360^0 circular orbit, for 64 frames, obtaining 75-200 kcounts per frame. A series of three acquisitions was performed on separate time points of the chest-abdomen region and abdomen-pelvis region. All acquisition sets were processed using a Hamming-Hann filter, and attenuation corrected as described previously. After reconstruction and attenuation correction, the images were examined to determine that the reconstructed slices (transverse, coronal, or sagittal) were appropriate for delineating organs/tumors. Once the proper slices were selected, a region was drawn around the area of interest and the counts per second in the region of interest were derived, based on the 18% threshold value. The counts per second and the calibration factor ultimately yield the activity present in the respective region at a particular time point.

Planar activity values from serial conjugate views are derived from the buildup factor technique of Siegel (14). These images were acquired using a 128 x 128 matrix, a 15% energy window centered on the photopeak of ^{131}I, for 500 kcounts. This method has been shown to be more accurate than other conjugate view techniques (15). The resultant integral time-activity data (both planar and SPECT) were incorporated into an automated dosimetry method described previously by the authors (16). For the red marrow dose (RM), we used the sacral scintigraphy method of Siegel et al (17). It has been shown to be most effective in our clinical studies. Briefly, a region is drawn around the sacrum (a triangular region on the planar images, drawn so as not to include the iliac vessels or bladder), and the cumulated activity is multiplied by a conversion factor of 10.1, since 9.9% of the red marrow resides in the sacrum.

Once quantification is performed, the time-activity data are integrated to determine the cumulated activity. Planar data are integrated by either an exponential or trapezoidal integral. The exponential integral is determined from the effective half-time ($T_{1/2e}$) and y-intercept (initial activity) of the exponential function described by the log of activity versus time. The trapezoidal integral is the sum of the trapezoidal areas defined by the data, with additional estimates of activity before and after the period spanned by the data. The choice between the exponential integral and trapezoidal integral is based on the following criteria: 1) if the effective half-time is greater than the physical half-life, the

trapezoidal integral is used, 2) if the slope of the time-activity curve is not negative, the trapezoidal is used, 3) if the r-coefficient of the slope is < -0.80, the exponential integral is used, and 4) if the trapezoidal integral is within ± 10% of the exponential, the exponential integral is used. The exponential integration is the method of choice, and as such, the SPECT data were fit by the exponential method. The dose estimates were then derived using the conventional MIRD formulation, most recently described in the MIRD Primer (18) as:

$$D_k = \tilde{A}S,$$

where D_k is the mean absorbed dose to a target tissue k, $\tilde{A}$ is the cumulated activity, and S is the MIRD defined S value. The S values used for organs in our calculations are those found in MIRD Pamphlet 11 (19), whereas tumors are treated as spherical unit-density sources. We have included a modification of the standard MIRD (Medical Internal Radiation Dose) schema to account for tumors. Tumors are treated as spherical unit-density sources to compute tumor-to-tumor (self-to-self) doses, and when a tumor is located within a MIRD tabulated organ, the host-organ-to-tumor (and vice-versa) dose is computed using the penetrating emission component of the host organ (self-to-self) S factor. The mass of the organ is also adjusted accordingly to compensate for the mass of the tumor(s) residing in the organ.

The effective half-time ($T_{1/2e}$) of an organ/tumor is determined from the slope of the time-activity curve described. In our methodology, if the resultant effective half-time is longer than the physical half-life, then the physical half-life is used in the integration calculation.

RESULTS

Table 1 provides typical examples of the organ and tumor quantification (in MBq) values obtained from SPECT and planar imaging of a patient, at comparable time-points postinjection. As can be seen from Table 1, most of the SPECT-based values are lower than those obtained from the buildup factor technique using planar conjugate views. Tables 2 and 3 list the organ dose estimates (in mGy/MBq) derived from SPECT data and those obtained using our conventional planar-based method, respectively.

Table 4 shows the relationship between the SPECT estimates as a function of the planar values. As the table demonstrates, the SPECT quantities are within a reasonable range of the planar estimates. As expected, the majority of the doses derived from SPECT are lower than those obtained with planar images. The lower values can be attributed, in part, to the fact that due to the limited spatial resolution of SPECT, counts in a region are spread over a larger area than in planar images, and as a result are decreased. However, this is more commonly the case with regions that are beyond the spatial resolution of a gamma camera [< 2.5 times the Full Width at Half Maximum (FWHM) (20)], and is not as prominent with large organs, as is the case in this study. Rather, we believe the lower values are a result of more accurate data from SPECT since the superimposition of activity in an organ or tumor is resolved, and the possibility of inaccurate background correction is removed. As a result, the final estimated doses are the product of more accurate determination of activity distribution.

The higher dose estimates for organs in the chest-abdomen region can be attributed to the use of a broad beam value for the linear attenuation coefficient (μ), since the chest region is not composed of uniformly attenuating tissue. By using a broad beam value of μ, a number of scatter events are not removed in the processed data. The estimates are still within an acceptable range, although a narrow beam value of μ based on transmission imaging would be more accurate.

Table 1

Organ and Tumor Activity (in MBq) Derived from SPECT and Planar Images for Patient 1629 (Tumor = Liver Tumor RM= Red Marrow (sacrum))

ORGAN	TPI	PLANAR	SPECT	ORGAN	TPI	PLANAR	SPECT
Lungs	24	8.14	7.41	Lungs	48	3.91	4.18
Liver	24	36.55	35.2	Liver	48	25.28	24.88
Spleen	24	4.37	3.76	Spleen	48	3.22	2.48
Kidneys	24	6.53	5.7	Kidneys	48	4.46	4.85
RM	24	1.22	1.22	RM	48	1.27	1.12
Tumor	24	2.29	2.17	Tumor	48	2.24	1.85

Table 2

Tabulated Organ Doses (in mGy/MBq) Based on SPECT Data (RM=Red Marrow (sacrum))

PATIENT	INJECTION #	LUNGS	LIVER	SPLEEN	KIDNEYS	RM
1486	2	8.95E-01	9.08E-01	1.89E+00	6.68E-01	9.65E-01
1585	1	1.33E+00	8.65E-01	1.76E+00	9.70E-01	1.75E+00
1601	2	1.82E-01	1.78E+00	3.95E-01	2.68E-01	4.43E-01
1613	2	4.70E-01	4.97E-01	5.49E-01	5.70E-01	4.38E-01
1615	1	8.76E-01	1.02E+00	1.72E+00	7.41E-01	9.22E-01
1619	1	4.22E-01	6.89E-01	1.42E+00	1.11E+00	3.76E-01
1629	1	2.78E-01	1.21E+00	8.38E-01	7.76E-01	3.35E-01

Table 3

Tabulated Organ Doses (in mGy/MBq) Based on Planar Images (RM=Red Marrow (Sacrum))

PATIENT	INJECTION #	LUNGS	LIVER	SPLEEN	KIDNEYS	RM
1486	2	1.03E+00	1.09E+00	2.17E+00	7.65E-01	1.09E+00
1585	1	1.28E+00	8.84E-01	1.80E+00	1.12E+00	1.78E+00
1601	2	1.80E-01	1.78E+00	4.11E-01	2.73E-01	4.54E-01
1613	2	5.22E-01	5.81E-01	6.62E-01	7.54E-01	4.46E-01
1615	1	8.11E-01	9.43E-01	1.62E+00	7.65E-01	9.05E-01
1619	1	4.16E-01	6.78E-01	1.57E+00	1.20E+00	3.84E-01
1629	1	2.73E-01	1.30E+00	9.03E-01	7.57E-01	3.68E-01

Table 4

SPECT Organ Values as a Percentage of Planar Organ Values (SPECT/Planar)

PATIENT	INJECTION #	LUNGS	LIVER	SPLEEN	KIDNEYS	RM
1486	2	87	83	87	87	89
1585	1	104	98	98	87	98
1601	2	101	100	96	98	98
1613	2	90	86	83	76	98
1615	1	108	108	106	97	102
1619	1	101	102	90	93	98
1629	1	102	93	93	103	91

Table 5 represents the estimated tumor doses from both SPECT and planar methods, and locations targeted post-injection. The dose estimates are within approximately 20% of each other, indicating that reliable information can be obtained from SPECT. The tumor in patient 1486 was located in the neck region, without adjacent activity. The remainder of the lesions in the other patients were located in organs (liver, lung), and demonstrated a larger variability between the SPECT and planar doses. The SPECT estimates are probably more reliable, since one must consider whether appropriate background correction can be performed on planar views when a tumor resides in an organ, or if the tumor structure can be accurately delineated from organ activity. Tumor volumes were calculated using a modified version of the described SPECT quantification method using a computer program that was designed around this particular goal. The major differences in the tumor volume application is the use of a Bandpass filter and a threshold value of 17%, which were empirically determined to be suitable.

Table 5

Comparison of SPECT and Planar Calculated Tumor Doses (mGy/MBq) Showing the Relationship between SPECT and Planar Values (SP/PL) SP=SPECT, PL=Planar

		TUMOR	DOSE	DOSE	
Patient	**Injection #**	**Location**	**Planar**	**SPECT**	**SP/PL**
1486	2	Rt. Neck	11.02	10.56	0.96
1601	2	Liver	0.36	0.33	0.92
1601	2	Liver	0.16	0.15	0.94
1615	1	Lt. Lung	9.12	7.15	0.78
1615	1	Rt. Lung	17.65	14.92	0.85
1629	1	Liver	27.46	24.56	0.89

DISCUSSION

The method proposed herein provides a simple and accurate, yet practical method for determining regional activity quantitation based on SPECT data, when certain factors are accounted for (attenuation and scatter), and using a calibration factor to convert from counts per unit time to activity. The techniques presented here for scatter compensation and photon attenuation, (namely, a narrow energy window (15%) and Chang's attenuation correction), respectively, are used routinely in the majority of clinical nuclear medicine settings. For example, while there are other more sophisticated methods of Compton scatter and attenuation compensation (e.g., Maximum Likelihood Estimation, Dual/Triple Energy Window settings), many of these processes require modification(s) to existing nuclear medicine cameras and computer systems, or require the determination of a constant for scatter correction for a particular set of acquisition parameters. As for attenuation compensation, the method of acquiring a separate transmission image to determine an effective patient-specific attenuation coefficient can be time-consuming, placing additional constraints on patients and can be subject to technical error.

The concept of using a narrow energy window as a means of scatter discrimination may seem crude or insufficient. However, to date, no other means of correcting for scatter have become as widely accepted and applied, and it is a practice most clinical centers use with confidence and would not require any validation. The use of a constant attenuation coefficient for attenuation correction could be left open to debate since there are many investigators who propose methods for nonisotropic

attenuation correction, and these techniques do have merit. As our data indicate, a constant linear attenuation coefficient may not be suitable for all patients. However, given the fact that the dose estimates derived from our SPECT-based technique are within an acceptable range to those derived from planar images, the technique does have value, except in the thorax, where linear attenuation may not be valid. Many of the conventional measures available for activity quantification, SPECT or planar, may not be routine. The use of a calibration factor, which is subject to the same conditions as patient scanning, seems to provide a method for adequate correction of these problems. Our method provides a technique that is easy to use and an application that can yield sufficiently accurate data for quantitative analysis. We have demonstrated that a simple, yet effective, SPECT-based technique to overcome the limitations of planar imaging for activity quantitation is possible without the need for sophisticated scatter correction methods, given the constraints of the average clinical setting. Our method was validated for ^{131}I, although the concept can be applied to any radionuclide used for imaging.

Future goals regarding SPECT quantification include the development of a simple method for determining accurate three-dimensional dose distributions which can be implemented as easily as the quantification method described. These methods may enable the calculation of accurate patient-specific dosimetry for therapy with radiolabeled antibodies.

ACKNOWLEDGMENTS

The authors wish to thank Doug Dunlop, RT(N) for assistance with imaging. This work was supported in part by USPHS Grant CA 39841 from the NIH.

REFERENCES

1. Goldenberg DM, DeLand F, Kim E, Bennet S, Primus FJ, van Nagell JR, Estes N, De Simone P and Rayburn P. Use of radiolabeled antibodies to carcinoembryonic antigen for the detection and localization of diverse cancers by external photoscanning. N Engl J Med 298:1384-1388, 1978.
2. Goldenberg DM, Horowitz JA, Sharkey RM, Hall TC, Murthy S, Goldenberg H, Lee RE, Stein R, Siegel JA, Izon DO, Burger K, Swayne LC, Belisle E, Hansen HJ and Pinsky SM. Targeting, dosimetry, and radioimmunotherapy of B-cell lymphomas with iodine-131-labeled LL2 monoclonal antibody. J Clin Oncol 9:548-564, 1991.
3. Sharkey RM, Goldenberg DM, Goldenberg H, Lee RE, Balance C, Palace D, Verge D and Hansen HJ. Murine monoclonal antibodies against carcinoembryionic antigen. Cancer 71:3478-3485, 1993.
4. Goldenberg DM. Monoclonal antibodies in cancer detection and therapy. Am J Med 94:297, 1993.
5. Leichner PK, Koral KF, Jaszcack RJ, Green AJ, Chen GTY and Roeske JC. An overview of imaging techniques and physical aspects of treatment planing in radioimmunotherapy. Med Phys 20:569-577, 1993.
6. Macey DJ and Giap HB. Quantitative SPECT. In: Clinical SPECT Imaging, Kramer EL and Sanger JJ, Editors, New York: Raven Press Ltd., 69-78, 1995.
7. Rosenthal MS, Cullom J, Hawkins W, Moore SC, Tsui BMW and Yester M. Quantitative SPECT imaging: A review and recommendations by the focus Committee of the Society of Nuclear Medicine Computer and Instrumentation Council. J Nucl Med 36:1489-1513, 1995.
8. Tsui BMW, Zhao T, Frey EC and McCartney WH. Quantitative single-photon emission computed tomography: Basics and clinical considerations. Sem Nucl Med 24:38-65, 1994.

9. Chang LT. A Method for attenuation correction in radionuclide computed tomography. IEEE Trans. Nuclear Science NS-25:638-643, 1978.
10. Jasczak RJ, Greer KL, Floyd E, Harris CC and Coleman RE. Improved SPECT quantification using compensation for scattered photons. J Nucl Med 25:893-900, 1984.
11. Koral KF, Wang X, Rogers WL, Clinthorne NH and Wang X. SPECT compton-scattering correction by analysis of energy spectra. J Nucl Med 29:195-202, 1988.
12. Koral K, Swaikem FM, Buchbinder S, Clintohorne NH, Rogers WL and Tsui BMW. SPECT dual-energy-window compton correction: scatter multiplier required for quantification. J Nucl Med 31:90-98, 1990.
13. King MA, Hadememnos GJ and Glick SJ. A dual-photopeak window method for scatter correction. J Nucl Med 33:605-612,1992.
14. Siegel JA. The effect of source size on the buildup factor calculation of absolute volume. J Nucl Med 26:1319, 1985.
15. van Rensburg AJ, Lotter MG, Heyns AP and Minnaar PC. An evaluation of four methods of ^{111}In planar image quantification. Med Phys 15:853-861, 1988.
16. Dunn RM, Juweid ME, Behr TH, Sharkey RM and Goldenberg DM. An automated internal dosimetry scheme for radiolabled antibodies. Med Phys 22;1549-1550, 1995.
17. Siegel JA, Lee RE, Palace D, Horowitz JA, Sharkey RM and Goldenberg, DM. Sacral scintigraphy for bone marrow dosimetry in radioimmunotherapy. Int J Appl Radiat Instru Part B., 16:553-559, 1989.
18. Loevinger R, Budinger T and Watson E. MIRD Primer for Absorbed Dose Calculations. New York: Society of Nuclear Medicine, 1988.
19. Snyder W, Ford M, Warner G and Watson S. "S" Absorbed Dose per Unit Cumulated Activity for Selected Radionuclides and Organs, MIRD Pamphlet No. 11. New York, Society of Nuclear Medicine, 1975.
20. Kojima A, Matsumoto M, Takahashi M and Yoshida H. Effect of spatial resolution on SPECT quantification values. J Nucl Med 30:508-514, 1989.

QUESTIONS

Mattsson: Could you quantify the accuracy of your SPECT-based technique for organ activity determination?

R. Dunn: Yes, we could. We performed phantom simulations with known amounts of activity and performed quantitative analysis to verify our technique. These phantom measurements were within 5% of the actual activity.

PATIENT-SPECIFIC DOSIMETRY BASED ON QUANTITATIVE SPECT IMAGING AND 3D-DFT CONVOLUTION

Akabani G[1], Hawkins WG[2], Eckblade MB[2] and Leichner PK[1]
Department of Radiation Oncology[1] and Department of Radiology[2]
University of Nebraska Medical Center, Omaha, Nebraska 68198

ABSTRACT

The objective of this study was to validate the use of a 3-D discrete Fourier Transform (3D-DFT) convolution method to carry out the dosimetry for I-131 for soft tissues in radioimmunotherapy procedures. **Methods:** To validate this convolution method, mathematical and physical phantoms were used as a basis of comparison with Monte Carlo transport (MCT) calculations which were carried out using the EGS4 system code. The mathematical phantom consisted of a sphere containing uniform and nonuniform activity distributions. The physical phantom consisted of a cylinder containing uniform and nonuniform activity distributions. Quantitative SPECT reconstruction was carried out using the Circular Harmonic Transform (CHT) algorithm. **Results:** A comparison of the radial dose profile between MCT calculations and the 3D-DFT convolution method based on the mathematical phantom resulted in close agreement. The root mean square error (*RMSE*) between the two methods was less than 0.1% with a maximum difference of less than 21%. The results obtained from the physical phantom gave a *RMSE* of less than 0.1% and a maximum difference of 13%, and a comparison of isodose contours resulted in good agreement. An analysis of the underestimation in the absorbed dose rate based on the number of missing slices from the physical phantom with a uniform activity distribution indicated a maximum underestimation of up to 20%. Finally, SPECT data from two patients who had undergone I-131 radioimmunotherapy (RIT) were used to assess and compare absorbed dose rates and isodose-rate contours by means of 3D-DFT convolution and MCT; a comparison of methods resulted in a *RMSE* of less than 0.02% and maximum difference of less than 13%. **Conclusions:** The 3D-DFT convolution method calculated absorbed doses and dose rates for a given activity distribution in a time efficient manner. Results demonstrate that 3D-DFT convolution is a precise tool to carry out a dosimetric analysis for soft tissue. This method can be used on a patient-specific basis to carry out the dosimetry of tumors, organs and user-defined volumes of interest (VOIs). Moreover, this method can be implemented on personal computers on a routine basis to expeditiously carry out a dosimetric analysis of soft tissue VOIs.

INTRODUCTION

The development of patient-specific dosimetry for administered radionuclides and radiolabeled compounds is essential for a better understanding of tumor response and normal-tissue toxicity. This is particularly relevant in clinical trials in cancer therapy with large administered activities and

potentially high radiation absorbed doses in tumors and normal tissues. As discussed in a previous publication, in clinical trials the absorbed dose is usually calculated rather than measured, and calculations are usually based on imaging procedures (1). Therefore, a necessary first step in nuclear medicine dosimetry was the development of algorithms and computer software for the quantitative determination of the activity of radionuclides and radiolabeled compounds in tumors and normal tissues as a function of time following their administration to patients.

Initially, activity quantitation for patients was based on planar gamma camera views. However, planar gamma camera images did not provide the volumetric information needed for dosimetry nor did they provide sufficient information about the distribution of activity within tumors or normal organs. Therefore, in most cases only a mean value of absorbed dose could be estimated from planar gamma camera views. Additionally, it was difficult and error-prone to resolve superposition of activities in tumors and normal organs. To improve dosimetry in radionuclide therapy, including radioimmunotherapy (RIT), it was essential to develop quantitative emission-computed tomography (ECT). Both single-photon emission computed tomography (SPECT) and positron-emission tomography (PET) have been employed for the quantitation of radioactivity in patients, perhaps most notably in clinical RIT. An overview of quantitative planar imaging, SPECT and PET quantitation, dosimetry and treatment planning in clinical RIT has been given elsewhere (1). In ongoing clinical trials in RIT at our institution, quantitative SPECT studies provide the information necessary for improved calculations of absorbed dose distributions.

After the spatial and temporal distribution of radioactivity has been determined for a patient, patient-specific radiation absorbed dose calculations can be carried out. In principle, Monte Carlo calculations of the transport of radiation could be used for patient-specific dosimetry. In practice, such calculations are computationally very intensive and time consuming (2,3). An alternative method is to use point dose kernels which permit the assessment of absorbed dose rate and dose in a more efficient manner (4-7).

In this report, we generalize previous work on a unified approach to photon and beta particle dosimetry (6) and introduce a point source kernel for I-131 which includes not only photons and beta particles but also monoenergetic electrons. We show that a three-dimensional convolution method using a discrete Fourier transform (3D-DFT) permits efficient computations of absorbed dose rates for I-131. This radionuclide was chosen for the present study because it is widely used in diagnostic and therapeutic nuclear medicine and because its spectrum is sufficiently complex to test this approach to dosimetry. We demonstrate explicitly in mathematical and physical phantom studies and in a patient study that the 3D-DFT method is as accurate as Monte Carlo calculations. This means that in conjunction with quantitative SPECT, based on the circular harmonic transform (CHT) algorithm (8-11), we have developed and clinically implemented a system for patient-specific soft-tissue dosimetry.

Each SPECT (or PET study) represents a time point ("snapshot") in the distribution of radioactivity in a patient and this information is stored in a 3D matrix. In the 3D absorbed dose calculations described in this report, every voxel in this matrix represents both a source and a target volume. These calculations, therefore, yield distributions of absorbed dose rates and, consequently, absorbed dose-rate gradients which are characterized by isodose-rate contours, and absorbed dose-rate volume histograms. An important feature of the output of absorbed dose calculations in our approach to patient-specific dosimetry is the superposition of isodose-rate contours on SPECT images. Additionally, minimum, maximum and mean values of absorbed dose rates are computed for each volume of interest (VOI). These features provide a complete description of absorbed dose rates at each time point. The absorbed dose is obtained by integrating over several time points which include at least two SPECT studies and several whole-body images, acquired over a period of days.

The results of this work differ from previous investigations (2,5,7) in several aspects. The 3D-DFT absorbed dose calculations are shown to yield the same results as Monte Carlo calculations, thereby validating the 3D-DFT method. In practice, this means that 3D absorbed dose calculations can be carried out on computers in nuclear medicine departments and on currently available personal computers. Furthermore, all calculations are based on 3D SPECT matrices and do not require additional input from other imaging modalities, such as computed tomography (CT) or magnetic resonance imaging (MRI) although these may be helpful in identifying VOIs. Finally, a more complete description of absorbed dose rates and dose is provided than was done previously.

MATERIALS AND METHODS

Monte Carlo transport calculations were carried out by the use of the EGS4 system code (12,13). The material used was water with a density of 1.00 g/cm^3. Electron and photon transport calculations were carried out with a cut off energy of 10 keV. Patient SPECT data was acquired using the Picker 2000 gamma camera system (Picker Ohio Imaging, Bedford Heights OH) and reconstruction was carried out using the Circular Harmonic Transform (CHT) algorithm (8). Transverse SPECT slices were reconstructed in 128^2 matrices. The basic element of the SPECT matrix was a cubic voxel with a side dimension of 0.467 cm. Calculations were carried out for I-131, a widely used radionuclide in diagnostic and therapeutic nuclear medicine.

Radionuclide Kernel

A single kernel containing all types of emitted radiations was generated for use in the 3D-DFT convolution method. This approach was consistent with a previous development by Leichner (6) for beta particles and photon absorbed dose distributions around a point source. In this work, the basic convolution kernel was calculated by means of Monte Carlo transport. Photon and electron transport were carried out in a lattice of tissue where the source region was located at the voxel of origin (with coordinate indexes $i = 0, j = 0, k = 0$) containing a uniform activity distribution. The decay scheme and beta spectrum for I-131 were obtained from the National Nuclear Data Center (NNDC, Brookhaven Nat. Lab., Upton, NY) and by using the Program RADLST (14). Monte Carlo transport calculations were then carried out and energy deposition was computed for every voxel of the lattice. The number of histories transported was 10 million. The cubic voxel dimensions were the same as in the SPECT matrix. This kernel representation was not continuous but rather discrete based on the absorbed dose to every individual voxel of the lattice. Table 1 presents the initial elements of the discrete kernel for I-131 based on the voxel index defined as the sum of $i^2 + j^2 + k^2$, and radial distance. Figure 1 illustrates the absorbed dose kernel as a function of radial distance. Statistical errors were calculated based on energy deposition for voxels having the same index, $i^2 + k^2$. Therefore, these statistical errors were proportional to the radial distance from the center of the lattice and inversely proportional to the number of voxels with the same index.

Table 1
Discrete Absorbed Dose Kernel Representation in Water for I-131 in an Infinite Lattice Based on Voxel Index and Radial Distance

Index ($i^2+j^2+k^2$)	Radial Distance (cm)	No. of Voxels	Absorbed Dose (Gy/Bq s)
0	0.00000	1	2.733×10^{-10}
1	0.46693	6	6.329×10^{-12}
2	0.66033	12	5.911×10^{-13}
3	0.80874	8	2.706×10^{-13}
4	0.93385	6	1.940×10^{-13}
5	1.04410	24	1.524×10^{-13}
6	1.14370	24	1.260×10^{-13}
8	1.32070	12	9.765×10^{-14}
.	.	.	.
.	.	.	.

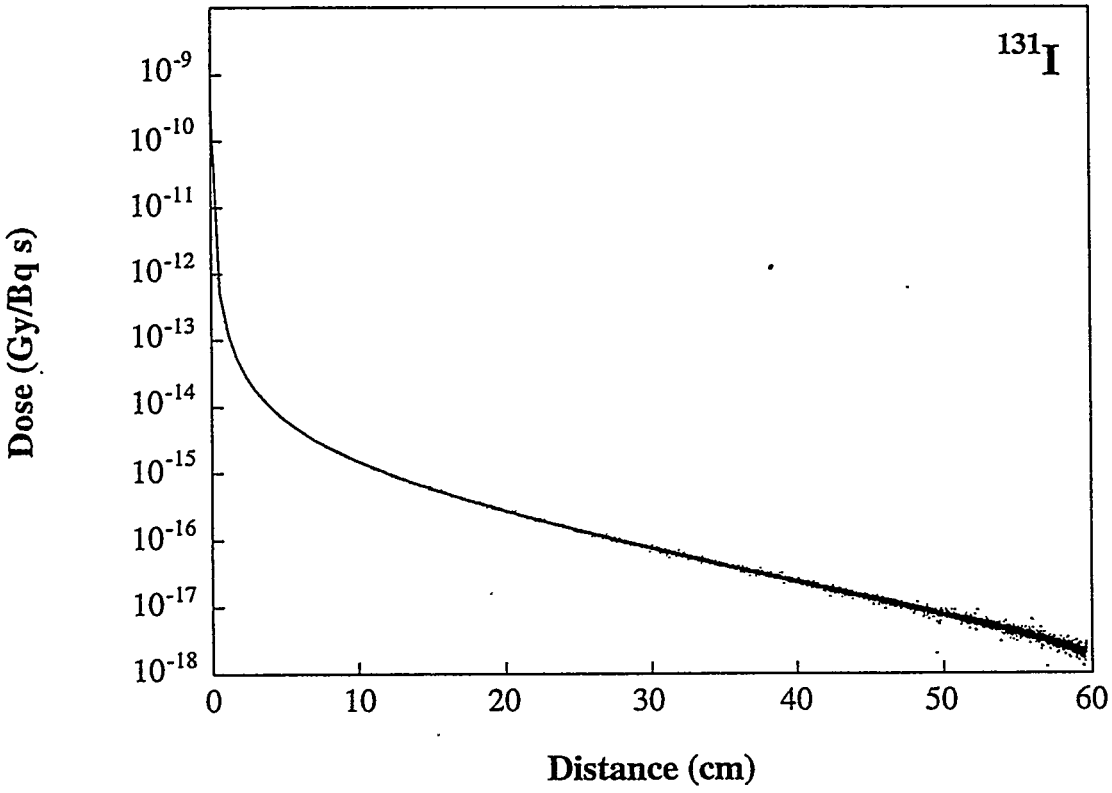

Figure 1. Dose kernel for I-131 based on a cubic voxel of 0.467 cm side. This kernel contains both electron and photon components and was calculated using the EGS4 Monte Carlo transport code. The material used was water with a density of 1.00 g/cm^3.

This kernel representation takes advantage of the symmetry of a cubic lattice and, thus, it reduces the amount of computer memory used to store the kernel. A 128^3 matrix required 8.4 MB of memory; however, when symmetry was applied and the kernel was transformed into an ASCII format, the file size was reduced to approximately 300 kB. After calculating the dose kernel, a M^3 matrix was

generated which contained a three-dimensional dose kernel that was to be used during the 3D-DFT convolution process where M was the matrix size of the SPECT images. This process is carried out by calculating the index value, $i^2 + j^2 + k^2$, and, thus, the corresponding kernel value for every voxel of the matrix. The origin of the indices (i, j, k) is located at the center of the matrix. This kernel representation is irrespective of the radiations being emitted and can be applied to any other radionuclide decay scheme.

Monte Carlo Source Sampling

To implement Monte Carlo transport calculations, it was necessary to carry out source sampling based on the activity distribution in SPECT images. To this end, a triple rejection technique based on conditional activity distributions was used to sample the indices i, j, k over the three-dimensional matrix. This was done by collapsing the activity distribution over the z-axis and carrying out an initial rejection technique. After the k index was evaluated, a second pass through the rejection technique was used to assess the j index by collapsing the corresponding z plane over the y-axis, and finally, the i index was simply evaluated based on the evaluated k and j indices. These probability distributions were expressed as

$$h^z(k) = \sum_i \sum_j A(i,j,k), \tag{1}$$

$$h^y(j,k) = \sum_i A(i,j,k), \text{ and} \tag{2}$$

$$h^x(i,j,k) = A(i,j,k), \tag{3}$$

where $h^z(k)$ was the probability distribution on the z-axis; $h^y(j,k)$ was the conditional probability distribution on the y-axis given the k index, and $h^x(i,j,k)$ was the conditional probability distribution on the x-axis given the j and k indices. Consider a matrix of size, $M \times M \times N$, where M is the slice matrix dimension and N the number of reconstructed SPECT slices. There will be one single probability function for the z-axis and the corresponding h^z_{max}, N conditional probability distributions for the y-axis and their corresponding $h^y_{max}(k)$, and $M \times N$ conditional probability distributions for the x-axis and their corresponding $h^x_{max}(j,k)$. Once the voxel indices (i, j, k) were calculated, the coordinates (x, y, z) were sampled based on a uniform activity distribution in a given voxel. This was expressed as follows:

$$\begin{aligned} x &= i\Delta + (ran - 0.5)\Delta \\ y &= j\Delta + (ran - 0.5)\Delta \\ z &= k\Delta + (ran - 0.5)\Delta \end{aligned} \tag{4}$$

where Δ was the cubic voxel side dimension and *ran* is a random number. This method was extremely efficient in comparison to a simple rejection technique that samples simultaneously the x-, y- and z-axis; however, it required twice the computer memory for source sampling.

Photon and electron Monte Carlo transport calculations were carried out to assess the energy deposition patterns and absorbed dose rates based on a given activity distribution. To obtain reliable

results from Monte Carlo transport calculations, a minimum of 4 million histories was required to carry out a comparative study.

3D-DFT Convolution

The basic equation for the assessment of the absorbed dose rate to a point in space from a given activity distribution can be expressed in terms of the convolution integral

$$D(r_o) = \int_{Vol} k(r - r_o)A(r)dr^3 \tag{5}$$

or

$$D(r_o) = k(r_o) * A(r_o), \tag{6}$$

where $D(r_0)$ gives the dose rate at point r_0, $A(r)$ expresses the spatial activity distribution, and $k(r)$ represents the radiation dose kernel for a given radionuclide for all radiative components. The Fourier transform (FT) of the convolution in (6) is

$$FT\{D(r)\} = FT\{k(r)\}FT\{A(r)\}. \tag{7}$$

In other words, the convolution of two functions in the spatial domain corresponds to the product of the Fourier Transform of the two signals in the frequency domain. However, the SPECT data were represented in a discrete three-dimensional matrix rather than a continuous function. Thus, a Discrete Fourier Transform (DFT) was used as a fundamental operation for the assessment of absorbed dose and dose-rate distributions in discrete space. In discrete space, the convolution of two discrete functions, $k(n)$ and $A(n)$ is defined by

$$D(n) = \sum_{m=-\infty}^{m=\infty} k(n-m)A(n) \tag{8}$$

and this can be denoted again as

$$D(n) = k(n) * A(n). \tag{9}$$

When applying the DFT this becomes

$$DFT\{D(n)\} = DFT\{k(n)\}DFT\{A(n)\}. \tag{10}$$

This states that the DFT of the convolution of two discrete functions is the product of the individual DFT of the functions. The DFT converts the convolution into multiplication. This property was used to reduce the computations needed for convolution by using the equation as follows:

$$D(n) = IDFT\{DFT\{k(n)\}DFT\{A(n)\}\}, \tag{11}$$

where IDFT represents the Inverse Discrete Fourier Transform.

A three-dimensional DFT and a three-dimensional IDFT were developed at our facilities to carry out this process in a computationally efficient manner (15).

RESULTS

Comparison of Monte Carlo Transport and 3D-DFT Convolution for Mathematical Phantoms

To assess the applicability and accuracy of the 3D-DFT convolution method, three tests were carried out to evaluate the radial dose profile for a sphere containing different activity distributions. The sphere was set up at the center of a 128^3 matrix containing different activity distributions of I-131. The regions inside and outside the sphere were assumed to be made up of water with a density of 1.00 g/cm^3. Monte Carlo sampling was carried out as described previously using the triple conditional rejection technique. The sphere setup was based on the indices i, j, k where

$$(i - 64)^2 + (j - 64)^2 + (k - 64)^2 \leq 16^2. \tag{12}$$

The root mean square error (*RMSE*) of each data set was calculated to assess the overall difference in the results obtained between the 3D-DFT convolution method and Monte Carlo transport. The root mean square error was calculated as expressed by

$$RMSE = \frac{\sqrt{\sum_{i,j,k} (\alpha_{i,j,k} - \beta_{i,j,k})^2}}{\sum_{i,j,k} \beta_{i,j,k}}, \tag{13}$$

where $\alpha_{i,j,k}$ and $\beta_{i,j,k}$ are the results obtained from Monte Carlo transport and the 3D-DFT convolution method, respectively. Moreover, the maximum difference was calculated as expressed by

$$\partial = \frac{\max|\alpha_{i,j,k} - \beta_{i,j,k}|}{\beta_{i,j,k}}. \tag{14}$$

Test 1. Uniform distribution in a sphere

A sphere containing a uniform distribution of I-131 was used to assess the radial dose profile from the center of the sphere. Monte Carlo transport was carried out for 4 million histories and results were normalized to absorbed dose per unit transformation (Gy/Bq s). Figure 2A shows the comparison of the results as calculated from Monte Carlo transport and the 3D-DFT convolution method where the absorbed dose profile is expressed as a function of radial distance (cm) from the center of the sphere. The agreement between Monte Carlo transport and the 3D-DFT convolution method reflects the precision of the 3D-DFT convolution for regions inside and outside the sphere. The differences between the methods are due to the stochastic nature of Monte Carlo transport and computational approximations associated with the 3D-DFT convolution method. The *RMSE* for the whole data set was 0.04% and the maximum difference, ∂, was 21%.

Test 2. Two concentric spheres with uniform activity distributions

Two concentric spheres with uniform distributions of I-131 were used to assess the radial dose profile. The concentration ratio between the inner sphere and outer sphere was 10:1. Monte Carlo transport calculations were carried out for 4 million histories. Figure 2B illustrates the dose profile for this geometrical arrangement. The radial dose profiles for Monte Carlo transport and 3D-DFT were in very close agreement. The *RMSE* for the whole data set was 0.04% and the maximum difference, ∂, was 10%.

Test 3. Nonuniform activity distribution in a sphere

A sphere containing an activity distribution inversely proportional to the radial distance from the center of the sphere was used to assess the radial dose profile. In this case, Monte Carlo transport was carried out for 40 million histories. Figure 2C illustrates the dose profile for both Monte Carlo transport and 3D-DFT convolution. Again, the differences between Monte Carlo transport and 3D-DFT convolution were due to the stochastic behavior of the Monte Carlo transport. The *RMSE* for the whole data set was 0.02%, and the maximum difference, ∂, was 1.5%.

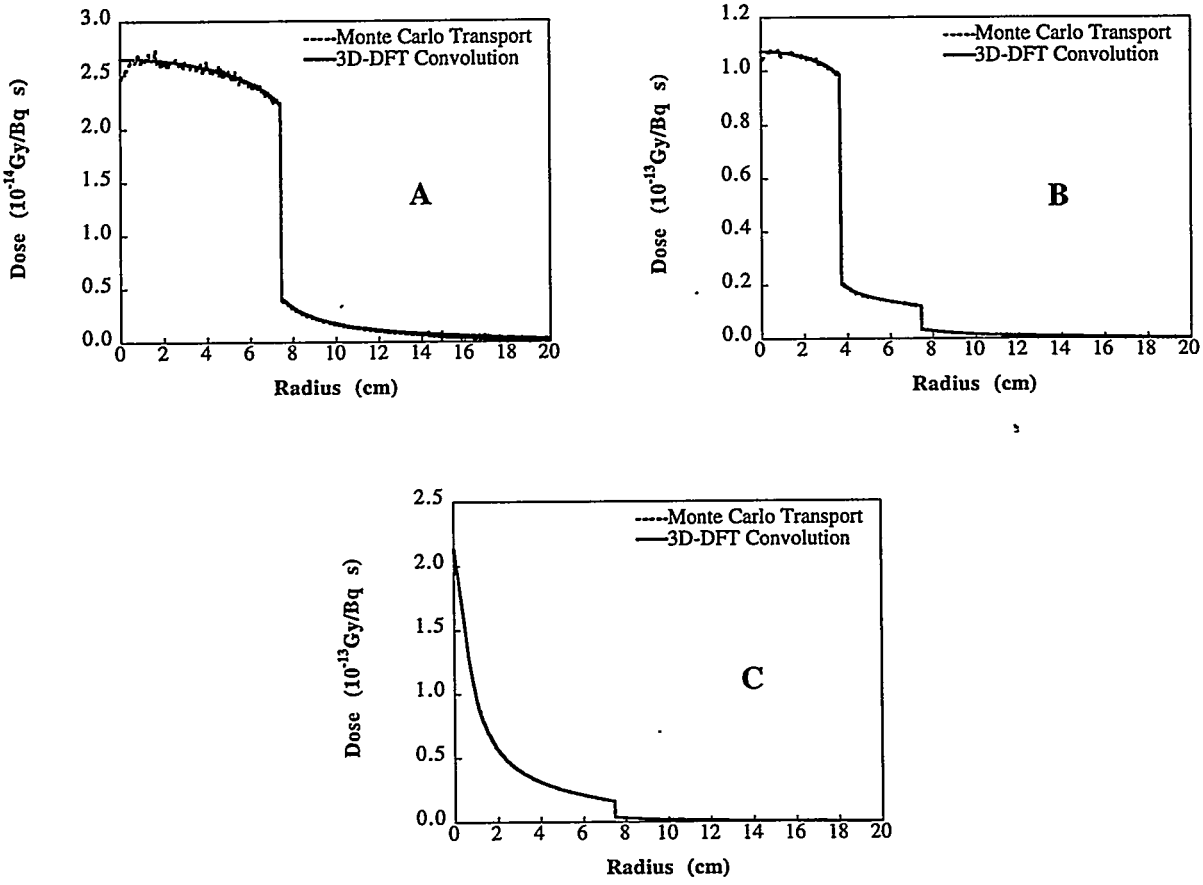

Figure 2. Radial dose profiles as calculated with Monte Carlo transport and the 3D-DFT convolution method for different activity distributions of I-131 in a sphere with a radius of 7.47 cm. A) Uniform activity distribution. B) Two concentric regions with an activity concentration ratio of 10:1. C) Activity concentration proportional to $(m^2+1)^{-1/2}$, where $m^2=i^2+j^2+k^2$.

Comparison of Monte Carlo Transport and 3D-DFT Convolution for Physical Phantom Studies

Uniform and nonuniform phantom studies were carried out to assess the applicability of the 3D-DFT convolution method with our current methods for quantitative SPECT imaging. A cylindrical phantom with an inside diameter of 21.5 cm and an inside height of 18.5 cm was filled with water; I-131 was uniformly distributed throughout the phantom with a measured activity concentration of 0.53 μCi/ml. SPECT reconstruction was carried out using the CHT algorithm where the number of reconstructed slices was 32. The calculated average activity concentration was 0.52 μCi/ml with a standard deviation of 8%. It is important to mention that all regions outside the phantom were considered to be made up of water. Monte Carlo transport calculations were carried out for 50 million histories. Figure 3 illustrates a comparison of the isodose-rate contours as calculated by Monte Carlo transport and the 3D-DFT convolution methods, respectively. The *RMSE* was 0.02% and the maximum difference, ∂, was 13%.

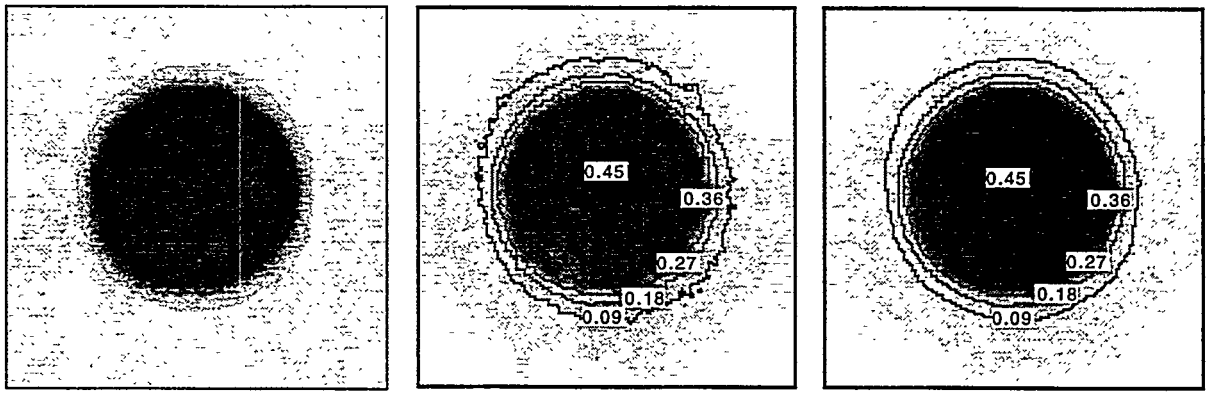

SPECT image Monte Carlo Transport 3D-DFT Convolution

Figure 3. Isodose-rate (cGy/hr) contours of a cylindrical phantom containing a uniform distribution of I-131. Reconstruction was carried out using the CHT algorithm. The measured concentration was 0.53 μCi/ml and the calculated mean concentration was 0.52 μCi/ml with a s.d. of 8%.

A nonuniform phantom study was carried out to assess the applicability of the 3D-DFT convolution method for nonuniform regions. The phantom consisted of a cylinder containing a hot, cold and background activity regions. Two inner cylinders were used to represent the hot and cold region. These cylinders each had a volume of 570 ml and an inside diameter of 7.26 cm. One inner cylinder was filled with plain water simulating a cold region. The second inner cylinder had a measured activity concentration of 3.55 μCi/ml simulating a hot region. The measured activity concentration for the background region was 1.28 μCi/ml. SPECT reconstruction was carried out using the CHT algorithm, and Table 2 shows a comparison between the measured and calculated activity concentrations in the cold, background and hot regions. Monte Carlo transport calculations were carried out for 40 million histories. Figure 4 illustrates a comparison of isodose-rate contours between the results obtained using Monte Carlo transport and the 3D-DFT convolution method. The *RMSE* for the whole data set was 0.01%, and the maximum difference, ∂, was 12.4%.

The agreement between Monte Carlo transport calculations and the 3D-DFT convolution method shows the applicability of this latter method for the assessment of dose rates in soft tissue where activity distributions are evaluated based on the CHT algorithm.

Table 2

Measured and Calculated Activity Concentrations in a Non-homogeneous Phantom. Calculated Activities Were Assessed Using the CHT Algorithm.

	Measured Activity (μCi/ml)	Calculated Activity (μCi/ml)	Difference (%)
Cold Region	0.00	0.15	-
Background	1.28	1.27	-0.78
Hot Region	3.55	3.14	-11.55

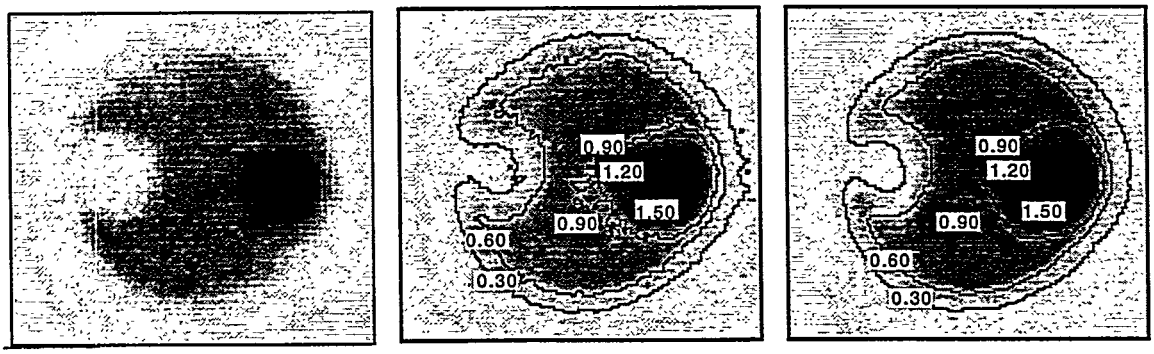

SPECT image Monte Carlo Transport 3D-DFT Convolution

Figure 4. Comparison of Monte Carlo transport and 3D-DFT convolution isodose-rate (cGy/hr) contours of a SPECT cylindrical phantom for I-131 containing a cold, background and hot region. Calculated concentrations for background and hot region were 1.27 and 3.14 μCi/ml, respectively.

In many instances, the SPECT data do not contain all possible activity distributions over the body; thus, absorbed dose rates to regions that are close to the initial and last SPECT slice may be underestimated because activity regions that are located above the first and below the last reconstructed SPECT slices are not taken into account. To quantitatively assess this possible underestimation, the cylindrical phantom containing a uniform activity distribution of I-131 was used. Twenty-five slices were reconstructed and absorbed dose rates were calculated using the 3D-DFT convolution method. The percentage differences in absorbed dose rates were calculated based on one, two, four and eight missing slices, where these slices have the same activity concentration and were located prior to slice No. 1. Figure 5 illustrates the profile of the difference of the mean absorbed dose rate as a function of slice number based on the number of missing slices. This difference is proportional to the number of missing slices; however, as expected, this difference becomes smaller for those regions that are further away from the boundary. This dose rate underestimation needs to be avoided if precise absorbed dose rate estimates are to be carried out in the clinical arena. Thus, when carrying out a SPECT reconstruction, regions or volumes of interest of high activity content must be fully reconstructed to account for all activity regions.

Patient-specific Dosimetry Using Quantitative SPECT Imaging

To assess the feasibility of using the 3D-DFT convolution method in clinical trials, SPECT data from two previous patients who had undergone I-131 RIT were used. Patient-specific dosimetry was carried out using a SPECT reconstruction matrix of 128 X 128 by *N* slices. All regions were assumed

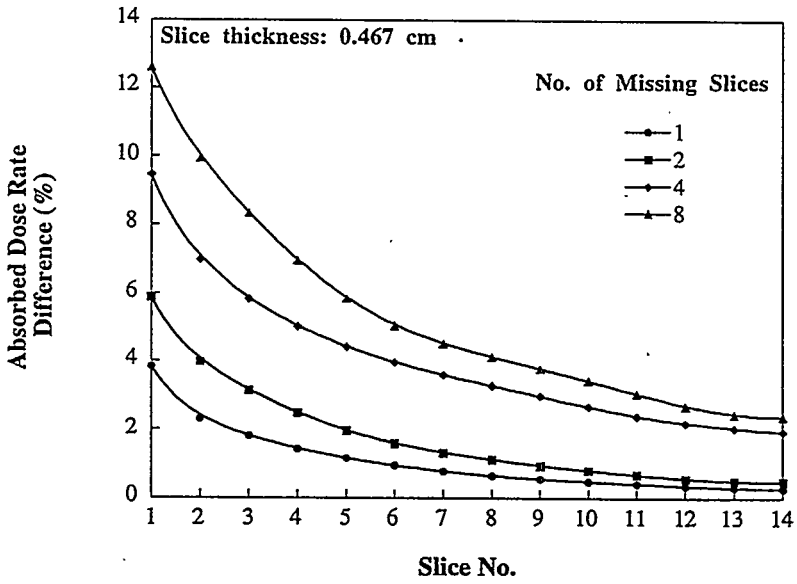

Figure 5. Percentage difference of absorbed dose rate as a function of slice. No. based on the number of missing slices for a cylindrical phantom with a uniform distribution of I-131.

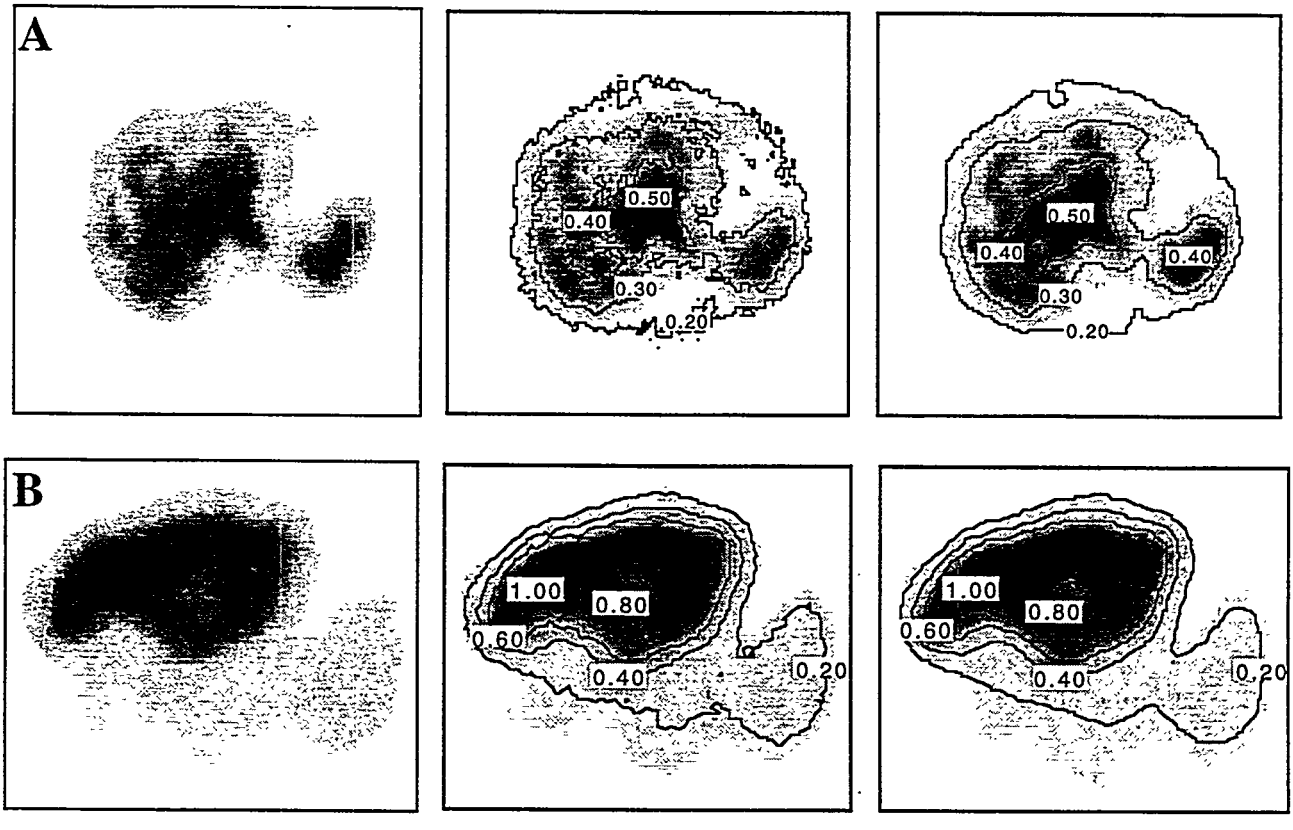

SPECT image Monte Carlo Transport 3D-DFT Convolution

Figure 6. Comparison of MCT and 3D-DFT convolution isodose-rate contours (cGy/hr). Figure shows SPECT slices of the liver and spleen of two patients who had undergone I-131 RIT.

to be made of tissue with a density of 1.04 g/cm^3 and a convolution kernel for I-131 was calculated for this material type and density. The basic element of the matrix was a cubic voxel with a side dimension of 0.467 cm. The CHT algorithm was used to carry out quantitative SPECT imaging, and voxel counts were converted into activity (Bq). Absorbed dose rates based on the 3D-DFT convolution method were calculated using Equation 11; similarly, Monte Carlo transport calculations were carried out for 40 million histories to assess the dose-rate profile. As described previously, the Monte Carlo source sampling was based on the triple conditional rejection technique. A comparison of the results obtained with Monte Carlo transport calculations and the 3D-DFT convolution method delivered an overall root mean square error, *RMSE*, of less than 0.02%, and a maximum difference, ∂, of less than 13%. Figure 6 shows the isodose contours obtained using both methods for a transverse slice. With this method it was possible to assess dose-rate gradients for regions and organs of the body and, furthermore, given a VOI, it was possible to assess a dose-rate volume histogram. As an example, the liver was selected as a VOI where all regions were determined in all reconstructed slices by means of image registration. Consequently, it was possible to carry out an analysis of the VOI based on dose-rate volume histograms and calculate the maximum, minimum, and mean dose rate and its corresponding standard deviation. Figure 7 shows the differential and cumulative dose-rate volume histogram where the mean absorbed dose rate and standard deviation were A) 0.42 and 0.06 (cGy/hr), and B) 0.81 and 0.14 (cGy/hr), respectively.

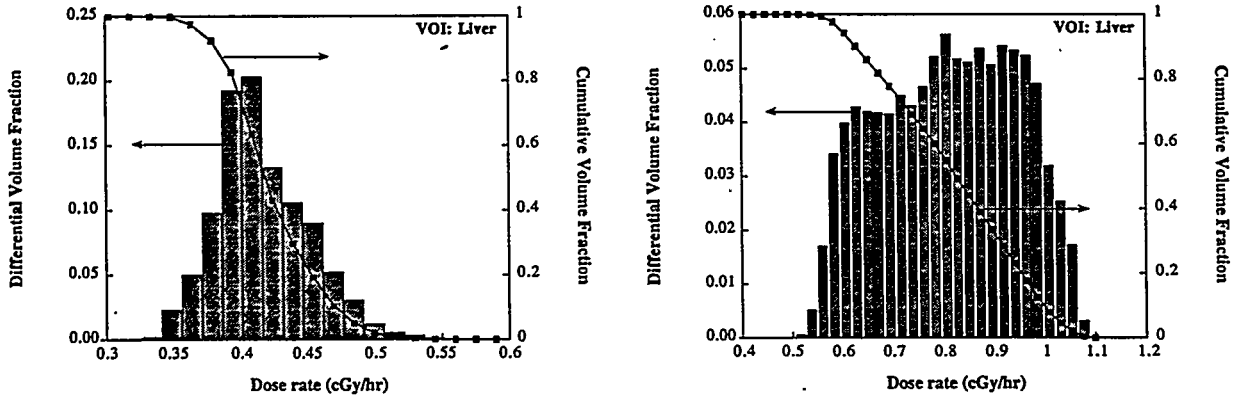

Figure 7. Examples of differential and cumulative dose-rate volume histograms for the liver based on quantitative SPECT imaging and 3D-DFT convolution for two patients who had undergone I-131 RIT. The mean absorbed dose rate and standard deviation were A) 0.42 and 0.06 (cGy/hr), and B) 0.81 and 0.14 (cGy/hr), respectively.

DISCUSSION AND CONCLUSIONS

The 3D-DFT convolution method presented here was used to calculate absorbed doses and dose rates for a given activity distribution in a time efficient manner. The comparison of results of Monte Carlo transport calculations and 3D-DFT convolution shows that the latter method is a precise tool to carry out absorbed dose and dose-rate profiles for any given spatial activity distribution. Therefore, the 3D-DFT convolution method can be used on a patient-specific basis to carry out radiation dosimetry of tumors, organs and user-defined VOIs. This method can be implemented on personal computers and nuclear medicine workbenches on a routine basis to expeditiously carry out the dosimetric analysis of user-defined regions. In contrast to the current MIRD methodology (16), this method allows us to generate isodose-rate contours, dose-rate gradients, dose-rate volume

histograms (both differential and cumulative) and carry out statistical analysis, rather than simply assessing average absorbed doses or dose rates based on assumed uniform activity distributions over predefined organs and regions. Consequently, this dosimetric method may help assess the effectiveness of a specific radionuclide therapy on a patient-specific basis, rather than simply assessing average absorbed doses to gross anatomical regions.

However, it is important to address the limitation of this convolution method. The first limitation of the 3D-DFT convolution method is that it is only valid for those regions of the body with a uniform density; therefore, the results will underestimate or overestimate absorbed doses to the lungs, bone and interface regions. However, a study by Sauer (17) indicates that it is possible to implement a convolution and superposition method for the assessment of absorbed dose rates for nonuniform regions and interfaces as is the case of soft tissue-bone and soft tissue-lung interfaces. To delimit regions and organs of different material type and density, it may be necessary to use CT-SPECT or MRI-SPECT fusion to determine regions and organs of interest with higher precision than by simply using SPECT images.

The second limitation is based on the number of reconstructed SPECT slices that describe the spatial activity distribution over the body. As shown in this study, an underestimation of the absorbed dose rate to regions and organs of the body may occur if activity regions that are beyond the first and last reconstructed slice are ignored. For the case of I-131, this dose rate underestimation can be up to 20% for regions close to the boundaries of reconstruction. However, this limitation can be avoided as long as the VOIs are located well within the first and last SPECT-reconstructed slices.

ACKNOWLEDGMENTS

This work was supported in part by DOE Grant DE-FG02-91ER61195 and NCI Grant CA58272-03.

REFERENCES

1. Leichner PK, Koral KF, Jaszczak RJ, Green AJ, Chen GTY and Roeske JC. An overview of imaging techniques and physical aspects of treatment planning in radioimmunotherapy. Med Phys 20, Pt. 2:569-577, 1993.
2. Johnson TK. MABDOS: A generalized program for internal radionuclide dosimetry. Comput Meth Progr Biomed 27:159-167, 1988.
3. Meredith RF, Johnson TK, Plott G et al. Dosimetry of solid tumors. Med Phys 20, Pt. 2:583-592, 1993.
4. Berger MJ. Beta-ray dosimetry calculations with the use of point kernels. In: Cloutier RJ, Edwards CL, Snyder WS, eds. Medical Radionuclides: Radiation Dose and Effects. Oak Ridge, TN: AEC symposium series No. 20, CONF 691212. (1970).
5. Sgouros G, Barest G, Tekumthala J, Chui C, Mohan R, Bigler RE and Zanzonico PB. Treatment planning for internal radionuclide therapy: Three-dimensional dosimetry for nonuniformly distributed radionuclides. J Nucl Med 31:1884-1891, 1990.
6. Leichner PK. A unified approach to photon and beta particle dosimetry. J Nucl Med 35:1721-1729, 1994.
7. Giap HB, Macey DJ and Podoloff DA. Development of a SPECT-based treatment planning system for radioimmunotherapy. J Nucl Med 36:1885-1894, 1995.
8. Hawkins WG, Leichner PK and Yang N-C, The circular harmonic transform for SPECT and boundary conditions on the Fourier transform of the sinogram. IEEE Trans Med Ima 7:135-148, 1988.

9. Leichner PK, Hawkins WG, Yang N-C. Quantitative SPECT in radioimmunotherapy. Antibody Immunoconj Radiophar 4:25, 1990.
10. Hawkins WG, Yang N-C and Leichner PK. Validation of the CHT algorithm for quantitative SPECT. J Nucl Med 32:141-150, 1991.
11. Leichner PK, Vriesendorp HM, Hawkins WG et al. Quantitative SPECT for ^{111}In-labeled antibodies in the livers of beagle dogs. J Nucl Med 32:1442-1444, 1991.
12. Nelson WR, Hirayama H and Rogers DWO. The EGS4 Code System. Stanford Linear Accelerator Center. Report 265 (1985).
13. Bielajew AF and Rogers DWO. PRESTA, The Parameter Reduced Electron-step Size Transport Algorithm for Electron Monte Carlo Transport. National Research Council of Canada, pub. PIRS-0042 (1991).
14. Burrows TW. The Program RADLST. Information Analysis Center Report. Report. BNL-NCS-52142. Brookhaven National Laboratory, 1988.
15. Burrus CS and Parks TW. The discrete Fourier transform. In: Burrus CS and Parks TW, eds. DFT/FFT and Convolution Algorithms, 1st edition. New York: John Wiley & Sons; 1985: 21-80.
16. Snyder WS, Ford MR, Warner GG and Watson SB. 'S', Absorbed Dose per Unit Cumulated Activity for Selected Radionuclides and Organs, MIRD Pamphlet No. 11, Society of Nuclear Medicine, New York (1975).
17. Sauer OA. Calculation of dose distribution in the vicinity of high-Z interfaces for photon beams. Med Phys 22:1685-1690, 1995.

THREE-DIMENSIONAL DOSE-VOLUME HISTOGRAM (DVH) ANALYSIS FOR BREMSSTRAHLUNG SPECT IMAGES OBTAINED BY INFUSIONAL BRACHYTHERAPY USING PHOSPHORUS-32

Parsai EI[1], Ayyangar KM[1], Dobelbower RR[1] and Siegel JA[2]
Medical College of Ohio[1]
Department of Radiation Therapy, Toledo, Ohio 43699
and Cooper Hospital/University Medical Center[2]
One Cooper Plaza, Camden, NJ, 08103

ABSTRACT

Spatial dose-rate distribution to the target and normal tissues from a beta-emitting radionuclide can be estimated using SPECT imaging and standard MIRD techniques. For patients receiving infusional brachytherapy the "megarad" dose delivered to the target organ causes concern about the degree of dose nonuniformity. Quantitative evaluation of absorbed dose requires not only three-dimensional dose calculation, but also tools such as DVHs that make this analysis possible and reliable. In the present work, quantitative dosimetry was performed for four patients with pancreatic cancer who were infused with colloidal P-32 directly into their tumors under CT guidance. A clinically applicable methodology was then developed to determine the 3-D absorbed dose distribution from transaxial reconstructed SPECT images for these patients. Calibration curves were generated using phantom studies to determine the activity per voxel from the attenuation-corrected measured counts per voxel in the reconstructed SPECT images. The calculation was extended to determine absorbed dose (Gy) at each voxel position from its activity content. Since the measured voxel dimension was a cube of 8.64 mm per side for a 64x64 matrix, the dose from neighboring voxels was estimated and found to be 0.4% and hence, any other contribution from the neighboring voxels was neglected. Map of the 2-D isodose distributions generated was then projected on the reconstructed SPECT and CT images through CT-SPECT image fusion and calculation was extended to determine 3-D isosurface dose distribution. Three-dimensional DVHs were then generated to measure the degree of dose nonuniformity in the target volume. The techniques used for the 3-D dosimetry and the results of the DVH analysis are presented.

INTRODUCTION

According to a recent survey of the American Cancer Society (1), there are an estimated 28,000 new cases of pancreatic cancer in the United States each year. Pancreatic cancer is often nonresectable because of tumor spread to the very rich local lymphatic system and/or extension of tumor into adjacent structures such as the portal vein, superior mesenteric vein or artery, duodenum, jejunum, kidneys, spleen, stomach, and colon. Patients with local disease treated by curative resection

display a median survival time of approximately 12-month and a 5-year survival rate of 6.4% (2). New therapeutic options, such as monoclonal antibodies, have not shown substantial curative effect, but have a limited adjuvant effect. A major limitation of this therapy is that they often do not yield greater than 1% tumor dose deposition (3). Clinical research with radiolabeled polyclonal antibodies has also been conducted and resulted in maximum tumor dose deposition of about 20% of the infused dose (4).

The infusional brachytherapy technique, a new radiation modality, resulted from a number of experimental and clinical observations. It requires direct infusion of colloidal P-32 into the tumor site under computed tomography (CT) guidance. It consists of injecting 2.5 million particles of macroaggregated albumin (MAA) followed by injection of colloidal P-32 into the cancerous tissue under CT guidance using a biopsy needle. For a 1110 MBq (30 mCi) injection of colloidal P-32 distributed in a 30 cc volume, the resultant dose deposition is approximately 7300 Gy. Data from the patients who have undergone this treatment in a Phase I study indicate that no significant toxicity has been observed and that the median survival time has improved. Order et al. (5) have shown that treating patients using this technique has resulted in an increase in the average median survival time for patients with nonresectable pancreatic cancer when compared with the recent report of the Radiation Therapy Oncology Group (RTOG) (6).

MATERIALS AND METHODS

A GE Maxxus - 4000I gamma camera was used to acquire SPECT images, and a number of tests were performed to determine its optimal operational characteristics. To find which collimator is optimal for bremsstrahlung SPECT imaging, 6.8 mCi of P-32 was drawn into a syringe in about 0.8 ml volume and placed at the center of 20 cm polystyrene phantom. The system was then set to acquire data in tomography mode for 32 projections and 180° at 20 sec acquisition time intervals for each camera head with the LEHR collimator. The same test then was performed after replacing the low-energy collimator with the medium-energy collimator. These raw data then were reconstructed by filtered backprojection, using a Butterworth window of order 15 with a cutoff frequency at 0.3 of the Nyquist frequency in the transaxial plane. Siegel et al. (7), have described further phantom studies performed to optimize the bremsstrahlung energy window setting to improve both resolution and contrast, and also to validate volumetric analysis on the reconstructed SPECT slices. Experimental data showed that an energy setting of 100 keV ±25% , with a medium energy (parallel hole) general purpose collimator (MEGP) and a 39% threshold for volumetric quantitation is optimal for this type of study. The 39% threshold was determined through the use of hollow spheres filled with P-32 chromic phosphate and a series of SPECT images (7). The pixel size information was determined through the use of two line sources each containing 37 MBq (1 mCi) of P-32 chromic phosphate placed parallel to one another along the camera's x and y direction and 10 cm apart. Images were obtained with 100k total counts and pixel position was determined from the centroids of the count profiles. The distance between the two centroids was measured and divided by the number of pixels. This gave the pixel size in X and Y planes.

The patient's data used in the present study were acquired on a Siemens Multispect-2 dual-headed gamma camera system (Siemens Gammasonics, IL), interfaced to a Macintosh ICON-IV computer. A program was written to create a new 2-D array to read these data in binary, removing the header information, and writing it in a binary format. The data with no header were then stored on a 3.5 inch floppy diskette which could be read by an Apple computer (Power Macintosh 7500), and the SPECT images could be displayed. The data were then saved in DOS format and transferred into our UNIX workstation through FTP software as already described.

Dosimetry Considerations for P-32

The MIRD formula, explained in detail in the MIRD Publication Pamphlet No. 1 (8), is the most commonly used technique for calculation of absorbed dose. However, there are a number of uncertainties associated with this methodology, one being the coefficient of variation (MIRD Pamphlet No. 5 (9), which appears next to the absorbed fraction column. This is a statistical limitation especially when it is 50% or higher. This value represents a significant uncertainty in the calculation of the absorbed fraction. Another limitation of this convention (as per MIRD Pamphlet No. 11 (10)) assumes that the source is uniformly distributed within a standard size organ, which varies with each patient. The authors of MIRD formulas, in all their discussions, urge the users to be aware of the assumptions and limitations used in generating the data.

The modified Loevinger function, which is an empirical equation for calculating the beta ray point-source dose distribution in air and in water (11,12), is another technique used for calculation of absorbed dose. This function, listed below, was written in FORTRAN language to be used for verification of the measured dose obtained from the 3-D dosimetry.

$$J(x) = \kappa/(\gamma x)^2 \left\{ c\left[1-(\gamma x/c)e^{1-(\gamma_{x/c})}\right] + \gamma x e^{1-\gamma_x}\right\},$$

$$\textit{where} \quad c\left[1-(\gamma x/c)e^{1-(\gamma_{x/c})}\right] = 0$$

and J(x) represents the absorbed dose rate at a distance "x" cm from a point source of beta radiation, γ is an absorption coefficient for β particles in the medium, and κ is a normalizing constant which ensures that the total energy absorbed over all space is the average β-particle energy per disintegration (13).

Beyond what the available conventional techniques provide, a 3-D approach is needed to more accurately calculate radiation absorbed doses.

Methods Used for 3-D Dosimetry

After the SPECT image data were transferred to the PC from the GE-Maxxus computer through FTP software to the UNIX workstation, a number of programs developed for nuclear medicine data handling were used to properly display the image and analyze the data. Firstly, a program read the binary information and removed the manufacturer's header from each file and added a header segment to each slice known to the software through another FORTRAN program. At this point the MCO-developed 3-D software was used to generate count surfaces in 3-D space and, via the Advanced Visual System (AVS) system, the images were displayed. A computer algorithm was also written in FORTRAN to convert the binary data to files that were readable by spreadsheet software such as EXCEL for data analysis and quantitation. This program (TX6TOEXCEL) was used for plotting of pixel contents as a function of distance or the number of pixels.

To evaluate the tools developed for generating the dose from the SPECT images, an experiment was designed using four point sources of Tc-99m. Table 1 describes specifics of these sources, which were placed inside a cylindrically-shaped polystyrene head phantom. The sources were labeled 1 through 4, and positioned at different depths in holes drilled along the height of the phantom. The phantom was carefully placed on the patient support assembly (PSA) and the system was set for 32 projections, 20 sec each and 180° rotation for each camera head. These images were stored into 64x64 matrices.

Table 1
Specifications of the Tc-99m 4-Source Experiment and Measured Calibration Factor

Source Number	Activity (μCi)	Volume (ml)	Attenuating Distance (cm)	Calibration Factor (Cts/μCi)
1	165	0.2	1	1292
2	220	0.2	8	733
3	100	0.06	8	772
4	240	0.2	1	1113

This raw data were reconstructed in the transaxial planes by a filtered backprojection algorithm using the same reconstruction parameters described previously. The reconstructed images were then imported into the UNIX workstation for analysis and quantitation.

To determine a depth-dependent calibration curve using a P-32 point source, a specially designed cylindrically-shaped body and head phantom was constructed using slabs of polystyrene materials. Twelve holes (0.95 cm diameter) were drilled along the long axis of the cylinder centered at various depths from the axial surface. For each hole, a polystyrene rod exactly fitting the hole was machined so that when not in use, it would be plugged to provide a uniform medium. A diagram of this phantom is shown in Figure 1. Using this phantom, a set of calibration curves were generated by the following experiment. A solution of 92.5 MBq (2.5 mCi) of colloidal P-32 in 0.5 ml was drawn in a glass syringe. The length of this source was measured to be 3.0 cm long and the outer diameter of the syringe was 0.9 cm. With the source at each hole position, SPECT imaging was performed using the GE-4000I. The raw data were then reconstructed and transferred to the UNIX workstation, and volumetric analysis was applied to the various slices. After 3-D reconstruction of the SPECT images, a computer program was developed to look at each slice and to add all the counts and all the pixels containing those counts in that slice and list those two sums. In performing the summing of counts, an empirically determined 39% threshold was used for optimal volumetric analysis, since it provided the best correlation between known and measured volumes (7). The results of the data analysis obtained from each hole were written to a file, which was then transferred to an Excel spreadsheet, and the results were plotted as a function of distance to the edge of the phantom.

Since the exact activity of P-32 used in this experiment was known, 92.5 MBq (2.5 mCi), the counts per pixel could be converted to activity per pixel. This was accomplished by dividing the known activity by the sum of the counts of all slices at each hole position. The activity in each pixel (activity per count per pixel) was plotted as a function of distance in radial direction (cylindrical coordinate system) to the edge of the phantom. The calibration curves correlating the activity at each pixel to a depth in the phantom were then generated to be used in the calculation of isodose distributions. The SPECT images then were converted to activity images and then to dose images through the following steps: 1) the data were transferred to the UNIX workstation; 2) the slices were made using our in-house developed 3-D software; 3) the patient contour was traced out on each image (using two small compton backscatter sources). The contours were drawn with respect to a common origin defined on the first SPECT image. Through the use of a computer program, all images were scanned for the maximum count, and all images were filtered for counts greater than 39%. Each nonzero pixel was then examined, and the pixel counts were converted to activity. The location of each pixel was checked with the contour of that slice, and the shortest distance of the point to the contour was calculated. For this depth, a calibration factor was determined from a table.

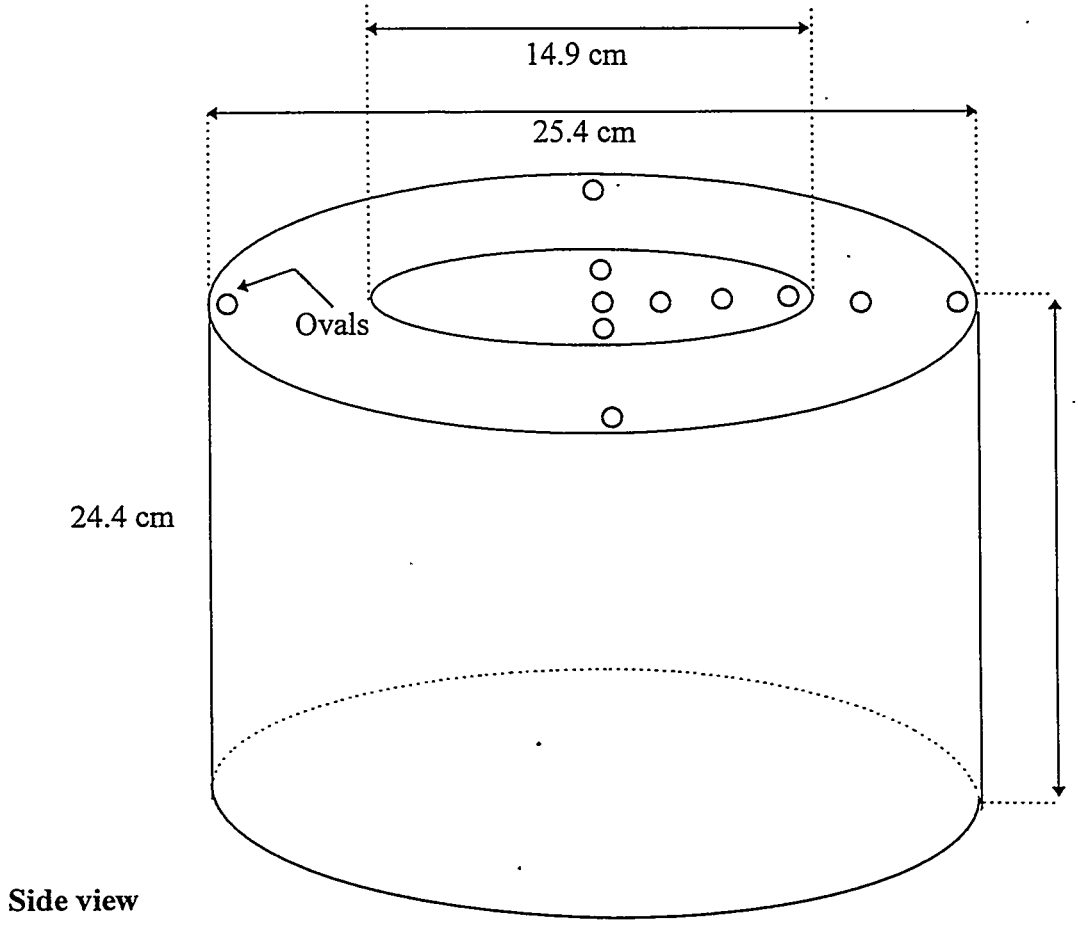

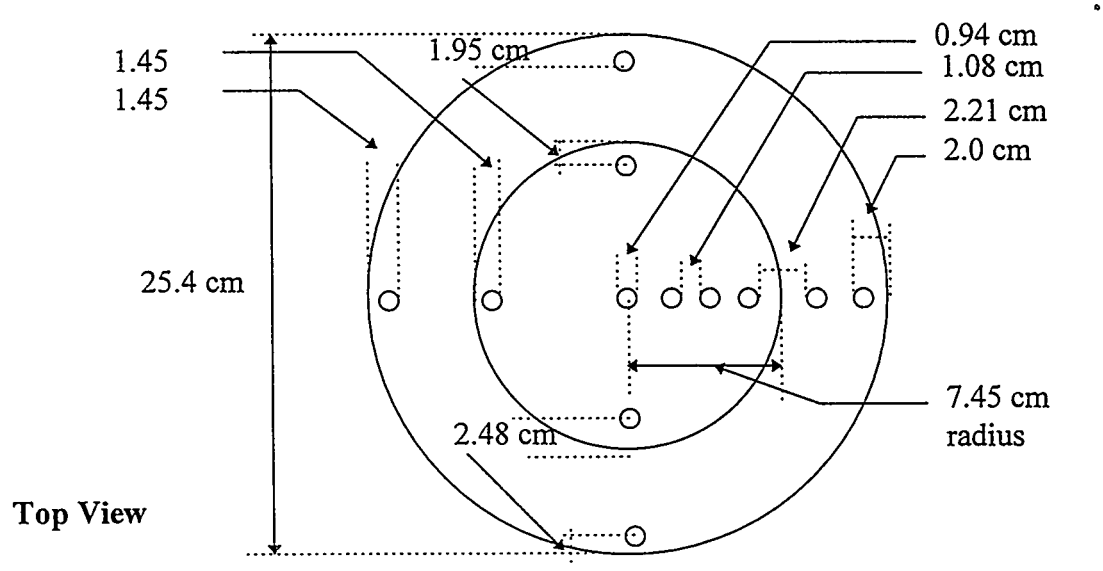

Figure 1. Polystyrene phantom designed for 3-D dosimetry.

The table read by the program as an input file was determined by converting the calibration curve obtained from the body phantom to a table with two columns. Distance from the edge was placed in the first column, and activity per count per pixel was placed in the second column. Based on the calculated distance, a calibration factor was obtained from the table. By multiplying the pixel counts by the calibration factor, the counts were converted to activity.

The activity at each pixel then was converted to dose, making the following two assumptions: first, the biological half-life of P-32 colloid is infinite, and second, the average range of the beta particles was smaller than the length of a voxel. The average range of beta particles of P-32 is 3 mm and the maximum range is 8-9 mm, where each pixel in our Maxxus system represents a volume of (8.64 mm X 8.64 mm X 8.64 mm). Hence, for all practical purposes, we can treat each voxel as being large enough for beta particle to deposit its energy. Based on this assumption, a dose conversion factor of 0.11 mGy/MBq-s (1.48 rad/μCi-h) from the MIRD tables were used for dose calculations. By using the factor (14.3 d * 24 h *1.44 *2 * calib. factor *1000), the original counts from the image then were converted to a new set of numbers or new counts. A scaling factor of 1000 was used so that each new count would be represented as thousands of rads.

DVH Method:

The content of each voxel is converted to dose using the activity per voxel and the calibration data, whereby a dose-volume matrix (DVM) is obtained. The 3-D model of the organ of interest from CT is then fused with the DVM. Each voxel of DVM that is within the organ of interest is then found. All voxels of equal dose are then collated and placed in corresponding dose-volume bins, from which the DVHs are generated.

RESULTS

Originally, the data acquired and processed with the GE gamma camera were compared with the processed data from the UNIX workstation. In Figure 2-a, where counts are plotted as a function of distance using the GE software, a FWHM of 12.5 mm is measured for the two lines sources shown. A similar plot from the workstation shown in Figure 2-b gave a FWHM of 12.9 mm on average, which indicated the integrity of the transferred data. In Figure 3, the iso-count distributions (shown in lines) are calculated and displayed around the 4 small sources of Tc-99m (shown as small solid cylinders). These data were acquired through SPECT imaging utilizing a head phantom. Figures 4-a and 4-b display the activity distribution for a P-32 point source and show a plot of activity/count-pixels as a function of distance from the edge of the body and head phantom, respectively. Even though the agreement among these measured data is not good for all measured depths, they are however, within the experimental error as shown in Figure 5. This diagram is a plot of measured data points for both head and body phantom combined and displayed on the same axes. A straight line is drawn as a best fit for the data points shown. Figure 6 displays the calculated isodose lines obtained from a patient's data, who was treated with colloidal P-32 for pancreatic cancer on a 2-D transaxial SPECT slice. The images were obtained by bremsstrahlung SPECT and each slice shows a nice patient body contour obtained by using the two compton backscatter sources, as well as the area of high P-32 activity. The isodose lines displayed and projected on the 2-D transaxial slice are 5, 4, 3, 2 and 1 kGy (500, 400, 300, 200, and 100 krad) lines outwardly. The same data expanded in 3-D are shown in Figure 7, where body contour was obtained from the data acquired for bremsstrahlung SPECT and a 3 kGy (300 krad) isosurface dose is shown around the site of P-32 injection. Figures 8-a and 8-b show the DVHs for two of the patients treated with this technique.

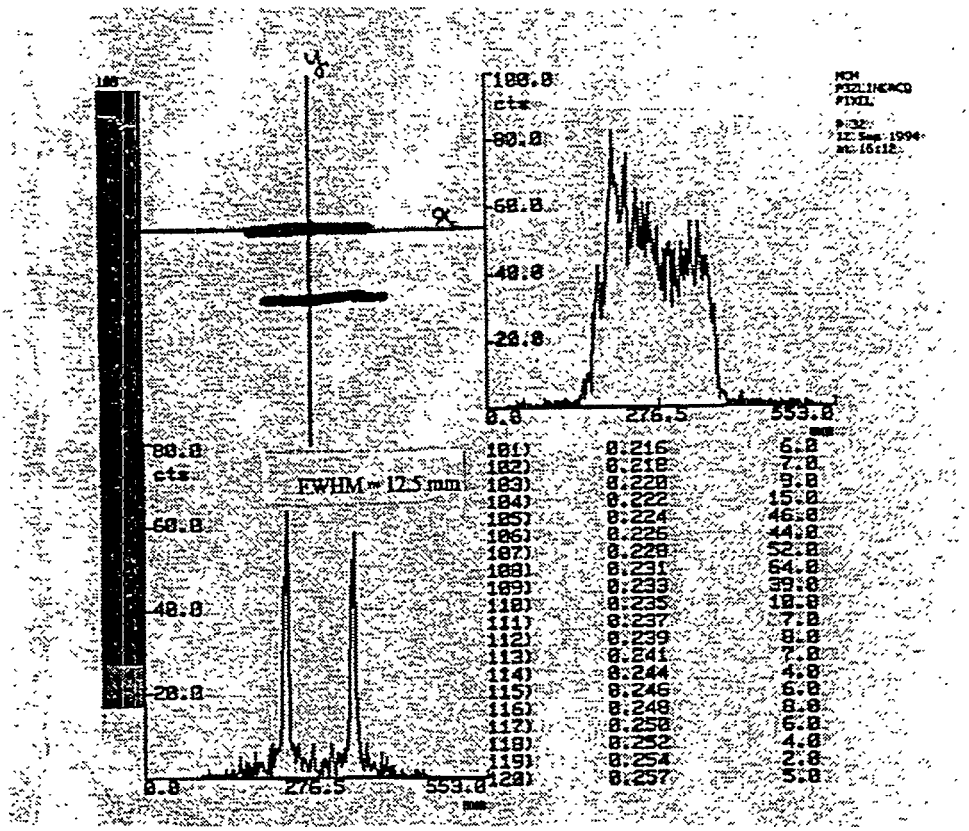

Figure 2-a. Plot of counts versus distance in both X (along the P-32 line sources) and Y (crossing the line sources) planes. This diagram was generated using the GE software.

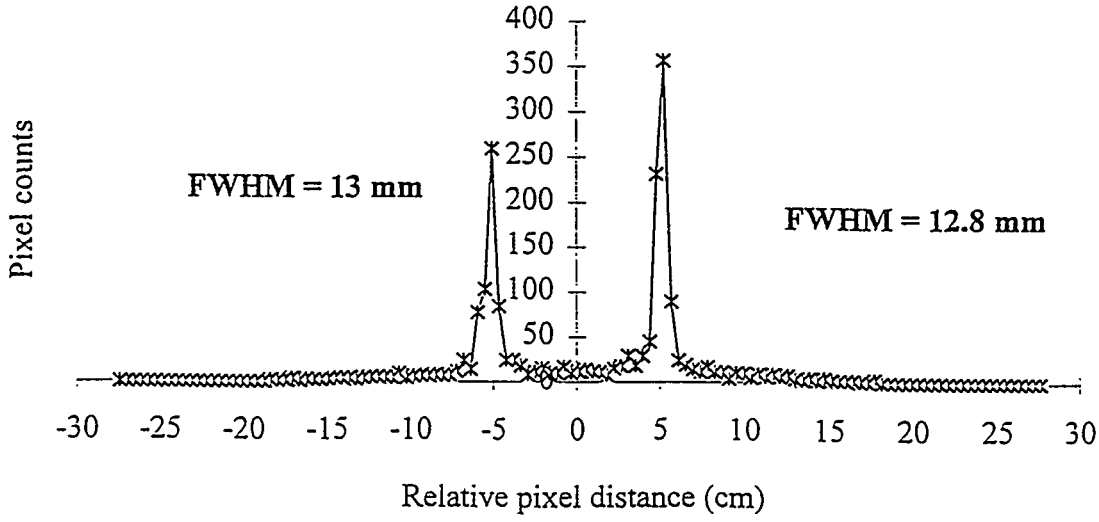

Figure 2b. In air planar measurement of the camera's point spread function using line sources placed along the detector's X-axis.

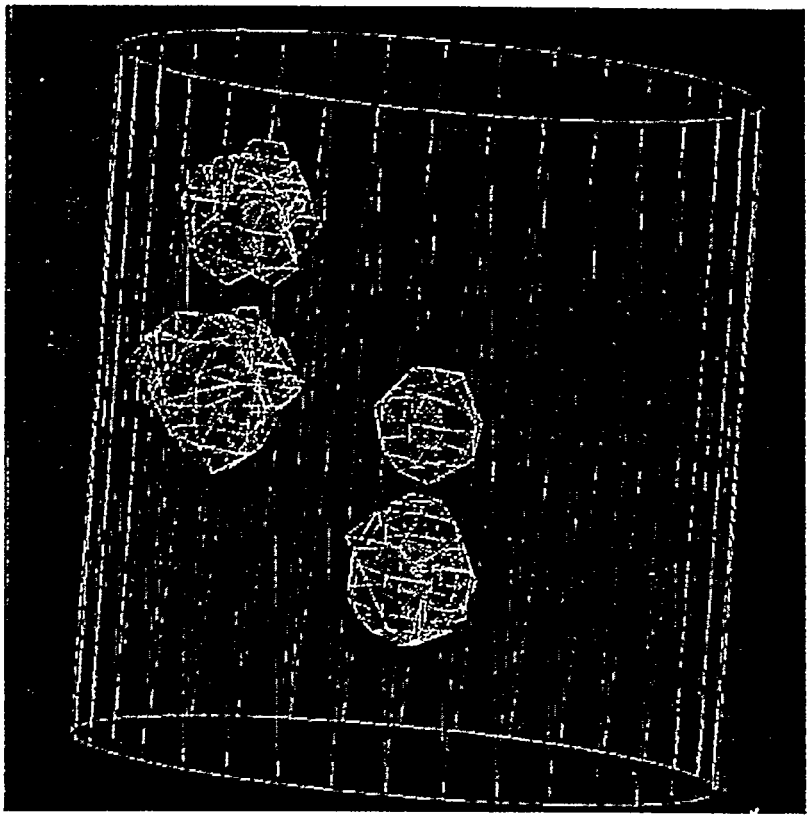

Figure 3. Isocount distributions (lines) around the Tc-99m point sources (small solid cylinders) using a head phantom and SPECT imaging data.

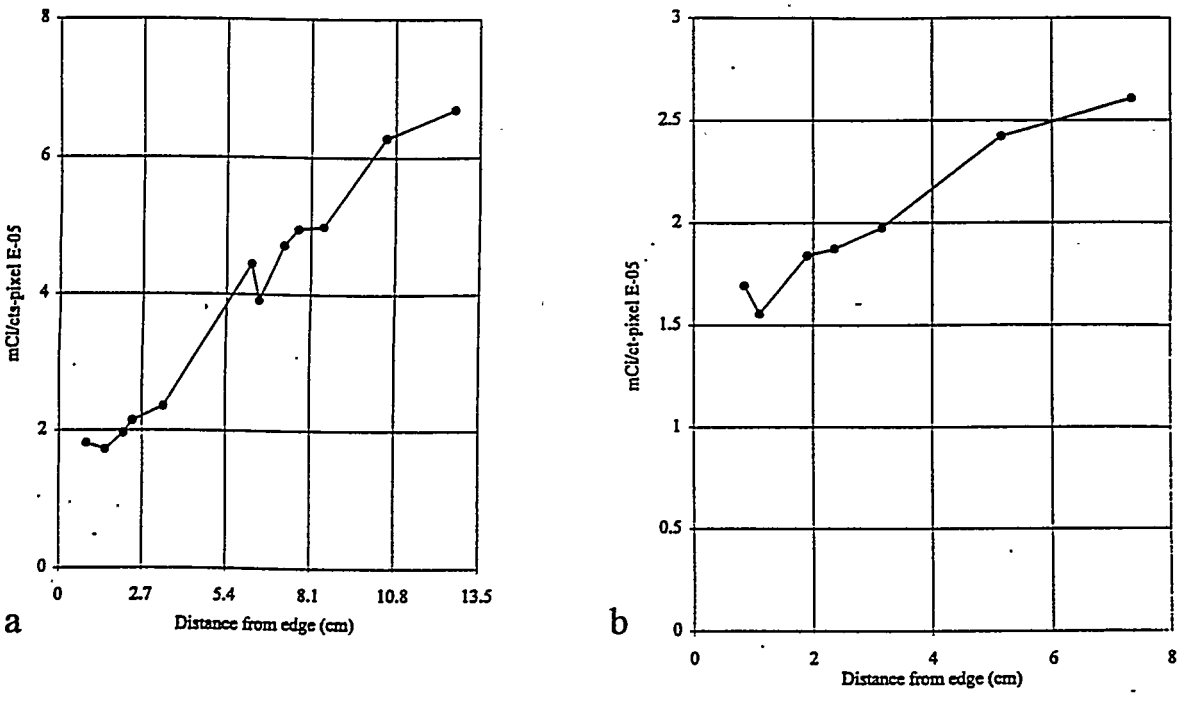

Figure 4. a) Activity distribution for a point source as a function of distance from the edge for the body phantom and b) for the head phantom.

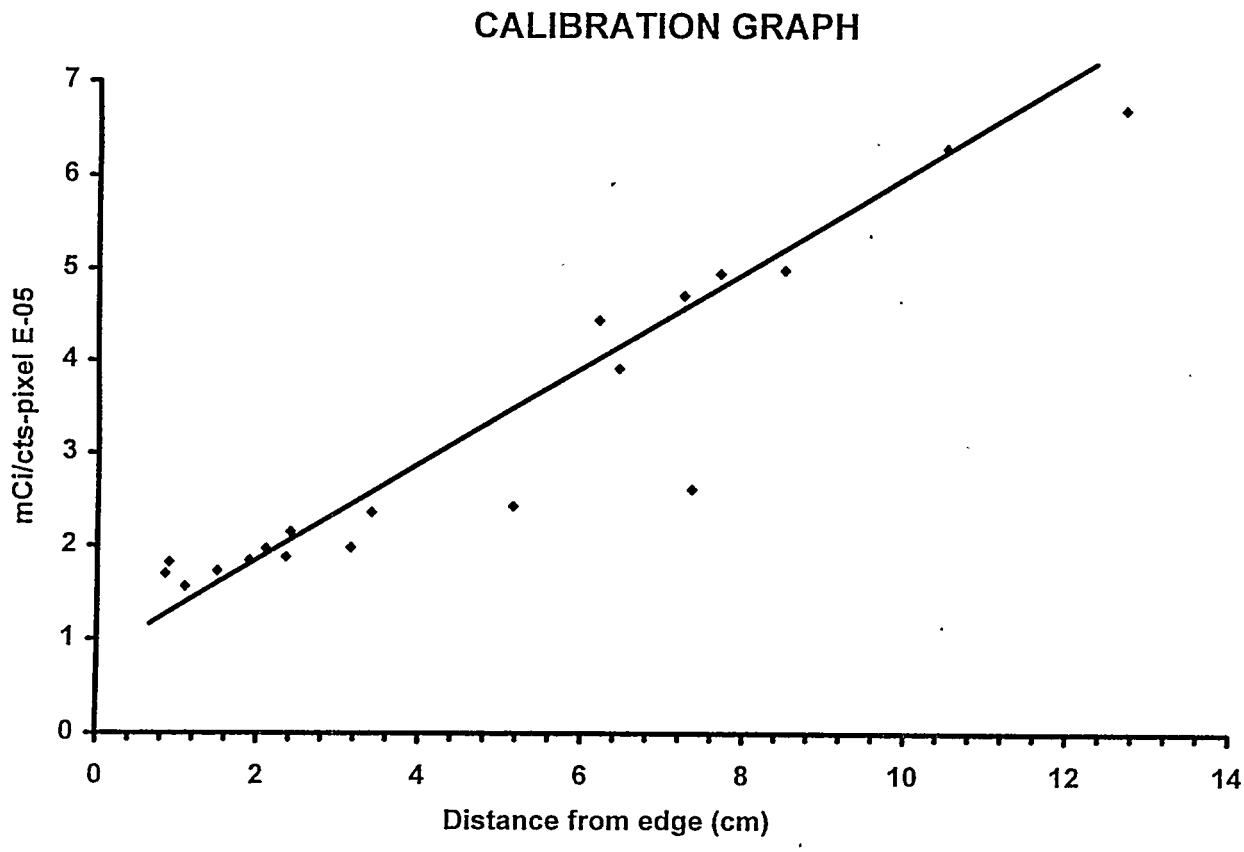

Figure 5. Activity distribution plotted vs. distance from the phantom edge obtained by plotting head and body phantom data on the same graph.

CONCLUSIONS

Data from the GE-Maxxus and from the Siemens gamma camera were read into a UNIX box and through various tests the accuracy and completeness of the transferred information was verified. Other factors such as the system's linearity of response, resolution, and efficiency were measured for P-32 bremsstrahlung SPECT imaging and a set of parameters were chosen for optimum results. This included the choice of the collimator, energy windows prior to collection of data, and algorithm parameters in reconstructing the images. Calibration values (counts/activity) were determined in 3-D space from the Tc-99m experiment without applying the attenuation correction algorithm provided by the manufacturer. In the case of P-32, the calibration values were converted to reflect the activity in a given pixel from the number of counts obtained from SPECT data. Using the calibration curve, the image obtained from bremsstrahlung SPECT data was converted to activity and then to dose. Two-dimensional isodose lines were generated and displayed on SPECT slices using the patient's data and 3-D isodose surface distributions were generated directly from SPECT image data.

The absorbed dose results were verified utilizing the modified Loevinger's point function in a computer program written in FORTRAN for calculation of dose. The anatomic site of injection was also verified through CT-SPECT image co-registration (14). The technique developed for calculation of DVHs accurately represented dose-volume relationship in the target organ and the dose-volume matrix.

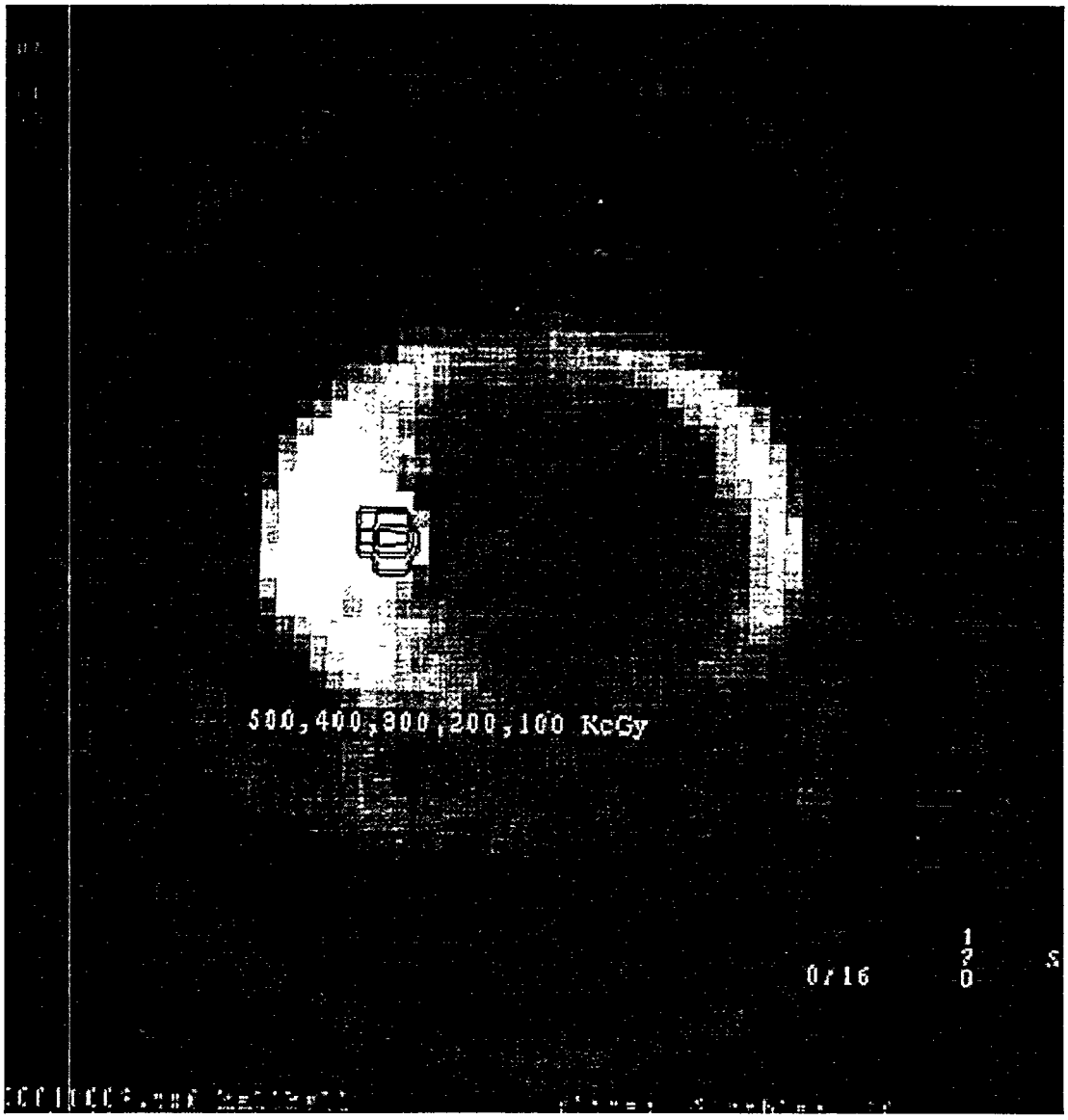

Figure 6. Isodose distribution displayed on a transaxial SPECT slice and generated from bremsstrahlung SPECT imaging of P-32 from a patient with cancer of the pancreas. The isodose lines shown are 5, 4, 3, 2, and 1 kGy.

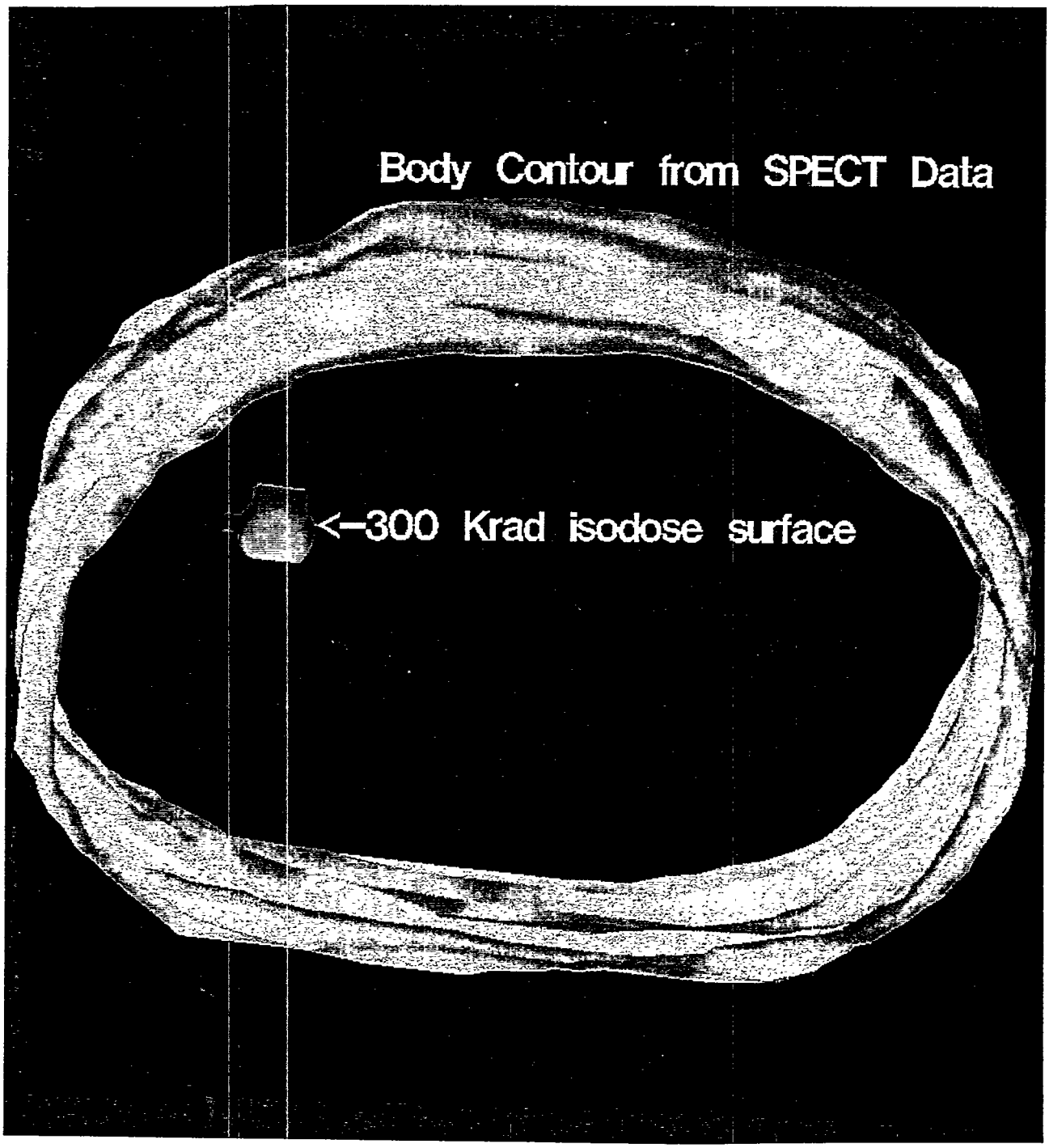

Figure 7. Three-dimensional isodose surface distribution and outer boundary of a patient determined from bremsstrahlung SPECT data.

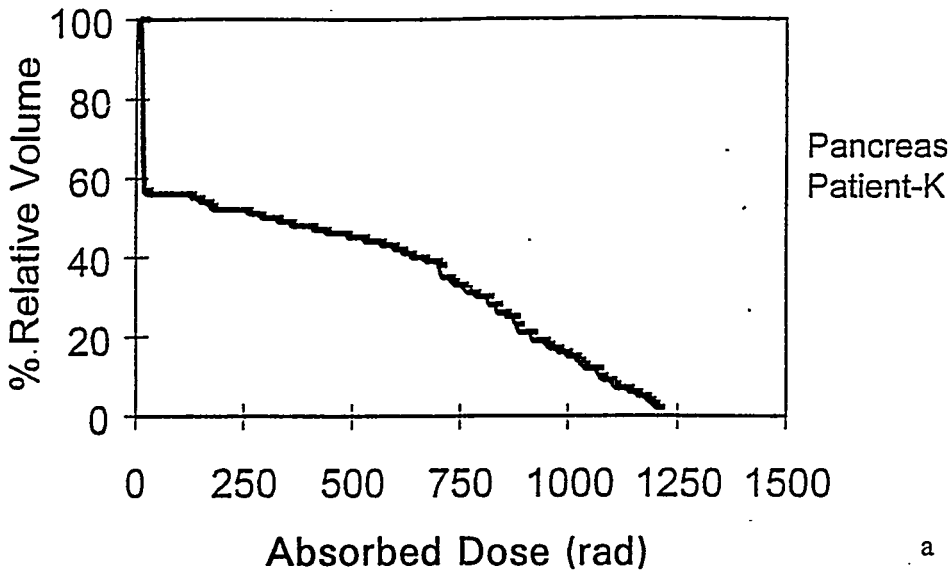

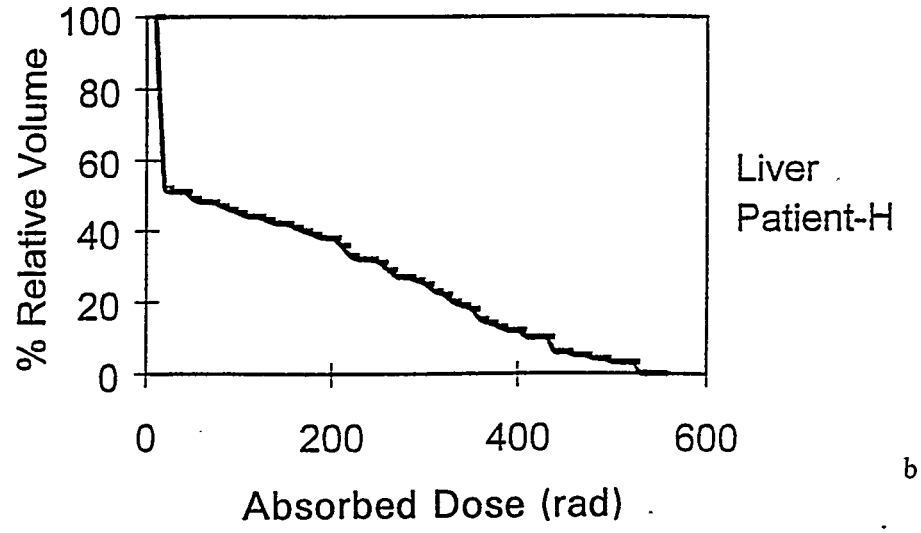

Figures 8-a and 8-b. Two examples of patient DVHs calculated from the bremsstrahlung SPECT data.

REFERENCES

1. American Cancer Society (ACS) Cancer Facts and Figures, Atlanta, GA, 1994.
2. Jordan GL, Jr. Pancreatic Resection for Pancreatic Cancer. In: Dobelbower, RR (ed.) Gastrointestinal Cancer Radiation Therapy, pp. 116-143, Springer-Verlag, New York, 1987.
3. Larson SM, Cheung NK and Leibel SA. Radioisotope conjugates biologic therapy of cancer, DeVita VT, Hellman S. and Rosenberg SA, (eds.) L.B. Lippincott Co., Philadelphia, PA, 21(3):496-511, 1991.
4. Stillwagon GB and Order SE. Polynomial antibodies in therapy. Biologic therapy of cancer. DeVita VT, Hellman S and Rosenberg SA, (eds.) L.B. Lippincott Co., Philaldephia, PA, 22(6): 588-601, 1991.
5. Order SE, Siegel JA, Lustig RA, Principato R., Zeiger LS, Johnson E, Zhang H, Lang P and Wallner PE. Infusional brachytherapy in the treatment of non-resectable pancreatic cancer. A

new radiation modality (Preliminary report of the phase I study). Antibody, Immunoconjugates and Radiopharmaceuticals 7(1):11-27, 1994.
6. Tepper JE, Noyes D, Krall JM, Sause WT, Wolkov HB, Dobelbower RR, Thompson J, Owens J and Hanks GE. Intraoperative radiation therapy of pancreatic carcinoma: A report of RTOG-8505. Int J Rad Oncol Biol Phys 21:1145-1149, 1991.
7. Siegel JA, Zeiger LS, Order SE and Wallner PE. Quantitative bremsstrahlung single photon emission computed tomographic imaging: Use for volume, activity, and absorbed dose calculations. Int J Radiat Oncol Biol Phys 31:953-958, 1995.
8. Loevinger R and Berman M. A schema for absorbed dose calculations for biologically-distributed radionuclides. J Nucl Med Suppl. No. 1 MIRD Pamphlet No 1, pp 7-14, 1968.
9. Snyder WS, Ford MR, Warner GG, et al. Estimates of absorbed fractions for monoenergetic photon sources uniformly distributed in various organs of a heterogeneous phantom. MIRD Pamphlet No 5, J Nucl Med 10: Suppl. No. 3, pp. 5-12, 1969.
10. Snyder WS, Ford MR, Warner GG and Watson SB. "S," Absorbed Dose per Unit Cumulated Activity for Selected Radionuclides and Organs. MIRD Pamphlet No. 11, Society of Nucl Med, 1975.
11. Cross WG, Freedman NO and Wong PY. Beta-ray dose distributions from point sources in an infinite water medium. Health Phys 63(2):160-171, 1992.
12. Berger MJ. Distribution of absorbed dose around point sources of electron and beta particles in water and other media. MIRD Pamphlet No. 7; J Nucl Med 12: Suppl. 5:5-23, 1971.
13. Hine G and Brownell G. Radiation Dosimetry. Academic Press, New York, NY, 1956, p 709.
14. Parsai EI, Ayyangar KM, Dobelbower RR and Siegel JA. Clinical fusion of three-dimensional images using bremsstrahlung, SPECT and CT. J Nucl Med 38(2):319-324, 1997.

QUESTIONS

Humm: In what form is the P-32 injected and what is the biological clearance half-time in the tumor at the injection site?

Parsai: We used a colloidal form (chromic phosphate). The biological half-time is assumed long, so the rate of clearance is the physical half-life.

Fisher: Is it too early to describe the clinical effectiveness of infusional brachytherapy using P-32 chromic phosphate for treatment of pancreatic cancer?

Parsai: This is a question for medical doctors but from our discussions with physicians and papers written on the subject, I understand that the survival time is increased and quality of life post diagnosis has improved.

Sgouros: How do you interpret the rapid initial drop in the DVH's?

Parsai: The volume of tissue in the calculation matrix containing normal tissue and tumor was larger than the tumor area where maximum dose was intended to be delivered.

Harper: Were any of these procedures carried out using surgical exposure?

Parsai: No, this is an outpatient procedure

USING SPECT IN THE CALCULATION OF THE ADMINISTERED ACTIVITY IN THYROID RADIONUCLIDE THERAPY: ELIMINATION OF THE WEIGHT ESTIMATE

Muller SH, Valdés Olmos RA, Hoefnagel CA
Department of Nuclear Medicine
Netherlands Cancer Institute, Antoni van Leeuwenhoek Huis
Plesmanlaan 121
1066 CX Amsterdam
The Netherlands

ABSTRACT

Purpose. To find a scintigraphic method for the determination of the dosage (administered activity) in ^{131}I therapy of the thyroid which avoids the unreliable scintigraphic volume determination.
Method. The requested dosage is often specified as the amount of activity which must be administered to reach the desired uptake per gram (activity concentration or specific activity, MBq/g). If no additional information from CT, MRI or US is available, uptake and weight (size) are determined from scintigraphy. Scintigraphic size determination is rather inaccurate, in particular in the case of an inhomogeneous distribution e.g. cysts or nodules. Using a SPECT study of the thyroid with ^{123}I, it is possible to determine the activity concentration directly, without the necessity of determining the size of the thyroid. Such a procedure requires that a reference bottle containing a known concentration of radionuclide is scanned simultaneously with the patient. The reference should contain a concentration which is comparable to that in the thyroid, typically 10% to 20% of the injected dosage for a 20 cm^3 bottle. After reconstruction, the average count value of a small ROI (< 1cm^2) or the maximum count value is determined in an area with viable thyroid tissue and in the center of the reference. The ratio of these two count values multiplied by the known activity concentration in the reference bottle directly yields the uptake per gram per injected dosage, without the need to determine the size of the thyroid.
Results. Phantom studies have shown that this method yields reliable ratios independent of the size of the reference bottle if the diameter is more than 20 mm . Data for three patients with a uniform uptake in the thyroid show agreement within 20% between the concentration determined from planar scintigraphy + CT and direct determination of the concentration.
Discussion. This method avoids the inaccuracies involved in the volume determination and the need for additional CT, MRI or US examinations. An additional advantage is that the local activity concentration in a small region is obtained, enabling the determination of the uptake in that part of the thyroid that should be treated which can be useful in the case of an inhomogeneous uptake, e.g, cysts or nodules.

INTRODUCTION

^{131}I sodium iodide is used in radionuclide therapy of hyperthyroidism [1]. The absorbed dose in the thyroid tissue is determined by the dosage (administered activity), by the uptake and clearance of ^{131}I and by the functioning mass of the gland. Treatment outcome is determined by the dose and radiosensitivity of the gland. Measuring all factors before treatment and adjusting the dosage should improve the efficacy of the treatment [2].

In studies of the impact of dose calculation on treatment outcome, uptake and mass are usually measured. Uptake can easily and reliably be determined from planar scintigraphy. The accuracy of the mass estimate depends strongly on the method. Mass estimates from planar scintigraphic studies alone are not reliable [2,3]. The accuracy of SPECT (single-photon emission computed tomography) is limited due to the uncertainty about the threshold value separating thyroid tissue from its environment [4]. CT (computerized tomography), MRI (magnetic resonance imaging) or US (ultrasound) would yield more accurate estimates, but require considerable postprocessing to measure the volume. Moreover, the patient has to undergo another examination in addition to the scintigraphic scan which is used to determine the uptake. In the case of nodular goiter, determination of the functioning volume is even more difficult [1]. Retention is estimated from 20 or 4 hour uptake [5], although variation in actual retention may result in doses differing by a factor of two or more [6]. Radiosensitivity cannot be determined presently, and the variation in this factor is unknown.

If not all factors (uptake, mass, retention) are carefully controlled, accuracy of the dose calculation is uncertain. Depending on the accuracy of the dose calculation, studies on the use of a calculated dosage instead of an empirical dosage may or may not show an improved treatment outcome [7,8,9]. Therefore, although a careful calculation of administered activity is probably preferable, currently the uncertainty about the impact on treatment outcome and the effort required for the calculation do not simulate the calculation of dosage in clinical practice [1,2,10]. Clinical acceptance of dosage calculation will improve if the trade-off between cost and effort is improved.

In first approximation, the dose is linearly related to the ratio of uptake and volume [2]. Following the usual procedure, this ratio is determined from the uptake in the whole thyroid and the weight (size) of the thyroid. Instead of measuring uptake and volume separately, we propose a method which directly determines the activity concentration from a ^{123}I SPECT examination without time-consuming postprocessing. The elimination of additional examination such as CT, MRI or US may make this method more acceptable for clinical routine use.

METHODS AND PATIENTS

The dosage is specified as the amount of activity which must be administered to reach the desired uptake per gram (activity concentration or specific activity, e.g. MBq per gram) in viable tissue [2]. Using a SPECT study of the thyroid, it is possible to determine the activity concentration directly, avoiding the determination of the size of the thyroid. Such a procedure requires that a reference bottle (with a diameter of more than 20 mm) containing a known concentration of radionuclide is scanned simultaneously with the patient. The reference should contain a concentration which is comparable to that in the thyroid, typically 10% to 20% of the injected dosage for a 20 cm^3 bottle. After reconstruction using a smoothing filter, the average count value of a small region of interest (ROI) (< 1 cm^2) or the maximum count value is determined in an area with viable thyroid tissue. The same values are determined in the center of the reference bottle. The ratio of these two values multiplied by the known concentration in the reference bottle directly yields the uptake per gram (per injected activity).

Several assumptions underlying this method were verified in vitro using a phantom with the approximate dimensions of the adult neck. This phantom consisted of a two liter bottle with a square area of 10x10 cm^2 and smaller cylindrical bottles and spheres near its surface (either inside to simulate thyroids or outside to simulate references of different sizes). Using ^{99m}Tc solutions, both the influence of concentration ratios and the influence of the size of the bottles and spheres were evaluated. The small energy difference between ^{99m}Tc and ^{123}I (140 versus 159 keV) allows the use of ^{99m}Tc for the phantom experiments.

In vivo this method was compared to the method which determines the uptake from planar scintigraphy and volume from a CT scan in four patients: one male (age 57, half of the thyroid previously resected), and three females (age 42, 75, 85). Three patients had a diffuse uptake in the thyroid, the eldest patient had a multinodular goiter. Scintigraphic scans (Planar and SPECT) were obtained 4 hours postinjection of 90 MBq ^{123}I. After 24 hours, only a planar scan was made. A CT scan was obtained from each patient. One or two reference bottles of 20 cm^3 volume were taped in a shallow depression of the neck and filled with 5 to 20 MBq ^{123}I. The uptake from planar scintigraphy was obtained by dividing the number of counts in an ROI around the thyroid with an ROI around the whole reference bottle (each corrected for the background) and multiplying by the amount of activity in the reference bottle.

SPECT scans were obtained using the following parameters: ADAC Dual Head Camera, LEHR collimator, 64x64x16 matrix, 48 azimuths, 30-45 seconds per azimuth, 20% window, zoom 1.85, reconstruction filter back projection (Butterworth 3D, order 3, cut-off 0.7). The long axis of the cylinders and reference bottles was always oriented perpendicular to the reconstructed SPECT slices.

RESULTS

No difference was found between ratios determined using the average count value of a small ROI or the maximum count value in the area of interest, as should be expected considering the rather strong smoothing during the back-projection.

Phantom Experiments

Less than 5% difference was found between identical cylinders mounted inside or outside on the surface of the neck bottle. The relationship between diameter of a cylinder or sphere mounted on the outer surface of the neck bottle and measured concentration is shown in Figure 1. All objects were filled with the same ^{99m}Tc solution. Small spheres underestimate the concentration more than thin cylinders with the same radius. This is due to the averaging effect of the noise reducing filtering in the SPECT backprojection calculation. The figure shows that for a cylindrical bottle with an inner diameter of more than 20 mm less than 10% underestimation results. Therefore, in the patient studies, a commonly used 20 cm^3 bottle with a diameter of 25 mm was chosen as a reference. If the diameter becomes larger than 40 mm, attenuation effects cause a decrease of counts in the center of the bottle.

Using a series of 25 mm bottles filled with a range of concentrations (maximum dilution 8 times), a linear relationship between true concentration and measured SPECT value was found with a slope of 1 (+/- 0.03, 1SD).

Patient Studies

The data for all patients are shown in Table 1. The values given for the reference with a concentration of 0.3 MBq/g (patients 1 and 2) are probably too high due to imperfect dose calibration (see discussion). Patient 4 had a nodular goiter. The volume used in this calculation is the volume of the whole thyroid. The volume of the largest nodule as measured on the CT scan was 45 cm^3.

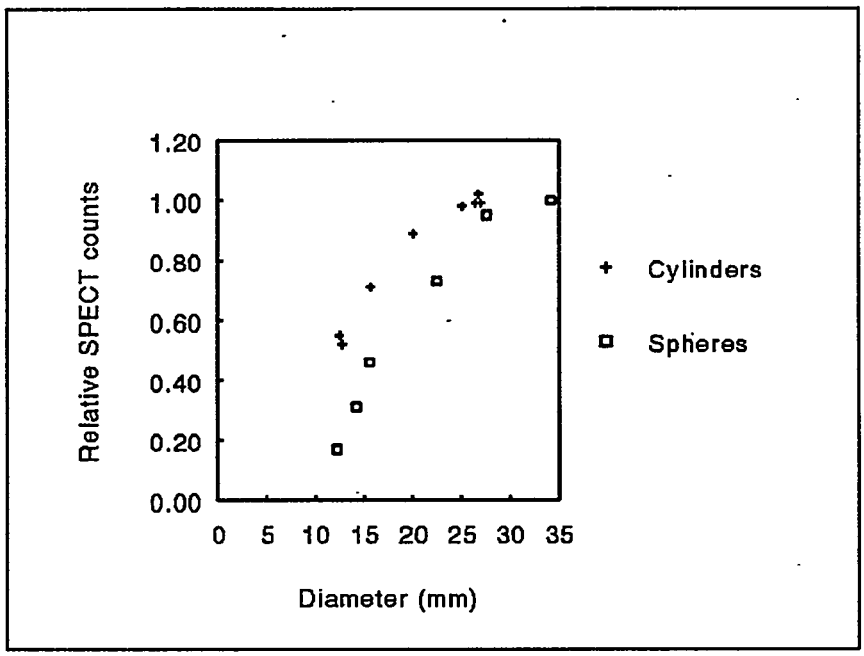

Figure 1. Relation between diameter and maximum SPECT count value for cylinders and spheres of different sizes. Values are relative to that of the largest sphere (diameter 34.2mm).

Table 1

Overview of Data for All Patients: Volume of the Thyroid as Measured by CT, Activity Concentration in the Reference Bottle, and Activity Concentration in the Thyroid Determined with the Uptake from Planar Scintigraphy Combined with the CT Volume, and Determined Directly from the SPECT Scan.

Patient # (age)	Volume CT (cm^3)	Reference MBq/g	Planar + CT MBq/g	SPECT MBq/g
1 (42)	28	0.8 0.3	0.9 1.2	1.1 1.4
2 (57)	52	0.8 0.3	0.31 0.46	0.26 0.41
3 (75)	45	0.4	1.6	1.3
4 (85)	150	1.1 0.36	0.1 0.1	0.42 0.40

DISCUSSION

Phantom Experiments

The phantom studies have shown that the direct determination of activity concentration is technically feasible with a cylindrical reference bottle provided that the diameter of a cylinder is more than 20 mm. In that case less than 10% underestimation will result. It is also important that the

thyroid should be sufficiently large, which will usually be the case for patient hyperthyroidism. Because of the linear relationship between actual and measured concentration, the concentration in the reference bottle may differ from that in the thyroid. The price of ^{123}I will limit the amount of activity used for the reference, but sufficient activity must be used to avoid excessive noise. If a 20 cm^3 bottle is used, it is recommended that only 10 to 20% of the activity be administered.

Patient Studies

In general, the agreement between the methods is quite good for patients with a homogeneous uptake in the thyroid (less than 20% deviation). The new method is certainly superior to methods which determine volume from scintigraphy. Errors in the volume calculation with planar scintigraphy (and therefore in concentration) may easily exceed 50% [3]. SPECT can determine volume more accurately, but requires considerable effort [4], and if a SPECT scan is available, the new method can be used more easily.

If a study with a larger number of patients would confirm that both methods yield comparable results, the new, simpler method can be used to calculate dosage instead of the method using an additional CT, MRI or US scan without discontinuity.

As the true concentration is not known, it is impossible to decide which method is more accurate. In the case of nodular goiter the new method is probably superior, because it yields the local uptake if the nodule is sufficiently large. This is illustrated by the data for patient 4, where planar uptake combined with CT volume of the whole thyroid yields an activity concentration which is only 25% of that found using the direct method. On the CT scan, the volume of the largest nodule was 45 cm^3, but precise identification of the nodule in the planar images was impossible due to the hot background from the surrounding thyroid. Also determination of the uptake from the SPECT images was ambiguous, as it was not clear which volume and threshold should be used. Any concentration between 0.05 and 0.3 MBq/g is possible. The direct method yielded the even slightly higher value of 0.42 MBq/g. Unfortunately, the true concentration in the nodule is not known. Future phantom experiments are necessary to test the value of the method in the case of nodular goiter.

^{123}I was chosen as a radionuclide to use in the SPECT study instead of ^{131}I because the quality of the images is much better (159 keV instead of 364 keV) and because ^{131}I may cause transient radiation damage, resulting in reduced uptake of the therapy dosage [10]. Using ^{123}I, dose calibration must be performed carefully [12], preferably using a copper shield to reduce the impact of low energy characteristic X-rays. The large difference in concentrations between the two references for the first two patients was probably due to inadequate dose calibration (without copper shield) of the reference bottles. As the calculation of concentrations is made relative to the standard, the results for both methods are equally affected by this error. The half-life of ^{123}I is only 13 hours. Quantitative SPECT imaging after 24 hours is not possible, but retention can be determined from planar scintigraphy.

Summarizing, the method for direct determination of the concentration from SPECT has the following advantages.

- Background corrections are not necessary, as the concentration in the surrounding tissue is very low, and is negligible in the SPECT image.
- The method is quick and easy to use; no additional examinations are required.
- Because the reference bottle and thyroid are in a similar environment (both close to the surface of the neck) attenuation effects can be neglected. Only in the case of very large goiters is a correction required. It might even be possible to use 180° SPECT instead of the full 360° SPECT, gaining a factor two in SPECT acquisition time.

CONCLUSION

Direct determination of activity concentration is feasible, avoiding the inaccuracies involved in the volume determination and the need for additional CT or MR examinations. An additional advantage is that the local activity concentration in a small region is obtained, enabling the determination of the uptake in that part of the thyroid that should be treated. This may be useful in the case of inhomogeneous uptake, e.g. cysts or nodules.

REFERENCES

1. Clarke SEM. Radionuclide therapy of the thyroid. Eur J Nucl Med 18:984-991, 1991.
2. Becker DR. Radioactive iodine (^{131}I) in the treatment of hyperthyroidism. In: Beckers V. (ed) Thyroid diseases, Pergamon Press, Paris, pp 145-158, 1982.
3. Huysmans DAKC, De Haas MM, Van den broek WJJM, Hermus ARMM, Barentsz JO, Corstens FHM and Ruijs SHJ. Magnetic resonance imaging for volume estimation of large multinodular goiters, A comparison with scintigraphy. Brit J Radiol 67:519-523, 1994.
4. Mortelmans L, Nuyts J, Van Pamel G, Van den Maegdenbergh V, De Roo M and Suetens P. A new thresholding method for volume determination by SPECT. Eur J Nucl Med 12:284-290, 1986.
5. Hayes AA; Akre CM and Gorman CA. ^{131}Iodine treament of Graves' disease using modified early ^{131}iodine uptake measurements in therapy dose calculations. J Nucl Med 31:519-522, 1990.
6. Fueger GF. Dosimetrie and dosierung der radiojodtherapie mit 131-jod. Acta Med Austriaca 14:87-98, 1987.
7. Huysmans DAKC, Hermus ARMM, Corstens FHM and Kloppenborg PWC. Long-term results of two schedules of radioiodine treatment for toxic multinodular goiter. Eur J Nucl Med 20:1056-62, 1993.
8. Franklyn JA, Daykin J, Drolc Z. Farmer M and Sheppard MC. Long-term follow-up of treatment of thyrotoxicosis by three different methods. Clin Endocrinol 34:71-6, 1991.
9. Jarlov AE, Hegedus L., Kristensen LO, Nygaard B and Hansen JM. Is calculation of the dose in radioiodine therapy of hyperthyroidism worth while? Clin Endocrinol 43:325-9, 1995.
10. EANM Task Group Radionuclide Therapy. Radionuclide Therapy: From Palliation to Cure. Monograph [^{131}I] Iodide. 1993.
11. Park HM, Perkins OW, Edmondson JW, Schnute RB and Manatunga A. Influence of diagnostic radioiodines on the uptake of ablative dose of iodine-131. Thyroid 4:49-54, 1994.
12. Harris CC, Jaszczak RJ, Greer KL, Briner WH and Coleman RE. Effects of characteristic x-rays on assay of 123I by dose calibrator, J Nucl Med 25:1367-70, 1984.

QUESTIONS

Humm: Did you look at the variation in the number of counts on the central axis SPECT slice for calibration bottles of different size with the same specific activity? Scatter fraction will increase with increasing bottle size.

Muller: Yes, I looked a little at variation in size and at this size (20cc) the bottle is so large that SPECT procedures are no longer a major concern, but I agree that this point requires a more careful investigation. Anyway, I recommend that the bottle size be adapted to the expected size of half the thyroid.

Cloutier: Would it be important to put a tissue-equivalent material around your bottle?

Muller: No, due to the SPECT imaging from all sides and the superficial position of the thyroid, this would not be important. In clinical practice it would moreover be an unwelcome complication.

PRACTICAL SIMPLIFICATIONS FOR RADIOIMMUNOTHERAPY DOSIMETRIC MODELS

Shen S, DeNardo GL, O'Donnell RT, Yuan A,
DeNardo DA, Macey DJ and DeNardo SJ
Radiodiagnosis and Therapy Section
University of California at Davis Medical Center,
Sacramento, California 95816

ABSTRACT

In the development of dosimetric methods for radioimmunotherapy, practical simplifications in the dosimetric models were introduced. This study evaluated the magnitude of uncertainty associated with practical simplifications for: 1) organ mass of the MIRD phantom; 2) radiation contribution from target alone; 3) interpolation of S value; 4) macroscopic tumor uniformity; and 5) fit of tumor pharmacokinetic data.

We found:

1) 50% of 54 lymphoma patients had a body mass that deviated by >19% from that of reference man, and had a spleen mass that deviated by >120% from that of reference man;
2) for therapeutic radionuclides ^{90}Y, ^{131}I and ^{67}Cu, > 93% of the total mean radiation dose was from activity in the target for liver, spleen, lungs and kidneys;
3) interpolation of log mass values vs. log S(p) or log S values were performed using existing organ S values from MIRD Pamphlet No. 11. These S values from interpolation were compared to those derived from MIRD Pamphlet No. 8 for 4-100 g spheres for doses from activity in the sphere only. The differences between these methods were <4% for ^{67}Cu and ^{131}I, but a difference of 18% was found for ^{111}In since the latter imaging radionuclide has primary p emissions;
4) as great as a 3-fold regional difference in tumor dose was found due to macroscopic nonuniformity in large tumors (>100 g) using SPECT;
5) the difference in doses for 30 tumors between mono- and biexponential methods were evaluated for ^{131}I, ^{67}Cu and ^{111}In labeled Lym-1. The mean differences were 4 and 5% for ^{67}Cu and ^{111}In, but was 14% for ^{131}I, reflecting the influence of the longer physical half-life.

The present study supports and expands observations made by others that uncertainties in dosimetry due to simplifications can range from substantial to inconsequential depending on the assumptions made, choice of radionuclide and organ size. However, carefully selected simplifications for a specific application can be made without detrimental consequences to the dose-response model.

INTRODUCTION

Radiation dosimetry is potentially useful for assessment and prediction of efficacy and toxicity for radionuclide therapy. The usefulness of these dose estimates relies on the establishment of a dose-response model using accurate pharmacokinetic data and a radiation dosimetric model. Due to the complexity in radiation dose estimation, many practical simplifications have been introduced in the dosimetric modeling for clinical trials of radioimmunotherapy. Although research efforts are generally needed to improve the simplifications used at each stage of model development, practical simplifications are often possible for specific applications without significant consequences to the dose-response model.

The purpose of the present study was to evaluate the range of the deviation associated with practical simplifications in dosimetric modeling and to determine which simplifications were good approximations for specific applications of radioimmunotherapy. The following five simplifications were evaluated: 1) organ mass of reference man; 2) radiation contributed from the target alone; 3) interpolation of S value; 4) macroscopic tumor uniformity; and 5) fit of tumor pharmacokinetic data.

MATERIALS AND METHODS

Patients

Patients with advanced non-Hodgkin's lymphoma, chronic lymphocytic leukemia or breast cancer were treated with radiolabeled antibodies (1-5). Fifty-four ^{131}I-Lym-1, five ^{67}Cu-2IT-BAT-Lym-1, five ^{111}In-2IT-BAD-Lym-1 lymphoma patients, and four ^{111}In/^{90}Y-Bre-3 breast cancer patients were included in this analysis.

Four large tumors (>100 g) were used in analysis of tumor macroscopic nonuniformity. Ten tumors in ^{131}I-Lym-1 studies, 10 tumors in ^{67}Cu-2IT-BAD-Lym-1 studies and 10 tumors in ^{111}In-2IT-BAD-Lym-1 studies were selected for analysis of tumor data fitting. These 30 tumors all had a mass ≥ 4 g.

Evaluation of Simplifications

Organ mass of MIRD phantom. Current dosimetry techniques use population-averaged organ masses (MIRD phantom) for patient organ dose calculations (6, 7, 8). Because radiation dose is defined as energy deposited per unit mass, deviation of the organ mass of individual patients from that of the MIRD phantom may result in substantial error in organ dose estimates.

Fifty-four lymphoma patients treated with ^{131}I-Lym-1 were analyzed. Six patients had a splenectomy. The spleen mass for 42 patients was determined using x-ray CT images prior to treatment with ^{131}I-Lym-1. In the remaining 6 patients, CT images were not available so that spleen mass was determined from SPECT images acquired one day after administration of ^{131}I-Lym-1.

An irregular region of interest (ROI) was drawn manually to identify the spleen on each tomographic slice. The area of each ROI was multiplied by the slice thickness to obtain the spleen volume in each slice. All slices were subsequently summed to yield the total-spleen volume. The deviation in body and spleen mass for each individual patient was determined from masses assigned for the MIRD phantom (6).

Radiation contributed from the target alone. The radiation contribution can be considered in 3 parts: a) nonpenetrating radiation from activity only in the target; b) penetrating radiation from activity only in the target and c) penetrating radiation from activities in all sources other than the target including the remainder of the body. Because the absorbed dose contributed by penetrating

radiation in irregular small target volumes is difficult to calculate and represents a small fraction, this is often ignored. The present study evaluated the deviation introduced by ignoring part c) or both parts b) and c).

Yttrium-90, ^{131}I, ^{67}Cu, and ^{111}In were considered in this analysis. Yttrium-90 is a pure beta emitter and energy deposited in organs by ^{131}I or ^{67}Cu is dominated by nonpenetrating radiation. Indium-111 emits predominantly penetrating radiation. The analysis of organ dose included 54 patients from ^{131}I-Lym-1 studies; five from ^{67}Cu-Lym-1 studies and four from ^{111}In/^{90}Y-Bre-3 studies. Biodistribution of ^{90}Y-Bre-3 was assumed to be identical to that of ^{111}In-Bre-3 to derive radiation dosimetry for ^{90}Y. The cumulated activity for the remainder of the body was obtained in each case by subtracting cumulated activity in liver, spleen, lungs and kidneys from the total body (9).

Interpolation of S value. S values for tumors or organs in individual patients are not directly provided by the MIRD tables. One method used to obtain S values for tumors (10) or individual organs (including both penetrating and nonpenetrating radiation from activity in the target) was based on interpolating existing S values for organs found in MIRD Pamphlet No. 11 (8). Iodine-131, ^{67}Cu, and ^{111}In were considered in this analysis. Interpolation of log mass values vs. log S(p) (10) or log S values were performed. S values tested for interpolation were for the source as target (S(t←t)) for liver, spleen, kidneys, testes, thyroid, adrenals and ovaries.

The validity of this simple interpolation was evaluated for spherical sources. The S value for penetrating and nonpenetrating radiation from activity in a spherical tumor can be calculated using the MIRD formula (7) where penetrating absorbed fractions ϕ_p were obtained using MIRD data for

$$S_{p+np}(t\leftarrow t) = S_p(t\leftarrow t) + S_{np}(t\leftarrow t)$$
$$S_{p+np}(t\leftarrow t) = \Sigma\,(\Delta_p\phi_p + \Delta_{np})/m \qquad (1)$$

tumors from 4-100 g (11). The mean energies emitted per nuclear transition Δp and Δnp were obtained from MIRD data (12). Deviation for interpolated S values from the S values derived using Equation 1 were assessed for tumors from 4g to 100 g for ^{131}I, ^{67}Cu and ^{111}In.

Macroscopic tumor uniformity. The current dosimetric approach assumes a uniform distribution of activity in organs and tumors. We have observed a macroscopic nonuniform activity distribution in large tumors using gamma camera imaging. Four large tumors (>100 g) were analyzed in breast cancer patients treated with ^{90}Y/^{111}In-Bre-3 and in lymphoma patients treated with ^{131}I-Lym-1. SPECT images of tumors were acquired and the concentration ratio between highest and lowest uptake within each tumor were compared.

For purposes of illustration, in one study, tumor radiation doses were calculated using SPECT and planar-imaging data. A tumor zone of high uptake (outer shell) and low uptake (inner sphere) were divided using the maximum gradient of counts profile in SPECT slices (13). The ratio of counts between high- and low-uptake zones was determined from SPECT images acquired one day after injection of radiolabeled antibody. The total activity in the tumor immediately after injection, and daily up to day 10 was determined using quantitative planar imaging. Activity in each tumor zone was determined by assuming a constant ratio for uptake between the two zones as measured from SPECT. Differences in radiation dose were compared assuming a uniform distribution for the whole tumor or for separate zones of high and low uptake. For this large tumor, all beta energy emitted within the whole tumor or the high- and low-uptake zones was assumed to be absorbed within that zone.

Fit of tumor pharmacokinetic data. A monoexponential function is frequently considered a useful simplification to fit pharmacokinetic data of tumors (14, 15). The deviation due to this simplification is generally considered to be dependent on the length of the uptake phase. A biexponential form of the function

$$A = A_0 \{\exp(-b\,t) - \exp(-c\,t)\} \qquad (2)$$

was considered more appropriate for tumor data fitting because it considers both the uptake and clearance phase (16). Ten tumors from ^{131}I-Lym-1, 10 tumors from ^{67}Cu-2IT-BAD-Lym-1, and 10 tumors from ^{111}In-2IT-BAD-Lym-1 studies were fitted with monoexpontential and biexponential functions. Percentage deviation in tumor dose was determined between these methods.

RESULTS

Evaluation of Simplifications

Organ mass of the MIRD phantom. The whole-body mass of individual patients deviated moderately from that of the MIRD phantom(69880g) (6), but spleen mass deviated substantially because splenomegaly was frequently found in patients with B-cell lymphoma (Figure 1). Only 50% of the patients had spleen mass deviations < 120% from spleen mass of the MIRD phantom (174g), consequently, the deviation for spleen radiation dose from that using the mass of the MIRD phantom was substantial for this group of patients.

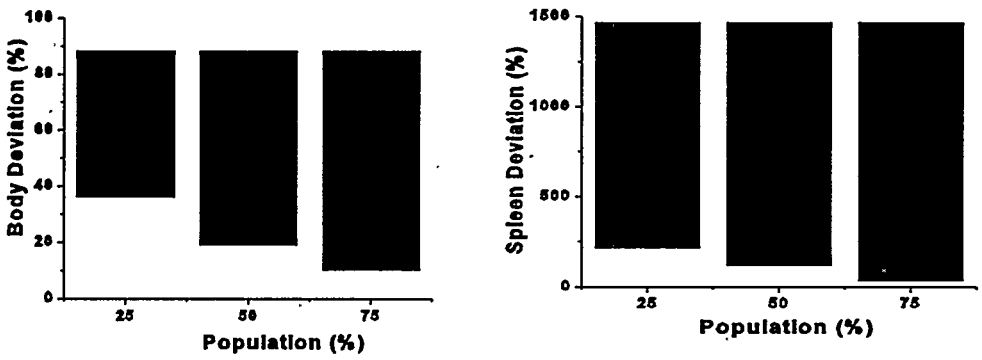

Figure 1. (Left) Whole-body and (Right) spleen mass of individual patients deviated from the mass of the MIRD phantom. Fifty percent of patients had spleen mass deviations ranging 120-1450% from that of the MIRD phantom.

Radiation contribution from target alone. The self-dose to organs was dominated by the nonpenetrating contribution from ^{131}I and ^{67}Cu (Table 1). The radiation dose from ^{131}I and ^{67}Cu in liver, spleen, lungs and kidneys showed an average deviation of 3.4% when penetrating radiation from sources other than the target was ignored. Self-radiation for ^{90}Y was essentially 100% of the total dose.

Table 1

Mean Percentage Contribution (range) of the Total Dose for Nonpenetrating Radiation from Activity only in Target (*np*), for Penetrating and Nonpenetrating Radiation from Activity only in Target (*np+p*).

	Liver	Spleen	Lungs	Kidneys
^{111}In				
np	28 (27-28)	37 (36-39)	36 (33-40)	30 (28-32)
np+p	88 (84-90)	79 (77-84)	68 (62-73)	59 (55-65)
^{131}I				
np	73 (68-74)	87 (82-90)	88 (87-89)	90 (73-93)
np+p	97 (91-99)	98 (91-100)	98 (96-99)	95 (77-98)
^{67}Cu				
np	86 (84-87)	93 (90-94)	90 (89-92)	93 (91-94)
np+p	99 (98-100)	97 (95-99)	96 (94-98)	93 (92-94)

Interpolation of S values. The log organ mass value vs. log S values were interpolated using existing S values from MIRD Pamphlet No.11 (8) [Figure 2 (Left)]. Correlations of linear regression fitting of these data were high ($r^2 > 0.99$) for all three radionuclides. The S values were interpolated as 0.321x tissue mass $^{-0.9809}$ for ^{67}Cu, 0.3874 x tissue mass $^{-0.9602}$ for ^{131}I, and 0.07296 x tissue mass $^{-0.8492}$ for ^{111}In. The S(*p*) values were interpolated as 0.002136 x tissue mass $^{-0.6390}$ for ^{67}Cu, 0.01132 x tissue mass $^{-0.7032}$ for ^{131}I, and 0.024656 x tissue mass $^{-0.7620}$ for ^{111}In. These results were in agreement with those reported by other investigators (10). Good agreement was found between spherical source S values derived from this interpolation and values derived from MIRD Pamphlet No. 8 (11) for the therapeutic radionuclides ^{131}I and ^{67}Cu [Figure 2 (Right)]. A difference of 18% was found for ^{111}In reflecting the greater effect of source geometry for this radionuclide with predominating penetrating emissions.

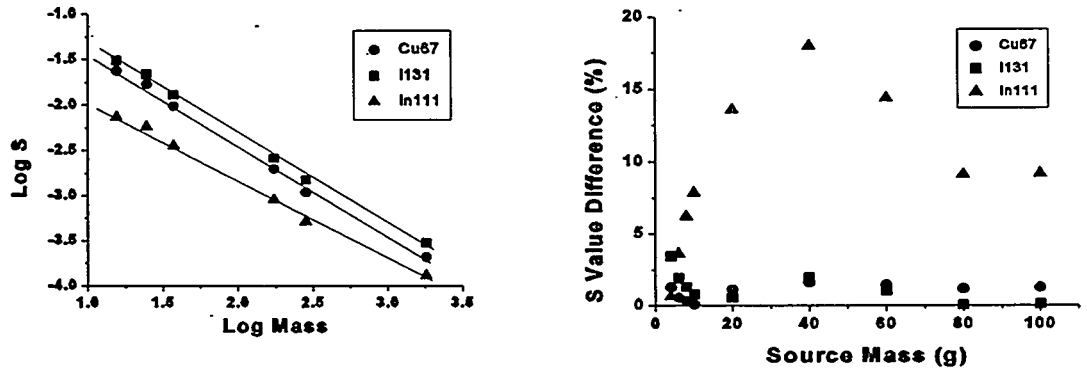

Figure 2. (Left): Interpolation of log organ mass values vs. log S values using existing S values from MIRD Pamphlet No. 11. (Right): Percentage difference in S values interpolated and derived using MIRD Pamphlet No. 8 data for spherical sources.

Macroscopic tumor uniformity. Substantial difference in activity concentration within the tumor was observed using SPECT (Table 2a). Variation in macroscopic ^{90}Y dose was illustrated for one large tumor assuming uniform distribution within low- and high-uptake zones (Table 2b). The uptake in the total tumor, low-uptake zone and high-uptake zone were 11.1%, 5.6% and 5.5%, respectively.

Table 2a

Macroscopic Nonuniformity Observed within Large Tumors. Ratio of Voxel Counts in Low-Uptake to High-Uptake Zones in Tumor ROI on SPECT Slices

	Tumor 1	Tumor 2	Tumor 3	Tumor 4
Volume (ml)	349	111	268	268
Radionuclide	^{111}In	^{111}In	^{131}I	^{111}In
Count Ratio (%)	0.30	0.51	0.71	0.62

Table 2b

Macroscopic Tumor Radiation Dose Variation in High- and Low-Uptake Zones

	Total Tumor			Low -take Zone			High-Uptake Zone		
	vol (ml)	T_b days	Gy/GBq average	vol (ml)	T_b days	Gy/GBq average	vol (ml)	T_b days	Gy/GBq average
Tumor 1	349	49	14.9	248	51	10.6	101	47	25.2

Fit of tumor pharmacokinetic data. The difference between dose estimates derived using monoexponential fitting and biexponential fitting was small for ^{67}Cu and ^{111}In, but was relatively large for ^{131}I [Figure 3 (Left)]. The effect of radionuclide half-life on the tumor data fit using a monoexponential function was illustrated in Figure 3 (Right). For radionuclides with short physical half-lives, the monoexponential function appears to be a good approximation even when biological data exhibit a prolonged uptake phase.

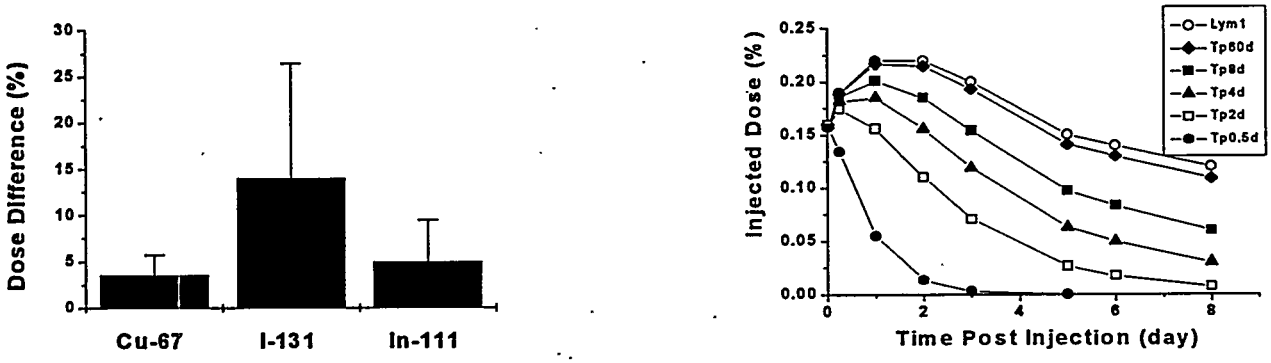

Figure 3. (Left): Mean percentage difference in radiation doses to tumors fitted with monoexponential function ($A_o e^{-b\,t}$) or biexponential function ($A_o e^{-b\,t} - A_o e^{-c\,t}$) for the tumor pharmacokinetic data with Lym-1 antibody. (Right): Tumor activity for isotopes with different physical half-lives (T_p), extrapolated from ^{131}I-Lym-1 data (T_p=8 d). T_p of 60 days corresponds to ^{125}I, and T_p of 0.5 d corresponds to ^{123}I.

DISCUSSION

The organ mass for individual patients can deviate substantially from that of the MIRD phantom especially when organ size is associated with disease, such as splenomegaly in patients with lymphoma. Consequently, the simplification of using the MIRD phantom for individual patients can introduce substantial errors in organ dose estimates [Figure 1 (Right)]. For lymphoma patients in the present study, a modified S value was needed to adjust the deviation in mass for calculation of the spleen dose for individual patients.

Although penetrating radiation from nontarget sources, including the remainder of the body, has been considered a major contributor to the total radiation dose in diagnostic nuclear medicine, the present study suggests that this contribution is about 5% for therapeutic radionuclides such as ^{131}I or ^{67}Cu (Table 1). This small contribution from source regions outside the target is due to the dominant nonpenetrating radiation from ^{131}I and ^{67}Cu (12). Based on these results, the total radiation dose to target organs can be well represented by dose from activity in the target alone for therapeutic radionuclides in organs visualized on patient images.

The use of interpolated S values does not have a theoretical basis, however, good approximation of S values for source organs as the target can be obtained for therapeutic radionuclides such as ^{131}I or ^{67}Cu with this simple procedure (Figure 2 (Left)). Interpolation of S values is practical for derivation of S values for organs in individual patients when the source is the target. Because the dose contribution from sources other than the target is small for ^{131}I or ^{67}Cu, the dose estimates considering only the source as target represents a good approximation for radioimmunotherapy.

Although tumor pharmacokinetic data usually do not exhibit an instantaneous uptake phase, a simplification using monoexponential fitting for tumors provided good approximations for radionuclides which have a relatively short half-life. For radionuclides with short half-lives, tumor radiopharmacokinetics are almost monoexponential even when biological data exhibit a prolonged uptake phase (Figure 3 (Right)). If radiation dose estimates are needed only for the radionuclides with short half-lives, less imaging data points (~ 3 points) are required for monoexponential fitting compared to biexponential fitting.

Substantial errors (10-fold or greater) have been reported due to nonuniformity in activity distribution in tumors at the microscopic level (17-19). Although the simplification of uniform distribution of activity and absorbed dose is one of the largest errors in the dosimetry of radionuclide therapy, this problem is very difficult to correct at present because of the spatial resolution limits of the gamma camera for imaging patients. For this type of "noncorrectable" limit with current technology, reproducibility and documentation become more important. Nevertheless, when tumor nonuniformity at the macroscopic level can be observed by gamma camera imaging, tumor dose estimation can be corrected accordingly. We have illustrated a preliminary correction method using both planar and SPECT imaging.

In summary, simplification at each step of clinical research provides valuable means and insights for solving complicated problems. The results of the present study support and expand observations made by others that errors in dosimetry due to simplifications can range from substantial to inconsequential depending on the assumptions made, choice of radionuclide and organ size. However, carefully selected simplifications for a specific application can be made without significant error in radioimmunotherapy dosimetry.

ACKNOWLEDGMENTS

This work was supported by grants from the National Cancer Institute (PHS CA 47829) and the Department of Energy (DE-FG03-84ER-60233).

REFERENCE

1. DeNardo SJ, DeNardo GL, O'Grady LF, Hu E, Sytsma VM, Mills SL, Levy NB, Macey DJ, Miller CH and Epstein AL. Treatment of B cell malignancies with ^{131}I-Lym-1 monoclonal antibodies. Int J Cancer 3:96-101, 1988.
2. DeNardo GL, DeNardo SJ, Meares CF, Kukis DL, Diril H, McCall MJ, Adams GP, Mausner LF, Moody DC and Deshpande SV. Pharmacokinetics of copper-67 conjugated Lym-1, a potential therapeutic radioimmunoconjugate, in mice and in patients with lymphoma. Antibody, Immunoconj Radiophar 4:777-785, 1991.
3. Shen S, DeNardo GL, DeNardo SJ, Salako QA, Morris G, Banks D, Yuan A and DeNardo DA. Dosimetric evaluation of ^{64}Cu-2IT-BAT-Lym-1 in ^{67}Cu-2IT-BAT-Lym-1 for radioimmunotherapy. J Nucl Med 37:146-150, 1996.
4. DeNardo SJ, Mirick GR, Kroger LA, O'Grady LF, Erickson KL, Yuan A, Lamborn KR, Hellstrom I, Hellstrom KE and DeNardo GL. The biological window for chimeric L6 radioimmunotherapy. Cancer (Suppl) 73:1023-1032, 1994.
5. DeNardo SJ, Zhong GR, Salako Q, Li M, DeNardo GL and Meares CF. Pharmacokinetics of chimeric L6 conjugated to ^{111}In-and ^{90}Y-DOTA-peptide in tumor bearing mice. J Nucl Med 36:829-836, 1995.
6. Snyder WS, Ford MR and Warner GG. Estimates of Specific Absorbed Fractions for Photon Sources Uniformly Distributed in Various Organs of a Heterogeneous Phantom. MIRD Pamphlet No. 5, Revised, Society of Nuclear Medicine, New York 1978.
7. Loevinger R and Berman M. A revised schema for calculating the absorbed dose from biologically distributed radionuclides. MIRD Pamphlet No.1, Society of Nuclear Medicine, New York, 1976.
8. Snyder WS, Ford MR, Warner GG and Watson SB. "S," Absorbed Dose per Unit Cumulated Activity for Selected Radionuclides and Organs. MIRD Pamphlet No. 11, Society of Nuclear Medicine, New York, 1975.
9. Coffey JL and Watson EE. Calculating dose from remaining body activity: a comparison of two methods. Med Phys 6:307-308, 1979.
10. Meredith RF, Johnson TK, Plott G, Macey DJ, Vessella RL, Wilson LA, Breitz HB and Williams LE. Dosimetry of solid tumors. Med Phys 20:583-592, 1993.
11. Ellett WH and Humes RM. Absorbed fractions for small volumes containing photon-emitting radioactivity. MIRD Pamphlet No. 8, Society of Nuclear Medicine, New York, 1971.
12. Weber DA, Eckerman KF, Dillman LT and Ryman JC. MIRD: Radionuclide data and decay schemes. Society of Nuclear Medicine, New York, pp:72-75, 1989.
13. Gilland DR, Jaszczak RJ, Turkington TG, Greer KL and Coleman RE. Volume and activity quantitation with iodine-123 SPECT. J Nucl Med 35:1707-1713, 1994.
14. Leichner PK, Yang N, Frenkel TL, Loudenslager DM, Hawkins WG, Klein JL and Order SE. Dosimetry and treatment planning for Y-90-labeled antiferritin in hepatoma. Int J Radiat Oncol Biol Phys 14:1033-1042, 1988.
15. Eary JF, Pollard KR, Durack LD, Bice AN, Lewellen TK, Matthews D, Press OW, Nelp WB, Appelbaum FR and Bernstein I. Post therapy imaging in high dose I-131 radioimmunotherapy

patients. Med Phys 21:1157-1162, 1994.
16. Howell RW, Goddu SM and Rao DV. Application of the linear-quadratic model to radioimmunotherapy: confirmation of the advantage of long-lived radionuclides. J Nucl Med 35:1861-1869, 1994.
17. Yorke ED, William LE, Demidecki, Heidorn DB Roberson PL and Wessels BW. Multicellular dosimetry for beta-emitting radionuclides: autoradiography, thermoluminescent dosimetry and three-dimensional dose calculations. Med Phys 20:543-550, 1994.
18. Humm JL, Macklis KB, Cobb LM and Chin LM. Internal dosimetry using data derived from autoradiographs. J Nucl Med 34:1811-1817,1993.
19. Erdi AK, Wessels BW, DeJager R, Erdi YE, Atkins FB, Yorke ED, Smith L, Huang E, Smiddy M, Murray J, Varma VM, McCabe R, McNellis R, John C, Ney A, Nochomovitz L and Hanna MG. Tumor activity confirmation and isodose curve display for patients receiving iodine-131-labeled 16.88 human monoclonal antibody. Cancer (Suppl) 73:932-944,1994.

QUESTIONS

Rao: Is the tumor macro-nonuniformity you showed time dependent?

Shen: Yes, in this particular tumor, the clearance half-time of the low-uptake zone was about 30% longer than that of the high-uptake zone.

HUMAN DOSIMETRY OF β^+ RADIOPHARMACEUTICALS BASED ON PET RECTILINEAR SCANS. VALIDATION OF THE METHOD WITH [^{18}F]ALTANSERIN

Brihaye C, Lemaire C and Luxen A
University of Liège
Cyclotron Research Center
B30, Sart-Tilman
B-4000 Liège (Belgium)

ABSTRACT

In order to estimate the absorbed doses from positron-emitting radiopharmaceuticals based on human biodistribution data, a method to measure the activity in various source organs has been developed. The acquisitions were performed using rectilinear scans with an ECAT 951/31R PET camera, which is a more rapid and easier mode of acquisition to determine organ biodistribution than using a whole-body scanning mode. The most important advantage of this mode of acquisition is that the activity in the remainder of the body can be estimated. Since it is not possible to apply an attenuation correction for rectilinear scans, a calibration was performed with an humanoid phantom containing known activities of ^{68}Ga in various source organs. Correlation factors between the number of counts per second in the ROI drawn on the organs and the activity in the organs were deduced for the anterior-posterior and lateral views. The method was validated by administering 185 MBq of [^{18}F]Altanserin, which is an antagonist of $5HT_2$ receptors, to six volunteers and measuring the activities in the organs at different times after injection. Urine was collected and assayed by gamma spectrometry. At the first scan (10 minutes after administration), i.e. before any excretion, the sum of the activities measured in all the organs including the remainder of the body is between 95 and 105 % of the administered activity. For the following scans (30 minutes, 1 hour, 3 hours and 5 hours after injection), the sums of the activities in the organs plus the cumulative activity in the urine are in agreement (85-92%) with the administered activities.

The absorbed doses resulting from the administration of 1 MBq of [^{18}F]Altanserin were estimated using the MIRDOSE3 program and the following mean values were obtained: gall bladder wall 0.031 mGy, LLI wall 0.022 mGy, ULI wall 0.053 mGy, pancreas 0.025 mGy, red marrow 0.019 mGy, spleen 0.037 mGy and urinary bladder wall 0.071 mGy. The mean effective dose equivalent and the effective dose are 0.031 and 0.027 mSv/MBq, respectively.

INTRODUCTION

Among the radiopharmaceuticals currently used in positron-emission tomography, few of these have been evaluated from a dosimetric point of view using human biodistribution data. Moreover, some of these absorbed doses were estimated using a restricted number of experimental points

describing the biokinetics. The case of ^{15}O is different since its short half-life ($T_{1/2}$ = 122 s) does not permit the experimental measurement of activity distribution in the organs. Table 1 summarizes the experimental conditions reported in the literature for the estimation of the absorbed doses for [^{18}F]FDG, [^{18}F]Fluoro-DOPA, [^{13}N]Ammonia and [^{11}C] L-Methionine, which are the most frequently used β^+ labeled radiopharmaceuticals (1). It can be seen from this table that the optimal conditions for obtaining complete biodistribution data are rarely fulfilled.

Table 1
Source of Data Used to Calculate Absorbed Dose Estimates Reported in the Literature

Radiopharmaceutical	Frequency of application in Europe(application/week) from ref.(1)	Experimental conditions for obtaining biodistribution data.	Ref.
[^{18}F]FDG	180	Dog biodistribution data 1 hr after injection. Human biodistribution for the brain and the urinary bladder. Biokinetic data for 7 organs in human obtained from PET studies.	(2) (3)
[^{13}N]Ammonia	25	Estimation of the absorbed doses based on a dynamic model of ammonia metabolism in man.	(4)
[^{11}C]Methionine	18	In fact, the reported absorbed doses are for C-11 DL-tryptophan and DL-valine and based on 30-min tissue distribution of these C-14 labeled amino acids in dog.	(5)
[^{18}F]Dopa	13	Administration of the radiopharmaceutical in 2 dogs killed at 1 and 2 hours after injection.	(6)

Another factor, which is the importance of the so-called "remainder of the body", has to be considered when determining biodistribution data. From biodistribution data for [^{18}F]Altanserin obtained in rats following the conventional method, the absorbed doses were calculated with the MIRDOSE3 program for the following 3 conditions.

1. All the individual organs are considered as separate source organs (adrenals, brain, LLI, SI, stomach, ULI, heart contents, kidneys, liver, lungs, muscle, cortical bone, trabecular bone, spleen, testes and urinary bladder contents).
2. The main organs (brain, heart contents, kidneys, liver, lungs and urinary bladder contents) are considered as source organs and the other organs are integrated into the remainder of the body.

3. Following the method for [^{18}F]FDG, the brain, the heart contents and the urinary bladder contents are considered as source organs, the other organs being included into the remainder of the body.

The estimated absorbed doses for the three conditions are presented in Table 2. It can be seen that, if the value of the remainder of the body increases, the estimated radiation dose decreases for some organs and the values of the effective dose equivalent and the effective dose are also lower.

It can be concluded that in order to estimate the radiation absorbed doses accurately, it is imperative to know the biokinetics of the tracer for all organs which show selective uptake, and the remainder of the body. In this work, a method based on PET rectilinear scans is proposed. The method, which is sensitive and rapid, was validated in vivo with [^{18}F]Altanserin administered to six volunteers.

Table 2

Radiation Dose Estimates for F-18-Altanserin using Three Different Calculation Methods

Target organ	Radiation Dose Estimates (mGy/MBq)		
	Using all organs as source organs	Using main organs as source organs	Brain, heart and ur. blad. contents as source organs
Adrenals	3.35e-02	1.50e-02	1.40e-02
Brain	1.21e-02	1.17e-02	1.19e-02
Breasts	8.29e-03	9.99e-03	1.02e-02
Gallbladder wall	1.74e-02	1.71e-02	1.48e-02
LLI wall	2.30e-02	1.43e-02	1.54e-02
SI	5.27e-02	1.45e-02	1.51e-02
Stomach	3.04e-02	1.36e-02	1.39e-02
ULI wall	2.66e-02	1.44e-02	1.47e-02
Heart wall	1.14e-02	1.25e-02	1.21e-02
Kidneys	2.21e-02	2.15e-02	1.34e-02
Liver	3.20e-02	3.18e-02	1.34e-02
Lungs	1.75e-02	1.80e-02	1.21e-02
Muscle	1.03e-02	1.18e-02	1.23e-02
Ovaries	1.73e-02	1.47e-02	1.57e-02
Pancreas	1.51e-02	1.53e-02	1.47e-02
Red marrow	2.10e-02	1.26e-02	1.31e-02
Bone surfaces	2.90e-03	1.30e-02	1.36e-02
Skin	7.88e-03	9.24e-03	9.78e-03
Spleen	1.45e-02	1.30e-02	1.34e-02
Testes	9.05e-03	1.17e-02	1.27e-02
Thymus	9.87e-03	1.21e-02	1.25e-02
Thyroid	9.67e-03	1.18e-02	1.27e-02
Ur. Blad. wall	4.43e-02	4.51e-02	4.59e-02
Uterus	1.74e-02	1.60e-02	1.70e-02
Total body	1.23e-02	1.24e-02	1.23e-02
EFF DOSE EQUIV	2.29e-02 mSv/MBq	1.75e-02 mSv/MBq	1.58e-02 mSv/MBq
EFF DOSE	2.26e-02 mSv/MBq	1.68e-02 mSv/MBq	1.56e-02 mSv/MBq

MATERIALS AND METHODS

PET Rectilinear Scans

With an ECAT 951/31R PET camera, it is possible to scan the majority of organs using two different acquisition modes, the rectilinear scan and the whole-body scan. The rectilinear scan mode was designed to position the patient and is not quantitative. This mode is rapid and does not require postprocessing to get the images. Moreover, in this mode, an image containing an anterior-posterior view and a lateral view is reconstructed on-line occupying about 0.4 Mb of memory. The whole-body scan mode is quantitative and requires about 40 Mb of memory. The data has to be retroprocessed and Z-filtered, which takes about 10 minutes per view. If a calibration is done to make the rectilinear scan mode quantitative, the method would be well suited for obtaining biodistributation data.

Description of the Humanoid Phantom Used for Calibration

For the calibration, a humanoid phantom (Alderson Research Labs, Inc. Long Island City N.Y. Remcal Ser. No 118.) was used. The phantom was modified to include organs which were not present originally. These organs include brain, SI, LLI, ULI and urinary bladder, which were made from lucite and polypropylene tubing following the dimensions for an adult reported by M. Cristy (10).

Calibration

Known activities of ^{68}Ga (3.7 - 37 MBq) were introduced into the organs of the phantom and rectilinear scans were performed for 2 minutes per field of view (10.4 cm). Correlation factors between the number of counts per second in the ROI drawn on the organs and the activity in the organs were deduced for the anterior-posterior and lateral views.

Examples of views are shown in Figures 1 and 2 for brain and heart, and lungs and liver.

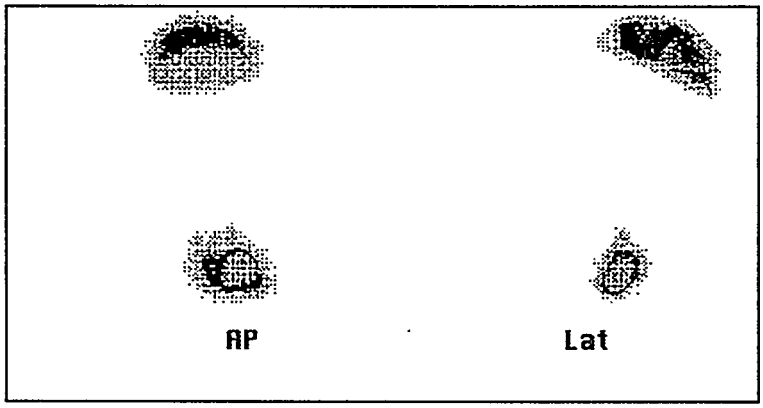

Figure 1. Anterior-posterior and lateral views acquired by rectilinear scan mode for activity present in the brain and the heart of a humanoid phantom.

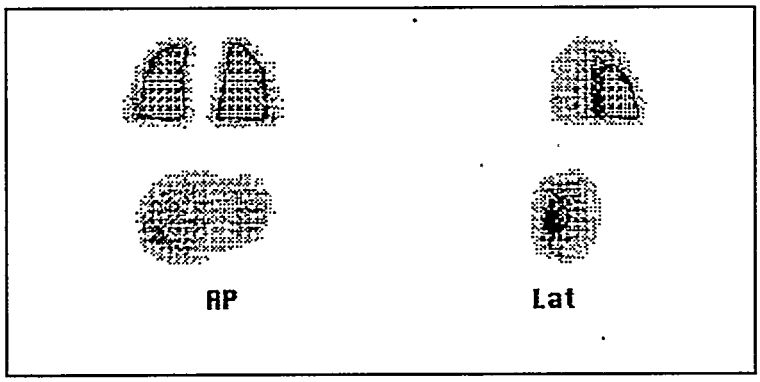

Figure 2. Anterior-posterior and lateral views acquired by rectilinear scan mode for activity present in the lungs and the liver of a humanoid phantom

RESULTS AND DISCUSSION

In Vivo Validation of the Method

To evaluate the quantitativeness of the method in vivo, six volunteers (male, 22-29 years) were injected with 185 MBq of [^{18}F]Altanserin, (a radioligand for the study of serotonin 5HT$_2$ receptors (7-9)), and rectilinear scan acquisitions (2 minutes per field of view) were performed at 10, 30, 60, 180 and 300 minutes postinjection. Urine was collected and assayed for activity by gamma spectrometry. Views obtained 30 min, 3 hr and 5 hr p.i. are presented in Figures 3, 4 and 5.

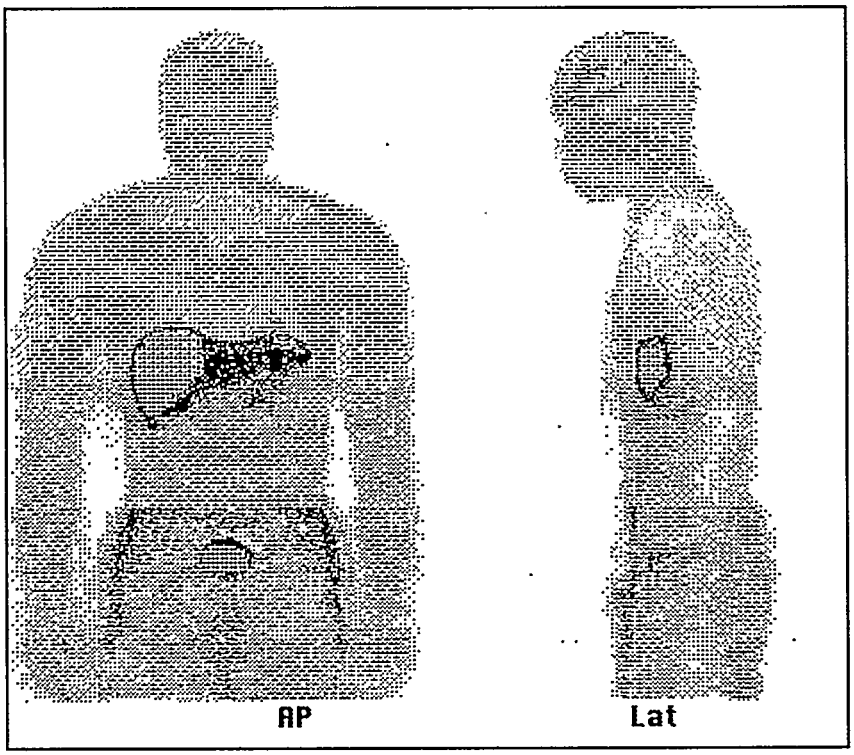

Figure 3. Anterior-posterior and lateral views at 30 minutes postinjection.

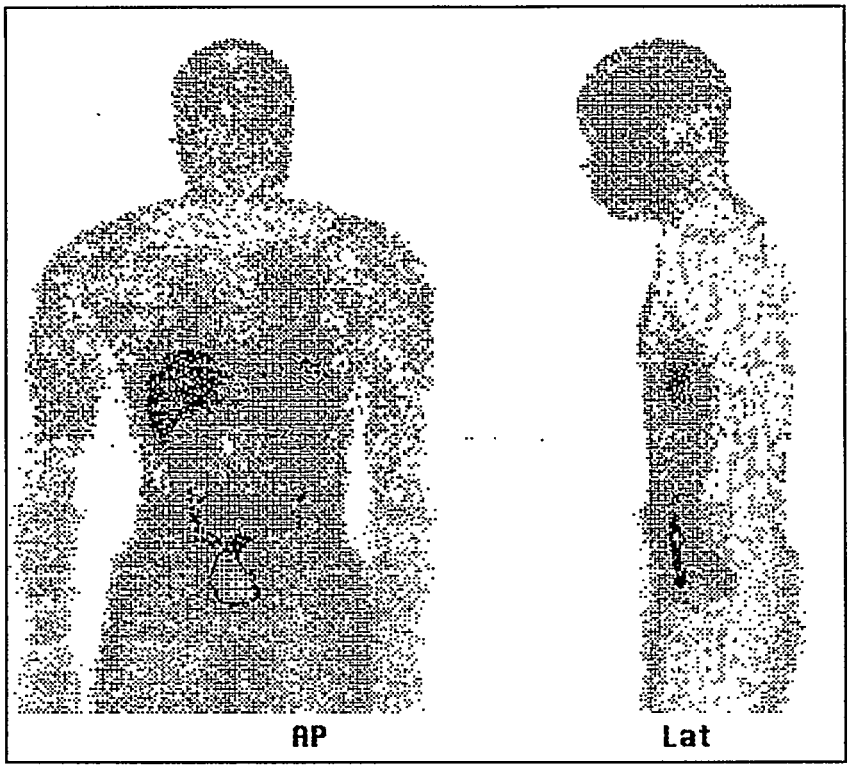

Figure 4. Anterior-posterior and lateral views at 3 hours postinjection.

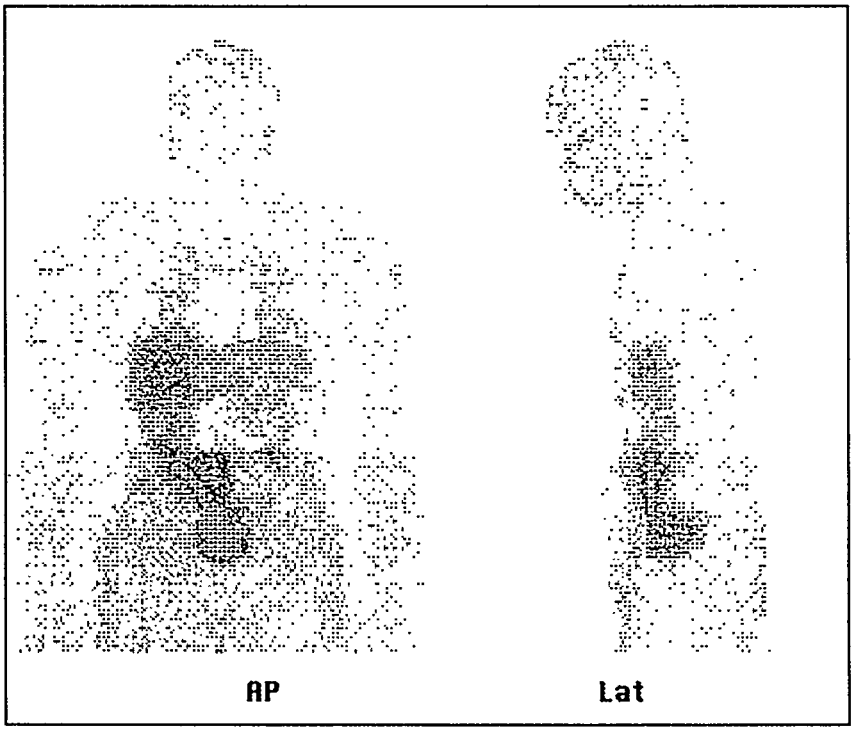

Figure 5. Anterior-posterior and lateral views at 5 hours postinjection.

For the first scan (10 minutes after administration), i.e. before any excretion, the sum of the activities calculated from the correlation factors in all the organs, including the remainder of the body, and corrected to the time of administration, is between 95 and 105 % of the administered activity. For the following scans (30 min, 1 hour, 3 hours and 5 hours), the sums of the activities corrected to the injection time plus the cumulative activity in the urine are in agreement (85-92%) with the administered activity. These values show that after calibration, the rectilinear scan acquisition mode is quantitative for a biodistribution data collection.

Estimates of the Radiation Doses from [^{18}F]Altanserin

For each organ, including the experimental remainder of the body, the variation of the decay-corrected activity as a function of the time period after administration was fitted in exponential terms by a nonlinear-least-squares technique. The curves are presented in Figure 6 for the liver, left kidney, lungs, spleen, urinary bladder and the remainder of the body. Organ residence times were calculated from these functions, and dose estimates were generated using the MIRDOSE3 program. The mean results (n=6) and the standard deviation are presented in Table 3.

Table 3
Absorbed Dose Estimates for [^{18}F]Altanserin

Target organ	Absorbed dose (mGy/MBq)
Adrenals	0.024 ± 0.004
Brain	0.0065 ± 0.0009
Breasts	0.014 ± 0.003
Gallbladder wall	0.031 ± 0.006
LLI wall	0.022 ± 0.004
Small Intestine	0.036 ± 0.006
Stomach	0.021 ± 0.003
ULI wall	0.053 ± 0.006
Heart wall	0.020 ± 0.008
Kidneys	0.059 ± 0.007
Liver	0.072 ± 0.004
Lungs	0.022 ± 0.004
Muscle	0.017 ± 0.004
Ovaries	0.024 ± 0.004
Pancreas	0.025 ± 0.003
Red Marrow	0.019 ± 0.004
Bone Surfaces	0.018 ± 0.003
Skin	0.013 ± 0.005
Spleen	0.037 ± 0.002
Testes	0.016 ± 0.004
Thymus	0.017 ± 0.005
Thyroid	0.016 ± 0.003
Urin. Bladder Wall	0.071 ± 0.002
Uterus	0.025 ± 0.004
Total Body	0.019 ± 0.005
EFF DOSE EQUIV (mSv/MBq)	0.031
EFF DOSE (mSv/MBq)	0.027

*mean value ± std. Dev

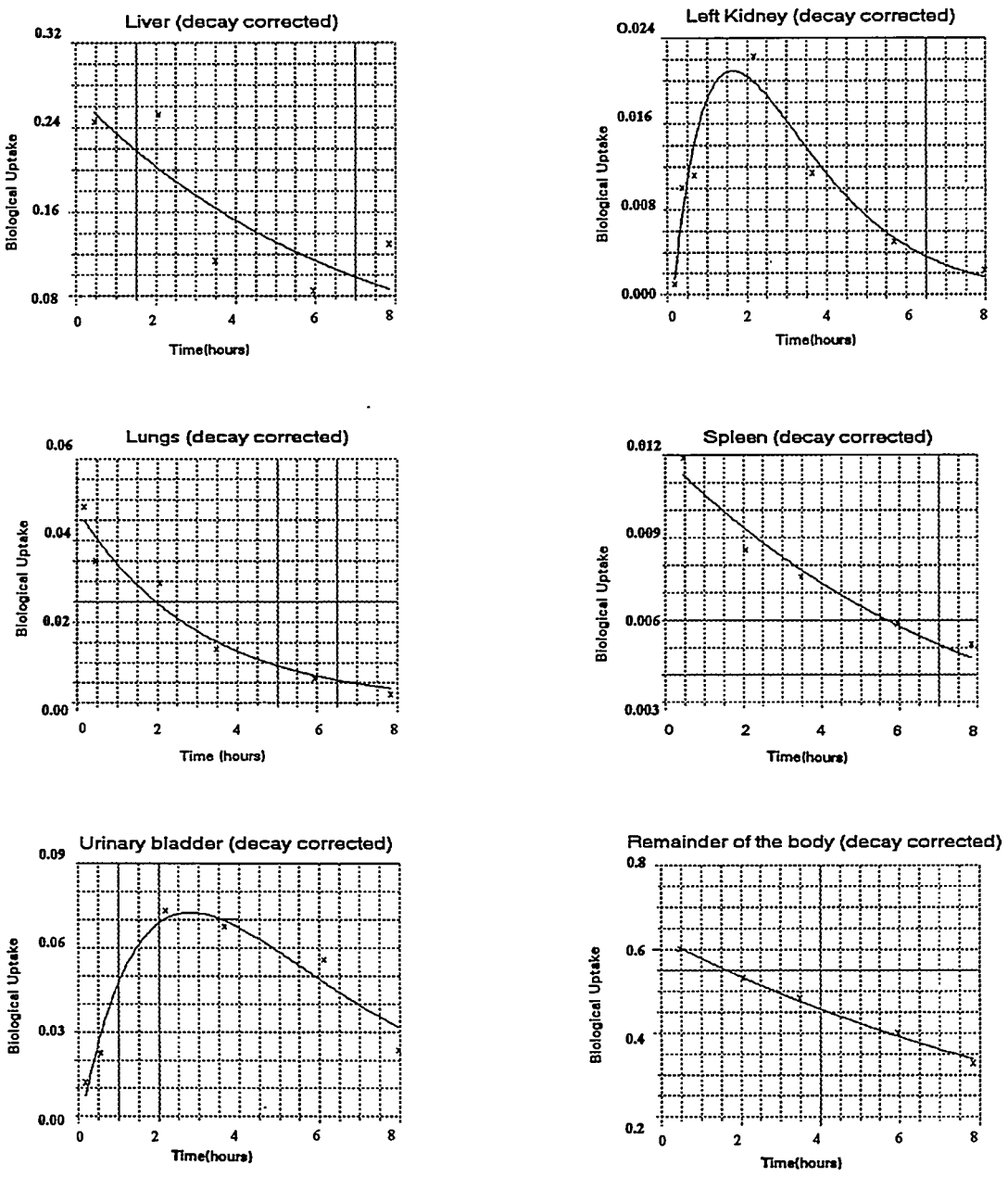

Figure 6. Variation of the human biological uptake of [^{18}F] Altanserin as a function of the time after administration for the liver, left kidney, lungs, spleen, urinary bladder and the remainder of the body.

CONCLUSION

In this work, it has been shown that a PET rectilinear scan acquisition mode, after calibration, is a powerful and easy tool for obtaining biokinetic data of positron-emitting radiopharmaceuticals in humans. In the future, it could be applied to other routinely used PET radiopharmaceuticals in order to more accurately estimate the absorbed doses.

REFERENCES

1. Meyer G-J, Waters SL, Coenen HH, Luxen A, Mazière B and Langström B. PET radiopharmaceuticals in Europe: Current use and data relevant for the formulation of summaries of product characteristics (SPCs). Eur J Nucl Med 22(12):1420-1432,1995.
2. Jones SC, Alavi A, Christman D, Montanez I, Wolf AP and Reivich M. The radiation dosimetry of 2-[F-18]fluoro-2-deoxy-D-glucose in man. J Nucl Med 23(7):613-617, 1982.
3. Mejia AA, Nakamura T, Masatoshi I, Hatazawa J, Masaki M and Watanuki S. Estimation of absorbed doses in humans due to intravenous administration of fluorine-18-fluorodeoxyglucose in PET Studies. J Nucl Med 32(4):699-706, 1991.
4. Lockwood AH. Absorbed doses of radiation after an intravenous injection of N-13 ammonia in man: Concise communication. J Nucl Med 21(3):276-278, 1980.
5. Hübner KF, Andrews GA, Buonocore E, Hayes RL, Washburn LC, Collman IR and Gibbs WD. Carbon-11-labeled amino acids for the rectilinear and positron tomographic imaging of the human pancreas. J Nucl Med 20(6):507-513, 1979.
6. Harvey J, Firnau G and Garnett ES. Estimation of the radiation dose in man due to 6-[^{18}F]fluoro-L-dopa. J Nucl Med 26(8):931-935, 1985.
7. Lemaire C, Cantineau R, Guillaume M, Plenevaux A and Christiaens L. Fluorine-18-altanserin: A radioligand for the study of serotonin receptors with PET: radiolabeling and in vivo biologic behavior in rats. J Nucl Med 32(12):2266-2272, 1991.
8. Biver S, Goldman S, Luxen A, Monclus M, Forestini M, Mendlewicz J and Lostra F. Multicompartmental study of fluorine-18 altanserin binding to brain $5HT_2$ receptors in humans using positron emission tomography. Eur J Nucl Med 21(9):937-946, 1994.
9. Sadzot B, Lemaire C, Maquet P, Salmon E, Plenevaux A, Degueldre C, Hermanne JP, Guillaume M, Cantineau R, Comar D and Franck G. Serotonin $5HT_2$ Receptor imaging in the human brain using positron emission tomography and a new radioligand, [^{18}F]altanserin: Results in young normal controls. J Cerebr Blood Flow and Metab 15(5):787-797, 1995.
10. Cristy M. Mathematical Phantoms Representing Children of Various Ages for Use in Estimates of Internal Dose. ORNL Report ORNL/NUREG/TM-367, 1980.

QUESTIONS

T. Smith: You have described your technique for a ^{18}F-labeled substance which has a half-life of 110 min. Although this is relatively short, it is considerably longer than some other positron radiopharmaceuticals. Would your technique be satisfactory for shorter-lived radionuclides than ^{18}F?

Brihaye: The method I presented was also applied to ^{11}C compounds. The problem is that a correction must be applied for the loss of counts during the scan due to decay. This can be easily done as following. If t_{scan} is the duration of the scan and $A_{measured}$ is the experimental count rate measured during the scan, the count rate reported to the start of the scan A_o can be calculated by the relation

$$\frac{A_o = A_{measured} \cdot \lambda \cdot t_{scan}}{\left[1 - e^{-\lambda t_{scan}}\right]}.$$

For ^{15}O, the correction factor would be too high, so that the method could not be applied.

Rao: Since most of the positron-emitting pharmaceuticals have short half-lives (~ minutes), how do you account for scan time in determining the biodistribution?

Brihaye: The same question was asked by Terry Smith. Let t_{scan} be the duration of the scan. During the scan, there is a loss of counts due to the decay of the short-lived radionuclide, so that the apparent count rate, A_{app} is not correct. The apparent count rate can be corrected and the accurate count rate, reported to the time of beginning of the scan, A_o, can be derived as follows:

$$A_o = \frac{A_{app} \cdot \lambda \cdot t_{scan}}{\left[1 - e^{-\lambda t_{scan}}\right]}.$$

QUANTITATIVE WHOLE-BODY PHARMACOKINETICS OF YTTRIUM-86 COMPLEXES WITH PET AND RADIATION DOSE CALCULATION OF ANALOGOUS YTTRIUM-90 RADIOTHERAPEUTICALS

Rösch F[1], Herzog H[2], Neumaier B[1], Müller-Gärtner HW[2], Stöcklin G[1]
Institute für Nuklearchemie[1] und Medizin[2], KFA Jülich, Germany
Mailing address: Prof. Dr. Rösch, Institut für Kernchemie,
Johannes Gutenberg-Universität Mainz, D-55099 Mainz, Germany

ABSTRACT

Painful bone metastases are palliatively treated with β^- emitting isotopes such as yttrium-90. Because it is a pure β^- emitter, data on the pharmacokinetics and radiation doses caused by individual ^{90}Y radiotherapeuticals to metastases and unaffected organs is lacking. To obtain quantitative biokinetics of ^{90}Y-Citrate and ^{90}Y-EDTMP the β^+ surrogate yttrium-86 ($T_{1/2}$ = 14.7 h, 33% β^+) was prepared and applied as ^{86}Y-Citrate and ^{86}Y-EDTMP for whole-body PET measurements. Five patients with multiple bone metastases of prostate cancer received about 200 MBq of ^{86}Y-citrate and five received ^{86}Y-EDTMP.

Dynamic PET scans were recorded over the liver, followed by several quantitative whole-body PET scans from 4 to 72 h p.i. The reconstructed transversal PET images were evaluated to obtain time-activity curves in normal bone, bone metastases and liver. Based on these ^{86}Y uptake kinetics, the radiation doses from the ^{90}Y compounds were calculated according to the MIRD recommendations. The doses delivered by ^{90}Y-Citrate would be 25.5 ± 10.6 mGy (per MBq injected) to the tumor and 2.5 ± 0.4 mGy/MBq for the whole red bone marrow. For ^{90}Y-EDTMP, these doses would be 17.8 ± 1.7 mGy/MBq and 1.8 ± 0.6 mGy/MBq, respectively.

The positron emitter ^{86}Y and PET provide quantitative information applicable to the clinical use of yttrium-90. This approach may also be useful for planning endoradiotherapy dosages as well as for controlling the success of the treatment.

Introduction

Approximately 80% of patients with prostatic carcinoma develop metastatic bone disease, and nearly half of them experience bone pain (1). Among the modalities for management of bone pain, endoradionuclide therapy is a well established approach. For some time phosphorus-32, strontium-89 and yttrium-90 have been available as ^{32}P-phosphate, ^{89}Sr-chloride and ^{90}Y-citrate (2-4). Chelates of phosphonates of samarium-153 and rhenium-186, namely, ^{153}Sm-EDTMP (ethylene diamine

tetramethylene phosphonate) and ^{186}Re-HEDP (1,1-hydroxyethylidine diphosphonate) are recently reported to have therapeutically useful biodistributions.

The radiation doses to bone metastases as well as to normal bone and radiosensitive organs such as the bone marrow depend on the activity administered and on the pharmacokinetics of the radiopharmaceutical. Its accurate determination is a critical step in the development of a radiotherapeutical. For humans, such data are available qualitatively in the case of those β^--emitting radionuclides that simultaneously emit a measurable percentage of low-energy photons such as samarium-153. Consequently, some target to nontarget accumulation ratios were deduced for ^{153}Sm-EDTMP by means of whole-body gamma camera images. Radiation doses were subsequently derived by Logan et al. (5), Eary et al. (6) and Bayouth et al. (7).

Yttrium-90 is a pure β^--emitter without any accompanying γ-radiation. It is available in a convenient generator system for no-carrier-added syntheses and is efficiently incorporated into radiopharmaceuticals. To date, the calculations of the human doses of radiation from yttrium-90 radiopharmaceuticals have been indirect, based on several empirical approaches.

Although ^{90}Y-citrate has been available for three decades, data from humans on its biodistribution and radiation doses to individual organs are not available. ^{90}Y-EDTMP is not yet routinely used. It has great potential usefulness, however, since phosphonate ligands like EDTMP promote the selective uptake of trivalent metallic radionuclides in bone and bone metastases. ^{153}Sm-EDTMP, for instance, is currently under clinical trial in the U.S.. The present paper describes the application of the approach to use PET to quantitatively assess the pharmacokinetics of yttrium-90 radiopharmaceuticals in humans, using the positron-emitting isotope yttrium-86 ($T_{1/2}$ = 14.74 hr, 32% β^+) (8).

Materials and Methods

Patients

Ten men with prostatic carcinoma and scintigraphically-proven bone metastases were studied. Five patients each were chosen for investigation with ^{86}Y-citrate and ^{86}Y-EDTMP. Their age ranged from 54 to 84. The patients had normal hematological parameters. Bone scintigrams with ^{99m}Tc-MDP were available for all subjects. None had received either radiotherapy or chemotherapy in the preceding 4 weeks. All had normal kidney and liver function. Prior to the study each patient gave written informed consent.

Preparation of Yttrium-86 Compounds

Yttrium-86 was produced at the Jülich compact cyclotron CV28 via the (p,n) reaction on 96.3% enriched $^{86}SrCO_3$ target material. Chemical processing led to no-carrier-added and radiochemically pure ^{86}Y(III) (9,10). The ^{86}Y-citrate and ^{86}Y-EDTMP complexes were synthesized by adding one drop of ^{86}Y(III) stock solution (10^{-4} M HCl) to ligand solutions of the following composition: for citrate, 3 ml aqueous solution of 7.5 mg/ml sodium citrate, pH 7.4, overall sodium citrate concentration 0.087 M, overall ionic strength 0.17 M, with 2 ml saline added to obtain isotonicity; for EDTMP, 2 ml aqueous solution of 21.8 - 36.5 mg/ml EDTMP adjusted with NaOH to pH 7.5, with 1 ml saline added to obtain isotonicity. The mixed solutions were sterile filtered, and assays of pyrogenicity were performed by standard methods. Radiochemical yields were found to be > 98% for both complexes.

PET Measurement and Data Analysis

PET measurements were done with the Scanditronix/GE scanner PC4096-15WB (11). As whole-body transmission scans were recorded before the first PET scan, all emission data could be corrected for attenuation. The patient was very carefully positioned for each measurement by means of laser beams in order to match the position of the transmission scan. The patients had an intravenous line placed in each arm. The radiopharmaceuticals were administered intravenously in a volume of 4-5 ml.

Dynamic PET scans were started simultaneously with the injection of the radiopharmaceutical and continued for 40 to 90 min. The field of view covered either the liver and/or individual metastases in vertebrae. Simultaneously, blood clearance and urinary excretion was determined by conventional methods. Later, up to four whole-body PET scans were acquired, the first at about 3 h post injection (p.i.) and the last up to 76 h p.i. The whole-body scans consisted of a series of single scans, each lasting for 4-6 min, extending from the neck to the femur.

Depending on the extent of the whole-body scan, the reconstruction of the emission data yielded in up to 210 transversal images for each measurement. Those images could be reconstructed as anterior, lateral, coronal or sagittal sections. The images had units of yttrium-86 activity concentration, i.e. kBq/cm^3. The accuracy of the activity determination in structures not confounded by the partial-volume effect was validated by phantom measurements. The activity concentration in kBq/cm^3 in the metastases was directly obtained by analyzing regions of interest (ROI) in the transversal slices, using a 30% isocontour level in three adjacent slices and averaged taking into account the ROI areas. Furthermore, ROIs were marked over normal bone, liver and kidneys. Activity concentration for the liver is given as a mean of at least two different ROIs; that for the kidneys as a mean of one ROI per left and right kidney. Finally, all data were corrected for the decay of yttrium-86.

Calculation of Radiation Dose

The decay-corrected pharmacokinetic data for the yttrium-86 radiopharmaceuticals were considered to be valid for the analogue yttrium-90 labeled compounds. The calculation of the radiation doses was performed as described in detail (8) in accordance with MIRD Pamphlets No. 11 and No. 5 (12,13). A dose constant of 0.54 g·Gy/MBq·h (2 g·rad/μCi·h) for yttrium-90 and a specific density of bone of 1.5 g/cm^3 were used. The radiation dose to the red marrow was considered to be from activity equally stored in cortical and trabecular structures of healthy bone, i.e. the corresponding individual MIRD radiation dose S factors delivered from yttrium-90 stored in cortical and trabecular bone were applied. The sizes of the metastses evaluated here were at least several cm^3. Therefore, the dose caused by the β^--emitter ^{90}Y is considered to be independent of the volume of the metastases.

In order to calculate the cumulated activities for both normal bone and metastases, the activity was considered not to be released after the uptake processes, which were completed at about 40 hr p.i. for ^{86}Y-citrate and about 1 hr for ^{86}Y-EDTMP. That means that the short early periods of uptake could be neglected for the calculation of the cumulated activities. The activities averaged at 48 and 72 hr for both ^{86}Y-citrate and ^{86}Y-EDTMP, respectively, were regarded as final levels of $A_{metastasis}$. After this point, the effective half-time was assumed to be equal to the physical half-life of ^{90}Y ($T_{1/2}$ = 64 hr), so that the cumulated activity $\tilde{A} = A_0 \cdot 64\ h \cdot \ln 2$.

Results

Pharmacokinetics

Figure 1 shows the early phase of ^{86}Y-citrate uptake (0 - 60 min p.i.) in patient #4. Initially, a 10 cm broad body section over the liver was monitored that included some parts of the kidneys as well as a metastasis in the os ilium. Those images served as measurements of the individual uptake kinetics of bone metastases, normal bone (not shown here), liver and kidneys. Error bars show deviations derived from the ROI determination in individual metastases, from two different ROIs for the liver, and from individual ROIs per left and right kidney.

Yttrium-86 accumulated continuously in bone metastases and also in normal bone, but at a much lower level. ^{86}Y-citrate concentrated in the liver rapidly, reaching a maximum of about 20% ID at 2-3 min p.i. The isotope was then released with a mean $T_{1/2} = 90 \pm 20$ min. Maximum accumulation in the kidneys occurred somewhat later than for the liver, at about 3-5 min p.i.. Within the first hour p.i., the release from this organ occurred with a $T_{1/2} = 80 \pm 30$ min.

Figure 2 shows the early uptake kinetics of ^{86}Y-EDTMP in patient #6. Uptake by bone metastases was faster than that of ^{86}Y-citrate and the accumulation of yttrium-86 in the liver was significantly lower. As for ^{86}Y-citrate, absolute values of yttrium-86 activity concentration varied significantly for individual bone metastases. In the kidneys, yttrium-86 uptake reached a maximum at about 2-5 min p.i., followed by a biphasic release. The liver, in contrast to the injection of ^{86}Y-citrate, showed a much lower accumulation of radioyttrium.

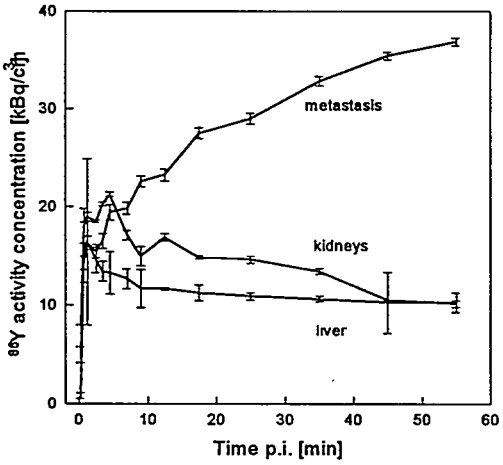

Figure 1. Decay-corrected time-activity curves of the early uptake kinetics of ^{86}Y-citrate in bone metastases, liver and kidneys.

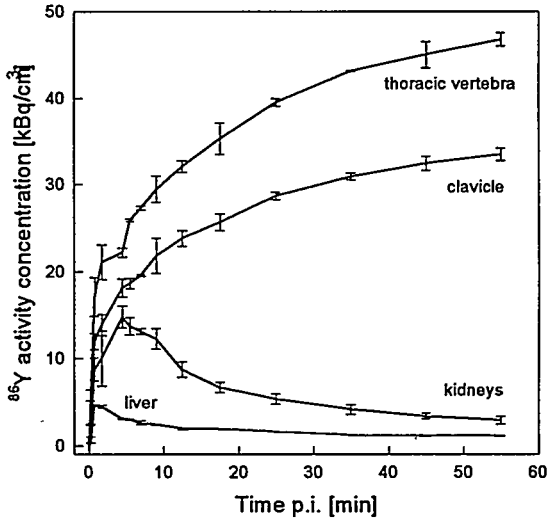

Figure 2. Decay-corrected time-activity curves of the early uptake kinetics of ^{86}Y-EDTMP in bone metastases, liver and kidneys.

The overall uptake kinetics covered a period of up to 3 days p.i. Figures 3 and 4 show complete time-activity curves for all the individual bone metastases of patient #4, who received ^{86}Y-citrate, and of patient #6, who received ^{86}Y-EDTMP. After correction for decay, the activity concentration in bone metastases was essentially constant already after ≈ 1.5 hr p.i. In contrast, and also typical for the ^{86}Y-citrate group, activity concentrations in the metastases increased more slowly and reached final levels at approximately 2 days p.i.

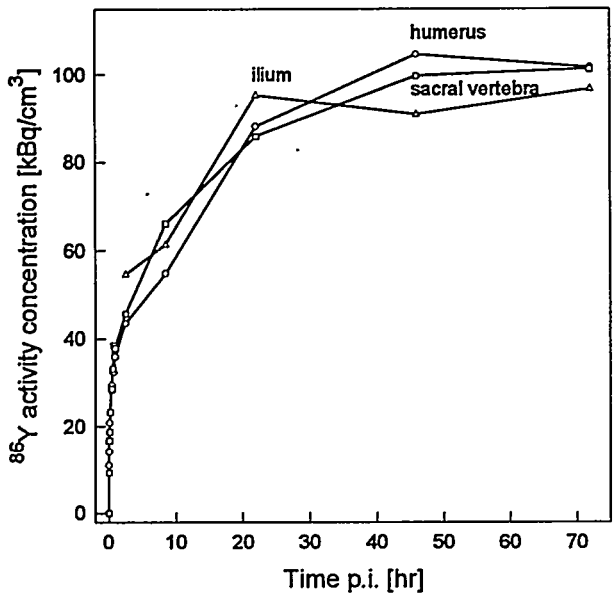

Figure 3. Complete decay-corrected time-activity curves of various bone metastases for ^{86}Y-citrate.

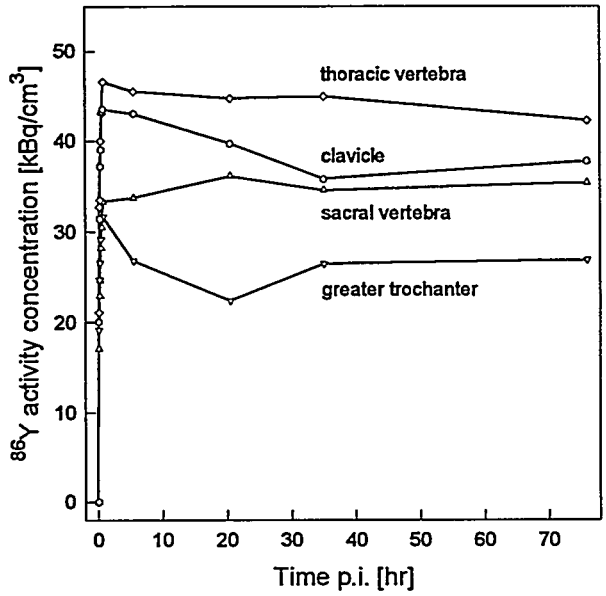

Figure 4 . Complete decay-corrected time-activity curves of various bone metastases for ^{86}Y-EDTMP.

The maximum activity concentrations in the ^{86}Y-citrate group were about 50% higher than those in the ^{86}Y-EDTMP group. For both radiopharmaceuticals, once the yttrium-86 activity concentration reached saturation it did not decline, indicating negligible clearance from the metastases. Average values of the uptake of ^{86}Y-citrate per cm^3 of bone metastases as well as the organ uptake for the total skeleton and for the liver are summarized in Table 1.

Although the kinetics of uptake were similar within each group, the maximum yttrium-86 activity concentrations, expressed as % ID/cm^3, varied, not only between patients but also between metastases in the same patient (cf. Fig. 2 for example). Average values of the uptake for both the two ^{86}Y-complexes are summarized in Table 1.

Table 1

Individual Uptake of the Two Different ^{86}Y Complexes at Different Times Postinjection

Radioyttrium complex ligand	Time p.i.(h)	Uptake in various organs (% ID)		
		Bone metastases (per cm^3)	Skeleton (total)	Liver (total)
Citrate	4	0.050 ± 0.018	25.8 ± 4.5	13.6 ± 2.0
	20	0.071 ± 0.028	34.2 ± 5.7	13.9 ± 2.0
	48	0.085 ± 0.037	36.2 ± 5.9	11.2 ± 1.8
	72	0.102 ± 0.013	44.0 ± 1.4	10.0 ± 2.2
EDTMP	4	0.051 ± 0.004	23.5 ± 8.0	at the background level
	20	0.050 ± 0.004	24.2 ± 7.7	
	48	0.054 ± 0.008	23.5 ± 7.8	
	72	0.053 ± 0.003	24.8 ±2.7	

The different uptake kinetics of ^{86}Y-citrate and ^{86}Y-EDTMP by bone metastases in turn determine the ratio of yttrium-86 activity concentration ratios between bone metastases and normal bone. In a given patient those ratios vary significantly, from 3:1 to 15:1. Similar ratios of 8±2 were obtained at about 1 h p.i. for ^{86}Y-EDTMP and at about 2 days p.i. for ^{86}Y-citrate. There is evidence that the yttrium-86 uptake kinetics in normal bone are somewhat faster than in bone metastases. The healthy bone seems to be more rapidly covered by ^{86}Y-EDTMP to a final level. The bone metastases may increasingly incorporate yttrium-86 due to the weaker apatite matrix.

For ^{86}Y-citrate, the yttrium-86 activity concentration in the liver peaked at 2-3 min p.i. and then decreased continuously over the whole period of measurement. At 20 hr p.i. and 72 hr p.i. this organ contained about 14% and 10% of the total administered activity.

Biochemical Analysis

Radiochemical analysis of blood samples showed that the stability of the two yttrium-86 radiopharmaceuticals differed in vivo. Gel chromatography revealed that 5 min after the injection of ^{86}Y-citrate, > 60% of the yttrium-86 in the blood was bound to serum proteins. In contrast, the ^{86}Y-EDTMP complex was much more stable; at 5 min p.i., yttrium-86 bound to serum proteins accounted for only 7% of the blood yttrium-86 activity.

Radiation Doses for ^{90}Y Radiopharmaceuticals

Using the uptake kinetics measured with yttrium-86, radiation doses were calculated for the yttrium-90 analogues. The individual patient data are summarised in Table 2, which includes mean values and standard deviations of the radiation doses to the bone metastases, the red marrow and the liver for each radiopharmaceutical.

The average dose to the bony metastases, per MBq yttrium-90 injected, would be greater for ^{90}Y-citrate, 26 ± 11 mGy/MBq, than for ^{86}Y-EDTMP, 18 ± 2 mGy/MBq ($p > 0.05$). ^{90}Y-citrate also would deliver a higher dose to the total red marrow (2.5 ± 0.4 mGy/MBq) than ^{90}Y-EDTMP (1.8 ± 0.6 mGy/MBq) ($p < 0.05$). Due to the negligible uptake of ^{86}Y-EDTMP by the liver, only the uptake of ^{90}Y-citrate is relevant; i.e. 1.8 ± 0.3 mGy/MBq for the whole organ.

Table 2

Individual Radiation Dose Calculated for the Injection of One MBq of the ^{90}Y Complexes

Radioyttrium complex ligand	Patient #	Radiation dose (mGy/MBq ^{90}Y injected)		
		Bone metastases[a]	Bone marrow[b]	Liver
Citrate	1	22 ± 8	2.0	1.8
	2	25 ± 7	3.0	1.6
	3	35 ± 1	2.5	
	4	36 ± 3	2.9	2.1
	5	10 ± 1	2.3	
	mean	26 ± 11	2.5 ± 0.4	1.8 ± 0.3
EDTMP	6	20 ± 5	1.5	
	7	16 ± 2	1.9	
	8	17 ± 2	1.5	
	9	19 ± 6	1.2	
	10	17 ± 3	2.7	
	mean	18 ± 2	1.8 ± 0.6	

[a] Data could not be compared by t-test. A rank sum test showed no significant difference.
[b] A t-test revealed a significant difference ($p < 0.05$) between ^{86}Y-citrate and ^{86}Y-EDTMP.

DISCUSSION

As expected, both the ^{86}Y radiopharmaceuticals localized primarily in the skeleton. Metastases accumulated ^{86}Y-EDTMP rapidly, attaining maximum concentrations by about 1.5 hours p.i. ^{86}Y-citrate accumulated much more slowly, requiring about 2 days to reach a maximum, but that level was higher than that achieved by ^{86}Y-EDTMP. Once deposited, the yttrium-86 of both radiopharmaceuticals remained in bone metastases or normal bone.

Data on the accumulation of yttrium-86 permitted calculation of the radiation doses that would be delivered by ^{90}Y radiopharmaceuticals. Such calculations indicate that ^{90}Y-citrate will deliver a slightly higher dose to metastases than ^{90}Y-EDTMP, 26 ± 11 vs 18 ± 2 mGy/MBq ^{90}Y administered The ROI technique of evaluating the activity uptake into a single metastasis, however, is influenced by the partial-volume effect. Therefore, it is expected that the activity in some parts of the metastasis as well as the related radiation dose is higher than the data derived from the ROI mean.

The corresponding doses to the total bone marrow per MBq of administered ^{90}Y, as derived from the accumulation of ^{90}Y in healthy bone, will be 2.5 ± 0.4 (citrate) and 1.8 ± 0.6 (EDTMP) mGy/MBq. Owing to preferential deposition of the therapeuticals in bone metastases, the local dose to bone marrow in the vicinity of a metastasis could be up to 15-fold higher. This, in turn, will increase the average radiation dose to the total bone marrow.

Some parts of the Y^{3+} released by the dissociation of the citrate complex bind to serum and are taken up by the liver. The sequestration and subsequent slow release of yttrium from those sites accounts for the slow accumulation of the radionuclide in bone and for the greater whole-body radiation dose, in the case of ^{86}Y-citrate. On the other hand, it prevents a significant portion of yttrium-86 from being excreted rapidly. This corresponds to the whole-body retention of the two ^{86}Y

complexes. In turn, it allows for redistribution of yttrium-86, providing a steady transfer of the radionuclide from the liver to bone metastases.

CONCLUSION

The present study suggests that the approach to employing β^+-emitting yttrium-86 as a substitute for β^--emitting yttrium-90 and direct in vivo measurement by PET, provides a quantitative comparison of the pharmacokinetics and radiation doses from different ^{86}Y-complexes. This technique could be superior to other methods used to estimate in vivo radiation doses of ^{90}Y radiopharmaceuticals. Finally, a preliminary ^{86}Y-PET trial in an individual patient can serve as a precise basis for calculating the dose of yttrium-90 to be used subsequently in radiotherapy. In determining the activity of ^{90}Y-citrate and ^{90}Y-EDTMP that can be safely administered to a patient, the absorbed dose to bone metastases as well as to the red marrow should be considered.

ACKNOWLEDGMENTS

This work was supported by grant Ro 985/2-1 of the Deutsche Forschungsgemeinschaft. We thank the team of the CV28 cyclotron for the irradiations and L. Theelen for technical assistance.

REFERENCES

1. Campa JA III and Payne R. The management of intractable bone pain: A clinician's perspective. Semin Nucl Med 22:3-10, 1992.
2. Harbert JC. Radionuclide therapy of bone pain. In: Nuclear Medicine Therapy. Thieme Medical Publishers, Inc., New York, 1987.
3. Lewington VJ. Targeted radionuclide therapy for bone metastases. Eur J Nucl Med 20:66-74, 1993.
4. Kutzner J, Hahn K, Grimm W, Rösler HP, Eckmann A and Bender S. ^{90}Yttrium-citrate for pain-therapy by bone metastases. NUC Compact 21:128-132, 1990.
5. KW, Volkert WA and Holmes RA. Radiation dose calculations in persons receiving injection of Samarium-153 EDTMP. J Nucl Med 28:505-509, 1987.
6. Eary JF, Collins C, Stabin M, Vernon C, Petersdorf S, Baker M, Hartnett S, Ferency S, Addison SJ, Appelbaum F and Gordon EE. Samarium-153-EDTMP biodistribution and dosimetry estimation. J Nucl Med 34:1031-1036, 1993.
7. Bayouth JE, Macey DJ, Kasi LP and Fosella FV. Dosimetry and toxicity of samarium-153-EDTMP administered for bone pain due to skeletal metastases. J Nucl Med 35:63-69, 1994.
8. Herzog H, Rösch F, Stöcklin G, Lueders C, Qaim SM and Feinendegen LE. Measurement of pharmacokinetics of yttrium-86 radiopharmaceuticals with PET and radiation dose calculation of analogous yttrium-90 radiotherapeutics. J Nucl Med 34:2222-2226, 1993.
9. Rösch F, Qaim SM and Stöcklin G. Nuclear data relevant to the production of the positron emitting radioisotope ^{86}Y via the ^{86}Sr(p,n) and ^{nat}Rb(^{3}He,2n) processes. Radiochimica Acta 61:1-8, 1993.
10. Rösch F, Qaim SM and Stöcklin G. Production of the positron emitting radioisotope ^{86}Y for nuclear medical application. Appl Radiat Isot 44:677-681, 1993.
11. Rota Kops E, Herzog H, Schmid A, Holte S and Feinendegen LE. Performance characteristics of an eight-ring whole-body PET scanner. J Assist Comput Tomogr 14:437-445, 1990.

12. Snyder WS, Ford MR, Warner GG and Watson SB. "S" Absorbed Dose per Unit Cumulated Activity for Selected Radionuclides and Organs. MIRD Pamphlet No. 11, Society of Nuclear Medicine, New York, 1975.
13. Snyder WS, Ford MR, Warner GG and Fisher LH jr. Estimates of Absorbed Fractions for Monoenergetic Photon Sources Uniformly Distributed in Various Organs of a Heterogeneous Phantom. MIRD Pamphlet No. 5. J Nucl Med 10:5s-52s, 1969.

QUESTIONS

Kwok: Can you tell us in greater detail how you calculated the bone marrow dose, especially the marrow near bone metastases?

Roesch: The radiation dose to the bone metastases was calculated from ^{90}Y activity accumulated in the skeleton. Following the MIRD scheme, it was assumed that ^{90}Y is equally stored in trabecular and cortical structures of the bone surface. Accordingly, the corresponding S factors for trabecular and cortical bone.

Brihaye: ^{86}Y and ^{90}Y have different decay schemes. Do you think it could have influence on the chemical stability of the EDTMP complexes?

Roesch: There are at least two processes responsible for the accumulation of radioyttrium in bone structures. One is the substitution of Y(III) for Ca(II) in the hydroxyapatite. The other is the chemical complex stability of the Y(III) complexes. For both of these processes, there is no isotopic effect for the two carrier-free yttrium isotopes ^{90}Y and ^{86}Y. The different modes of decay do not influence these physicochemical processes. Consequently, uptake mechanism measured for ^{86}Y compounds is the same as for ^{90}Y analogues.

Hetherington: Since ^{90}Y is a reactor produced isotope and ^{86}Y is cyclotron produced, is there a possibility that a difference in specific activity could cause a difference in the biological behavior of the compounds of the two isotopes?

Roesch: You are right, that for most of the reactor produced β^- emitting isotopes used in endotherapy, problems in the accumulation behavior are to be expected which are due to the low specific activity of those isotopes. This, in particular is true for receptor-based types of uptake mechanism.

In the case of ^{90}Y, however, the situation is different. ^{90}Y is one of the few β^- emitters that is available in no-carrier-added concentration when it is obtained via the $^{90}Sr/^{90}Y$ generator system.

Actually, this easy availability and the carrier-free status of ^{90}Y, together with its 100% β^- decay, make this isotope a very promising and potential candidate for endoradiotherapy.

Fisher: What geometry did you assume for bone metastases and what is the assumed absorbed fraction for ^{90}Y in these metastases ($\phi = 1.0$?)?

Roesch: We did not assume a geometry for bone metastases. Each individual metastasis was analyzed by defining regions of interest (ROI) from the transversal PET images. The volume and di-

ameter of the corresponding spheres differed. Usually, volumes ranging from 1 to 10 centimeter cubes were quantified. For these volumes, absorbed fractions for ^{90}Y were adopted from the MIRD recommendations.

Behr:. Congratulations! I think you have a very elegant and powerful tool for assessing dosimetry of Y-labeled radiopharmaceuticals. My only concern is the relatively short imaging time available. You mentioned 72 hours imaging. I think with antibody imaging this may be a little short to assess tumor targeting and pharmacokinetics adequately. Could you comment on this? How long could you stretch the imaging period?

Roesch: Generally speaking, the approach of using Y-86 as a surrogate for Y-90 labeled radiotherapeuticals is of course applicable only to those compounds having a biological half-time comparable to the physical half-life of Y-86. It is 14.7 hrs. We have measured uptake kinetics up to 3 days post injection. This was adequate for the biological half-time of bone-affine ^{90}Y-complexes. In the case of ^{90}Y-labeled monoclonal antibodies, measurement may be extended up to 4 days post injection provided the regions of interest show increasing or at least constant accumulation of the ^{90}Y radiotherapeutical.

THE BIODISTRIBUTION AND DOSIMETRY OF ^{117M}SN DTPA WITH SPECIAL EMPHASIS ON ACTIVE MARROW ABSORBED DOSES

J Stubbs[1] and H Atkins[2]
[1]Radiation Dosimetry Systems of Oak Ridge, Inc, Knoxville, TN
[2]Brookhaven National Laboratory, Upton, NY

ABSTRACT

^{117m}Sn(4+) DTPA is a new radiopharmaceutical for the palliation of pain associated with metastatic bone cancer. Recently, the Phase II clinical trials involving 47 patients were completed. These patients received administered activities in the range 6.7-10.6 MBq/kg of body mass. Frequent collections of urine were acquired over the first several hours postadministration and daily cumulative collections were obtained for the next 4-10 days. Anterior/posterior gamma camera images were obtained frequently over the initial 10 days.

Radiation dose estimates were calculated for 8 of these patients. Each patient's biodistribution data were mathematically simulated using a multicompartmental model. The model consisted of the following compartments; central, bone, kidney, other tissues, and cumulative urine. The measured cumulative urine data were used as references for the cumulative urine excretion compartment. The total-body compartment (sum of the bone surfaces, central, kidney, and other tissues compartments) was referenced to all activity not excreted in the urine. Scintigraphic images indicated the skeleton was the primary site of total-body retention within a few days postinjection, thus bone retention was considered equal to the total-body retention after 4 days postadministration. Transfer rate coefficients for this model were iteratively adjusted using a nonlinear least squares regression algorithm (CONSAM31) until each simulated time-activity curve statistically "fit" each measured or inferred time-activity curve (e.g., total-body time-activity curve). These curves were numerically integrated to yield source organ residence times. The total-bone residence times were equally divided between the cortical and trabecular bone surfaces. Total-bone residence time averaged 270 hours (range 84-390 h). These patients excreted an average of 41% (range 14%-89%) of the administered activity in the urine.

MIRDOSE3.1 was used to calculate the absorbed doses for each subject separately and descriptive statistics for the study population were calculated. The mean absorbed doses (range) were: active marrow, 2.5 (0.78-3.8) mGy/MBq; bone surfaces, 17 (5.1-24) mGy/MBq; urinary bladder wall, 0.38 (0.19-0.62) mGy/MBq; all other organs, <0.19 mGy/MBq. The mean total dose to active marrow was 1.7 Gy (range 0.56-2.9 Gy) with an average 32% of the subjects' active marrow receiving doses >1.5 Gy (range 6%-44%).

QUESTIONS

Rao: I would like to make a comment on a statement you made regarding the LD_{50} bone marrow dose for humans being about 500 cGy. While that is correct for acute irradiation, for incorporated radionuclides (with long physical half-lives), the LD_{50} dose can be significantly higher than 500 cGy because of dose-rate effects. Don't you agree?

Stubbs: Yes, but it is useful for comparative purposes and helps put the marrow doses we calculate in perspective.

Srivastava: I have a comment and a question. The comment is really a minor correction to what was stated. Tin-117m DTPA was developed at Brookhaven National Laboratory during the early and mid-eighties. Diatide (then Diatech) was given exclusive rights to commercialize this agent in June, 1994.

The question is whether there is some kind of a consensus that has been developing among the expert dosimetrists, most of them are gathered here today, that individualized dosimetry is the best approach or even required in this class of patients? Is it perhaps to help with treatment planning?

Stubbs: The general consensus, at this time, is that it's not necessary to perform individualized dosimetry for these palliative agents. The pain response as a function of lesion absorbed dose or degree of skeletal involvement has not been investigated. Some papers to be presented at next month's Society of Nuclear Medicine meeting are alluding to skeletal burden having an inverse relationship to pain response for a given level of administered activity. Cytopenia is clearly related to higher levels of administered activity. Currently, no relationship has been established between marrow absorbed dose and cytopenia for these compounds. However, there may be some utility in assessing a patient's absorbed doses for marrow and lesions, particularly as our knowledge of marrow dosimetry and marrow response to low dose beta-irradiation increases. Though at the present time, I may be one of the few to hold that opinion.

Sgouros: What was the hematologic toxicity in terms of grade in the patient population treated in this study? Have you been able to correlate the dosimetry estimates with the toxicities obtained in this study?

Stubbs: I do not know the toxicity grades for these patients but we saw platelet and neutrophil drops ranging from nil to 50-65%. We have looked into correlating marrow toxicity (% drop in platelet and neutrophil counts) against several marrow absorbed dose parameters. That data will be presented next month at the Society of Nuclear Medicine meeting.

HEMATOLOGIC TOXICITY IN THE RADIOIMMUNOTHERAPY OF SOLID CANCERS WITH ^{131}I-LABELED ANTI-CEA NP-4 IgG_1: DEPENDENCE ON RED MARROW DOSIMETRY AND PRETREATMENT

Behr TM, Sharkey RM, Juweid ME, Dunn RM, Vagg RC, Siegel JA and Goldenberg DM
Garden State Cancer Center
at the Center for Molecular Medicine and Immunology
Newark, NJ 07103

ABSTRACT

The aim of this study was to determine the relationship between red marrow dosimetry and hemotologic toxicity (leuko-/thrombocytopenia) in radioimmunotherapy with the ^{131}I-labeled antibody NP-4. A total of 57 patients with CEA-expressing tumors were treated in a phase I/II dose escalation trial (e.g., 29 colorectal, 9 lung, 7 pancreas, 6 breast and 4 medullary thyroid cancer patients). Most patients were heavily pretreated (chemotherapy, external beam). The patients underwent a diagnostic study (296 MBq [8 mCi]), followed by the therapeutic dose (1628-9916 MBq [44-268 mCi] of ^{131}I-labeled NP-4 IgG). Imaging was performed from 4 up to 240 h p.i. (planar and SPECT). Blood clearance was determined from blood samples, and whole-body clearance from whole-body scanning. Cumulated activities were calculated and dose estimates were derived from the MIRD schema (red marrow dosimetry from blood data and sacral imaging). Red marrow doses ranged from 0.45-7.06 Gy, and whole-body doses from 0.31-3.44 Gy. Sacral/blood ratios were 0.70±0.29 (0.20-1.45). The red marrow was the dose-limiting organ. Blood counts reached their nadir 3-5 weeks p.i., recovering within 9-11 weeks p.i. A strong correlation between marrow doses and myelotoxicity was observed. Differences in pharmacokinetics were found between different types of CEA-producing tumors. Blood half-times were significantly lower in colorectal when compared to all other cancer types ($p<0.001$), as were also the whole-body half-times. As a consequence of the lower red marrow doses (0.59±0.30 vs. 0.95±0.19 mGy/MBq [2.19±1.09 vs. 3.54±0.73 rad/mCi]; $p<0.001$), less hematological toxicity was seen in these patients. In patients without prior radiation or chemotherapy, the maximum tolerated dose (MTD) had not been reached at 6 Gy [600 rad](no toxicity > 2), whereas pretreated patients had higher toxicities (MTD approx. 3.5 Gy [350 rad]). All patients with grade four toxicity had prior external irradiation of ≥10% of their marrow or chemotherapy within the last six months. Patients with bone metastases or chemotherapy with cisplatinum or mitomycin were at especially high risk for developing more severe toxicity. These data suggest that there is a good correlation between red marrow doses and hemtologic toxicity. Previous chemotherapy or radiation, as well as metastatic bone involvement, are important risk factors for the development of more severe toxicity. Variability in MAb clearance may be explained by different clearance rates of tumor-type related CEA-subspecies (CEA-receptor mediated clearance of MAb-CEA complexes). Thus, a higher maximum tolerated dose may be achieved in colorectal cancer than in other tumor types.

INTRODUCTION

In hematological neoplasms, radioimmunotherapy (RAIT) has become a potential third mode of therapy, alongside chemotherapy and external-beam radiation (1,2). This success is probably due to a combination of high radiosensitivity (1,2) and a high antigen accessibility in lymphoma tissue. Unfortunately, both factors do not apply to many types of solid tumors, which are known to be relatively radioresistant and to be characterized by a fairly high interstitial pressure (3), which, combined with poor perfusion of larger lesions and a "binding site barrier" effect (4), results in poor accessibility for the antibody. Therefore, objective therapeutic effects of RAIT in solid tumors have rarely been reported. This is certainly also due to the fact that most RAIT trials reported for solid tumors have involved end-stage patients with bulky tumor masses who have already failed standard treatment regimens, such as surgery, chemotherapy or external beam radiation. However, some recent studies have shown promising results with RAIT in certain types of solid tumors, especially in medullary thyroid, ovarian and colorectal cancer, particularly in patients with small-volume disease (5).

In most standard-dose (i.e., nonmyeloablative) RAIT trials, the red marrow was identified as the only dose-limiting organ (1,6). However, to the best of our knowledge, no study has examined in more detail the relationship between red marrow dose and resulting myelotoxicity. Furthermore, only a few reports exist on other factors which may influence the degree of myelotoxicity in RAIT. Therefore, in this report, we analyze in more detail the factors influencing the red marrow toxicity in clinical RAIT of patients with CEA-expressing tumors who were treated with the ^{131}I-labeled anti-CEA murine monoclonal antibody NP-4 (IgG_1 subtype). These studies may serve as a basis and rationale for the design of further clinical RAIT studies.

PATIENTS, MATERIALS AND METHODS

Monoclonal Anti-CEA Antibody And Radiolabeling

The monoclonal anti-CEA antibody NP-4 used for this study has been described previously (5,7). It belongs to the IgG_1 subclass and is specific for CEA, reacting with a class-III peptide epitope of the CEA molecule, according to the classification of Primus et al. (8). It has an affinity of 10^8 l/mol (7) and does not react with antigens that share CEA-related epitopes, e.g., nonspecific cross-reactive antigens (7).

Radioiodination with $Na^{131}I$ (New England Nuclear, Billerica, MA) was performed by the chloramine-T or iodogen method (9). The specific activity was 444-592 MBq/mg [12-16 mCi/mg]. Eighty-five-95% of the activity was native-size IgG by size-exclusion HPLC, with less than 10% aggregated IgG and less than 5% unbound iodine.

Patients

A total of 57 patients underwent radioimmunotherapy (5) with ^{131}I-labeled anti-CEA NP-4 IgG, with a total of 80 therapeutic injections (20 patients were injected repeatedly, up to four times). Among them were 29 colorectal, 9 lung, 7 pancreatic, 6 breast and 4 medullary thyroid cancer patients, as well as one biliary and one salivary gland cancer patient. All had histologically-proven CEA-expressing cancers. The patients were at least four weeks beyond major surgery, three weeks beyond chemotherapy or external-beam radiation, and had a performance status of 60 or greater on the Karnofsky scale. Patients with serum creatinine levels higher than 1.5 mg/dl or bilirubin levels above 2 mg/dl were excluded. Also excluded were patients with white blood cell counts of $< 3000/\mu l$ (or a granulocyte count of $< 1500/\mu l$), as well as patients with less than 100,000 platelets/μl. Most of

the patients were in very advanced metastatic tumor stages and were heavily pretreated with radio- and/or chemotherapy (5).

CEA and HAMA Determinations and Blood Chemistry

CEA serum levels were determined using a CEA-EIA, which has been described in detail earlier (10). HAMA levels were determined as described previously (11). The normal range of HAMA in most patients without prior exposure to mouse proteins was a titer below 100. Routine blood chemistry parameters, blood cell counts, and differential blood counts were obtained at the same time-points, and occasionally more frequently.

Radioimmunotherapy Protocol

The therapy was designed as a dosimetry-based protocol with the intention to retreat patients several times. Patients entered into the RAIT protocol first underwent a diagnostic-dosimetric study, with 0.5 - 2.5 mg of protein labeled with 296-1110 MBq [8.0 - 30.0 mCi] of ^{131}I, on an outpatient basis for assessment of tumor targeting and dosimetry. Based on the results of this diagnostic study, patients were admitted to the hospital for the initial therapeutic dose. The amount of administered activity was calculated to deliver no more than 1.50 Gy to the red marrow (as a blood-based dose) from the diagnostic and therapeutic studies in the first six patients. Thereafter, the dose was raised in 1-Gy increments (six patients per group) until more than one patient per group developed toxicity higher than grade three. This limit was reached at 4.5 Gy to the red marrow. An upper limit for the injected activity was defined at 9250 MBq [250 mCi] (± 10 percent) per injection. This dose level (4.5 Gy to the red marrow or 9520 MBq total activity) was subsequently maintained for the rest of the study. In patients where bone marrow had been harvested and stored, the allowed upper dose limit to the red marrow was 5.5 Gy. If there was no toxicity greater than grade three, the patients were eligible for retreatment after all hematologic parameters had returned to normal for at least two weeks, regardless of their HAMA status. The retreatment activity was calculated to deliver the same marrow dose as had been the patient's previous limit. Red marrow and organ toxicity was graded according to standard toxicity criteria. Patients developing grade four toxicity or showing progressing disease under treatment were excluded from retreatment. Therapeutic injections were performed with 4.5 - 22.7 mg of protein labeled with 1628-9916 MBq [44.0 - 268.0 mCi] ^{131}I.

Imaging and Pharmacokinetic Analysis

Anterior and posterior planar images of the head, neck, chest, abdomen and pelvis were obtained in diagnostic studies from 4 h up to 192 h postinjection using a high-energy parallel-hole collimator. In therapeutic settings (i.e., higher activities), imaging was started on the day when the retained whole-body activity reached 1110 MBq [30 mCi] or less, and continued for at least three imaging sessions. SPECT of the pelvis, abdomen and chest was regularly performed on at least two occasions, with additional studies when indicated by the particular clinical presentation.

MAb blood-clearance rates were determined by counting samples at various times after the end of the infusion. Mostly, blood samples were collected at 5 min, 30 min, 1, 2, 4, 8, 24, 48, 72, 96 and 120 hours after the end of the antibody infusion until the end of imaging. Clearance rates were calculated for each patient using the least-squares analysis, as described previously (5,12,13). The clearance data are expressed as the biological clearance times as follows: half-time-alpha (distribution phase); half-time-beta (elimination phase); and (overall) half-time, $T_{½}$ (number of hours required for 50% of the activity to be cleared from the blood).

Total-body clearance rates were determined from whole-body scans obtained at 4, 24, 48, 72 and 96 hours until the end of the imaging time, or, for patients receiving therapeutic doses, by a hand-held

rate meter (at 1 m distance from the patient), with measurements initiated immediately at the end of infusion, followed by twice-daily readings until the end of the study.

Plasma samples taken at 1 and 24 hours after antibody administration were analyzed by low- or high-pressure size-exclusion chromatography either on a Sephacryl-300 column (1.6 x 90 cm; Pharmacia, Piscataway, NJ) or on a GF-250 column (DuPont, Wilmington, DE), as described in more detail elsewhere (5).

Dosimetry

For organ and tumor dosimetry, the sacrum, as a region representative of the red marrow (13,14), and ROIs of organs and tumors were generated from the anterior and posterior planar views obtained during each imaging session on at least three occasions. Appropriate adjacent soft-tissue regions of the chest, abdomen and pelvis served as background regions. The activities in these regions were generated using the build-up factor methodology for Compton scatter compensation (15). The individual time-activity curves of organs and tumors were fit to an exponential function using a nonlinear, least-squares analysis or a trapezoidal method, and then integrated to obtain the cumulative activity in each region. The blood time-activity concentration data were fit by a biexponential function to obtain the cumulated activity in the blood. The red marrow cumulated activity was calculated from these blood data by multiplying this concentration by 1,500, the assumed weight in grams of the marrow in an average adult (blood-based doses, assuming a blood/marrow ratio of 1.0). Imaging-based red marrow dosimetry was calculated from sacral scintigraphy (13,14) by assuming 9.9% of the total red marrow is located in the sacrum (13,14). The mean dose in mGy was calculated for organs and tumors according to the Medical Internal Radiation Dose (MIRD) schema, with correction for the remainder of the whole-body activity (16,17). The masses of normal organs were generated from MIRD standard tables (18).

RESULTS

Patient Characteristics

All 57 patients in this study presented advanced metastatic stages of their disease, and most were heavily pretreated with chemotherapy and/or radiation. Thirty-eight patients had undergone previous chemotherapy, 20 had external-beam radiation and 18 had both. These conventional treatment regimens had either failed or were abandoned because of severe side effects, such as prolonged myelosuppression, pulmonary toxicity or myocardial insufficiency. Two of the 57 patients had undergone previous radioimmunotherapy using the ^{131}I-labeled anti-CEA antibodies NP-2 or NP-3 IgG at our institution before entering the NP-4 treatment protocol.

Pharmacokinetics

Influence of HAMA on biokinetics and dosimetry. At HAMA titers below 300, no effect on the clearance rates of the antibody from the blood and whole-body was apparent, whereas with titers above this threshold a rapidly increasing plasma and whole-body clearance rate was observed. This was reflected by decreasing red marrow and whole-body doses.

Influence of circulating antigen and tumor type on pharmacokinetics. Circulating CEA, as well as the type of CEA-expressing cancer, had a marked influence on the pharmacokinetics of NP-4 IgG. Figure 1 shows that over a similar range of circulating plasma CEA, HAMA-negative colorectal

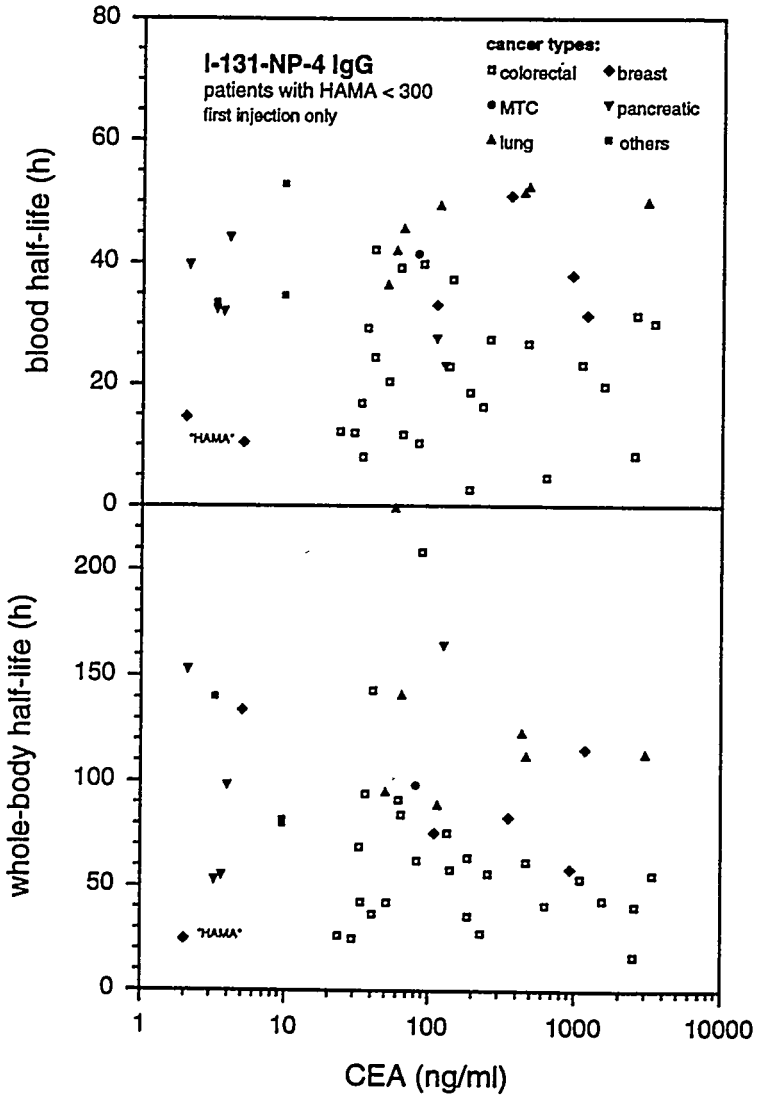

Figure 1. Blood and whole-body half-times in relation to the plasma CEA level and the tumor type.

cancer patients cleared the antibody significantly faster from blood and whole-body than all other types of CEA-producing cancer (blood T½ 21.4 ± 11.1 h versus 35.8 ± 13.2 h; $p<0.01$). Two breast cancer patients were exceptions; however, since their CEA levels were both below 5 ng/ml, the role of circulating antigen as a reason for this rapid blood clearance was unlikely. Indeed, it was subsequently shown by in vitro complexation studies that HAMA not detected by the assay employed was responsible (these patients are marked as HAMA" in Figure 1). Similar differences between colorectal cancer and other CEA-expressing tumors were also observed in the whole-body half-times (61.9 ± 39.9 h versus 96.1 ± 48.2 h for colorectal versus other tumor types; $p<0.01$). Typically, a high liver uptake was seen in early scans in these rapidly-clearing patients, with subsequent metabolic release of a LMWF (low-molecular weight fraction) that was at least partially composed of iodide, as indicated by its uptake in the thyroid and stomach. In contrast to the rapid metabolic breakdown caused by HAMA, no enhanced bone marrow or splenic uptake was seen in these patients.

Dosimetry

Red marrow and whole-body doses. Red marrow doses ranged from 0.45 to 7.06 Gy, and whole-body doses from 0.31 to 3.44 Gy. Consistent with the shorter blood and whole-body half-times, the radiation doses to red marrow and whole-body were significantly lower in HAMA-negative patients with colorectal than with other types of cancer (0.59 ± 0.30 vs. 0.95 ± 0.19 mGy/MBq [2.2 ± 1.1 vs. 3.5 ± 0.7 rad/mCi] for the red marrow, $p<0.001$; and 0.16 ± 0.08 vs. 0.24 ± 0.05 mGy/MBq [0.6 ± 0.3 vs. 0.9 ± 0.2 rad/mCi] for the whole-body, $p<0.001$). Patients with elevated HAMA (titers > 300) had significantly decreased blood and whole-body half-times, thus decreased red marrow and whole-body doses. At HAMA titers above 1000, all red marrow doses were below 0.3 mGy/MBq [1.0 rad/mCi], and the whole-body doses were below 0.1 mGy/MBq [0.3 rad/mCi].

Figure 2 shows the predictability from the diagnostic estimates of the radiation dose to the red marrow and whole-body in the first therapy injection in patients with HAMA titers < 300. There was

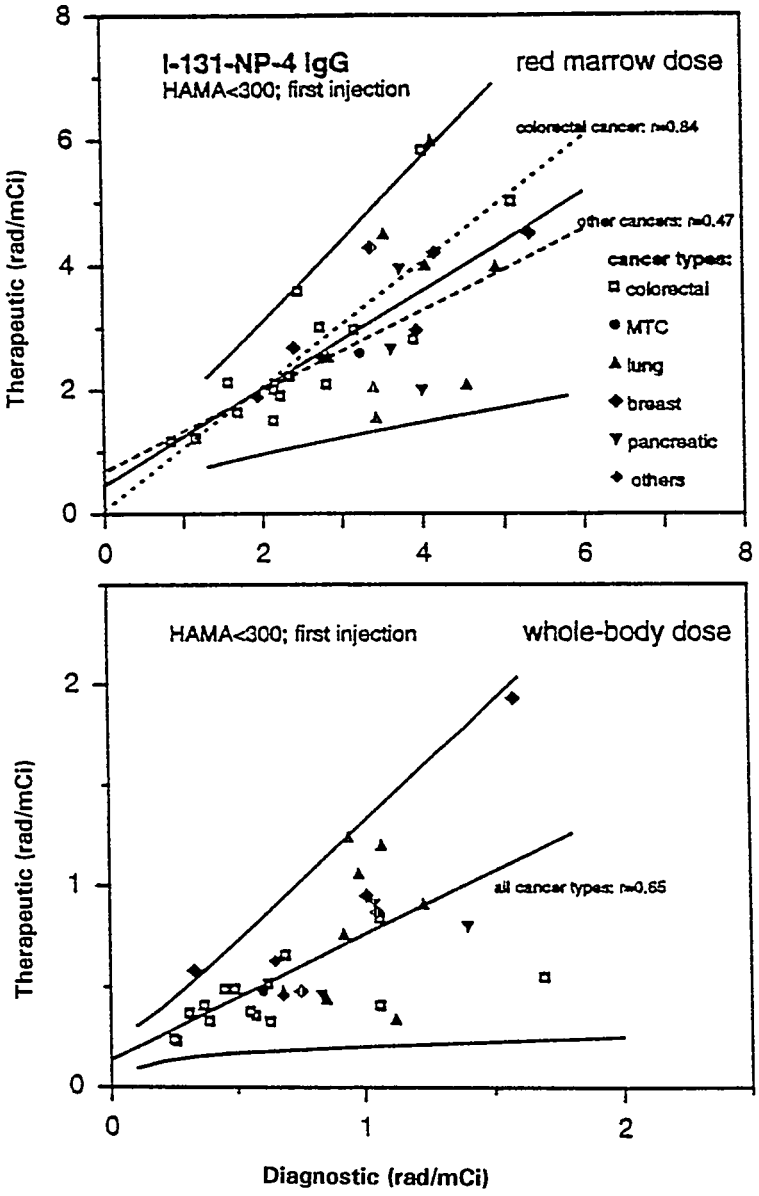

Figure 2. Predictability of the actually observed therapeutic doses from the diagnostic dose estimates.

a good correlation between diagnostic and therapeutic dosimetry in colorectal cancer patients (dotted line; r=0.84), with the regression line being close to the identity line between both studies. In the other cancer types, the observed therapy doses tended to be slightly lower than what had been predicted by the dosimetric study (Fig. 2, upper panel, dashed line). However, the sample size was too small for reaching statistical significance with respect to the potential difference between colorectal and other cancer types, as is the case for the whole-body doses as well (Fig. 2, lower panel). The solid lines in Figure 2 represent the overall regression line together with the 95-percent prediction intervals for red marrow (upper panel) and whole-body doses (lower panel). It is noteworthy that not in a single case would the red marrow or whole-body dose have been underestimated by more than 30 percent, whereas in 24.4 percent of cases, the red marrow dose was overestimated by more than 30 percent. When estimated from the blood, red marrow doses were approximately 30 percent higher than those obtained from imaging of the sacrum as a region representative of the bone marrow (14). Table 1 summarizes the overall red marrow, whole-body and organ dosimetry of ^{131}I-NP-4 IgG.

Table 1 Organ Dosimetry of ^{131}I-NP-4 IgG in HAMA-Negative (i.e., titer < 300) Patients		
	Radiation Absorbed Dose (mGy/MBq)	
Organ	Mean ± SD	Range
whole-body	0.20 ± 0.10	0.07 - 0.46
red marrow		
blood	0.81 ± 0.39	0.18 - 1.44
sacrum	0.59 ± 0.34	0.03 - 1.30
ratio sacrum/blood	0.19 ± 0.08	0.05 - 0.39
liver	0.49 ± 0.22	0.14 - 1.08
spleen	0.96 ± 0.40	0.27 - 1.60
lung	0.62 ± 0.33	0.14 - 1.19
kidney	0.96 ± 0.26	0.70 - 1.43
thyroid	7.04 ± 5.63	0.72 - 15.10
urinary bladder wall	0.72 ± 0.03	0.67 - 0.75
testes/ovaries	0.49 ± 0.16	0.34 - 0.78
brain/lenses	0.02 ± 0.01	0.02 - 0.03

Bone Marrow Toxicity

Myelotoxicity in relation to red marrow doses and pretreatment. The red marrow was the only dose-limiting organ. In the dose escalation part of this trial, no red marrow toxicity higher than grade 3 was observed until 3.5 Gy (blood-based), whereas one grade-4 toxicity (white blood cells and platelets) was seen at the 4.5-Gy level to the red marrow. This dose level was therefore maintained for the rest of the study, unless autologous bone marrow had been harvested and stored. In the latter case, 5.5 Gy was the intended red marrow dose (5 patients). However, in none of them was actual bone marrow grafting necessary to overcome myelotoxicity.

Table 2 summarizes the results of the retrospective analysis of the red marrow toxicities seen in 44 assessable patients in correlation to the actually observed red marrow doses. The patients were divided into different categories according to their extent of pretreatment (external beam radiation and/or chemotherapy), as well as the time that elapsed since this treatment, potentially compromising the bone marrow reserve and, therefore, its ability to cope with radiation exposure. In a total of 14 assessable patients without any previous chemo- or radiotherapy, no white blood cell toxicity greater than grade 2 was observed despite red marrow doses of up to 6.13 Gy. In the same group of patients, the highest platelet toxicity observed was in a colorectal cancer patient with a grade 3 thrombocytopenia at a red marrow dose of 3.4 Gy. Interestingly, this patient had an elevated HAMA at the time of his therapeutic injection (titer 761), and showed an intense and unusually-persistent bone marrow uptake, so that the actual bone-marrow dose may be much higher than estimated from the blood-based dosimetry.

Table 2

Bone Marrow Toxicity in 44 Assessable Patients, in Relation to Red Marrow Dose and Pretreatment (first RAIT only)

Red marrow dose (Gy)	Toxicity grade					Total
	0	1	2	3	4	
Leukopenia:						
<2	7 (3[a]/2[b]/1[c]/1[d])	3 (0/2/1/0)	0	0	0	10 (3/4/2/1)
2.0-2.99	9 (3/1/5/0)	3 (1/0/2/0)	0	0	0	12 (4/1/7/0)
3.0-3.99	6 (2/3/1/0)	1 (0/1/0/0)	3 (3/0/0/0)	0	2 (0/0/1/1)	12 (5/4/2/1)
4.0-4.99	3 (1/1/0/1)	0	1 (0/0/0/1)	0	0	4 (1/1/0/2)
5.0-5.99	1 (0/1/0/0)	1 (1/0/0/0)	2 (0/1/1/0)	0	0	3 (0/2/1/0)
>6.0	0		0	2 (0/0/2/0)	0	3 (1/0/2/0)
Total	26 (9/8/7/2)	8 (2/3/3/0)	6 (3/1/1/1)	2 (0/0/2/0)	2 (0/0/1/1)	44 (14/12/14/4)
Thrombocytopenia:						
<2	7 (3/2/2/0)	1 (0/1/0/0)	1 (0/1/0/0)	1 (0/0/0/1)	0	10 (3/4/2/1)
2.0-2.99	7 (3/1/3/0)	2 (1/0/1/0)	1 (0/0/1/0)	2 (0/0/2/0)	0	12 (4/1/7/0)
3.0-3.99	5 (4/0/1/0)	0	3 (0/3/0/0)	1 (1/0/0/0)	2 (0/0/1/1)	11 (5/3/2/1)
4.0-4.99	2 (1/0/0/1)	1 (0/1/0/0)	0	1 (0/0/0/1)	1 (0/0/1/0)	5 (1/1/1/2)
5.0-5.99	0	1 (0/1/0/0)	1 (0/1/0/0)	0	1 (0/0/1/0)	3 (0/2/1/0)
>6.0	1 (1/0/0/0)	0	0	2 (0/0/2/0)	0	3 (1/0/2/0)
Total	22 (12/3/6/1)	5 (1/3/1/0)	6 (0/5/1/0)	7 (1/0/4/2)	4 (0/0/3/1)	44 (14/11/15/4)

a) patients without any prior radio- or chemotherapy (with exception of $Na^{131}I$ thyroid ablation)
b) patients with prior irradiation of less than 10 % of the bone marow and/or no chemotherapy within the last 6 months
c) patients with prior irradiation of 10 - 20 % of the bone marrow and/or chemotherapy within 1 - 6 months prior to RAIT
d) patients with irradiation of more than 20 % of the bone marrow and/or chemotherapy within the last 4 weeks before RAIT

In more heavily pretreated patients, severe leukocyte toxicities (grade 3 and 4) occurred at red marrow doses over 3.0 Gy, and platelet toxicities were seen even at doses below 2.0 Gy. All patients with grade 4 toxicities had prior irradiation of more than 10 percent of the bone marrow and/or chemotherapy within the last 6 months before radioimmunotherapy, and all of them had, additionally, multiple bone metastases.(three lung cancer and one breast cancer patient). One breast cancer patient developed grade 4 platelet and white blood cell toxicity at a red marrow dose of only 3.71 Gy. She had undergone high-dose chemotherapy with adriamycin, vincristine, cyclophosphamide and mitomycin together with autologous bone marrow transplantation six months before radioimmunotherapy, and was on an immunotherapy trial with interferon four weeks before RAIT. A bone marrow biopsy after the development of this severe toxicity showed diffuse bone marrow infiltration by tumor cells, replacing the normal marrow space almost completely. A second bone marrow transplantation with marrow that was stored from her first ABMT became necessary.

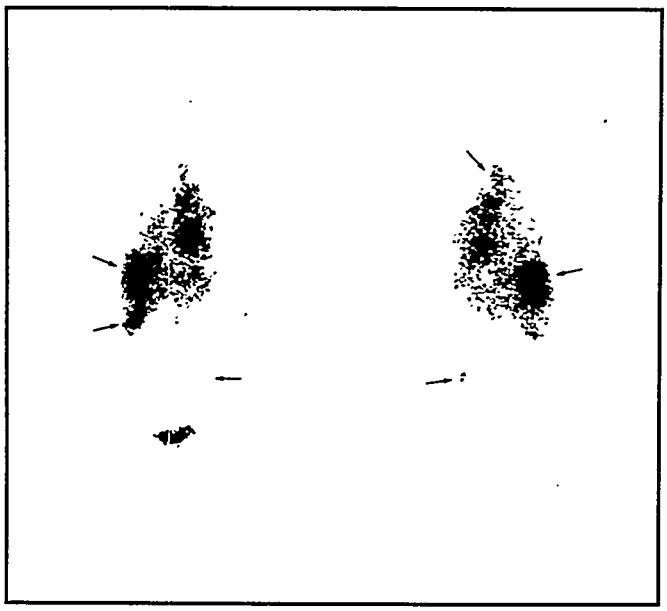

Figure 3. Whole-body scan of patient #949, a 62-year-old woman with extensively metastasized breast cancer, 72 h after injection of 2579 Mbq [69.7 mCi] ^{131}I-NP-4 IgG. The presence of bone metastases was identified as an additional risk factor for more severe myelotoxicity. The arrows show multiple sites of involvement (bone, liver).

Myelotoxicity in relation to cancer type and bone (marrow) involvement with tumor. The presence of bone or bone marrow metastases was identified as an for additional important risk factor the development of red marrow toxicity (Figure 3). Of eleven patients with bone involvement, four had grade 4, one additional Grade 3 platelet toxicity, and only three had no bone marrow toxicity. Interestingly, these three had no more than two bone lesions, whereas patients with higher toxicities had multiple sites of involvement. A correlation between cancer type and red marrow toxicity was observed as as well. Only one grade 3 white blood cell and five grade 3 platelet toxicities were seen in a total of 26 assessable colorectal cancer patients, and no toxicity higher than grade 2 was observed in 3 patients. In contrast, at comparable radiation doses, assessable medullary thyroid cancer four grade 4 and two grade 3 toxicities were seen in seven lung cancers, and one grade 4 toxicity in five assessable breast cancer patients.

Generally, patients who were pretreated with mitomycin and/or cisplatinum tended to have very severe bone marrow toxicities after RAIT. However, these chemotherapeutic agents were given mostly to lung and breast cancer patients who also had higher red marrow doses due to their longer serum half-times, and most had also bone marrow involvement and/or additional external beam radiation. Therefore, the definitive role of these chemotherapeutic agents as especially high risk factors is uncertain.

Typically, white blood cell and platelet counts began to drop, platelets usually preceeding leukocytes, two to three weeks after RAIT, reaching their nadir four to seven weeks after the RAIT injection (Figure 4). The time to recovery was typically nine to eleven weeks post-RAIT. With adequate treatment (platelet transfusions, cytokines), all but two patients recovered without any sequelae from their grade 3 or 4 toxicities. Both of these two patients died in grade 4 platelet toxicity from a bleeding stomach ulcer because they refused platelet tranfusion or any treatment other than analgesics.

In the case of retreatment, the toxicities observed were additionally dependent upon HAMA titers (the higher the HAMA, the lower the red marrow dose, thus the less the red marrow toxicity), the time that elapsed between the prior treatment and the retreatment injection (the shorter the time, the higher the toxicity), as well as the time between the recovery of previous marrow toxicity and the subsequent RAIT (the shorter the time, the higher the toxicity). Since the HAMA problem was the dominant feature, these data were not analyzed in more detail.

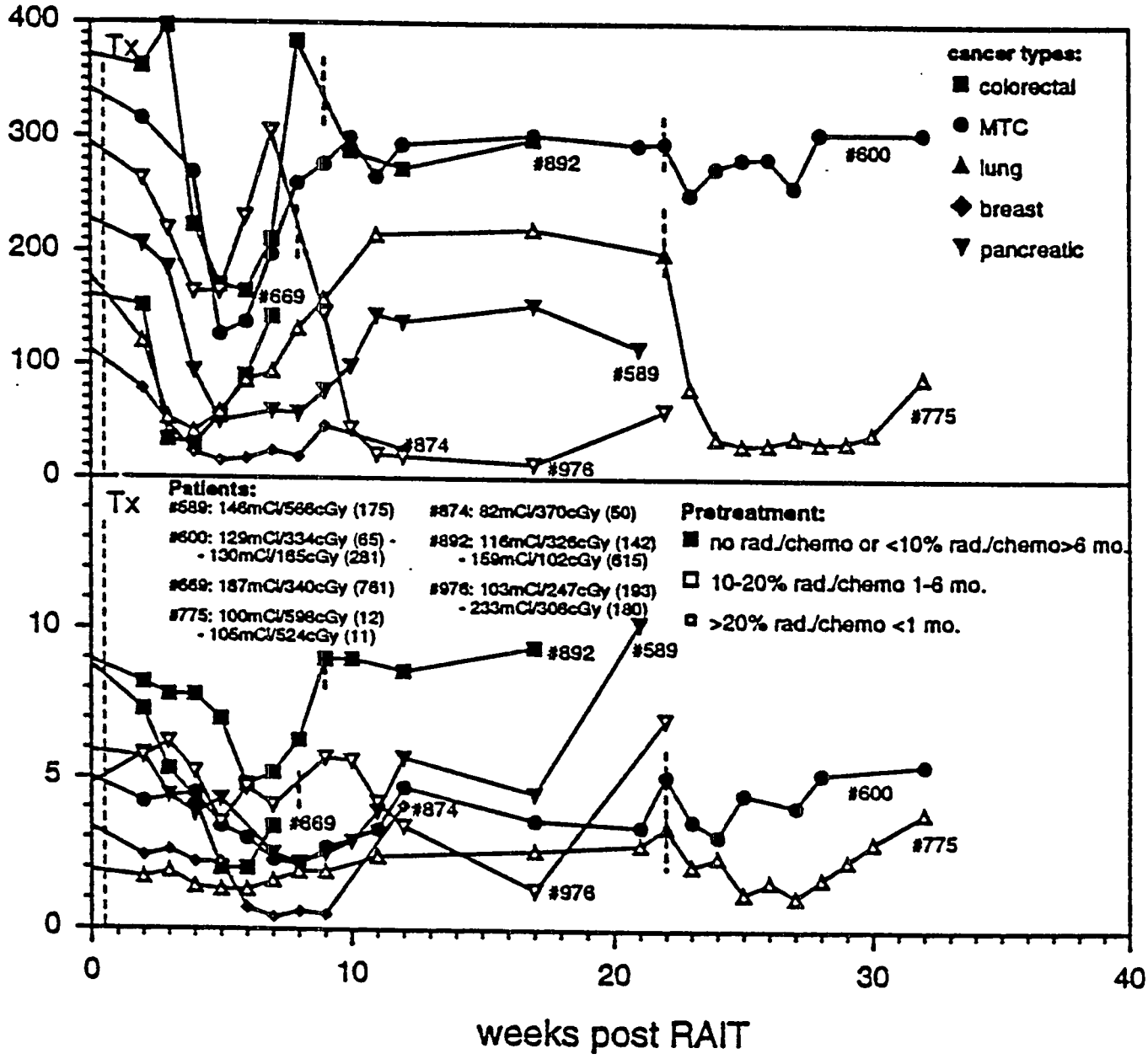

Figure 4. Typical white blood cell and platelet curves for seven representative patients with different cancer types and differences in pretreatment. Dashed lines indicate time-points of (re-)treatment. Values in parentheses after injected mCi and red marrow doses represent HAMA titers at the time of antibody injection.

DISCUSSION

The present Phase I/II RAIT study was designed as a dosimetry-based protocol with the intent that patients would receive several retreatments. As was shown earlier for other anti-CEA MAbs (5,19), their clearance rate is influenced not only by HAMA, but also by complexation with circulating antigen. In a previous study we demonstrated that this clearance rate is dependent on the

histogenetic tumor type; a fundamental difference between colorectal cancer and all other tumor types was found (19). Over a similar range of plasma CEA, colorectal cancer patients cleared the antibody significantly faster than did patients with other CEA-expressing malignancies. This was especially pronounced in colorectal cancer patients with liver metastases. Microheterogeneities in the chemical structure of the CEA produced by different cancer types may be responsible for the differences in clearance rates (5,19-21). The different and, in individual cases, unpredictable clearance rates of the radiolabeled antibodies clearly underline the necessity of an individualized, dosimetry-based treatment planning, and not just standard dosing based on body surface area. In view of this concept, it is very interesting that the therapeutic dosimetry seems to be fairly predictable from the diagnostic injection, despite the fact that different protein doses were given for each injection.

As seen in other RAIT trials (1,2,12,13,22,23), myelosuppression was the only dose-limiting toxicity. The difference in radiosensitivity was minimal between patients who never had any external-beam radiation or chemotherapy before, and those who had less than 10 percent of their red marrow irradiated or who were given chemotherapy more than 6 months before RAIT. In this subset of patients, the maximum tolerated dose has not been reached in our study, despite individual doses of over 6 Gy [600 rad]. In contrast, patients with irradiation of more than 10 percent of their blood-forming bone marrow, or who had recently undergone chemotherapy, started to develop grade 3 or higher toxicities at 3 Gy [300 rad] or even less (MTD approximately 4 Gy [400 rad] to the red marrow).

The presence of diffuse or widespread bone metastases seems to be a risk factor by itself for the development of marrow toxicity. Two reasons are apparent. First, the replacement of red marrow by the tumor itself and, second, the fact that the real dose to the blood-forming elements will be underestimated by a dosimetry based on the peripheral blood, since elements in the bone marrow itself are targeted, irradiating the neighboring progenitor blood cells. The severe toxicity in a breast cancer patient who had recently undergone high-dose chemotherapy with autologous bone marrow grafting, and who was treated shortly after an interferon trial and who had diffuse bone-marrow tumor involvement, is easily understandable based on this multiplicity of risk factors. It cannot be decided at this time whether the lower toxicities observed in colorectal cancer patients, compared to lung or breast cancer patients, are due to differences in the pretreatment (less aggressive chemotherapy and radiation), to the lower likelihood of bone involvement or to the more rapid antibody clearance, or probably to a combination of these factors. It has been described earlier that certain chemotherapeutics (e.g., mitomycin) are associated with an especially high myelotoxicity of RAIT (6,22).

The fact that red marrow doses of over 6 Gy [600 rad] were tolerated in patients without any myelotoxic pretreatment without developing dose-limiting toxicity, seems to be of especial importance with respect to the design of adjuvant radioimmunotherapy trials. The combination of a relatively high tolerance of the uncompromised red marrow togtether with an anticipated high radioantibody uptake in small tumor cell clusters (24,25) in the adjuvant situation should lead to good therapeutic efficacy without severe toxicty.

ACKNOWLEDGMENTS

These studies were supported in part by grants from the Deutsche Forschungsgemeinschaft (DFG Be 1689/1-1/2) and the National Institutes of Health (CA39841 and CA54425).

REFERENCES

1. Goldenberg DM (ed.). Cancer Therapy with Radiolabeled Antibodies. CRC Press, Boca Raton 1995.
2. Press OW, Eary JF, Appelbaum FR, Martin PJ, Nelp WB, Glenn S, Fisher DR, Poster B, Matthews DC, Gooley T and Bernstein ID. Phase II trial of ^{131}I-B1 (anti-CD20) antibody therapy with autologous stem cell transplantation for relapsed B cell lymphoma. Lancet 346:336-340, 1995.
3. Jain RK, and Baxter LT. Mechanisms of heterogenous distribution of monoclonal antibodies and other macromolecules in tumors: Significance of elevated interstitial pressure. Cancer Res 48:7022-7032, 1988.
4. Juweid M, Neumann R, Paik C, Perez-Bacete MJ, Sato J, van Osdol W and Weinstein JN. Micropharmacology of monoclonal antibodies in solid tumors: Direct experimental evidence for a binding site barrier. Cancer Res 52:5144-5153, 1992.
5. Behr TM, Sharkey RM, Juweid ME et al. Phase I/II clinical radioimmunotherapy with an ^{131}I-labeled anti-CEA murine monoclonal antibody. J Nucl Med In press, 1997.
6. Divgi CR, Scott AM, Dantis L, Capitelli, Siler K, Hilton S, Finn RD, Kemeny N, Kelsen D, Kostakoglu L, Schlom J and Larson SM. Phase I radioimmunotherapy trial with iodine-131-CC49 in metastatic colon carcinoma. J Nucl Med 36:586-592, 1995.
7. Sharkey RM, Goldenberg DM, Goldenberg H, Lee RF, Ballance C, Pawlyk D, Varga D and Hansen HJ. Murine monoclonal antibodies against carcinoembryonic antigen: immunological, pharmacokinetic, and targeting properties in humans. Cancer Res 50:2823-2831, 1990.
8. Primus FJ, Newell KD, Blue A and Goldenberg DM. Immunological heterogeneity of carcinoembryonic antigen: antigenic determinants on carcinoembryonic antigen distinguished by monoclonal antibodies. Cancer Res 43:686-692, 1983.
9. Weadock KS, Sharkey RM, Varga DC and Goldenberg DM. Evaluation of a remote radioiodination system for radioimmunotherapy. J Nucl Med 31:508 -511, 1990.
10. Primus FJ, Kelley EA, Hansen HJ and Goldenberg DM. 'Sandwich'-type immunoassay for carcinoembryonic antigen in patients receiving murine monoclonal antibodies for diagnosis and management of cancer. Clin Chem 34:261-264, 1988.
11. Hansen HJ, Sullivan CL, Sharkey RM and Goldenberg DM. HAMA interference with murine monoclonal antibody-based immunoassays. J Clin Immunoassays 16:294-299, 1993.
12. Sharkey RM, Juweid M, Shevitz J, Behr T, Dunn R, Swayne LC, Wong GY, Blumenthal RD, Griffiths GL, Siegel JA, Leung S, Hansen HJ and Goldenberg DM. Evaluation of a CDR-grafted (humanized) anti-carcinoembryonic antigen (CEA) monoclonal antibody in preclinical and clinical studies. Cancer Res 55:5935s-5945s, 1995.
13. Siegel JA, Pawlyk DA, Lee RE, Sasso NL, Horowitz JA, Sharkey RM and Goldenberg DM. Tumor, red marrow, and organ dosimetry for ^{131}I-labeled anti-carcinoembryonic antigen monoclonal antibody. Cancer Res 50:1039s-1042s, 1990.
14. Siegel JA, Lee RE, Pawlyk DA, Horowitz JA, Sharkey RM and Goldenberg DM. Sacral scintigraphy for bone marrow dosimetry in radioimmunotherapy. Nucl Med Biol 16:553-559, 1989.
15. Wu RK and Siegel JA. Absolute quantitation of radioactivity using the buildup factor. Med Phys. 11:189-192, 1984.
16. Pawlyk DA, Siegel JA, Sharkey RM and Goldenberg DM. Automating large-scale processing of dosimetry data. J Nucl Med 34:160P (abstract 780), 1993.
17. Dunn RM, Juweid ME, Behr TM, Siegel JA, Sharkey RM and Goldenberg DM. An automated

internal dosimetry scheme for radiolabeled antibodies. Med Phys 22:1549-1550, 1995.
18. Snyder WS, Ford MR, Warner GG and Watson SB. 'S' Absorbed Dose per Unit Cumulative Activity for Selected Radionuclides and Organs. MIRD Pamphlet No.11. Society of Nuclear Medicine, New York 1976.
19. Behr TM, Sharkey RM, Juweid ME, Dunn RM, Ying Z, Zhang CH, Siegel JA, Gold DV and Goldenberg DM. Factors influencing the pharmacokinetics, dosimetry, and diagnostic accuracy of radioimmunodetection and radioimmunotherapy of CEA-expressing tumors. Cancer Res 56:1805-1816, 1996.
20. Hernando JJ, von Kleist S and Grunert F. A repertoire of monoclonal antibodies reveals extensive epitope heterogeneity in CEA purified from neoplasms originating from different organs. Int J Cancer 56:655-661, 1994.
21. Thomas P, Toth CA, Saini KS, Jessup JM and Steele G. The structure, metabolism and function of the carcinoembryonic antigen gene family. Biochim Biophys Acta 1032:177-189, 1990.
22. Welt S, Divgi CR, Kemeny N, Finn RD, Scott AM, Graham M, St.Germain J, Richards EC, Larson SM, Oettgen HF and Old LJ. Phase I/II study of iodine-131-labeled monoclonal antibody A33 in patients with advanced colon cancer. J Clin Oncol 12:1561-1571, 1994.
23. Meredith RF, Bueschen AJ, Khazaeli MB, Plott WE, Grizzle WE, Wheeler RH, Schlom J, Russell CD, Liu T and LoBuglio AF. Treatment of metastatic prostate carcinoma with radiolabeled antibody CC49. J Nucl Med 35:1017-1022, 1994.
24. Blumenthal RD, Sharkey RM, Haywood L, Natale AM, Wong GY, Siegel JA, Kennel SJ and Goldenberg DM. Targeted therapy of athymic mice bearing GW-39 human colonic cancer micrometastases with ^{131}I-labeled monoclonal antibodies. Cancer Res 52:6036-6044, 1992.
25. Sgouros G. Radioimmunotherapy of micrometastases: Side-stepping the solid-tumor hurdle. (Editorial) J Nucl Med 36:1910-1912, 1995.

QUESTIONS

Shen: Comment. It is very practical and effective that you correlate marrow dose to toxicity grades. When we took one more step to correlate marrow dose to blood counts, we had to address marrow cell proliferation, multilayer structure from stem cell to mature cell and marrow reserve due to previous chemotherapy. We need defined criteria for patient selection in order to have good correlations.

Zadasny: Did you present red marrow doses based on blood samples or the sacral dosimetry method?

Behr: The values were based on blood samples assuming a specific activity ratio of marrow/blood = 1.0. The sacral method was used only by planar gamma camera views. We are looking at using a SPECT method to further refine, and expect an even better correlation between the resulting doses and myelotoxicity.

Muller: The correlation between bone marrow toxicity and toxicity is described as "good", but is it statistically significant?

Behr: Yes, probably, especially if you stratify the patients with regard to previous treatment.

Muller: But in that case the numbers become very small.

Behr: I agree, but you would need studies in hundreds of patients in order to get numbers in each category.

Sgouros: Did you examine correlation of administered activity with whole-body dose?

Behr: Yes, we did. Actually there was a pretty good correlation between the whole-body doses and the resulting myelotoxicity as well. The correlation was better, however, between red marrow doses and mylotoxicity. This is the reason why we just showed this correlation. I think, since the red marrow is the target organ we are interested in, it makes more sense to look at the dose to this organ, not to the whole-body. Since there is a pretty good correlation between red marrow doses and whole-body doses, the correlation between the dose and myelotoxicity is not very surprising anymore.

BIOKINETICS AND DOSIMETRY AFTER REPEATED INJECTIONS OF ^{111}In-DTPA-D-Phe^{1}-OCTREOTIDE

Andersson P[1], Forssell-Aronsson E[1], Grétarsdóttir J[1], Johanson V[2], Wängberg B[2], Nilsson O[3], Fjälling M[4] and Ahlman H[2]
Departments of [1]Radiation Physics, [2]Surgery and [3]Pathology and [4]Nuclear Medicine
Göteborg University
Sahlgrenska University Hospital
S-413 45 Göteborg, Sweden

ABSTRACT

The biokinetics and dosimetry of ^{111}In-DTPA-D-Phe^{1}-octreotide were studied in a 55-year old woman with metastatic spread of a midgut carcinoid tumor to the liver, skeleton, para-aortic and mediastinal lymph nodes. For dose planning, the patient received an intravenous injection of a diagnostic amount of ^{111}In-DTPA-D-Phe^{1}-octreotide (D, 280 MBq per 10 g). Treatment was given four times with ^{111}In-DTPA-D-Phe^{1}-octreotide (T1-T4) with 3-20 week intervals. In the first three therapeutic administrations T1, T2 and T3, the patient received 40 μg DTPA-octreotide labeled with 3.0, 3.5 and 3.1 GBq ^{111}In, respectively. In the fourth T4, 1.3 and 1.5 GBq ^{111}In-DTPA-D-Phe^{1}-octreotide were given 24 h apart. Each fraction contained 20 μg DTPA-octreotide.

Anterior and posterior whole-body scintigraphy was performed repeatedly up to 550 h after each injection. During the first 60 h after T1-T3, a 1 mm lead shield was mounted on the gamma camera to avoid dead-time losses. Cumulated activity and residence times were estimated from the time-activity curves for whole body, liver, spleen, kidneys, urinary bladder and a bone metastasis. Mean absorbed doses were calculated with the MIRDOSE 3 program.

The relative ^{111}In content (%/IA) in the whole body, liver with metastases, and a bone metastasis was lower after T1-T3 than after D. The relative ^{111}In content was higher in all studied organs and tissues after the fractionated T4 compared with T1-T3.

The absorbed dose per unit injected activity was highest for D and T4. The whole body received a total mean absorbed dose of 1.2 Gy. The total mean absorbed dose to a hypothetical 140 g tumor in the abdomen was estimated to be 17 Gy.

INTRODUCTION

Several neuroendocrine tumors express large numbers of high affinity cell surface receptors for somatostatin. Octreotide, a long-acting somatostatin analogue, is used clinically for symptomatic treatment of neuroendocrine tumors, i.e. it inhibits hormone secretion from the tumor cells.

Scintigraphy using ^{111}In-DTPA-D-Phe^1-octreotide is a sensitive and accurate method to localize neuroendocrine tumors.

Measurements of ^{111}In activity concentration in biopsies of tumor and normal tissues in patients with neuroendocrine tumors, after preoperative injection with ^{111}In-DTPA-D-Phe^1-octreotide, have revealed very tumor-to-normal tissue ratios (1). Furthermore, binding studies and electron microscopic autoradiography of cultured human neuroendocrine tumor cells have shown internalization of ^{111}In after incubation with ^{111}In-DTPA-D-Phe^1-octreotide (2). These findings indicate the possibility of using the enhanced biological effect from intracellularly-emitted Auger electrons from ^{111}In after administration of ^{111}In-DTPA-D-Phe^1-octreotide.

A 55-year old woman with a severe midgut carcinoid syndrome (duration of several years) underwent radiotherapy with ^{111}In-DTPA-D-Phe^1-octreotide, injected intravenously (3). The patient had metastatic spread to the liver, para-aortic and mediastinal lymph nodes, and also to the skeleton. Due to the large tumor burden in the liver (>50%), the patient was not suitable for ischemic treatment of the liver metastases (hepatic arterial embolization). The decision to attempt radiotherapy with ^{111}In-DTPA-D-Phe^1-octreotide was based on a) the high tumor-to-normal tissue ^{111}In activity concentration ratios observed in surgical biopsies after injection of a diagnostic amount of ^{111}In-DTPA-D-Phe^1-octreotide, b) the demonstrated internalization of ^{111}In into tumor cells of the patient when studied in primary culture (2), and c) the obvious limitations for interventional treatment due to the extent and dissemination of the patient's disease.

Previous studies with repeated injections of radiolabeled monoclonal antibodies have shown different biokinetics with different amounts of antibodies (4-6). However, in other studies such differences were not observed (7). For correct dose planning prior to a treatment, it is thus important to know if the biokinetics of a diagnostic amount of radiopharmaceutical differ from those of a therapeutic.

The aim of this work was to study the biokinetics and dosimetry of ^{111}In after repeated injections of different amounts of ^{111}In-DTPA-D-Phe^1-octreotide.

MATERIAL AND METHODS

Injections

For dose planning, the patient received 280 MBq of ^{111}In bound to 10 g of DTPA-octreotide by intravenous injection (D). Then the patient was treated four times with ^{111}In-DTPA-D-Phe^1-octreotide (T1-T4). In the three therapeutic administrations (T1, T2 and T3), the patient received 40 μg DTPA-octreotide labeled with 3.0, 3.5 and 3.1 GBq ^{111}In, respectively. The radiopharmaceutical was given as 4-6 slow i.v. injections via a central venous catheter. In the fourth therapeutic administration (T4), the therapy amount was given as two fractions: 1.3 and 1.5 GBq ^{111}In-DTPA-D-Phe^1-octreotide 24 h apart. Each fraction contained 20 μg DTPA-octreotide and was given as 2-3 slow i.v. injections via a central venous catheter. The time intervals between the consecutive administrations D, T1, T2, T3 and T4 were 3, 8, 5 and 20 weeks, respectively (Table 1). The study was approved by the Ethics Committee of Göteborg University and the Isotope Committee of Sahlgrenska University Hospital.

Table 1
^{111}In Activity and the Amount of DTPA-D-Phe^{1}-Octreotide Given to the Patient

	^{111}In activity (MBq)	Amount of DTPA-D-Phe^{1}-octreotide (μg)
Diagnosis (D)	280	10
Therapy 1 (T1)	3000	40
Therapy 2 (T2)	3600	40
Therapy 3 (T3)	3100	40
Therapy 4 (T4)	1300+1500	20+20

Radiopharmaceutical

DTPA-D-Phe^{1}-octreotide and ^{111}In-chloride were obtained from Mallinckrodt Medical B.V. (The Netherlands). At D and T1, the radiolabeling of DTPA-D-Phe^{1}-octreotide with ^{111}In was performed by adding ^{111}In-chloride to each vial containing 10 μg DTPA-D-Phe^{1}-octreotide and incubating for 30 minutes. At T2, T3 and T4, the radiolabeling of DTPA-D-Phe^{1}-octreotide with ^{111}In was performed by adding 1 ml saline to each vial containing 10 μg DTPA-D-Phe^{1}-octreotide. The content of these vials was then added to vials containing ^{111}In-chloride and incubated for 30 minutes. The specific activity was 280-880 MBq ^{111}In per 10 μg DTPA-D-Phe^{1}-octreotide. Chromatography of the radiopharmaceutical was performed using instant thin layer chromatography (ITLC-SG, Gelman Instrument Company, MI, USA) with sodium-citrate (0.1 M, pH 5) as the mobile phase. Before administration, the radiopharmaceutical was diluted with saline.

Measurement of ^{111}In Concentration in Tissue Samples

Seven days after the diagnostic study (D) the patient underwent surgery. Tumor and normal tissue biopsies were excised and the ^{111}In activity concentration was measured in a gamma counter equipped with a 7.6 cm (diameter) X 7.6 cm NaI(Tl) well crystal (3 cm hole diameter, 6 cm depth) and a single-channel pulse-height analyzer. Corrections were made for detector background and for physical decay. The ^{111}In activity concentrations, C (%IA/g), and tumor-to-blood ^{111}In activity concentration ratios, T/B, were calculated as described earlier (1).

Scintigraphy

Scintigraphy was performed repeatedly up to 550 h after i.v. injection of ^{111}In-DTPA-D-Phe^{1}-octreotide. Anterior and posterior whole body scintigrams were acquired using a gamma camera (General Electric AC/T, UK) equipped with a medium energy parallel-hole collimator and connected to a GE STARCAM computer system. The energy windows were centered over the 172 keV and 245 keV peaks with a window width of 20%. The scanning speed was 5.6-27 cm/min. In the diagnostic study (D), no voiding of the urinary bladder was performed between the injection and the first acquisition. During the acquisitions performed within the first 60 h after T1, T2 and T3, a 1 mm lead shield was mounted on the collimator to avoid dead time losses in the gamma camera.

Calibration of the gamma camera was performed using a thin surface source according to the method of Fleming (8). The calibration factor between the sensitivity of the ionization chamber and the gamma camera was then determined. The thin surface source was also used to determine the correction factor for the lead shield.

Biokinetics and Dosimetry

The ^{111}In activity content in the whole body, liver with metastases, spleen, kidneys and urinary bladder was determined mainly according to the method of Fleming (8). Regions of interest (ROIs) were drawn around the whole body, lungs, legs, liver with metastases, spleen, urinary bladder and the left kidney in the gamma camera images. For this patient the right kidney region was superimposed on the liver region and was not included. Instead, the content of ^{111}In in the kidneys was assumed to be twice that of the left one. Consequently, when calculating the content of the liver, the assumed content in the superimposed right kidney region was subtracted.

To correct for differences in effective thickness (and hence attenuation) the whole-body ROI was divided in three regions: lungs, legs and the rest of the body. The mean effective thickness of each of these regions was estimated from a lateral gamma camera image (assuming a lung density of 0.3 g/cm^3). The mean effective thicknesses of the organs were estimated from typical CT images of patients.

Corrections were also made for background. For whole-body, lungs and legs, a background region was placed outside the body. The background region used for the other organs was placed in the abdomen outside the visualized organs. Background correction from over- and underlying tissue was made based on the mean thickness of the organ, assuming homogeneous activity distribution in the background region.

The ^{111}In activities in whole body, organs and tumors were estimated using the geometric mean of corresponding number of counts (corrected for background and attenuation) from anterior and posterior ROIs (8). The activity content was expressed as the fraction of the injected activity,. The activity content in the whole body was calculated as the sum of ^{111}In activity in the lungs, legs and the rest of the body. The activity content in the remainder of the body was calculated as the content in the whole body minus the content in the organs.

A ROI was also placed over a bone metastasis in the right femur. The corresponding background region was placed at the same location on the opposite femur. The tumor-to-background ratio for the bone metastasis was estimated from the anterior images.

The time-activity curve for an open one- or two-compartment model was fitted to the measured time-activity data for each source organ. The residence time for any organ was estimated as the cumulated activity divided by the injected activity. The mean absorbed doses were calculated by the MIRDOSE 3 program, using the adult female phantom (9).

The absorbed doses in tumors were estimated from the mean of ^{111}In activity concentration in the three excised liver metastases and the measured time-activity curve for the bone metastasis. To estimate mean absorbed doses to different tumor sizes, the weight (10) and self-dose S values (9) for ovaries, thyroid or kidneys were used.

RESULTS

The content of ^{111}In in the whole body, liver with metastases, spleen, kidneys, urinary bladder and one selected bone metastasis was evaluated from the gamma camera images (Figure 1, Figure 2a). The pituitary and thyroid were not distinguished in the images. The content of ^{111}In was in general different between the diagnostic (D) and therapeutic administrations T1-T3. Differences were also obtained between T4 and T1-T3 (Figure 1, Figure 2a).

After 48 h, the whole-body content of ^{111}In was about 40% and 30% for D and T1-T3, respectively. After 48 h, the whole-body retention of ^{111}In for D seemed to remain constant, but slowly decreased for T1-T3. For T4, the content of ^{111}In was always higher than T1-T3, throughout the time studied (Figure 1a).

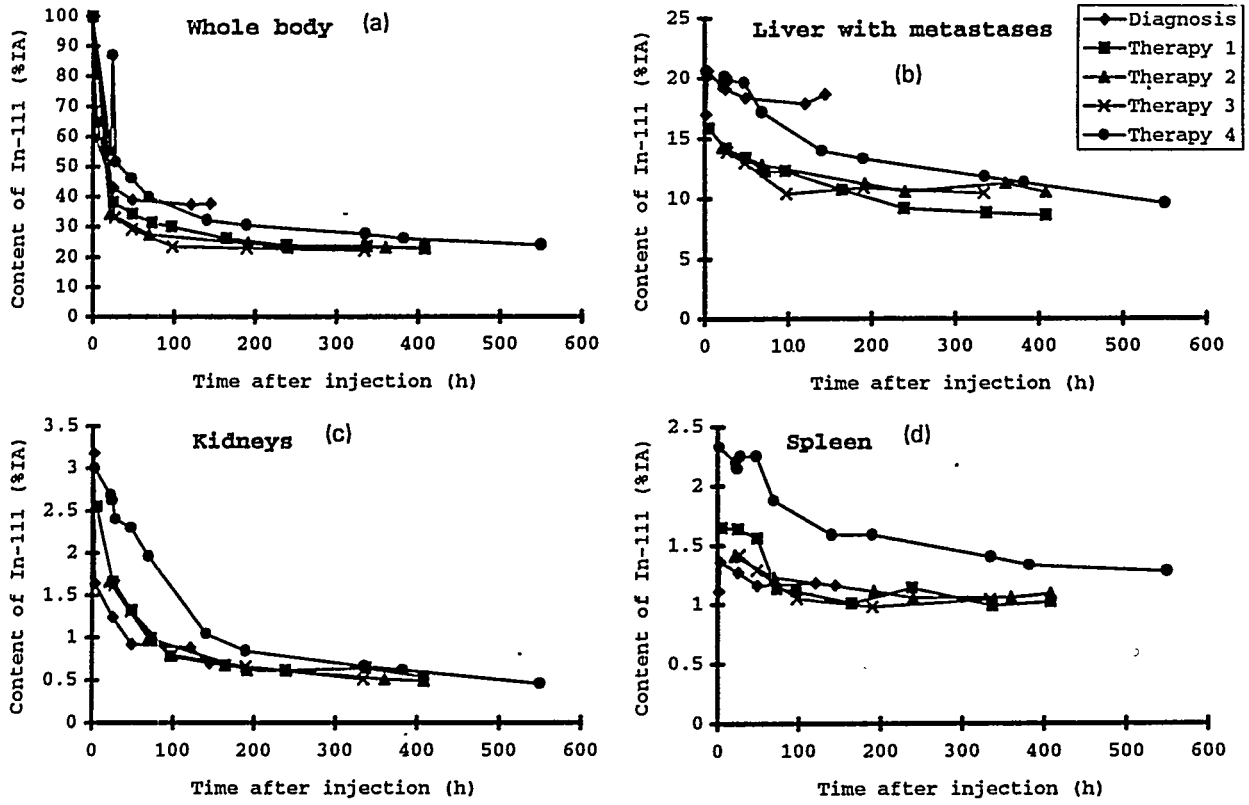

Figure 1. Content of ^{111}In (a) in whole body, (b) liver, © kidneys and (d) spleen after I.V. injection of ^{111}In-DTPA-D-Phe^{1}-octreotide. Values are corrected for physical decay.

A high uptake was seen in the liver with metastases (Figure 1b). After D, the uptake increased to about 20% during the first few hours, and then slowly decreased during the time of study. For D, the ^{111}In content in the liver with metastases was about 50 % higher than for T1-T3, and for T4 it was higher than for T1-T3. The ^{111}In content in the kidneys was different (up to a factor of 2) between D, T1-T3, and T4. There was a fast initial decrease (during 50-150 h) and then a much slower release of ^{111}In, during the time of study (Figure 1c). The content of ^{111}In in the spleen was higher for T4 than for D and T1-T3 (Figure 1d).

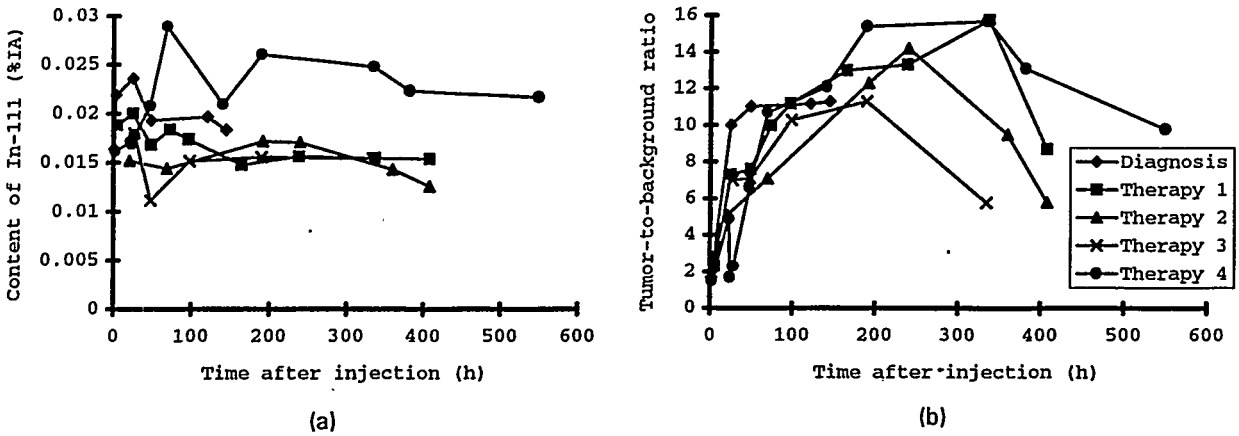

Figure 2. (a) Content of ^{111}In (values are corrected for physical decay) and (b) tumor-to-background ratio for a bone metastasis, after I.V. injection of ^{111}In-DTPA-D-Phe^{1}-octreotide.

In the bone metastasis there was a higher content of ^{111}In after D than after T1-T3 (Figure 2a). After 48 h, the content of ^{111}In was higher for T4 than for D and T1-T3. Tumor-to-background ratios for the bone metastasis, estimated from the images, are shown in Figure 2b.

The ^{111}In concentrations (%IA/g) and the tumor-to-blood ratios in the excised tumor biopsies 7 days after I.V. injection of ^{111}In-DTPA-D-Phe^1-octreotide are shown in Table 2. The uptakes in all of the liver metastases was higher than in the primary tumor.

The mean absorbed doses to the target organs, calculated using MIRDOSE 3, are shown in Table 3. Liver with metastases, spleen and kidneys received the highest absorbed doses. The total mean absorbed dose to hypothetical tumors with the shape, size and location as the ovaries, thyroid and kidneys were estimated to about 8.5 Gy, 13 Gy and 17 Gy, respectively (Table 4).

Table 2

Tumor-to-Blood Activity Concentration Ratios (T/B) and ^{111}In Concentrations, C, in Tumor Biopsies Excised 7 Days after I.V. Injection of ^{111}In-DTPA-D-Phe^1-Octreotide. Values are Corrected for Physical Decay.

Tumor biopsy	T/B	C (%IA/g)
Midgut carcinoid (primary tumor)	150	0.008
(liver metastasis)	400	0.020
(liver metastasis)	470	0.024
(liver metastasis)	650	0.033

Table 3

Absorbed Dose per Unit Injected Activity and Total Mean Absorbed Dose for Different Organs after I.V. Injections of ^{111}In-DTPA-D-Phe^1-Octreotide at the Diagnostic (D), Therapeutic (T1-T3) and Fractionated Therapeutic (T4) Administrations

Organ	Absorbed dose per unit injected activity (mGy/MBq)					Total mean absorbed dose (Gy)
	D	T1	T2	T3	T4	
Total body	0.12	0.08	0.08	0.07	0.12	1.2
Liver with metastases	1.18	0.80	0.75	0.73	1.10	11.0
Spleen	0.55	0.65	0.51	0.50	0.87	8.2
Kidneys	0.41	0.36	0.32	0.32	0.56	5.0
Urinary bladder wall	0.22	0.15	0.07	0.10	0.22	1.8
Red marrow	0.09	0.06	0.06	0.05	0.09	0.9
Muscle	0.08	0.06	0.06	0.05	0.09	0.9
Ovaries	0.09	0.06	0.05	0.05	0.10	0.9

Table 4

Absorbed Dose per Unit Injected Activity and Total Mean Absorbed Dose for Different Hypothetical Tumors (see text) after I.V. Injections of ^{111}In-DTPA-D-Phe^{1}-Octreotide from the Diagnostic (D), Therapeutic (T1-T3) and Fractionated Therapeutic (T4) Administrations

Assumed tumor size (g)	Absorbed dose per unit injected activity (mGy/MBq)					Total mean absorbed dose (Gy)
	D	T1	T2	T3	T4	
4	1.1	0.58	0.50	0.44	1.1	8.5
20	1.7	0.90	0.79	0.69	1.7	13
140	2.4	1.4	1.2	1.1	2.5	17

DISCUSSION

The ^{111}In biokinetics after T1, T2 and T3 were similar. A difference between the ^{111}In content in D and T1-T3 in the whole body and in the metastatic liver was seen (Figure 1 a,b). Also for the bone metastasis, there seemed to be a difference in the ^{111}In content (Figure 2a). These differences were not seen in normal organs, e.g. spleen and kidneys (Figure 1 c,d). In D and T1-T3, 10 μg and 40 μg of DTPA-D-Phe^{1}-octreotide was used, respectively. Saturation of available receptors may be one explanation for the lower uptake of ^{111}In-DTPA-D-Phe^{1}-octreotide when using higher amounts of DTPA-D-Phe^{1}-octreotide.

Fractionated administration was initiated in the fourth therapy due to the differences in biokinetics between D and T1-T3, allowing a further study of the possible receptor saturation. T4 resulted in a higher ^{111}In content in all organs and tissues studied. In T4 the absorbed dose per unit injected activity increased by a factor of 1.8-2.4 for the tumors compared with T1-T3. For normal organs this factor was 1.5-2.0.

The total mean absorbed dose to the liver with metastases was about 11 Gy. This estimated absorbed dose to the normal liver tissue is probably an overestimation, as the metastases had several times higher ^{111}In activity concentration than the normal liver parenchyma (1). Furthermore, the metastases caused an increase in total liver volume, which was not considered in the calculations. Therefore, the absorbed dose to the liver metastases was higher than to the normal liver tissue, which should have received a much lower absorbed dose than 11 Gy. The total absorbed dose in tumors with size, location and shape similar to ovaries, thyroid and kidneys was calculated to be about 8.5 Gy, 13 Gy and 17 Gy, respectively. The absorbed dose consists of the self-dose and the cross-dose contribution. The cross dose depends on the location of the tumors in the body. The cross dose contributed about 10 % to the total absorbed dose for the tumor with size, location and shape similar to kidneys and ovaries. For the "thyroid tumor" this contribution was about 4 %. The estimated value of 17 Gy to a tumor of size, shape and location similar to a kidney after injection of 12.6 GBq ^{111}In-DTPA-D-Phe^{1}-octreotide differs from the radiation therapy study by Krenning et al. (15), where a patient was given 20 GBq ^{111}In-DTPA-D-Phe^{1}-octreotide, and had an estimated cumulated absorbed dose of 13 Gy to a similar sized tumor. The different methods used to determine the total absorbed dose and the fact that different types of neuroendocrine tumors have a large variation in uptake of ^{111}In-DTPA-D-Phe^{1}-octreotide (1) may explain such a discrepancy.

In this study the uptake in red marrow was not determined, and red marrow was not included among the source organs. Therefore, the absorbed dose per injected activity in the marrow may have been low at 0.05-0.06 mGy/MBq for T1-T3. An estimation for T1-T3 of the highest possible mean

absorbed dose to the red bone marrow, assuming that the content of ^{111}In in the remainder was only distributed in the red bone marrow, was 0.2 mGy/MBq (3).

The biokinetics and dosimetry of ^{111}In in patients have previously been studied up to 48 h (11-13) and up to 72 h (14) after injection of diagnostic amounts, and up to 400 h after injection of therapeutic amounts, of ^{111}In-DTPA-D-Phe^1-octreotide (15). In this study, the ^{111}In content in the liver was about five times higher than for the other studies with diagnostic amounts, probably due to a very large tumor burden (more than 50%, estimated by CT). The ^{111}In content in the remainder of the body was also higher in this patient mainly due to uptake in bone metastases.

When using intraoperative detection of tumors it is important to have high tumor-to-normal tissue activity concentration ratios. In this patient, the tumor-to-background ratios, evaluated by gamma camera measurements, initially increased with time (Figure 2b). The observed decrease after 200-300 h is, however, not statistically significant. At 200 h the coefficient of variation (SD/mean) was about 8%, and increased to 60% at 550 h due to poor counting statistics.

In summary, the biokinetics were different after the various injections. This may be due to different amounts of DTPA-octreotide given, different specific activity of the radiopharmaceutical, iterated injections, different administration schedules, and/or differences in tumor burden and gradual therapeutic response to both octreotide and ^{111}In during the course of repeated therapies. For correct dose planning, it is crucial that the dosimetry for the subsequent therapy can be predicted.

ACKNOWLEDGMENTS

We thank Mallinckrodt for generously supplying the radiopharmaceutical. This work was supported by the Swedish Cancer Society (3427), the Swedish MRC (5220),the King Gustav V Jubilee Clinic Cancer Research Fundation, Swedish Medical Society and Sahlgrenska University Hospital Research Funds.

REFERENCES

1. Forssell-Aronsson E, Fjälling M, Nilsson O, Tisell LE, Wängberg B and Ahlman H. ^{111}In activity concentration in human tissue samples after i.v. injection of ^{111}In-DTPA-Phe^1-octreotide. J Nucl Med 36:7-12, 1995.
2. Andersson P, Forssell-Aronsson E, Johanson V, Wängberg B, Nilsson O, Fjälling M and Ahlman H. Internalization of ^{111}In into human neuroendocrine tumor cells after incubation with ^{111}In-DTPA-D-Phe^1-octreotide. J Nucl Med 37(12):2002-2006, 1996.
3. Fjälling M, Andersson P, Forssell-Aronsson E, Grétarsdóttir J Johanson V, Tisell L.E, Wängberg B, Nilsson O, Berg G, Michaneck A, Lindstedt G and Ahlman H. Systemic radionuclide therapy using Indium-111-DTPA-D-Phe^1-octreotide in midgut carcinoid syndrome. J Nucl Med 37(9):1519-1521, 1996.
4. Forssell-Aronsson E, Grétarsdóttir J, Jacobsson L, Mattsson S, Holmberg SB, Hafström L, Karlsson B and Lindholm L. Pharmacokinetics and dosimetry of the radioiodine-labeled monoclonal antibodies C-215 and C-245 studied in two patients with adenocarcinoma. In: Fifth International Radiopharmaceutical Dosimetry Symposium, Proceedings of a Conference held at Oak Ridge, Tennessee, May 7-10, 1991 (Edited by A Schlafke-Stelson and EE Watson). CONF-910529, pp: 113-129, 1992.
5. Carrasquillo JA, Abrams PG, Schroff RW et al. Effect of antibody dose on the imaging and biodistribution of indium-111 9.2.27 antimelanoma monoclonal antibody. J Nucl Med 29:39-47, 1988.

6. DeNardo GL, DeNardo SJ, O'Grady LF et al. Fractionated radioimmunotherapy of B-cell malignancies with ^{131}I-Lym-1. Cancer Res (Suppl) 50:1014s-1016s, 1990.
7. Trang JM, LoBuglio AF, Wheeler RH et al. Pharmacokinetics of a mouse/human chimeric monoclonal antibody (C-17-1A) in metastatic adenocarcinoma patients. Pharmaceutical Research 7(6):587-592, 1990.
8. Fleming J.S. A technique for the absolute measurement of activity using a gamma camera and computer. Phys Med. Biol 24:176-180, 1979.
9. Stabin MG. MIRDOSE: Personal computer software for internal dose assessment in nuclear medicine. J Nucl Med 37:538-546, 1996.
10. Snyder WS, Ford MR, Warner GG. MIRD Pamphlet No.5, Revised. Oak Ridge National Laboratory. Oak Ridge, TN. 1978.
11. Krenning EP, Bakker WH, Kooij PPM et al. Somatostatin receptor scintigraphy with Indium-111-DTPA-D-Phe-1-octreotide in man: Metabolism, dosimetry and comparison with iodine-123-Tyr-3-octreotide. J Nucl Med 33:652-658, 1992.
12. Bajc M, Palmer J, Ohlsson T and Edenbrandt L. Distribution and dosimetry of Indium-111-DTPA-D-Phe-1-octreotide in man assessed by whole body scintigraphy. Acta Radiologica 35:53-57, 1994.
13. Leide-Svegborn S, Nosslin B, Mattsson S. Biokinetics and dosimetry of ^{111}In-DTPA-D-Phe^1-octreotide in patients. In: Sixth International Radiopharmaceutical Dosimetry Symposium, Proceedings of a Conference held in Gatlinburg, Tennessee, May 7-10, 1996, AT S-Stelson, MG Stabin, RB Sparks and RE Toohey, Editors, 1997.
14. Forssell-Aronsson E, Lanhede B, Fjälling M, Wängberg B, Tisell LE, Ahlman H and Mattsson S. Pharmacokinetics and dosimetry of ^{111}In-DTPA-D-Phe^1-octreotide in patients with neuroendocrine tumors. In: Sixth International Radiopharmaceutical Dosimetry Symposium, Proceedings of a Conference held at Gatlinburg, Tennessee, May 7-10, 1996, AT S-Stelson, MG Stabin, RB Sparks and RE Toohey, Editors, 1997.
15. Krenning E.P, Bakker WH, Kooij PPM et al. Radiotherapy with a radiolabeled somatostatin analogue [^{111}In-DTPA-Phe^1] octreotide. In: Wiedenmann B, Kvols LK, Arnold R, Rieken EO, eds. Molecular and cell biological aspects of gastroenteropancreatic neuroendocrine tumor disease. Ann N Y Acad Sci 733:496-506, 1994.

QUESTIONS

Behr: What is the rationale for using ^{111}In as a therapeutic isotope? You will have much crossover radiation by gamma rays which do not contribute at all to tumor doses. Furthermore, you were receiving only 17 Gy as the maximum tumor dose. Do you expect any therapeutic results from such low doses considering the generally assumed radioresistance of neuroendocrine tumors?

Andersson: Today, only ^{111}In-octreotide is available commercially. It is true that ^{111}In is not an optimal radionuclide for therapy, due to the large fraction of energy emitted as photons. However, due to the high tumor/normal tissue ratios, the fact that ^{111}In was internalized into the tumor cells, the high LET (and probably RBE) for internalized In-111, and that liver artery embolization was not suitable for this patient, we decided to give therapeutic amounts of ^{111}In-octreotide. The estimated mean absorbed dose of 17 Gy to a kidney tumor is probably too low for complete tumor remission. In this case the effects of the therapy (octreotide and ^{111}In-octreotide) were 1) marked reductions of the two main tumor markers 5-HIAA and cortisol (80% and 45%, respectively), 2) stationary tumor

volume, and 3) symptom palliation. It is not probable that these results are explained by effects from unlabeled octreotide alone.

Brill: What is the localization of the somatostatin receptor? If it is intranuclear, the Auger electrons from ^{111}In are a viable therapy vehicle. If it is on the cell membrane, the therapy dose would be too low to be useful. Where is it localized?

Andersson: The somatostatin receptor is localized on the cell membrane. However, as I described, electron microscopic autoradiography showed that ^{111}In is internalized, maybe via receptor-mediated endocytosis, and is located both in the cytoplasm and nucleus.

Roesch: This is just a comment to the previous question. The use of ^{111}In for therapeutic purposes might be reasonable due to its Auger electron emission assuming the isotope is finally internalized into the cell. And exactly this was reported by Dr. Andersson. On the other hand, to introduce β^- emitting isotopes from the lanthanide series such as ^{169}Yb into DTPA-octreotide could cause problems resulting from the lower in vivo stability of the radiochemical label.

Andersson: ^{111}In is not an optimal radionuclide for therapy, due to the large fraction of energy emitted as photons. Since no other radionuclide, bound to octreotide, was available, ^{111}In-octreotide was used. However, if there is an enhanced effect from Auger electrons, when the radionuclide is internalized, then ^{111}In might be of interest as a radiotherapy nuclide. Further work regarding labeling of octreotide with more suitable radionuclides should be performed, and the in vitro and in vivo stability, binding properties and pharmacokinetics of such new radiopharmaceuticals should be studied.

Dunn: Did you take into account bone metastases activity contribution when determining the red marrow dose? Also, was the activity in the liver tumors taken into account for the liver dose estimate?

Andersson: The red marrow doses were estimated from the content of ^{111}In in the liver, kidneys, spleen, urinary bladder and assuming a homogenous distribution of the remaining ^{111}In in the remainder of the body. Due to the large number of the bone metastases and that the ^{111}In distribution in the bone and bone marrow was not known, a more correct estimation of the red marrow dose could not be performed. However, if the ^{111}In activity not located in the liver, kidneys, spleen and urinary bladder is assumed to be in the bone marrow, the red marrow dose would be about 0.2 mGy/MBq. Then the red marrow would receive < 1 Gy at each therapy occasion. The number of leukocytes was reduced (10-45%) after each injection. Concerning the absorbed dose to the liver, the In-111 activity in the liver metastases was included in the calculations and I only presented the results for liver with metastases. Since previous studies have shown that the uptake in liver tissue is lower than in liver metastases of midgut carcinoid tumors, and that the increased total liver volume in this patient was not taken into account, the absorbed dose to normal liver tissue is much lower than the values presented.

CLINICAL WHOLE-BODY DOSIMETRY AND THERAPY OF METASTASES WITH I-131

Kopp J and Heidenreich P
Clinic of Nuclear Medicine
Zentralklinikum, Augsburg D-86156, F.R.G.

ABSTRACT

Since 1986 we have used the MIRD concept together with individual biokinetic data from the patient in radioiodine therapy of metastases from thyroid cancer, neuroblastoma and pheochromocytoma. To measure individual biokinetic data the patient receives a small amount of I-131 intravenously. Immediately after the injection and for a period of five days, images of the radioiodine distribution are made with a large-field gamma camera. The biokinetic data are obtained by a region-of-interest technique. Volumes and masses of organ and tumor mostly come from CT and NMR examinations.

We calculate the activity that gives the maximum safe dose to the organ at risk and also the resulting dose to the leading metastases. This activity is administered to the patient in one course to achieve the maximum biologic effect to the tumor. We report about the methods and the results of therapies using up to 33 GBq of I-131.

INTRODUCTION

An individual dose estimation should be done before a nuclear medicine therapy especially in case of:

- benign thyroid diseases
- ablative therapy of the thyroid remnant after resection of a carcinoma
- therapy of thyroid cancer metastases which show I-131-uptake
- therapy with I-131-MIBG (malignant pheochromocytoma, neuroblastoma or carcinoid).

The intention of our dosimetric approach for metastases is to determine the amount of radioactivity which produces the maximum safe dose to the organ at risk. Knowing this activity, we can calculate the resulting dose to the tumor or metastases and therefore estimate the therapeutic effects.

In 1986 we started with a patient suffering from metastases of a pheochromocytoma. Now we have based more than 50 therapies on that dosimetry, most of which were given to patients with metastases of a thyroid carcinoma. Dosimetry is based on the considerations of the Society of Nuclear Medicine's MIRD committee. The use of the MIRDOSE3 program of ORISE is very helpful in performing the dose calculations.

MEASUREMENT OF INDIVIDUAL BIOKINETIC DATA

To get the retention curves for whole body, organs that accumulate the radionuclide and leading metastases, we use a digital gamma camera computer system. Immediately after intravenous administration of a test dose of the radionuclide we acquire a whole-body scan in both ventral and dorsal projection. The geometric mean of the containing counts is the reference value for the maximum uptake in a specified region. The velocity of camera or table movement during the acquisition and the dimension of the camera head in that direction gives the acquisition time per pixel. Dorsal and ventral views, acquired over four to five days, show the distribution of activity in metastases and organs of interest. On the second day postinjection an additional whole-body scan is made for documentation.

A region-of-interest technique determines the counts for metastases, organs, the residual body and if necessary, the values for background correction. The regression function of the geometric mean of the counts gives the maximum uptake and effective half-time for the integration of the retention function.

To validate the result of the effective half-time of the radionuclide in the residual body, daily probe measurements are made.

CALCULATION OF DOSE PER ACTIVITY

The mass of metastases and organs is derived by sonography, x-ray computer tomography or magnetic resonance imaging. If the individual organ or patient mass does not fit into one of the standard phantoms, the S values can either be interpolated or corrected by a factor f_m (1) as follows:

$$f_m = \frac{mass_{phantom}}{mass_{individual}} \quad for\ nonpenetrating\ radiation$$

and

$$f_m = \left(\frac{mass_{phantom}}{mass_{individual}} \right)^{0.7} \quad for\ penetrating\ radiation.$$

The calculation of the dose per activity for the organ at risk (e.g. red bone-marrow, lungs etc.) and leading metastases is now done with the help of ORISE's MIRDOSE3 program.

THERAPEUTIC DECISION

In the absence of better and more reliable data we assume the TD5/5 of external beam radiation therapy to be the tolerance dose for our organ at risk (2). The results from whole-body irradiation therapy of leukemia support our experience that this assumption underestimates the real tolerance doses. They seem to be at least twice as high and therefore we are on the safe side according to risk for the patient.

Tolerance dose and dose per activity of the organ at risk gives us the maximum activity to be administered to the patient. Knowing the amount of activity we can administer, we calculate the resulting dose to metastases. From that we classify the therapeutic approach as possibly curative or

palliative. To be curative the metastases should receive more than 150Gy. If the red marrow is the only organ at risk and our dosimetric results indicate that we have to go over the 5% risk level to become curative, or the patient already shows problems with the blood producing system, we collect stem cells and stay prepared for a reimplantation if necessary.

CONCLUSION

Since 1986 we have based our therapeutic decision for more than 50 cases on the described method of dosimetry. In more than 40 cases the amount of radioactivity we administered in a single dose ranged from 3.1 to 33.5 GBq. In more than 10 cases we renounced therapy with no chance of real benefit for the patient. In our opinion it is essential to utilize powerful nuclear medicine therapy in the best way possible. To achieve that we believe that one has to include the assessment of risk and benefit for the patient before the treatment is started. Our evaluation is one way towards optimization of therapy with radionuclides. To go further a lot of scientific work is still to be done, especially with respect to radiobiology.

REFERENCES

1. Kaul A, Henrichs K and Roedler HD. Radionuclide biokinetics and internal dosimetry in nuclear medicine. La Ricerca Clin Lab 10:629-660, 1980.
2. Rubin P. The Frank Bushke lecture. Late effects of chemotherapy and radiation therapy. A new hypothesis. Int J Radiat Oncol Biol Phys 10:5, 1984.

ABSORBED DOSE TO NONTARGET ORGANS AT ^{131}I-TREATMENT OF HYPERTHYROIDISM

Jönsson H, Mattsson S, Bramstång T and Landberg T
Departments of Radiation Physics and Oncology
Malmö University Hospital, S-205 02 Malmö, Sweden

ABSTRACT

Radiation dose estimates are normally calculated for healthy individuals. There is also, however, an interest in obtaining absorbed dose data for various disease states. The individual thyroid uptakes and effective half-times in 516 patients, (433 females and 83 males), treated with ^{131}I-iodide for hyperthyroidism at Malmö University Hospital have therefore been collected and partly used to estimate the absorbed dose to different organs in the hyperthyroid patient. The patients have been divided into three different groups according to their diagnoses; diffuse goiter, multinodular goiter and adenoma (solitary). They were also separated according to sex and age. The uptake in the thyroid of a test activity of ^{131}I-iodide was measured at 3, 24 and 48 hours, and a fourth measurement was made 3-9 days after the administration. A high uptake at 24 hr was related to a short effective half-time. With increasing age, the 24-hr uptake decreased and the effective half-time increased. Patients with a diffuse goiter had a higher 24-hr uptake and a shorter effective half-time than those with a multinodular goiter. The fractional excretion of ^{131}I in urine was found to be the same in the test and therapeutic situation, indicating similar kinetics in these two situations.

For female patients of age 18-45 years (n=92), the absorbed dose was estimated for approximately 20 organs in the body using four currently used dose calculation methods. The absorbed dose to the uterus was assumed to represent the absorbed dose to an embryo. The estimated mean absorbed dose to the uterus or embryo was 0.06 mGy/MBq. The mean absorbed dose to the bladder varied from 0.28 to 0.64 mGy/MBq with an average of 0.45 mGy/MBq, and the dose to the stomach varied from 0.58 to 0.60 mGy/MBq with an average of 0.59 mGy/MBq. For an administration of 300 MBq of ^{131}I the effective dose, excluding the thyroid as a target organ, was estimated to be 50 mSv.

INTRODUCTION

^{131}I-iodide is widely used for treatment of hyperthyroidism. To treat the patient with radioiodine, the absorbed dose to the thyroid must be calculated to ensure that the treatment gives the desired effect. The absorbed dose also needs to be calculated to organs other than the thyroid to estimate the risks of late effects in the patient. This is becoming more important as younger patients are treated with radioiodide. For women of childbearing age, the absorbed dose to the embryo is of special importance. For an embryo/early fetus, the absorbed dose is approximately the same as the absorbed

dose to the uterus. When the pregnancy is known, treatment with radioiodine is prohibited, but several cases have been reported where a pregnant woman unintentionally has received treatment with radioiodide (1).

The aim of the study was to determine if there is any difference in iodine biokinetics in individuals with different diagnoses, and if there were differences due to age or sex. Absorbed doses for different organs and tissues for female patients, 18-45 years old, and the effective dose, excluding the thyroid as a target organ, were estimated.

MATERIALS AND METHODS

During the years 1984-1989, 516 patients were treated with ^{131}I-iodide at Malmö University Hospital. Uptake and retention data from these patients have been used to calculate the absorbed dose to different organs in the patients. The patients were divided according to the diagnoses: diffuse goiter (n=282), multinodular goiter (n=122) and adenoma (n=62). Fifty patients had other diagnoses. The uptake of ^{131}I-iodide in the thyroid was measured at 3 hr, 24 hr, 48 hr and once in the period 3-9 days after the intake of a test activity. The effective half-time, T_{eff}, of the thyroid retention was calculated. The volume of the thyroid was estimated as the volume of two ellipsoidal lobes from a scintigram of the test activity of ^{131}I-iodide. The uptake at 24 hr after intake was plotted against the effective half-time for the three different diagnoses. The 24-hr uptake and effective half-time were also plotted against the age of the patient for each of the three diagnoses. The excretion of ^{131}I in urine was measured up to 24 hr after the administration of test and therapeutic activity respectively.

The absorbed dose per MBq ^{131}I-iodide orally administered was calculated for approximately 20 organs for female patients of age 18-45 years (n=92). Four different methods were used for the calculations:

1. The tables in ICRP Publication 53 (2) representing an adult female and also a 15 year old male (3) were extrapolated for uptakes higher than 55%, and values in between tabulated values were interpolated. The biological half-time for retention of iodine in the thyroid was set to 65 days for all patients, corresponding to an effective half-time of 7.2 days;
2. ICRP computer program (4). The program is based upon the present algorithms used by ICRP Task Group on "Dose to patients from radiopharmaceuticals" (2). The individual uptake of ^{131}I-iodide in the thyroid and the calculated individual effective half-time of the thyroid retention were used as input data with the adult female phantom (3);
3. MIRDOSE3 (5) for 15-yr-old phantom (3). The individual uptake of ^{131}I-iodide in the thyroid and the calculated individual effective half-time of the thyroid retention were used as input data;
4. MIRDOSE3 (5) for nonpregnant adult female phantom (6). The individual uptake of ^{131}I-iodide in the thyroid and the calculated individual effective half-time of the thyroid retention were used as input data.

RESULTS

Table 1 shows the number of patients according to diagnosis, sex and age.

Table 1
Distribution of Patients According to Diagnosis, Sex and Age

Diagnosis	Total number of patients	Percentage of men	Percentage of women	Percentage of women ≤45 years	Percentage of women >45 years
Diffuse goiter	282 (55%)	19 %	81 %	36 %	64 %
Multinodular goiter	122 (24%)	11 %	89 %	8 %	92 %
Adenoma	62 (12%)	11%	89%	13%	87%
Other	50 (10%)	-	-	-	-

Biokinetic data for patients with diffuse goiter, multinodular goiter and adenomas are shown in Table 2. Patients with diffuse goiter are younger (mean age = 51 years) than patients with multinodular goiter or adenoma (mean age = 64 years and 63 years, respectively) ($p<0.001$). Patients with diffuse goiter also have a higher uptake ($p<0.001$) (mean value for 24-hr uptake was 62%) and a shorter effective half-time (mean value was 4.9 days) than patients with the other two diagnoses, multinodular goiter (49% and 5.9 days) and adenoma (42% and 5.9 days) ($p<0.001$). The age of the patients and the effective half-time do not differ between multinodular goiter and adenoma, while patients with adenoma have lower uptake of iodide than patients with multinodular goiter ($p<0.001$).

Table 2
Mean Age, 24-hr Uptake and Effective Half-time, T_{eff}, for Patients with Different Diagnoses

Diagnosis	Age (range) (y)	24-hr uptake ± SE (%)	T_{eff}, ± SE (d)
Diffuse goiter (n=282)	51 (14-90)	62 ± 1	4.9 ± 0.1
Multinodular goiter (n=122)	64 (22-92)	49 ± 1	5.9 ± 0.1
Adenomas (n=62)	63 (24-87)	42 ± 1	5.9 ± 0.1

Between males and females, no difference could be seen in age, 24-hr uptake or effective half-time (Table 3). Females of age 45 and younger have a significantly higher uptake (mean value 62%) and a shorter effective half-time (mean value 4.9 days) than females of age higher than 45 years (53% and 5.5 days), ($p<<0.001$) (Table 3).

Table 3
Mean Age, 24-hr Uptake and Effective Half-time for Males and Females of of all Ages and for Females ≤45 Years and Females >45 Years

	Age (range) (y)	24-h uptake ± SE (%)	T_{eff}, ± SE (d)
Males (n=83)	55 (19-84)	55 ± 2	5.3 ± 0.1
Females (n=433)	57 (14-92)	56 ± 1	5.4 ± 0.1
Females ≤45 y (n=103)	-	62 ± 1	4.9 ± 0.1
Females >45 y (n=330)	-	53 ± 1	5.5 ± 0.1

The fractional urinary excretion of ^{131}I during 24 hr after the test and after the therapeutic administrations are compared in Figure 1. The figure shows similar kinetics for both situations with a linear coefficient of 1.01 and a correlation coefficient, r=0.95. Bockisch et al. (7) compared the

uptake and the effective half-time after application of test and therapeutic activity and found the two situations to be slightly different. The uptake was lower and the effective half-time faster in the therapeutic situation, which was assumed to be due to radiation effects of the therapeutic activity. This might be the case also for the few patients in Figure 1 who had a higher urinary excretion of ^{131}I after the therapeutic activity than after the test activity. However, for the group as a whole there is no significant difference between the diagnostic and therapeutic situations.

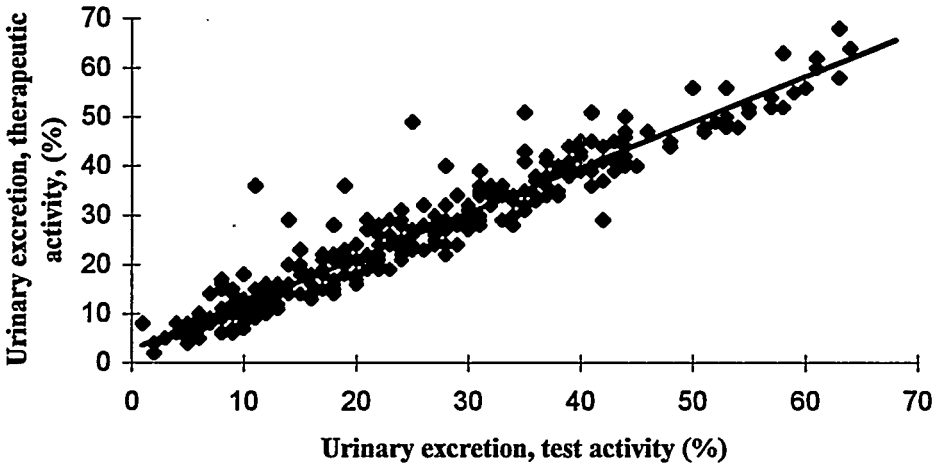

Figure 1. The fractional 24-hr urinary excretion after a test and a therapeutic administration indicate similar biokinetics in the two situations.

The results (mGy/MBq) for several organs from the different dose calculation methods can be seen in Figure 2. At an individual treatment, the mean activity administered was 300 MBq (range: 70-2200 MBq). The resulting total absorbed doses calculated using the ICRP computer program (4) are given in Table 4 together with the standard error and the range.

The mean absorbed dose to the stomach was estimated to 190 mGy; the maximum dose to one patient's stomach was 1300 mGy. The bladder received a mean absorbed dose of 160 mGy, while the ovaries and the uterus received about 20 mGy each. The highest absorbed dose to the uterus was 150 mGy. The mean absorbed dose to the red marrow was 40 mGy. The effective dose, with thyroid excluded as a target organ, (8,9) was calculated to have a mean value of 50 mSv when 300 MBq was administered orally.

DISCUSSION

The International Commission on Radiological Protection (ICRP) has calculated the absorbed dose to various organs after intake of ^{131}I-iodide (2). The calculations have been carried out for people with an uptake of iodide of 0, 5, 15, 25, 35, 45 and 55% and for females with a biological half-time of iodide of 65 days. Patients with hyperthyroidism have a higher uptake of iodide than normal individuals, often higher than 55%, and a shorter biological half-time than persons with a normal thyroid function (Table 2). The different biokinetics make the data in ICRP Publication 53 (2) inappropriate for use when calculating the absorbed dose or when estimating the risk of cancer after a

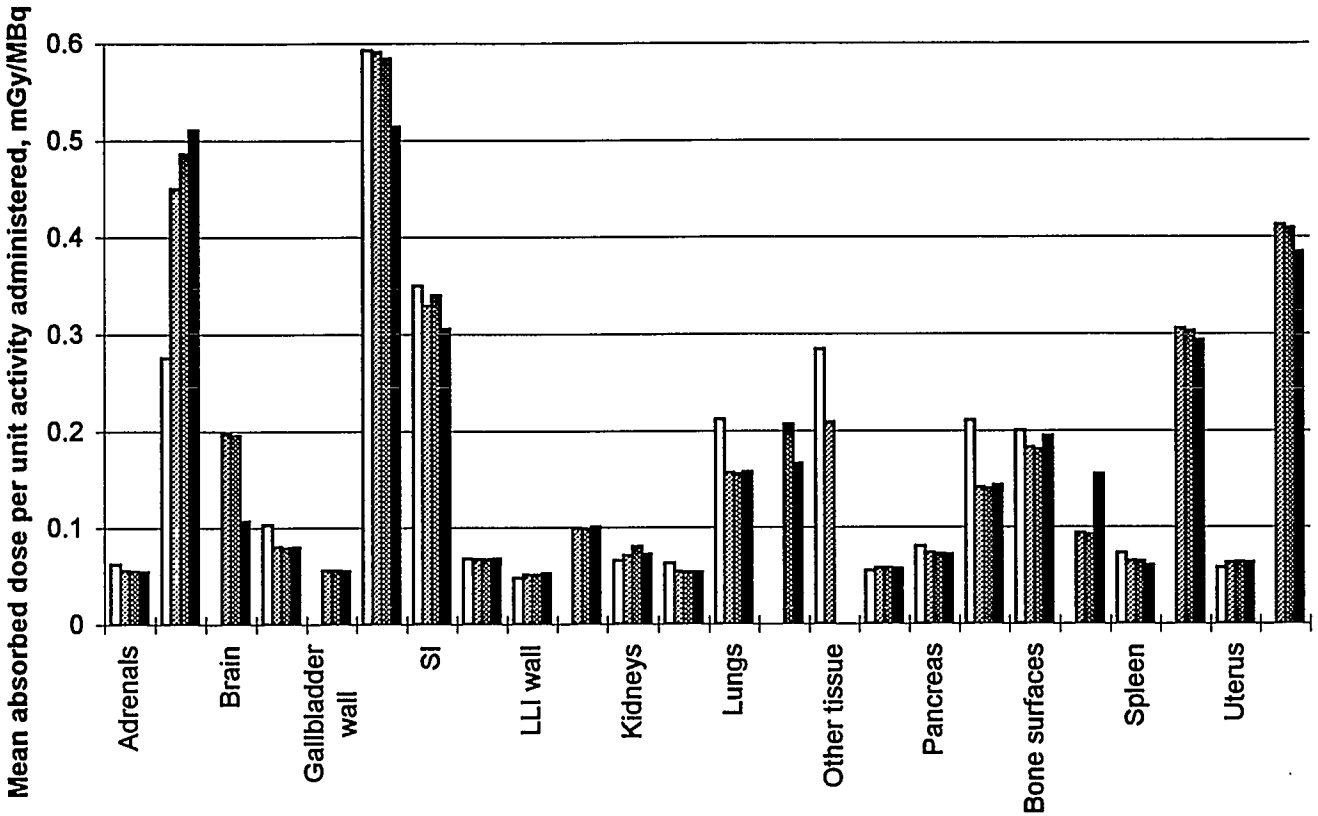

Figure 2. The absorbed dose per orally administered MBq ^{131}I calculated in four different ways. White bar. ICRP Publication 53, Light grey bar: ICRP computer program, Dark grey bar: MIRDOSE3 for 15-yr-old; Black bar: MIRDOSE3 for nonpregnant adult female.

Table 4
The Absorbed Dose per MBq Orally Administered ^{131}I-iodide
and the Total Absorbed Dose from an ^{131}I-iodide Therapy for Female Patients 18-45 Years Old

Organ	Mean value mGy/MBq	Range	Mean value ± SE mGy	Range
Adrenals	0.056	0.044-0.066	18 ± 2	4 - 98
Bladder	0.45	0.28-0.64	160 ± 19	29 - 1400
Bone surface	0.18	0.087-0.27	55 ± 5	11 - 210
Brain	0.20	0.086-0.30	59 ± 5	11 - 210
Breasts	0.080	0.045-0.11	24 ± 2	6 - 110
Gallbladder wall	0.056	0.010-0.062	18 ± 2	1 - 110
Stomach	0.59	0.58-0.60	190 ± 19	42 - 1300
SI	0.33	-	110 ± 11	23 - 720
ULI wall	0.067	0.065-0.068	22 ± 2	5 - 140
LLI wall	0.051	0.049-0.054	17 ± 2	4 - 120
Heart wall	0.10	0.058-0.14	30 ± 3	7 - 140
Kidneys	0.071	0.067-0.075	23 ± 2	5 - 160
Liver	0.055	0.042-0.066	17 ± 2	4 - 94
Lungs	0.16	0.075-0.23	47 ± 4	9 - 180
Ovaries	0.058	0.056-0.060	19 ± 2	4 - 130
Pancreas	0.074	0.063-0.083	23 ± 2	5 - 140
Red marrow	0.14	0.072-0.20	43 ± 4	9 - 170
Skin	0.094	0.049-0.13	28 ± 2	6 - 120
Spleen	0.065	0.052-0.077	21 ± 2	5 - 120
Thymus	0.31	0.13-0.46	91 ± 8	16 - 320
Uterus	0.063	0.058-0.069	21 ± 2	5 - 150
Other tissue	0.21	0.095-0.31	62 ± 5	12 - 230

treatment with radioiodide. The absorbed dose per MBq of ^{131}I-iodide administered calculated using ICRP Publication 53 (2) is different, (Figure 2) due to the use of a constant effective half-time 7.2 days, which is valid for females with a normal thyroid function. The effect of assuming too long of an effective half-time is that the absorbed dose to the bladder is underestimated, as too much ^{131}I is assumed to decay in the thyroid. The absorbed dose to the thyroid is in the same way overestimated. The absorbed doses calculated with the ICRP computer program (4) and MIRDOSE3 (5), both using the 15-yr-old (3), are almost identical. The difference in the values calculated with MIRDOSE3 (5) using the nonpregnant adult female phantom (6) is due to differences in some of the organ masses in the phantoms.

Stabin et al. (10) calculated dose estimates to the bladder, uterus, gonads, marrow, thyroid and whole body for the hyperthyroid adult female using the standard MIRD technique. The absorbed dose was estimated for maximum thyroid uptakes from 20% to 100% using two different thyroid uptake biologic half-times of 2.9 hr and 6.1 hr and assuming the biologic half-time of the thyroid retention to be a function of maximum thyroid uptake. In this work, the range of the maximum uptake in the thyroid was 30-90%, and a biological thyroid uptake half-time of 8 hr was used (2). Different values of the biological half-time for the thyroid retention were used in the calculations. Stabin et al. (10)

used the dynamic bladder model of Cloutier et al. (11), while in this work the kidney-bladder model published by ICRP (2) was used. Briere et al. (12) calculated the absorbed dose to the uterus and ovaries using the MIRD Pamphlet No. 11 (13). The absorbed dose to the uterus was also measured with LiF dosimeters.

Table 5
Comparison between Absorbed Dose per MBq ^{131}I-iodide Administered Orally

Organ	This work mGy/MBq	Stabin et al. (10) mGy/MBq	Briere et al. (12) mGy/MBq
Bladder	0.28-0.64	0.60-1.0	-
Ovaries	0.056-0.060	0.026-0.047	0.037 calculated mean
Red marrow	0.072-0.20	0.062-0.15	-
Uterus	0.058-0.069	0.036-0.063	0.047 calculated mean 0.049 measured mean
Total body	0.17-0.63	0.16-0.45	-

The highest absorbed dose is received by the stomach. Studies have been made to investigate the incidence of cancer in patients receiving radioiodide for hyperthyroidism. In the study made by Holm et al. (14), it was observed that the risk for stomach cancer increased over time and increased with activity administered. The study used the tabulated values in ICRP Publication 53 (2) and data from Edmonds and Smith (15) to estimate the absorbed dose from ^{131}I. The latter showed that patients receiving radioiodide for thyroid cancer had a higher mortality of cancer of the bladder and of leukemia, 0.4 and 4.9 deaths per 10^4 patient-year-Gy to the bladder wall and red marrow, respectively.

In the present work, the mean absorbed dose to the uterus after a representative radioiodide therapy is estimated to 20 mGy with a range of 5 mGy - 150 mGy. The absorbed dose to an embryo in an early pregnancy is assumed to be the same as to the uterus.

The effective dose, in which the thyroid as a target organ has been excluded, was calculated to have a mean value of 50 mSv when 300 MBq ^{131}I-iodide was administered. The thyroid is excluded so as to estimate the risk for late effects to the other organs in the body after therapy with ^{131}I-iodide (8, 9). In these calculations, the thyroid is considered as a source organ, but is excluded as a target organ. The absorbed dose to the thyroid is excluded as the thyroid is the target for the treatment and the absorbed dose is very high.

CONCLUSION

Patients with diffuse goiter have a higher uptake and a faster effective half-time than patients with multinodular goiter and adenoma (solitary). The biokinetic data differ with age but not with sex. Younger patients have a higher uptake and a shorter half-time than older patients. When the absorbed dose to non-target organs or tissues is to be calculated for a patient with hyperthyroidism, the individual biokinetic data must be used. For example, the absorbed dose calculated using ICRP Publication 53 (2) data for healthy person overestimate the absorbed dose to the red marrow by 50% on average, relative to calculations using actual thyroid uptake and retention data. For female patients 18-45 years old, the absorbed dose to various organs has been calculated. For one patient, the overestimation for the absorbed dose to the red marrow was as high as 250%. The stomach receives the highest absorbed dose, with a maximum of 1300 mGy. An oral administration of ^{131}I-iodide may

result in an absorbed dose to the stomach of 180 mGy per treatment (range 40-1300 mGy). The effective dose, where the contribution from the thyroid to itself has been excluded, was calculated to have a mean value of 50 mSv when 300 MBq ^{131}I-iodide was administered orally.

REFERENCES

1. Berg G, Fagerberg B, Jacobsson L et al. Radioiodine treatment of hyperthyroidism in a pregnant woman - clinical experience and 8 year follow-up of the off-spring. To be published in J Nucl Med.
2. International Commission on Radiological Protection: Radiation Dose to Patients from Radiopharmaceuticals. ICRP Publication No 53. Annals of ICRP 18. Pergamon Press, Oxford, 1988.
3. Cristy M and Eckerman K. Specific Absorbed Fractions of Energy at Various Ages from Internal Photon Sources. ORNL/TM-8381. Oak Ridge National Laboratory, Oak Ridge, TN, USA, 1987
4. Johansson L, ICRP Task Group on "Dose to Patients from Radiopharmaceuticals", 1995.
5. Stabin M G. MIRDOSE: Personal computer software for internal dose assessment in nuclear medicine. J Nucl Med 37(3):538-546, 1996.
6. Stabin M G, Watson E E, Cristy M et al. Mathematical Models and Specific Absorbed Fractions of Photon Energy in the Nonpregnant Adult Female and at the End of each Trimester of Pregnancy. ORNL/TM-12907. Oak Ridge National Laboratory, Oak Ridge, TN, USA, 1995.
7. Bockisch A, Jamitzky T, Derwanz R and Biersack H J. Optimized dose planning of radioiodine therapy of benign thyroidal diseases. J Nucl Med 34(10):1632-1638, 1993.
8. Beentjes L B and Timmermans C W M. Patient doses in the Netherlands. Radiat Prot Dosim 36:265-268, 1991
9. United Nations Scientific Committee on the Effects of Atomic Radiation, Sources and Effects of Ionizing Radiation, pp 262-263, United Nations, New York, 1993.
10. Stabin M, Watson E E, Marcus C S and Salk R D. Radiation dosimetry for the adult female and fetus from iodine-131 administration in hyperthyroidism. J Nucl Med 32(5):808-813, 1991.
11. Cloutier R J, Smith S A, Watson E E, Snyder W S and Warner G G. Dose to the fetus from radionuclides in the bladder. Health Phys 25(2):147-161, 1973.
12. Briere J and Philippon B. Absorbed dose to ovaries or uterus during a ^{131}I-therapeutic of cancer or hyperthyroidism: comparison between in vivo measurements by TLD and calculations. Int J Appl Radiat Isot 30(10):643-646, 1979.
13. Snyder W S, Ford M R, Warner G G and Watson S B. "S", Absorbed Dose per Unit Cumulated Activity for Selected Radionuclides and Organs, MIRD Pamphlet No. 11, Society of Nuclear Medicine, New York, 1975.
14. Holm L E, Hall P, Wiklund K et al. Cancer risk after iodine-131 therapy for hyperthyroidism. J Natl Cancer Inst 83(15):1072-1077, 1991.
15. Edmonds C J and Smith T. The long-term hazards of the treatment of thyroid cancer with radioiodine. Br J Radiol 59(1):45-51, 1986.

QUESTIONS

Behr: Did I understand you correctly that you did not measure uptake of ^{131}I in other organs than the thyroid directly, but just were relying on your measurements in the thyroid not using excretion measurements? Don't you think you will underestimate the doses to other organs with specific uptake, e.g., the stomach?

Jonsson: We used the ICRP intestinal model.

Behr: Don't you think real measurements from the actual studies would be better than just model assumptions?

Jonsson: Of course real measurements are better than a model assumption. However, this is a retrospective study. For new patients we will include uptake measurements for other organs such as the stomach.

Stubbs: What is the interpretation of effective dose for hyperthyroid treatment with $Na^{131}I$ when the thyroid absorbed dose times weighting factor for thyroid is excluded?

Jonsson: By calculating the effective dose excluding the thyroid you can estimate the risk for late effects for the other organs.

T. Smith: Is the difference you observed between your bladder dose values and those of Stabin simply due to the use of different bladder voiding periods?

Jonsson: Yes, and if the dynamic bladder model was used we would get different dose values.

Akabani: Comment. How can you consider the risk-benefit analysis for a patient who is undergoing radionuclide therapy? It is clear that there is no model capable of assessing the effective dose as a measure of the risk of future illnesses or diseases. Effective dose may be only used or calculated for those patients undergoing diagnosis, not therapy. Please, some comments.

Mattsson: Comment. The idea to calculate an effective dose value for volumes outside the treated region (Beentjes, LB and Duijsings JH, Radiation Risk from Radiotherapy 1996. Proc. Xth Int. Congr. Radiation Research, 1171-1174, Würzburg, Aug 27-Sept 1, 1995) has been used in both external and internal radiotherapy to get an idea of the risk for late radiation induced stochastic effects after the therapy. It might be of value when optimizing the treatment technique and when estimating population doses.

The Application of Image Registration and Mathematical Modeling to the Dosimetry of Intralesional Therapy

Flux G D, Ott R J and Webb S
Institute of Cancer Research & Royal Marsden NHS Trust
Sutton, London SM2 2PT

ABSTRACT

The efficacy of intralesional therapy as a treatment for recurrent high grade glioma has been studied at our Center. In this trial up to 650 MBq of an ^{131}I-labeled monoclonal antibody (MAb) was delivered directly into the solid component of the tumor via one or two indwelling catheters. In all cases a poor diffusion of the radiolabeled antibody through the tumor resulted in noticeably inhomogeneous activity distributions. A number of authors have addressed the issue of inhomogeneous activity distributions with the aid of registered image data (1-2). In this study we have developed a method of three-dimensional dosimetry to ascertain the dose distribution resulting from intralesional therapy, incorporating temporal as well as spatial inhomogeneities. This method used a mathematical model in conjunction with registered SPECT and CT image data to determine the distribution of activity as a function of time. The spatial heterogeneity of activity following infusion, determined from SPECT scans at various time points, was found to result in a correspondingly heterogeneous distribution of absorbed dose to the tumor. Dose-volume histograms were obtained from these dose distributions enabling the heterogeneity to be quantified. In three cases the mean dose to the tumor using this method was also determined in order to make comparisons with results obtained using conventional MIRD dosimetry. In the former case these mean doses were found to be 7 Gy, 20 Gy and 30 Gy, while the corresponding doses using MIRD dosimetry were 23 Gy, 15 Gy and 11 Gy.

INTRODUCTION

The prognosis of patients presenting with high grade glioma is poor, with a median survival of patients treated with surgery alone of 12-14 weeks (3). External beam radiotherapy can increase this to 42-52 weeks (4), although this can entail damage to normal brain tissue. Tumors may however be targeted with monoclonal antibodies (MAbs).

A study carried out at the Royal Marsden National Health Service Trust (RMNHST) determined the feasibility of administering a therapeutic quantity of an ^{131}I-labeled Mab by means of direct infusion into the solid component of the tumor via an indwelling catheter. In this study the catheter was inserted stereotactically following a CT scan of the patient wearing a Gill-Thomas-Cosman stereotactic head frame to which was attached a Brown-Roberts-Wells localization device (5). The CT images were used to define the tumor and to determine the correct placement and trajectory of

the needle. Up to 650 MBq of labeled antibody was then infused over 15-24 hours. Following infusion SPECT scans were obtained on subsequent days for about a week.

METHODS

Image Registration

One feature of this study was that a large number of scans were obtained for each patient. These included the initial CT scan and 5-7 SPECT scans as well occasional follow-up CT scans and MRI and PET scans to aid the delineation of the anatomical and functional tumor volume. To optimize the information available from these scans, they were registered using either stereotactic coordinates obtained from the head frame or external markers attached to the patient's skin.

For each of the SPECT scans, markers were attached at reproducible positions using skin blemishes such as scars, freckles, subcutaneous cysts, etc., as well as recognized anatomical landmarks such as the outer canthi. The markers themselves consisted of perspex discs containing a spherical cavity into which could be injected a liquid suitable for the imaging modality. The cavity was stopped with a small screw, enabling the markers to be re-used. For SPECT scans, the markers were filled with ^{99m}Tc, and a dual energy window was employed, thereby obtaining separate marker and activity image sets which were automatically registered. Markers of various sizes were constructed and the size used was chosen such that it would appear as a series of discs on several image slices. A centroiding algorithm was then employed to localize the center of the marker. This enabled sub-slice coordinates to be obtained, thereby improving the accuracy of registration. Image data were registered by determining the least squares fit between the two sets of matching points according to an algorithm developed by Arun et al. (6). One of the SPECT scans was obtained with the patient wearing the stereotactic head frame as well as the markers, so that all scans could be registered to the initial CT image set. Registration of these images with the initial CT scan enabled the clinician to determine whether the activity had been injected at the correct point and to monitor the change in activity distribution over time (Figure 1).

Registration Accuracy

The accuracy of registration was determined both for phantom and for patient data. Accuracies of ~1mm were found for both the frame-based and marker-based methods, in the latter case for as few as three markers. In the case of patient data the frame-based method was found to be more accurate due to the immobilization of the patient with accuracies of ~2.0 mm, compared with ~4.0 mm for the marker-based method on CT and SPECT data of slice separations 6.4 mm and 8.0 mm, respectively (7).

Mathematical Modeling

It was evident from the registered image sets that the distribution of activity was not homogeneous throughout the tumor, implying that the absorbed dose distribution was also non-uniform. In order to determine this dose distribution, a mathematical model was developed to describe the distribution of activity as a function of time from the commencement of infusion. The starting point for this model was a basic diffusion equation (8).

$$C(r,t) = \frac{M}{8(\pi\kappa t)^{3/2}}\left[\exp\left(\frac{-r^2}{4\kappa t}\right)\right], \qquad (1)$$

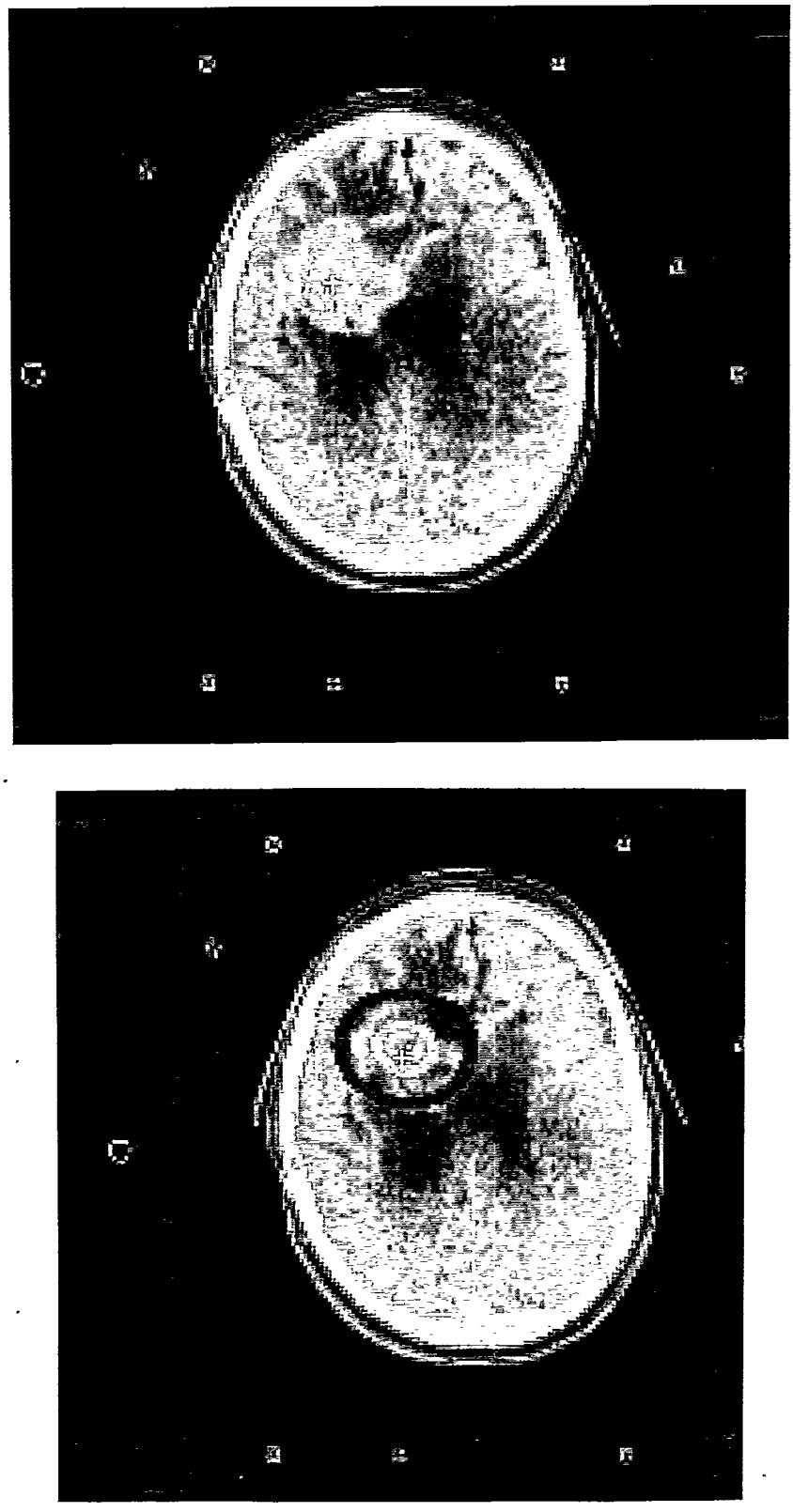

Figure 1. (Top) CT transaxial slice depicting tumor in the top left quadrant. The nine cross sections of the bars of the frame can be seen surrounding the head. (Bottom) The same slice with the activity distribution as imaged at two days postinfusion overlaid. The white cross signifies the point at which the catheter was placed.

where C(r,t) is the concentration of activity (in MBq mm^{-3}) at radial distance r and time t, M is the total amount of activity within the volume (in MBq), and κ is the diffusion constant (in mm^2h^{-1}).

Modifications were made to this equation to incorporate

(i) a biphasic effective decay rate with decay constants λ_a and λ_b h^{-1}, with the second phase commencing at time t_x h,
(ii) a finite duration of infusion over time t_f h, with an initial rate of infusion Q_0 MBq h^{-1}, and
(iii) a cessation of diffusion at time t_D h (7).

This yielded

$$C(r,t) = \frac{Q_0 e^{-\lambda_b t} e^{(-\lambda_b-\lambda_a)t_x}}{4\pi\kappa r}\left[erfc\left(\frac{r}{2(\kappa t_D)^{1/2}}\right) - erfc\left(\frac{r}{2[\kappa(t_D-t_f)]^{1/2}}\right)\right] \quad (t>t_x\geq t_D>t_f), \qquad (2)$$

where erfc is the complementary error function, ie

$$erfc(\rho) = 1 - \frac{2}{\sqrt{\pi}}\int_0^{\rho} e^{-\zeta^2} d\zeta. \qquad (3)$$

Equation 2 gives the distribution of activity as a function of time following the commencement of infusion. If the correct parameters are inserted, a profile generated by this equation should match that obtained from a scan. Of the unknown parameters in this equation, two (the initial rate of infusion and the duration of infusion) are known directly. The effective half-lives may be determined directly from the registered image data by considering the effective decay on the SPECT scan within the tumor volume as outlined on the CT scan. The diffusion parameters can then be determined from the image data, according to Equation 2.

An example is given here for one patient. In this case it was found that the image profiles matched the equation for the following values:

$Q_0 = 24.7$ MBq h^{-1}

$t_f = 15.5$ h

$\lambda_a = 25.8$ h

$\lambda_b = 76.3$ h

$t_x = 94.4$ h

$\kappa = 1.8$ $mm^2 h^{-1}$

$t_D = 51.3$ h

For each of the scans, the equation matched the image profile well (Figure 2).

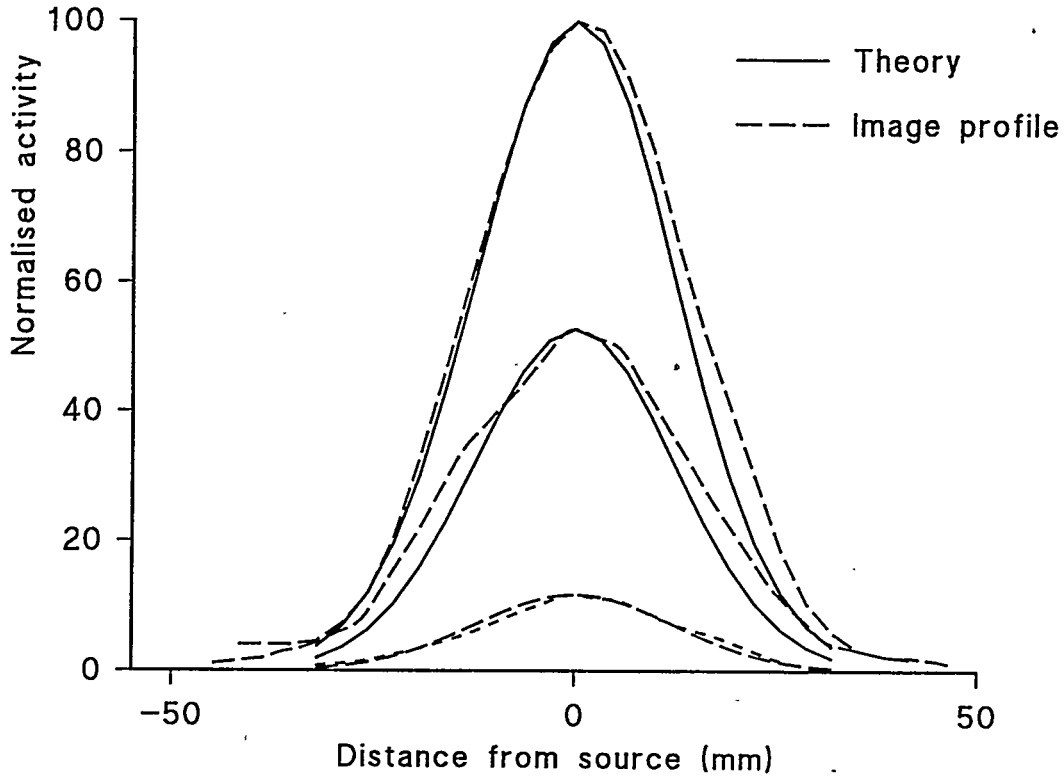

Figure 2. Profiles of activity as directly imaged and as given by Equation 2. These profiles are taken at times 2, 3 and 9 days postinfusion.

In order to obtain the distribution of the total number of decays, N(r), it is necessary to integrate Equation 2 with respect to time, yielding

$$N(r) = \frac{Q_0}{4\pi\kappa r}\left\{\left[erfc\left(\frac{r}{2(\kappa t_D)^{1/2}}\right)\right] - erfc\left(\frac{r}{2[\kappa(t_D - t_f)]^{1/2}}\right)\left(\frac{e^{-\lambda_a t_D}}{\lambda_a} - \frac{e^{-\lambda_a t_x}}{\lambda_a} - \frac{e^{-\lambda_b t_x}}{\lambda_b}\right)\right.$$

$$\left. + \int_0^{t_D} e^{-\lambda_a t}\, erfc\left(\frac{r}{2(\kappa t)^{1/2}}\right) dt - e^{-\lambda_a t_f} \int_0^{t_D - t_f} e^{-\lambda_a t}\, erfc\left(\frac{r}{2(\kappa t)^{1/2}}\right) dt\right\}. \quad (4)$$

This equation may be convolved with the point source dose kernel for ^{131}I to obtain the dose distribution. The dose kernel used in this study was that of Telenczak (9), and is essentially a Monte Carlo generated look-up table of absorbed dose as a function of distance from a point source of 1 MBq of ^{131}I. Dose values were obtained within a cubic matrix by integration of Equation 4 over each voxel to obtain the total number of decays occurring within that voxel. The assumption was then made that these decays all occurred at the center of the voxel and the contribution to the absorbed dose value to that and surrounding voxels was given by multiplication of the relevant entry in the look-up table.

RESULTS

This method of dosimetry enables absorbed dose profiles and dose-volume histograms to be produced. Dose profiles clearly show an inhomogeneous dose distribution, with extremely high dose values close to the point of infusion, falling rapidly to very low values (Figure 3).

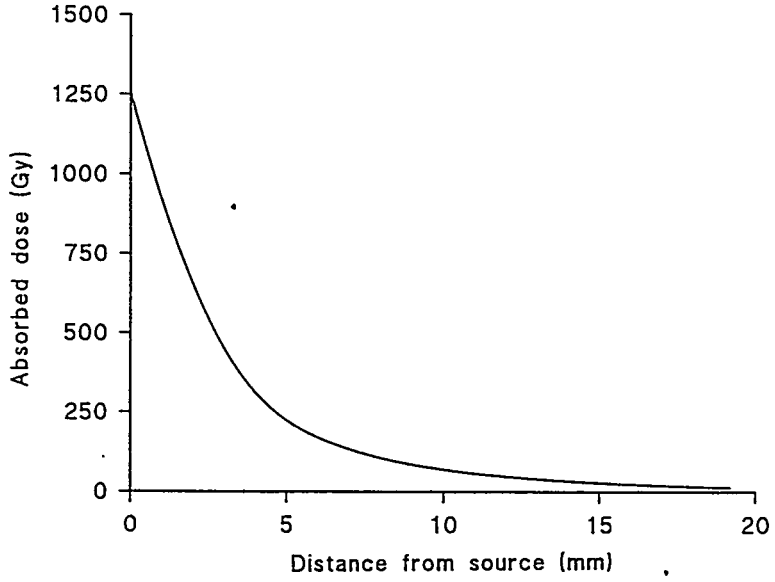

Figure 3. Absorbed dose profile.

The dose-volume histogram shown here is windowed to show a maximum of 100 Gy, which is received by only a small volume of the tumor (Figure 4). The results obtained were compared with those derived using standard MIRD dosimetry (10) by integrating the absorbed dose distribution and dividing by the tumor volume to obtain a mean value (Table 1).

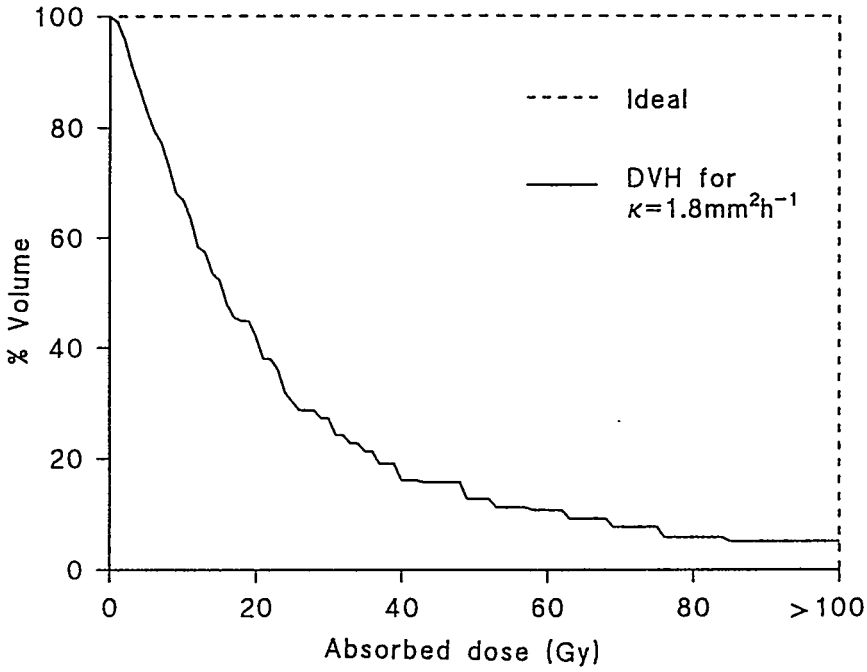

Figure 4. Integral dose-volume histogram, giving absolute values of dose.

Table 1
Comparison of Mean Doses as Obtained from Model-based and MIRD Methods

Patient	Mean dose using model (Gy)	Mean dose using MIRD (Gy)
A	27	7
B	15	20
C	11	30

It can be seen that in these three cases the mean doses obtained agree to within a factor of <4. Given that both methods use a number of assumptions, these initial results are encouraging. Further work is required however to fully validate this method.

DISCUSSION

This method of dosimetry has a number of advantages over standard methods. Firstly, it is possible to obtain a three-dimensional dose distribution allowing for temporal as well as spatial heterogeneity of activity distribution. Also, because the initial amount of activity infused and its effective decay rates are known, it is possible to quantify the dose distribution without the need of a calibration scan. Furthermore, the results are not highly dependent on registration accuracy, as would be the case if the image data were used to determine the time-dependent activity distribution. While this method has been developed to deal exclusively with infusion of activity at a single point, we are currently working to extend this to apply to infusion within a cavity that may have been surgically resected and to intravenous administration.

Intralesional therapy may deliver a high dose to the tumor while minimizing doses to sensitive organs. The principle problem however lies in obtaining a homogenous distribution throughout the tumor. This may be possible by careful selection of the infused agent such that it has the optimized diffusion and radiation emission characteristics. This method of dosimetry enables the production of dose-volume histograms (and therefore tumor-control and normal-tissue-complication probabilities) and provides a method by which individual treatment plans may be scored.

ACKNOWLEDGMENTS

The authors would like to thank Ms. S. Chittenden for her work on this project, including the derivation of results using the MIRD method of dosimetry as displayed above. The project was carried out under the guidance of Dr R Thomas. One of us (G. D. Flux) was sponsored during this period by the Cancer Research Campaign.

REFERENCES

1. Sgouros G, Chui S, Pentlow KS et al. Three-dimensional dosimetry for radioimmunotherapy treatment planning. J Nucl Med 34(9):1595-1601, 1993.
2. Giap HB, Macey DJ, Bayouth JE and Boyer AL. Validation of a dose point kernel convolution technique for Iodine-131 internal dosimetry. J Nucl Med 35(5):160P, 1994.
3. Bloom HGE. Intracranial tumors: Response and resistance to therapeutic endeavors 1970-1980 Int J Rad Oncol Biol Phys 8:1083-1113, 1982.
4. Walker MD, Green SB, Byar DP et al. Randomized comparisons of radiotherapy and

nitrosoureas in the treatment of malignant glioma after surgery. N Eng J Med 303(23):1323, 1980.
5. Gill SS, Thomas DGT, Warrington AP and Brada M. Relocatable frame for stereotactic external beam radiotherapy. Int J Rad Oncol Biol Phys 20 599-603 1991.
6. Arun KS, Huang TS and Blostein SD. Least-squares fitting of two 3D point sets. IEEE Trans on Pattern Analysis and Machine Intelligence. PAMI-9(5):698-700, 1987.
7. Flux GD. Multimodality image registration and its application to the dosimetry of intralesional radionuclide therapy. PhD thesis, University of London 1995.
8. Crank J. The Mathematics of Diffusion. Oxford University Press, London 1967.
9. Telenczak P. Apport de la microscopie ionique analytique et des methodes de Monte Carlo (EGS4-PRESTA) pour l'optimisation des parametres dosimetriques en radiotherapie metabolique. Doctoral Thesis No. 846 Universitie Paul Sabbatier, Toulouse, 1987.
10. Loevinger R and Berman M. A Revised Schema for Calculating the Absorbed Dose from Biologically Distributed Radionuclides. MIRD Pamphlet No.1 Revised. New York: Society of Medicine, 1976.

QUESTIONS

Sgouros: How do you interpret the nonphysics component of the effective half-time? If it represents some kind of loss how do you distinguish that from diffusion? Did the effective half-time change depending on the patient? How did the diffusion constant compare with Jain's estimate for antibodies?

Flux: The biological half-time of the isotope is presumed to be due to wash-out from the tumor after it enters the vasculature. In this study the activity was not seen to diffuse as far as the edge of the tumor in significant quantities. The rate of diffusion and the effective half-time were measured independently directly from the sequential image data. The effective half-time did vary with the patient, and usually occurred in two phases. The diffusion constants also varied and frequently the diffusion had ceased by the time of the first scan so that we were only able to obtain 'windows' within which the rate of diffusion had occurred. More work is required in determining these diffusion rates.

Humm: You compared mean doses using your dose calculation method with the MIRD method. If, however, the dose to a large volume of the tumor is almost zero, as you showed, such a comparison is meaningless. Only a dose-volume histogram is meaningful, from which one can predict the fraction of all survivors. A mean dose of 10,000cGy or 1,000,000cGy would still result in 50% cell survival if only half the tumor was irradiated.

Flux: Yes, I agree. The purpose of obtaining a mean dose from the model-based method of dosimetry was simply that this is the only way of determining to what degree the two methods of dosimetry agreed. Given that this method is as yet not fully validated, and that it uses different information and rests on a different set of assumptions than the MIRD method, it is important to determine the correlation between the two.

Parsai: Why would you want to use I-131 MAb rather than other beta emitters such as P-32?

Flux: A question for the radiochemists. One aim of this trial was to determine the efficacy of this particular antibody, which I believe could not be labeled to P-32.

R. Dunn: MIRD does not implicitly account for dose estimates for tumors. How were tumors treated to arrive at dose estimates?

Flux: It was necessary to use S factors taken from organs of approximately the same size as the tumors, with appropriate weighting factors incorporated to allow for the tumor mass.

Kennel: If the isotope is bound to antibodies, you would expect a biphasic diffusion from the injection site. A fast one from antibody not bound and a slower one due to release of the antibody or degradation of the antibody. Thus the time of measurements for diffusion are critical.

Flux: Yes, but we have no way to model this.

RADIATION DOSE ESTIMATES FROM INTRAPERITONEAL RADIOIMMUNOTHERAPY WITH ^{177}LU-CC49

Meredith RF[1], Macey DJ[1], Plott WE[1],
Brezovich IA[1], Khazaeli MB[2], Alvarez R[3], Partridge E[3], Russell CD[4], Wheeler RH[2],
Liu T[2], Elliott DG[2], Schlom J[5] and LoBuglio AF[2]
Departments of [1]Radiation Oncology, [2]Medicine, [3]OB/Gynecology and [4]Nuclear Medicine
University of Alabama at Birmingham, Birmingham, AL 35233 and
[5]National Cancer Institute, Bethesda, MD

ABSTRACT

Twenty-seven patients with ovarian cancer who failed surgery and chemotherapy were treated with intraperitoneal radioimmunotherapy using the murine anti-TAG-72 antibody CC49. The CC49 was radiolabeled with ^{177}Lu which emits beta particles ($\bar{E}$ = 149 keV) that are slightly less energetic than ^{131}I; Lu-177 also has less abundant gamma emissions. Dose escalations were performed from 370-1665 MBq/m^2(10-45 mCi/m^2) with $\geq$3 patients/dose group. Hematologic toxicity increased with dose escalation and resulted in grade 2-4 toxicity at 1665 MBq/m^2. Biokinetic studies revealed systemic absorption with peak blood levels at 48h. HPLC of blood showed stability of the radiolabeled complex 5 days post therapy. Dosimetry data collection included serial whole-body probe counts, gamma-camera scans and blood sampling. The MIRD formalism was used for dosimetry calculation. S values for ^{177}Lu were computed for the MIRDOSE II program by Dow Chemical (Freeport, TX). Regression analysis of data was used to derive the effective half-time of radioactivity in the whole body, blood, tumors and organs. Marrow dose was calculated using blood pharmacokinetics. Clearance from the abdominal cavity was assumed to be similar to that measured from the whole body. Clearance curves were more consistent using the geometric mean of anterior + posterior counts than with anterior counts alone. Total-body doses ranged from 89-594 mGy (0.11-0.25 mGy/MBq). For marrow, the dose ranged from 111-806 mGy (0.14-0.34 mGy/MBq). Three patients demonstrated tumor localization that could be quantitated from the Anger camera images; the radiation absorbed doses were 11.7, 17.6 and 18.7 mGy/MBq. The tumor-to-normal tissue ratio was higher with intraperitoneal ^{177}Lu-CC49 therapy than that reported in many radioimmunotherapy studies using systemic administration.

INTRODUCTION

Despite recent improvements in chemotherapy, disease eradication in the peritoneal cavity remains a major challenge in disease control and long-term survival of ovarian cancer patients. Several studies have shown promising therapeutic results with intraperitoneal radioimmunotherapy of ovarian cancer (1-8). Radiation dose estimates have been presented from previous studies using ^{90}Y, ^{131}I and ^{186}Re (2-4, 9-10). Adding to the experience with intraperitoneal radioimmunotherapy for

ovarian cancer, we have completed a Phase I study using the high-affinity, second generation anti-TAG-72 antibody, CC49 tagged with the radionuclide, ^{177}Lu (11). Pharmacokinetic data have been collected from the 27 patients in this Phase I study with the objective of providing radiation absorbed dose estimates for the total body, red marrow, abdominal organs and tumors that were visualized in serial radionuclide images.

METHODS

Study Design

A dose-escalating trial of intraperitoneal ^{177}Lu-CC49 antibody was conducted for patients with chemotherapy-resistant ovarian cancer limited to the abdominal cavity +/- retroperitoneal nodes. Additional clinical details of this study are reported separately (12-13). Parameters monitored include marrow toxicity, antitumor and immune responses, and in vivo pharmacokinetic data after a single intraperitoneal infusion of radiolabeled antibody at dose levels of 370-1665 MBq/m^2 .

CC49 preparation The monoclonal antibody CC49 is a high affinity murine IgG that reacts against tumor-associated glycoprotein TAG-72, which is expressed by the majority of common epithelial tumors (14,15). It has been used by our group and others in several clinical radioimmunotherapy trials, following preclinical studies that showed improved targeting and therapeutic efficacy compared to a related lower affinity antibody (15-19). CC49 was radiolabeled with ^{177}Lu using the bifunctional PA-DOTA chelator (11). CC49 and CC49 conjugated to the chelator PA-DOTA was provided by the National Cancer Institute. ^{177}Lu is a rare earth radionuclide produced by neutron capture with a physical half-life of 6.7 days and emits beta particles ($\bar{E}$ = 149 keV) that penetrate 0.2 to 0.3mm in soft tissue. ^{177}Lu also emits a small proportion of two low-energy gamma rays (113, 208 keV) that permit imaging with an Anger camera, and reduces the radiation hazard to health care personnel compared to ^{131}I. ^{177}Lu was obtained from the University of Missouri Reactor Center. In the initial portion of this study, CC49 was radiolabeled by Dow Chemical Laboratories in Midland, MI. The final quality control checks and individual preparations were performed at The University of Alabama at Birmingham (UAB) laboratories. The radiolabeled product (IND #4427, NSC #647944) had a specific activity of 300 MBq/mg with 88.5 - 93.9% immunoreactivity. Unlabeled CC49 (BB IND #3496, NSC #620537) was added to bring each individual dose to a total of 20 mg CC49. For patients 14-27, all radiolabeling preparation and quality control were performed at UAB on the day of administration. As a precautionary measure to reduce toxicity with the product administered on the day of preparation, dose levels were reduced to 925 MBq/m^2 and escalated at 185 MBq/m^2 per group with the UAB radiolabeled product.

Agent administration Prior to the administration of radiolabeled CC49, the flow and mixing of fluid in the peritoneal cavity was assessed from infusion of 185 MBq ^{99m}Tc-albumin and 500 ml saline through a Tenchkoff catheter which had previously been placed for access into the peritoneal cavity. If loculation was indicated from the radionuclide images, the patient did not receive the radiolabeled antibody. Patients who demonstrated free flow of fluid in the peritoneal cavity received the individually prepared doses of ^{177}Lu-CC49. The CC49 was infused by gravity in a volume of 50 ml, followed immediately by 1L of saline. The patient then changed position at least every 15 minutes for the next 2 hours to promote homogeneous distribution. Vital signs were monitored every 15 minutes during and immediately after the infusion.

Toxicity criteria Patients were evaluated for evidence of toxicity during hospitalization and periodically thereafter using Common Toxicity Criteria from Cooperative Group Trials. Hematologic toxicity was evaluated weekly for six weeks, or longer if blood counts had not returned to baseline.

Clinical monitoring Although this was a Phase 1 study, all patients were evaluated for tumor response. Patients had pretreatment CT scans which were repeated at 6 weeks. Standard criteria defining tumor response were used for those patients with measurable disease, including >50% tumor reduction as partial response and > 25% increase or the appearance of new lesions as progression. Their CT scans were repeated at several week intervals. Patients with nonmeasurable disease were monitored for clinical evidence of recurrence, and radiographic studies were utilized as indicated after the 6 week post-treatment CT scan.

Pharmacokinetics Pharmacokinetics of the radiolabeled antibody in the systemic circulation was assessed from the radioactivity and protein levels measured in serial blood samples as described in our previous studies (17). Figure 1 illustrates the model used to describe the in-vivo pharmocokinetics and compartments in which ^{177}Lu-CC49 was assumed to be distributed.

Radioimmunoscintigraphy Radionuclide images were acquired on three or more separate days after intraperitoneal radiolabeled antibody administration using a Sophy DSX Anger camera fitted with a medium-energy parallel-hole collimator. Whole-body images were acquired on each occasion and SPECT of the abdominal cavity on one or more occasions. Three photopeaks of the ^{177}Lu spectrum were selected (51 Kev, 113 Kev, 207 Kev) with windows of 30%, 20%, and 20%, respectively. Planar images were acquired with a 128 x 128 matrix for 400 K counts. A 512 x 128 matrix was used to acquire whole-body images. The scan speed was determined from the count rate of static images (k counts/sec). The time for each frame of SPECT acquisition was also determined from the static image count rate. For SPECT, a 64 x 64 matrix was used with a step and shoot mode for 64 projection images acquired over 360°. Scans were interpreted for areas of localization that corresponded with known tumor deposits and other areas/organs where localization was observed. Local count-density data were utilized for dosimetry calculations.

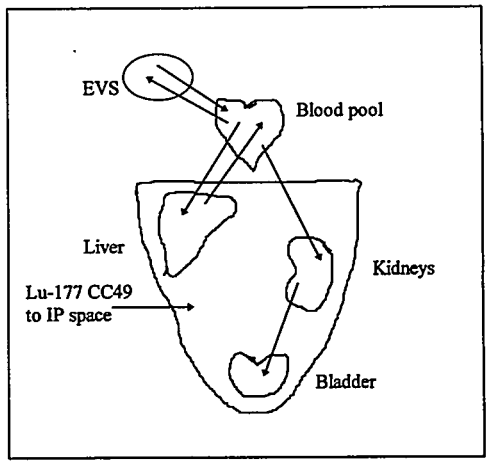

Figure 1. ^{177}Lu-CC49 is infused into the intraperitoneal (IP) space. It slowly enters the blood pool and is distributed to the extravascular space (EVS) and liver with excretion through the urinary tract.

Whole-body probe counts One minute serial whole-body probe counts with a collimated NaI crystal detector were acquired at a distance of 3 meters from the umbilicus of each patient over a period of up to 19 days after administration of ^{177}Lu-CC49. For initial patients, counts were collected only from the anterior position; later patients had counts taken from both the anterior and posterior directions to compensate for any movement of activity in the body. The counts acquired on each day were normalized to the initial counts recorded when all the administered ^{177}Lu was in the whole body of each patient.

Dosimetry Radiation doses to the red marrow, total body and tumors were calculated following the MIRD formalism (20). S values for tumor with ^{177}Lu were derived using the nuclear data tables (21). Total-body retention on each day was derived from the probe counts. Residence times were calculated from trapezoidal integration of whole-body retention data represented as percent of infused activity. Red marrow doses were calculated using the following:

$$\bar{D}_{rm} = \bar{D}_{rm \leftarrow blood} + \bar{D}_{rm \leftarrow RB},$$

where $\bar{D}_{rm}$ is the total dose to red marrow dose from ^{177}Lu in the blood and remainder of the total body.

$\bar{D}_{rm \leftarrow blood}$ is the contribution from ^{177}Lu in the blood, and

$\bar{D}_{rm \leftarrow RB}$ is the contribution from ^{177}Lu in the remainder of the body.

Activity in the red marrow was related to measured blood plasma activity concentrations using the reported marrow-to-blood activity concentration ratio (22). As activity measurements were made using plasma rather than whole blood, a constant factor of 0.19, the nominal value of the extracellular fluid fraction of the marrow space, was used to relate the specific activity of the plasma to that of the red marrow (22). Scaling of marrow mass based on estimates of the marrow volumes of individual patients was not included, since reciprocal factors would have been required for normalizing the corresponding S values. Dose estimates for tumor were based on the following:

$$\bar{D}_{tumor} = \bar{D}_{tumor \leftarrow tumor} + \bar{D}_{tumor \leftarrow TB},$$

where $\bar{D}_{tumor}$ is the total radiation dose to the tumor,

$\bar{D}_{tumor \leftarrow tumor}$ is the tumor self dose contribution,

and $\bar{D}_{tumor \leftarrow TB}$ is the radiation dose from activity in the total body.

For purposes of assigning S values for self-dose, all tumors were assumed to be spherical. The tumor masses/volumes were estimated from CT images. Tumor activities for at least three time points were derived from the geometric means of counts after background subtraction was applied. Attenuation correction was performed for body thickness for the count rates recorded in regions of interest that defined the perimeters of each tumor on serial, planar Anger camera images (23). A monoexponential fit to these data points gave the rate of clearance of radioactivity from each tumor. The peak tumor uptake was assumed to have occurred instantaneously after infusion. The maximum tumor uptake was estimated by extrapolating the count data from the three data points to the end of infusion. Since the count rates on which tumor activities were calculated were corrected for background activity in the patients body, the area of the tumor residence curve was assumed to represent cumulated activity for the tumor in excess of that due to background activity distributed uniformly in the whole body. Consequently, the calculated cumulated activity in the patient was regarded as activity uniformly distributed in the whole body plus that associated with excess activity in the tumor. The S value used for calculating the total body-to-tumor dose contribution was not adjusted for nonuniformity of activity in the body.

Assumptions used in calculating radiation dose for intraabdominal organs (intestines and peritoneum) included the following: 1) monoexponential clearance of radioactivity at the rate measured for the whole body; 2) 100% of the administered ^{177}Lu was considered to be distributed instantaneously and uniformly in the peritoneal cavity, and later throughout the whole body; and 3) the activity in the peritoneal cavity was assumed to serve as a uniform volume source of fluid surrounding the abdominal organs (24). Radiation dose estimates for the peritoneal surface, small intestine, and large intestine were calculated from the following:

$$\bar{D}_{IP\ organ} = \left[\bar{D}_{IP\ wall \leftarrow IP\ fluid}\right]_{np} + \left[\bar{D}_{IP\ organ \leftarrow TB}\right]_{p},$$

where $\bar{D}_{IP\ organ}$ represents the total IP cavity organ wall dose,

$\left[\bar{D}_{IP\ wall \leftarrow IP\ fluid}\right]_{np}$ is the organ wall dose from the nonpenetrating betas emitted by ^{177}Lu,

and $\left[\bar{D}_{IP\ wall \leftarrow IP\ fluid}\right]_{p}$ is the penetrating contribution from photons in the whole body.

The wall dose for all the IP organs was assumed to be 1/4 of the beta dose calculated for the IP fluid with a uniform distribution of ^{177}Lu and taken to represent the radiation dose to the sensitive layer of cells located at approximately 1/4 of the average range of the betas emitted by ^{177}Lu in soft tissue. Radiation doses to the intestines were not calculated because the activity was assumed to be surrounding them, not distributed within them. The MIRD model was used to calculate the radiation dose contribution to the bladder wall from ^{177}Lu in urine, based on the assumptions of an average volume of 200 ml and voiding interval of 3.5 hours (25). The total bladder wall dose was considered to be the sum of the IP wall dose plus the contribution from activity in urine and defined as:

$$\bar{D}_{Bl\ wall} = \bar{D}_{IP\ organ} + \bar{D}_{Bl\ wall \leftarrow urine},$$

where $\bar{D}_{Bl\ wall}$ is the total bladder wall dose,

$\bar{D}_{IP\ organ}$ is as defined previously for the IP organ wall dose,

and $\bar{D}_{Bl\ wall \leftarrow urine}$ is the bladder wall dose from activity in the urine.

The total-body dose to abdominal regions was taken to correspond to the mass among these regions in Reference Man (MIRD Pamphlet No. 5, Revised) (25). Radiation dose contributions to each organ from activity distributed in the whole body was obtained by multiplying cumulated activity in the whole body using ^{177}Lu S values. A modified version of MIRDOSE2 with ^{177}Lu S values was obtained by personal communication with Dow Chemical. The total radiation dose to each organ/region was calculated by summing the dose contributions from all sources in the total body.

Statistics Linear compartmental modeling was used to estimate pharmacokinetic parameters. One compartment and multiple compartment models were fitted to the serial biokinetic sample data. The one compartment model was chosen to best fit most of the data parsimoniously and pharmacokinetic estimates derived were used to describe the data for dosimetry calculations (26, 27). Descriptive statistics were calculated, including mean, standard error and standard deviation.

RESULTS

Twenty-seven ovarian cancer patients were treated at 7 dose levels from 370-1665 MBq/m^2 ^{177}Lu-CC49 administered intraperitoneally. Clinical results have been reported (12,13). Following a single administration of ^{177}Lu-CC49, HPLC evaluation of blood, and peritoneal fluid samples collected over five days confirmed that the ^{177}Lu-CC49 complex was stable in vivo (28). The pharmacokinetics of radioactivity in peritoneal fluid samples was more variable than in blood. This variability can be explained from the nonuniform distribution of this radiopharmaceutical in the intraperitoneal fluid space and variance in the intraabdominal area of sampling. These results were therefore not used for dose calculations. The peak concentration detected in blood occurred at approximately 48 hours after administration. This is illustrated for patient #22 in comparison to whole-body retention of radioactivity, cumulated urinary excretion and tumor retention (Figure 2).

For the entire group of patients, the effective whole-body half-time was 97.6 ± 17.2 hours;

urinary excretion for 23 patients ranged from <3% to 34% (mean = 16.4 ± 10.9%) in the first 72 hours. Patient #10 is the only patient to receive a second treatment. Evaluable data from both courses is included but, for consistency, the whole-body half-time from the second course was excluded from the statistical analysis, which was restricted to single dose therapy. Whole-body retention data were more consistent using the geometric mean of anterior + posterior counts than with anterior counts alone, although the difference was not statistically significant. A comparison of whole-body retention based on anterior counts alone versus the geometric mean for patient #27 is shown in Figure 3.

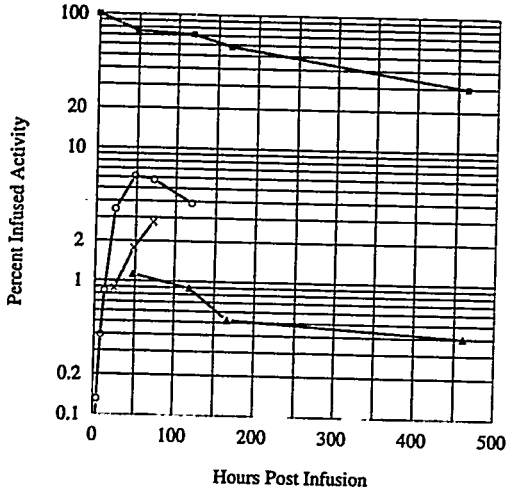

Figure 2. Radioactivity levels presented as percent of infused administered activity are compared for the whole body (■), blood (○), tumor (▲) and cumulated urinary excretion (x) for patient #22 as a function of time after infusion.

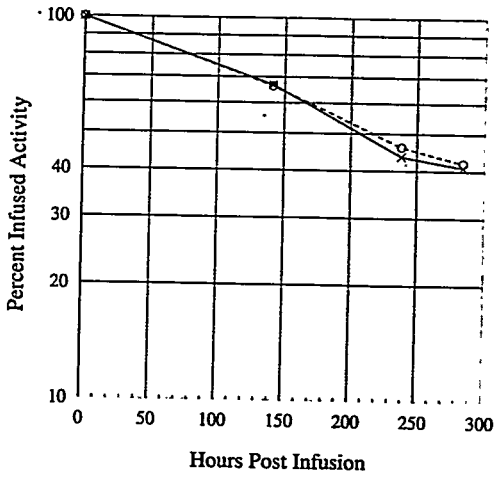

Figure 3. Retention curves for the percent of administered activity are compared as a function of time after administration for whole-body probe count data obtained from anterior only counts versus the geometric mean of anterior and posterior counts in patient # 27.

Marrow suppression increased with administered activity and was considered dose-limiting at 1665 MBq/m^2. Data collection was adequate to allow dosimetry calculations for 24 of the 27 patients. Table 1 compares the neutropenia and thrombocytopenia toxicity grades with the administered activity, total-body effective half-time of radioactivity, and radiation dose estimates to total body and bone marrow for individual patients.

Localization of ^{177}Lu-CC49 in tumor regions was observed in 9 of 13 patients who had gross disease, 7 of 9 with small nodules and 3 of 5 patients with microscopic disease. Figure 4 illustrates localization of ^{177}Lu in the abdomen that likely represents tumor nodules.

Figure 4. Localization of ^{177}Lu in tumor deposits in the anterior abdomen are demonstrated on this lateral section image of patient #5.

Table 1
Total-body and Red Marrow Doses

PT #	DOSAGE LEVEL MBq/m²	INFUSED MBq	TOTAL-BODY $T_{1/2}$-eff hours	TOTAL-BODY		RED MARROW		TOXICITY GRADE	
				DOSE mGy	DOSE mGy/MBq	DOSE mGy	DOSE mGy/MBq	WBC	PLATELET
01	370	611	79.8	89	.145	156	.256	0	0
02	370	673	86.2	105	.156	111	.165	0	0
03	370	681	102.4	126	.185	173	.254	0	1
04	666	1140	84.2	173	.152	354	.311	0	0
05	666	1225	83.1	186	.151	285	.232	0	0
06	666	1199	106.9	232	.193	356	.297	2	0
07	925	1402	135.7	345	.246	462	.330	0	0
08	925	1650	59.1	177	.107	332	.201	1	0
09	925	1587	74.1	219	.138	298	.188	1	0
10	1110	1776	74.0	238	.134	336	.189	1	0
11	1110	1924	68.2	396	.206	426	.221	1	1
12	1110	1991	119.1	428	.215	543	.273	0	1
13	1480	2564						0	1
14	925	1684	101.1	324	.192	393	.234	1	0
15	925	1602						2	3
16	1110	1839	88.7	295	.161	390	.212	1	3
17	1110	1972	113.3	405	.205	672	.341	2	1
18	1110	2002	107.5	390	.195	301	.151	2	1
19	1110	1902	71.6	246	.129	419	.220	2	1
20	1295	2013						1	1
21	1295	2150	104.3	407	.189	300	.139	0	0
22	1295	2157	115.6	430	.199	438	.203	0	1
23	1665	2927	109.0	579	.198	783	.268	4	3
24	1665	2819	92.6	472	.167	456	.162	2	2
25	1665	3263	100.6	594	.182	778	.238	2	3
26	1665	3079	106.5	582	.193	806	.267	3	1
27	1665	3411	93.0	575	.169	563	.165	3	1

Marked specific bone marrow uptake was not evident, although low intensity bone localization was noted for shoulders and large bones among some of the higher dose patients in the Anger camera images. Table 2 provides calculated dose estimates for normal organs, including a contribution to the bladder from urine.

Table 2
Normal Abdominal Organ Doses

	Mean (mGy/MBq)	S.D
Peritoneum* from IP fluid	8.086	3.436
Peritoneum from Remainder Body	0.178	0.035
Small Intestine from Remainder Body	0.178	0.035
Large Intestine from Remainder Body	0.178	0.035
Bladder Wall from Remainder Body	0.135	0.035
Bladder Wall from Urine	0.146	0.043

*This includes peritoneum covering the wall of the intestines and bladder

Most of the dose to normal intraabdominal organs is absorbed by the peritoneum covering them; there was modest dose from penetrating radiation from the remainder of the body. Table 3 provides calculated tumor radiation dose estimates for specific tumor nodules whose location and volume could be adequately defined. Table 3 also shows the tumor-to-marrow ratios for patients 5, 10 and 22.

Table 3
Tumor Dose and Tumor/Marrow Ratio

PATIENT NUMBER	INFUSED MBq	MARROW DOSE mGy	TUMOR MASS g	TUMOR DOSE Gy	TUMOR DOSE mGy/MBq	TUMOR/ MARROW
5	1228	285	1.0	21.7	17.7	76
10	1776	336	7.2	46.6	26.2	139
22	2157	438	12.0	25.2	11.7	58

Although this was a Phase 1 study, antitumor effects were noted. One of 13 patients with measurable disease (#10) had a partial response. Most of the other patients with gross disease progressed within 3 months (one was not evaluable since she was taken off the study with stable disease at 11 weeks and one remains stable at 7 months). Seven of 9 patients with <1 cm nodules progressed within 2-21 months, while two remain without evidence of disease at 4-5 months. Four of five patients with microscopic or occult disease remain stable with no evidence of disease at 6-35 months, and one with microscopic disease showed evidence of progression at 10 months.

DISCUSSION

The current study represents the first therapy trial with intraperitoneal administration of ^{177}Lu-CC49 in patients. The only previous clinical experience with this radiopharmaceutical was conducted

by the National Cancer Institute as a Phase I intravenous study for nonovarian adenocarcinomas (29).

Administration of ^{177}Lu-labeled antibody was accomplished in the present clinical trial with fewer radiation safety concerns than for ^{131}I. Although five days of hospitalization were utilized in these studies for the convenience of frequent blood, urine and peritoneal fluid sample collection, outpatient treatment will be standard when pharmacokinetics parameters do not have to be monitored so vigilantly.

As noted with other intraperitoneal radioimmunotherapy studies, hematologic toxicity was the dose limiting factor in this study. The maximum tolerated dose of ^{177}Lu-CC49 was less than expected from comparison of the emission characteristics of ^{177}Lu with ^{131}I and ^{186}Re, which have dose limiting toxicity (DLT) of about 4.44-5.92 GBq (2, 4) and 5.55 GBq/m^2, respectively when given as a single intraperitoneal treatment. The DLT from intraperitoneal ^{131}I-labeled antibodies may be strongly dependent on the antibody used or other factors since Heal et al. (30) reported no gradeable marrow suppression with up to 3.70 GBq whereas other groups (3) report severe marrow toxicity with doses of 4.77 GBq or greater. However, the calculated marrow dose was less for ^{177}Lu-CC49 at its MTD than for ^{131}I-CC49 as studied by our group as well as others (15-19). Prior chemotherapy may be a factor here, since all patients had been heavily pretreated. However, even with that taken into account, both the DLT toxicity per administered dose and the calculated marrow dose was lower for the ^{177}Lu-CC49 than for heavily pretreated breast cancer patients (18, 31) that received a mean administered dose of >3.70 GBq/m^2 ^{131}I-CC49 and had a mean marrow dose of 0.34 mGy/MBq, or for ovarian cancer patients treated with ^{186}Re-NRLU-10 whose marrow doses were >1 Gy when toxicity was noted (9). The lower DLT of ^{177}Lu compared to ^{131}I may be related to a small amount of late dissociation of the chelator and radionuclide with localization of the ^{177}Lu to bone that is not detectable in Anger camera images acquired. In contrast to the National Cancer Institute (NCI) study of intravenous ^{177}Lu-CC49 (29), which showed intense specific uptake of radioactivity in the bone marrow that resulted in severe hematologic toxicity at 925 MBq/m^2, our intraperitoneal studies have demonstrated little, infrequent bone localization and only mild marrow suppression at similar and higher activity levels. An explanation for the difference in marrow localization observed with route of administration remains to be elucidated. Dose estimates from the NCI study were reported as 108-135 rem/GBq ^{177}Lu from prolonged retention in the bone marrow (29).

Early bowel toxicity in this study was rare, mild and transient. No late bowel complications have been noted, with follow-up approaching 3 years for some of the patients. This is lower than reported from a number of other clinical trials using intraperitoneal therapy with radiolabeled antibodies, chemotherapy or colloidal P-32 (32-34). Mechanisms and biological factors that may account for this difference in toxicity have not been thoroughly explored.

The calculated radiation dose estimates will vary with different assumptions and dosimetry methods. Despite these differences, doses to the various organs are not strikingly different (9) for ^{186}Re where ≥10% of the radioactivity transited through the intestine and the residence time for the peritoneal activity was assigned for the small intestine and intraabdominal organs. Radiation dose estimates for the small intestine in the ^{186}Re study were calculated by assigning the peritoneal activity to the large intestine (9,10). It is anticipated that doses calculated from our current patient studies may be overestimates since assumptions were simple. For instance, urinary excretion was not accounted for in using 100% of the administered activity in dose calculations. Neither was accumulation of radioactivity to tumor. One of the difficulties in determining radiation doses to abdominal organs that do not show specific localization or transit through the intestines as in this study is that available models are designed with radioactivity moving through hollow organs such as the small intestine rather than a radioactive solution bathing the outside wall.

Miniature TLD's have also been used to determine intraperitoneal doses from

radioimmunotherapy Stewart et al. (3) noted nonspecific radiation of <5 Gy by TLD determination from up to 5.85 GBq ^{131}I-labeled antibodies (0.78 mGy/MBq, SE=0.22). The marrow doses in that study were estimated to range from 75 to 325 cGy for intraperitoneal administration of 4.03-5.44 GBq, which are generally higher than estimates from other groups.

Radiation dose estimates for tumors were generally found to be higher than that achieved with intravenous administration of similar radiopharmaceuticals at the MTD. The tumor/marrow ratio observed in our results was greater than the values seen with intravenous administration of radiolabeled CC49 or other radiolabeled antibodies. The ratio is consistent with that noted by Rowlinson et al. (35), who found that tumor/normal tissue activity ratio was about 50 times greater after intraperitoneal versus intravenous administration, using a human colon adenocarcinoma cell line in a nude mouse model. Other researchers using intraperitoneal radioimmunotherapy with ^{131}I or ^{186}Re have also noted tumor to normal ratios on this order (1,9,10,36,37), while that from a ^{90}Y tracer study (38) predicted less than a 5-fold increase in tumor compared to normal tissues. Most of these estimates have been derived from radionuclide images. However, the study of Larson et al. (39) used tumor and normal tissue biopsy material 4-14 days after administration of ^{131}I-B72.3 in patients with peritoneal carcinomatosis and compared these with radiation dose estimates derived from uptake calculations. They found that tumor uptake was widely variable, but in one patient reached as high as 40% of the injected activity.

Our results are similar to earlier reports from radionuclide imaging (40) and dosimetry (36,39) studies of intraperitoneal administration of radiolabeled antibodies which have demonstrated selective tumor localization and slow absorption into the blood pool (41). Also similar to results for several antibodies using at least three radionuclides (^{131}I, ^{186}Re, ^{90}Y) (1-2, 3-8,32), our current results show the greatest antitumor effects when disease volume is small and reduced efficacy for patients with large tumor nodules (7).

SUMMARY

Intraperitoneal therapy with ^{177}Lu-CC49 was well tolerated by most patients and resulted in higher tumor doses and greater tumor/marrow ratios than that generally achieved with intravenous administration. Early therapeutic responses are encouraging with four of five patients treated for microscopic disease alive without evidence of disease at >6-35 months.

ACKNOWLEDGMENTS

The authors gratefully acknowledge the help and advice received from the Radiation Internal Dose Information Center, Oak Ridge, TN. The authors also wish to thank Max Austin, M.D. and Larry Kilgore, M.D. for patient care, Cherita Fagan and JoLane Headley for nursing assistance, M.A. Markiewicz for pharmacy services, Rob Williams for technical assistance, and Carolyn Maddox and Sharon Garrison for manuscript preparation. This work was supported by NCI CM 87215, NIH 1 R01 CA/OD67828-01 and NIH M01 RR 00032.

REFERENCES

1. Epenetos A, Munro A, Stewart S, Rampling R, Lambert HE, McKenzie CG, Soutter P, Rahemtulla A, Hooker G, Sivolapenko GB, Snook D, Courtenay-Luck N, Dhokia B, Krausz T, Taylor-Papadimitriou J, Durbin H and Bodmer WF. Antibody-guided irradiation of advanced ovarian cancer with intraperitoneally administered radiolabeled monoclonal antibodies. J Clin Oncol 5(12):1890-1899, 1987.
2. Stewart JSW, Hird V, Snook D, Sullivan M, Myers MJ and Epenetos AA. Intraperitoneal ^{131}I- and ^{90}Y-labeled monoclonal antibodies for ovarian cancer: Pharmacokinetics and normal tissue dosimetry. Int J Cancer Supp 3:71-76, 1988.
3. Stewart JSW, Hird V, Snook D, Sullivan M, Hooker G, Courtenay-Luck N, Sivolapenko G, Griffiths M, Myers MJ, Lambert HE, Munro AJ and Epenetos AA. Intraperitoneal radioimmunotherapy for ovarian cancer: Pharmacokinetics, toxicity, and efficacy of I-131-labeled monoclonal antibodies. Int J Radiat Oncol Biol Phys 16:405-413, 1989.
4. Stewart JSW, Hird V, Snook D, Dhokia B, Sivolapenko G, Hooker G, Papadimitriou JT, Rowlinson G, Sullivan M, Lambert HE, Coulter C, Mason WP, Soutter WP and Epenetos AA. Intraperitoneal yttrium-90-labeled monoclonal antibody in ovarian cancer. J Clin Oncol 8(12):1941-1950, 1990.
5. Kavanagh J, Rosenblum M, Kudelka A, Gano J, Murray L, Maguire R, Burke T, Cunningham J and Wharton T. Tissue distribution of intraperitoneal B72.3-GYK-DTPA ^{90}Y with and without EDTA in ovarian cancer. In: Proc Adv Innovative Oncol: Biomodulation, Chemoimmunotherapy and Selected Phase II Drugs 38-40, 1991.
6. Jacobs AJ, Fer M, Su FM, Breitz H, Thompson J, Goodgold H, Cain J, Heaps J and Weiden P. A phase I trial of a rhenium 186-labeled monoclonal antibody administered intraperitoneally in ovarian carcinoma: Toxicity and clinical response. Ob Gyn 82(No.4 prt 1):586-593, 1993.
7. Hird V, Stewart JSW, Snook D, Dhokia B, Coulter C, Lambert HE, Mason WP, Soutter WP and Epenetos AA. Intraperitoneally administered ^{90}Y-labelled monoclonal antibodies as a third line of treatment in ovarian cancer. A phase 1-2 trial: Problems encountered and possible solutions. Br J Cancer 62(Suppl. X):48-51, 1990.
8. Salk D, Lesley T, Wiseman G, Breitz H, Bjorn M, Su FM, Smith L, DeNardo G, Xynos F and Weiden P. A phase I clinical trial of a fractionated dose intraperitoneal administration of rhenium-186 monoclonal antibodies in ovarian cancer [Abstract]. Antibody Immunoconj Radiopharm 5:359, 1992.
9. Breitz HB, Durham JS, Fisher DR and Weiden PL. Radiation-absorbed dose estimates to normal organs following intraperitoneal ^{186} Re-labeled monoclonal antibody: Methods and results. Cancer Res Suppl 55:5817s-5822s, 1995.
10. Breitz HB, Durham JS, Fisher DR, Weiden, PL, DeNardo GL, Goodgold HM and Nelp WB. Pharmacokinetics and normal organ dosimetry following intraperitoneal rhenium-186-labeled monoclonal antibody. J Nucl Med 36:754-761, 1995.
11. Schlom J, Siler K, Milenic DE, Eggensperger D, Colcher D, Miller LS, Houchens D, Cheng R, Kaplan D and Goeckeler W. Monoclonal antibody-based therapy of a human tumor xenograft with a ^{177}lutetium-labeled immunoconjugate. Cancer Res 51(1):2889-2896, 1991.
12. Meredith RF, Partridge EE, Alvarez RD, Khazaeli MB, Plott G, Russell CD, Wheeler RH, Liu T, Grizzle WE, Schlom J and LoBuglio AF. Intraperitoneal radioimmunotherapy of ovarian cancer with ^{177}Lu-CC49. J Nucl Med 37(9):1491-1496, 1996.
13. Alvarez RD, Partridge EE, Khazaeli MB, Plott G, Russell,CD, Liu T, Grizzle WE, Schlom J, LoBuglio AF and Meredith RF. Intraperitoneal radioimmunotherapy or ovarian cancer with ^{177}Lu-

CC49: A Phase I Study (Submitted).
14. Schlom J, Colcher D, Siler K, Thor A, Bryant G, Johnston WW, Szpak CA, Sugarbaker P, Carrasquillo JA, and Reynolds JC. Tumor targeting with monoclonal antibody B72.3: Experience and clinical results. Cancer Treatment & Research 51:313-335, 1990.
15. Schlom J, Eggensperger D, Colcher D, Molinolo A, Houchens D, Miller LS, Hinkle G, and Siler K. Therapeutic advantage of high-affinity anticarcinoma radioimmunoconjugates. Cancer Res 52(5):1067-1072, 1992.
16. Divgi CR, Scott AM, Dantis L, Capitelli P, Siler K, Hilton S, Finn RD, Kemeny N, Kelsen D, Kostakoglu L, Schlom J and Larson SM. Phase I radioimmunotherapy trial with iodine-131-CC49 in metastatic colon carcinoma. J Nucl Med 36(4):586-592, 1995.
17. Meredith R, Bueschen A, Khazaeli M, Plott W, Grizzle W, Wheeler R, Schlom J, Russell C, Liu T and LoBuglio A. Treatment of prostate carcinoma with radiolabeled antibody CC49. J Nucl Med 35:1017-1022, 1994.
18. Murray J, Macey D, Rosenblum M, Kasi L, Grant E, Zhang H, Katz R, Rieger P, LeBherz D, Bhadkamkar V, South M, Booser D, Dhingra K, Greiner J, Schlom J and Podoloff D. Phase II trial of ^{131}I-CC49 murine MAB plus alpha interferon in refractory breast cancer. Antibody Immunoconj Radiopharm 7(1):84, 1994.
19. Murray J, Macey D, Kasi L, Reieger P, Cunningham J, Bhakamkar V, Zhang H and Schlom J. Phase II radioimmunotherapy trial with ^{131}I-CC49 in colorectal cancer. Cancer 73:1057-1066, 1994.
20. Loevinger R and Berman M. A Revised Schema for Calculating the Absorbed Dose from Biologically Distributed Radionuclides. MIRD Pamphlet No. 1, Revised. New York: Society of Nuclear Medicine, 1976.
21. ICRP Publication 38, Radionuclide Transformations Energy and Intensity of Emissions. Task Group Committee 2 of the International Commission on Radiological Protection on data used in ICRP Publication 30, Pergamon Press Inc., New York, 1983.
22. Sgouros G. Bone marrow dosimetry for radioimmunotherapy: Theoretical considerations. J Nucl Med 34:689-694, 1993.
23. Thomas SR, Maxon HR, Kereiakes JG. *In vivo* quantitation of lesion radioactivity using external counting methods. Med Phys 3:253-255, 1976.
24. Watson EE, Stabin MG, Davis JL and Eckerman KF. A model of the peritoneal cavity for use in internal dosimetry. J Nucl Med 30:2002-2011, 1989.
25. Snyder WS, Ford MR and Warner GG. Estimates of Specific Absorbed Fractions for Photon Sources Uniformly Distributed in Various Organs of a Heterogeneous Phantom. MIRD Pamphlet No. 5, Revised. New York: Society of Nuclear Medicine, 1978.
26. Labaune JP. Handbook of Pharmacokinetics, toxicity assessment of chemicals. New York: John Wiley & Sons, 1989.
27. Snedecor G and Cochran W. Statistical Methods. 7th Ed, Ames Iowa. The Iowa State Univ Press, 1980.
28. Khazaeli M, Meredith R, Partridge E, Liu T, Alvarez R, Schlom J and LoBuglio A. Phase I trial of ^{177}Lu-CC49 monoclonal antibody in patients with recurrent or persistent ovarian cancer. Advances in the application of monoclonal antibodies in clinical oncology, Conference Proc. May, 1994, Molyvos, Greece.
29. Mulligan T, Carrasquillo JA, Chung Y, Milenic DE, Schlom J, Feuerstein I, Paik C, Perentesis P, Reynolds J, Curt G, Goeckeler W, Fordyce W, Cheng R, Cowan K and O'Shaughnessy J. Phase I study of intravenous ^{177}Lu CC49 murine monoclonal antibody in patients with advanced adenocarcinoma. Clin Cancer Res 1:1447-1454, 1995.

30. Heal AV, Tyson I, Greenberg H, Roberts W, Nicosia S., Berman C and Silbiger M. Pharmacokinetics, dosimetry and clinical evaluation of 131-I-HMFG-1 MoAb in the therapy of colorectal and ovarian carcinoma. Antibody Immunoconj Radiopharam 5(1):1-12, 1992.
31. Macey DJ, Grant EJ, Rosenblum MG, Zhang HZ, Katz RL, Rieger PT, LeBherz D, South M, Griner JW, Schlom J, Podologg DA and Murray JL. Effect of recombinant interferon alpha on biodistribution and toxicity of ^{131}I-labeled monoclonal antibody CC49 in breast cancer: A phase II trial. (In Press)
32. Muto M, Finkler N, Kassis A, Howes AE, Anderson LL, Lau CC, Zurawski VR, Weadock K, Tumeh SS, Lavin P and Knapp RC. Intraperitoneal radioimmunotherapy of refractory ovarian carcinoma utilizing iodine-131-labeled monoclonal antibody OC125. Gyn Oncol 45:265-272, 1992.
33. Markman M, Rowinsky E, Hakes T, Reichman B, Jones W, Lewis, JL Jr, Rubin S, Curtin J, Barakat R, Phillips M, Hurowitz L, Almadrones L and Hoskins W. Phase I trial of intraperitoneal taxol: A gynecologic oncology group study. J Clin Oncol 10:1485-1491, 1992.
34. Vergote IB, Vergote-DE Vos LN, Abeler VM, Aas M, Lindegaard MW, Kjorstad KE and Trope CG. Randomized trial comparing cisplatin with radioactive phosphorus or whole-abdomen irradiation as adjuvant treatment of ovarian cancer. Cancer 69:741-749, 1992.
35. Rowlinson G, Snook D, Busza A and Epenetos AA. Antibody-guided localization of intraperitoneal tumors following intraperitoneal or intravenous antibody administration. Cancer Res 47:6528-6531, 1987.
36. Ward B, Mather S, Hawkins L, Crowther ME, Shepherd JH, Granowska M, Britton KE and Slevin ML. Localization of radioiodine conjugated to the monoclonal antibody HMFG2 in human ovarian carcinoma: Assessment of intravenous and intraperitoneal routes of administration. Cancer Res 47:4719-4723, 1987.
37. Buckman R, De Angelis C, Shaw P, Covens A, Osborne R, Kerr I, Reed R, Michaels H, Woo M, Reilly R, Law J, Baumal R, Groves E and Marks A. Intraperitoneal therapy of malignant ascites associated with carcinoma of ovary and breast using radioiodinated monoclonal antibody 2G3. Gyn Oncol 47:102-109, 1992.
38. Hnatowich DJ, Chinol M, Siebecker DA, Gionet M, Griffin T, Doherty PW, Hunter R and Kase KR. Patient biodistribution of intraperitoneally administered yttrium-90-labeled antibody. J Nucl Med 29:1428-1434, 1988.
39. Larson S, Carrasquillo J, Colcher D, Yokoyama K, Reynolds JC, Bacharach SA, Raubitchek A, Pace L, Finn RD, Rotman M, Stabin M, Neumann RD, Sugarbaker P and Schlom J. Estimates of radiation absorbed dose for intraperitoneally administered iodine-131 radiolabeled B72.3 monoclonal antibody in patients with peritoneal carcinomatoses. J Nucl Med 32:1661-1667, 1991.
40. Carrasquillo J, Sugarbaker P and Colcher D. Peritoneal carcinomatosis: Imaging with intraperitoneal injection of ^{131}I-labeled B72.3 monoclonal antibody. Radiology 167:35-40, 1988.
41. Chatal J, Saccavini J, Gestin J, Thedrez P, Curtet C, Kremer M, Guerreau D, Nolibe D, Fumoleau P and Guillard Y. Biodistribution of indium-111-labeled OC125 monoclonal antibody intraperitoneally injected into patients operated on for ovarian carcinomas. Cancer Res 49:3087-3094, 1989.

QUESTIONS

Roesch: I was surprised to see that the ^{177}Lu labeling of your tracer was 100% intact even four days after administration in vivo. Could you give some information concerning the chelator which was used for the radiochemical binding of ^{177}Lu?

Meredith: PA-DOTA chelator was used.

Breitz: What did the peritoneal fluid sample fluid clearance show?

Meredith: Similar $t_{½}$ (effective) as whole body for patients with sufficient samples for evaluation.

Breitz: What was the specific activity for the marrow dose?

Meredith: 8 mCi/mg

Breitz: Why was MTD so low?

Meredith: MTD was lower than expected but it has not been fully studied to determine why the MTD seemed low.

CURRENT STATUS OF CELLULAR DOSIMETRY

Humm JL
Dept. of Medical Physics
Memorial Sloan-Kettering Cancer Center
1275 York Avenue
New York, NY 10021

ABSTRACT

The radiotoxicity resulting from the deposition of an absorbed dose D within any organ tissue will depend upon the spatial distribution of the energy deposition at the cellular and subcellular level. The biological response is produced by damage inflicted on the critical targets within a cell. Therefore, the proximity with which a pharmaceutical transports the radionuclide to these sites determines the biological response. Heterogeneity of the radionuclide distribution can effect an unanticipated enhancement of biological toxicity/mutagenicity, or elicit a reduced response. The former can occur if the source becomes selectively bound to the surface of a cell, internalized or incorporated within the cellular genome. Such mechanisms of enhanced cellular dose can produce disproportionate effects at low doses, and perhaps raise the risk of carcinogenesis from low exposures to selected radiopharmaceuticals. Unfortunately, enhanced toxicity through cellular-targeting mechanisms is unlikely to be sustained at therapeutic doses. This is because the distribution of current therapeutic agents is not uniform at the global tissue level, due to physiological barriers, heterogeneity of target expression and cell cycle effects. The probability of tumor control does not depend upon the average dose, but rather upon the cumulative effect of the radiation burden to the individual cells. Thus, emphasis in radiopharmaceutical dosimetry has been placed upon determining the microscopic distribution of those agents of current interest in diagnostic and therapeutic nuclear medicine. Improvements in our ability to quantify the radiolabel distribution at the tissue and cellular levels will enable us to improve predictions of the biological response from internal emitters. This knowledge can be applied to optimizing the design of nuclear medicine therapy protocols ranging from ^{131}I treatment of thyroid cancer to radiolabeled monoclonal antibodies and beyond.

Radionuclide Decay Schemes

The radiations emitted when a radionuclide decays are usually classified as alpha particles, beta particles or gamma rays. The ranges of the particles emitted by a radionuclide determine the significance of performing cellular dosimetry.

Photon Emissions

Photon emissions accompany virtually all radionuclide decay schemes, and for some isotopes,

e.g. ^{99m}Tc, are the prevalent radiation and the only one considered in dosimetry calculations. Photon radiations are attenuated according to the exponential law $I_x = (I_0/4\pi r^2)\exp^{[-\mu x]}$ where I_0 is the emitted photon intensity or fluence, I_x is the intensity at distance x from the source and m is the attenuation cross section for tissue. Photons do not possess a range *per se*, but the distance they travel before undergoing an interaction can be described by a mean path length in tissue which is given by $1/\mu$, the inverse of the attenuation cross section. It ranges from 0.2 cm to 14.1 cm for photon energies from 10 keV to 1 MeV. These mean path lengths greatly exceed the dimensions of cells. As a consequence, the selective deposition of radiation dose due to the accumulation of photon sources within subcellular compartments of the cell is insignificant. However, for radionuclides with a significant component of low energy X-ray fluorescent photons, e.g. ^{125}I, the absorbed fraction to a targeted tumor or organ can be large (1,2). Nevertheless, photon sources have not been specifically used as agents for targeted therapy. Their role remains diagnostic, and to provide dosimetric information for subsequent therapy with pure beta emitters, e.g. ^{111}In and ^{90}Y.

Beta Emitters

For particulate radiations, the subcellular concentration of a radionuclide can become important. The dose versus distance for a point source of beta particles obeys the relationship first described by Loevinger et al. (3), which consists of an inverse square geometric term and a power term to account for absorption. Over distances which are short relative to the mean range of the beta emissions, dose falls according to the inverse square law, i.e. for a source of activity within a cell nucleus, the dose to that cell nucleus is practically independent of the energy of the beta emission. This is shown in Figure 1, which compares the dose versus distance for ^{131}I (mean range 367 μm) and ^{90}Y (mean range 3900 μm). This same observation applies to the gamma emissions of brachytherapy sources. The physical interpretation of absorption for beta rays, is the disappearance of particles from the source fluence, when an electron reaches the end of its range. When dealing with a beta spectrum, electrons are constantly vanishing from the fluence spectrum, beginning with the lowest energy end of the spectrum. However, since most beta spectra contain only a small yield of very low-energy electrons, the importance of electron absorption is insignificant at the dimensions of individual cells, except for very low-energy beta sources such as tritium. The steep $1/r^2$ fall off in dose with distance means that the dose to a cell nucleus from a point source decreases by a factor of 4 in moving from 10 μm to 20 μm distance away. For this reason, radionuclide targeting can significantly increase the dose to individual cell nuclei even for long-range beta sources such as ^{90}Y (4).

The dose to an individual cell can be classified into two components: self-dose and the cross-fire dose. The self-dose depends only upon the number of sources which target that cell and their subcellular distribution, and is independent of the cell density in the culture vial or tissue under study, and beta particle energy (with the exception of the few very low-energy beta sources such as tritium). The cross-fire dose is highly dependent upon the beta emission ranges, and for a targeting radionuclide carrier depends also upon the cell density. This latter point is especially important when performing *in-vitro* cell survival studies with radionuclides, and has no counterpart in external beam *in-vitro* radiobiology. Schneider-Gaedicke et al. (6) attempted to tease apart the contribution from self- and cross-fire dose in an *in-vitro* study, using ^{131}I labeled OC125 antibody directed against two CA-125 antigen positive cell lines, to estimate the dosimetric enhancement to cell nuclei as a consequence of cell-surface binding.

The design of an external beam exposure of a cell culture dish is to irradiate the dish uniformly. Under these conditions all cells receive the same radiation dose, and the fraction of cell survivors is independent of the number of cells in the dish. The surviving fraction, under these conditions, is most commonly described by the linear quadratic relation, although other functional forms have been used.

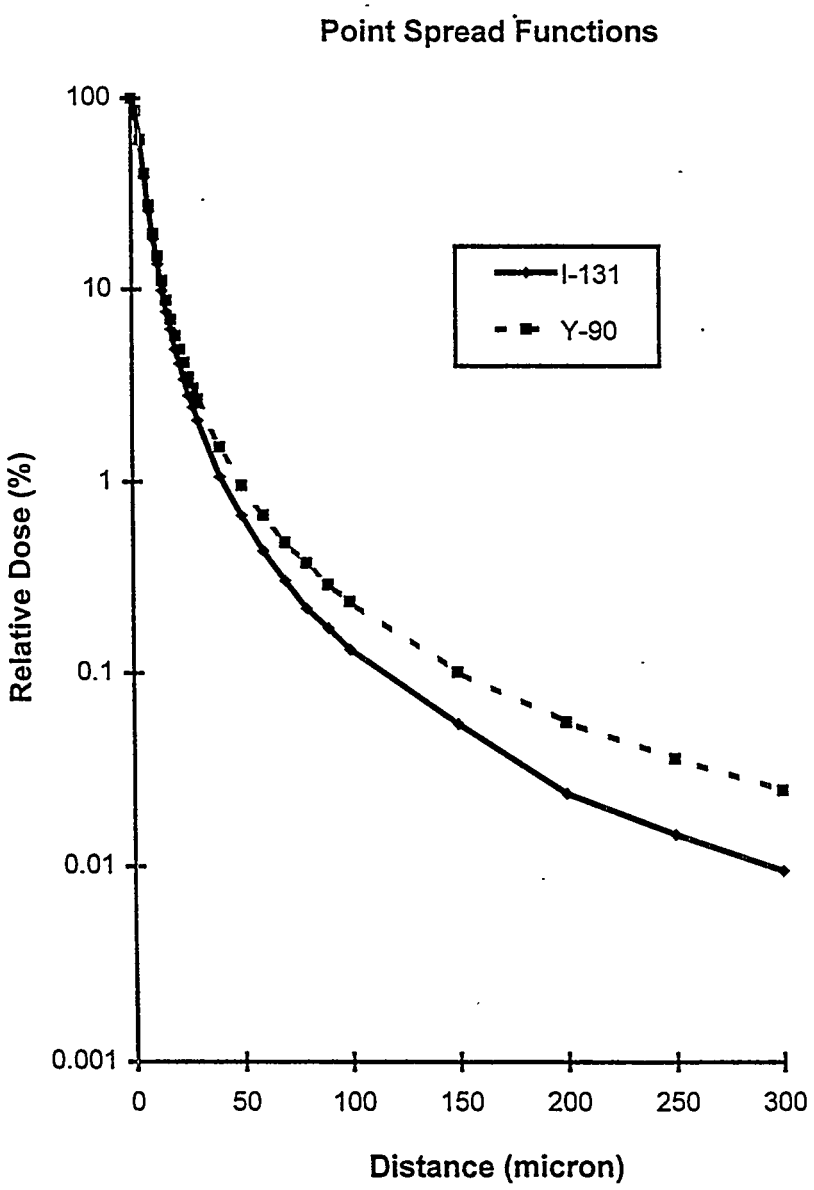

Figure 1. Radiation dose as a function of distance from a point source of ^{131}I and ^{90}Y, determined using Berger's point kernels (5), summed over the entire beta spectra.

This is equivalent to a perfectly uniform distribution of radionuclide within the cell culture, so as to establish charged particle equilibrium across the entire cell-containing volume. For this to be true, the vial must be sufficiently large so that edge effects are negligible. In practice, edge effects are present with *in-vitro* experiments involving radionuclides. The dose at a planar hot/cold interface, of width greater than the range of the highest-energy beta particle, is exactly one half of the equilibrium dose (7). The consequence of a uniform radionuclide distribution within any cell-containing vessel is a nonuniform dose distribution. The reduced dose experienced by the cells at the periphery of the culture vial will result in a departure from the linear-quadratic relationship between average dose and effect. One way to overcome this departure is to determine the dose distribution to the cell culture, and then apply the dose-response equation in a piecewise fashion using the microdosimetric-specific energy spectrum, or its macroscopic equivalent, the dose-volume histogram. This approach has not

been used for *in-vitro* studies, but has been applied for nonuniform beta source distributions from tissue sections (8,9). Monte Carlo methods to determine the dose to individual cells from beta sources is highly inefficient, due to the small dose delivered by a single electron track traversal of the cell. For many situations, it may be unnecessary to calculate the dose to individual cells, but more appropriate to calculate nonstochastic dose profiles determined by an assumed beta source distribution (10). Several theoretical studies have been performed to determine the radiation dose to cells or cell nuclei from radionuclides in common usage in nuclear medicine (11,4,12,13) distributed within different compartments of the cell.

Alpha Emitters

When evaluating an alpha radiolabeled targeting molecule, the interpretation of *in-vitro* radiobiological experiments becomes almost impossible, without a careful analysis of the biodistribution of the radiolabel (14,15). For example, a survival curve (Figure 2) was generated using a Monte Carlo simulation of three different radiolabeled antibody distributions: 1) a uniform distribution of activity, with charged particle equilibrium, representing a nonspecific antibody; 2) radiolabeled antibody bound to 100% of the cell population which expresses the antigen on the cell surface; and 3) half of the radiolabeled antibody bound to the cell population of which only 50% express the antigen. For all three simulations the number of source decays within the culture dish was the same. Thus the total energy deposited and the dose averaged over the dish is identical in all three cases. The differences in the survival curves reflect the differences in the dose deposition pattern within the cell nuclei. In case 1), the distribution of dose obeys a Poisson distribution, and the cell-survival curve is linear with a slope which is inversely proportional to the D_0 for the cell line modeled. In case 2), the dose to the cell nuclei is substantially greater than in case 1), because the sources have been selectively localized close to the sensitive target-cell nuclei. Antigen binding has changed the microscopic pattern of energy deposition at the cellular level, resulting in more dose within the cell nuclei, and less wastage of radiation energy in the intercellular spaces. In case 3), the cell-survival curve is biphasic. The initial slope of the survival curve is governed by the antigen-positive cells, the nuclei of which receive significant burdens from the decay of radiolabels directly on the cell membrane. However, once 50% of the cells have been selectively inactivated, the slope becomes markedly shallower reflecting the progressive cell nuclear dose to antigen negative cells. What is not intuitive, is that in this simulation, the surviving fraction at high average dose is lower for a nonspecific antibody, than for a specific antibody which binds to less than 100% of the cells. This is because radiolabels which bind to the cell-surface antigen of cells raise the contribution to the self-dose to those cells, yet reduce the dose contribution from cross-fire, by displacing them to greater distances from the antigen-negative cell population.

In-vitro studies have been performed using alpha-particle emitters such as radon (16,17), as well as alpha sources appended to monoclonal antibodies (18). These studies confirm the sensitive dependence of the result on the configuration of alpha sources relative to the cells. Humm (19) and Humm and Chin (20,15) demonstrated the importance of calculating the dose to every cell nucleus in order to accurately predict the cell-surviving fraction S. They proposed the determination of S by summing the probability of each individual cell's survival, i.e. $\Sigma\, p_i$, where p_i is the probability of the i'th cell's survival upon receiving a dose D_i. To determine the relation between p_i and D_i, Humm and Chin (15) used the expression $\exp[-D_i/D_0]$, where D_0 is the reciprocal of the slope of a cell survival curve, familiar from radiobiology. It may not be so straightforward, since it has been shown by Charlton and Sephton (21), as well as Roeske and Stinchcombe (22), that the D_0 used to define the bulk sensitivity of the cell line may not be equivalent to the inherent sensitivity (D_i) of the individual, yet identical, clonogens which make up the collective cell culture.

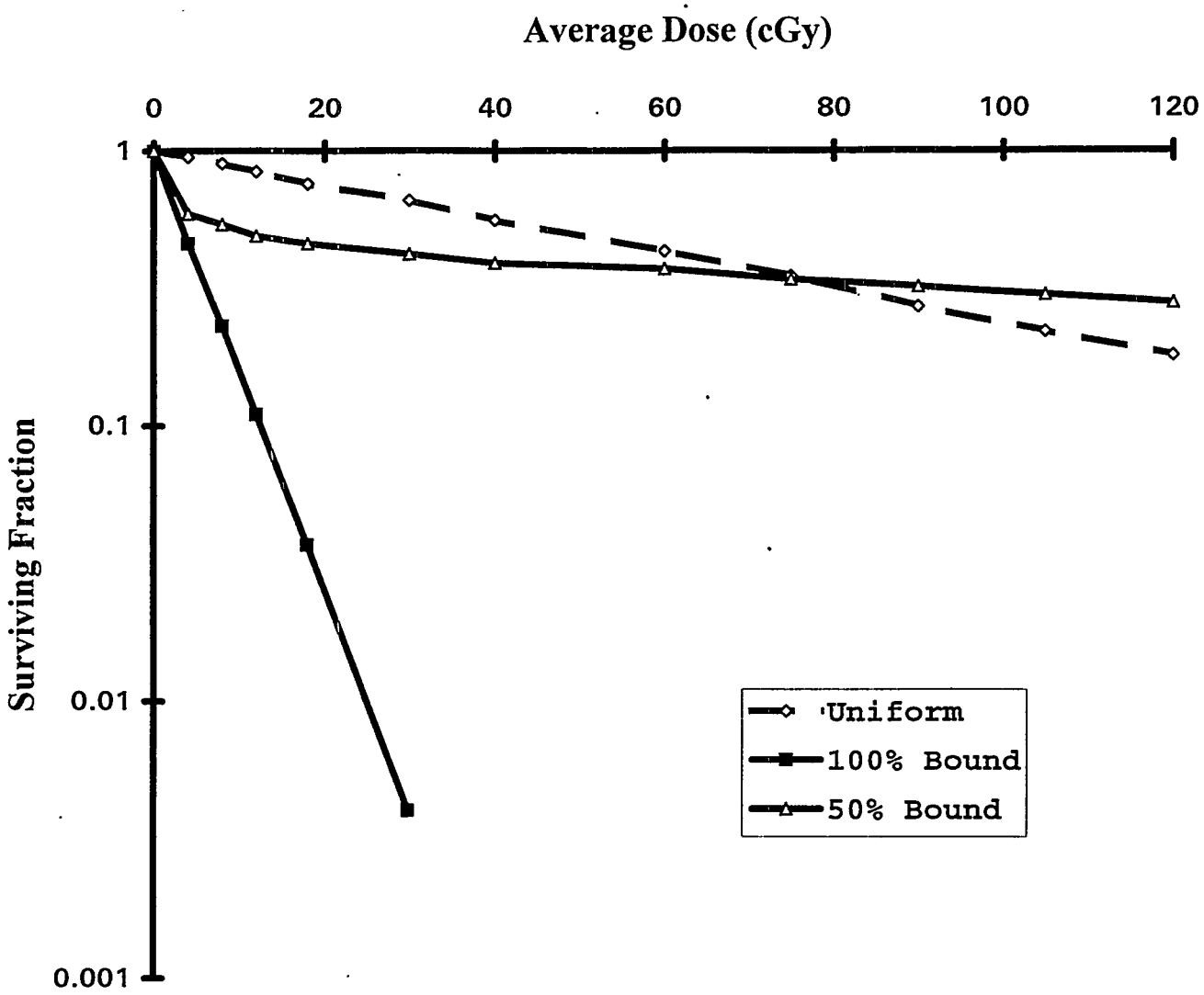

Figure 2. Survival curves obtained by Monte Carlo simulations of the energy deposition within cell nuclei from the alpha-particle emissions of ^{211}At-labeled antibodies. The three simulations represent survival curves for: 1) a uniform source distribution within the cell culture medium, 2) an ^{211}At-labeled antibody which binds uniformly to all cells within the medium, and 3) an ^{211}At-labeled antibody, half of which binds uniformly to 50% of the cells (assumed antigen positive) and the other half remaining unbound, i.e. uniformly distributed throughout the cell culture medium. The initial slope of the survival curve for cases 2) and 3) are 1/5.3 cGy, which is determined by the density of cells in the culture vial.

Auger-Electron Emitters

Radionuclides which exhibit a component of either electron capture or internal conversion in their decay scheme result in the introduction of an inner shell vacancy within the atom. This vacancy can be the source of a cascade of inner shell electron transitions, with the emission of several low-energy electrons, called "Auger electrons" (23,24). Most of these electrons possess energies less than a kiloelectron volt, and travel only nanometers in unit density tissue. The consequence of so short-range emissions, is that the concept of average dose, even to an object as small as a cell nucleus, breaks down. Electrons deposit energy along their tracks, principally as isolated ionizations, until

close to the end of their range. The energy deposition in the "track ends" is typified by a cluster of closely associated ionizations. The LET of track ends is greater than during the rest of the electron pathlength, and Goodhead (25) has shown that the RBE of electron track ends can be more than two times greater than during the rest of the electron track. However, the biological effectiveness of Auger electrons can be significantly greater than 2, when the radionuclide is targeted directly to the cellular genome (26,27,28). Almost all of the radionuclides used for imaging in nuclear medicine possess some component of electron capture or internal conversion, and it is for this reason, that a considerable interest has been expressed in the properties and dosimetry of these radionuclides . The high radiotoxicity of Auger electrons was discovered by those investigating the radiobiological properties of ^{125}I-iododeoxyuridine. Iodine-125 decays 100% by electron capture to metastable ^{125}Te, followed by the almost instantaneous de-excitation by either gamma emission (7%) or internal conversion (93%). The survival curves for ^{125}IUdR were substantially steeper than either ^{131}I incorporated into the DNA (28,29), or ^{125}I attached to the cell membrane (28,30), or within the cytoplasm (31). The survival curve for ^{125}I attached to DNA intercalating agents exhibited a survival much steeper than exhibited by the extranuclear ^{125}I localization studies, but less steep than the ^{125}IUdR curves (32).

Radiobiological Models of Radiation Cell Toxicity

Studies with Auger-electron emitters led to the hypotheses that the most important target for radiation cell death is the nuclear DNA and that direct ionizations in the DNA by any form of radiation is the principle cause of radiation cell death (33,34,24). Ionizations produced in DNA strands result in single and double strand breaks. Most of these breaks are readily repaired by the cell. A cell unable to repair or which misrepairs those breaks is most likely to lose its clonogenic potential. What distinguishes one type of radiation from another is not the number of initial strand breaks produced per unit dose (these numbers are almost independent of the radiation type), but the spatial distributions of breaks along the DNA strands. Low-LET radiations, such as beta and gamma rays, result in individual strand breaks which are not closely associated with each other along the length of the cellular genome (35). High LET radiations, in contrast, produce closely compacted single strand breaks, less readily fixed by the enzymatic apparatus of the cell. Monte Carlo track structure simulations of the pattern of ionizations within a model of the DNA duplex found the production of larger clusters of single strand DNA breaks following the decay of ^{125}I compared to an alpha particle traversal of the DNA molecule (36) providing a scientific explanation of the experimental finding that the cell survival curve for ^{125}IUdR was comparable to that of alpha particles (28,37).

The data obtained with Auger-electron emitters provide overwhelming support for the notion that the DNA is the principal target for radiation cell death. However, it may not be the only one (38), and its significance may be dependent upon the mode of cell death. Currently, the two modes of radiation induced cell death are "mitotic" and "apoptotic". The former is the result of irreparable damage to one of the cells functioning genes, necessary for the cells colony forming ability, and may not be manifest until several cell cycles. The second, often referred to as interphase cell death, occurs when the cell dies prior to reaching mitosis, i.e. within a few hours post irradiation. Apoptotic cell death may be induced by radiation deposition events in the cell nucleus and membrane (39,40). In addition, the apoptotic cell death pathway can be modulated by a variety sensitizing agents (41,42), enhanced by antibody binding to cell surface receptors (Macklis - unpublished data), or by tumor necrosis factor (43) or inhibited by basic fibroblast growth factors (44). The evaluation of cellular response to a radiation insult, therefore, becomes extremely complex, due to the acute sensitivity of the cell to the subcellular spatial distribution of the sources, which is dependent on the chemical

nature of the radionuclide and its carrier, which itself can alter the biological response. For these reasons, the radiobiology of internal emitters is much more complex to evaluate than external beam radiation therapy.

For Auger emitters, the radiobiological response of a cell culture is dependent on the radionuclide and where the carrier transports it within the cell. This implies that an RBE must be associated to each radiopharmaceutical, and not just the radionuclide. This approach would render an overwhelming task for radiation dosimetry. In order to introduce a rationale into radiopharmaceutical dosimetry, Howell et al (45), and Humm, Howell and Rao (46) have proposed that the dose contribution to the cell nucleus be determined by the RBE weighted sum contribution from each subcellular compartment. This microcompartmental modeling approach enables the problem of dosimetry to be broken down into the determination of the subcellular distribution of each radiopharmaceutical. Five compartments have been suggested:

1) the extracellular fluid,
2) bound to the cell membrane,
3) uniformly distributed within cytosol,
4) uniformly distributed within the cell nucleus, and
5) directly appended to the DNA.

For a given isotope, the radiotoxicity per decay can be ascribed an RBE for each subcellular compartment. In this way, the overall toxicity to the cell can be calculated, by summing the fraction of decays within each subcellular compartment multiplied by the corresponding RBE for that subcellular compartment, predetermined from *in-vitro* studies. This simple, but functional approach to the evaluation of radiopharmaceuticals would provide a rationale way towards the estimation of the radiotoxicity of new radiopharmaceuticals.

Obviously, the use of novel radiopharmaceuticals in man requires extreme vigilance. In vitro studies do not answer questions pertaining to the selective localization of the agent in dose limiting tissues, such as bone marrow, the G.I. tract etc.. Radiotracers often become concentrated in the phagocytic cells, such as the macrophages of the lung (47) or spleen (48) or Kupffer cells of the liver (49). The phagocytic cells of the immune system are probably not at substantial risk of neoplastic transformation, and do not constitute a dose limiting toxicity. Other radiopharmaceuticals of current clinical interest include the thymidine precursors for cancer therapy (50) and diagnosis (51) do require information careful scrutiny of the level of incorporation of the agent into the DNA of bone marrow and other normal tissues with rapid turnover. This information is not easy to obtain from clinical studies, but autoradiography of tissue samples may lead to a determination of the labeling index for these agents (52).

The Measurement of Doses at the Cellular Level

Rossi (53) developed an entire science devoted to the measurement of stochastic energy deposition within volumes commensurate with the size of cells. For a review of this subject, see Rossi and Zaider (54). In order to accurately measure the dose within very small volumes, they used a proportional counter (Rossi chamber) composed of tissue-equivalent walls and filled with a tissue-equivalent gas operated at low pressure. By regulating the gas pressure, they were able to simulate spherical volumes down to 0.3 μm diameter by operating the chamber at gas pressure down to 10 Torr. Below this pressure, the technique encounters difficulties due to the increase in statistical noise associated with the proportional counter gas amplification (55). These chambers have been extremely

useful in measuring the spectrum of energy deposition resulting from a given radiation source or field. Although these chambers have been used to determine the energy-deposition spectrum resulting from an incorporated radionuclide, such as radon gas, their principal application has been in the evaluation of external beams, especially mixed neutron-photon fields. Theoretical microdosimetry has been intimately coupled with radiobiology, especially attempts to derive a physical underpinning of the meaning of quality factor (54). Proportional counter based microdosimetry can provide basic physical information of the spectrum of energy deposition by a radionuclide within a simulated cellular volume. But this technique is unable to account for the distribution of a target radionuclide within tissue, and therefore had limited impact upon practical internal emitter radionuclide dosimetry. For a review of microdosimetry in targeted therapy see Humm, Roeske et al (56).

Information of the doses received by cells for a patient receiving a therapeutic or diagnostic quantity of radionuclide cannot be obtained. Laplace (57) declared that an intelligence acquainted with all the forces acting in nature at a given instant, as well as the momentary positions of all things in the universe, would be able to comprehend in one single formula the motion of all bodies, provided that its intellect were sufficiently powerful to subject all data to analysis. Extending this naiveté to the dosimetrists ideal world, one might speculate that the biological toxicity could be known exactly, if it were possible to calculate the dose to each and every cell within the human body. Such an endeavor is currently impossible. Humm, Macklis et al. (8,9,58) proposed to serially section an entire tissue biopsy specimen, and perform autoradiography and histological staining on every tissue section. The amount of information contained within a 1 cm^3 cube of tissue (10^8 cells and assume 10^9 autoradiographic grains) would require the segmentation of $> 10^9$ objects. Special image analysis macro routines were assembled for the automatic detection of both grains and stained cell nuclei, and the centers of each recorded in two files, one for sources (grains), the other for targets (cell nuclei). Good accuracy for both grain (>90%) and cell nuclei (>70%) can be achieved with well prepared sections (9). However, this accuracy requires a X400 magnification, reducing a microscope mounted camera field of view to approximately 200 μm X 200 μm. Therefore 2,500 image frames require analysis per square centimeter of tissue section. This represents 625 Mbytes of image memory per slide. Even with a motorized computer controlled stage, fully automated software for image capture, and specialized morphology and measurement boards to accelerate data acquisition and analysis, it would require about 1 minute per 1,000 objects detected, i.e. approximately 2 years to detect 10^9 objects.

A major limitation of autoradiography is that it provides information of the activity distribution within tissue at only a single time point; the moment of tissue fixation. Although, techniques have been proposed, using two isotopes with double emulsion layers, to derive information of the activity. distribution at two time points, these techniques are extremely complex and time consuming. Others have proposed the combination of spatio-geographic information obtained by autoradiography with cumulative dose information using thermoluminescent dosimeters (59,60) and MOSFET dosimeters (61). Both approaches, however, require the insertion of a miniature dosimeter attached to the end of a catheter needle in order to measure the cumulative dose delivered, thereby disrupting the activity distribution at the point of measurement.

Because of these insuperable shortcomings, one must ask whether autoradiography is practical and provides useful dosimetric information? It certainly is able to supplement the average dose estimates obtained by other means by providing more information of the microscopic source distribution relative to the tissue histology. This may be critical in understanding the radiobiological effectiveness of one radiopharmaceutical versus another, and assist the prediction of normal tissue toxicity at tracer doses. For example, it can determine the fraction of bone marrow cells which incorporate ^{125}IUdR, and thereby provide useful information with which to estimate bone marrow

toxicity. It is unlikely that such information can be gleaned from gamma-camera images alone, although Daghighian et al. (62,63,64) have proposed a method to do this from a multiexponential fit of the tissue-clearance constants, where each clearance constant is interpreted as a different cell-association mechanism, or subcellular compartment.

New more rapid and reproducible alternatives to film autoradiography are now becoming available, e.g. phosphor storage plates, CCD cameras, (65,66). Although these technologies are not yet able to achieve cellular resolution, they can be used for the rapid and accurate quantitation of, for example, the distribution of a short lived radionuclide, such as ^{212}Bi (τ = 1 hour) within a dose-limiting organ (67), or the uptake of radiolabeled antibody within micrometastatic disease (68).

DISCUSSION

Do we need dosimetry at the cellular level? The MIRD committee has and continues to refine the S factor method of organ dosimetry. Organ-level dosimetry may be perfectly adequate for the majority of radiopharmaceuticals used in the clinic, even though most of the radionuclides employed in nuclear medicine, e.g. ^{99m}Tc, ^{67}Ga, ^{201}Tl, ^{111}In, ^{51}Cr are Auger-electron emitters. Some of these have been the subject of intense study (69,70,71,72,49). Whenever, a radiopharmaceutical localizes uniformly within an organ, i.e. does not selectively localize within the cells of one of the dose-limiting tissues, then the average absorbed dose is most probably a reliable measure of tissue toxicity. If one can correctly account for the dose rate at which the radiation is delivered, then it should be possible to use such average doses in the same way as dose is used in external beam radiotherapy. Because radionuclide therapies irradiate the entire body, they are a form of liquid TBI (total-body irradiation). Therefore, all forms of radionuclide therapy encounter the bone marrow as the first-order toxicity. Second order toxicity, e.g. lung, G.I. tract or kidney, are rarely encountered, and are highly radiopharmaceutical and patient dependent. There is currently, a great deal of interest in improving our understanding of dose effect relations for bone marrow. The early work of Benua et al (73), which correlated bone marrow complications with doses >2 Gy to the blood, forms the backbone of thyroid dosimetry today. Yet, the extrapolation of these ideas to other diseases with other radiopharamceuticals, e.g. radiolabeled monoclonal antibodies have been decidedly less convincing (74,75). Patients who enter radioimmunotherapy trials have frequently undergone extensive prior chemotherapy. The interaction of radiation dose to bone marrow with the previous patient history of chemotherapy appears to be a major stumbling block to establishing clean and decisive dose-response relations for marrow (75). If dosimetry fails to predict bone-marrow toxicity for nuclear medicine therapies, other than the radioiodine treatment of thyroid cancer, then the relevance of time consuming, expensive quantitative gamma-camera procedures might be called into question. To incorporate any compromise of the stem cell's ability to reconstitute the bone-marrow population as a result of previous therapies, it will be necessary to investigate biological dosimeter, that can give a baseline of the ability of cell population to sustain further insults. Biological assays of radiation response are currently an active area of research (76,77).

One new potential cellular dosimeter is the fluorescent probe proposed by Makriogiorgos et al (78,79), who are exploring the substance coumarin. This is a chemical compound which reverts to a fluorescent form upon association with a hydroxyl radical formed along the track of an ionizing particle. Hydroxyl radicals are one of the major products produced by radiation interactions with water. The OH$^{\cdot}$ radicals are thought to be the principal component of indirect damage to the DNA. By loading a cell with coumarin, attaching it to the DNA or membrane of the host cell, one may be able to directly determine the dose to the cell population. Makrigiorgos (78) has demonstrated that coumarin retains its fluorescent signal over several months. Therefore, it is possible to expose a cell

population to a protracted exposure for several weeks, and then readout the cumulative dose on a cell by cell basis using a spectrophotometer or a flow cytometer.

Other approaches have been to evaluate the damage directly using plasmid sequences. Martin et al (80,81) incorporated ^{125}I at a known locus in a linearized plasmid of known base composition. He then measured the pattern of strand breaks relative to the site of the ^{125}I decay. By applying Monte Carlo techniques to model the pattern of individual ionizations relative to the DNA strands and base, Charlton and Humm (33) were able to determine the threshold energy (17.5 eV) required for the production of a single strand break. For a double strand break, it was necessary to produce two single strand breaks in opposite strands within 10 base pairs of one another. Such studies provide a connection between the physics of radiation energy loss, and DNA damage. The connection to biological effect is considerably more complex. It has recently been shown that the sustained damage to the DNA is dependent upon the enzymatic repair capacity of the cell, which is dependent upon the tertiary structure (the degree of supercoiling) of the DNA molecule, as well as the chemical environment, i.e. the presence or absence of radical scavengers (82,35). Physicists have responded by modeling radical diffusion (83,84,85). The objective of all of these efforts is to complete the chain of events from the initial physical interactions, to the radiation chemistry, the cellular damage and its repair or fixation. Dosimetry aims to characterize and quantify these processes at every level with whatever techniques that are available.

CONCLUSIONS

Incorporated radionuclide dosimetry needs to be performed at all levels from macrodosimetry to microdosimetry in order to fully understand the complexity of dose-response relations. Gamma-camera imaging remains the only way of obtaining the activity distribution of a radiopharmaceutical in patients over time. Although impaired by the coarse resolution of the gamma camera technology, gamma cameras do enable the organ doses to be calculated from a sequential set of planar or SPECT images.

The lack of resolution of gamma and PET cameras to determine the distribution of a radiopharmaceutical at the cellular level means that the dose estimates for organs derived from them are probably only first-order approximations of the radiotoxicity . There is a need to supplement organ dosimetry by information on the radiolabel distribution at the cellular and subcellular level, especially in the evaluation stage of new radiopharmaceuticals. Most of this work can be performed in preclinical studies with animal models. Nevertheless, whenever possible, patient biopsy material can be used for autoradiography and histology in order to determine any selective localization of the radiolabel with respect to the cellular architecture of the specimen. High-speed autoradiographic procedures are under development with which to quantitate the local deposition at the microscopic level.

The goal of radiation dosimetry is to provide exact and precise physical measures, with which to determine the biological consequences of radiation damage. This has not proven to be easy even for well-controlled external-beam experiments. As a consequence, several factors such as: LET, dose rate, fractionation, oxygen status etc. have been required for the successful interpretation of radiobiological experiments. Studies designed to underpin the biological effects of radiation delivered by internal emitters contain significantly greater complexities. A principal cause of these difficulties is the non-uniformity of the radionuclide distribution, resulting in a cellular dose distribution which is non-uniform. The biological implications of nonuniform dose distributions are extremely poorly understood, also in external beam therapy. How to determine the biological consequences of partial-volume irradiation to dose-limiting tissues, such as the lung, have been the subject of several

ingenious dose-volume histogram reduction schemes (86). The validity of these models is a topic of much speculation, because of their lack of testability. For this reason, it is unlikely that a small set of physical dosimetric descriptors will ever be available, with which to uniquely define the biological toxicity of a given radiopharmaceutical procedure.

Finally, I would like to speculate that dosimetry will become more multidisciplinary with a greater emphasis on the investigation of chemical and biological indicators of radiation response.

REFERENCES

1. Furhang E, Chui CS and Sgouros G. Radionuclide photon dose kernels for internal dosimetry. Med Phys 23:759-764, 1996.
2. Furhang E, Chui CS and Sgouros G. A Monte Carlo approach to patient-specific dosimetry. Med Phys 23:1523-1529, Sept. 1996.
3. Loevinger R, Japha EM and Brownell GL, Radiation Dosimetry, Chap.16, Academic Press Inc., New York, 1956.
4. Humm JL and Cobb LM. Nonuniformity of tumor dose in radioimmunotherapy. J Nucl Med 31:75-83,1990.
5. Berger MJ. Improved point kernels for electron and beta-ray dosimetry. NBSIR 73-107, National Bureau of Standards, 1973.
6. Schneider-Gaedicke E, Humm JL, Lau CC, Macklis RM, Bastert G and Knapp RC. Analysis of cytotoxicity of 131I-labeled OC125 F(ab')2 on human epithelial ovarian cancer cell lines. Radiother Oncol 23:150-159,1992.
7. Charlton DE. The flow of electron kinetic energy through an interface. Phys Med Biol 18:71-77, 1973.
8. Humm JL, Macklis RM, Bump K, Cobb LM and Chin LM. Internal dosimetry using data derived from tissue auto-radiographs. J Nucl Med 34:1811-1817, 1993.
9. Humm JL, Macklis RM, Yang Y, Bump K and Chin LM. Image analysis for the study of radionuclide distribution in tissue sections. J Nucl Med 35:11217-1225, 1994.
10. Howell RW, Rao DV and Sastry KSR. Macroscopic dosimetry for radioimmunotherapy: Nonuniform activity distribution in solid tumors. Med Phys 16:66-74, 1989.
11. Jungermann JA, Yu KHP and Zanelli CI. Radiation absorbed dose estimates at the cellular level for some electron emitting radionuclides for radioimmunotherapy. Int J Appl Radiat Ios 35:883-888, 1984.
12. Faraggi M, Gardin I, de Labriolle-Vaylet, C, Moretti JL and Bok BD. The influence of tracer localization on the electron dose rate delivered to the cell nucleus. J Nucl Med 35:113-119, 1994.
13. Goddu SM, Howell RW and Rao DV. Cellular dosimetry: absorbed fractions for monoenergetic electron and alpha particle sources and S-values for radionuclides uniformly distributed in different cell compartments. J Nucl Med 35:303-316, 1994.
14. Fisher DR, Frazier ME and Andrews Jr. TK. Energy distribution and the relative biological effects of internal alpha emitters. Radiat Prot Dosim 13:223-227, 1985.
15. Humm JL and Chin LM. A model of cell inactivation by alpha particle internal emitters. Radiat Res 134:143-150,1993.
16. Rotmensch J, Atcher RW, Hines JJ, Toohill M and Herbst AL. Comparison of short lived high LET alpha emitting radionuclides lead-212 and bismuth-212 to low X-rays on ovarian carcinoma. Gyn Oncol 35:297-300, 1989.
17. Scharwtz JL, Rotmensch J, Atcher RW, Jostes RF, Cross FT, Hui TE, Chen D, Carpenter S,

Evans HH, Mencl J, Bakele G and Rao PS. Inter-laboratory comparison of different alpha-particle and radon sources: cell survival and relative biological effectiveness. Health Phys 62:458-461, 1992.
18. Kozak RW, Atcher RW, Gansow OA, Friedman AM, Hines JJ and Waldman TA. Bismuth-212-labeled anti-Tac monoclonal antibody: alpha-particle emitting radionuclides as modalities for radioimmunotherapy. Proc Matl Acad Sci USA 83:474-478, 1986.
19. Humm JL. A microdosimetric model of astatine-211 labeled antibodies for radioimmunotherapy. Int J Radiat Onc Biol Phys 13:1767-1773,1987.
20. Humm JL and Chin LM. Cellular dosimetry. ACNP/SNM Joint Symposium on Dosimetry of Administered Radionuclides. American College of Nuclear Physicians, Society of Nuclear Medicine, Ed. Adelstein SJ, pp 306-330, 1990.
21. Charlton DE and Sephton R. A relationship between microdosimetric spectra and cell survival for high LET radiation. Int J Radiat Biol 59:447-457, 1991.
22. Roeske JC and Stinchcombe TG. Relationship between cell survival and specific energy spectra for therapeutic alpha particles. Radiat Res 145:268-273, 1996.
23. Charlton DE and Booz J. A Monte Carlo treatment of the decay of ^{125}I. Radiat Res 87:10-23,1981.
24. Humm JL and Charlton DE. A new calculational method to assess the therapeutic potential of Auger electron emission. Int J Radiat Onc Biol Phys 17:351-360,1989.
25. Goodhead DT. Relationship of microdosimetric techniques to applications in biological systems. In "Dosimetry of Ionizing Radiation", Ed. Kase KR, Bjarngard BE, and Attix FH, Academic Press, Orlando, pp 1-89, 1987.
26. Bradley EW, Chan PC and Adelstein SJ. The radiotoxicity of iodine-125 in mammalian cells. I. Effects on the survival curve of radioiodine incorporated into DNA. Radiat Res 64:555-563, 1975.
27. Chan PC, Lisco E, Lisco H and Adelstein SJ. The radiotoxicity of iodine-125 in mammalian cells. II. A comparative study on cell survival and cytogenetic responses to ^{125}IUdR, ^{131}IUdR and ^{3}HTdR, Radiat Res 67:332- 343, 1976.
28. Hofer KG. Radiation biology and potential therapeutic applications of radionuclides. Bull Cancer (Paris) 67:343-353, 1980.
29. Whaley JM and Little JB. Efficient mutation by ^{125}I and ^{131}I decays in DNA of human cells. Radiat Res 123:68-74, 1990.
30. Lindmo T, Boven E, Mitchell JB, Morstyn G and Bunn PA. Specific killing of human melanoma cells by ^{125}I-labeled 9.2.27 monoclonal antibody. Canc Res 45:5080-5087, 1985.
31. Kassis AI, Howell RW, Sastry KSR and Adelstein SJ. Positional effects of Auger decays in mammalian cells in culture. In: International Workshop on DNA damage by Auger Emitters, Eds. Baverstock K and Cahrlton DE, Taylor and Francis, London, pp 1-13, 1988.
32. Martin RF, Bradley TR and Hodgson GS. Cytotoxicity of an ^{125}I-labeled DNA binding compound that induces double stranded DNA breaks. Canc Res 39:3244-3247, 1979.
33. Charlton DE and Humm JL. A method of calculating initial strand breakage following the decay of 125-I. Int J Radiat Biol 53(3):353-365,1988.
34. Charlton DE, Nikjoo H and Humm JL. Calculation of initial yields of single and double strand breaks in cell nuclei from electrons, protons and alpha particles. Int J Radiat Biol 56(1):1-19, 1989.
35. Ward JF. Mechanisms of radiation action on DNA in model systems - their relevance to cellular DNA. In "The Early Effects of Radiation on DNA". Eds. Fielden EM and O'Neill PO, NATO ASI Series H, Springer Verlag, New York, Vol 54, pp 1-16, 1991.

36. Charlton DE. The range of high LET effects from ^{125}I decays. Radiat Res 107:163-171, 1986.
37. Howell RW, Narra VR, Rao DV and Sastry KSR. Radiobiological effects of intracellular ^{210}Po alpha emissions: A comparison with Auger emitters. Radiat Prot Dosim 31:325-328, 1990.
38. Hofer KG, van Loon N, Schneidermann MH and Charlton DE. The paradoxical nature of DNA damage and cell death induced by ^{125}I decay. Radiat Res 130:121-124, 1992.
39. Macklis RM, Lin JY, Atcher RW, Hines JJ and Humm JL. Cellular kinetics, dosimetry and radiobiology of alpha particle radioimmunotherapy. Induction of apoptosis. Radiat Res 130:220-226,1992.
40. Palayoor ST, Humm JL, Atcher RW, Hines JJ and Macklis RM. G2M arrest following exposure to 212-Bi alpha particle irradiation: Implications for biologically targeted high LET radiopharmaceutical therapy. Nuc Med Biol 20:795-805,1993.
41. Meyn RE, Stephens LC, Voehringer DW, Story MD, Mirkovic N and Milas L. Biochemical modulation of radiation induced apoptosis in murine lymphoma cells. Radiat Res 136:327-334, 1993.
42. Langley RE, Palayoor ST, Coleman CN and Bump EA. Modifiers of radiation induced apoptosis. Radiat Res 320-326, 1993.
43. Bellomo G, Perotti M, Taddei F, Mirabelli F, Finardi G, Nicotera P and Orrenius S. Tumor necrosis factor alpha induces apoptosis in mammary adenocarcinoma cells by an increase in intranuclear free Ca^{2+} concentration and DNA fragmentation. Canc Res 52:1342-1346, 1992.
44. Fuks Z, Persaud RS, Alfieri A, McLoughlin M, Ehleiter D, Schwartz JL, Seddon AP, Cordon-Cordo C and Haimovitz-Friedman A. Basic fibroblast growth factor protects endothelial cells against radiation induced programmed cell death *in vitro* and *in vivo*. Canc Res 54:2582-2590, 1994.
45. Howell RW, Rao DV, Hou DY, Narra VR and Sastry KSR. The question of biological effectiveness and quality factor for Auger emitters incorporated into proliferating mammalian cells. Radiat Res 128:282-292, 1991.
46. Humm JL, Howell RW and Rao DV. Dosimetry for Auger electron emitters: Report No.3 of AAPM Nuclear Medicine Task Group No.6. Med Phys 21:1901-1915, 1994.
47. Makrigiorgos GM, Berman RM, Baranowska-Kortylewicz J, Vinter DW, Iqbal A, Van den Abeele AD, Adelstein SJ and Kassis AI. Inhomogeneous deposition of radiopharmaceuticals for estimation of radiation risks: experimental evidence and dosimetric implications. J Nucl Med 31:1358-1363, 1990.
48. Cobb LM and Butler SA. Treatment of the murine lymphoma A31 with intravenous sterlized 114mIn loaded A31 cells. Radiother Oncol 10:217-230, 1987.
49. Gardin I, Colas-Linhart N, Petiet A and Bok B. Dosimetry at the cellular level of Kupffer cells after cells after technetium-99m-sulpher colloid injection. J Nucl Med 33:380-384, 1992.
50. Macapinlac HA, Larson SM, Daghigian F, Finn R, Zhang J, Humm JL, Squire O and Kemeny N. Pilot clinical trial of 5-[^{125}I]iodo-2'-deoxyuridine in the treatment of colorectal cancer metastatic to the liver. J Nucl Med 37:25S-29S, 1996.
51. Tjulajev J, Muraki A, Ginos J, Berk J, Koutcher J, Ballon D, Beattie B, Fin R and Blasberg R. Iododeoxyuridine uptake and retention as a measure of tumor growth. J Nucl Med 34:1152-1162, 1993.
52. Mariani A, Cei A, Collechi P, Baranowska-Kortylewicz N, Van den Abbeele A, DiLuca R, DiStefano R, Viacava P, Ferdeghini E, DiSacco S, Salvadori P, Bevilacqua G, Adelstein S, Mosca F and Kassis. A. Tumor targeting in vivo and metabolic fate of 5-[iodine-125]iodo-2'-deoxyuridine following intratumoral injection in patients with colorectal carcinoma. J Nucl Med 34:1175-1183, 1993.

53. Rossi HH. Microscopic energy distributions in irradiated matter. In "Radiation Dosimetry", Ed. Attix FH, Roesch WC and Tochlin E, Academic Press, New York, Vol. I, pp 43-92, 1968.
54. Rossi HH and Zaider M. Microdosimetry and its Applications. Springer-Verlag, Berlin, 1996.
55. Fano U. Ionization yield of radiations. II. The fluctuation of the number of ions. Phys Rev 42:26-29, 1947.
56. Humm JL, Roeske JC, Fisher DR and Chen GTY. Microdosimetric concepts in radioimmunotherapy. Med Phys 20,2, Pt. 2,1993.
57. Laplace PS. Theorié analytique des probabilités, Paris, Preface, 1820.
58. Humm JL, Macklis RM, Lu XQ, Yang Y, Bump K, Beresford B and Chin LM. Spatial accuracy of cellular dose estimates obtained from 3D reconstructed serial tissue autoradiographs. Phys Med Biol 40:163-180, 1995.
59. Griffith MH, Yorke ED, Wessels BW, DeNardo GL and Neacy WP. Direct dose confirmation of quantitative autoradiography with micro-TLD measurements for radioimmunotherapy. J Nucl Med 29:1795-1809, 1988.
60. Wessels BW, Yorke ED and Lambiotte M. Multicellular level dosimetry and low dose rate effects. ACNP/SNM Joint Symposium on Dosimetry of Administered Radionuclides. American College of Nuclear Physicians, Society of Nuclear Medicine, Ed. Adelstein SJ, pp 295-305, 1990.
61. Gladstone DJ, Lu XQ, Humm JL, Bowman HF and Chin LM. A miniature MOSFET radiation dosimeter probe. Med Phys 21:1721-1728, 1994.
62. Daghighian F, Pentlow KS, Larson SM, Graham MC, DiResta GR, Yeh SDJ, Macapinlac H, Finn RD, Arbit E and Cheung NKV. Development of a method to measure the kinetics of radiolabeled monoclonal antibodies in human tumor with applications to microdosimetry: positron emission tomography studies of iodine-124 labeled 3F8 monoclonal antibody in glioma. Eur J Nucl Med 20:402-409, 1993.
63. Daghighian F, Humm JL, Macapinlac HA, Izzo J, Zhang JJ, Finn R, Kemeny N and Larson S. I-125-5'-Iododeoxyuridine in the Treatment of Colorectal Cancer Metastatic to the Liver: II Pharmacokinetics and Dosimetry. J Nucl Med 37: 29S-32S, 1996.
64. Daghighian F, Barendswaard E, Welt S, Humm JL, Scott A, Willingham MC, McGuffie E, Old LJ and Larson SM, Enhancement of radiation dose to the nucleus by vesicular internalization of iodine-125-labeled A33 monoclonal antibody. J Nucl Med 37:1052-1057, 1996.
65. Humm JL, Chin LM, Lanza RC, Schaeffer CM, Speidel M and Greene R. Digital imaging for autoradiography - In "Computed Digital Radiography in Clinical Practice". Eds. Greene R and Oestmann J, Thieme Medical Publishers Inc., pp 167-172, 1991.
66. Humm JL. Problems and Advances in the Dosimetry of Radionuclide Targeted Therapy. In "Systemic Radiotherapy with Monoclonal Antibodies, Eds. M.L. Sautter-Bihl, H. Bihl and M. Wannenmacher, pp 37-65, Springer Verlag, 1996.
67. Speidel MT, Humm JL, Bellerive MR, Mulkern R, Atcher RW, Hines JJ and Macklis RM. Assessment of dosimetry and early renal radiotoxicity after treatment with an alpha particle emitting radiopharmaceutical. Antib Immunoconj Radiopharm 4(4):681-692,1991.
68. Finstad CF, Humm JL, Federici MG, Lloyd KO, Barakat R, Divgi C, Larson SM and Hoskins SM. Localization and quantitation using phosphor storage plates of radiolabeled monoclonal antibody MX35 $F(ab')_2$ in patients in micrometastatic epithelial ovarian cancer. Proc Amer Assoc Canc Res Abst. 4193, 37: 611, 1996.
69. Rao DV, Govelitz GF and Sastry KSR. Radiotoxicity of thallium-201 in mouse testes: Inadequacy of conventional dosimetry. J Nucl Med 24:145-153, 1983.
70. Kassis AI, Sastry KSR and Adelstein SJ. Intracellular distribution and radiotoxicity of chromium-51 in mammalian cells: Auger electron dosimetry. J Nucl Med 26:59-67, 1985.

71. Rao DV, Sastry KSR, Grimmond HE, Howell RW, Govelitz GF, Lanka VK and Mylavarapu VB. Cytotoxicity of some indium radiopharmaceuticals in mouse testes. J Nucl Med 29:375-384, 1988.
72. Rao DV, Narra VR, Howell RW, Lanka VK and Sastry KSR. Induction of sperhead abnormalities by incorporated radionuclides: Dependence on sub-cellular distribution, type of radiaton, dose rate, and presence of radioprotectors. Radiat Res 125:98-97, 1991.
73. Benua RS, Circale NR, Sonenberg M and Rawson RW. The relation of radioiodine dosimetry to results and complications in the treatment of metastatic thyroid cancer. Am J Roentgenol 87:171-182, 1962.
74. Eary JF, Krohn KA, Press OW, Fisher D and Bernstein ID. Radioimmunotherapy treatment planning based on radiation absorbed dose or patient size. J Nucl Med 37, Abst. 162, 43S, 1996.
75. Sgouros G, Divgi CR, Scott AM, Williams J and Larson SM. Hematologic toxicity in radioimmunotherapy: an evaluation of different predictive measures. J Nucl Med 37, Abst.165, 43-44S, 1996.
76. Gaulden ME. Biological dosimetry of radionuclides and radiation hazards. J Nucl Med 24:160-164, 1983.
77. Doloy MT, Malarbet JL, Guedeney G, Bourguignon M, Leroy A, Reillaudou M and Masse R. Use of unstable chromosome aberrations for biological dosimetry after the first postirradiation mitosis. Radiat Res 125:141-151, 1991.
78. Makrigiorgos GM, Baranowska-Kortylewicz J, Bump E, Sahu SK, Berman RM and Kassis AI. A method for detection of hydroxyl radicals in the vicinity of biomolecules using radiation induced fluorescence of coumarin. Int J Radiat Biol 63:445-458, 1993.
79. Makrigiorgos GM, Folkard M, Huang C, Bump E, Baranowska-Kortylewicz J, Sahu SK, Michael BD and Kassis AI. Quantification of radiation induced hydroxyl radicals within nucleohistones using a molecular fluorescent probe. Radiat Res 138:177-185, 1994.
80. Martin RF and Haseltine WA. Range of radiochemical damage to DNA with decay of iodine-125. Science 213:896-898, 1981.
81. Martin RF and D'Cunha GD. ^{125}I decay in synthetic oligodeoxynucleotides. In "Biophysical Aspects of Auger Processes". Eds. Howell RW, Narra VR, Sastry KSR, and Rao DV. American Institute of Physics, Woodbury, NY, pp 153-163, 1992.
82. Ward JF. Some biochemical consequences of the spatial distribution of ionizing radiation-produced free radicals. Radiat Res 86:185-195, 1981.
83. Roots R, Chatterjee P, Chang P, Lommel L and Blakely EA. Characterization of hydroxyl radical induced damage after sparsely and densely ionizing radiation. Int J Radiat Biol 47:157-166, 1985.
84. Chatterjee A, Koehl P and Magee JL. Theoretical consideration of the chemical pathways for radiation induced strand breaks. Adv Space Res 6:97-105, 1986.
85. Wright HA, Hamm RN, Turner JE, Howell RW, Rao DV and Sastry KSR. Calculations of physical and chemical reactions with DNA in aqueous solution from Auger cascades. Radiat Prot Dosim 31:59-62, 1990.
86. Kutcher GJ and Burman C. Calculation of complication probability factors for nonuniform normal tissue irradiation: The effective volume method. Int J Radiat Oncol Biol Phys 16:1623-1630, 1989.

QUESTIONS

Shen: Your work and the work of others demonstrated nonuniform distribution of cancer cells in tumor as well as nonuniform distribution of radionuclide in cancer cells. People began to realize this

is one of major factors for poor correlation between macrotumor dose and response. Can you share your thoughts on how to build linkage between submacrodistribution information revealed by autoradiography and patient studies to improve tumor dose-response in clinical studies?

Humm: I have discussed this question with Mike Stabin and both of us agreed that there needs to be a bridge between macrodosimetry with gamma cameras and microdosimetry from autoradiographs. Biopsy samples unfortunately only provide information of a radiolabel distribution at one time point, and from a small fraction of the whole tumor. In spite of this undersampling of the data, I believe that the analysis of autoradiographs can provide an indication of the magnitude of MAb binding heterogeneity or possible geometric enhancement due to the selective binding of radiolabeled MAb. It is in this spirit that microscopic analyses may be useful.

Rao: I would like to comment further on the use of autoradiographs. They are useful only to know why therapy is working or not, qualitatively, but can not be used to calculate dose that would give response. Autoradiographs obtained at one time point are of limited help in calculating the dose.

Humm: I agree with you. Autoradiographs provide valuable auxilliary information with which to evaluate the radiotoxicity of a therapeutic or diagnostic radiopharmaceutical. They give you a single time slice of the radiolabel distribution, which as we know is changing with time. Really what we need is a gamma camera with 10μm resolution capability, but such a device does not exist. For this reason, we still need autoradiographic techniques to provide us with cellular and subcellular radiolabel distributions with which to estimate dose modifying factors to take into account the effectiveness of measured radiolabel distribution. This has not yet been done, but I believe will be necessary in the future if dosimetry is to predict biological response.

ACCURACY IN PHYSICAL PARAMETERS FOR ABSORBED DOSE CALCULATIONS ON CELL- AND SUBCELLULAR LEVELS FOR LOW-ENERGY ELECTRON-EMITTING RADIONUCLIDES

Hindorf C, Tagesson M and Strand S-E
Division of Radiation Physics, Lund University Hospital
S-221 85 LUND, SWEDEN

ABSTRACT

Different methods to calculate absorbed dose for low-energy electrons emitted from radionuclides at the cellular and subcellular levels in radionuclide therapy have been studied, and the accuracy in the physical parameters have been evaluated. Special attention has been paid to dose point kernels and the semiempiric energy loss relationship developed by Cole.

Cole's relationship underestimates the energy loss of electrons by up to ≈30 % for energies between 20 eV and 10 MeV compared to other reported data. The differences are larger in the low-energy region (E<10 keV) than in the high-energy region (E>10 keV). Absorbed fractions for monoenergetic electrons with energies between 0.5 keV and 10 MeV for sphere diameters between 2 μm and 14 μm, were calculated using Cole's relationship. The result shows larger absorbed fractions compared to Berger's improved dose point kernel. For example for ϕ=10 μm and E=100 keV, the difference is ≈20%.

Cole's relationship should be appropriate to use for cellular absorbed dose calculations if one is aware of the limitations (underestimation of energy loss and continuous slowing down approximation). The comparison with Berger's dose point kernel shows rather large discrepancies, which in part could be explained by an error in the Monte Carlo algorithm used by Berger and by straggling, which is considered in Berger's kernel. The differences are, however, not fully explained and need further investigation.

Monte Carlo simulations or microdosimetry, which include stochastic effects of the energy deposition, should be a better alternative to use for absorbed dose calculations at the cellular and subcellular levels for electron-emitting radionuclides. However the poorly known physical energy loss data in the low energy region will also affect these methods.

INTRODUCTION

Currently most absorbed dose calculations for incorporated radionuclides are reported as the mean absorbed dose to organs. To better predict radiobiological effectiveness, however, the absorbed dose should be calculated on the cellular level, due to the nonuniform radionuclide distribution on organ, cellular and subcellular levels and the highly localized energy deposition resulting from the use of radionuclides emitting low-energy electrons (1-3).

Some of these latter methods used to estimate dose at the cellular or subcellular level are listed in Table 1. The dose point kernel approach describes the mean absorbed energy per disintegration as a function of distance from the source in a homogenous medium. To obtain an absorbed dose distribution, a convolution of the dose point kernel and the activity distribution must be performed. The Monte Carlo generated kernels are often considered to be the most accurate (4-5). The semiempiric energy-range relationship, proposed by Cole (7) offers a simple method for calculating the absorbed dose in water, as discussed below. Monte Carlo simulation takes the stochastic effect of energy deposition into account and provides an excellent tool to calculate absorbed dose even in small and geometrically complex regions. Microdosimetry, as described in ICRU 36 (13), is a theoretical tool developed to better predict the biological effect of energy deposition from radiation in a region, and should therefore take into account random fluctuations in energy deposition. The expectation values calculated from the microdosimetric, stochastic quantities equals the nonstochastic quantities (e.g. mean absorbed dose) as shown in ICRU 33 (17).

Table 1
Previously Used Methods to Calculate Absorbed Dose at the Cellular and Subcellular Levels for Electrons

Method	**References**
Point kernels	
Fit to experimental data	(4)
Using electron transport theory	(5)
Monte Carlo simulated	(6)
Semiempiric energy-range relationship	(7-10)
Monte Carlo simulations	(11-12)
Microdosimetry	(13-14)

Inaccuracy in calculated absorbed dose values may result from uncertainties in both the physical and biological input parameters. The biological parameters, the most difficult to accurately determine, can vary with many factors. In cellular dosimetry, the biokinetics on the cellular and subcellular level must be known. The physical parameters such as the calculation method, energy-loss data and radionuclide data, are often assumed to be accurately known. At the cellular level, as shown in this work, however, even inaccuracies in these parameters will introduce errors in the absorbed dose values. The aim of this work was to investigate the influence on the absorbed dose values, at the cellular level, of inaccuracies in following three physical parameters: choice of calculation method, energy-loss data and radionuclide data.

METHODS

Calculation Method

Two methods to calculate absorbed dose on a cellular level, a Monte Carlo-simulated dose point kernel and a semiempiric energy-range relationship, have been compared. Absorbed fractions per emitted monoenergetic electron in the center of a sphere were calculated. The sphere was used as a geometric model of a cell; seven sphere radii between 1 μm and 7 μm were considered in the calculations.

Semiempiric Energy-Range Expression

The range of electrons emitted from a heated filament in air and from foils of plastic for electron-energies between 20 eV and 50 keV has been measured by Cole (7). He reported an energy-range relationship (Equation 1) for electron-energies between 20 eV and 20 MeV, which fitted both his and other's measured data.

$$E = 5.9(R+0.007)^{0.565} + 0.00413R^{1.33} - 0.367, \quad (1)$$

where E is the electron energy in keV and R is the range, in μm, of the electrons. To obtain a relation for the energy loss, Cole derivated the energy-range equation:

$$\frac{dE}{dR} = 3.316(R+0.007)^{-0.435} + 0.0055R^{0.33}. \quad (2)$$

A small error is introduced here due to a miscalculation. The first coefficient in Equation 2 should be 3.334 instead of 3.316 as reported by Cole. In Equation 2, dE/dR is the energy loss in keV/μm in a unit density medium. Absorbed fractions were calculated per monoenergetic electron emitted at the center of a sphere using Cole's semiempiric relations. The equation used for the calculation of deposited energy in a sphere has been reported by Kassis et al. (10).

$$\varepsilon(r,E) = E - E(R(E)-r) \qquad 0 \le r \le R(E), \quad (3)$$

where ε(r, E) is energy deposited in the sphere, E is the initial electron energy, r is the radius of the sphere, R(E)-r is the residual range, and E(R(E)-r) is the residual energy of the electron at the boundary of the sphere. The values of the electron ranges, R(E), were obtained from Cole's equation. When the discrepancy between the defined energy and the calculated was sufficiently small (<0.1%), the range-value was accepted. The absorbed fraction in the sphere, ϕ(r, E), was then calculated as:

$$\phi(r,E) = \frac{\varepsilon(r,E)}{E}. \quad (4)$$

Monte Carlo-Simulated Dose Point Kernel

In 1973, Berger published a dose point kernel (6) that takes energy-loss straggling and energy transport of secondary emitted bremsstrahlung radiation into account. The kernel is also extended to a low-energy region (25-0.5 keV). The kernel is obtained by two different Monte Carlo codes, one for E>20 keV and one for E≤20 keV. Berger tabulated a scaled kernel in water for 36 energies between 0.5 keV and 10 MeV. Berger has also tabulated the fraction of emitted energy absorbed in a sphere, which he calculated by integration over the point kernel. These tabulated absorbed fractions were used for comparison to the results generated in this work.

Energy-Loss Data

For electron energies between 10 MeV and 10 keV, a comparison was made between Cole's energy-loss data and the stopping power-data for water given in ICRU 37 (18). For energies below 10 keV, the Bethe theory is not valid. Cole's data are then compared to those by Ashley (19) and Ritchie (20), which were theoretically calculated data for liquid water down to 20 eV.

For low energies, Humm et al. (21) have done a fit which better describes Cole's experimental data (Equations 6 and 8). The energy-range relations (Equations 5 and 7) are reported by Howell (22). For electrons of energies 60 eV<E ≤400 eV,

$$R = 1.523805 \cdot 10^{-3} + 0.038154E - 7.01803 \cdot 10^{-4}E^2 + 0.036283E^3 \quad (5)$$

$$\frac{dE}{dR} = 29.5 - 666.67R, \quad (6)$$

and for electrons of energy E ≤ 60eV,

$$R = 0.01233E + 2.25E^2 - 23.333E^3 \quad (7)$$

$$\frac{dE}{dR} = a + bR + cR^2 + dR^3 + eR^4 \quad (8)$$

with the coefficients: a=10.5; b=1.126 X 10^3; c=-9.251 X 10^5; d=2.593 X 10^8; and e=4.964 X 10^{10}. In the comparison of energy-loss data done in this work, Equations 1 and 2 were used for electron energies over 400 eV; for electrons of energies below 400 eV, Equations 5-8 were used.

Radionuclide Data

To estimate the influence of choice of input radionuclide data, absorbed fractions were calculated for ^{131}I, using either of two different β spectra (23,24) or the mean energy (23). Cole's semiempiric relationship was used. The β spectra were normalized.

RESULTS

The absorbed fractions in a sphere calculated with Berger's dose point kernel and Cole's semiempiric energy-range relationship are shown in Figure 1a; the ratio of the two values is shown in Figure 1b. Cole's absorbed fractions are higher than Berger's by up to 30% for higher energies. The difference is slightly less for larger spheres.

Different electron energy-loss data are shown in Figure 2a. The comparison for different energy loss-data shows that Cole underestimates the energy loss for several energies (Figure 2b). At energies over 10 keV, the difference between ICRU 37 and Cole is as much as ±10%. Data at energies below 10 keV show the caracteristic increase of energy-loss per length unit with decreasing energy, with a maximum at approximately 100 eV. Using the different energy loss data for lower energies result in deviations of up to 25% (Figure 2c).

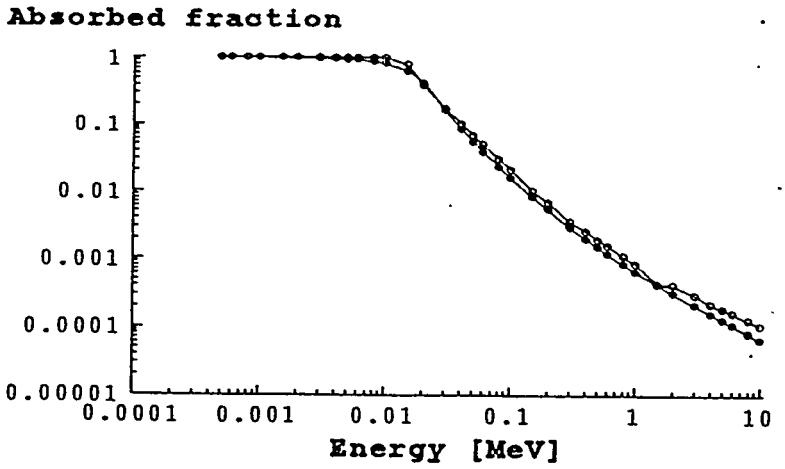

Figure 1a. Absorbed Fraction in a sphere with radius 5 μm. Filled circle-tabulated values by Berger (6) and Circle - values calculated in this work by Cole's relationship.

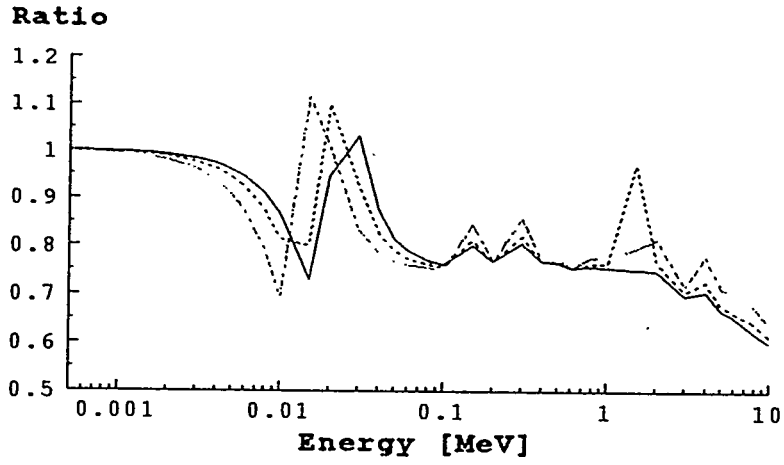

Figure 1b. Ratio of absorbed fraction (Bergers tabulated values (6) divided by values calculated in this work by Cole's relationship) in a sphere for different sphere radii, r. (Dotted line - r=3 μm, Dashed line - r=5 μm, Solid line - r=7 μm)

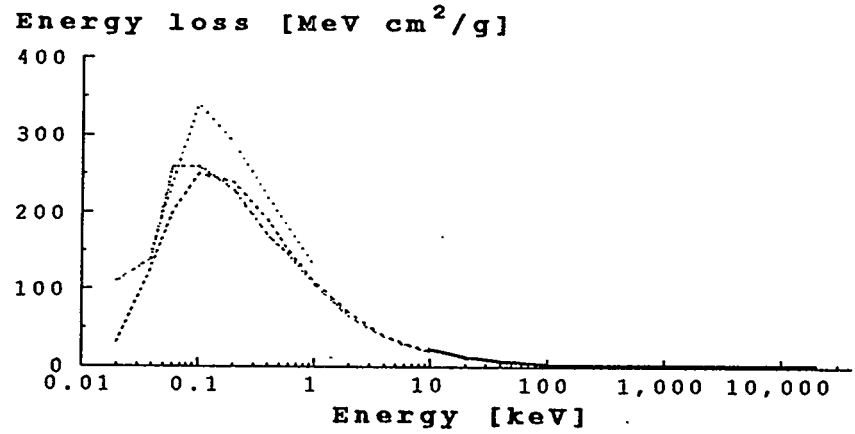

Figure 2a. Different electron energy-loss data. Solid line-ICRU 37 (18), Dotted line (7), Dashed line-Ashley (19) and Dash-dotted line-Ritchie. (20).

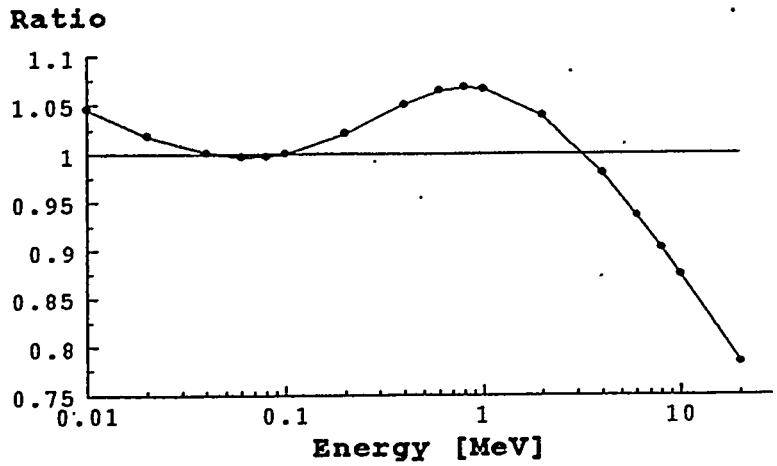

Figure 2b. Ratio of electron-loss data for energies over 10 keV, unit density. (ICRU 37, water divided by Cole.)

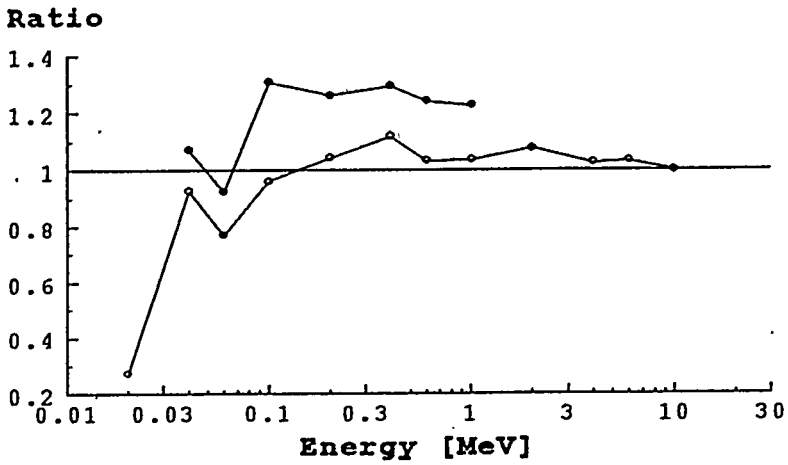

Figure 2c. Ratio of electron energy-loss data for energies over 10 keV, unit density. (ICRU 37, water divided by Cole.)

The different β spectra used in the calculation of absorbed fractions are shown in Figure 3a, and the calculated absorbed fractions are shown in Figure 3b. The use of different spectra results in deviations of up to 30% in the absorbed fractions.

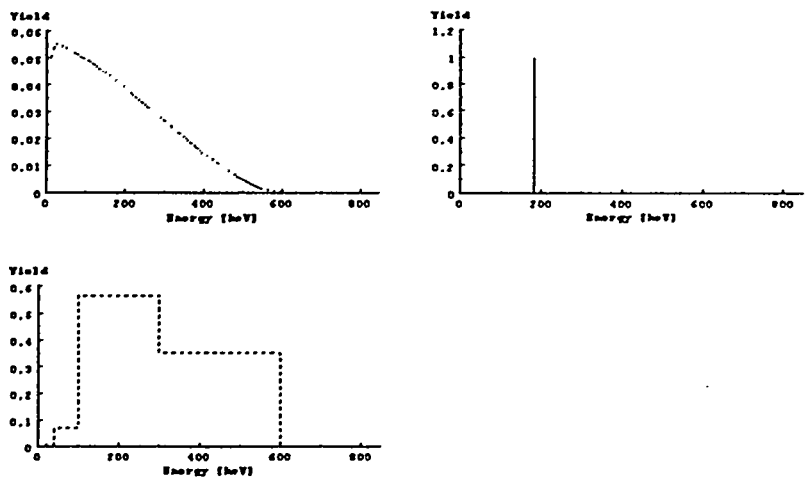

Figure 3a. Beta spectra and mean energy for ^{131}I. Dotted line = β spectra from Browne et al. (23), dashed line = β spectra from Simpkin & Mackie (24) and solid line = mean energy (23).

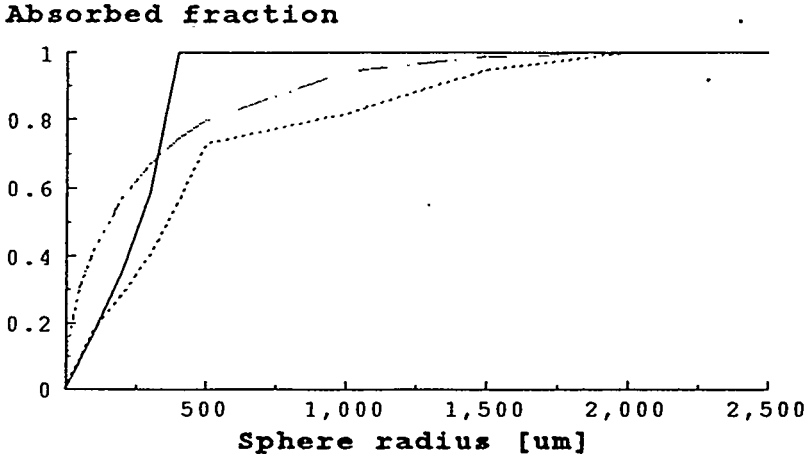

Figure 3b. Absorbed fraction with different radionuclide data for ^{131}I. (Dotted line = Browne et al. (23), dashed line = Simpkin & Mackie (24) and solid line = mean energy (23).

DISCUSSION

Cole's semiempiric energy-range relationship offers a simple method for calculating the absorbed dose on a cellular level. The method is, however, a rather simple description of the underlying physics, as it is based on a fit to experimental data measured in air and plastic. The semiempiric relationship uses the continuous slowing down approximation and neglects delta particles. Cole's neglect of straggling results in an overestimation of the absorbed dose near the source and an underestimation far from the source. Berger has included straggling and energy transport by secondary bremsstrahlung in his improved dose point kernel, thus his method theoretically should be a more appropriate description of the physics. Berger has, however, included a sampling error in his Monte Carlo code. Thus, his kernel gives results which differ somewhat from those reported by Simpkin and Mackie (24). The difference is higher at higher electron energies. These differences between Cole's and Berger's methods should explain some of the differences in the absorbed fractions calculated with the two methods. Monte Carlo simulations, which include stochastic effects in the calculation of absorbed dose on a cellular and subcellular level should be a better method to use, but one limitation is the poorly known energy loss data for low-energy electrons (25).

Our comparison of energy loss data shows that Cole estimates lower energy loss at most energies compared to ICRU 37 (18) This should result in lower absorbed doses and absorbed fraction, however, our calculations show that Cole's method estimates higher absorbed fractions than Berger. The explanation for this is unclear. The miscalculation done by Cole when deriving Equation 1, leads to an error of 0.5 %, which is negligible in the comparison done in this work.

The use of different radionuclide data, not only the use of the mean energy compared to β-spectra, but also the use of different β-spectra in the calculations, result in large deviations in the calculated absorbed doses. The deviations obtained by using the two different β-spectra reported in this work in estimating the absorbed dose are mainly due to differences in the energy binning of the spectra.

Table 2
Summary of the Uncertainties in the Absorbed Dose Calculations According to the Choice of Physical Parameters as Shown in this Work

Investigated parameter	Estimated deviation
Calculation method	up to 30%
Energy loss data	up to 25%
Radionuclide data	up to 30%

CONCLUSION

The results of absorbed dose calculations varies depending on what calculation method, energy loss-data and radionuclide data are chosen. Because of the rather large deviations of absorbed dose on the cellular level, which we found in this comparison due to the choice of input parameters, the accuracy of calculated absorbed doses in small volumes must be considered. When the dimensions get even smaller, i.e. at the subcellular level, the deviations in the absorbed dose might be even larger, as indicated in this work.

ACKNOWLEDGMENTS

This project has been supported by grants from the Swedish Cancer Foundation grant 2353-B95-09XAB, the Mrs Bertha Kamprad Foundation, the Gunnar, Arvid and Elisabeth Nilsson Foundation, the Lund University Medical Faculty and the Lund University Hospital Funds.

REFERENCES

1. Makrigiorgos GM, Ito S, Baranowska-Kortylewicz J, Vinter DW, Iqbal A, Van den Abbeele AD, Adelstein SJ and Kassis AI. Inhomogeneous deposition of radiopharmaceuticals at the cellular level: Experimental evidence and dosimetric implications. J Nucl Med 31(8):1358-1363, 1990.
2. Kassis AI. The MIRD approach: Remembering the limitations. J Nucl Med 33(5):781-782, 1992.
3. Humm JL. Dosimetric aspects of radiolabeled antibodies for tumor therapy. J Nucl Med 27:1490-1497, 1986.
4. Loevinger R. The dosimetry of beta sources in tissue. The Point-source function. Radiology 66:55-62, 1956.
5. Berger MJ. Distribution of Absorbed Dose around Point Sources of Electrons and Beta Particles in Water and other Media. Medical International Radiation Dose (MIRD) Committee Pamphlet No. 7, The Society of Nuclear Medicine, New York, 1971.
6. Berger MJ. Improved Point Kernels for Electron and Beta-ray Dosimetry. National Bureau of Standards, NBSIR 73-107, Washington, 1973.
7. Cole A. Absorption of 20-eV to 50,000-eV electron beams in air and plastic. Radiat Res 38:7-33, 1969.
8. Goddu SM, Howell RW and Rao DV. Cellular dosimetry: Absorbed fractions for monoenergetic electron and alpha particle sources and S values for radionuclides uniformly distributed in different cell compartments. J Nucl Med 35:303-316, 1994.

9. Goddu SM, Rao DV and Howell RW. Multiellular dosimetry for micrometastases: Dependence of self-dose versus cross-dose to cell nuclei on type and energy of radiation and subcellular distribution of radionuclides. J Nucl Med 35:521-530, 1994
10. Kassis AI, Adelstein SJ, Haydock C and Sastry SR. Radiotoxicity of ^{75}Se and ^{35}S: Theory and application to a cellular model. Radiat Res 84:407-425, 1980.
11. Nikjoo H, Goodhead DT, Charlton DE and Paretzke HG. Energy deposition in small cylindrical targets by monoenergetic electrons. Int J Radiat Biol 60(5):739-756, 1991.
12. Pomplun E. A new DNA target model for track structure calculations and its first application to I-125 Auger electrons. Int J Radiat Biol 59(3):625-642, 1991.
13. ICRU Report 36. Microdosimetry. International Commission on Radiation Units and Measurements, Bethesda, USA, 1983.
14. Feinendegen LE, Loken MK, Booz J, Muhlensiepen H, Sondhaus CA and Bond VP. Cellular mechanisms of protection and repair induced by radiation exposure and their consequences for cell system responses. Stem Cells 13(Suppl. 1):7-20, 1995.
15. Leichner PK and Kwok CS. Tumor doimetry in radioimmunotherapy: Methods of calculation for beta particles. Med Phys 20(2):529-534, 1993.
16. Prestwich WV, Nunes J and Kwok CS. Beta dose point kernels for radionuclides of potential use in radioimmunotherapy. J Nucl Med 30(6):1036-1046
17. ICRU Report 33. Radiation Quantities and Units, Washington, USA, 1980.
18. ICRU Report 37. Stopping Powers for Electrons and Positrons. International Commission on Radiation Units and Measurements, Bethesda, USA, 1984.
19. Ashley JC. Stopping power of liquid water for low-energy electrons. Radiat Res 89:25-31, 1982.
20. Ritchie RH, Hamm RN, Turner JE and Wright HA. The interaction of swift electrons with liquid water. In: Proceedings of the Sixth Symposium on Microdosimetry, Brussels, Belgium (J. Booz and H.G. Ebert, Eds.), pp. 345-354. Commission of the European Communities, Harwood, London, 1978. [EUR 6064 d-e-f.]
21. Humm JL, Howell RW and Rao DV. Dosimetry of Auger-electron-emitting radionuclides: Report No. 3 of AAPM Nuclear Medicine Task Group No. 6. Med Phys 21(12):1901-1915, 1994.
22. Howell RW. Personal communication, 1995.
23. Browne E, Firestone RB and Shirley VS. Table of Radioactive Isotopes. John Wiley & Sons, 1986.
24. Simpkin DJ and Mackie TR. EGS4 Monte Carlo determination of the beta dose kernel in water. Med Phys 17(2):179-186, 1990.
25. Paretzke HG, Turner JE, Hamm RN, Ritchie RH and Wright HA. Spatial distributions of inelastic events produced by electrons in gaseous and liquid water. Radiat Res 127:121-129, 1991.

QUESTIONS

Brihaye: Did you consider other geometries than spheres (i.e. cube...) and do you think that the geometry of the cell could have an influence on the absorbed dose calculations?

Hindorf: No, I haven't considered other geometries besides spheres and yes, I believe that the shape chosen to model the cell will influence the calculated absorbed dose.

CELLULAR DOSIMETRY OF ^{99m}Tc, ^{123}I, ^{111}In, ^{67}Ga AND ^{201}Tl ELECTRON EMISSIONS IN AN HEXAGONAL CELLS ARRANGEMENT AND SUBCELLULAR DISTRIBUTION OF RADIOACTIVITY

Gardin I[1], Faraggi M[2], Stievenart JL[1], Le Guludec D[2], Bok BD[1]
[1]Department of Nuclear Medicine, Beaujon Hospital
100 Bd du Gal Leclerc, F-92110 Clichy, France
[2]Department of Nuclear Medicine, Bichat Hospital
46 rue H. Huchard, F-75018 Paris, France

ABSTRACT

The electron radiation dose delivered to the cell nucleus depends strongly on the distribution of the radiopharmaceutical within the cells. Thus, an analytical model was developed to compute the self-dose emanating from the cell itself and the cross-dose emanating from the surrounding cells, for uniform distributions of radioactivity within the cell, within the cell nucleus and on the cell membrane. A close-packed hexagonal cells arrangement was assumed with a cell radius (R_{cel}) ranging from 4 to 12 µm, a nuclear radius (R_{nu}) ranging from 3 to 6 µm and a constant uptake per cell. This model was applied to compute the mean energy E, per disintegration and per cell, deposited within the cell nucleus for the most commonly used radionuclides in diagnostic nuclear medicine.

With every radionuclide and for fixed R_{cel} and R_{nu} values, E_{cross} variations are less than 5%. Conversely, with the same conditions, E_{self} depends widely on the subcellular distribution of radioactivity. For example, with ^{99m}Tc, R_{nu}=4 µm and R_{cel}=5 µm, E_{self} is 2.7, 1.43 and 0.08 keV/dis.cel, for respectively a cell, a cell nucleus and a membrane distribution. The ratio E_{self}/E_{cross} is always less than 0.1 for a cell membrane distribution. Thus, for this distribution, the contribution of the self-dose may be neglected versus the cross-dose for the same radioactivity per cell. For a cell nucleus distribution, E_{self}/E_{cross} may reach 17.4. This value was found for ^{201}Tl, where R_{nu}= 3 µm and R_{cel}= 9 µm. Intermediate values result from a homogeneous intracellular distribution.

Thus, the knowledge of the intracellular distribution of a radiopharmaceutical is a prerequisite for an accurate computation of the actual electron dose to the cell nucleus.

INTRODUCTION

The electron radiation dose delivered to the cell nucleus depends strongly on the distribution of the radiopharmaceutical within the cells and from one cell to another. It has been shown that spermhead survival in mouse testes induced by incorporated Auger emitters, differs from one subcellular localization of the radionuclide to another (i.e. cell nucleus versus cytoplasm) (1). A heterogeneous uptake of the radiopharmaceutical may be responsible for dose heterogeneity. For instance, after ^{99m}Tc-sulphur colloid injection, we have shown that most of the liver radioactivity is

incorporated in only 0.2% of Kupffer cells (2). Thus, the mean electron dose delivered to these cells is 15,000 times the mean dose to the liver calculated by the MIRD method (3).

These examples show that conventional dosimetry is not always sufficient to take into account the dose heterogeneity. Dosimetric computations at the cellular level would be more accurate. This approach has become increasingly important but remains underutilized in routine diagnostic nuclear medicine. One reason for this is probably a lack of available mathematical models. Thus, we propose a model to compute the mean dose delivered to the cell nucleus in a close-packed hexagonal cells arrangement, by taking into account the self-dose emanating from the cell itself and the cross-dose emanating from the surrounding cells. This model was applied to radionuclides routinely used in diagnostic nuclear medicine (^{99m}Tc, ^{123}I, ^{111}In, ^{67}Ga and ^{201}Tl).

MATERIALS AND METHODS

Mean Dose

The mean dose delivered by electron emissions $\bar{D}_{nu}$, which is absorbed by a target central cell nucleus, may be expressed by the sum of two terms. The first one concerns the self-dose ($\bar{D}_{self}$) which results from the radionuclide localized in the target cell itself. The second term refers to the cross-dose ($\bar{D}_{cross}$) which comes from electrons emanating from all the other cells.

$$\bar{D}_{nu} = \bar{D}_{self} + \bar{D}_{cross}$$

The self-dose may be expressed as

$$\bar{D}_{self} = \frac{\tilde{A}}{m_{nu}} \cdot E_{self}$$

where $\tilde{A}$ is the cumulated activity in the source, m_{nu} is the target nucleus mass, and E_{self} is the self-energy absorbed in the cell nucleus target. The same expression may be written for the cross-dose.

E_{self} (the self energy absorbed in the cell nucleus target) and E_{cross} (the cross energy) are given by.

$$E_{self} = \sum_i n_i \cdot E_i \cdot \phi_i(self) \text{ and}$$

$$E_{cross} = \sum_i n_i \cdot E_i \cdot \phi_i(cross),$$

where E_i is the energy of the ith electron emission and n_i is the number of emitted electrons per disintegration. ϕ_i (self) and ϕ_i (cross) represent the fraction of the energy E_i emitted by the source that is absorbed in the cell nucleus.

Spectra of the Radionuclides

The study was performed with the radionuclides commonly used in nuclear medicine diagnostic procedures. The radiation spectra for electron emissions were taken from Howell (4). The total energy emitted per disintegration (dis) is 16.2 keV/dis for ^{99m}Tc, 27.5 keV/dis for ^{123}I, 34.8 keV/dis for ^{111}In, 33.8 keV/dis for ^{67}Ga and 45.4 keV/dis for ^{201}Tl.

Cells Arrangement

The model was applied to concentric spherical nuclei and cells. The cell radius (R_{cel}) ranged from 4 to 12 μm, the nuclear radius (R_{nu}) ranged from 3 to 6 μm and the cytoplasmic thickness ranged from 1 to 6 μm.

Three source distributions were chosen to simulate various subcellular localizations of radionuclide: the full sphere for a radioactivity distributed within the nucleus or within the whole cell, and the surface of the sphere for a localization on the cell membrane.

To model the cross-dose, a close-packed hexagonal cells arrangement was assumed, with the same amount of radioactivity on each cell. The self and the cross-energy computations were carried out for one disintegration per cell. Thus, E_{self} and E_{cross} were expressed in keV/dis.cel.

Absorbed Fractions Computation

Firstly, the distribution of the absorbed dose around a point isotropic source emitting electrons was computed. In the case of a point source, Berger (5) expressed the absorbed fraction as a dimensionless quantity, the scaled absorbed dose functions $F(r/r_0, E_0)$, where r_0 is the maximal electron range, and r the distance between the point source and the observation point. The relationship between F and ϕ_0 for an electron of energy E_0 is given by

$$F(r/r_0, E_0) \cdot \frac{dr}{r_0} = 4\pi\rho r^2 \phi_0(r/r_0, E_0) \cdot dr,$$

where ρ is the medium density. The cells and interstitial spaces are considered to have a density of 1 g/cm^3.

To compute F, we used the analytical functions published by Prestwich et al. (6). Then, geometry factors g(nu←h) were used to calculate the absorbed fraction ϕ_0 for extended sources. ϕ_0 is related to this factor by the following relationship:

$$\phi(nu \leftarrow h) = \frac{1}{r_0} \int_0^{\infty} g(nu \leftarrow h) \cdot F(r/r_0, E_0) \cdot dr.$$

This geometry factor must be evaluated for both self and cross contributions and for each of the three radioactivity distributions (h).

The three corresponding geometry factors were taken from Gardin et al. (7) for the self contribution and from Goddu et al. (8) in the case of the cross contribution.

Calculations

Briefly, to compute E_{cross} the program operates as follows. For each electron energy, the program verifies that the distance between the source and the target is less than 1.2 times the electron range. If this is the case, the contribution of dose to these cells is calculated. Then the next distance is computed. This procedure continues until the distance between the source and the target is greater than 1.2 times the electron range. Thus, the number of cells which contribute depends on the maximum electrons range of each radionuclide (i.e. 249, 304, 602, 794 and 326 μm respectively for ^{99m}Tc, ^{123}I, ^{111}In, ^{67}Ga and ^{201}Tl). The program was written in Pascal on a personal computer.

RESULTS

Self-Dose

Table 1 gives E_{self} values in keV/dis.cel, the self-absorption in the cell nucleus, for various subcellular distributions of the five radionuclides studied. Values in Table 1A refer to a nuclear radius of 4 μm and a cytoplasmic thickness of 1μm. Values in Table 1B refer to the same nuclear radius (i.e. 4 μm) and a cytoplasmic thickness of 4 μm.

Table 1
Values of E_{self} (keV/dis.cel) for Various Subcellular Distributions of the Five Radionuclides Considered

A. R_{nu} = 4 μm and R_{cel} = 5 μm

	Nucleus	Membrane	Cell
^{99m}Tc	2.65	0.084	1.43
^{123}I	5.04	0.337	2.83
^{111}In	4.77	0.426	2.74
^{67}Ga	6.04	0.263	3.54
^{201}Tl	13.81	0.977	8.10

B. R_{nu} = 4 μm and R_{cel} = 8 μm

	Nucleus	Membrane	Cell
^{99m}Tc	2.65	0.017	0.37
^{123}I	5.04	0.13	0.84
^{111}In	4.77	0.11	0.83
^{67}Ga	6.04	0.056	0.93
^{201}Tl	13.81	0.13	2.2

These Tables show that E_{self} depends heavily on the subcellular distribution of radioactivity and on the cell dimensions.

The highest self-absorption is obtained for a distribution of radioactivity within the cell nucleus. For this localization, with R_{nu}=4 μm and R_{cel}=5 μm, the absorbed fraction ϕ(self) reaches a value ranging from 14 to 30%, depending on the radionuclide. On the other hand, ϕ(self) is less than 3% in the case of a cell membrane distribution and the same cell dimensions.

Cross-Dose

E_{cross} values, the cross-irradiation dose in the cell nucleus for various subcellular distributions of the five radionuclides, are given in Table 2. Data in Table 2A refer to R_{nu}=4 μm and R_{cel}=5 μm. Data in Table 2B are given for R_{nu}=4 μm and R_{cel}=8 μm.

Table 2
Values of E_{cross} (keV/dis.cel) for Various Subcellular Distributions of Five Radionuclides

A. R_{nu} = 4 µm and R_{cel} = 5 µm

	Nucleus	membrane	cell
^{99m}Tc	5.12	5.2	5.2
^{123}I	8.32	8.5	8.45
^{111}In	11.31	11.56	11.51
^{67}Ga	10.36	10.46	10.45
^{201}Tl	11.02	11.45	11.18

B. R_{nu} = 4 µm and R_{cel} =8 µm

	Nucleus	membrane	cell
^{99m}Tc	1.24	1.24	1.24
^{123}I	1.87	1.97	1.92
^{111}In	2.65	2.69	2.66
^{67}Ga	2.49	2.51	2.5
^{201}Tl	2.55	2.62	2.58

From these tables, it may be seen that the cross-irradiation dose depends on the cell dimensions as was found for the self-energy. On the other hand, the cross-dose does not depend on the subcellular distribution of radioactivity. We have found with every radionuclide and for fixed R_{cel} and R_{nu} values, that E_{cross} variations are less than 5%.

Self-Dose Versus Cross-Dose

From Tables 1 and 2, the ratio E_{self}/E_{cross} has been computed (see Table 3A (R_{nu}=4 µm et R_{cel}=5 µm) and Table 3B (R_{nu}=4 µm et R_{cel}=8 µm)).

Table 3
E_{self}/E_{cross} Values for Various Subcellular Distributions of Radioactivity and the Five Radionuclides Considered

A. R_{nu} = 4 µm and R_{cel} = 5 µm

	Nucleus	membrane	cell
^{99m}Tc	0.52	0.02	0.27
^{123}I	0.61	0.04	0.34
^{111}In	0.42	0.04	0.24
^{67}Ga	0.58	0.03	0.34
^{201}Tl	1.25	0.09	0.72

B. R_{nu} = 4 μm and R_{cel} =8 μm

	Nucleus	membrane	cell
^{99m}Tc	2.13	0.013	0.29
^{123}I	2.70	0.06	0.44
^{111}In	1.80	0.04	0.31
^{67}Ga	2.43	0.02	0.37
^{201}Tl	5.42	0.05	0.85

These tables show that this ratio depends on the dimensions of the cells. The thinner the cytoplasm, the smaller the E_{self}/E_{cross} ratio. For a membrane distribution of radioactivity, the self contribution is very small as compared to the cross contribution. For all the cells dimensions studied, E_{self}/E_{cross} is always less than 0.1 in the case of a cell membrane distribution. For a cell nucleus distribution, E_{self}/E_{cross} may reach 17.4. This value was found for ^{201}Tl, R_{nu}= 3 μm and R_{cel}= 9 μm. Intermediate values result from a homogeneous intracellular distribution.

DISCUSSION

An analytical model was developed to compute the self-dose emanating from the cell itself and the cross-dose emanating from the surrounding cells with a close-packed hexagonal cells arrangement, and uniform subcellular distributions of radioactivity. This model was applied to some commonly used radionuclides in diagnostic nuclear medicine.

Makrigiorgos et al. (7) and Goddu et al. (8) have also proposed a model to compute the self and the cross-dose contributions. Our model differs from Goddu's one in three ways:

i) The analytical method to compute F: Goddu et al. calculated F from Cole's energy loss expression;

ii) The close-packed cells arrangement: Goddu et al. used a cubic cells arrangement;

iii) The number of cells considered to calculate the cross-dose: a spherical multicellular cluster with a maximum radius of 200 μm was used in the model of Goddu et al.

In the case of the self-dose contribution, our model has been previously validated (9). For the cross-dose contribution, we have compared our E_{self}/E_{cross} ratios with those obtained by Goddu et al. (8), for R_{nu}=4 μm, R_{cel}=5 μm, a cell nucleus and a cell membrane distribution of radioactivity. The values obtained by our method were from 1.33 to 3.1 times smaller than those of Goddu et al. In our opinion, the main reason for this discrepancy comes from the fact that Goddu et al. computed the cross contribution in the case of a cluster with a maximum radius of 200 μm. This radius is smaller than the electron range of the radionuclides studied. Thus the cross-dose contribution is under-estimated as compared to an infinite medium.

The advantages of our model are obvious. It is quite simple and can easily be implemented on a personal computer. It can be extended to all kinds of subcellular distributions of radioactivity. Only three different subcellular localizations of the radiopharmaceutical were considered. In the case of a pure cytoplasmic distribution, it is not necessary to develop a specific model. Dosimetric values can be easily deduced from the previous ones. Nevertheless, some limits exist. The geometry of most cells is more complex than a close-packed hexagonal cells arrangement. Even in the same tissue, the size may vary from cell to cell.

Many radiobiological data have shown the influence of the biodistribution of the

radiopharmaceuticals on the cell-survival rate. Nevertheless, Rao et al. (1) have pointed out that dosimetric computations alone are not always able to predict the radiobiological consequences. But knowledge of the dose actually delivered at the cellular level has remained a prerequisite to a better understanding of a dose-effect relationship.

A constant uptake per cell was assumed in this model. This assumption is not always valid. It has been shown that the cells' affinity for a radiopharmaceutical may be very different from one cell to another, even in the same tissue (2). This phenomenon may be responsible for an increased self-dose in highly radiolabeled cells.

E_{self} depends widely on the subcellular distribution of radioactivity and on the cell dimensions (see Table 1). This result is in agreement with other findings (10) (11). The self-absorption by the target nucleus can reach several keV/dis.cel when the radiopharmaceutical is located within the cell. This result may be explained by the fact that Auger electrons have a shorter range than the cell nucleus radius, and a large fraction of the emitted energy is deposited in the vicinity of the source.

E_{cross} is independent of the subcellular distribution of the radiopharmaceutical studied (variation less than 5%). Thus, the model may be simplified by using only one geometry factor rather than three.

The ratio E_{self}/E_{cross} is always less than 0.1 for a cell membrane distribution (Table 3). Thus, for this distribution, the contribution of the self-dose may be neglected for the same amount of radioactivity per cell.

These findings show the need to make computations at the cellular level. The knowledge of the intracellular distribution of a radiopharmaceutical is a prerequisite for an accurate computation of the actual electron dose to the cell nucleus.

REFERENCES

1. Rao DV, Narra VR, Howell RW, Lanka VK and Sastry KSR. Induction of sperm head abnormalities by incorporated radionuclides: dependence on subcellular distribution, type of radiation, dose rate, and presence of radioprotectors. Radiat Res 125:89-97, 1991.
2. Gardin I, Colas-Linhart N, Petiet A and Bok B. Dosimetry at the cellular level of Kupffer cells after technetium-99m-sulphur colloid injection. J Nucl Med 33:380-384, 1992.
3. Loevinger RL, Budinger TF and Watson EE. MIRD primer for absorbed dose calculations. New York: The Society of Nuclear Medicine, 1988.
4. Howell RW. Radiation spectra for Auger-electron emitting radionuclides: Report No. 2 of AAPM Nuclear Medicine Task Group No. 6. Med Phys 19:1371-1383, 1992.
5. Berger MJ. Improved point kernels for electron and beta ray dosimetry. NBSIR 1973;(Washington, DC: US Department of Commerce, Bureau of Standards):73-107.
6. Prestwich WV, Chan L, Kwok CS and Wilson B. Dose point kernels for beta emitting radioisotopes. 4th International Radiopharmaceutical Dosimetry Symposium, Oak Ridge, Tenn, USA: 1985, Conf. 851113 (DE 86010102): 545-561.
7. Makrigiorgos GM, Adelstein SJ and Kassis AI. Limitations of conventional internal dosimetry at the cellular level. J Nucl Med 30:1856-1864, 1989.
8. Goddu SM, Rao DV and Howell RW. Multicellular dosimetry for micrometastases: dependence of self-dose versus cross-dose to cell nuclei on type and energy of radiation and subcellular distribution of radionuclides. J Nucl Med 35:521-530, 1994.
9. Gardin I, Faraggi M, Huc E and Bok B. Modelling of the relationship between cell dimensions and mean dose delivered to the cell nucleus: application to five radionuclides used in nuclear medicine. Phys Med and Biol 40:1001-1014, 1995.
10. Faraggi M, Gardin I, de Labriolle-Vayley C, Moretti JL and Bok B. The influence of tracer

localization on the electron dose rate delivered to the cell nucleus by some radionuclides used in diagnostic nuclear medicine procedures. J Nucl Med 35:113-119, 1994.
11. Goddu SM, Howell RW and Rao DV. Cellular dosimetry: Absorbed fractions for monoenergetic electron and alpha particle sources and S-values for radionuclides uniformly distributed in different cell compartments. J Nucl Med 35:303-316, 1994.

QUESTIONS

Rao: Our group has published similar calculations on cellular dosimetry. Can you compare your results with those published by us?

Gardin: Yes, of course, I have compared these values with yours in the case of a nuclear radius of 4 μm and a cytoplasmic thickness of 1 μm. This comparison will be in the written version. In the case of the self-energy, the comparison was made in a previous paper published in Physics in Medicine and Biology (1995).

In the case of the cross-dose we always found that our values are higher than yours. I think it is because you used a limited number of cells, depending on the cluster size and the range of the electrons, when we used an infinite medium.

C. Wang: If one calculates cellular dose, then one should use the microdosimetry quantity "specific energy". If one uses the quantity "specific quantity", then one should calculate the distribution of specific energy. Mean value (dose) has little meaning in interpreting biological effect.

Gardin: I don't agree with this point of view. I think that dosimetry at the cellular level is also a convenient manner to make dosimetric calculations. Mean dose delivered to the cell nucleus is an easy parameter which can be used to draw cell survival curves and for RBE ratios computation. I don't know why a mean organ dose is an interesting parameter and not a mean cellular dose. Of course, if one is interested in the statistical variations of energy deposition and what is appended during an electron interaction, microdosimetry is more convenient. These two approaches are not opposed but complementary.

Rao: Comment. I'd like to briefly talk about the concept of dose in general. Mean absorbed dose is calculated for a purpose i.e., to predict biological effect whether it is a therapeutic effect or radiation risk. There are some in the radiation research community who believe that dose whether (micro, cellular or macro) will not be adequate to predict the response, and some other method (fluence) needs to be used. The appropriate method of calculating the dose should come from experimental data. Therefore, I believe we should spend more time determining the biological effects in vivo first, and then use different dosimetry methods that best explain the observed biological effects. Such an approach should result in appropriate dosimetry methods relevant to practical problems.

CELLULAR UPTAKE OF ^{212}BiOCl BY EHRLICH ASCITES CELLS : A DOSIMETRIC ANALYSIS

Roeske JC[1], Whitlock JL[2], Harper PV[3], Stinchcomb TG[4], Schwartz JL[5], Hines JJ[6] and Rotmensch J[2]
[1]Department of Radiation and Cellular Oncology, The University of Chicago, Chicago, IL 60637
[2]Department of Obstetrics and Gynecology, The University of Chicago, Chicago, IL 60637
[3]Department of Radiology, The University of Chicago, Chicago, IL 60637
[4]Department of Physics, DePaul University, Chicago, IL 60614
[5]Department of Radiation Oncology, University of Washington, Seattle, WA 98195
[6]Chemistry Division, Argonne National Laboratory, Argonne, IL 60439

ABSTRACT

Bi-212 is an alpha-emitting radionuclide being investigated as a therapeutic agent in the intraperitoneal treatment of micrometastatic ovarian carcinoma. In evaluating a new therapeutic modality, cell-survival studies are often used as a means of quantifying the biological effects of radiation. In this analysis, Ehrlich ascites cells were irradiated under conditions similar to therapy in various concentrations of Bi-212. Immediately following irradiation, a cell survival assay was performed in which cells were plated and colonies were counted after 10-14 days. Both a macrodosimetric and a microdosimetric approach were used in analyzing these data. These models used as input the fraction of activity within the cell and in solution, the distribution of cell sizes, and the variation of LET along individual alpha-particle tracks. The results indicate that the energy deposited within the nucleus varies significantly among individual cells. There is a small fraction of cell nuclei which receive no hits, while the remaining cells receive energy depositions which can differ significantly from the mean value. These dosimetric parameters are correlated with measured cell survival and will be a useful predictor of outcome for therapeutic doses.

INTRODUCTION

Ovarian cancer is one of highest causes of mortality among gynecologic cancers in the western world. The American Cancer Association has estimated approximately 19,000 new cases were diagnosed in 1986, of which 60% of these eventually died due to complications from the disease (1). The malignancy originates in the ovaries and is generally detected during Stage III or IV when it has metastasized to the surface of the peritoneum. At this stage, only a 10-20% 5-year survival is observed (1). Treatment of this disease involves surgical debulking of the tumor, followed by a regimen of chemotherapy and/or radiation therapy (2,3). Because of the diffuse nature of peritoneal disease, treatment of the entire abdomen to 25 Gy (2500 rad) is prescribed with external-beam radiation therapy (3). This dose is inadequate for the control of macroscopic disease, but is limited by normal tissue tolerance. To augment the external beam dose, Au-198 colloids (4) and radioactive

chromic phosphate (P-32 colloids) (5-7) have been administered directly into the peritoneal cavity. However, with lack of specificity, there is no tumor to normal tissue dose advantage (4-7). Furthermore, loculation and the formation of colloidal clumps can occur resulting in a nonuniform-dose distribution.

We are currently investigating the use of an alpha-particle emitter (Bi-212) for the treatment of ovarian micrometastases in the peritoneal cavity. Bi-212 has been chelated to monoclonal antibodies and its therapeutic effectiveness has been demonstrated in vitro and in mice (8-13). With a physical half-life of 60.55 minutes, Bi-212 releases more than 90% of its energy through two alpha-decay modes, 36% with an average energy of approximately 6.05 MeV and 64% with an energy of 8.78 MeV from Po-212 (14). Alpha particles may be advantageous in the treatment of ovarian micrometastases because of their short range (40-90 μm), high-linear energy transfer (LET) and independence of dose-rate effects (15). In addition, the use of a short-lived emitter which delivers its radiation while it is still in solution eliminates some of the problems presented by colloids. However, the dosimetry of alpha emitters is a challenge because the size of the sensitive target within the cell, the nucleus, is of the same order of magnitude as the range of the alpha particle.

It is generally accepted that the dosimetric analysis of alpha particles requires knowledge of the distribution of energy deposited within the cellular target (16). Microdosimetry is the study of the stochastic nature of energy deposition in small targets as a quantitative means of understanding the biophysical and biological interactions of radiation with matter. The fundamental quantities in classical microdosimetry are specific energy (energy per unit mass) and lineal energy (energy per unit path length through the target) (16). The basic criterion for determining the necessity of microdosimetry was established by Kellerer (17) and described by Polig (16). This principle states that the stochastic nature of energy deposition within the target must be taken into account when the relative deviations of the local dose from the mean exceeds 20%. For example, a spherical target with a diameter of 5 microns requires an average dose of at least 100 Gy from alpha particles for the use of the average dose to be warranted (16).

The goal of this work is to provide both a macrodosimetric and a microdosimetric analysis of Bi-212 cell-survival experiments for Ehrlich ascites cells. These cells are irradiated in conditions similar to therapy and hence the results of this analysis will be used to design therapeutic trials.

MATERIALS AND METHODS

Bi-212 Generator

The generator is a cation-exchange column supporting Ra-224, a daughter of Th-228. Pb-212 was eluted from the radium column with 2 N nitric acid and Bi-212 was eluted with 0.15 M hydroiodic acid and neutralized with acetate buffer (18). This preparation was used in initial studies. However, this procedure was modified to make it more suitable for future clinical studies by changing the eluant of the Ra-224 column to 2 N HCl. Trace contaminants of Th-228 were recovered by passing the eluant from the Ra-224 column through a column prepared as follows. A solution of crown ether dissolved in n-octanol was layered on 10 μm PVC particles (Ambuchrome CG) which were then placed in a chromatographic column. The eluate from the Ra-224 column was passed through this column where the Pb-212 is retained. It was then washed in large volumes of 2 N HCl until the long-lived contaminants were reduced to a negligible level. The Pb-212 was allowed to decay for 2-4 hours to allow for the regeneration of Bi-212 removed from the previous washings. The Bi-212 was then eluted with 0.9 N HCl followed by 5 ml of distilled water. This eluant was passed through a second column to remove traces of Pb-212 and a short column of support material was used to remove traces of crown ether and octanol. It was then neutralized with 1 N sodium hydroxide

to pH 7 using phenol red indicator and diluted to 30 ml with water to render it isotonic.

Survival Assay

Ehrlich ascites carcinoma cells were grown in-vitro in NCTC 135 (Gibco), supplemented with 10% fetal bovine serum (Intergen), antibiotic free. For the clonogenic assay, the cells were trypsinized and washed twice in a serum-free medium. Two milliliters of serum-free medium containing Ehrlich ascites cells at a concentration of 10^6 cells/ml were added to each of six 12x75 mm^2 tubes (Falcon) containing a sterile stir bar. Activities of Bi-212 ranging from 0.3-1.2 MBq/cc (8-32 μCi/cc) were added to each tube. The tubes were then placed on a stir plate, and incubated at room temperature for 4 hours.

At the end of the incubation period, the cells were pelleted by centrifugation and an aliquot of the remaining supernatant was removed to determine the activity remaining. The cells were resuspended in serum-containing medium and the concentration was determined using a hemacytometer. One hundred to 10,000 cells were plated in duplicate in 100 mm^2 tissue-culture dishes (Falcon). Control data points consisted of cells incubated in medium without activity. Fifteen milliliters of culture medium were added, and the cells were incubated at 37°C and 5% carbon dioxide in a humidified atmosphere. Ten to fourteen days after plating, the dishes were washed once with 0.85% sodium chloride and stained with crystal violet. Only colonies of greater than 50 cells were counted.

Ehrlich ascites cells were examined under a 40x objective of a Zeiss microscope. Using a Quantex Imaging Analysis System, the distribution and sizes of the cells and the nuclei were determined. Of the 50 cells examined, the average cellular diameter was 20.7 μm, and the average nuclear diameter was 7.5 μm. These values are used in the dosimetry calculations described below.

Macrodosimetry

Cell-survival analysis is performed using both a macrodosimetric and microdosimetric approach. The macrodosimetric approach calculates the average dose to the cell nucleus using a Monte Carlo approach (19). For details of the Monte Carlo calculation, the interested reader is referred to the paper "Analysis of ovarian dose of women employed in the radium watch dial industry : A macrodosimetric and microdosimetric approach" also published in these proceedings. Cell survival is plotted versus the average cell nucleus dose, and fitted to the function

$$S(D) = \exp(-D/D_o) \quad (1)$$

using the least-squares maximum-likelihood estimator. In this function, D is the average absorbed dose and D_0 is the dose required to reduce the population surviving fraction to 1/e.

Microdosimetry

The previously described macrodosimetric approach assumes that every cell receives exactly the same dose. In reality, the energy deposited within cellular targets by alpha particles is highly nonuniform. This is due to two effects. The first involves the variation in path lengths as the alpha particle traverses various chords through the target. The second factor is the variation in energy deposited along these path lengths due to the Bragg peak. Thus it is necessary to consider the microdosimetric distributions in analyzing cell-survival curves for alpha emitters. The principal microdosimetric function is the specific-energy distribution, which is the microdosimetric analogue of absorbed dose. Survival is related to the specific-energy distribution by

$$s(D) = \int_0^{zmax} f(z)\ \exp(-z/z_o)\ dz, \qquad (2)$$

where f(z) is the specific-energy distribution, and z_o is the specific energy at which the surviving fraction is reduced to 1/e. Use of the function $\exp(-z/z_o)$ assumes that the cells are radiologically independent. This formulation has been used extensively in the analysis of alpha-particle cell-survival curves (20-22).

The microdosimetric approach used is described by Stinchcomb and Roeske (19). Briefly, this approach involves calculating the function $f_1(z)$, which is the specific-energy distribution for a single hit. This function takes into account the chord-length distribution for a given source-target geometry, and the variation in stopping power along the particle's path. The multiple hit distribution, f(z) is the n-fold convolution of $f_1(z)$, where n is the number of alpha-particle hits to the cell nucleus. Stinchcomb and Roeske (19) have demonstrated that equation 2 can be simplified to relate the observed survival to the single-event specific-energy spectrum as follows:

$$s(D) = \exp[-\langle n\rangle\{1-T_1(z_o)\}], \qquad (3)$$

where <n> is the average number of hits to the cell nucleus, and $T_1(z_o)$ is the Laplace transform of the single-event spectrum. It has been shown that when cell survival can be represented by a simple exponential (Equation 1), the relationship between D_o and z_o (23) is given by

$$1/D_o = 1/\langle z_1\rangle\ \{1-T_1(z_o)\}. \qquad (4)$$

Thus, by determining D_o as described above, and knowing $f_1(z)$, z_o may be determined. This expression can be solved iteratively or explicitly for z_o if an analytical expression for $f_1(z)$ exists.

Both the macrodosimetric and microdosimetric calculations consider the dose from the alpha-particle emissions of Bi-212 and its progeny. However, there is a beta-particle component which contributes approximately 7% to the total dose. Given that the RBE of alpha particles may range from 5-20, the effect of the beta particle is negligible. Hence, it can be neglected.

The dosimetric analysis we have performed is as follows. Initially, we consider the survival of cells irradiated by Bi-212 DTPA. This compound minimizes the attachment of Bi-212 to cells (24,25), and hence the source is assumed to consist entirely of activity outside of the cell. We determined the values of D_o and z_o which satisfy equations 1 and 3 for this source configuration. We then analyzed the survival of Bi-212 OCl. Since the survival of cells irradiated by Bi-212 OCl is much lower than that from Bi-212 DTPA, the implication is that there is a cellular component of activity which results in enhanced cell kill. Using the value of z_o obtained above, we determine the most likely source distribution to produce the observed survival with Bi-212 OCl.

RESULTS

The results of this analysis are illustrated below in Figures 1-4. Shown in Figures 1 a and b are the single-event specific energy spectra for sources located inside and outside the Ehrlich ascites cells, respectively. The shapes of these spectra are of particular interest. The single-event spectrum for sources located inside the cell has two peaks. The main peak is due to sources located inside the cell nucleus, while the lower peak occurring at the higher specific energy is due to sources located in the cytoplasm. In the second case, where sources are located outside the cell, the single-event spectrum is nearly triangular in shape up to the peak, and has a long tail. The triangular shape is similar to that of the chord length distribution through a spherical target. The long tail is due to the variation in LET and the Bragg peak.

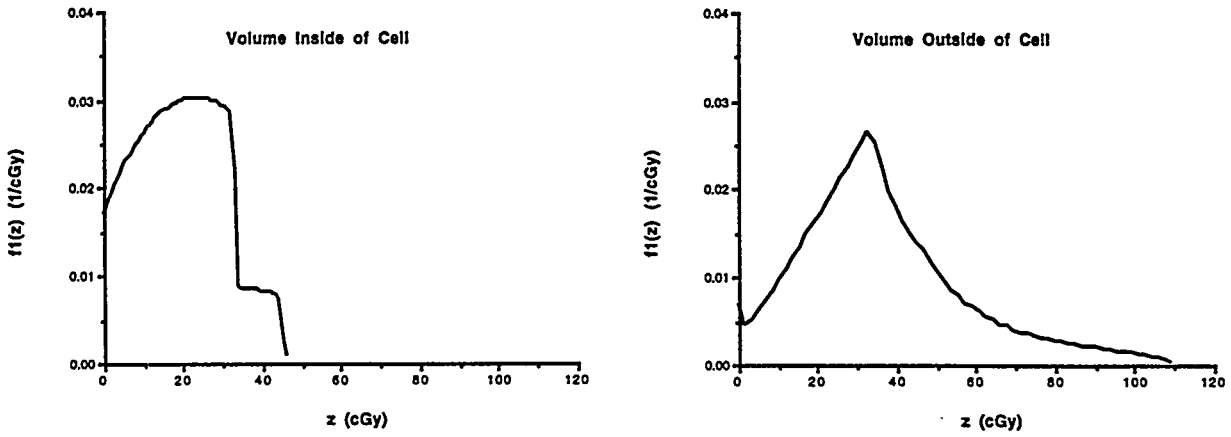

(a) (b)

Figure 1. Single-event spectra for sources located a) inside the cell and b) outside the cell.

Figure 2 a and b are the multi-hit specific-energy spectra (f(z)) for both the low- and high-dose survival points. Both of these analysis were performed for Bi-212 chelated to DTPA. Previous studies have demonstrated that this complex does not bind to cells and remains in solution (24,25). Thus, the energy deposited is due only to sources which decay outside the cells. The multi-hit specific-energy spectra demonstrate a number of features. First, the distribution of specific energy is highly nonuniform. There is a significant fraction of cells which receive energy-deposition events both greater and less than the mean absorbed dose. Second, for the low-dose case, there is a small fraction of cells which are completely missed by the alpha-particle emission. Thus, these cells have a 100% probability of surviving and reduce the therapeutic efficacy.

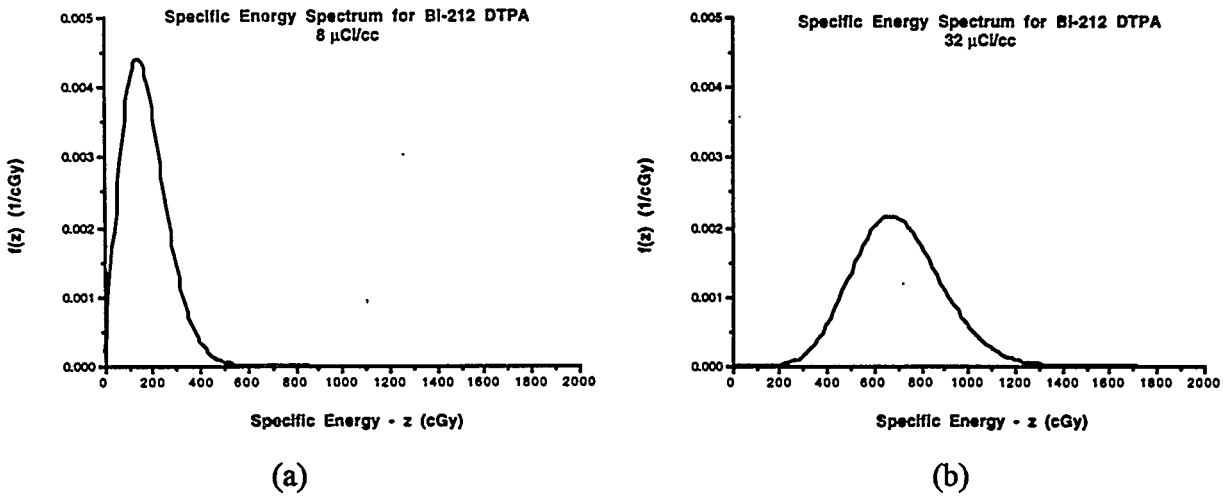

(a) (b)

Figure 2. Multiple event specific energy spectra for a) low concentration and b) high concentration.

The natural log of the surviving fraction as a function of absorbed dose is plotted in Figure 3. Also plotted is the best fit as obtained from equations 1 and 3. Note that regardless of the analysis (macrodosimetric vs. microdosimetric) the same fit is obtained. However, the parameters associated with these fits are different. For the macrodosimetric analysis, the value of D_0 is 0.837 Gy (83.7 rad). However, from the microdosimetric analysis, the value of z_0 is 0.575 Gy (57.5 rad). These values are significantly different because the microdosimetric analysis includes cells which receive energy-deposition events significantly less than the mean value. Thus, in order to achieve the same survival, the individual cell sensitivity (as obtained from z_0) must be greater.

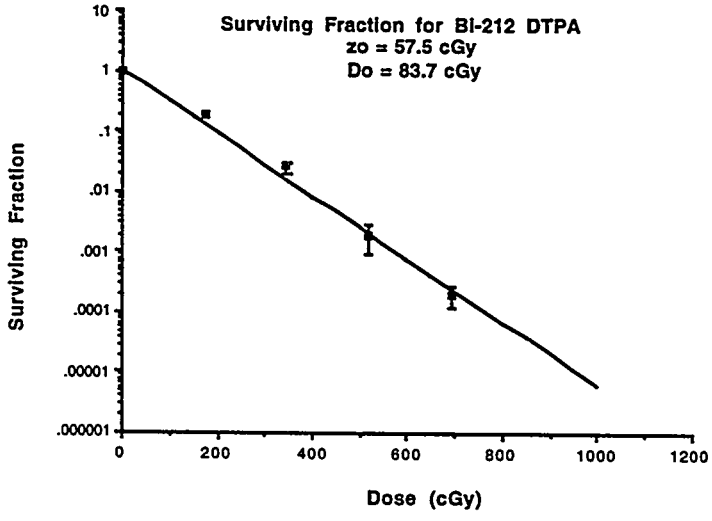

Figure 3. Fit of Bi-212 DTPA cell survival data using both the macrodosimetric and microdosimetric approach.

We have also considered the survival from Bi-212 OCl. In parallel experiments, cells were exposed to both the Bi-212 DTPA and Bi-212 OCl. If the activity distribution were the same in both

cases (e.g. activity limited to solution) we would expect the same surviving fraction for the same quantity of activity administered. However, the surviving fraction from the Bi-212 OCl is significantly less than that observed from Bi-212 DTPA. This suggests that these cells are receiving a dose component from activity localized on or within the cells. In order to estimate the number of sources which would have to decay within a cell to produce the observed survival level, we worked backwards to determine the specific energy distribution which would produce the observed survival at each dose point. The results of this analysis are summarized graphically in Figure 4. For the case where the sources are assumed to be uniformly distributed throughout the cells, the number of sources (~ 50/cell) is relatively constant versus activity. However, at a concentration of 0.6 MBq/cc (16 μCi/cc), the number of sources is significantly less. The cause of this deviation is not known at this time. Note that the fraction of activity administered which accumulated within cells is estimated to be 1-2% of the total activity.

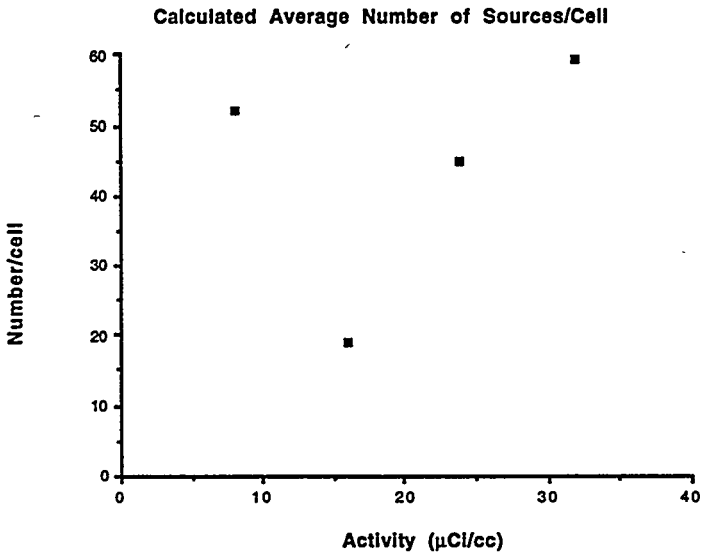

Figure 4. Estimated number of sources/cell required to produce observed cell survival for Bi-212 OCl.

DISCUSSION

The purpose of this study was twofold. The first was to determine the response of Ehrlich ascites cells to alpha-particle irradiation. This was evaluated through the analysis of cell survival produced by Bi-212 DTPA. Results using the macrodosimetric approach showed that the data were fit with a single exponential having a population parameter D_o equal to 0.837 Gy (83.7 rad). When the same analysis was performed using a microdosimetric approach, it was observed that the individual cell survival parameter z_o was 0.575 Gy (57.5 rad). Note that the latter quantity is significantly less than the former because the microdosimetric analysis considers the entire distribution of energy deposited within the cell population. As is evident in Figure 2, the specific energy deposited is often much different than the mean value. Hence, the individual cell survival parameter (z_o) would have to be much less than the population survival parameter (D_o) in order to take into account those cells which receive energy depositions less than the mean value.

A second purpose of this analysis was to evaluate the uptake of Bi-212 OCl by Ehrlich ascites

A second purpose of this analysis was to evaluate the uptake of Bi-212 OCl by Ehrlich ascites cells. In the above analysis, we estimated the number of sources required to decay within the cell to produce the enhanced cell kill for Bi-212 OCl relative to Bi-212 DTPA. For each data point we calculated that approximately 1-2% of the administered activity would need to be distributed uniformly within the cell. Preliminary studies have indicated that approximately 2% of the activity is associated with the cells, which is consistent with the calculational results. This is a potentially important role of microdosimetry in the analysis of cell-survival experiments. Given a simple source distribution and a calculated survival parameter (z_o), it may be possible to determine the complex source distribution to produce an observed survival value.

The microdosimetric analysis of Bi-212 OCl experiments represents a crude estimate of the cellular uptake. In order to verify these theoretical estimates, experiments need to be performed to determine the cellular-activity uptake. These experiments consist of exposing cells to known activities of Bi-212 OCl, separating the cells from the medium at different time points (eg. 15,30,60, 90 minutes) and counting the activity associated with the cells. In addition, in order to determine the cellular distribution, we also need to know whether this activity is associated within the cell nucleus or cytoplasm. Details of these experiments have been described by Jostes (25) and involves lysing the cell and measuring the activity associated with the nuclear contents. These experiments, however, are difficult due to the short half-life of Bi-212 and the relatively small amounts of activity associated with cells. In addition, it is also desirable to measure the cellular uptake versus different concentrations, and under saturation conditions where the activity is much greater than the number of cells present.

Finally, the role of cell-survival studies in planning therapeutic strategies should be discussed. It is estimated that alpha-particle emitters will be most effective in targeting disease ranging from 1 - 10^7 cells. The effectiveness will be limited for larger tumors as the diffusion times are generally much greater than the radionuclide half-life (particularly for Bi-212). However, these survival studies indicate that alpha emitters will be effective for single cells or small clumps of cells. For these targets, it will be important to know the variation in specific energy deposited within the cell nucleus, and importantly, the fraction of cells receiving zero hits. These parameters will ultimately determine the therapeutic benefit of this modality.

ACKNOWLEDGMENTS

The authors gratefully acknowledge the support of the Boughton Trust and the University of Chicago Mother's-Aid Lying-In Hospital. We also thank Dr. Melvin Greim for his guidance in the measurement of cellular dimensions.

REFERENCES

1. Ozols RF and Young RC. Ovarian cancer. Curr Prob Cancer 11:37-122, 1987.
2. Fuks Z, Yahalom J and Brenner H. Radiation Therapy of Gynecologic Cancers, pp:147-172, Alan R. Liss Inc., New York, 1987.
3. Horyon J and Caput T. Gynecologic Cancer in Clinical Oncology, pp:79-82, W.B. Saunders, New York, 1977.
4. Andrews GA, Root S, Kerman HD and Bigelow RR. Intracavitary colloidal radiogold in the treatment of effusion caused by malignant neoplasm. Ann Surg 137:375-381, 1953.
5. Boye E, Lindegoard MW, Paus E, Skretting A, Davy M and Jacobsen E. Whole-body distribution of radioactivity after intraperitoneal administration of P-32 colloids. Br J Radiol 57:395-402, 1984.

6. Currie JL, Bagne F, Harris C, Sullivan DL, Suruit EA, Wilkinson RH and Creasman WT. Radioactive chromic phosphate suspension: Studies on distribution dose absorption, and effective therapeutic radiation in phantoms, dogs and patients. Gyne Onc 12:193-218, 1981.
7. Ott RJ, Flower MA, Jones A and McCready VR. The application of SPET to determine the radiation dose from P-32-chromic phosphate therapy of peritoneal cavity. Eur J Nucl Med 11:305-308, 1985.
8. Kozak RW, Atcher RW, Gansow OA, Friedman AM, Hines JJ and Waldmann TA. Bismuth-212-labeled anti-Tac monoclonal antibody: Alpha-particle-emitting radionuclides as modalities for radiotherapy. Proc Natl Acad Sci USA 83:474-478, 1986.
9. Kurtzman SH, Russo A, Mitchell JB, DeGraff W, Sindelar WF, Brechbiel MW, Gansow OA, Friedman AM, Hines JJ, Gamson J and Atcher RW. Bismuth-212 linked to an antipancreatic carcinoma antibody: Model for alpha-particle-emitter radiotherapy. JNCI 80:449-452, 1988.
10. Macklis RM, Kinsey BM, Kassis AI, Ferrara JL, Atcher RW, Hines JJ, Coleman CN, Adelstein SJ and Burakoff SJ. Radioimmunotherapy with alpha-particle-emitting immunoconjugates. Science 240:1034-1026, 1988.
11. Rotmensch J, Atcher RW, Hines J, Grdina D, Schwartz JS, Toohill M and Herbst A. The development of alpha-emitting radionuclide lead 212 for the potential treatment of ovarian carcinoma. Am J Obstet Gyne 160(4):789-797, 1989.
12. Rotmensch J, Atcher RW, Schlenker R, Hines J, Grdina D, Block BS, Press M, Herbst A and Weichselbaum RR. The effect of alpha-emitting radionuclide lead 212 on human ovarian carcinoma: A potential new form of therapy. Gyne Onc 32:236-239, 1989.
13. Rotmensch J, Atcher RW, Hines J, Toohill M and Herbst AL. Comparison of short-lived high-let alpha-emitting radionuclide lead-212 and bismuth-212 to low-LET x-rays on ovarian carcinoma. Gyne Onc 35:297-300, 1989.
14. Weber DA, Eckerman KF, Dillman LT and Ryman JC. MIRD:Radionuclide Data and Decay Schemes, The Society of Nuclear Medicine, New York, 1989.
15. Hall EJ. Radiobiology for the Radiologist, Harper and Row, pp:13-78, 1973.
16. Polig E. The localized dosimetry of internally deposited alpha-emitters. Curr Top Rad Res 13:189-327, 1978.
17. Kellerer AM. Analysis of patterns of energy deposition; a survey of theoretical relations in microdosimetry, in: Proceedings of the Second Symposium on Microdosimetry, Stresa, Italy, ed. H.G. Ebert (Commission of the European Communities, Brussels, 1970) EUR 4452 d-f-e, pp:107-134, 1970.
18. Atcher RW, Friedman AM and Hines JJ. An improved generator for the production of Pb212 and Bi212 from Ra224. Appl Radiat Isot 39:283-286, 1988.
19. Stinchcomb TG and Roeske JC. Analytic microdosimetry for radioimmunotherapy. Med Phys 19(6):1385-1393, 1992.
20. Charlton DE and Sephton RA. A relationship between microdosimetric spectra and cell survival for high-LET irradiation. Int J Radiat Biol 59:447-457, 1991.
21. Humm JL and Chin LM. A model of cell inactivation by alpha particle internal emitters. Rad Res 134:143-150, 1993.
22. Stinchcomb TG and Roeske JC. Analysis of survival of C-18 cells after irradiation in suspension with chelated and ionic bismuth-212 using microdosimetry. Rad Res 140:48-54, 1994.
23. Roeske JC and Stinchcomb TG. Relationships between cell survival and specific energy spectra for therapeutic alpha particle emitters. Rad Res 145(3):268-273, 1996.
24. Scwartz JL, Shadley JD, Atcher RW, Tang J, Whitlock JL and Rotmensch J. Comparison of radon-daughter-induced effects in repair-proficient and repair-deficient CHO cell lines. Env

Molec Mut 16:178-184, 1990.
25. Jostes RF, Hui TE, Janes AC, Cross FT, Schwartz JL, Rotmensch J, Atcher RW, Evans HH, Mencl J, Bahale G and Rao PS. In vitro exposure of mammalian cells to radon: Dosimetric considerations. Rad Res 127:211-219, 1991.

QUESTIONS

Akabani: I am very excited about your work. I have followed it very closely and have done very similar calculations. You assumed a uniform concentration of ^{12}Bi-DTPA in the medium, how will it be reflected in a clinical setting for the treatment of intraperitoneal tumors?

Roeske: In the clinical situation, we plan to use ^{212}BiOCl, which we know is taken up by cells. This should increase the therapeutic response as a higher dose will be delivered to the cells.

Stubbs: You showed that ^{212}Bi decays in a 2-step process where both alpha and beta particles are emitted. What fraction of the total emitted decay energy is contributed by the beta particles?

Roeske: The beta particle component is about 5% of the total alpha particle dose. However, because of the higher RBE of the alpha particles, the biological effects of the beta particles can be neglected.

BIOLOGICAL CONSEQUENCES OF THE LYMPHOCYTE IRRADIATION INDUCED BY ^{99M}TC-HMPAO WHITE BLOOD CELLS LABELING

de Labriolle-Vaylet C, Petiet A[1], Sala-Trepat M[2], Gardin I[1], Bok B[1] and Colas-Linhart N[1]
Saint-Antoine and X Bichat[1] Schools of Medicine, Institut Curie[2], Paris, France

ABSTRACT

^{99m}Tc-HMPAO labeling of white blood cells results in the incorporation of radioactivity not only into polymorphonuclear leukocytes, but also into lymphocytes. A significant irradiation may result from the uptake of this radiopharmaceutical into the lymphocytes. The aim of the study was to calculate the mean dose delivered to the ^{99m}Tc-HMPAO labeled lymphocytes, to count chromosomal aberrations in these cells, and to evaluate their viability by measuring their plating efficiency. Under standard labeling conditions, the mean activity associated with lymphocytes was 325 ± 10.8 kBq/10^6 lymphocytes, resulting in a mean cellular dose of approximately 8 Gy. This mean dose could not be used to predict the biological consequences of this labeling, as microautoradiographic studies showed that the labeling was not homogeneous (4% intensely labeled cells), but the uptake variability could not be quantified. The frequency of chromosomal aberrations (dicentrics and rings) was 1.08 ± 0.09. No abnormality was observed in unlabeled lymphocytes. The plating efficiency of the labeled lymphocytes was reduced as compared with control cells, but some lymphocytes were still able to form cellular clones, so labeled lymphocytes were not dead according to the radiobiological definition. Discarding lymphocytes from the cell suspension before ^{99m}Tc-HMPAO labeling to avoid the injection of viable irradiated cells is recommended, especially in children.

INTRODUCTION

^{99m}Technetium hexamethylpropyleneamine oxine (^{99m}Tc-HMPAO) has been used to radiolabel leukocytes in vitro in order to localize inflammatory or infectious foci (1,2). This labeling is routinely performed on mixed leukocyte preparations, but the tracer is not specific, and it is incorporated not only into polymorphonuclear leukocytes but also into mononuclear cells (3). The use of ^{99m}Tc-HMPAO instead of ^{111}In-oxinate for cell labeling has many advantages, including disponibility, low cost, better image quality and lower radiation dose to the whole body. But during its deexitation, ^{99m}Tc emits low-energy (Coster-Kronig, Auger) and intermediate-energy electrons (internal conversion), whose range is of the same order of magnitude as the cell size (4). So a significant cell irradiation may result from the presence of this radioisotope within the lymphocytes. These cells are very radiosensitive and are able to form clones. The aim of our study was to calculate the mean dose delivered to the labeled lymphocytes and to evaluate the biological consequences of this labeling by scoring the chromosomal aberrations and assessing the labeled lymphocyte viability.

MATERIALS AND METHODS

Labeling Data

The leukocytes were labeled under standard labeling conditions for infection diagnosis. Mixed leukocytes isolated from 60 ml of blood were incubated with 325 MBq of ^{99m}Tc-HMPAO. The final radioactivity on lymphocytes was evaluated after selective sedimentation. The spontaneous release of the tracer was measured during the two first hours after labeling.

Labeling Homogeneity

The homogeneity of the labeling was studied using track microautoradiography (5) performed on lymphocytes isolated immediately after labeling. Quantitative data were based on the examination of 1350 cells.

Cell Dosimetry

The mean dose delivered to lymphocytes was calculated in two steps (6). First, we considered the external dose, D_{ext}, which was delivered during the incubation phase of labeling (t = 10 min). The activity in the incubation medium was 320 MBq in a volume of 5 ml. Second, we considered the internal dose, D_{int}, which is derived from the ^{99m}Tc incorporated into the cells. A lymphocyte was considered to be a sphere (diameter = 10 µm) with a homogeneous distribution of the radionuclide. To calculate the fraction of the emitted energy that was actually absorbed by the lymphocyte, we used the model proposed by Berger (7) and previously described to evaluate the dose absorbed by Kupffer cells (8). Finally, the mean total absorbed dose to the lymphocytes, D_{tot} or the sum of D_{ext} and D_{int}, was calculated.

Chromosome Analysis

The chromosome analysis was carried out exclusively on complete first division metaphases identified as homogeneously stained chromosomes after fluorescent plus Giemsa staining (9). The dicentrics and rings were counted and the yield of unstable chromosomal aberrations was calculated for cell samples (mean number of aberrations/cell).

Viability of the Labeled Lymphocytes

The labeled lymphocyte viability was evaluated by measuring the plating efficiency (PE) of two different donors. The labeled mononuclear cells were incubated at 37°C in microtiter plates (10 cells/well) in RPMI medium, supplemented with 0.5% PHA (Gibco, Cergy, France), 10% interleukin 2 (Boehringer, Meylan, France) and irradiated lymphoblastoid feeder cells (10^4/well) (GM 1899A, Camden, NJ, USA). All plates were incubated at 37°C for 18 days and the wells were scored using an inverted phase-contrast microscope. Controls were lymphocytes incubated in saline or in cold HMPAO.

RESULTS

Labeling Data

The global leukocyte labeling efficiency was 37.9 ± 13.5% (n=28). The mean radioactivity associated with lymphocytes was 325 ± 10.8 kBq/10^6 lymphocytes. Spontaneous release of the tracer from lymphocytes in plasma at 37°C was not significant during the first two hours after labeling.

Labeling Homogeneity

Microautoradiographic studies performed immediately after labeling showed that 4% of the labeled cells appeared as dense black spots corresponding to highly labeled cells. Therefore the labeling is not homogenous (Figure 1). The range between minimal and maximal radioactive uptake could not be quantified.

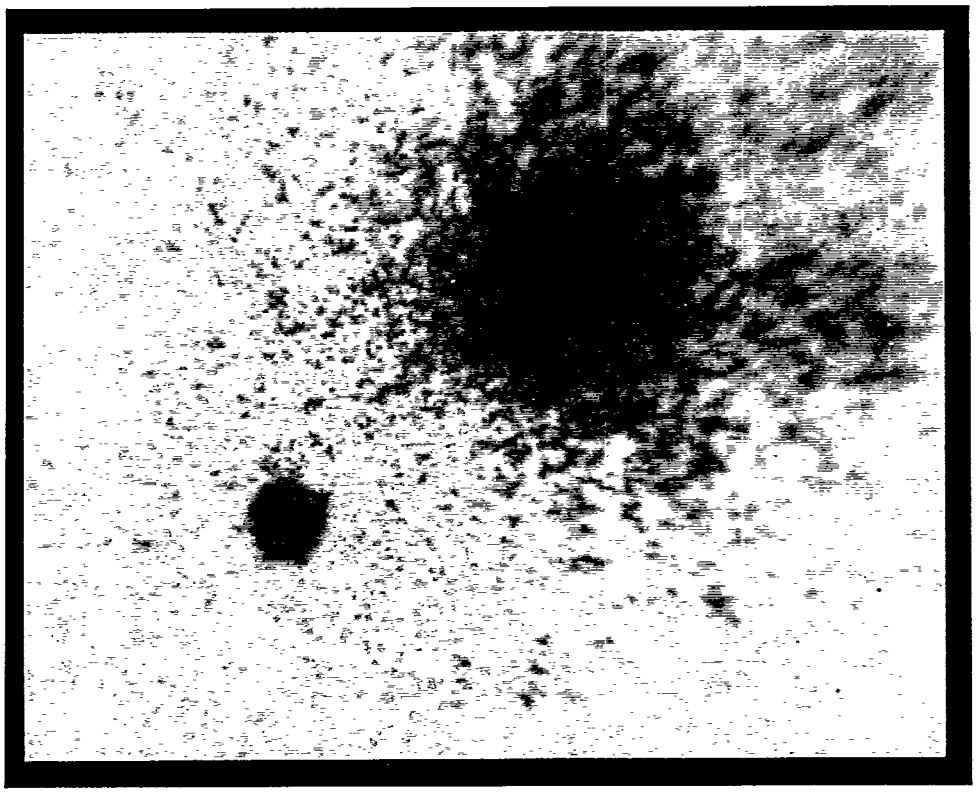

Figure 1. Track microautoradiography shows that the lymphocyte Tc-99m-HMPAO labeling is not homogeneous. One of these two cells is intensely labeled, but the uptake variability cannot be quantified.

Cell Dosimetry

Under the above conditions, the external dose was 0.08 Gy and the internal dose was 7.8 Gy. The mean total dose was 7.9 Gy.

Chromosome Analysis

The number of dicentrics and rings in the labeled lymphocytes was 108 for 100 cells examined. No abnormality was observed in control lymphocytes.

Viability of the Labeled Lymphocytes

The plating efficiency of controls was comparable to the mean values observed in the laboratory (23%) (10). The plating efficiency for labeled lymphocytes was 11% for donor one and 6.5% for donor two. For both donors, the differences between PE before and after labeling were significant ($p \text{ inf } 10^{-2}$). Moreover both PE, after labeling, were significantly different from zero ($p \text{ inf } 10^{-2}$).

DISCUSSION

Because of the heterogeneity of the lymphocyte labeling demonstrated by microradiography, the mean dose calculated here overestimates the absorbed dose to weakly labeled cells and underestimates the absorbed dose to intensely labeled cells. This limitation prevented us from considering the dose estimate as sufficiently reliable to evaluate the biological consequences of this labeling. Thus we have attempted to identify typical biological damage induced by the labeling. We observed a high number of dicentrics and rings, but these anomalies are unstable. However, it is accepted that the mechanism responsible for the formation of dicentrics is similar to that causing translocations, which are stable abnormalities, compatible with cell survival (9).

After labeling, the plating efficiency of labeled lymphocytes was reduced (48% and 28% respectively, of the control plating efficiency), but some lymphocytes remained viable, according to the radiobiological definition of viability, i.e. they are able to form clones. These findings suggest that it would be preferable to exclude the lymphocytes from the cell suspension, especially when HMPAO labeling is used to detect infection in children.

REFERENCES

1. Peters AM, Osman S, Henderson BL, Kelly JD, Danpure HJ, Hawker RJ, Hodgson HJ, Neirinckx RD and Lavender JP. Clinical experience with ^{99m}Tc-hexamethylprophylene amineoxime for labelling leucocytes and imaging inflammation. Lancet (2):946-949, 1986.
2. Peters AM. The Utility of [^{99m}Tc] HMPAO-Leukocytes for Imaging Infection. Semin Nucl Med (24):110-127, 1994.
3. Danpure H, Osman S and Caroll MJ. The development of a clinical protocol for the radiolabelling of mixed leucocytes with Tc-99m hexamethyl-propyleneamine oxime. Nucl Med Commun (9):465-475, 1988.
4. Howell RW. Radiation spectra for Auger-electron emitting radionuclides: Report No. 2 of AAPM Nuclear Medicine Task Group No.6. Med Phys (19):1371-1383, 1992.
5. Barbu M, Colas-Linhart N and Bok B. Technetium 99m autoradiography of labelled white cells. Acta Haemat.(71):13-17, 1984.
6. Bassano DA and Mc Afee JG. Cellular radiation doses of labeled neutrophils and platelets. J Nucl Med (20):255-259, 1979.
7. Berger MJ. Improved point kernels for electron and beta-ray dosimetry. NBSIR. Washington, DC: US Dept. of Commerce, National Bureau of Standards:73-107, 1973.
8. Gardin I, Colas-Linhart N, Petiet A and Bok B. Dosimetry at the cellular level of Kupffer cells after technetium-99m-sulphur colloid injection. J Nucl Med (33):380-384, 1992.
9. IAEA (International Atomic Energy Agency). Biological dosimetry: chromosomal aberration analysis for dose assessment. Technical Report, Series No. 260, 1986.
10. Sala-Trepat M, Cole J, Green MHL, Rigaud O, Vilcoq JR and Moustacchi E. Genotoxic effects of radiotherapy and chemotherapy on the circulating lymphocytes of breast cancer patients. III: Measurement of mutant frequency to 6-thioguanine resistance. Mutagenesis (5):593-598, 1990.

MORPHOLOGICAL STUDIES OF RAT LUNG CELLS AFTER INTERNAL IRRADIATION INDUCED BY 99M TECHNETIUM LABELED MICROSPHERES

Robinson M, Petiet A, Colas-Linhart N and Bok B
Laboratoire de Biophysique, Faculté de Médecine X Bichat
BP 416, 75870 Paris cedex 18, France

ABSTRACT

Lung imaging using i.v. injection of ^{99m}technetium (^{99m}Tc) labeled microspheres results in a heterogeneous distribution of labeled microspheres within the lungs; which was visualized in rats using a microautoradiography "track" method. Consequently, the absorbed radiation doses to the lung cells in close contact with the labeled microspheres (i.e. endothelial and epithelial cells) were estimated to be 6 Gy and 2 Gy respectively, in rats. The purpose of the present study was to evaluate potential ultrastructural damage induced by ^{99m}Tc electron irradiation, particularly early phenomena such as apoptosis. Eighteen male Wistar rats were divided into three groups. The first group was submitted to an i.v. injection of ^{99m}Tc microspheres (2.10^5 particles, 50 MBq), the second received unlabeled microspheres and the third was treated with a saline injection alone (control group). Animals were sacrificed at 4 hours (effective half-life of this radiopharmaceutical) and 6 hours (physical half-life of ^{99m}Tc) after injection. Ultrathin sections of the lungs were performed and analyzed using electron microscopy.

No acute radiation effects were observed. No ultrastructural injuries were noted in the first group. There is no morphological difference in lung cells between the three groups. No evidence of radiation-induced apoptosis was noted in the lung cells closely apposed to the labeled microspheres. Only inflammatory response (leukocyte infiltration) was observed in the first and second group. Previous cellular dosimetric estimations do not seem to be correlated with early morphological damages at the cellular level.

INTRODUCTION

Lung scintigraphy with ^{99m}technetium (^{99m}Tc) albumin microspheres has been widely used since 1968 (1). The potential radiobiological consequences of pulmonary imaging were studied in male Wistar rats using histological techniques. Lesions at the tissue and at the cellular level following radiotherapy have been described in the lungs (2). Little is known about potential damage following internal irradiation such as human lung scintigraphy.

In a previous study, we applied an appropriate experimental microautoradiography track method (MAR) adapted to the detection of high-internal-conversion electrons of ^{99m}Tc (3). The mean uptake of radioactivity by individual ^{99m}Tc (600 MBq) labeled microspheres (4.10^6 particles, Sferotec-S, SORIN, Italy) using MAR was 94 Bq/microsphere. The visualization yield was Y=33 ± 3%

(m ± SD for 5 experiments). Secondly, MAR was used to study the pulmonary microdistribution of the ^{99m}Tc labeled microspheres in serial lung sections. A very heterogeneous tridimensional distribution of labeled particles was demonstrated, with interparticle distances ranging from 57 to 4,400 μm.

Using the mean activity, calculated mean absorbed doses reached approximately 6 Gy for the closest endothelial cell nuclei and 2 Gy for epithelial cell nuclei (4). These high radiation doses led us to suppose that pulmonary lesions and the apoptosis phenomenon could be observed at the cellular level. The distance traveled by high-energy (142 keV) internal-conversion electrons in the lung medium is 800 μm. Therefore, lung cells directly apposed to the labeled microspheres and also neighboring cells, were examined under electron microscopy.

MATERIALS AND METHODS

This study was carried out in 18 male Wistar rats (weighing 320 ± 60 g) divided into 3 groups. The rats were anesthetized with urethane (2g/kg) and a catheter was introduced into the trachea. The first group was submitted to an i.v. injection of ^{99m}Tc labeled microspheres (2.10^5) corresponding to an activity of 50 MBq. The second group received the same number of unlabeled microspheres and the third was given only an injection of saline. The rats were sacrificed at 4 hours (effective half-time of the labeled particles) and 6 hours (physical half-life of ^{99m}Tc) after injection. Before excision, the lungs were inflated via the trachea with a perfusion of fixation fluid (1.5% glutaraldehyde in a 0.1 M cacodylate buffer, pH=7.4).

Transmission Electron Microscopy

The lungs were fixed with the same aldehyde mixture, washed in buffer, post-fixed in a ferricyanide-reduced osmium solution made up of 1% potassium ferricyanide and 1% osmium tetroxide made in a cacodylate buffer. Thereafter, the lung tissue was dehydrated and embedded in Epon. Thin sections were performed to localize an area with microspheres (groups one and two). Then, ultrathin sections were obtained and stained with lead citrate and uranyl acetate. Approximately 60 micrographs per animal were taken on a Philips EM 300 electron microscope and analyzed.

RESULTS

Thin Sections

The heterogeneous distribution of microspheres was confirmed. Although 90% of the microspheres in the examined sections were trapped individually within a given capillary, in some cases, several microspheres were found together within the same capillary (Figure 1).

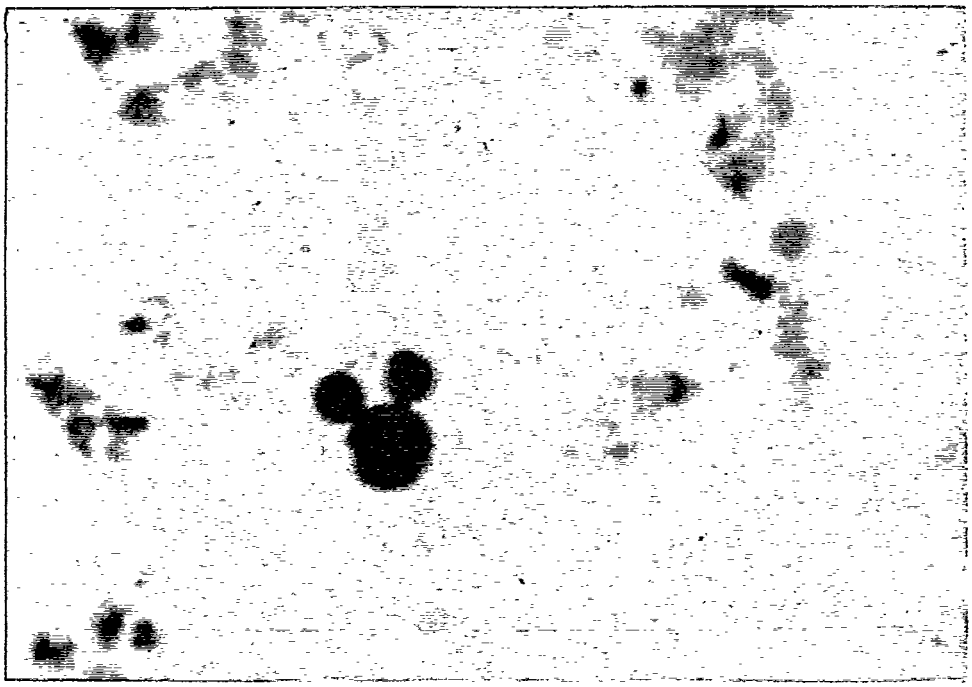

Figure 1. (Magnification X 400). Alveolar profile from rat lung. Three microspheres are trapped in the same capillary. The alveolar septa contain abundant capillaries filled with erythrocytes. The alveola spaces are lined by flat extensions of the alveolar epithelial cells.

Ultrathin Sections (Figures 2-4)

Figure 2. (Magnification X 4500). Six hours after an i.v. injection of unlabeled microspheres in rat. Four microspheres are lodged in lumina of capillary: sizes are different. You can note a polynuclear (P) and the epithelial cells (E).

Figure 3. (Magnification X 8200). Micrograph taken 4 hours after an i.v. injection of labeled microspheres in rat. The microspheres fill totally lumina of capillaries and are apposed directly to the endothelial cells (→).

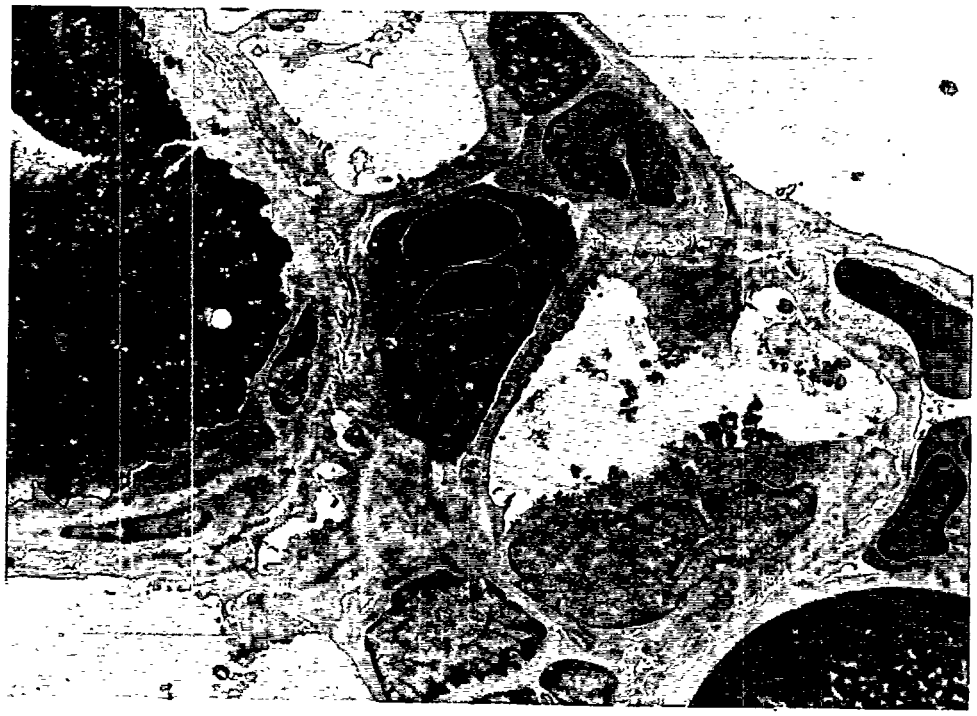

Figure 4. (Magnification X 12500). Six hours after an i.v. injection of labeled microspheres in rat. Two microspheres can be observed: one has begun to disintegrate.

The density of the chromatin was slightly increased and interstitial edema was visualized in the lungs of the three groups. However these phenomena were not specific and could be induced by the *in situ* fixation method.

Inflammatory response (several polynuclear cells in the capillary lumina) was found in groups one and two which appeared to be due to the introduction of microspheres rather than by the ^{99m}Tc.

DISCUSSION

In the chronology of physicochemical and biological events after an irradiation, established by Bacq and Alexander (5), morphological lesions can be observed within minutes or hours. Radiation-induced morphological damage can be revealed by electron microscopic analysis (6). The phenomenon of apoptosis can be induced by insults such as UV and ionizing radiation (7-8). It is now recognized that apoptosis or "active cell death" has been implicated in a wide variety of physiological processes such as carcinogenesis and tumor development (9). This mode of cell death is characterized by distinct steps of membrane blebbing and chromatin condensation. The lag time for radiation-induced apoptosis was about 3 hours and most cell death occurred within 12 hours (10).

Numerous electron micrographs have been analyzed (approximately 400 for irradiated lungs). Nevertheless, no signs of apoptosis have been clearly demonstrated. Observed changes at the nuclear level, such as increase of chromatin density, could not be attributed to radiation-induced apoptosis and corresponded to lung section artefacts.

The introduction of microspheres induced inflammatory responses. ^{99m}Tc was not responsible for these reactions, since high leukocyte infiltration was also observed after unlabeled microsphere injection. In addition, irradiation induced by ^{99m}Tc labeled microspheres did not produce morphological lesions.

The calculated mean delivered dose to endothelial and epithelial cells was very high; 6 and 2 Gy, respectively. The authors of a previous study (11) observed that a 1 Gy dose kills 15-25% of the pulmonary cells, 2 Gy kills 40-55% of these cells and beyond 3 Gy, each supplementary Gray kills about 50% of the surviving cells. Although these doses were calculated according to hypotheses which are valid only in the case of external radiotherapy, we expected morphological damages or signs of cell death. Conventional dosimetry calculations do not appear to be correlated with morphological alterations at the cellular level. Other authors have also reported that quantification of biological damage using standard dosimetry techniques are generally unsuccessful (12).

Further biological investigations are needed to evaluate the functional status of irradiated pulmonary cells and to study potential relationships with the dose.

ACKNOWLEDGMENTS

We thank JC Barrault (Sorin Biomédica) for supplying the Sferotec-s kits used in the study. This study is part of the PhD Thesis by Marjorie Robinson granted by Electricité de France (E.D.F.).

References

1. Zolle I, Rhodes BA and Wagner HN, Jr. Properties and use of radioactive albumin microspheres. J Nucl Med (9):363, 1968.
2. Rodeman HP, Bamberg M. Cellular basis of radiation-induced fibrosis. Radioth Oncol (35):83-90, 1995.

3. Barbu M, Colas-Linhart N and Bok B. ^{99m}Tc autoradiography of labeled white cells. Acta Haemat (71):13-14, 1984.
4. Robinson M, Colas-Linhart N, Guiraud-Vitaux F, Petiet A and Bok B. Heterogeneous distribution of technetium 99m-labeled microspheres in rat lungs: microautoradiographic evidence and dosimetric consequences. Accepted for publication in J Nucl Med, 04 April, 1996.
5. Bacq ZM and Alexander P. Fundamentals of radiobiology, completely revised 2nd edition, edited by Pergamon Press, pp 555, Oxford, England, 1971.
6. Harmon BV and Allan DJ. X-ray induced cell death by apoptosis in the immature rat cerebellum. Scanning Microscopy (2):561-568, 1988.
7. Warters RL. Radiation-induced apoptosis in murine T-cell hybridoma. Cancer Res (52):883-890, 1992.
8. Clarke AR, Purdie CA, Harrison DJ, Morris RG, Bird CC, Hooper ML and Willie AH. Thymocyte apoptosis induced by p53-dependent pathways. Nature (362):849-852, 1993.
9. Stewart BW. Mechanisms of apoptosis : integration of genetic, biochemical, and cellular indicators. J Natl Cancer Inst (86):1286-1296, 1994.
10. Hendry JH, Potten CS, Chadwick C and Bianci M. Cell death (apoptosis) in the mouse small intestine after low doses: effects of dose-rate 14.7 MeV neutrons and 600 MeV (maximum energy) neutrons. Int J of Radiat Biol (42):611-620, 1982.
11. Tubiana M and Bertin M. Radiobiologie-Radioprotection, edited by Presses Universitaires de France, pp. 43-44, Paris, France, 1989.
12. Watt DE and Khan S. Cross-sections for the biological effectiveness of electrons in mammalians cells. 3rd International Symposium on Biophysical Aspects of Auger Processes, Abstract L13. University of Lund, Sweden, 1995.

FACTORS INFLUENCING TUMOR DOSIMETRY IN THE RADIOIMMUNOTHERAPY OF CEA-EXPRESSING CANCERS WITH ^{131}I-LABELED MURINE AND HUMANIZED ANTI-CEA MONOCLONAL ANTIBODIES

Behr TM, Sharkey RM, Dunn RM, Juweid ME, Siegel JA and Goldenberg DM
Garden State Cancer Center
at the Center for Molecular Medicine and Immunology
Newark, NJ 07103

ABSTRACT

Achieving a sufficiently high radiation dose is probably the key to therapeutic success in radioimmunotherapy (RAIT) of solid tumors. The aim of this study was, therefore, to examine which factors influence tumor dosimetry in the RAIT of CEA-expressing cancers. Data from 119 tumors in 93 patients with CEA-expressing tumors (e.g., colorectal, lung, breast, ovarian, pancreatic, and medullary thyroid carcinomas) were analyzed. They underwent RAIT with the ^{131}I-labeled IgG_1 anti-CEA antibodies NP-4 ($K_a=10^8M^{-1}$), MN-14 ($K_a=10^9M^{-1}$) or its humanized form (hMN-14), as well as the anti-colon-specific antigen-p MAb, Mu-9. Imaging was performed from 4 to 240 h p.i. (planar and SPECT). The targeting kinetics and cumulated activity of tumors and organs were determined from imaging data and blood clearance. Doses were calculated according to the MIRD schema. An inverse logarithmic relationship between tumor size and MAb uptake was found for both anti-CEA Mabs (i.e., the smaller the lesion, the higher the uptake; uptakes ranging from 10^{-3} to 1 % ID/g, doses from 0.3-59.5 mGy/MBq [1-220 rad/mCi]), whereas no such relationship was found for Mu-9. Tumor uptake was the most important factor determining the dose ($r=0.91$), with the biological half-time of the MAb in the tumor (range 21-398 h) being the next most important dose-determining factor ($r=0.51$). The tenfold difference in affinity did not lead to significant differences in tumor uptake between both anti-CEA Mabs, but to longer biological tumor half-times of MN-14 as compared to NP-4. Colorectal and medullary thyroid cancers had higher tumor uptakes and tumor-to-red marrow dose ratios than other cancers ($p<0.01$). Maximal tumor uptake occurred between 4 and 48 h p.i., correlating to differences in the blood half-times. Biological blood and tumor half-times of the anti-CEA Mabs were significantly shorter in colorectal than in other cancers. HAMA decreased the tumor uptake and tumor-to-non-tumor ratios by increasing MAb clearance. HAHA (anti-human=anti-idiotypic) antibodies had no effect on the biodistribution, but selectively decreased tumor uptake, and thus the dose. These data suggest that the tumor uptake is the most important dose-determining factor. Differences in affinity are reflected by different half-times, not uptake values. In contrast to HAMA, HAHA seems to affect exclusively the tumor uptake without influencing the overall biodistribution. Especially favorable conditions for anti-CEA antibodies seem to prevail in colorectal and medullary thyroid cancer, as well as patients with minimal disease, where cytotoxic tumor doses may be expected and therapeutic responses have been obtained.

INTRODUCTION

Whereas radioimmunotherapy (RAIT) of lymphoma and other hematological tumors is increasing in acceptance as a new potent mode of treatment (1,2), its success in solid tumors is still limited (3,4). In preclinical models, RAIT of colorectal cancer has been shown to be more effective than an equitoxic chemotherapy of 5-fluorouracil and leucovorin (5). In an adjuvant (minimal metastatic disease) model, RAIT was shown to be highly effective for achieving even long-term cures (6). The biological, physiological, biophysical and biochemical conditions in such animal models, however, can be fundamentally different from the clinical situation (7). Mathematical models (8-10) of parameters determining tumor targeting and uptake (e.g., tumor size, vascular permeability, interstitial pressure as well as the presence of a "binding site barrier") have been verified mostly by animal studies (8-11). Therefore, a closer examination of factors that influence tumor dosimetry in patients is warranted, since achieving sufficiently high tumor doses is paramount to accomplishing therapeutic efficacy in the RAIT of solid tumors (3). Therefore, the aim of this study was to focus on factors which may influence the tumor dosimetry of solid, CEA-expressing tumors, in order to identify those subgroups of patients where radioimmunotherapy may be promising. These findings could be used as a guideline in the design of future clinical trials.

MATERIALS AND METHODS

Antibodies and Radiolabeling

NP-4 and MN-14 are IgG_1-subclass murine anti-CEA monoclonal antibodies (12,13). Both are directed against the same class-III peptide epitope of the CEA molecule, according to the classification of Primus et al. (14). The affinity of MN-14 was determined to be tenfold higher than that of NP-4 (10^9 l/mol versus 10^8 l/mol) (13). Recently, a humanized, CDR-grafted, form of MN-14 has been developed and introduced into clinical trials (15). The studies of Sharkey et al. showed identical biodistribution and tumor targeting properties of the humanized and murine forms of MN-14 (15,16). Mu-9 is a murine monoclonal antibody of the IgG_1 subtype, directed against the colon-specific antigen-p mucin (CSAp), which is present in approximately 60 to 70 percent of colorectal cancers (17). This antibody has the advantage of recognizing an epitope which is not present in the circulation.

The antibodies were purified and labeled with $Na^{131}I$ (New England Nuclear, N.Billerica, MA), as described in detail recently (18). The immunoreactivity of labeled anti-CEA Mabs and Mu-9 was more than 80 percent in all cases.

Patients, Antibody Administration and Imaging

The data from a total of 93 patients with CEA-expressing adenocarcinomas who underwent RAIT with the ^{131}I-labeled high-affinity IgG anti-CEA monoclonal antibody MN-14 (n=41), its humanized, CDR-grafted form, hMN-14 (n=19), the lower affinity anti-CEA IgG, NP-4 (n=19), or the anti-CSAp antibody, Mu-9 (n=14), were analyzed in this study (among them 59 colorectal, 9 medullary thyroid, 6 lung, 3 pancreatic and 9 ovarian cancer patients).

Before antibody injection, all patients were premedicated with Lugol's solution and potassium perchlorate to decrease the thyroid and gastric uptake, respectively. All patients entered into the RAIT protocol first underwent a diagnostic-dosimetric study with 0.5-2.5 mg of protein, labeled with 296-1110 MBq [8.0-30.0 mCi] ^{131}I, for assessment of tumor targeting and dosimetry. Usually, within two weeks after the dosimetric injection, the patients were admitted to the hospital for therapy (4.0-27.5 mg, 1103-8839 MBq [29.8-238.9 mCi]).

Scanning of patients was performed with a Sophy-DS-X or DS-7 camera (Sopha Medical Systems, Columbia, MD). Anterior and posterior planar images were obtained in diagnostic studies daily from 4 to 168 hr p.i. (occasionally up to 336 hr) with a high-energy parallel-hole collimator, collecting 500,000 counts on all days (128 x 128 matrix). In therapeutic settings (higher activities), imaging was started when the retained whole-body activity reached ≤ 1110 MBq (30 mCi). SPECT was performed routinely at 24, 48, 72 and 96 hours (64 projections over 360°, 64 x 64 matrix size), using a Hamming-Hann filter for reconstruction.

CEA and HAMA Determinations

Plasma CEA levels were determined by using a CEA-EIA that was described earlier (19). The serum samples were heat-extracted prior to CEA measurement to avoid falsification of results by human anti-mouse antibodies (HAMA) present in patients' sera (20). HAMA titers were determined using a commercially available enzyme-linked immunoabsorbent assay (ImmuSTRIP™ HAMA-EIA; Immunomedics, Inc., Morris Plains, NJ).

Human anti-humanized MN-14 (=anti-idiotypic) antibodies (for brevity's sake called HAHA in this study, although they represent, in reality, anti-idiotypic antibodies against the remaining murine portion of humanized MN-14) were determined by in vitro complexation studies, analyzed by HPLC (15). Any complexation > 10 percent was considered as positive for HAHA.

Pharmacokinetic Analysis

MAb blood clearance rates were determined by counting blood samples at various times after the end of the infusion, as described previously (1,3,4,12,13,17). The clearance data are expressed as the biological clearance times as follows: $T_{1/2}$-α: distribution phase; $T_{1/2}$-β: elimination phase; and (overall) half-time ($T_{1/2}$ = number of hours required for 50 percent of the activity to be cleared from the blood). Total-body clearance rates were determined from whole-body scans obtained from 4 hours p.i. until the end of imaging.

Dosimetry

Regions of interest of organs and tumors were generated from the anterior and posterior planar views obtained during each imaging session. Appropriate adjacent soft tissue regions served as background regions for the organs. The background regions for tumors were chosen in the normal, nontumor-bearing parenchyma of the respective organ, as close to the tumor as possible. The activities in these regions were generated by using the build-up factor methodology for Compton scatter compensation (21). The individual time-activity curves of organs and tumors were fit to a mono- or biexponential function by a nonlinear, least-squares analysis, or by the trapezoidal method, and then integrated to obtain the cumulated activity in each region. The blood time-activity concentration data were also fit by a mono- or biexponential function (see above) to obtain the cumulated activity in the blood. The red marrow cumulated activity was calculated from these data, based on blood, by multiplying this concentration by 1,500, the assumed weight in grams of the marrow in an average adult. The mean dose in mGy was calculated for organs according to the Medical Internal Radiation Dose (MIRD) schema, with correction for the remainder of the whole-body activity (22-24). For tumor dosimetry, the self-to-self, self-to-host, and host-to-self doses were considered. The masses of normal organs were generated from MIRD standard tables (25), and tumor volumes were obtained from CT or calculated by a voxel-counting procedure from SPECT data (1). If not otherwise stated, all data on the tumor pharmacokinetics and dosimetry reported in this paper rely exclusively on studies where imaging was started no later than 48 hr after antibody administration (i.e., diagnostic or low-activity therapeutic injections), in order to avoid any bias of the results due to

missing early phases of the tumor or organ kinetics (20). Reported maximum tumor uptake values were determined as the intercept of a pseudolinear back-extrapolation from the logarithm of measured uptake values with the ordinate, i.e., the virtual uptake at the time of MAb injection (4,22).

RESULTS

Patients, Cancer Types and Pharmacokinetics

Previous studies have shown identical pharmacokinetics of the anti-CEA antibodies, NP-4, MN-14, and its humanized form, hMN-14, within the same histogenetic tumor type (20). In contrast, profound differences were found between tumor types, especially between colorectal cancer at elevated plasma CEA levels and other CEA-expressing tumor types (20). This holds true for this patient population as well. As was also demonstrated in detail in previous studies (4,20), colorectal cancer patients had, at comparable plasma CEA levels, the unique feature of clearing anti-CEA antibodies faster from blood and whole-body than patients with other CEA-expressing tumors, a phenomenon which we could show to be most likely due to CEA-receptor-mediated clearance of immune complexes between the injected antibody and circulating antigen (4,20). This phenomenon was seen in the patients included in this study as well (data not shown), whereas the anti-CSAp antibody, Mu-9, shows normal clearance rates in these patients (20). Therefore, with anti-CEA antibodies, the blood half-times and the red marrow and whole-body doses in colorectal cancer patients were approximately only half as high as in patients with all other forms of CEA-expressing tumors ($p<0.001$). As was shown also in previous studies, tumor targeting and sensitivity were independent of the plasma CEA levels or the antibody protein dose applied (4,20).

Overall Tumor Dosimetry

In a total of 119 tumors, no significant overall differences could be observed between the various antibodies with respect to absolute tumor doses achieved, as well as with respect to tumor-to-normal organ ratios with murine and humanized MN-14, NP-4, and Mu-9, in HAMA- and HAHA-negative patients (data not shown).

Table 1 further differentiates according to different histogenetic cancer types. In colorectal cancer patients, tumor doses of the anti-CEA antibodies were significantly lower (about half the value) than with the anti-CSAp antibody, Mu-9 ($p<0.05$). Interestingly, no significant differences are noticeable between NP-4 and MN-14/hMN-14, despite the tenfold higher affinity of the latter. With Mu-9, the normal organ doses also were higher in colorectal cancer patients, which is a consequence of its lower blood and whole-body clearance as compared to the anti-CEA MAbs. This explains why no differences in the tumor-to-non-tumor ratios were found between the four antibodies.

Medullary thyroid cancer patients had the highest tumor doses (two- to threefold higher than all other cancer types), as well as the highest tumor-to-nontumor ratios. Here, no significant difference was observed between MN-14 and NP-4. Although absolute tumor doses were comparable to those of colorectal cancer patients in other cancer types, tumor-to-normal organ ratios generally were significantly ($p<0.05$) lower. This is due to the differences in antibody clearance, leading to higher red marrow and organ doses in these noncolorectal cancer patients.

Table 1
Tumor Dosimetry with Anti-CEA MN-14 and NP-4, as well as with Anti-CSAp Mu-9

Monoclonal Antibody	Tumor Dose mGy/MBq	Tumor/Nontumor ratios					
		T/red marrow	T/whole-body	T/kidney	T/liver	T/lung	n
Colorectal cancer:							
MN-14	1.9 ± 1.7	3.2 ± 2.2	11.7 ± 9.8	2.3 ± 2.2	3.3 ± 2.8	3.7 ± 2.1	33
hMN-14	1.8 ± 1.5	3.5 ± 1.9	12.0 ± 7.8	1.6 ± 1.3	3.0 ± 2.2	3.5 ± 2.0	12
NP-4	1.7 ± 0.2	2.9 ± 0.4	10.7 ± 1.5	N/D	2.8 ± 1.6	2.7 ± 0.4	10
Mu-9	4.0 ± 3.4	3.6 ± 2.5	14.1 ± 10.0	2.6 ± 2.6	3.8 ± 2.9	3.8 ± 3.0	19
medullary thyroid cancer:							
MN-14	4.9 ± 2.9	5.0 ± 3.3	18.2 ± 13.2	3.7 ± 2.3	3.0 ± 1.4	3.9 ± 1.5	9
NP-4	3.9 ± 0.8	4.0 ± 1.4	16.3 ± 4.3	2.8 ± 0.4	4.8 ± 1.0	4.2 ± 2.7	4
lung cancer:							
MN-14	1.9 ± 0.9	1.9 ± 0.9	7.6 ± 3.0	1.1 ± 0.8	2.4 ± 1.4	1.6 ± 0.7	8
hMN-14	0.5	0.7	3.0	0.7	0.8	0.8	1
NP-4	N/D	N/D	N/D	N/D	N/D	N/D	-
ovarian cancer:							
MN-14	2.4 ± 3.5	2.8 ± 3.6	12.9 ± 16.1	4.9 ± 6.2	5.2 ± 7.8	4.9 ± 6.3	8
hMN-14	1.8 ± 1.3	1.6 ± 1.0	5.8 ± 4.8	1.2 ± 0.6	1.9 ± 0.6	1.6 ± 1.2	5
NP-4	N/D	N/D	N/D	N/D	N/D	N/D	-
pancreatic cancer:							
MN-14	1.8 ± 1.4	1.3 ± 0.7	5.8 ± 4.2	2.4 ± 1.9	2.6 ± 2.5	1.9 ± 1.1	2
hMN-14	1.3	1.0	4.4	2.3	N/D	1.2	1
NP-4	N/D	N/D	N/D	N/D	N/D	N/D	-

Quantitative Tumor Uptake in Relationship to Tumor Mass and Cancer Type

Figure 1 shows the relationship between the tumor mass and the tumor uptake for the three antibodies and different tumor types. With both anti-CEA antibodies, NP-4 and MN-14, as well as with MN-14's humanized form, an inverse logarithmic relationship was found when analyzing the overall data of all tumor types. Usually, uptake values ranged between $5x10^{-3}$ and 10^{-1} %ID/g.

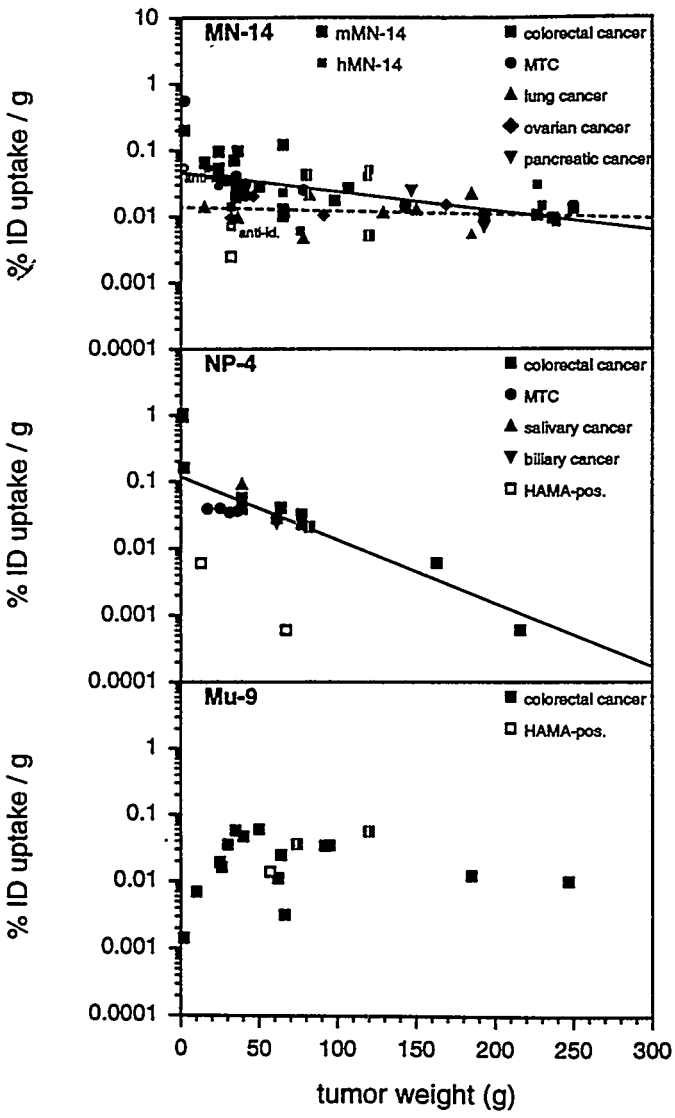

Figure 1. Relationship between tumor mass and tumor uptake. Open symbols represent data from HAMA and HAHA-positive patients, respectively.

Occasionally, in very small tumors (<2g), uptake values of up to more than 1 percent of the injected dose per gram were observed, which is higher than what would have been predicted by a logarithmic back-extrapolation from the data of larger tumors. There was no significant difference in tumor uptake between both anti-CEA antibodies, NP-4and MN-14, despite their tenfold difference in affinity (Figure 1). When differentiating further into different cancer types, at comparable tumor sizes, the percent tumor uptake values of MN-14 were similar for colorectal and medullary thyroid cancer (overall 0.045 ± 0.075 vs. 0.033 ± 0.010 %ID/g for colorectal versus MTC in the size range between 10 and 100g; solid line in Figure 1, upper panel). In contrast, the uptake values were significantly lower (0.011 ± 0.007 %ID/g) for most other types of CEA-expressing tumors (i.e., lung, pancreatic, etc.) at comparable sizes (dashed line in Figure 1, upper panel; the difference between the two regression lines is statistically significant at a $p=0.022$ level).

No tendency towards higher tumor uptake in smaller tumors was seen with the anti-CSAp antibody, Mu-9 (i.e., the slope of a regression line between tumor size and uptake is not significantly different from zero). Indeed, small tumors even tended toward lower uptake values than were observed in larger ones (Figure 1, lower panel).

Determinants of Tumor Dosimetry

Figure 2 shows the relationship between tumor uptake and tumor doses achieved. A strong linear relationship was found for all three antibodies between the logarithm of tumor uptake and the logarithm of the radiation doses to the tumors ($r=0.85$-0.91, slope highly significantly different from zero; $p<0.0001$). Interestingly, with MN-14 and its humanized form, at comparable absolute uptake values, all noncolorectal cancer lesions resulted in higher tumor doses than colorectal cancer lesions (Figure 2, top; dashed versus solid regression line; difference between both lines significant at $p=0.0232$). There may be an identical trend with NP-4 (cf. Figure 2, middle panel), but the difference is only subtle, and the number of observations is too few to reach statistical significance.

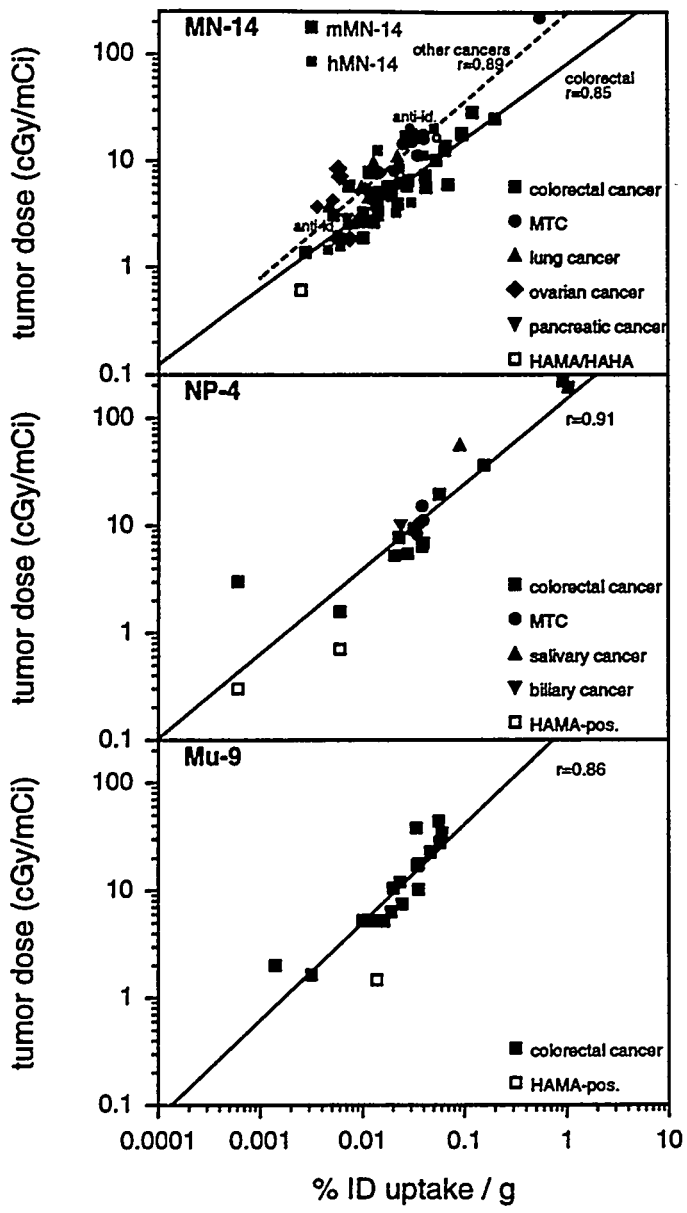

Figure 2. Correlation between the antibody uptake and the radiation doses.

Since the radiation dose to a given tissue is defined by the uptake and the effective half-time of the radioisotope in the tissue, this phenomenon must rely on differences in the biological half-times of the radiolabeled antibody in the tumor. Indeed, Figure 3 shows that the biological half-times of the anti-CEA antibodies in colorectal tumors were significantly shorter (48.6 ± 19.8 hr) than in all other types of cancer (132.9 ± 68.8 hr; $p<0.01$). The higher tumor doses in medullary thyroid cancer at comparable tumor sizes are, therefore, a consequence of a higher tumor uptake (which is similar to colorectal cancer, see above), and of a longer biological $T_{½}$ than in colorectal cancer, resulting in a longer residence time in the tumor. However, in contrast to the strong correlation between uptake values and doses, the overall correlation between tumor half-times and doses was, at r=0.51, rather weak (Figure 3).

A trend was noticed towards shorter tumor half-times with NP-4 as compared to MN-14. In most cancer types, biological tumor half-times of NP-4 were approximately half the values obtained with MN-14. Due to a relatively broad variation and the small number of observations, however, statistical significance was reached only in colorectal (33.7 ± 10.6 vs. 52.6 ± 23.5 hr for NP-4 and MN-14; $p<0.05$) and medullary thyroid cancer (61.4 ± 21.3 vs. 124.6 ± 36.7 hr for NP-4 and MN-14, respectively; $p<0.01$) (Figure 4).

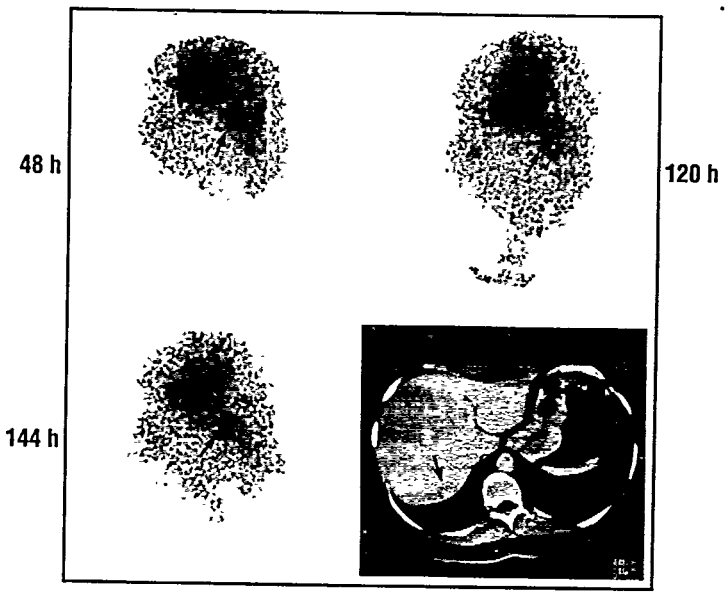

Figure 4a. Tumor targeting of a liver metastasis in a medullary thyroid cancer (pat. #1431) with NP-4 IgG shows slowly increasing tumor/background ratios (arrow): $T_{1/2}$ biological in the tumor = 53.8 h, whole-body $T_{1/2}$ = 52.8 h.

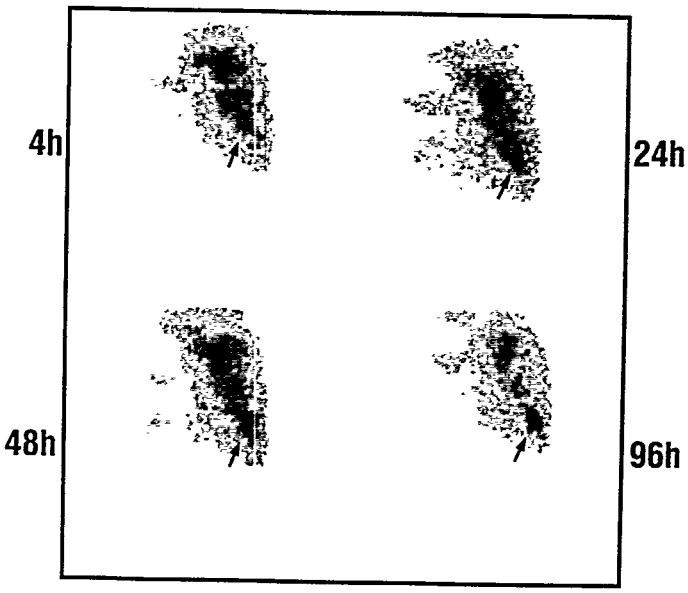

Figure 4b. Tumor targeting of a similar liver lesion of medullary thyroid cancer in another patient (#1465) with MN-14 shows improved tumor/background ratios, despite no significant differences in tumor uptake, which is due to a longer $T_{1/2}$ of MN-14 in the tumor at similar whole-body clearance: biological $T_{1/2}$ in the tumor = 137.5 h, whole-body $T_{1/2}$ = 65.2 h.

Influence of HAMA and HAHA on Tumor Dosimetry

The absolute tumor uptake, as well as the resulting radiation doses, were, by one to two orders of magnitude, lower in patients with pre-existing HAMA at the time of antibody injection, depending on the actual HAMA titer (cf. Figures 1-3). Also, tumor-to-red marrow and tumor-to-other normal organ ratios were significantly lower in these patients than in HAMA-negative patients. An exception to this rule was when HAMA developed several days after the antibody administration when tumor targeting had already reached its apogee. In this situation, tumor targeting was not compromised and the HAMA-induced enhanced background clearance led to markedly enhanced tumor-to-nontumor ratios.

Whereas HAMA hindered tumor accretion because of a rapid uptake of the injected antibody by the reticuloendothelial system of liver, spleen and bone marrow, with rapid metabolism and excretion

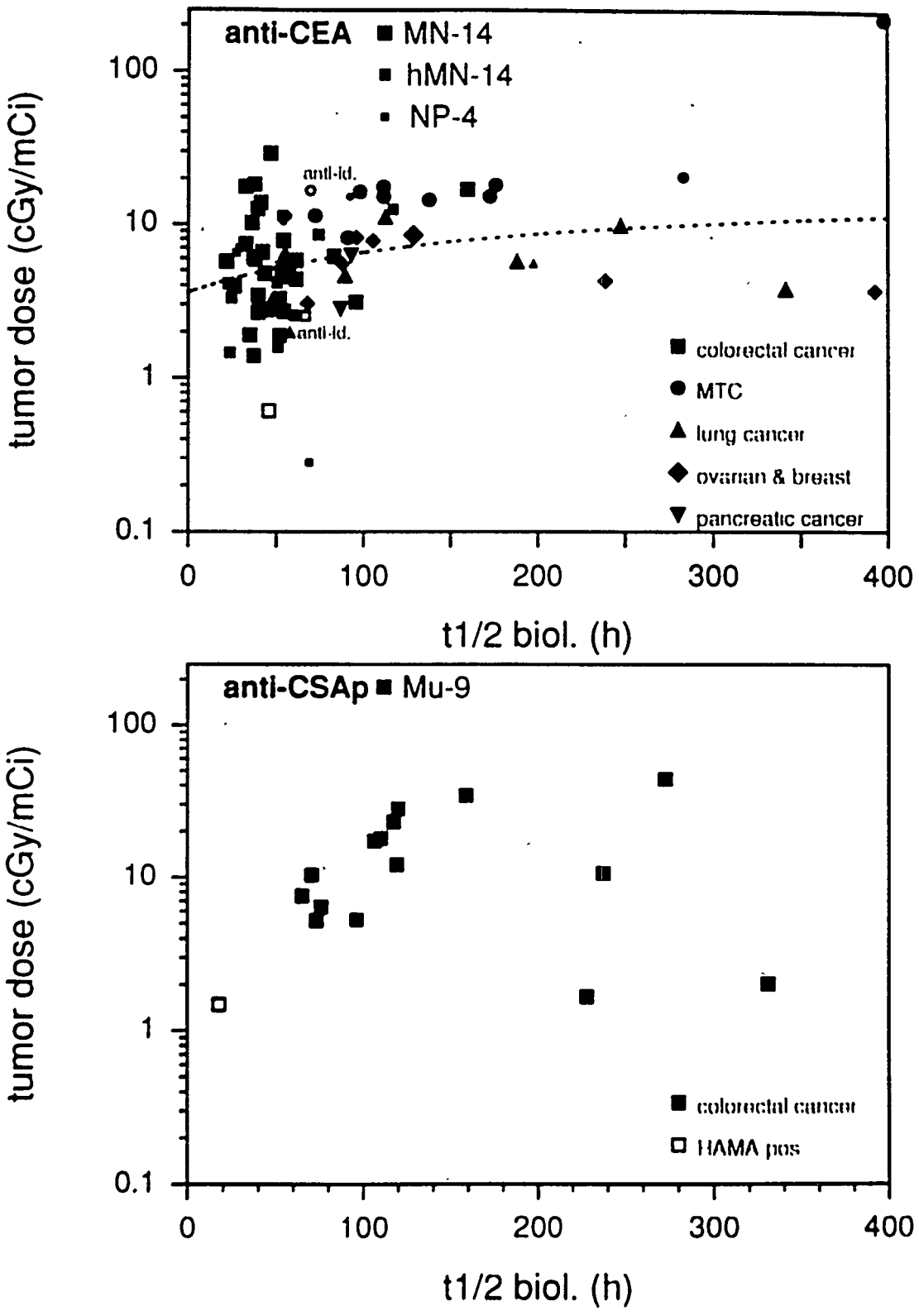

Figure 3. Relationship between the biological half-time of the radiolabeled antibody and tumor doses.

of the metabolites via the urine (4), the influence of human anti-humanized MN-14 (for simplicity's sake abbreviated as HAHA) on tumor uptake was different in patients with anti-idiotypic HAHA against the antigen-binding site of MN-14.

Figure 5. Tumor targeting in patient #1517: the left panel shows strong uptake of MN-14 in a peritoneal implant (arrow), whereas, after the development of anti-idiotypic HAHA, a second diagnostic study with hMN-14 shows only very faint targeting (right panel), despite no significant alterations in the overall pharmacokinetics (both scans 72 h p.i.).

Figure 5 is an image of patient #1517, a 31-year-old man with a history of poorly-differentiated metastatic colorectal cancer. His first exposure to murine IgG was an ^{111}In-labeled B72.3 (OncoScint™) study eight months prior to the first MN-14 IgG scan. At this time-point he was HAMA- and HAHA-negative. The scan with mMN-14 (0.6 mg) [300 MBq, 8.1 mCi ^{131}I] shows strong accumulation in a peritoneal implant (tumor uptake 1.5×10^{-2} %ID/g in a 30-g lesion), as well as delineation of the whole peritoneal cavity (peritoneal carcinomatosis). One week after receiving 6.0 mg of *murine* MN-14 IgG for RAIT, he developed HAMA, including an anti-idiotypic response (HAHA). A second diagnostic study with 10.0 mg hMN-14 three months later showed only very faint targeting (uptake only approximately 7×10^{-3} %ID/g in the 30-g implant, i.e., less half of the original value), and absence of targeting of the peritoneal carcinomatosis, despite no significant alterations in the overall pharmacokinetics (blood $T_{1/2}$ 17.65 h versus 18.63 h in the first study 3 months earlier).

Tumor-Targeting Kinetics

Different targeting kinetics were seen between the antibodies in patients with different tumor types. With MN-14, the maximal tumor uptake was seen in 10 out of 28 assessable patients by 4 hr (all of them had plasma $T_{1/2}$s shorter than 15 h), in 12 patients by 24 hr, and in 5 patients at 48 hr p.i. Consistent with the short blood half-time of anti-CEA antibodies in this cancer type, in 8 out of 14 colorectal cancer patients the maximum uptake was reached at 4 hr, whereas in 4 assessable lung cancer patients, two had the maximal tumor uptake at 48 hr, and one even at 72 hr p.i. In accordance with the longer serum half-times of Mu-9 in colorectal cancer patients, maximal tumor uptake was seen in 2 of 7 assessable patients at 24 hr, and in the other 5 out of 7 patients at 48 hr p.i.

DISCUSSION

Whereas in lymphoma, probably due to its radiosensitivity, complete response rates of over 80 percent have been reported with RAIT (1-3), the objective response rates are still rather low in solid tumors (3-4). In external beam radiation, depending on the tumor type, doses usually between 3000 and 7000 cGy are required for achieving responses in adenocarcinomas (26). Although some recent studies showed higher or at least a comparable effectiveness of low-dose-rate RAIT (27), the generally accepted view is that even higher radiation doses are necessary to achieve a similar

biological effectiveness, especially given the lower dose rate of RAIT with ^{131}I-labeled MAbs. A study examining the doses required in Na^{131}I therapy of differentiated thyroid cancer for achieving successful ablation of benign and malignant thyroid tissue demonstrated this principle also for radionuclide therapy: the higher the radiation dose, the higher the success rate (28). Our study, therefore, has attempted to identify those subgroups of patients which may be especially suitable for a radioimmunotherapeutic approach. Several preclinical studies have attempted to define the relationship between tumor size, antigen expression, interstitial pressure, vasculary leakage, etc., and tumor uptake with radiolabeled antibodies (8-11). Also, mathematical models were developed to describe these data (8-11). However, only very few studies exist that examine these parameters in patients.

An inverse relationship between tumor size (mass) and absolute tumor uptake of antibody is a well-known phenomenon from animal models (9,10) and a few clinical studies (4,22). In these small lesions, probably optimal conditions are found with respect to vascularization, antigen accessibilty, interstitial pressure, and several other factors. This favors the concept of radioimmunotherapy as a treatment modality for either minimal residual disease or in adjuvant settings (29). No such relationship exists with Mu-9, which recognizes a mucin found intracellularly, as well as in especially high concentrations in necrotic tumor tissue (17). This may explain why small lesions had an even lower Mu-9 uptake than larger ones. Perhaps the antigen is only accessible for the MAb when it is present in the extracellular matrix of tumors or necrotic areas, which are more abundant in larger tumors.

The observation that a tenfold difference in affinity does not lead to any significant difference in tumor uptake was observed in clinical studies by others as well (30,31), which is in contrast to data from animal or mathematical models (32,33). Our data seem to indicate, however, that the difference in affinity might cause a different retention of antibody in the tumor. Longer half-times in the tumor are consistent with the superior imaging qualities of MN-14 when compared to NP-4 (12,13,20). Earlier studies on the uptake of antibodies with different affinity usually relied on well-counter measurements of tumor biopsy specimens. This method may have advantages with respect to the accuracy of the absolute uptake determination, but this single time-point sampling does not allow the determination of the tumor biological $T_{1/2}$.

The significantly shorter tumor half-times in colorectal cancer patients, when compared to other cancer types, are most likely due to their significantly shorter blood half-times. In a recent study (20), we showed that colorectal cancer patients have a tendency to clear anti-CEA antibodies quickly from the circulation (most likely a CEA-receptor-mediated clearance of immune complexes between CEA and the MAb). In contrast, Mu-9 showed a normal pharmacokinetic behavior in these patients (20), since its mucin epitope is not recognized in the circulation. We have shown that different clearance rates are most likely due to microheterogeneities in the chemical structure of the CEA produced by different cancer types (20,34-36).

The highest tumor uptake values of MAb were observed for colorectal and medullary thyroid cancer patients. Due to their longer half-times, the latter had higher mean doses when compared to most colorectal tumors, which were reflected by promising anti-tumor effects (Figure 6). Taking into account the general hypervascularity (37) and, consequently, better antigen accessibility of medullary thyroid cancer lesions, as compared to hypovascular colorectal tumors, our study may suggest that CEA antigen content is highest in colorectal and medullary thyroid cancer. Uptake in all other cancer types was found to be significantly lower, suggesting a lower CEA content, which would be in accordance with the lower CEA plasma levels generally observed in patients with these other cancer types (62).

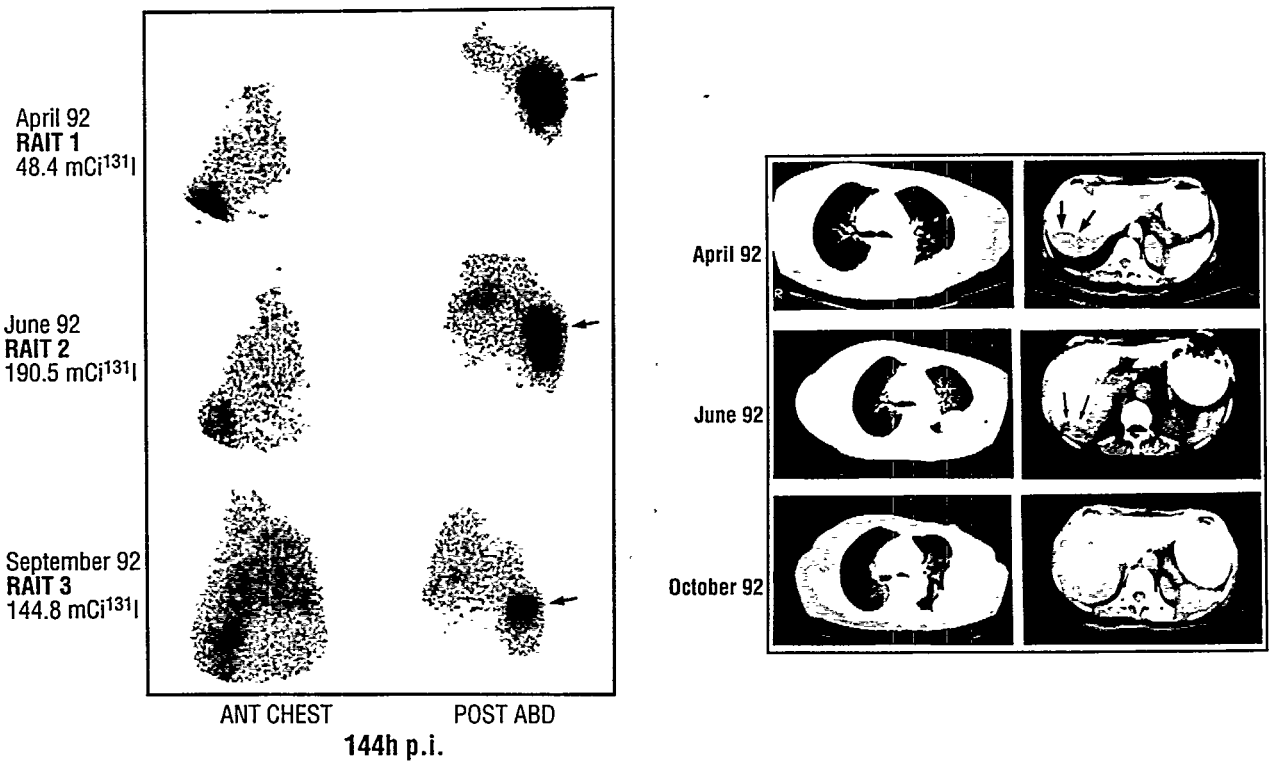

Figure 6. Targeting and therapeutic response to radioimmunotherapy with ^{131}I-MN-14 in a 72-year-old woman with metastatic medullary thyroid cancer (local recurrence in the neck, lung, pleural, and liver metastases (37)). The left panel shows the tumor targeting on the occasion of three therapy injections (144 h p.i. each). A large liver metastasis (arrow) disappeared completely one month after the third therapy injection (cf. CT, right panel), having received a total dose of approximately 65 Gy, whereas the pleural carcinosis and local recurrence progressed (total dose only 12 Gy). Plasma CEA and calcitonin dropped by approximately 60%. This patient underlines the necessity of achieving sufficiently high tumor doses in order to obtain therapeutic response in radioimmunotherapy.

Interestingly, anti-idiotypic responses, in contrast to conventional HAMA, do not seem to affect the overall biodistribution, but compromise the tumor targeting ability of the circulating antibody, most likely by blocking its antigen-binding site. This fundamental difference between classical HAMA and anti-idiotypic HAHA has recently been predicted from animal data by Pimm (38), but, to the best of our knowledge, has not yet been reported in human studies.

In summary, our study suggests that especially favorable tumor doses can be achieved in small lesions of colorectal cancer, as well as in medullary thyroid cancer, although comparably favorable conditions also may be found in other neoplasms with micrometastatic lesions. The predicted tumor doses may exceed by far the values generally obtainable with external beam radiation. Therefore, an adjuvant RAIT trial or a therapy of minimal disease in these tumor types seems to be warranted. Indeed, preclinical results in micrometastatic colorectal cancer are promising (6), and an earlier study, involving several different tumor lines in an animal model, has clearly shown the superiority of RAIT as compared to conventional chemotherapy (5).

ACKNOWLEDGMENTS

These studies were supported in part by grants from the Deutsche Forschungsgemeinschaft (DFG Be 1689/1-1/2) and the National Institutes of Health (CA39841 and CA54425).

REFERENCES

1. Goldenberg DM, Horowitz JA, Sharkey RM et al. Targeting, dosimetry, and radioimmunotherapy of B-cell lymphomas with iodine-131-labeled LL2 monoclonal antibody. J Clin Oncol 9: 548-564, 1991.
2. Press OW, Eary JF, Appelbaum FR et al. Phase II trial of ^{131}I-B1 (anti-CD20) antibody therapy with autologous stem cell transplantation for relapsed B cell lymphoma. Lancet 346: 336-340, 1995.
3. Goldenberg DM (ed.). Cancer Therapy with Radiolabeled Antibodies. CRC Press, Boca Raton, 1995.
4. Behr TM, Sharkey RM, Juweid ME et al. Phase I/II clinical radioimmunotherapy with an ^{131}I-labeled anti-CEA murine monoclonal antibody. J Nucl Med (in press), 1997.
5. Blumenthal RD, Sharkey RM, Natale AM et al. Comparison of equitoxic radioimmunotherapy and chemotherapy in the treatment of human colonic cancer xenografts. Cancer Res 54: 142-151, 1994.
6. Blumenthal RD, Sharkey RM, Haywood L et al. Targeted therapy of athymic mice bearing GW-39 human colonic cancer micrometastases with ^{131}I-labeled monoclonal antibodies. Cancer Res 52: 6036-6044, 1992.
7. Mach JP, Carrel S, Merenda C, Heumann D and Roenspies U. In vivo localization of anti-CEA antibody in colon carcinoma. Can results obtained in the nude mice model be extrapolated to the patient situation? Europ J Cancer Suppl. I: 113-120, 1978.
8. Jain RK. Determination of tumor blood flow: a review. Cancer Res 48: 2641-2658, 1988.
9. Hagan PL, Halpern SE, Dillman RO, et al. Tumor size: Effect on monoclonal antibody uptake in tumor nodules. J Nucl Med 27: 422-427, 1986.
10. Williams LE, Duda RB, Proffitt RT et al. Tumor uptake as a function of tumor mass: A mathematical model. J Nucl Med 29: 103-109, 1988.
11. Juweid M, Neumann R, Paik C et al. Micropharmacology of monoclonal antibodies in solid tumors: direct experimental evidence for a binding site barrier. Cancer Res 52: 5144-5153, 1992.
12. Sharkey RM, Goldenberg DM, Goldenberg H et al. Murine monoclonal antibodies against carcinoembryonic antigen: Immunological, pharmacokinetic, and targeting properties in humans. Cancer Res 50: 2823-2831, 1990.
13. Sharkey RM, Goldenberg DM, Murthy S et al. Clinical evaluation of tumor targeting with a high-affinity, anticarcinoembryonic-antigen-specific, murine monoclonal antibody, MN-14. Cancer 71: 2082-2096, 1993.
14. Primus FJ, Newell KD, Blue A and Goldenberg DM. Immunological heterogeneity of carcinoembryonic antigen: antigenic determinants on carcinoembryonic antigen distinguished by monoclonal antibodies. Cancer Res 43: 686-692, 1983.
15. Sharkey RM, Juweid M, Shevitz J et al. Evaluation of a CDR-grafted (humanized) anti-carcinoembryonic antigen (CEA) monoclonal antibody in preclinical and clinical studies. Cancer Res 55: 5935s-5945s, 1995.
16. Sharkey RM, Juweid M, Behr T et al. Comparison of tumor targeting with murine and

humanized anti-carcinoembryonic antigen monoclonal antibodies. Proc Am Assoc Cancer Res 86: 489 (abstract 2914), 1995.
17. Sharkey RM, Goldenberg DM, Vagg R et al. Phase I clinical evaluation of a new murine monoclonal antibody (Mu-9) against colon-specific antigen-p for targeting gastrointestinal carcinomas. Cancer 73: 864-877, 1994.
18. Weadock KS, Sharkey RM, Varga DC and Goldenberg DM. Evaluation of a remote radioiodination system for radioimmunotherapy. J Nucl Med 31: 508 -511, 1990.
19. Primus FJ, Kelley EA, Hansen HJ and Goldenberg DM. 'Sandwich'-type immunoassay for carcinoembryonic antigen in patients receiving murine monoclonal antibodies for diagnosis and management of cancer. Clin Chem 34: 261-264, 1988.
20. Behr TM, Sharkey RM, Juweid ME et al. Factors influencing the pharmacokinetics, dosimetry and diagnostic accuracy of radioimmunodetection and radioimmunotherapy of CEA-expressing tumors. Cancer Res 56: 1805-1816, 1996.
21. Wu RK and Siegel JA. Absolute quantitation of radioactivity using the buildup factor. Med Phys 11: 189-192, 1984.
22. Siegel JA, Pawlyk DA, Lee RE et al. Tumor, red marrow, and organ dosimetry for ^{131}I-labeled anti-carcinoembryonic antigen monoclonal antibody. Cancer Res 50: 1039s-1042s, 1990.
23. Pawlyk DA, Siegel JA, Sharkey RM and Goldenberg DM. Automating large-scale processing of dosimetry data. J Nucl Med 34: 160P (abstract 780), 1993.
24. Dunn RM, Juweid ME, Behr TM, Siegel JA, Sharkey RM and Goldenberg DM. An automated internal dosimetry scheme for radiolabeled antibodies. Med Phys 22: 1549-1550, 1995.
25. Snyder WS, Ford MR, Warner GG and Watson SB. 'S' absorbed dose per unit cumulative activity for selected radionuclides and organs. MIRD Pamphlet No.11. Society of Nuclear Medicine, New York 1976.
26. Cox JD, ed. Moss' Radiation Oncology - Rationale, Technique, Results. Mosby; St. Louis 1994.
27. Buchsbaum D, Khazaeli MB, Liu T, et al. Fractionated radioimmunotherapy of human colon carcinoma xenografts with ^{131}I-labeled monoclonal antibody CC49. Cancer Res 55: 5881s-5887s, 1995.
28. Maxon HR, Thomas SR, Hertzberg VS et al. Relation between effective radiation dose and outcome of radioiodine therapy for thyroid cancer. N Engl J Med 309: 937-941, 1983.
29. Sgouros G. Radioimmunotherapy of micrometastases: Side-stepping the solid-tumor hurdle. (Editorial) J Nucl Med 36: 1910-1912, 1995.
30. Gallinger S, Reilly RM, Kirsh JC et al. Comparative dual label study of first and second generation antitumor-associated glycoprotein-72 monoclonal antibodies in colorectal cancer patients. Cancer Res 53: 271-278, 1993.
31. Divgi CR, Scott AM, McDermott K et al. Clinical comparison of radiolocalization of two monoclonal antibodies (mAbs) against the TAG-72 antigen. Nucl Med Biol 21: 9-15, 1994.
32. Sung C, Shockley TR, Morrison PF, Dvorak HF, Yarmush ML and Dedrick RL. Predicted and observed effects in antibody affinity and antigen density on monoclonal antibody uptake in solid tumors. Cancer Res 52: 377-384, 1992.
33. Thomas GD, Chappell MJ, Dykes PW et al. Effect of dose, molecular size, affinity, and protein binding on tumor uptake of antibody or ligand: a biomathematical model. Cancer Res 49: 3290-3296, 1989.
34. Hernando JJ, von Kleist S and Grunert F. A repertoire of monoclonal antibodies reveals extensive epitope heterogeneity in CEA purified from neoplasms originating from different

organs. Int J Cancer 56: 655-661, 1994.
35. Chandrasekaran EV; Davila M, Nixon DW, Goldfarb M and Mendicino J. Isolation and structures of the oligosaccharide units of carcinoembryonic antigen. J Biol Chem 258: 7213-7222, 1983.
36. Thomas P, Toth CA, Saini KS, Jessup JM and Steele G. The structure, metabolism and function of the carcinoembryonic antigen gene family. Biochim Biophys Acta 1032: 177-189, 1990.
37. Juweid ME, Sharkey RM, Behr T et al. Radioimmunotherapy of medullary thyroid carcinoma with ^{131}I-labeled anti-CEA antibodies: Initial results. J Nucl Med 37:875-881, 1996.
38. Pimm MV. Possible consequences of human antibody responses on the biodistribution of fragments of human, humanized or chimeric monoclonal antibodies: a note of caution. Life Sciences 55: 45-49, 1994.

QUESTIONS

Shen: Your results are very encouraging. Have you tried to correlate tumor dose and tumor response in this group of patients?

Behr: The major problem with these patients is that they were typical patients of a phase-I/II therapy trial with lesions. It is not very surprising that you have had a hard time achieving sufficiently high tumor doses in these patients to be effective. However, we did see some correlation between tumor doses and therapeutic effects. In the patient with the liver metastasis from medullary thyroid cancer I showed, the tumor dose was approximately 65 Gy, very high, which is consistent with the therapeutic success seen. However, there were other patients with doses above 100 Gy and no therapeutic effect. This may be due to microheterogeneities in dose distribution or other microdosimetric problems discussed earlier today

Brill: This is more a comment than a question. The effect of HAMA decreased tumor uptake and increased blood clearance in your study, and this resulted in a bigger tumor to background ratio, and improved diagnostic image quality. The FDA has been very concerned about HAMA in diagnostic MoAb studies, which doesn't seem reasonable. Our experience with HAMA positive patients in diagnostic retreatment studies suggests it is a red herring in those situations, and is only important in therapy studies where it results in lower tumor doses, as you have shown.

BETA-CAMERA AND PINHOLE-SPECT IMAGING FOR DOSIMETRY APPLICATIONS

Ljunggren K[1], Tagesson M[1], Erlandsson K[1], Aas AT[2], Salford LG[2] and Strand S-E[1]
[1]Radiation Physics and [2]Neurosurgey Dept. Lund University
S-22185 Lund, SWEDEN

ABSTRACT

Animals inoculated with gliomas in the brain and treated with intratumoral injection of Tl-201 have previously shown promising results concerning survival. This study was undertaken to investigate methods for estimating the dosimetry in these animals. Two high-resolution techniques were used, beta-camera imaging and pinhole SPECT. Pinhole SPECT was used for detection of the administered Tl-201 activity in vivo. After sacrifice, the sliced rat brain was imaged with the beta camera. Histopathological examinations of the brain slices were compared to the beta-camera images. Treated animals survived several days longer than the controls. Necrosis was found in all the Tl-201-treated brain tumors, and tumor sizes were decreased. In some cases, the tumors had totally disappeared. Biokinetics of the activity in the tumor gave the cumulated activity. The beta-camera activity distribution matrix was used as input for calculating the absorbed dose rate. We have shown that these techniques are useful for determining the dosimetry in small laboratory animals undergoing radionuclide therapy.

INTRODUCTION

In evaluating new methods for treatment of tumors with radionuclides, preclinical evaluation must be done in animals. For evaluation of the therapeutic effect, dosimetry must also be determined. In this study we have explored two high-resolution techniques, beta-camera imaging and pinhole SPECT, to determine quantitative activity data for dosimetry calculations. Intratumoral Tl-201 therapy of Fisher 344 rats with RG62 glioma tumor, reported earlier by Sjöholm et al. (1), showed prolonged life compared to a control group. A prolonged activity retention was identified in the tumor region. Because of poor spatial resolution with ordinary scintillation camera imaging, we used pinhole SPECT, which gave information about the distribution of Tl-201 in the brain and also information about the dynamics. The beta camera provided the high-resolution (500 μm) imaging needed for detailed dosimetry, for comparison with histopathological examination.

MATERIALS AND METHODS

Tumor Model

Fisher 344 rats with developed malignant RG2 gliomas were stereotactically administered Tl-201 chloride (5 MBq each time) intratumorally on day 15, 17 and 19 after inoculation. At day 16, 18 and

20, one rat was imaged using pinhole SPECT. The brain was removed after imaging and was stored in formalin for histopathological examination. At day 16, one rat was sacrificed for beta-camera imaging, and one more rat was sacrificed at day 18. The brain was cut in two parts, each part containing half the tumor, one part for beta-camera imaging and the other dedicated for histopathological examinations was stored in formalin.

Beta-camera System

The "beta camera" (2-5) is a position sensitive light detector (Photec Ltd, UK) based on a photocathode with microchannel plates and a resistive anode adapted with a plastic scintillator (0.3 mm NE102A). The light from the scintillator is collected in a manner similar to conventional scintillation (Anger-type) cameras. The biological sample containing the radioactivity is mounted on the plastic scintillator. The scintillation light produced (427 nm), as a result of the β-particle interaction in the scintillator, is converted to an amplified electron pulse impinging on a resistive anode. The analog signal output from the resistive anode is digitized and collected event by event in an image memory.

Pinhole SPECT

Pinhole SPECT is a method that has been receiving increasing attention in the past few years for studying radiopharmaceutical distribution in small laboratory animals (6-10). Pinhole SPECT was performed here with a DIACAM scintillation camera and lead pinhole inserts of 2 or 4 mm diameter. The distance of the pinhole to the camera crystal was 20 cm, and to the center-of-rotation (COR), 3.5 cm. Ninety SPECT projections were acquired in 64x64 matrices over 360° rotation. The acquisition time was 40 s per angle and the energy window was 20% for 70 keV and 30% for 167 keV. The number of counts per projection was 5000-6000 and a total of 450,000 counts was collected.

The projection data were corrected for the geometric and intrinsic efficiency variations using a Co-57 flood source study. Correction was also made for the COR-shift but not for attenuation and scatter. Tomographic images were reconstructed using cone beam-filtered backprojection (11).

Dosimetry Calculations

Using the activity map from the beta-camera image, the dose rate in that slice can be calculated (12). The activity map was aligned with a density map of unit density. Decays of Tl-201 (13) were sampled according to the content of each voxel in the activity map. Only electrons were considered. The electrons were followed using a simple semi-Monte Carlo technique assuming the continuous slowing down approximation (CSDA). The electrons were allowed to deflect according to a multiscattering theory, based on an energy-dependent Gaussian mass scattering power (14). They were followed down to 12 keV, and then were considered to be locally absorbed. For macroscopic dosimetry, biokinetic data from pinhole SPECT and beta-camera images were used. S values for different tumor geometries were needed. Stabin, in the MIRDOSE software (15) provides S values for small spheres, down to a sphere of 0.26 cm radius (0.01 g), for many radionuclides. These S values assume that the activity is uniformly distributed throughout the sphere, and apply photon and electron absorbed fractions for the whole sphere. Due to the need to estimate S values for spheres smaller than those provided in MIRDOSE, we estimated the S values with our Monte Carlo program. The total tumor geometry is approximately spherical as found in the beta-camera imaging.

RESULTS

Beta-camera Images

In all beta-camera images, the Tl-201 activity was concentrated in the tumor tissue. A good correlation between the Tl-201 activity distribution and histopathology was found. Similar results were found for other metastasized tumors indicating a flow of the Tl-201 activity from the primary tumor, where the activity was injected, to the metastasis.

Figure 1 is a histological image of one of the brain slices and Figure 2, the corresponding beta-camera image. It is clearly shown that the activity is found both in the primary tumor, where the activity was injected, as well as in a large metastasis distant to the injection site. Notable is the extremely low activity in the rest of the brain.

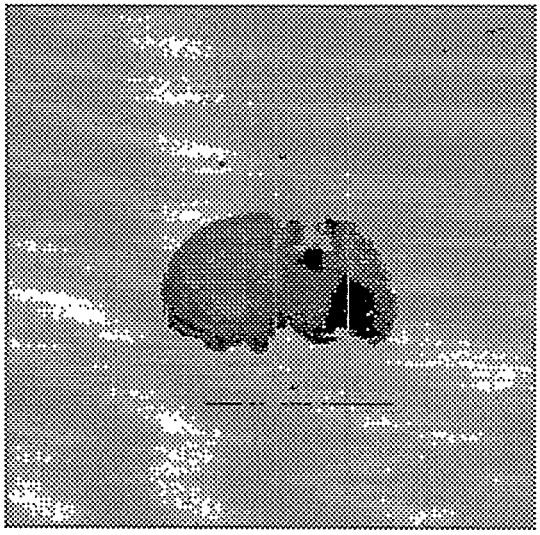

Figure 1. Histological slice (50 μm) of the brain where the primary tumor and the larger metastasis are shown.

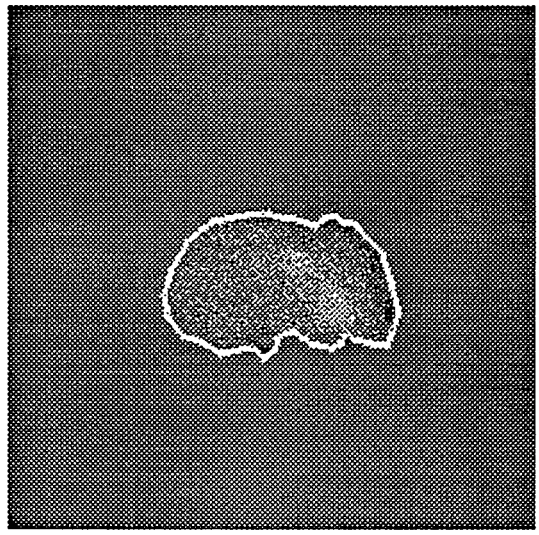

Figure 2. Beta-camera image of the brain slice in Figure 1, showing Tl-201 activity in the tumor areas. Note the low activity in nontumor tissue.

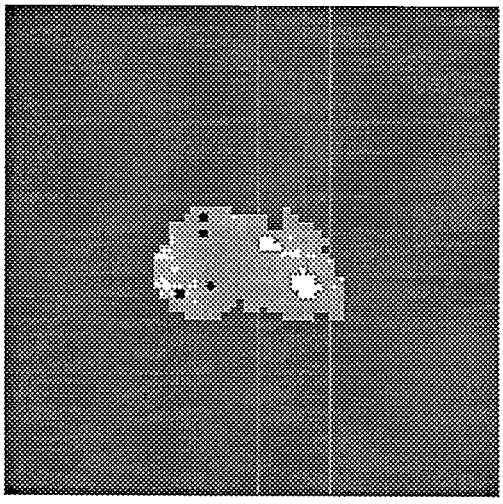

Figure 3. Absorbed dose-rate distribution in brain slice containing tumor.

Dosimetry

The dose rate from the activity distribution in Figure 2 is shown in Figure 3. The main contribution to the absorbed dose is from the conversion and Auger electrons, whereas the photon dose is negligible.

In Figure 4, S values (tumor-to-tumor) for Tl-201 in spheres of different diameters are compared with data from the MIRDOSE 3 program (15). Our simulations and the MIRDOSE 3 values agree well for larger tumors where data were available.

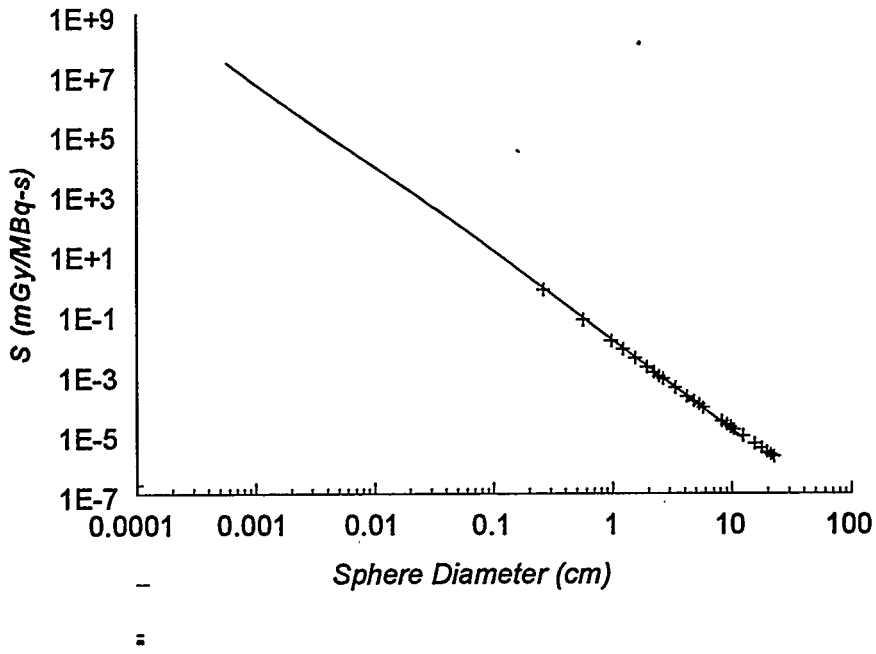

Figure 4. S values for Tl-201 uniformly distributed in spheres (- this work, + MIRDOSE 3).

Pinhole SPECT

The pinhole-SPECT method displayed the activity distribution in the tumor with a resolution of 5 mm. Figure 5 shows a 3-D representation of the Tl-201 activity distibution obtained with pinhole SPECT. Six slices obtained from one of the rat brains are shown in Figure 6. It can be seen that the activity is confined to the tumor region, whereas almost no activity is found in the normal brain tissue.

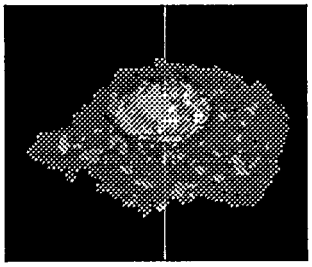

Figure 5. 3-D pinhole SPECT

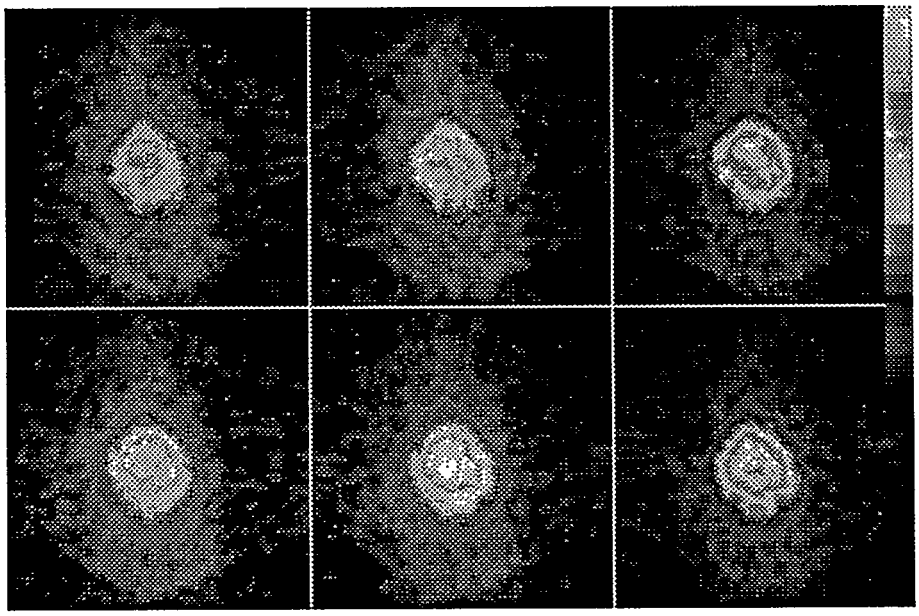

Figure 6. Pinhole-SPECT images of sagittal Tl-201 activity in glioma tumors in rat brain.

Comparison of Beta Camera to Pinhhole SPECT

Beta-camera images from the same animal as shown in Figure 6 are displayed in Figure 7. These images, with a much higher spatial resolution, verify that the Tl-201 activity is concentrated in the tumor tissue.

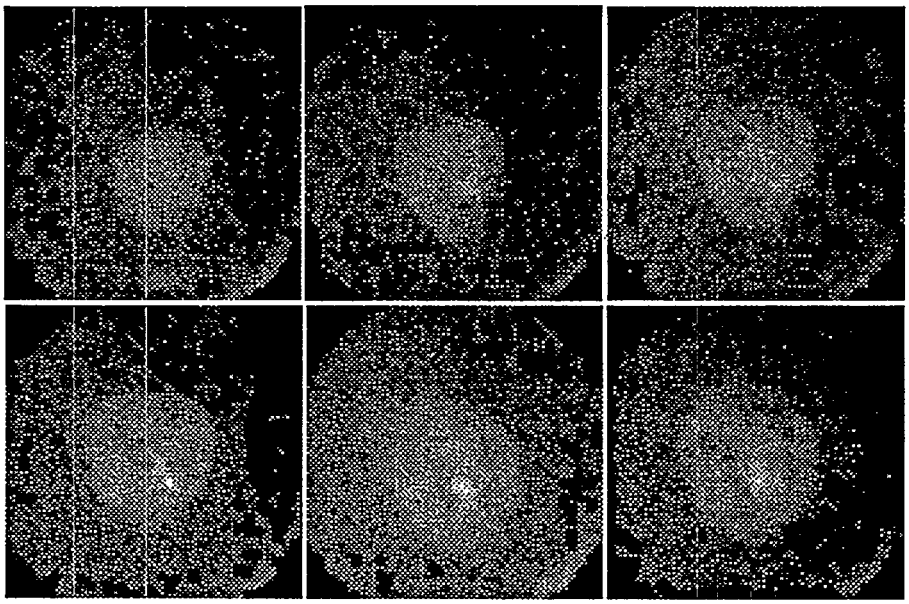

Figure 7. Consecutive beta-camera activity in sagittal slices of brain with tumor.

Tumor Absorbed Dose

Figure 8 shows the absorbed dose to spheres with different diameters as a function of cumulated activity. There is a strong dependence of the tumor dose on these two parameters. In the biokinetic studies for the actual treatments, we found that the cumulative activity was approximately 650 GBq-s. Thus for a mean tumor volume of 0.065 cm^3 (0.5 cm diameter), as found in the dissected tumors, the absorbed dose to the tumor will be 60 Gy, corresponding to 4 Gy/MBq.

SUMMARY

Therapeutic effects as a result of radionuclide therapy must be evaluated based on a proper dosimetry. For our earlier successful pilot study of the therapeutic effect of Tl-201 given intratumorally in glioma bearing rats (1), we now have explored two methods for determining the activity distribution with high-spatial resolution for small-scale dosimetry calculations. Pinhole SPECT was shown to be useful for tomographic imaging of the activity in the rat brain in vivo. For obtaining a more detailed activity distribution, the beta camera can provide supplementary imaging of tissue slices with a resolution of 500 μm.

Using these techniques, it is possible to obtain the input data needed for absorbed dose calculations. In the present study with Tl-201, absorbed doses to tumors in the order of 60 Gy were calculated. These absorbed doses seem to be sufficient to get a therapeutic effect in these animals. In fact, our data indicate that absorbed doses in the order of some tenths of a Gy can eliminate tumors. The high therapeutic effect of Tl-201 in our tumor model might be explained due to numerous

emissions of low-energy Auger electrons and Tl-201 activity localization in cell nuclei.

In conclusion, we have found that the pinhole SPECT and beta-camera techniques are useful in determining absorbed doses in small laboratory animals undergoing experimental radionuclide therapy.

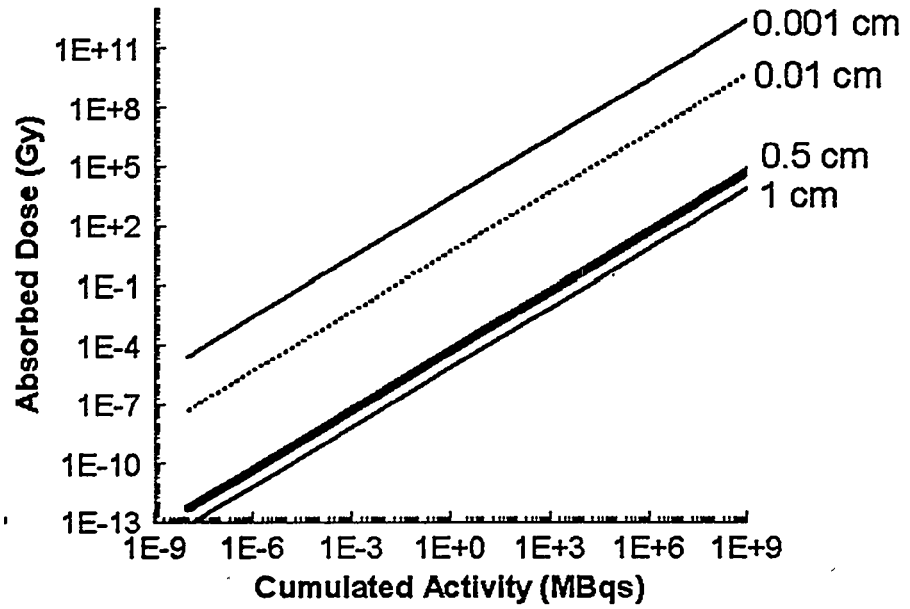

Figure 8. Absorbed dose for uniformly distributed ^{201}Tl activity in spheres with different diameters as a function of cumulated activity.

ACKNOWLEDGMENTS

The authors wish to express their thanks to Catarina Blennow and Kerstin Sturesson for helping us with the clinical material and to Prof. Arne Brun for histopathological examination.

This work was supported by Swedish Cancer Foundation 2353-B95-09XAB, Gunnar, Arvid and Elisabeth Nilsson's Foundation, Swedish Natural Science Research Council F-AA/FU 1621-313, B. Kamprad's Foundation, John and Augusta Persson Foundation, Royal Physiographic Society of Lund, Faculty of Medicine, Lund University and Lund University Hospital funds.

REFERENCES

1. Sjöholm H, Ljunggren K, Adeli R, Brun A, Ceberg C, Strand S-E and Salford LG. Necrosis of malignant gliomas after intratumoral injection of Tl-201 in vivo in the rat. Anti- Drugs 6:109-114,1995.
2. Ljunggren K and Strand S-E, Development of a digital imaging detector based on microchannel plates for biomedical samples emitting uncharged and charged particles. Nucl Instr Meth A273:784-786,1988.

3. Ljunggren K and Strand S-E. Beta camera for static and dynamic imaging of charged-particle emitting radionuclides in biologic Samples. J Nucl Med 31:2058-2063, 1990.
4. Ljunggren K, Strand S-E, Ceberg CP, Sjöholm H, Elmqvist D, Brun A and Salford LG. Beta camera low activity tumor imaging. Acta Oncologica 32:869-872, 1993.
5. Ljunggren K and Strand S-E. Reduction of noise in the Beta camera for low activity applications. IEEE Trans Nucl Sci 41:1666-1669,1994.
6. Strand S-E, Ivanovic M, Erlandsson K, Weber DA, Franceschi D, Button T and Sjögren K. High resolution pinhole SPECT for tumor imaging. Acta Oncologica 32:861-867,1993.
7. Strand S-E, Ivanovic M, Erlandsson K, Franceschi D, Button T, Sjögren K and Weber DA. Small animal imaging with pinhole single-photon emission computed tomography. Cancer 73:981-984, 1994.
8. Palmer J and Wollmer P. Pinhole emission computed tomography: method and experimental evaluation. Phys Med Biol 35:339-350, 1990.
9. Weber DA, Ivanovic M, Franceschi D, Strand S-E, Erlandsson K, Franceschi M, Atkins HL, Coderre JA, Susskind H, Button T and Ljunggren K. Pinhole SPECT: An approach to in vivo high resolution SPECT imaging in small laboratory animals. J Nucl Med 35:342-348,1994.
10. Li J, Jaszczak RJ and Coleman RE. Quantitative small field-of-view pinhole SPECT imaging: Initial evaluation. IEEE Trans Nucl Sci 42:1109-1113, 1995.
11. Feldcamp LA, Davies LC, and Kress JW. Practical cone-beam algorithm. J Opt Soc Am 1:612-619,1984.
12. Tagesson M, Ljungberg M and Strand S-E. Transformation of activity distributions in quantitative SPECT to absorbed dose distributions in a radionuclide treatment planning system. J Nucl Med 35:123, 1994.
13. Snyder WS, Ford MR, Bernad SR, Dillman LT, Eckerman KF, Poston JW and Watson SB. ICRP 38: Radionuclide Transformations, Energy and Intensity of Emissions, Pergamon Press, New York,1983.
14. Berger MJ, Monte Carlo calculation of the penetration and diffusion of fast charged particles. in: Methods in Computational Physics, edited by S Fernbach and M Rotenberg Vol 1:135-215, Academic Press, New York, New York, 1963.
15. Stabin M. MIRDOSE - the personal computer software for use in internal dose assessment in nuclear medicine. J Nucl Med 37:538-546, 1996.

COMPARISON OF 3D TUMOR DOSE DISTRIBUTIONS FOR CC49 AND 17-1A MONOCLONAL ANTIBODIES

Roberson PL[1] and Buchsbaum DJ[2]
[1]University of Michigan, Ann Arbor, MI 48109
[2]University of Alabama at Birmingham, Birmingham, AL 35233

ABSTRACT

A study of three-dimensional (3D) tumor uptake has been performed for 20 tumors at 5 time points postinjection for a 11.1 MBq (300 μCi) i.p. injection of ^{131}I-labeled CC49 monoclonal antibody (MoAb) in athymic nude mice bearing s.c. LS174T human colon cancer xenografts. Serial section autoradiography and computer reconstruction of the 3D activity distributions were used. This data set was compared to previously reported data for 17-1A MoAb for the same tumor model. CC49 is a second generation MoAb reactive with the TAG-72 mucinous antigen and with an affinity of 1.6×10^{10} M^{-1}, compared to 0.7×10^{8} M^{-1} for 17-1A binding to a 30-41 kDa cell surface glycoprotein. Consistent with extracellular binding and higher affinity, uptake for CC49 was significantly higher than for 17-1A. The CC49 uptake curve initially increased and remained at levels above 20% of injected dose per gram (ID/g) for more than 11 days, compared to the 17-1A curve which reached a bound MoAb maximum at day 4 of 13% ID/g, followed by a steady decline. Dose-rate distributions were highly variable and time dependent in both systems. The 17-1A tumor uptake was concentrated in the highly vascularized regions at early times, slowly diffused to poorly vascularized regions, but ultimately declined in the highly vascularized regions. With the CC49 extracellular binding and increased affinity, large uptake concentrations were observed even at later time points. However, tumor surface dose rates were lower than interior dose rates at later times. This data was used to test the hypothesis that higher affinity results in significantly increased dose rates and total doses at the sites with highly vascularized, rapidly proliferating cells. Results were correlated with spatial and time dependent effective dose calculations. A radially dependent dosimetry model was used to test the hypothesis, and to estimate the relative advantage of the higher affinity antibody. The dominant dosimetric effect was the dose-rate nonuniformity. The higher dose rates experienced by tumors in the CC49 compared to the 17-1A experiments were predicted to be relatively less efficient per unit dose in achieving cell kill.

INTRODUCTION

The advantage of increasing affinity for monoclonal antibodies is to increase the target-to-normal-tissue ratio of radionuclide uptake. It is assumed that an increased uptake translates to improved therapy. Questions arise concerning the distribution of uptake and the relative increase in therapeutic advantage. Factors affecting the therapeutic advantage include nonuniformity of uptake,

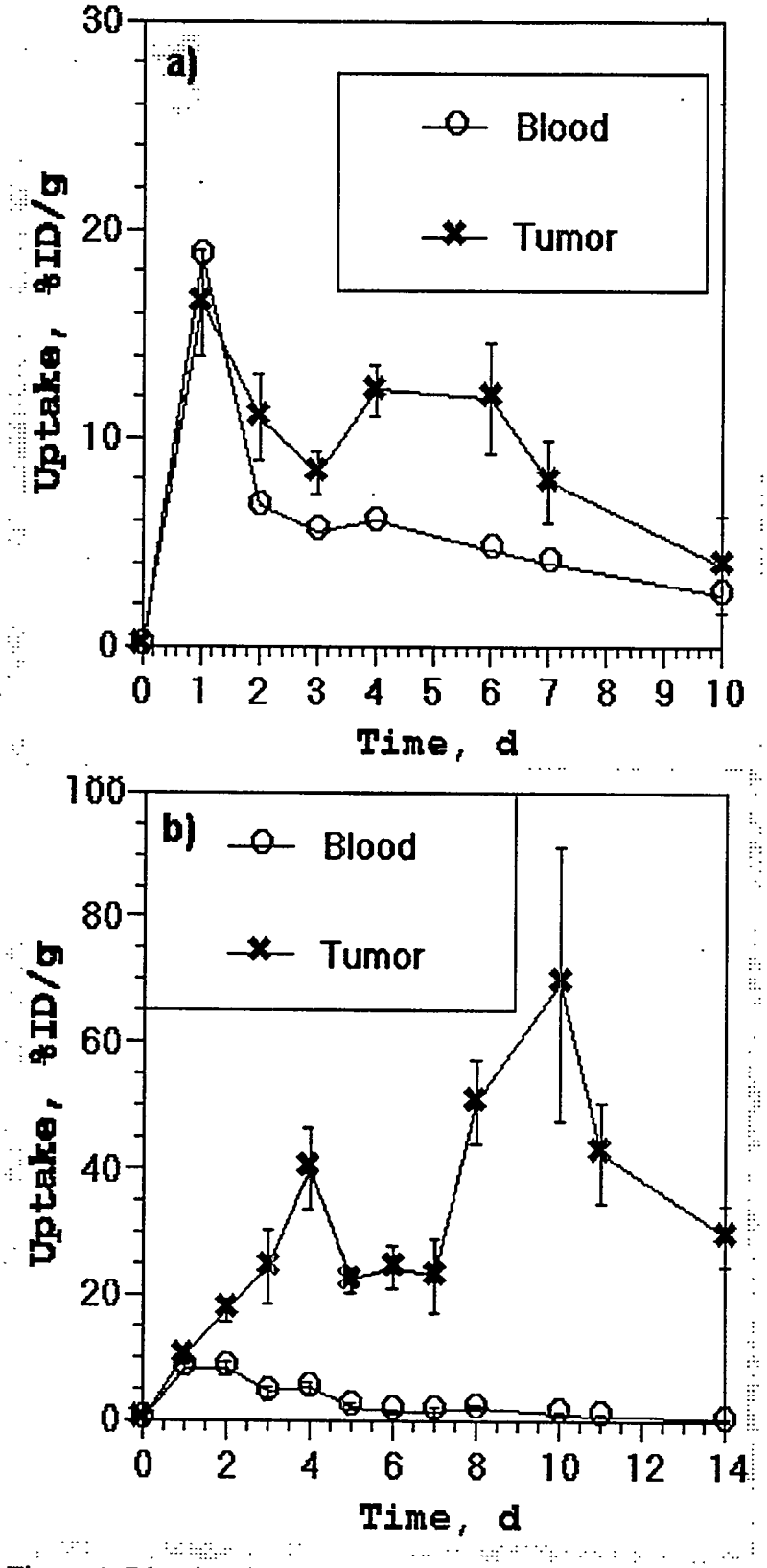

Figure 1. Blood and tumor uptake for 11.1 MBq (300 μCi) injection of ^{131}I-labeled MoAbs a) 17-1A and b) CC49. Uptake is in units of percent injected dose per gram.

radionuclide properties, time history of uptake, tumor architecture and tumor response to radiation.

The calculation of average dose to tumor for radioimmunotherapy is of limited utility because of the many factors affecting therapeutic advantage. Prediction of outcome can help design experimental regimens and provide a better chance of clinical success. Comparisons of therapy outcome are not expected to correlate simply with dose, but may be correlated with an effective dose. An effective dose was defined as a corrected value representing the appropriate dose if outcome were a simple function of dose. Effective doses are more useful as predictive estimates of outcome for comparative therapy regimens, rather than as separate, unique numbers to be attached to each treatment.

Here, we compared experiments performed with two ^{131}I-labeled MoAbs with different uptakes and dose nonuniformities. The posed question was: Is the apparent dosimetric advantage of the higher affinity CC49 antibody over the 17-1A antibody sustained under more thorough analysis?

MATERIALS AND METHODS

Athymic nude mice bearing subcutaneous LS174T human colon cancer xenografts were given i.p. injections of 11.1 MBq (300 μCi) ^{131}I-labeled 17-1A or CC49 MoAb. Tumors averaged approximately 10 mm in diameter and 0.5 g in mass. Tumors resected at 1,3,4,7 and 10 days postinjection (17-1A) or 3,4,7,10 and 11 days post-injection (CC49) were used for 3D analysis. Measurements for blood and tumor uptake are presented in Figure 1. Additional

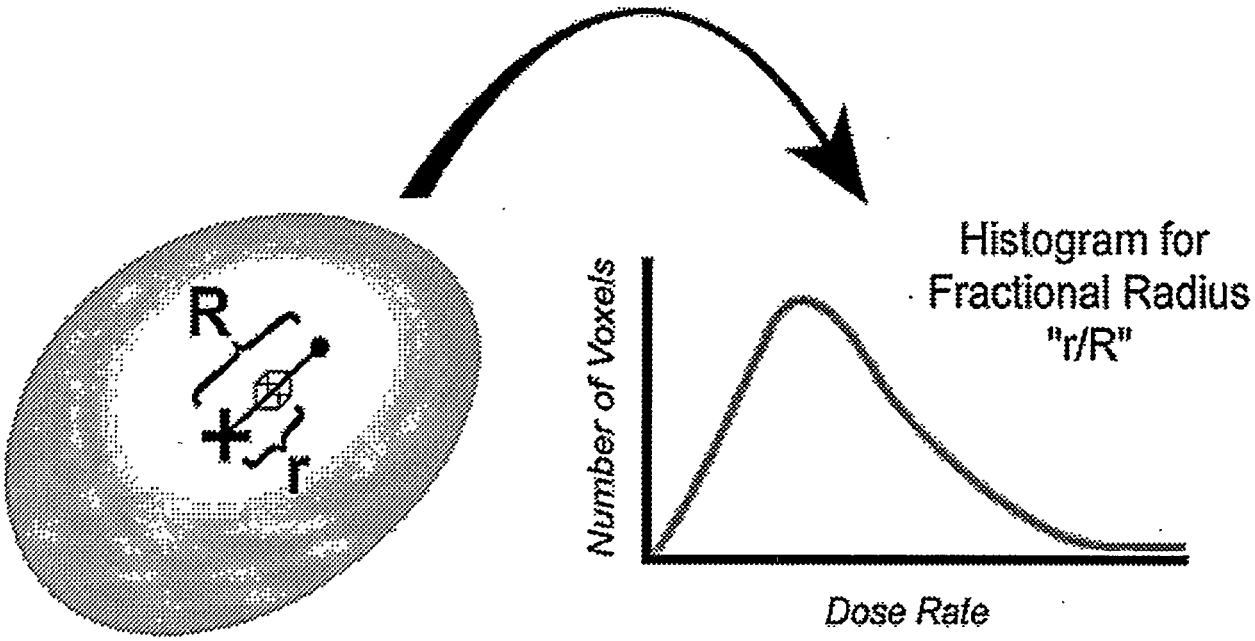

Figure 2. Derivation of radial dose-rate volume histograms from a 3D dose-rate distribution.

experimental details are reported elsewhere (1,2).

Monoclonal antibody 17-1A binds to a glycoprotein on the cell surface, and has a relatively low affinity (0.7×10^8 M^{-1}). It is internalized and the label is catabolized and cleared more rapidly (3). Monoclonal antibody CC49 has a higher affinity (1.6×10^{10} M^{-1}) and binds to the mucinous antigen TAG-72, which is secreted into the extracellular space (4).

Dosimetry

Three-dimensional activity density distributions were determined using serial section autoradiography. Sections cut per tumor varied between 15 and 30 at intervals from 100 μm to 500 μm, depending on tumor diameter. Each section was 32 μm thick. The film was calibrated for activity density, using an injection standard. Film data was read on a laser densitometer at 100 μm or 125 μm resolution. Each section was converted to two-dimensional activity density data. Surface and internal structures were used to align the sections to form a 3D activity density distribution. Activity density values between measured planes were calculated using linear interpolation. The activity density data were stored in 3D matrices with voxel sizes between 100 μm and 250 μm, depending on tumor size. A point kernel for ^{131}I (5) was used to generate a voxel kernel for each voxel size. Three-dimensional dose calculations were performed by folding the voxel kernel with the activity density matrix using fast-Fourier analysis. Additional information is reported elsewhere (6,7,8).

Summing reconstructed 3D tumor distributions is not well defined because each tumor has a unique architecture. A dominant characteristic of the LS174T xenograft data was the difference between uptake histories at the surface and interior of the tumors. This was attributed to the vascularization properties of the tumor type. To help standardize and average the data set while retaining essential data characteristics, the 3D dose distributions were converted into radial histograms. As illustrated in Figure 2, for each voxel, a path was followed from the tumor center of mass, passing through the voxel, to the tumor surface. A fractional radius was defined as the distance

from the center to the voxel divided by the distance from the center to the surface. The calculated dose rate for that voxel was added to one of 30 fractional radii. The result was a series of differential dose-volume histograms, each representing a tumor radius (8).

The space-time dependence of the dose rate was approximated using the radial histogram data. Data for each tumor was normalized to the average activity per gram from the uptake curve (Figure 1) for its time postinjection and represented an independent measurement of the local dose-rate nonuniformity. The radial histograms for each time point were averaged to yield a representative dose-rate nonuniformity. The space-time dependent description was represented by the uptake curve augmented by the dose-rate nonuniformity histograms. For any time, the activity density was taken from the uptake curve and the dose-rate nonuniformity was taken from the histograms. For each radius, the volumes with the highest (lowest) dose rate were matched with the like volumes with the highest (lowest) dose rates at other times (approximation of maximum heterogeneity).

Effective Dose

Calculations for the effective dose are described briefly. A more detailed description appears elsewhere (8). The effective dose, D_{eff}, was defined as the equivalent uniform absorbed dose required to produce the same fractional cell survival, S, as for a linear dose response with coefficient α:

$$D_{eff} \equiv 1/\alpha \ \ln(S). \tag{1}$$

For a varying dose rate,

$$S(t) = \frac{1}{V} \int_V \exp[-\alpha \ D(\vec{r},t) \ RE(\vec{r},t)] d^3r. \tag{2}$$

$$RE(\vec{r},t) = 1 + \left(\frac{2\int_0^t R(\vec{r},t')[\int_0^{t'} R(\vec{r},t'')\exp(-\mu(t'-t''))dt'']dt'/(\alpha/\beta)}{D(\vec{r},t)}\right), \tag{3}$$

where the formula for relative effectiveness was taken from Millar (9) and

$$D(\vec{r},t) = \int_0^t R(\vec{r},t')dt'. \tag{4}$$

$R(\vec{r},t)$ is the local dose rate as a function of time, μ is the cell repair constant, and α and β are parameters of the linear-quadratic model. The 3D spatial dependence of $R(\vec{r},t)$ was represented by the histograms at each radius. The time dependence was included by assigning a local time interval to each set of averaged histograms representing a time point postinjection. The integrals used to calculate the dose distributions from the dose-rate distributions assumed the approximation of maximum heterogeneity.

The effects of hypoxic and necrotic cells on the effective dose were estimated. The dependence of the oxic, hypoxic and necrotic fractions on vascular density was calculated assuming local equidistant blood vessels and nominal distances from the nearest blood vessel for hypoxic and necrotic regions to form. The average radial dependence of vascular density was assumed equal to the uptake at day 1 postinjection for the low affinity antibody (17-1A), as verified using H-E staining (6). The normalizations of the radial dependences of the tissue fractions were constrained to match the measured average fractional volume of necrotic tissue (30%). This yielded a hypoxic fraction of 10%. The linear-quadratic parameters were converted to α_o, β_o and α_H, β_H for oxic and hypoxic subpopulations. The ratio of oxic to hypoxic parameters were set to reproduce an oxygen enhancement ratio of 2, appropriate for low dose rates (10). The total S value was the weighted sum of the oxic and hypoxic S values.

Cell proliferation was assumed to be exponential. The S value was multiplied by $\exp[(\ln 2)t/t_d]$, where t_d was the tumor volume doubling time.

Parameters used in the calculation were $\alpha = 0.3$ (11), $\alpha/\beta = 25$ (12), and $\mu = 0.46\ h^{-1}$ (11). The tumor doubling time (t_d=3.4 d) was chosen to reproduce the observed LS174T regrowth doubling time delay for a 6 Gy ^{60}Co exposure of 15±1 day (1). This value was consistent with the value measured by Leith et al. (13) for LS174T of 3.3 d. The oxic and hypoxic parameters were determined to reproduce the fractional cell loss for the ^{60}Co exposure.

RESULTS

For 17-1A, the tumor uptake reached an early maximum (Fig. 1a), primarily representing free antibody near well-vascularized regions. The second maximum represented the effects of binding with the cell-surface antigens, which slowly clears as the antibody dissociates from the antigen site or is internalized, liberating the ^{131}I from the antibody. The higher affinity CC49 displayed a greater and more persistent uptake (Figure 1b). The tumor uptake was large compared to blood levels, initially rising and experiencing sustained levels above 20% ID/g.

Radial distributions representing the mean of the radial histograms are presented in Figure 3 for (a) 17-1A and (b) CC49. For 17-1A the uptake was initially concentrated at the tumor surface. The activity slowly diffused to the tumor center. At later times the uptake in the surface regions was either reabsorbed into the blood (washed out) or diluted by tumor regrowth in the well vascularized regions. For CC49, the uptake was consistently more concentrated at the tumor center. The radial distributions included the loss of energy external to the tumor, primarily appearing as lower dose rates at the tumor surface.

Doses and effective doses (Table 1) were calculated in the order of increasing model complexity to help judge the significance of the applied corrections. The simplest calculation used the area under the uptake curve to calculate the activity-time per unit mass and assumed only local deposition (uniform isotropic model from the Medical Internal Radiation Dose formalism (14)). The uncertainty quoted for the uniform isotropic model was estimated from the standard deviations of tumor uptake measurements (see Figure 1). The space-time dependence of the dose rate was integrated to calculate the total average dose. The difference between the uniform isotropic model calculation and the space-time dependent model calculation of average tumor dose was due to energy leaving the tumor. Neither of these calculations was expected to correlate with therapy outcome.

The effect of dose nonuniformity was estimated using Equations 1 through 4, assuming a uniform

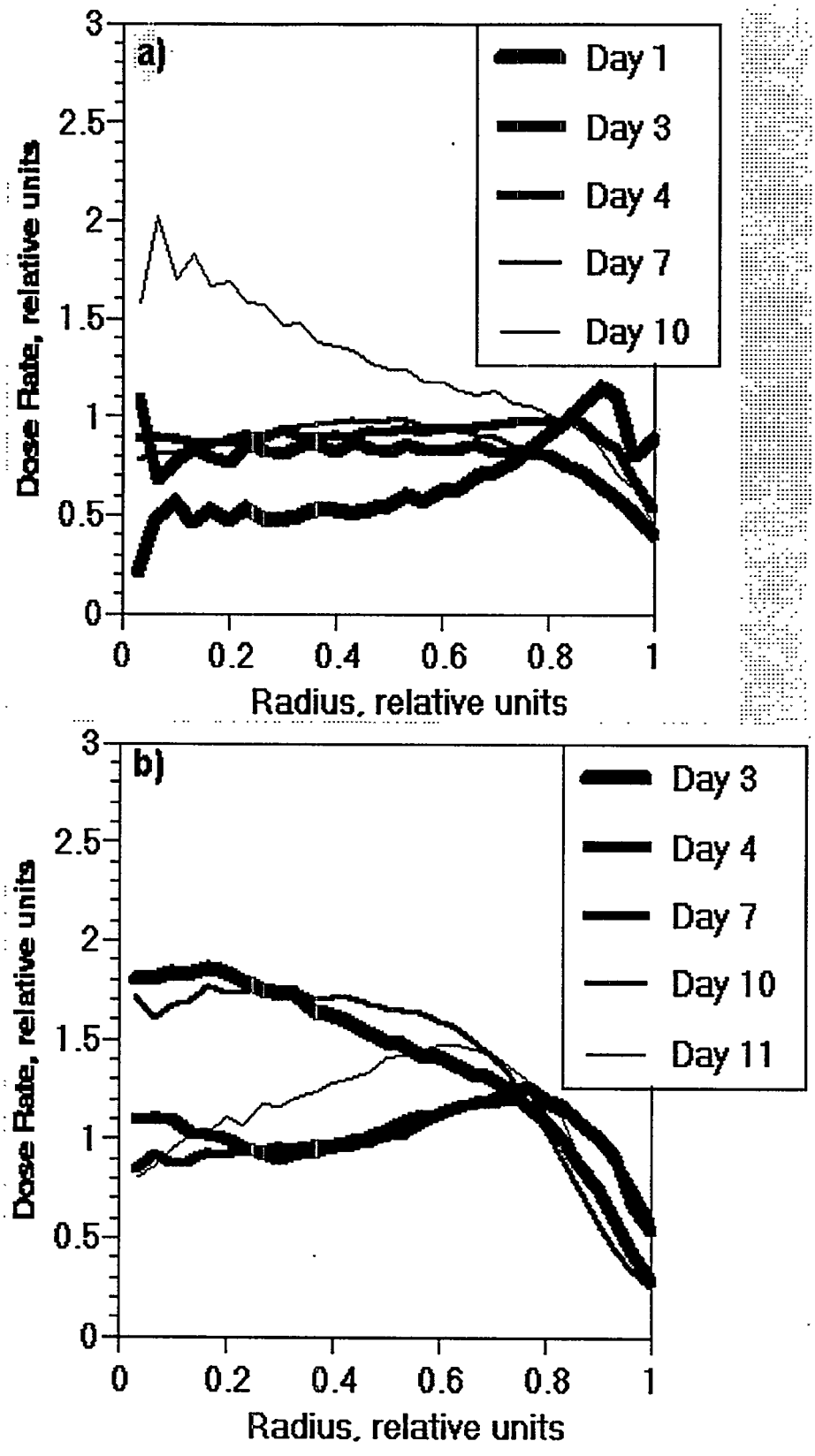

Figure 3. Radial dose-rate distributions for an 11.1 MBq (300 μCi) injection of ^{131}I-labeled MoAbs a) 17-1A and b) CC49. Curves are normalized to unit average dose rate assuming local dose deposition.

viable cell density. The result was a large loss in effective dose compared to the average dose. Also, the higher doses for CC49 were relatively less efficient given the dose nonuniformity. The calculated effective doses including cell proliferation assumed tumor cure as the endpoint (minimum fraction of viable cells and maximum effective dose, see Figure 4). Effective dose values are lower because a portion of the dose rate produced cell loss that compensated for cell proliferation and all dose deposited after the fractional cell survival minimum was disregarded. The calculations including cell status recognize that the tumors have a large contribution of necrotic tissue mainly in the tumor interior. However, the effective dose values were relatively unaffected by cell status. Dose, effective dose and cell loss curves are presented in Figure 4 for the complete calculation.

The ratios of doses for CC49 compared to 17-1A (last column, Table 1) were greater than a factor of four. However, the ratios of effective doses were less than two. The dominant effect was the reduction in effective dose due to the nonuniform dose distributions, with the higher doses being relatively less efficient. That is, for the same dose nonuniformity, the higher average dose is less efficient. Of lesser significance

is the difference due to the specific 3D dose distributions, where the 17-1A distribution had a slight advantage due to the relatively higher dose rates per unit uptake at the tumor surface (compare Figure 3a to 3b).

Table 1
Dose and Effective Dose

Dose Model	17-1A Dose, Gy	CC49 Dose, Gy	Ratio CC49/17-1A
Uniform/Isotropic	20.8 ± 1.4	102 ± 9	4.9
3D (energy loss)	17.0	86.9	5.1
Dose Nonuniformity (α=0.3 Gy^{-1}, α/β=25 Gy)	11.3*	19.7*	1.7
Proliferation (t_d=3.4 d)	5.1*	8.4*	1.6
Cell Oxygenation Status	5.3*	7.9*	1.5

* Effective Dose

The proliferation parameter (tumor doubling time) was determined from single fraction ^{60}Co experiments. For a 6-Gy fraction, tumor doubling time was chosen to reproduce the measured value of 15±1 d (1). The doubling time for 11.1 MBq (300 μCi) injection of 17-1A was 15±3 (1) compared to the model calculation of 22 d. The calculation for CC49 resulted in a doubling time of 30 d. A therapy experiment using an injection of 22.2 MBq (600 μCi) ^{131}I-labeled CC49 resulted in an initial doubling time of 20 d (2). However, average tumor growth rates were slower than for controls, yielding a mean doubling time of approximately 27 d. The proliferation model would require some modification to reproduce the outcomes of these therapy experiments for both 17-1A and CC49. However, results for the comparison between MoAbs are reasonably representative. The assumption most likely requiring modification for improved comparison to outcome is constant exponential proliferation.

DISCUSSION

The uptake for MoAb 17-1A was more concentrated at the tumor surface compared to the CC49 uptake. This was attributed to the type and location of the targeted antigen sites. The 17-1A uptake better matched the pattern of vasculature at early time points and slowly diffused from high vascular (mostly surface) to low vascular (mostly interior) regions. For single tumors having a sharp discontinuity of antigen at the tumor surface, the surface dose is expected to be lower than the central doses due to energy loss. Even a homogeneous uptake will produce a surface dose of approximately one-half of the central dose (15). Surface doses were modified by the uptake distribution, but remained relatively low. However, the dominant effect on the calculations is the overall inhomogeneity of dose. The difference between the 3D distributions was approximately a 20% to 40% effect, compared to factors of two to four attributed to inhomogeneity.

The dosimetry model contains several simplistic assumptions, including validity of the linear quadratic model, dose addition to retain maximum heterogeneity, and necrotic/hypoxic tissue fractions that were not correlated with antibody uptake within each radial shell. Dose rates are

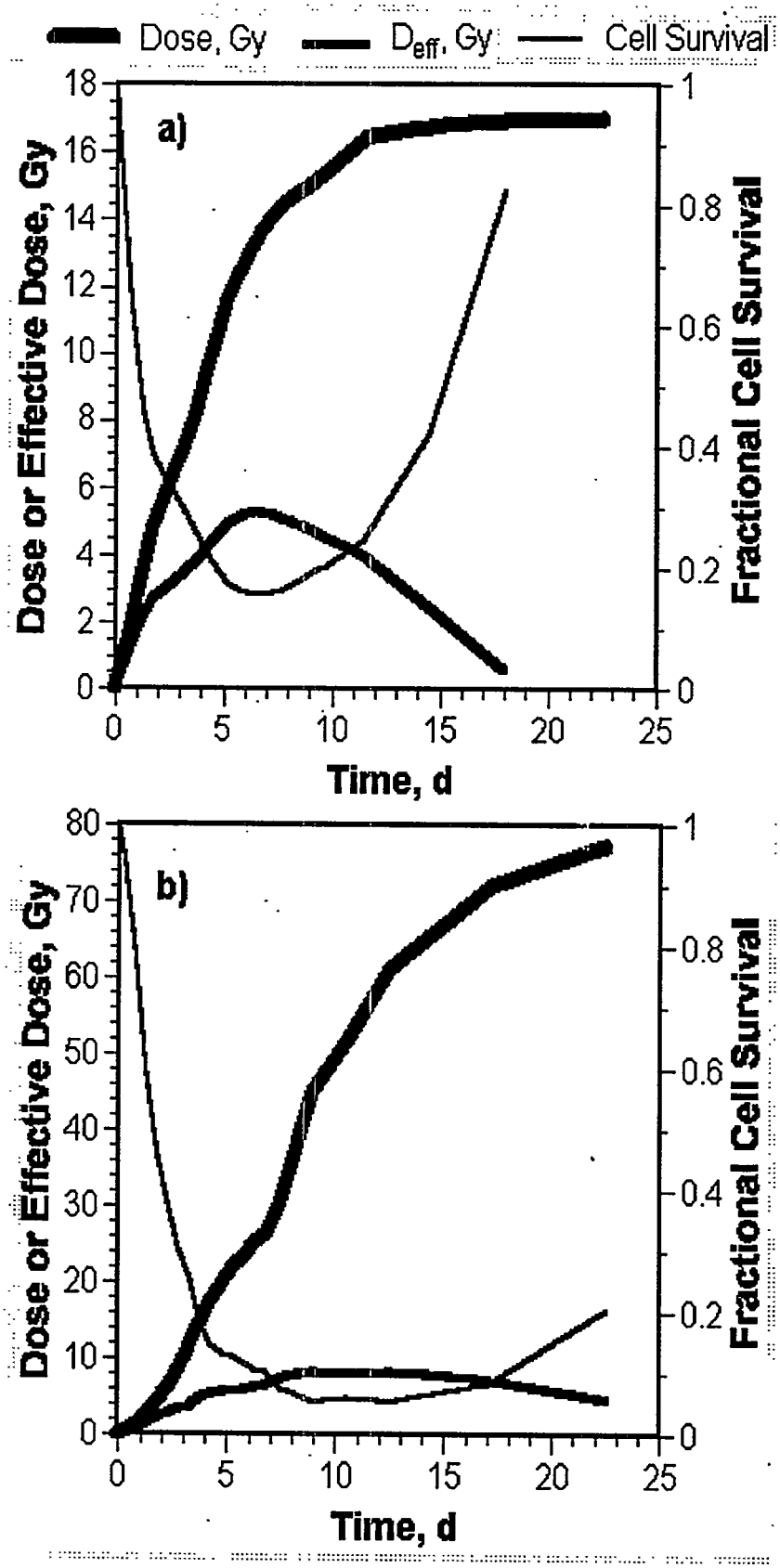

Figure 4. Dose, effective dose and fractional cell survival for an 11.1 MBq (300 μCi) injection of ^{131}I-labeled MoAbs, a) 17-1A and b) CC49.

sufficiently low for the antibody experiments that the linear-quadratic model provides only a small correction. The larger effect is for the single fraction ^{60}Co exposures, which was used to determine the tumor doubling time. The contribution to the uncertainty from the linear-quadratic model was linked with the contribution from the assumption of constant exponential proliferation, since the tumor doubling time depended on the fractional cell loss predicted by the linear-quadratic model. A model incorporating nonuniform proliferation could improve model prediction of recurrence time with experimental results.

The assumption of maximum heterogeneity is reasonable, but does contribute to uncertainty because the limits placed on probability for cure depend on the regions of least dose. Under maximum heterogeneity, the regions of least dose are matched over time. While assuming that the high and low uptake regions randomly shift from time to time is not reasonable, there is some evidence that the vascularity does change over time (16,17), changing the uptake patterns somewhat. Additional investigation of minimal dose-rate regions over time may be warranted.

The necrotic/hypoxic correlation with antibody uptake could also be important if it can be shown that the lowest dose rates are indeed in necrotic tissues. Although this appears not to be the case for CC49 (greater uptake in tumor interior), this remains an uncertainty. Confidence in this type of effective dose model would benefit from spatially correlated measurements of the antibody uptake, cell proliferation rate, antigen expression and necrotic fraction at the cellular level.

ACKNOWLEDGMENTS

The authors gratefully acknowledge Sheila Bright and Casey Jones for technical assistance and Steve Dudek, Emmanuel Christodoulou and Ming Zhu for assistance with data analysis. This work was supported by NIH grant CA44173.

REFERENCES

1. Buchsbaum DJ, Ten Haken RK, Heidorn DB, Lawrence TS, Glatfelter AA, Terry VH, Guilbault DM, Steplewski Z and Lichter AS. A comparison of ^{131}I-labeled monoclonal antibody 17-1A treatment to external beam irradiation on the growth of LS174T human colon carcinoma xenografts. Int J Radiat Oncol Biol Phys 18:1033-1041, 1990.
2. Buchsbaum DJ, Khazaeli MB, Liu T, Bright S, Richardson K, Jones M and Meredith R. Fractionated radioimmunotherapy of human colon carcinoma xenografts with ^{131}I-labeled monoclonal antibody CC49. Cancer Res(Suppl) 55:5881s-5887s, 1995.
3. Woo DV, Li D, Mattis JA and Steplewski Z. Selective chromosomal damage and cytotoxicity of ^{125}I-labeled monoclonal antibody 17-1a in human cancer cells. Cancer Res 49:2952-2958, 1989.
4. Schlom J, Eggensperger D, Colcher D, Molinolo A, Houchens D, Miller LS, Hinkle G and Siler K. Therapeutic advantage of high-affinity anticarcinoma radioimmunoconjugates. Cancer Res 52:1067-1072, 1992.
5. Prestwich WV, Nunes J and Kwok CS. Beta dose point kernels for radionuclides of potential use in radioimmunotherapy. J Nucl Med 30:1036-1046, 1989 and 30:1739-1740, 1989.
6. Roberson PL, Buchsbaum DJ, Heidorn DB and Ten Haken RK. Three-dimensional tumor dosimetry for radioimmunotherapy using serial autoradiography. Int J Radiat Oncol Biol Phys 24:329-334, 1992.
7. Roberson PL, Heidorn DB, Kessler ML, Ten Haken RK and Buchsbaum DJ. Three-dimensional reconstruction of monoclonal antibody uptake in tumor and calculation of beta dose-rate nonuniformity. Cancer 73:912-918, 1994.
8. Roberson PL and Buchsbaum DJ. Reconciliation of tumor dose response to external beam radiotherapy versus radioimmunotherapy with ^{131}Iodine-labeled antibody for a colon cancer model. Cancer Res (Suppl) 55:5811s-5816s, 1995.
9. Millar WT. Application of the linear-quadratic model with incomplete repair to radionuclide directed therapy. Br J Radiol 64:242-251, 1991.
10. Hall EJ. Radiobiology for the Radiologist. Philadelphia: J.B. Lippincott Co., 1994.
11. Fowler JF. Radiobiological aspects of low dose rates in radioimmunotherapy. Int J Radiat Oncol Biol Phys 18:1261-1269, 1990.
12. Wong JYC, Williams LE, Demidecki AJ, Wessels BW and Yan XW. Radiobiologic studies comparing yttrium-90 irradiation and external beam irradiation in vitro. Int J Radiat Oncol Biol Phys 20:715-722, 1991.
13. Leith JT, Padfield G, Faulkner L and Michelson S. Hypoxic fractions in xenografted human colon tumors. Cancer Res. 51:5139-5143, 1991.
14. Loevinger R and Burman M. A Revised Schema for Calculating the Absorbed Dose from Biologically Distributed Radionuclides. Medical Internal Radiation Dose Pamphlet No. 1, Revised. New York: Society of Nuclear Medicine, Inc., 1976.
15. Howell RW, Rao DV and Sastry KS. Macroscopic dosimetry for radioimmunotherapy: Nonuniform activity distributions in solid tumors. Med Phys 16:66-74, 1989.
16. Chaplin DJ, Olive PL and Durand RE. Intermittent blood flow in a murine tumor:

Radiobiological effects. Cancer Res 47:597-601, 1987.
17. Eskey CJ, Koretsky AP, Domach MM and Jain RK. ^{2}H-nuclear magnetic resonance imaging of tumor blood flow: Spatial and temporal heterogeneity in a tissue-isolated mammary adenocarcinoma. Cancer Res 52:6010-6019, 1992.

QUESTIONS

Shen: This is really a depth analysis using radiation biology. Have you examined heterogeneity of cell population in tumor? Do you expect any dose rate effect on α and λ in this tumor model?

Roberson: We have not examined heterogeneity of cell population. For a more complete comparison to mouse therapy experiments, we will have to study tumor regrowth phenomena, which should include the possibility of cell type heterogeneity. We have no information that would point to a dose-dependent α or λ. More investigations into tumor regrowth under antibody irradiation conditions may help to understand the results of the mouse therapy experiments.

Sgouros: Is it correct that you were able to get around the difficulty of kinetics in your autoradiography dosimetry by converting the spatial distribution of activity at each time-point to a spherical distribution?

Roberson: The dose-rate distribution was calculated for each tumor because of the requirement to perform the cross-fire dosimetry correctly. The dose-rate distributions were converted to "spherical" distributions, averaged and used with the spherical model of the oxic, hypoxic and necrotic fractions.

Behr: I think your study was powerful. However, I think, it would be more interesting and preferable to compare two different antibodies against the same epitope/antigen so that you can examine the effect of different affinity without having a few interfering factors such as internalization (as for 17-1A). Have you performed such studies, e.g. with B72.4 versus CC49?

Roberson: The difficulty of generating the extensive data base of reconstructed tumors limits the application of this technique. We work with antibodies destined for or in clinical trials. The 17-1A data was collected a few years ago. The CC49 data is our current interest.

Rao: The α and β parameters which you used in your calculations, are they experimentally determined for the cancer cell employed? If so, is it done in vitro or in vivo, for external beams or an internal radionuclide (^{131}I)? Finally, is the proliferation time which you used also determined experimentally and if so, how?

Roberson: The α/β value was taken from our in-vitro experiments. The values of α and tumor doubling time are related and were chosen to match the single fraction ^{60}Co experiment regrowth delay time. The value of α was fixed at 0.3, and the doubling time was fit to the data. The result for the doubling time was consistent with literature values for LS174T tumors.

^{90}Y DOSIMETRY IN THE NUDE MOUSE: EVALUATION OF THREE DOSIMETRY MODELS IN RELATION TO THE OBSERVED BIOLOGICAL EFFECTS IN THE RADIOIMMUNOTHERAPY OF HUMAN COLON CANCER XENOGRAFTS

Behr TM[1], Sgouros G[2], Sharkey RM[1], Dunn RM[1], Blumenthal RD[1], Kolbert K[2], Juweid ME[1], Siegel JA[1] and Goldenberg DM[1]
Garden State Cancer Center
at the Center for Molecular Medicine and Immunology[1]
Newark, NJ 07103
Department of Medical Physics[2]
Memorial Sloan-Kettering Cancer Center
New York, NY 10021

ABSTRACT

Due to the long path length of high-energy β-emitters, cross-organ radiation may become an important issue in small animal models. The aim of this study, therefore, was to evaluate three different dosimetry models in relation to observed biological effects in radioimmunotherapy (RAIT) with ^{90}Y-labeled immunoconjugates (IgG, F(ab)$_2$ and Fab) in nude mice. The maximum tolerated dose (MTD) of the ^{90}Y-labeled anti-CEA MAb MN-14 (Fab, F(ab)$_2$, and IgG), as well as the dose-limiting organ toxicities were determined in GW-39 colon cancer xenografted nude mice (s.c. or metastatic). The mice were treated without artificial support, with inhibition of the renal uptake of antibody fragments by D-lysine (1,2), with bone marrow transplantation (BMT), or with combinations of each. Blood counts, kidney and liver function parameters, histology, and tumor growth were monitored. The ^{90}Y dosimetry was calculated based on three different model assumptions: 1) taking only self-doses into account, using S factors for spheres (3); 2) correcting for cross-organ irradiation according to the model of Hui et al. (4); and 3) using actual mouse anatomy as represented by magnetic resonance imaging (MRI) with a three-dimensional internal dosimetry package (3D-ID) developed by Sgouros et al. (5). Self-doses of Model 1 were not sufficient to describe the observed biological effects, especially near organs with a high activity accretion. With Fab, rising liver enzymes were observed at injected activities ≥ 12 MBq, not explained by a self-dose of 4.3 Gy. Model 2 shows crossfire from the kidneys, resulting in an average liver dose of 2.45 Gy/MBq. With F(ab)$_2$ fragments, only the combination of BMT and lysine increased the MTD, explained by cross-organ radiation from the kidneys to the red marrow of the lumbar spine, described only by Model 3 (marrow self-dose ≤ 5 Gy, crossfire up to 0.8 Gy/MBq). Antitumor effects correlated well with calculated doses. These data show that for understanding the biological effects of ^{90}Y in a mouse model, accounting for cross-organ irradiation is mandatory. The best correlation between biological effects and the dosimetry was obtained by the third, MRI-anatomy-based model, which also allows the description of crossfire from abdominal organs to the red marrow.

INTRODUCTION

Whereas radioimmunotherapy has matured in the treatment of non-Hodgkin's lymphoma to an accepted third mode of treatment (6), in solid tumors, success is still limited and novel strategies and approaches are warranted. Since monoclonal antibody fragments and peptides are known to yield better target-to-nontarget ratios than IgG, they may be expected to be superior for radiotherapy. Their use for therapy is limited, however, by their high renal accretion (1,2,7).

This renal accretion of peptides and small proteins is a well-known phenomenon (1,2,7). Since radiometals (e.g., ^{90}Y, $^{186/188}Re$, ...) or other forms of residualizing labels (e.g., ^{131}I-dilactitol tyramine) are retained intracellularly (8), the kidney will most likely become the dose-limiting organ in therapy trials with such agents. We recently described methodologies to decrease this renal uptake (1,2,9). We demonstrated the effectiveness of cationic amino acids, amino sugars, as well as their polymers, to decrease renal accretion of antibody fragments, thus reducing the radiation dose to the kidney by almost one order of magnitude without affecting the biodistribution in any other organ or in tumor xenografts (1,9).

In the present study, we have evaluated the application of this methodology to cancer radioimmunotherapy with ^{90}Y-labeled immunoconjugates. Studies in human tumor-bearing nude mice were performed to determine the dose-limiting, radiation-induced, organ toxicities, and the feasibility of this methodology to overcome nephrotoxicity. Athymic nude mice are the most frequently used preclinical model for assessing the antitumor efficacy and toxicity of experimental cancer therapeutics. Due to the long path length of high-energy β^-emitters, cross-organ irradiation may become an important issue with this model. The aim of this study was, therefore, to evaluate three different dosimetry models in relation to observed biological effects in radioimmunotherapy (RAIT) with ^{90}Y-labeled immunoconjugates (IgG, $F(ab)_2$ and Fab) in nude mice. The relationship between the observed biological effects and the dosimetry was established, using different model assumptions in order to establish a model that allows prediction of biological effects from the doses applied.

MATERIALS AND METHODS

Human Tumor Xenograft Model, Antibodies and Biodistribution Studies

The human colon carcinoma cell line, GW-39 (10), was grown in 5-6 week-old female athymic nude mice (Taconic, Germantown, NY), as described previously. Also, the high-affinity murine anti-CEA monoclonal antibody, MN-14 ($K_a=10^9$ l/mol), has been described in detail previously (11). $F(ab)_2$ fragments were prepared by papain digestion (1). The bivalent fragments were reduced to monovalent fragments (Fab) by reduction with cysteine, as described earlier (1). Isothiocyanate benzyl-diethylene-tetraamine-pentaacetate (SCN-Bz-DTPA) conjugates of IgG, $F(ab)_2$ and Fab were prepared according to Brechbiel et al. (12).

For biodistribution studies, yttrium-88 was obtained as $^{88}YCl_3$ in 6 M HCl from the Los Alamos National Laboratory (Los Alamos, NM). Yttrium-90 was obtained from NEN DuPont (N.Billerica, MA) as $^{90}YCl_3$ in 0.05 M HCl. Labeled antibodies were administered within 3 hours of their preparation. Tumor-bearing animals were injected intravenously into the tail vein with approximately 20-50 μg of antibody protein (labeled with 148-185 kBq [4-5 μCi] of ^{88}Y). The mice were necropsied at 4, 8, 24, 72, 120 and 168 h for antibody fragments, and additionally at 336 h for intact IgG. The amount of activity in the tumors and tissues (liver, spleen, kidney, lung, intestine, blood and bone) was determined by gamma scintillation counting using an injection standard to account for physical decay, as described previously (1).

The biodistribution data were used to generate time-activity curves (13). They were fit to an

exponential function and integrated over time for dosimetry. When the regression coefficient for this exponential fit was worse than -0.90, the integral was computed trapezoidally. In most instances, the absorbed dose to the normal tissues was calculated from the exponential model. In this assumption, the cumulated activities from the first data point to time-zero and from the last data point to infinite time were extrapolated from the curve using the effective half-life of the agent. If the time-activity curves could not be fit by the exponential model, the trapezoidal integration was used. Here, the cumulated activity was extrapolated from the first data point to zero. The cumulated activity after the last sampling-time point was determined as follows: if the slope between the last and the next-to-last data point was positive, no loss of antibody binding from the tissue was assumed, and only the physical decay was considered; if this slope was negative, then the slope was used to define the terminal phase of the time-activity curve.

Dosimetry Models

Three different models, based on the MIRD schema, were used to calculate radiation dose estimates for the tissues, in order to evaluate which model is in best accordance with the biological effects observed. The first model was developed by Siegel et al. (3,14) and was described in detail previously (13,14); it accounts only for self-doses and not for eventual crossfire irradiation between different organs and tissues. For all tissues except the bone, the assumption of uniform distribution of activity in a spherical mass was maintained, and doses were calculated, using S factors generated for ^{90}Y in spheres of 0.1 to 1 g (3,14). For the blood, S values were obtained by extrapolation of the values reported by Hui and Poston (15). For the bone, a cylindrical shape with dimensions of 2-mm diameter x 10-mm length was used, as published earlier (16).

In the second model, absorbed fractions of beta energy $[\phi_\beta(r_t \leftarrow r_s)]$ reported by Hui et al. (4) were used. This model accounts for cross-organ contributions to the dose in the major abdominal and thoracic organs, as well as between bone and bone marrow. However, the contribution from any other major organ or the tumor to the red marrow is not considered.

The third model, leading to a calculation of S factors for ^{90}Y in nude mice, will be described in detail elsewhere (5). Briefly, mice were imaged using a 4.7-Tesla, small-animal spectrometer (General Electric). Serial, transverse images, spanning the liver and kidneys, with an effective spacing of 2 mm and a planar resolution of 0.1 mm per pixel (25 mm field-of-view) were obtained. These images were used to define the mouse organ anatomy for 3D-dosimetry calculations performed using 3D-ID, a three-dimensional internal dosimetry software package (17-19). Using this package, contours were drawn around the liver, spleen and kidneys of the mouse. The cumulated activity concentration associated with each organ was assigned to each 3-D contour set and a point-kernel convolution technique was used to obtain the absorbed dose distribution for each target volume. An ^{90}Y electron point-kernel, generated using INKERNEL, a program provided by Dr. Douglas Simpkin (20) was used. Contours around the spinal column/marrow region were also drawn to provide an estimate of the dose contribution to this region from activity in the liver, kidneys and spleen. Mean absorbed doses and dose-volume histograms to the target regions were generated.

Experimental Radioimmunotherapy

Tumor size was determined by caliper measurements in three dimensions immediately before therapy and at weekly intervals thereafter. Tumors were either left untreated (controls) or injected with a single dose of ^{90}Y-labeled MN-14 Fab, $F(ab)_2$ or IgG, with the activities indicated. Ten to twenty animals were studied in each treatment group. As a nonspecific therapy control, the Bz-DTPA-conjugated Fab' fragment of the anti-CD22 B-cell lymphoma monoclonal antibody LL2 was used, which was prepared as described earlier (1). Body weight was recorded weekly, and survival

was monitored. The maximum tolerated dose (MTD) was defined as the highest possible dose under the respective conditions that did not result in any animal deaths, with the next higher dose level resulting in at least 10% of the animals dying. Animals were observed until their death or until the tumor began to ulcerate through the skin.

For renal uptake reduction, D-lysine monohydrochloride (Sigma, St. Louis, MO) was dissolved in PBS at 175 mg/ml. The animals were injected i.p. with 200 μl of this solution (i.e., 35 mg of D-lys). For Fab therapies animals were given four hourly i.p. injections, starting 30 min before administration of the radiolabeled antibody. In the case of $F(ab)_2$, five 200-μl injections were performed every second hour, also starting 30 min before radioantibody administration, as has been established earlier as the optimal regimen (1,9). For bone marrow transplantation, marrow was harvested and transplanted by i.v. injection via the tail vein 72 h after RAIT with ^{90}Y-Fab or $F(ab)_2$ fragments, or 120 h after RAIT with ^{90}Y-IgG, as described previously (6).

Blood urea nitrogen (BUN) and creatinine, as well as glutamate oxaloactetate transaminase (GOT) and alkaline phosphatase (AP) were determined on the day of radioantibody administration, and at weekly intervals thereafter. Total and differential white blood cell and platelet counts were determined on the day of RAIT, and at weekly intervals thereafter. Fifty-μl heparinized specimens were collected by retroorbital bleeding. White blood cells (WBC) and platelets were determined.

For organ and tumor histology, the animals were sacrificed by cervical dislocation and necropsied at the times indicated. Organs were fixed in 10% formalin, embedded in paraffin and cut into 5-mm sections. Staining was performed with hematoxylin-eosin.

RESULTS

Biodistribution of Yttrium-Labeled MN-14 (Fab, $F(ab)_2$, IgG)

Whereas IgG showed a slow tumor uptake that reached its apogee at 72 to 120h p.i. (28.8 ± 6.5 % ID/g at 120h p.i.), maximum tumor uptake occurred with $F(ab)_2$ at 24h p.i. (10.4 ± 4.5 % ID/g). With Fab, the 24-h uptake (6.0 ± 1.2 % ID/g) was not significantly higher than the 4-h uptake. Although absolute tumor accretion was significantly higher with IgG than with fragments ($p<0.001$), at 4h p.i., Fab had the highest tumor uptake of all three immunoconjugates (5.4 ± 2.9 % ID/g for Fab vs. 2.7 ± 0.8 and 3.7 ± 1.0 % ID/g for $F(ab)_2$ and IgG, respectively; $p<0.01$). IgG showed a slow blood clearance with a $T_{½}$-α of about 4 h and a $T_{½}$-β of approximately 120 h. In contrast, both fragments cleared (Fab faster than $F(ab)_2$) with half-times less than 3 hours. High renal uptake was seen with both fragments, with Fab significantly higher than $F(ab)_2$ (at 24h p.i., 67.5 ± 5.3 % ID/g vs. 43.9 ± 10.0 % ID/g, $p<0.001$), whereas this uptake was negligible with complete IgG (less than 5 % ID/g at all time points).

Renal accretion could be inhibited significantly by the administration of cationic amino acids, amino sugars or polymers thereof (1,2,9). Hourly administration of D-lysine (4 x 35 mg i.p.) reduced the renal uptake approximately seven-fold for Fab, and bihourly administration led to five-fold reduction of the renal accretion of $F(ab)_2$ fragments without affecting the biodistribution in any other organ or the tumor.

Dosimetry According to Model One and Two

Table 1 shows the ^{90}Y-dosimetry of MN-14 in the subcutaneous GW-39 nude mouse model, taking into account only self-doses in spherically-shaped organs (Model 1). As shown previously (1,9), tumor doses are comparable for the bivalent and the monovalent fragment, but approximately five-fold higher for IgG. With both fragments, doses to the unprotected kidneys are significantly higher than with IgG, and approximately twice as high with the Fab when compared to $F(ab)_2$.

However, under lysine treatment, they were similar, and in the same order of magnitude as that observed with IgG.

Table 1

Comparative Dosimetry of ^{90}Y-labeled MN-14 IgG, F(ab)$_2$ and Fab in GW-39 Colon Cancer Xenograft-bearing Nude Mice, Taking into Account only Self-doses of Spherically-shaped Organs, using S Factors According to (***"Model 1"***) (3,14)

	^{90}Y-IgG		^{90}Y-F(ab)$_2$		^{90}Y-Fab	
	mGy/MBq	T/NT	mGy/MBq	T/NT	mGy/MBq	T/NT
GW-39	7392	---	1478	--	1339	--
liver	2505	3.0	801	1.8	362	3.7
spleen	801	9.2	339	4.4	169	7.9
kidney control D-lysine	 927 834	 8.0 8.9	 4747 1455	 0.3 1.0	 8934 1504	 0.1 0.9
intestine	593	12.5	280	5.3	127	10.6
lung	1322	5.6	218	6.8	104	12.8
blood	3716	2.0	467	3.2	266	5.0
bone	500	14.8	301	4.9	133	10.0
washed bone	308	24.0	263	5.6	107	12.5

Table 2 shows the dosimetry based on the same biodistribution data, but correcting for cross-organ irradiation according to the model of Hui et al. (4). The comparison of Tables 1 and 2 shows that with the long path-length of β particles of ^{90}Y, cross-organ irradiation becomes an important issue. For example, with a Fab fragment, liver doses are seven-fold higher without lysine, and still twice as high under lysine treatment than what would have been estimated only from self-β absorption (due mainly to cross-irradiation from the kidney). The same principle holds true for the spleen. Also, for F(ab)$_2$ the liver doses are considerably higher when taking this crossfire into account (for details, compare Tables 1 and 2). Interestingly, however, for IgG, with its less pronounced differences in activity distribution over the different organs, changes in dosimetric calculations are comparably minor.

Table 2

Comparative Dosimetry of ^{90}Y-labeled MN-14 IgG, F(ab)$_2$ and Fab in GW-39 Colon Cancer Xenograft-bearing Nude Mice, Using the Model Reported by Hui et al. (4) that Takes into Account Crossfire Radiation from Neighboring Organs (**"Model 2"**)

	^{90}Y-IgG		^{90}Y-F(ab)$_2$		^{90}Y-Fab	
	mGy/MBq	T/NT	mGy/MBq	T/NT	mGy/MBq	T/NT
GW-39	7392	--	1478	--	1339	--
liver						
control	2960	2.5	1938	0.8	2446	0.5
D-lysine	N/D	--	1170	1.3	729	1.8
spleen						
control	881	8.4	1692	0.9	941	1.4
D-lysine	N/D	--	464	3.2	230	5.8
kidney						
control	991	7.5	4768	0.3	8944	0.1
D-lysine	898	8.2	1475	1.0	1513	0.9
intestine						
control	934	7.9	1089	1.4	1585	0.8
D-lysine	N/D	--	559	2.6	389	3.4
lung	1472	5.0	290	5.1	137	9.8
red marrow	2523	2.9	546	2.7	303	4.4
bone	500	14.8	301	4.9	133	10.0

Experimental Radioimmunotherapy with ^{90}Y-Labeled Immunoconjugates

Toxicity of ^{90}Y-Fab. In order to establish the MTD of ^{90}Y-Fab, varying amounts of activity were injected, starting at 18.5 MBq [500 μCi] and decreasing in 10- to 20-percent steps. At each activity level, one group of animals (ten to twenty per group) received the Fab with no additional support, a second group was treated with D-lysine, a third was bone-marrow grafted 72 h after injection of the radioactivity, and a fourth received a combination treatment with lysine and BMT. Acute treatment-related death was defined as occurring within four weeks post RAIT.

Figure 1a shows the survival data, the BUN and blood cell profile for treatment of the GW-39-bearing mice for different selected treatment groups (i.e., lysine/no lysine; BMT/no BMT; combinations thereof) in comparison to untreated controls (i.e., no radioantibody administration). The slowly decreasing survival curve in these controls is due to tumor growth (50% death rate after 7 weeks). Animals treated with 14.8 MBq [400 μCi] and BMT without lysine protection died 2-3 weeks after RAIT. They showed steeply rising BUN levels in their serum (estimated dose to the kidney was approximately 130 Gy), beginning at one week after RAIT (Figure 1a second panel), whereas lysine-treated groups survived without any signs of renal compromise (estimated kidney dose was ~22 Gy), thus establishing the MTD with lysine and BMT at 14.8 MBq [400 μCi]. Death in the nonlysine-treated group corresponded to development of fluid in all body cavities (pleural effusions

and ascites), as well as generalized edema, consistent with acute renal failure. Major histological findings were a marked tubular dilatation and atrophy, whereas damage to the glomeruli seemed to be comparably minor. Leukopenia and thrombocytopenia were seen in all treated groups; the higher the activity the more severe the effects (see Figure 1a, two lower panels). A very subtle tendency, not statistically significant, was observed towards more pronounced red marrow toxicity in nonlysine-treated groups, when compared to the lysine-treated. No *acute* kidney toxicity was seen in the 7.4 or 9.3 MBq groups [200 or 250 μCi], regardless of kidney protection by the amino acid. However, at 5 weeks post RAIT, in the 9.3 MBq group without lysine, some animals showed rising serum BUN levels (Figure 1a) when the first deaths occurred. As was seen in the acute radiation-induced deaths at

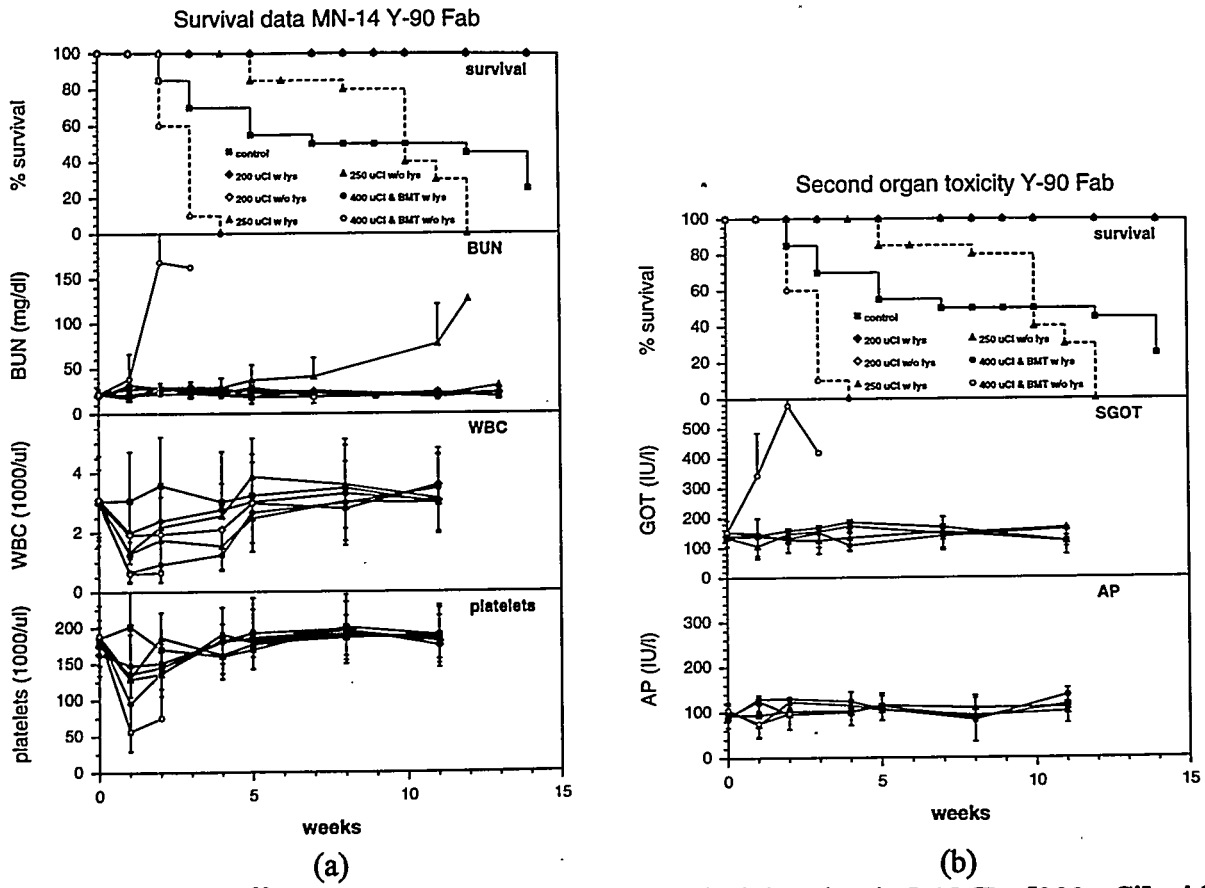

Figure 1. Effect of ^{90}Y-labeled MN-14 Fab at three typical dose levels 7.4 MBq [200 μCi] with/ without lysine, 9.3 MBq [250 μCi] with/without lysine, and 14.8 MBq [400 μCi] with BMT and with/without lysine) on animal survival: (a) kidney function and red marrow parameters (WBC and platelets) and (b) liver function parameters (SGOT and AP). 7.4 MBq is the MTD without artificial support, 9.3 MBq with lysine, and 14.8 MBq with lysine and BMT.

the 14.8 MBq [400 μCi] level, several animals developed ubiquitous fluid accumulation (pleural effusion, ascites, edema). At 10 weeks post RAIT, 60% of the animals were dead, and all had expired after 12 weeks. All marrow parameters had returned to normal, whereas BUN was continuously rising in these animals (estimated kidney dose was 83 Gy). The histological picture was characterized by widespread glomerular sclerosis, tubular atrophy, arteriolar intimal thickening, and fibrinoid necrosis. No deaths were observed in the lysine-treated group and kidney function parameters remained normal. The MTD of ^{90}Y-Fab under lysine protection was, therefore, established at 9.3 MBq [250 μCi]. No renal toxicity was observed in the 7.4 MBq [200 μCi] group, with or without

lysine (the assumed kidney absorbed dose without amino acid administration was 66 Gy). Thus, with respect to *chronic* toxicity, 7.4 MBq [200 μCi] is the established MTD without artificial support (i.e., without lysine or BMT), 9.3 MBq [250 μCi] with lysine alone, and 14.8 MBq [400 μCi] with BMT and kidney lysine treatment. No histological changes were appreciated in any of the lysine-treated groups (estimated kidney absorbed dose with 14.8 MBq with lysine was 22 Gy).

SGOT and AP also were monitored in these animals, since, according to the ^{90}Y-mouse dosimetry model used (Table 2), substantial cross-organ radiation doses to the liver could be expected. Indeed, animals treated with 14.8 MBq without lysine (estimated average liver dose 36 Gy) showed rising GOT levels as soon as one week post RAIT (Figure 1b). With lysine, as well as in the 7.4 MBq or 9.3 MBq group regardless of kidney protection, no such liver toxicity was observed. None of the groups showed any abnormalities in AP levels (an indicator of possible biliary damage).

Toxicity of ^{90}Y-F(ab)$_2$ fragments and IgG. The MTD of ^{90}Y-labeled F(ab)$_2$ fragments without artificial support, such as lysine administration or bone marrow transplantation, was established as 7.4 MBq, which would deliver approximately 3.45 Gy to the blood (Table 1), corresponding according to model 2 to approximately 4 Gy to the red marrow and 35 Gy to the kidneys (Table 2). This dose was accompanied by a moderate leukopenia and thrombocytopenia. No changes in serum BUN or creatinine were observed. This maximum tolerated activity could not be increased by lysine administration or bone marrow transplantation alone, whereas the combination of both increased the MTD by thirty percent to 9.6 MBq [260 μCi]. At this dose level, the animals developed severe leukopenia and thrombocytopenia, without significant differences whether lysine-treated or not. With lysine and bone marrow transplantation, the cell counts recovered fully in 3-5 weeks, whereas without lysine or BMT the animals died 2-3 weeks after RAIT in leuko- and thrombocytopenia, but without any signs of renal failure. The effect of lysine is surprising, since at an estimated renal dose of 46 Gy, no rising BUN or creatinine was observed, and histological changes observed in animals that were treated with ^{90}Y-labeled bivalent fragments (F(ab)$_2$) were very mild as compared to the severe destruction seen at higher doses of ^{90}Y-Fab.

The MTD of ^{90}Y-MN-14 IgG without additional support was reached at 3.7 MBq [100 μCi]. Severe bone marrow toxicity (WBC and platelets) was observed. The nadir of platelet counts was reached at two, and of WBC at 2-3 weeks after radioantibody administration. The time to recovery was, with approximately 5-6 weeks post radioantibody injection, longer than observed with fragments. With bone marrow support, this MTD was increased by 30% (4.8 MBq [130 μCi]). No other organ toxicity was observed with ^{90}Y-IgG, which is consistent with the comparably low doses to other organs (liver, kidney, etc.). Accordingly, lysine was unable to increase the MTD.

Comparative antitumor effects. When comparing antitumor effects of ^{90}Y-labeled MN-14 Fab, F(ab)$_2$ and IgG at their respective maximal MTDs (with maximal support, i.e., BMT and lysine, where applicable), calculated tumor doses were approximately 20 Gy for Fab (at an injected activity of 14.8 MBq), 14 Gy for F(ab)$_2$ (9.6 MBq), and 35 Gy for IgG (4.8 MBq). As with the 1.4-fold higher tumor dose, better tumor control was seen with Fab than F(ab)$_2$; tumor growth was controlled only for 7-9 weeks with the bivalent fragments, compared to over 12 weeks with the monovalent fragment. It is interesting to note, in this context, that tumor growth stopped almost immediately after the injection of Fab fragments, whereas with bivalent fragments, continuing growth over a 1-2 week period was seen before a radiation effect became obvious. Surprising, because of the tumor dosimetry, which is almost twice as high with IgG than with Fab, tumor growth control was best with the monovalent fragment. With complete IgG, tumor growth was controlled for ~10 weeks; after this time, especially larger tumors began to grow more rapidly.

An MRI-Anatomy-Based ^{90}Y-Dosimetry Model

Since many, but not all, of the observed biological effects could be explained by crossfire irradiation taken into account by Model 2, and especially the finding that with $F(ab)_2$, despite the apparent lack of nephrotoxicity, an increase in the MTD was possible only by combination of BMT and lysine, crossfire from major organs to the red marrow was very likely to play a role. Therefore, Model 3 was developed which takes crossfire from the abdominal organs to the red marrow of the lumbar spine into account. S factors resulting from this model will be published elsewhere (5).

Table 3

Comparative Dosimetry of the Abdominal Organs and the Red Marrow in the Lumbar Spine for ^{90}Y-labeled MN-14 IgG, $F(ab)_2$ and Fab in Nude Mice, Using an MRI Mouse Anatomy-based Model According to Sgouros et al. (5), also Taking into Account Crossfire Irradiation from Neighboring Organs to the Red Marrow (***"Model 3"***)

	^{90}Y-IgG mGy/MBq	**^{90}Y-F(ab)$_2$** mGy/MBq	**^{90}Y-Fab** mGy/MBq
liver			
control	3557	1252	806
D-lysine	N/D	1448	683
spleen			
control	1067	591	632
D-lysine	N/D	502	236
left kidney			
control	1734	6702	12728
D-lysine	N/D	2452	2687
right kidney			
control	1452	6446	12331
D-lysine	N/D	2293	2569
red marrow lumbar spine*			
total			
control	2563	662	523
D-lysine	N/D	588	349
crossfire contribution from the abdominal organs			
control	28	116	221
D-lysine	N/D	42	46

* The red marrow dose given in this table represents exclusively the dose to the marrow of the lumbar spine, which represents approximately 16.0 ± 3.6 % of the total active red marrow of the mouse (21,24).

Table 3 shows the dosimetry for the abdominal organs and the red marrow of the lumbar spine according to this model, and Figure 2 shows the resulting dose-volume histograms for red marrow, kidneys, and liver. Three differences between the doses in Model 2 and 3 are remarkable; generally,

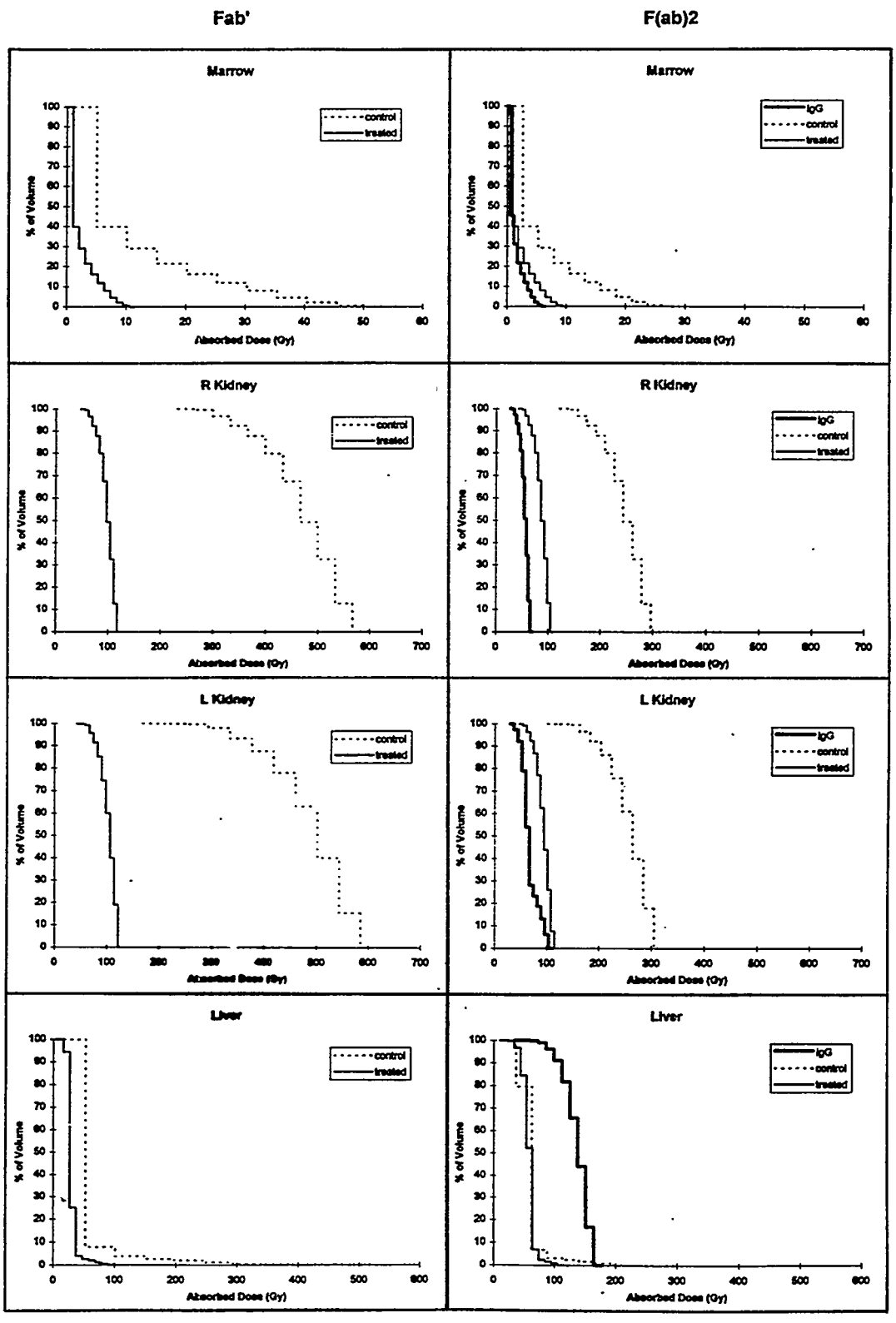

Figure 2. Dose-volume histograms, based on the model according to Sgouros et al. (ref. 5, Model 3) for the red marrow, kidneys and liver with ^{90}Y-labeled Fab (left column), $F(ab)_2$ and IgG (right column).

self-doses in the MRI-based model are slightly higher than in Model 2. Second, the contribution from the kidneys to the mean spleen and liver doses is lower than estimated from Model 2. However, the dose-volume histograms show, with ^{90}Y-Fab in those parts of the liver that are close to the right kidney, doses up to 8 Gy/MBq (Figure 2). This easily explains the observed liver toxicity. Third, and this is unique to Model 3, it shows a substantial contribution from the abdominal organs to the red marrow dose, which is up to 0.2 Gy/MBq for the monovalent, 0.1 Gy/MBq for the bivalent fragment, and still .03 Gy/MBq for IgG. This may explain why with $F(ab)_2$ only the combination of lysine and bone marrow transplantation could increase the MTD, since lysine decreases this contribution almost three-fold.

DISCUSSION

In two previous studies we could demonstrate in a preclinical model, as well as in a pilot clinical trial, the ability of cationic compounds to induce a transient functional proteinuria (1,2,9) that resulted in the reduction of the renal uptake, thus radiation dose, by almost one order of magnitude. In order to evaluate the usefulness of this methodology with respect to increased anti-tumor efficacy in radioimmunotherapy with such agents, we undertook experiments in GW-39 human colon cancer xenograft-bearing nude mice.

As can be expected from the several-mm path length of ^{90}Y, cross-organ irradiation seems to play an important role in small animal models. Dosimetry models which simply account for self-doses seem to be insufficient for the description and prediction of the observed biological effects. For example, the liver toxicity parameters, which were observed in the 14.8 MBq (400 μCi) ^{90}Y-Fab group when no lysine was given, are solely explainable by such cross-organ irradiation, since the whole inferio-posterior parts of the liver are within the range of the high-energetic β particles originating from the kidneys. Indeed, dose-volume histograms (cf. Figure 2) show that, with Fab fragments, those parts of the liver which are close to the kidneys get substantial crossfire doses which may explain the the rising liver parameters.

Surprising is the observed bone marrow toxicity of ^{90}Y-labeled fragments at comparably low bone marrow doses, especially also when compared to data known for ^{90}Y-IgG (this study, 13). This may be partially due to a combination of the considerably higher dose-rate delivered by the fragments when compared to IgG (Figure 3), and the fact that major portions of the bone marrow also are within the range of β particles from the kidneys and the tumor. Attempts to solve this problem have been proposed (4,22). Since the model of Hui et al. (Model 2) (4) only considers a contribution from the bone, not from major abdominal organs or the tumor, to the blood-forming red marrow, the development of an actual, anatomy-based mouse-model seemed, therefore, of utmost importance for correlating the observed biological effects of ^{90}Y to dosimetric calculations. The calculated S factors, together with a more detailed description of this third model, will be published elsewhere (5). Also, the toxicity data for $F(ab)_2$ fragments probably have to be interpreted on this basis. No biochemical signs of renal toxicity were observed, and chronic histological changes were very mild, making nephrotoxicity as the cause of death very unlikely, which is also in agreement with the dosimetry results. At these doses, as with ^{90}Y-Fab, no renal damage was observed. Since only the combination of lysine and bone marrow transplantation increased the MTD, we assume that the bone marrow is the dose-limiting organ, and the cross-organ radiation dose from the kidney is contributing to this limiting red marrow toxicity. This clearly suggests that Model 3 is superior to both other dosimetry models, since only this model accounts for cross-organ irradiation in the red marrow.

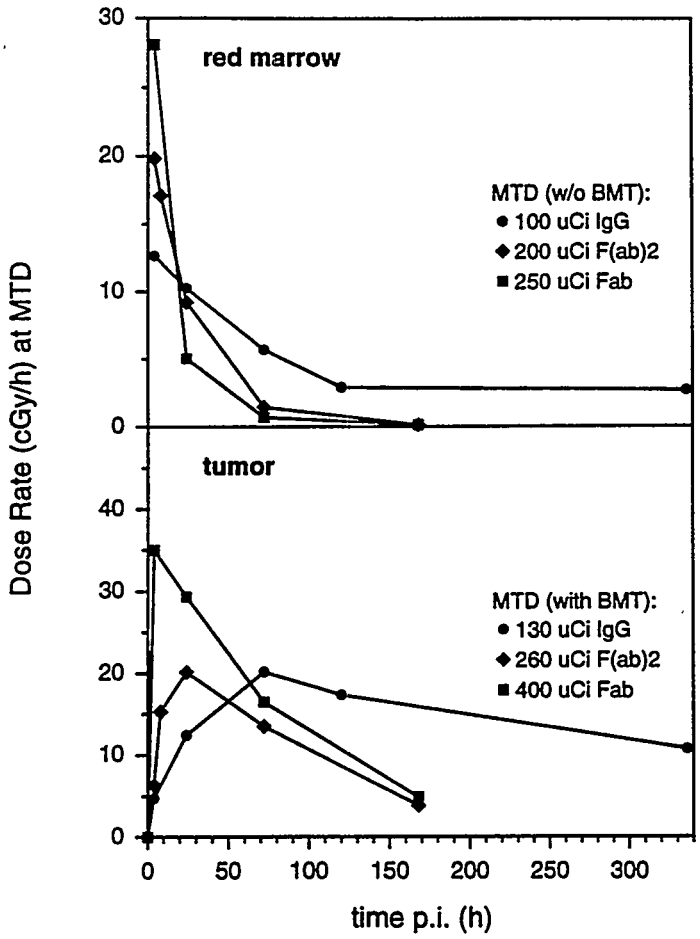

Figure 3. Comparison of dose rates in the bone marrow and tumor at the respective MTDs (100, 200 and 250 μCi w/o BMT for the marrow, 130, 260 and 400 μCi with lys and BMT for the tumor with IgG,F(ab)$_2$ and Fab, respectively).

In contrast to previous observations (13,23), tumor response also could be predicted fairly well from the dosimetry. With both fragments, tumor doses of 10 Gy or less achieved only a short retardation of tumor growth, whereas doses above 20 Gy were able to control tumor progression for more than 15 weeks. This clearly supports the concept that even relatively radioresistant solid tumors, such as colonic cancers, can respond to radioimmunotherapy provided sufficiently high radiation doses are achieved. Surprising, however, is the fact that despite an almost twice as high radiation dose to the tumor at their respective MTDs, IgG seemed to be less effective in controlling tumor growth as compared to Fab. In our view, there are two possible reasons for this observation. First is a difference in dose rate, which is higher with Fab than IgG. Figure 3 shows that the maximum dose rate with Fab is almost twice as high with IgG and is reached at 4h p.i., whereas not before 72h p.i. with IgG. Second is the fact that the antibody distribution is much more homogenous with monovalent as compared to bivalent immunoconjugates. Despite the long path length of ^{90}Y, a more homogenous dose distribution may contribute to enhanced antitumor effectiveness.

Summarizing, our study shows that ^{90}Y dosimetry in an animal model requires careful correction for cross-organ irradiation. The best correlation between biological effects and dosimetry was obtained with the MRI-anatomy-based model, which also allows the description of crossfire from abdominal organs to the red marrow. The dosimetry obtained by this model corresponded well to the observed effects with respect to toxicity, as well as to tumor responses.

ACKNOWLEDGMENTS

This work was supported in part by grants of the Deutsche Forschungsgemeinschaft (DFG Be 1689/1-1/2) and the National Institutes of Health (Outstanding Investigator Award CA39841, CA54425 and CA62444).

REFERENCES

1. Behr TM, Sharkey RM, Juweid ME, Blumenthal RD, Dunn RM, Griffiths GL, Bair HJ, Wolf FG, Becker WS and Goldenberg DM. Reduction of the renal uptake of radiolabeled monoclonal antibody fragments by cationic amino acids and their derivatives. Cancer Res 55:3825-3834, 1995.
2. Behr TM, Becker WS, Sharkey RM, Juweid ME, Dunn RM, Bair HJ, Wolf FG and Goldenberg DM. Reduction of renal uptake of monoclonal antibody fragments by amino acid infusion. J Nucl Med 37:829-833, 1996.
3. Siegel JA and Stabin MG. Absorbed fractions for electrons and beta particles in small spheres. J Nucl Med 29:803, 1988.
4. Hui TE, Fisher DR, Kuhn JA, Williams LE, Nourigat C, Badger CC, Beatty BG and Beatty JD. A mouse model for calculating cross-organ beta doses from yttrium-90-labeled immunoconjugates. Cancer 73:951-957, 1994.
5. Sgouros et al., manuscript in preparation.
6. Goldenberg DM (ed.). Cancer Therapy with Radiolabeled Antibodies. CRC Press, Boca Raton/Ann Arbor/London/Tokyo 1995.
7. Behr TM, Becker WS, Bair HJ, Klein M, Stühler Ch M, Cidlinsky KP, Scheele JR and Wolf FG. Comparison of complete versus fragmented ^{99m}Tc-labeled anti-CEA monoclonal antibodies for immunoscintigraphy in colorectal cancer. J Nucl Med 36:430-441, 1995.
8. Duncan JR and Welch MJ. 1993. Intracellular metabolism of indium-111-DTPA labeled receptor targeted proteins. J Nucl Med 34:1728 - 1738, 1993.
9. Behr TM and Goldenberg DM. Improved prospects for cancer therapy with radiolabeled antibody fragments and peptides ? J Nucl Med 37:834-836, 1996.
10. Goldenberg DM, Witte S and Elster K. A new human tumor serially transplantable in the golden hamster. Transplantation 4:760-764, 1966.
11. Sharkey RM, Goldenberg DM, Murthy S, Pinsky H, Vagg R, Pawlyk D, Siegel JA, Wong GY, Gascon P, Izon DO, Vezza M, Burger K, Swayne LC, Pinsky CM and Hansen HJ. Clinical evaluation of tumor targeting with a high-affinity, anticarcinoembryonic antigen-specific, murine monoclonal antibody, MN-14. Cancer 71:2082-2096, 1993.
12. Brechbiel MW, Gansow OA, Achter RW, Schlom J, Esteban JM, Simpson DE and Colcher D. Synthesis of 1-(*p*-isothiocyanobenzyl) derivatives of DTPA and EDTA: Antibody labeling and tumor imaging studies. Inorg Chem 25:2772-2781, 1986.
13. Sharkey RM, Motta-Hennessy C, Pawlyk D, Siegel JA and Goldenberg DM. Biodistribution and radiation dose estimates for yttrium- and iodine-labeled monoclonal antibody IgG and fragments in nude mice bearing human colonic tumor xenografts. Cancer Res 50:2330-2336, 1990.
14. Siegel JA and Stabin MG. Absorbed fractions for electrons and beta particles in spheres of various sizes. J Nucl Med 35:152-156, 1994.
15. Hui TE and Poston JW. A model of the circulating blood for use in radiation dose calculations. *In* Proceedings of the International Conference on Radiation Dosimetry and Safety. Taiwan. 151-168, 1987.
16. Loevinger R, Japha EM and Brownell GL. Discrete Radioisotope Sources. *In* Radiation Dosimetry. G.L. Hine and G.L. Brownell, editors. Academic Press, New York. 712, 1956.
17. Sgouros G, Barest G, Thekkumthala J, Chui C, Mohan R, Bigler RE and Zanzonico PB. Treatment planning for internal radionuclide therapy: Three-dimensional dosimetry for nonuniformly distributed radionuclides. J Nucl Med 31:1884-1891, 1990.

18. Sgouros G, Chiu S, Pentlow KS, Brewster LJ, Kalaigian H, Baldwin B, Daghighian F, Graham MC, Larson SM and Mohan R. Three-dimensional dosimetry for radioimmunotherapy treatment planning. J Nucl Med 34:1595-1601, 1993.
19. Kolbert K, Sgouros G, Scott AM, Baldwin B, Zhang J, Kalaigian H, Macapinlac HA, Graham MC and Larson SM. Dose-volume histogram representation of patient dose distribution in three-dimensional internal dosimetry. J Nucl Med 35:123P-124P (Abst), 1994.
20. Simpkin DJ and Mackie TR. EGS4 Monte Carlo determination of the beta dose kernel in water. Med Phys 17:179-186, 1990.
21. Behr TM, Sharkey RM, Blumenthal RD, Aninipot RL, Dunn RM, Sgouros G and Goldenberg DM. Red marrow dosimetry of ^{131}I- and ^{90}Y-labeled immunoconjugates in a nude mouse model (manuscript in preparation).
22. Goris ML, Nielsen KK and Napel SA. Dosimetry computation from tissue distribution data entered in an electronic mouse model with convolution of the beta ray deposition profile. J Nucl Med 35:161P (Abst), 1994.
23. Sharkey RM, Weadock KS, Natale A, Haywood L, Aninipot R, Blumenthal RD and Goldenberg DM. Successful radioimmunotherapy for lung metastasis of human colonic cancer in nude mice. J Natl Cancer Inst 83:627-632, 1991.
24. Sgouros G. Bone marrow dosimetry for radioimmunotherapy: Theoretical considerations. J Nucl Med 34:689-694, 1993.

QUESTIONS

Fisher: The mouse dosimetry model of Hui et al. does account for cross-organ contributions to the red marrow dose, primarily from ^{90}Y deposited on bone surfaces. The marrow component was developed to account for known ^{90}Y on bone surfaces and in marrow, measured from femoral bone samples and marrow punch biopsies. You attribute marrow toxicity to cross irradiation by ^{90}Y in kidneys. What fraction of total mouse marrow lies within the mean range of ^{90}Y beta particles from the kidneys? Perhaps an alternative explanation of the effect you observed is irradiation of red marrow by free ^{90}Y on bone surfaces.

Behr: I am well aware of the fact that the model of Hui et al. does account for crossfire from the bone surfaces to the red marrow and this crossfire was taken into account in our dose calculations according to this model. It does not, however, account for crossfire from abdominal organs to the red marrow. We performed a study to show which percentage of the red marrow lies within the mean range of ^{90}Y in abdominal organs; for this purpose ^{99m}Tc-labeled sulfur colloid was injected i.v. into mice and the affected parts of the skeleton were dissected and counted separately in a well counter. It turned out that approximately 25% of the total red marrow was within this range. Whether this is enough to explain the observed biological effects must remain undecided at this point. The fact, however, that only combinations of lysine and bone marrow transplantation could increase the maximum to tolerated dose with ^{90}Y-F(ab)$_2$ fragments strongly supports our crossfire hypothesis. We can rule out ^{90}Y on bone surfaces as a possible factor since our biodistribution studies showed the chelate to be stable with very low bone uptake over time. These measured data were the basis for all dose calculations. Furthermore, if free ^{90}Y was the reason for the observed biological effects (myelotoxicity), this effect should have been more pronounced like IgG, not with fragments, since IgG has the longer residence time in the body. Since the effect was more pronounced with fragments, loss of ^{90}Y out of chelation and its bone uptake is most unlikely.

Atcher: What evidence do you have that marrow toxicity is dose-rate dependent?

Behr: Well, its very simple; it is the only explanation for which I have evidence to explain our data at this point. The maximum tolerated red marrow dose with ^{90}Y-labeled fragments is lower by a factor of 3 to 4 than is the ^{90}Y-IgG. All modeling could not show additional crossfire that might explain this toxicity. However, there is clear evidence of differences in dose rate. Lacking other explanations I could think of, I postulate the dose rate to be the responsible factor although I am aware that most published studies emphasize that there is basically no influence of dose rate on human bone marrow stem cells.

Rao: I would like to comment on the dose-rate effects in bone marrow. In mice there are dose-rate effects in marrow. We performed some experiments in mice using acute radiation and a constant dose rate with an external beam for one week using a dose rate of 2 rads/hr, and we clearly did find dose-rate effects. I don't know at this time if there are dose-rate effects in humans.

Behr: I think dose-rate effects are the only possible explanation for the observed effects in the tumor (better antitumor efficacy of Fab from IgG despite lower doses) and the red marrow that we have at the moment. I think more work needs to be done to confirm this postulate.

ANALYSIS OF OVARIAN DOSE OF WOMEN EMPLOYED IN THE RADIUM WATCH DIAL INDUSTRY: A MACRODOSIMETRIC AND MICRODOSIMETRIC APPROACH

Roeske JC[1], Stinchcomb TG[2], Schieve L[3] and Keane A[4],
[1]Department of Radiation and Cellular Oncology, The University of Chicago, Chicago, IL 60637
[2]Department of Physics, DePaul University, Chicago, IL 60614
[3]Department of Epidemiology and Biostatistics, University of Illinois-Chicago, Chicago, IL 60612
[4]Environmental, Safety and Health Division, Argonne National Laboratory, Argonne, IL 60439

ABSTRACT

In the 1920s, painters in the radium watch dial industry frequently tipped their brushes with their tongues resulting in the ingestion of radium-226 and/or radium-228. Earlier dosimetric studies (1950-1990) attempted to correlate the magnitude of biological effects (eg. increased cancer incidence) with variations in radium uptake. Recently, there is a renewed interest on the part of epidemiologists studying additional possible effects (eg. low birthrate and sex ratio). The goal of this work is to review and update the determination of dose to the ovaries from both external and internal radiation hazards in an attempt to correlate ovarian dose with these additional possible effects. The dose to the ovaries can be attributed to four major sources - 1) external gamma irradiation from the containers of radium paint; 2) alpha and 3) beta particle emissions due to sources which decay within the ovaries; and 4) internal gamma irradiation released throughout the body. Data obtained in earlier dosimetric studies on the quantity of Ra-226 and/or Ra-228 ingested were used in this study. Dose is estimated on a macroscopic scale by calculating the average dose deposited within the entire ovary. In addition, a microdosimetric analysis is performed which considers the statistical variation of energy deposited within individual oocyte nuclei. Sources of uncertainty, and the use of these data in new epidemiological studies are discussed.

INTRODUCTION

Shortly after the discovery of radium in 1898 came the application of this new element to many areas of everyday life. One such application was in the radium dial industry. Radium salts were used to activate zinc sulfide rendering it luminous. By applying this luminous compound to the dials of watches or clocks, the numbers would glow in the dark. This characteristic was particularly useful on gauges of battleships and airplanes during World War I.

The radium dial industry was first introduced in the United States in 1913. The original plants were situated in Connecticut, New Jersey, and Illinois. Later, plants were opened in other states, primarily in Massachusetts, New York and Pennsylvania. In 1924, local dentists observed a number of cases of jaw necrosis among workers in the industry. Around the same time, Martland (1) described a

new disease in which severe anemia was noted in several dial painters. These findings suggested a possible occupational association.

An analysis of working habits revealed that dial painters were pointing their camel's hair brush with their lips. This resulted in the ingestion of relatively large quantities of radium. Simple calculations, based on the workers habits, revealed that the average worker ingested 15 - 215 μg of radium per week. In 1926, the government instituted occupational safety standards for dial painters including cessation of tipping brushes with lips. However, despite the abolition of brush tipping, considerable radiation exposure continued due to unsatisfactory working conditions (dust, poor ventilation, etc.). Although intake of radium continued, the associated risk was greatly reduced and radium induced malignancies were not observed in those employed after 1926.

In the 1950s, the US Atomic Energy Commission pursued active followup of the radium dial workers. Approximately 1600 pre-1930 workers were identified (~ 1500 females) and an additional 1200 women were identified from 1930-1949. Nearly 50% of the identified workers were further evaluated for radium body burdens (at ANL or MIT). Studies of adverse health effects included the following results (2). The most well established effects of internal radium exposure were bone sarcomas and head carcinomas. Cancers at other sites were investigated, but the results were often negative or marginally significant. A threefold excess of multiple myeloma was reported which was correlated to the duration of employment. Elevated risks were observed for breast and colon cancer. Suggestive results for lung cancer and leukemia were also reported. A fertility analysis of a fraction of the cohort suggested a reduction of the live birthrate which was correlated with radium intake (3).

Recently, there is renewed interest in exploring the effects of internally deposited radiation on reproductive functions among women in this cohort (4,5). Potential outcomes of interest include : a) demographic measures such as percent childlessness, total pregnancy rate, live birthrate, and time to first pregnancy as markers of fertility; b) live-birth sex ratio as a potential marker for mutagenic effects; and c) birth weight. These outcomes will be evaluated as a function of absorbed dose to the ovaries or other critical structures within the pelvis.

The goal of this report is to present a dosimetric framework for calculating the dose to the ovaries to be used in these current undertakings. The individual dose components are discussed and their relative effect on the total dose is elucidated. In addition, a microdosimetric analysis is presented to aid in the interpretation of the observed results.

MATERIALS AND METHODS

For this particular cohort, there are four distinct sources which contribute to the dose that the ovaries receive. These sources are : 1) photons emitted from radium external to the body; 2) alpha particles, 3) beta particles and 4) photon irradiation from internalized radium. Each of these four sources will be considered, and their effect on the total dose will be calculated.

1. Dose from Gammas Emitted by External Radium

Exposure readings obtained during the early 1930s suggested that the occupational exposure from external gamma irradiation was equivalent to that received from a paint container with 1200 μgm of radium at a distance of 0.5 m (6). Using the approach proposed by Polednak (3) the average daily exposure at the skin is

$$X = \Gamma\, A/r^2 = 0.004 \text{ R/hr}, \qquad (1)$$

where $\Gamma = 0.84$ R/g-hr, A is the activity in gm of Ra-226, and r is the distance in m. Based on a

conversion factor of 6 mGy/R (0.6 rad/R) (3) to determine the dose to the ovaries (including attenuation and scatter), and assuming 250 working days/yr, the external dose component is 48 mGy/yr (4.8 rad/yr) of employment.

2. Dose from Internal Alpha-Particle Emissions

The soft tissue dosimetry of radium has been discussed extensively by Keane and Schlenker (7). The average dose to tissue x at time t (days following initial uptake) is given by the following equation:

$$(D_t)_x = 1.38 \times 10^{-5} M_x^{-1} \sum [F_x (T_t)_x b_i E_{\alpha i}] \qquad (2)$$

where $(D_t)_x$ is the dose in mGy per Bq; 1.38×10^{-5} is a conversion constant; M_x is the mass of the tissue in kg; F_x is the fraction of energy emitted within the tissue that is absorbed; $(T_t)_x$ is the effective retention integral in days; b_i is the number of alphas emitted by the i^{th} member of the decay series per alpha emitted by the parent; and $E_{\alpha i}$ is the energy of the i^{th} alpha particle. Since the dimensions of the ovaries are much larger than the range of the alpha particles, $F_x = 1$. Thus, the remaining parameters must be evaluated for Ra-226 and Ra-228.

In their original work, Keane and Schlenker (7) made the assumption that the decay of Rn-222 in soft tissue is negligible due to its prompt clearance. Hence the dose is due entirely to Ra-226 alone. In the above equation, $b E_\alpha = 4.77$ MeV for Ra-226. For Ra-228, a major assumption is that there is no translocation of the daughter products. Thus the summation over all daughters in Equation 1 of $\sum b_i E_{\alpha i} = 31.9$ MeV (See Table 1).

Table 1
Alpha-Particle Emissions of Ra-226/228

Ra-226*	Ra-228
4.77 MeV - 100%	5.35 MeV - 100%
	5.67 MeV - 100%
	6.29 MeV - 100%
	6.78 MeV - 100%
	6.06 MeV - 36%, 8.78 MeV - 64%

* Note that only the decay from Ra-226 is considered. The Rn-222 daughter is assumed to be removed from the tissue prior to its decay.

The retention integral, $(T_t)_x$, is determined as follows. The method described by Keane and Schlenker uses the assumption that the observed and predicted values of $(\text{Ra-226/Ca})_{soft}/(\text{Ra-226/Ca})_{bone}$ are equal (7). For a more detailed description, the interested reader is referred to the original paper. For a given organ x, the infinite retention integral, $(T_\infty)_x$ can be approximated by

$$(T_\infty)_x = [(226\text{Ra/Ca})_x/(226\text{Ra/Ca})_{bone}] [Ca_x/Ca_{bone}] (T_\infty)_{bone} \qquad (3)$$

The finite retention integral at time t after systemic intake of activity is given by

$$(T_t)_x = [(T_t)_{soft}/(T_\infty)_{soft}] (T_\infty)_x \quad (4)$$

where the retention integrals are obtained from Schlenker (8) and modified by Rowland (9). Similar equations can be derived for Ra-228. The functional forms of the retention integrals are discussed below.

By multiplying the constants in Equation 2, the calculated alpha particle dose to the ovaries is 2.34 mGy/MBq-day and 15.7 mGy/MBq-day for Ra-226 and Ra-228, respectively. In order to obtain the total dose, these factors are multiplied by the product of the initial activity and the soft-tissue retention integral evaluated at the appropriate time after systemic intake.

3. Dose from Internal Beta Emitters

The same procedure described above can be used to determine the dose from beta particles. However, the primary difference will be in the energy released per decay. For Ra-226, there are no beta emissions associated with the decay, as all daughter products are assumed to be removed. The beta-particle component from Ra-228 contributes approximately 1 MeV (average beta energy). Since this value is much less than that of the alpha particles (31.9 MeV for Ra-228), and given that the alpha particle RBE may be 20 or more, the beta-particle dose component will be neglected.

4. Dose from Internal Gamma Emissions

The details of the organ dosimetry from internal photon sources are discussed by Schlenker (10) in the 1971 ANL report. Conceptually, the dose to a particular organ is determined by first calculating the cumulative activity within bone and soft tissue. This consists of the ingested activity scaled by the appropriate retention integral. The cumulative activity is multiplied by the dose per unit decay to the target organ. This factor takes into account the energy per decay, the physical processes of attenuation and scatter, and the relative source-target geometry. For Ra-226, the average organ dose is given by

$$D(t) = J \{[Q_s(\text{Ra-226})\, T_t(\text{Ra-226})_{total}] + [Q_s(\text{Rn-222})\, T_t(\text{Rn-222})_{total}] + [\Delta Q(\text{Ra-226}) Q_s(\text{Ra-226}) T_t(\text{Ra-226})_{soft}] + [\Delta Q(\text{Rn-222}) Q_s(\text{Rn-222}) T_t(\text{Rn-222})_{soft}]\} . \quad (5)$$

The terms for these equations are described as follows:

$D(t)$ = total dose to organ
J = initial ingested activity
$Q_s(y)$ = dose rate in target per unit activity of y in skeleton
$\Delta Q(y)$ = difference of dose rate in target per unit activity for extraskeletal and skeletal sources, divided by the dose rate in target per unit activity in skeleton
$T_t(y)_{total}$ = integral of the total-body retention function at time t
$T_t(y)_{soft}$ = integral of the soft-tissue retention curve at time t
A similar equation may also be derived for Ra-228.

Ingested Activity and Retention Integrals

All of the internal dose calculations are proportional to the ingested activity and the retention integral. For the radium dial workers, the retention integrals are based on whole-body measurements obtained in earlier studies. The radium body content was measured using a sodium iodide crystal scintillation counter. Additionally, the amount of radon expired through breathing was also measured. In both cases, the uncertainties associated with the measurements ranged from 10-15%. In some

cases, the quantity of Ra-228 remaining in the body at the time of measurement was minute due to its 6.7 year half-life. Thus, the quantity of Ra-228 ingested was estimated based on the paint content at the various times and places of employment (2). The interested reader is referred to the recent publication by Rowland (11) which describes the measuring techniques used over the years.

The retention function takes into account both the physical decay and biological removal processes of the radionuclide. When radium is initially ingested, it diffuses rapidly from the digestive tract into the circulation. A portion is excreted through the feces, and a smaller amount through the urine. That which becomes distributed throughout the body is retained in either soft tissue (for a relatively short time) or bone. Due to the similar chemical properties of calcium, radium has a high affinity for bone and thus bone has a much longer retention time than soft tissue (8,9). The retention function was used to extrapolate the measured activity in order to determine the initial intake. Historically, the Norris equations (12) were used to describe the temporal variation of ingested radium. However, these have been revised to obtain a better fit of the data (8,9,13). These modifications essentially change the relative partitioning of activity between the soft tissue and bone compartments. In these studies, the systemic intake of Ra-226 was calculated using Rowland's modification (9) of ICRP Publication 20 (13) whole-body retention equations.

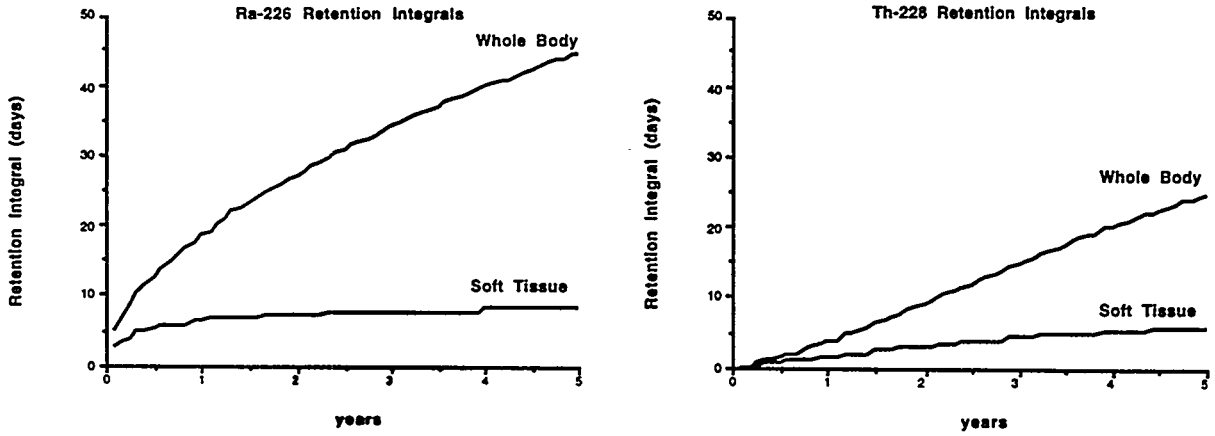

Figure 1. Retention integrals for Ra-226 and Th-228.

The time integral of the retention function is known as the retention integral. The product of the retention integral and the initial activity is the cumulative activity or the total number of decays occurring within a particular volume. Typical retention integrals for Ra-226 and Th-228 are shown in Figure 1. Of interest is that the soft tissue retention integral reaches a plateau within the first several years. However, the whole-body retention integral does not reach a plateau for approximately 40 years for Ra-226 and approximately 20 years for Th-228. Note that the retention integral of Th-228 (instead of Ra-228) is used for alpha-particle dose calculations, as the decay of Ra-228 does not directly result in any alpha emissions. However, in photon dose calculations, the Ra-228 retention integral is used. Both of these retention integrals are based on an initial acute intake. Thus, the time on the x-axis represents the time from ingestion to the calculation time. This calculation time is dependent upon the biological endpoint. For live birthrate, the time used will be from the start of employment to marriage.

Microdosimetric Analysis

The above description was based on a macroscopic dose calculation to the entire ovary.

However, due to the densely ionizing tracks of the alpha particles, and the relatively low-activity concentration, it is important to consider microdosimetric effects. To calculate the microdosimetric hit distributions and specific-energy spectra (microdosimetric analogue of absorbed dose) for the cell nuclei, a computer code was written based on a Monte Carlo approach. The cell nucleus is assumed to be spherical and to have an average radius of 9 μm based on measurements made of neonatal oocytes (14). Sources are assumed to be uniformly distributed throughout the ovary, which is the same assumption used in the macrodosimetric analysis.

Our Monte Carlo algorithm has been described previously (15), and will only be described briefly here. Microdosimetric quantities are determined by selecting each source, determining if the source decays based on the source's effective half life, randomly determining the energy of the alpha emission (based on branching ratios) and the directional cosines of alpha-particle track. Assuming the alpha particle will travel in a straight line, the parametric equations as given by Eckerman (16), can be solved to determine if the alpha particle intersects the nucleus.

$$x' = x + t\cos(\varphi_1) \tag{6}$$

$$y' = y + t\cos(\varphi_2) \tag{7}$$

$$z' = z + t\cos(\varphi_3) \tag{8}$$

$$r_n^2 = x'^2 + y'^2 + z'^2 \tag{9}$$

In these equations r_n is the radius of the nucleus, x,y,z are the coordinates of the alpha source, and x',y',z' are the intercepts of the alpha particle with the nucleus. The angles φ_1, φ_2 and φ_3 are the angles of the alpha-particle path relative to the x,y, and z axes, respectively. This computation may be simplified by taking advantage of the symmetry presented by the choice of a spherical target. The next process involves determining t, which is the distance traversed by the alpha particle. This distance is evaluated by substituting Equations 6-8 into Equation 9 for the primed values. By solving for t, two solutions are obtained; t_1 corresponding to the distance from the alpha source to where the alpha particle enters the nucleus, and t_2 corresponding to the distance between the alpha source and where the particle leaves the nucleus. Note that when the alpha-particle emission occurs within the nucleus (starter), t_1 is chosen to be zero, while t_2 is the intercept with the nuclear surface. If the alpha particle terminates its track within the nucleus (stopper) the value of t_2 is set to the maximum range of the particle. A hit occurs when the solutions for t_1 and t_2 are both real, positive numbers.

The specific energy for a given deposition event is calculated by integrating the function

$$z = \frac{1}{m_n} \int_{t_1}^{t_2} \frac{dE}{dx}\, dx, \tag{10}$$

where m_n is the mass of the cell nucleus, and dE/dx is obtained from ICRU Report 49 (17) for alpha particles in water. Integration is performed using a look-up table for the linear-energy transfer data. The energy is evaluated at the residual range for t_1 and t_2. This is defined as the range of the chosen alpha minus the distance t_1 or t_2. The difference in these two energies is the amount of energy deposited in the nucleus by the single hit. Specific-energy spectra and hit distributions are obtained by simulating the source distributions 5000 - 10000 times, and counting the frequency of hits and specific energy.

Two source configurations are considered; a low ingestion of activity and a high ingestion of activity. Initial intakes of 3.7×10^5 Bq (10 μCi) and 3.54×10^7 Bq (956 μCi) of Ra-226 are used for the low and high activity, respectively. These values are based on intakes as determined above.

RESULTS

Estimates of the ovarian dose are summarized as follows. Nearly 50% of the workers received ovarian doses of less than 100 mSv (10 rem), and approximately 90% received doses of less than 5 Sv (500 rem). Note that these values have incorporated a quality factor. The factors used for these dose estimates are 1 for both internal- and external-gamma emissions, and 20 for alpha-particle emissions. The factor 20 was chosen based on the radiation protection quality factor for alpha-particles as recommended by the NCRP (18). For each of these doses, nearly 99% of the total dose can be attributed to the alpha-particle component. Thus, the choice of a quality factor is not important as it will only shift the doses by a constant.

Although not explicitly mentioned, the choice of a time for use in the retention integral is critical. For evaluation of parameters such as birth weight, the time chosen for the retention integral is the time from the start of employment to either the time of conception or birth. However, for analyses where the endpoint is live birthrate, the time used in the retention integral is less clear. In these cases, we have chosen to use the time from the start of employment to the time of marriage, which would indicate the presumed beginning of a woman's reproductive period. In general, this time is often less than 5 years. Analysis of the retention integrals in Figure 1 shows that this is the steepest portion of the curve, particularly for Th-228. Thus, uncertainties in this time are more likely to result in large uncertainties in the absolute dose. An alternative for these studies would be to choose the retention integral based on the time from the start of employment to the age 45, which potentially represents a woman's entire reproductive capability. This would tend to overestimate the dose to the ovaries.

Analyses using both methods have demonstrated that in comparison to a low-dose group (0 - 0.05 Sv), the high-dose group (> 5 Sv) exhibited a significant decrease in the number of live births (1.8 vs. 1.1; $p = 0.05$). Use of the retention integral at age 45 resulted in a general increase in the total dose. However, for the most part, it did not shift workers from one group to another. These trends were also evident after multivariable adjustment for potential confounding factors and after exclusion of subjects who may contribute a potential classification or selection bias. The interested reader is referred to Schieve (4,5) for a more detailed description of the statistical methods and results.

Results of the microdosimetric analysis are shown graphically in Figures 2 and 3. Figures 2 a-b are the specific energy distributions for both a low exposure and a high exposure individual, respectively. The corresponding "hit" distributions are shown in Figures 3 a-b. The values on the x-axis in Figure 2 represent absolute specific energies and therefore do not include a quality factor. Note that in both the low and high exposure cases, the specific energy distribution is highly heterogeneous and differs significantly from the mean value. In Figure 2a, the mean dose is 7 mGy (0.7 rad). However, there are cells which receive significantly higher specific energies than the mean with a maximum occurring at 250 mGy (25 rad). In addition, the fraction of cells receiving zero specific energy (nearly 90%) is not shown on this graph. In the high exposure case, the mean dose is 680 mGy (68 rad) with cells receiving specific energies ranging from zero to a maximum of approximately 1.75 Gy (175 rad). In this case, fewer than 1% of the cell nuclei receive zero specific energy.

The hit distributions provide additional insight which is useful in the interpretation of the biological results. In the example from the low exposure group, nearly all the oocyte nuclei are completely missed. The mean number of hits is 0.1 with most cells receiving zero or one hit. Significantly less than 1% of the cells receive more than one hit. However, in the high-exposure

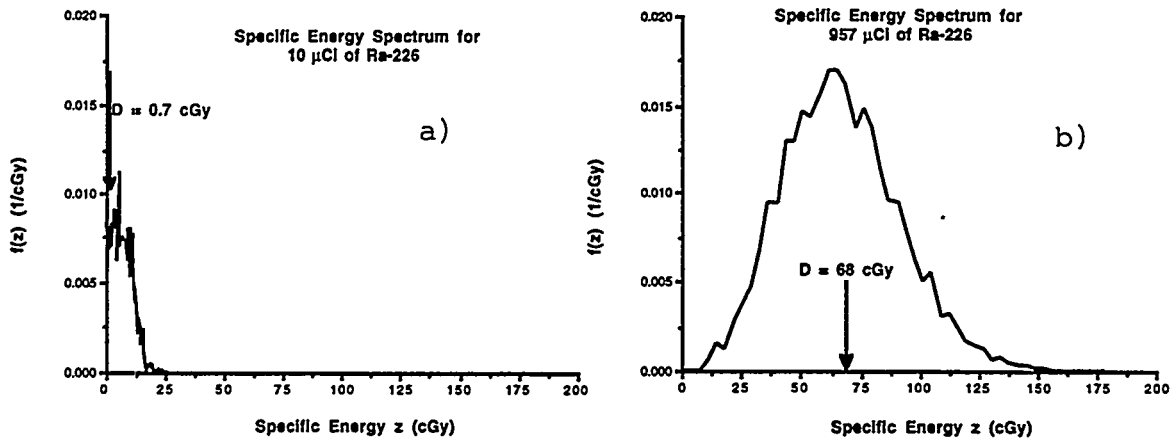

Figure 2. Specific-energy spectra for a) low exposure and b) high exposure.

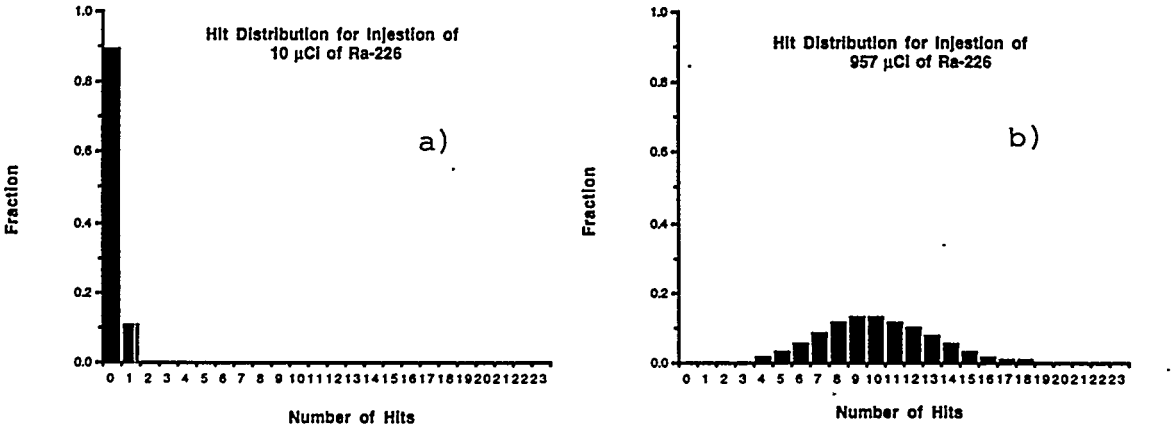

Figure 3. Hit spectra for a) low exposure and b) high exposure.

example, nearly all nuclei receive two hits or more. The average number of hits to the cell nucleus is approximately 10, with a small fraction of cell nuclei receiving 20 or more hits.

Furthermore, we have also plotted the fraction of cell nuclei receiving more than zero hits, more than one hit and more than two hits versus the average ovarian dose (Figure 4) in order to provide a link between macroscopic and microdosimetric quantities. Of particular interest is that the high-dose group (> 5 Sv) is the one for which the least number of live births is observed. Note that a large fraction of the oocyte cell nuclei receives more than 0,1 and 2 alpha-particle hits. This provides a possible explanation as to why the decrease in the number of live births occurs at these dose levels.

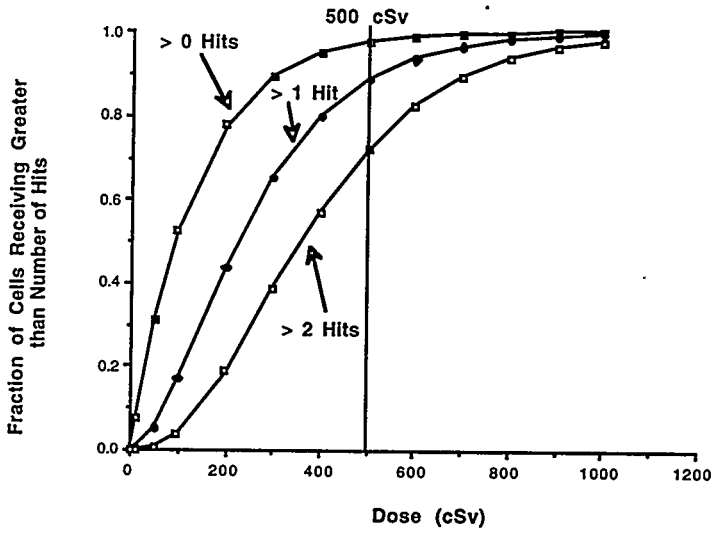

Figure 4. Fraction of cells receiving greater than the specified number of alpha-particle hits vs. the biological effective dose for ingestion of Ra-226.

DISCUSSION

The goal of this work was to review and update the dosimetry of ingested radium as applied to the radium dial workers. We have used these methods to calculate the average dose to the ovaries based on intake data and the retention of radium in man. In addition, we have examined the microdosmetry for the simple case of a uniform source distribution. Our dosimetric analysis has demonstrated a statistical correlation between a decrease in the live birthrate and those receiving ovarian doses of greater than 5 Sv. Inspection of the hit distribution to cell nuclei demonstrates that those in this high-dose range have nearly all oocyte nuclei receiving one or more alpha-particle hits. This is in contrast to the low-dose region where only a small percentage of the cell nuclei receive greater than two hits.

However, as in any dose calculation, certain caveats must be considered. In the estimation of the alpha particle dose from Ra-226, a major assumption was that Rn-222 and its daughters contributed no dose to the tissue in which its parent decayed. This is perhaps an oversimplification and could be rectified by using available retention data for Rn-222. Similarly, the assumption was made that all daughter products of Ra-228 decayed in place. Again, more data on the translocation of daughter products would be a useful refinement. Second, in the estimation of internal doses, all cases assumed an acute ingestion of radium. Future refinements would include modifying this for a continuous ingestion, if such data were available on the length of employment, etc. Third, there are a large number of uncertainties, including those associated with whole body measurements, calculation of retention integrals, the relative proportion of activity distributed between soft tissue and bone, and applying reference man data to particular individuals. Keane and Schlenker (7) estimated that the 95% confidence interval to be a factor of 4.8 of the calculated dose.

Previous analysis of a subset of this data had been performed by Polednak (3). His results showed that a significant decrease in live births occurred at doses of 1 Sv. Note that this is significantly lower than our determination of a threshold dose of 5 Sv. A possible explanation for this is that Polednak's data represents a much smaller data set and therefore lacks the ability to refine the high-dose category further. In addition, the difference in live birthrate that he observed between the

low-dose group and high-dose group was relatively small (2.5 vs. 2.0).

It is important to remember that comparisons between internal alpha-particle dose and external-gamma doses are not appropriate. The reason for this is as follows. Consider a volume irradiated by an external beam of photons to a dose of 2 Gy. If one were to sample every cell within that volume, the dose to each cell would be 2 Gy. However, consider the case where the alpha particle dose is 2 Gy. Based on the above examples, most of the cells irradiated will receive energy deposition events which differ significantly from the mean. Thus, for a dosimetric analysis of this type to be meaningful, microdosimetric quantities must be considered. In addition, the comparison between external dose and alpha-particle dose is hampered by the RBE of the alpha particle.

It is desirable to correlate biological outcome with microdosimetric parameters. However, in this case, correlation is difficult. The reason for this is that microdosimetric parameters are strong functions of the source distribution. For example, a source distributed only within the cell nucleus will have a distinctive specific energy spectrum compared to a source distribution which is limited to the spaces outside of the cell. In order to calculate microdosimetric parameters accurately, it is necessary to obtain serial autoradiography samples. These data may be available through animal studies.

The results of our simple microdosimetric analysis has shed light on the threshold nature of the dose response. Figure 4 shows the fraction of cells receiving more than zero, one or two alpha-particle hits. Of note is the relationship between the slope of these functions and the occurrence of a decreased number of live births. In particular, the slope of the curve for greater than zero hits becomes nearly zero at approximately 5 Sv. Data from mice and humans (19,20) have shown that oocytes are relatively sensitive to alpha-particle irradiation. Thus, it may be argued that those receiving at least 1 hit are killed or severely mutated such that it would result in the loss of the fetus. While this simplified analysis does not take dose into account, it provides a useful method for understanding the nature of the dose response which warrants further investigation.

ACKNOWLEDGMENTS

The authors thank Drs. Faith Davis, Robert Thomas, Robert Rowland, Andrew Stehney, Robert Schlenker, and John Rundo for their scientific support and counsel over the course of this project. Special thanks to Thomas Kotek, database manager for the Internal Emitter Project at Argonne, for his help in obtaining and understanding these data and to Candice Ipem and Mark Trusgnich for their hard work in abstracting the data. This work was supported in part by the US Department of Energy, Office of Energy Research, under contract W-31-109-ENG-38.

REFERENCES

1. Martland HS. Occupational poisoning in manufacture of luminous watch dials. JAMA 92:466-473, 1929.
2. Stebbings JH, Lucas H and Stehney AF. Mortality from cancers of major sites in female radium dial workers. Am J Indust Med 5:435-459, 1984.
3. Polednak AP. Fertility of women after exposure to internal and external radiation. J Env Path and Toxicol 4:457-470, 1980.
4. Schieve L. Comparative analysis of reproductive experience of women formerly employed in the radium dial industry. Ph.D. Dissertation. The University of Illinois-Chicago, 1996.
5. Schieve L, Davis F, Roeske JC, Handler A, Freels S, Stinchcomb T and Keane A. Evaluation of internal alpha radiation exposure and subsequent infertility among a cohort of women formerly employed in the radium dial industry. Radiation Res 147(2):236-244, 1997.

6. Bloomfield JJ and Knowles FJ. Health aspects of radium dial painting. II. Occupational environment. J Indust Hygiene 15:368-382, 1933.
7. Keane A and Schlenker RA. Soft tissue dosimetry of radium in humans - I. Alpha particle doses from the decay of ^{226}Ra and ^{228}Ra in soft tissues. Health Phys 44 (Suppl 1):81-89, 1983.
8. Schlenker RA, Keane A and Holtzman RB. The retention of ^{226}Ra in soft tissue and bone : Implications for ICRP20 alkaline earth model. Health Phys 42:671-680, 1982.
9. Rowland RE. Low level radium retention by the human body: A modification of the ICRP Publication retention equation. Health Phys 65:507-513, 1993.
10. Schlenker RA. Gamma-ray dosimetry of ^{226}Ra and ^{228}Ra in the human body. Radiological and Environmental Research Division Annual Report. Argonne National Laboratory (ANL 7860, Part II), 23-50, 1971.
11. Rowland RE. Radium in humans : A review of US studies, pp 35-64, Argonne National Laboratory, Argonne, IL 1994.
12. Norris WP, Speckman TW and Gustafson PF. Studies of the metabolism of radium in man. Am J Roentgenol Rad Therapy Nucl Med 73:785-802, 1955.
13. International Commission on Radiological Protection, "Alkaline earth metabolism in adult man", ICRP Publication 20, Pergamon Press, Oxford, 1973.
14. Forabosco A, Sforza C, DePol A, Vizzotto L, Marzona L and Ferrario, VF. Morphometric study of the human neonatal ovary. The Anatom Rec 231:201-208, 1991.
15. Stinchcomb TG and Roeske JC. Analytic microdosimetry for radioimmunotherapy. Med Phys, 19(6):1385-1393, 1992.
16. Eckerman KF, Ryman JC, Taner AC, and Kerr GD. Traversal of cells by radiation and absorbed fraction estimates for electrons and alpha particles. Proceedings of the Fourth International Radiopharmaceutical Dosimetry Symposium, Oak Ridge, TN 1985, S-Stelson AT and Watson EE, Editors, Conf-851113, pp:67-81, 1986.
17. International Commission on Radiation Units and Measurements, Stopping powers and ranges for protons and alpha particles, ICRU Report 49, Bethesda, MD 1993.
18. National Council on Radiation Protection and Measurements. Recommendations of limits for exposure to ionizing radiation. NCRP Report 91, Washington, D.C. 1987.
19. Thomas RG, Healy JW and McInroy JF. Plutonium in gonads : A summary of the current status. Health Phys. 48(1):7-17, 1985.
20. Russell LB and Russell WL. Frequency and nature of specific-locus mutations induced in female mice by radiations and chemicals : A review. Mut Res 296:107-127, 1992.

QUESTIONS

Toohey: Which estimates of radium intake were used? Specifically, was Rundo's correction of the Norris retention function applied, which would tend to increase the lower range of intake estimates and therefore the doses?

Roeske: The most recent radium intake values from ANL were used in these studies. These values are based on Rowland's modification of ICRP Publication 20 whole-body retention equations.

Eckerman: In your calculations you have neglected the daughter products of radium. These decay products should not be neglected. You might consider the treatment recently used by the ICRP; see Publications 67 and 71.

Rao: I have to agree with Keith that the daughter nuclides of Ra-226 may not be ignored in dosimetry. We have done some in vivo experiments with Ra-223 and found that the daughters are in equilibrium with the parent. Therefore, ignoring contributions from daughter products of Ra-226 in dosimetry may not be appropriate. I have a questions for you. The still births that you talked about are the consequence of radiation damage to mature oocytes. Early oocytes are sensitive and small in size. Have you taken account of large size of mature oocytes in your dosimetry?

Roeske: I agree that neglecting the Rn-222 daughter may result in an underestimate of absorbed dose. However, the results are expected to be the same, namely that the high-dose group will have a significant reduction in the live birthrate. As for the size of oocytes during the different stages of maturity, we have examined the microdosimetry for the average oocyte. It is not expected that the consideration of the size distribution will change these results.

SMALL-SCALE DOSIMETRY OF BONE AND BONE MARROW FOR ^{89}Sr AND ^{90}Y USING HISTOLOGICAL IMAGES

Akabani G and Leichner PK
Department of Radiation Oncology
University of Nebraska Medical Center, Omaha, Nebraska 68198

ABSTRACT

The objective of this study was to assess the variability of ^{89}Sr and ^{90}Y localized absorbed doses to bone tissues based on histological images. This work defines the concept of small-scale dosimetry based on terms of cumulated activity per unit volume in source region and establishes the variable of a modified S* value (Gy cm^3/Bq s). Methods: Histological images were obtained from beagle dog bones which closely resemble those of humans. Chord length distributions from histological images were used to assess the degree of trabeculation and its relationship with S* values for different bone tissues. A two dimensional Monte Carlo transport code was used to assess the energy deposition pattern of beta particles on these histological images. Electrons were transported pixel-by-pixel based on the material properties of each pixel. Trabecular bone, red bone marrow and fat cells were recognized in every histological image and Monte Carlo transport was then carried out based on different source configurations. The energy deposited in each bone region was expunged and S* values were calculated as a function of mean bone marrow cavity size and bone marrow volume fraction (BMVF). Results obtained from histological samples were then compared with a three-dimensional slab model where each bone region was simulated by a slab of different thicknesses. Bone surfaces were considered to have a thickness of 10 μm. Results: A total of 29 histological images were analyzed and S* values were calculated. Two source regions were assumed: the bone marrow and the bone surfaces. A comparison of results of S* values between histological images and the three-dimensional slab model resulted in very close agreement. The results from both models show that S* values are proportional to BMVF. Conclusions: This dosimetric technique based on histological images presents a direct approach to bone and bone marrow dosimetry on a patient-specific basis. Results demonstrate that the use of S* values as a function of BMVF conveys an estimate of absorbed doses to localized bone regions.

INTRODUCTION

Dosimetry of the bone and consequently, the determination of the optimal activity and frequency to administer a radionuclide to a patient, is a complex problem. It requires knowledge of the physiological, morphological, chemical, and physical properties of bone, as well as the biokinetic behavior and distribution (macro-distribution and cell-level distribution) of the radionuclide and the types of radiations emitted. The complexity of the bones that make up the skeleton makes it difficult

to interpret the effects of irradiation or to measure radiation dose. There are significant discontinuities in density and composition over spatial dimensions that are of the same order of magnitude as the ranges of radiations emitted by radionuclides (1, 2).

The intimate blending of bone matrix and bone marrow is a primary point in devising therapy of bone lesions; since specific modalities are not yet available for destroying the malignant cells, treatment is usually palliative. Presently, difficulties are encountered in calculating accurate doses and clinical experience is needed to determine a reasonable optimal dose with any particular radiopharmaceutical. There is a large number of clinical cases of bone dosimetry presented in the scientific literature (3-9). In many cases, it is difficult to compare or assess differences among these studies because of the lack of a comprehensive dosimetric system capable of taking into consideration the many parameters associated with each study.

Presently, the Medical Internal Radiation Dose (MIRD) schema for absorbed dose calculations is used to assess doses to bone (gross skeletal dosimetry) by using calculated radiation absorbed doses per unit cumulated activity (S values) for specific radionuclides. The MIRD methodology is well suited for diagnosis because it assumes that the activity is uniformly distributed in each bone; for the case of radioimmunotherapy and radionuclide therapy, this essentially ignores the local distribution of the radionuclide and its relationship to affected cell populations. It has been stated that the MIRD methodology requires further improvements if dose estimates are to be calculated for therapy purposes in individual patients and to be able to compare results with those obtained using localized external beam radiotherapy (10-12).

There are several challenges to meet in order to improve radiotherapy procedures. One of these is to improve the dosimetry and study the correlation of doses and/or dose distributions in bone tissues with the respective clinical or biological outcome. To meet this challenge and carry out clinical studies with confidence, absorbed dose calculations will require some degree of accuracy and an estimate of the uncertainty associated with the calculations. Furthermore, there will be the need to decide what dosimetric variables are to be used in order to correlate absorbed dose with toxicity or normal tissue complication probability and tumor control. Currently, average absorbed doses are correlated to a biological outcome; however, the possible use of dose-volume histograms for specific regions of the bone may convey more information related to a specific treatment rather than assessing only a single dose value.

To a large extent, the problem of bone dosimetry is based on radionuclide cell distribution and cell and tissue energy deposition (14- 20). Many issues associated with bone marrow dosimetry are based on how the radionuclide targets marrow, bone, bone surfaces, blood and other components. However, it is difficult to obtain an accurate distribution of a radionuclide. The long term objective is to provide a set of clinically implementable procedures regarding bone marrow dosimetry for a specific radionuclide as well as the respective inherent errors, and to provide the data collection requirements. To this end, this work addresses the beta dosimetry of bone marrow with the help of imaging techniques that can provide the information necessary to carry out studies that will address the proposed objective.

The difficulty of assessing absorbed doses to bone tissues is due to the lack of information on how the radioactive material is distributed throughout bone itself. Several problems have been encountered in obtaining good biokinetic data from measurements in man (21-23). In clinical practice, researchers use data obtained from several sources, such as imaging and blood sampling, to assess the macro-distribution of radionuclides in bone; however, these methods convey gross local information that is used to assess the activity fraction in bones with no reference to its internal distribution. On the other hand, marrow aspiration and bone marrow biopsy samples may convey information on radionuclide distribution at the small-scale level.

Small-scale dosimetry based on histological images and autoradiography at the microscopic level represents an excellent but extreme and tedious approach to the problem of bone dosimetry. It provides a large amount of information and it will always be limited to a small region of a bone. Nonetheless, some useful predictions of the local distribution and dosimetry of radionuclides that go beyond gross skeletal dosimetry can be made based on the information provided through this method, specially for localized bone lesions. Through the use of small-scale dosimetry it is possible to assess localized absorbed doses for various regions of the bone based on mapping a specific bone site.

Histological images of the bone convey information about cell populations, densities, and form of cell clustering in marrow cavities. The way cells arrange themselves is an important factor in dosimetric calculations for radionuclide therapy and radioimmunotherapy as large dose variations can occur in bone marrow because of varying cell arrangements and the way radioactive material is attached to these cells. The use of histological images enhances the capabilities of accurate bone dosimetry for cancer research by using the characteristics of the actual bone and cell populations rather than oversimplified assumptions such homogeneous distribution of a radionuclide in bone marrow.

SMALL SCALE DOSIMETRY

In this work, small scale dosimetry is defined as the assessment of doses to regions or tissues with spatial dimensions that are in the same order as the range of the corpuscular radiations being emitted. Using the MIRD nomenclature, the absorbed dose to target region r_k can be expressed as

$$\bar{D}(r_k \leftarrow r_h) = K \frac{\tilde{A}_h}{m_k} \sum_i n_i E_i AF_i (r_k \leftarrow r_h) \; [Gy], \tag{1}$$

where K is a conversion factor, $\tilde{A}_h$ is the cumulated activity in source region r_h expressed in (Bq s), m_k is the mass of the target region r_h expressed in (g), n_i is the intensity per decay of radiation type I, E_i is the energy of radiation type I expressed in (MeV), and AF_i ($r_k \leftarrow r_h$) is the absorbed fraction of energy for radiation type I from source region r_h to target region r_k. Let V_s be the localized volume of a bone tissue sample, then Equation 1 can be expressed in an equivalent form as

$$\bar{D}(r_k \leftarrow r_h) = K \frac{\tilde{A}_h / V_s}{m_k / V_s} \sum_i n_i E_i AF_i (r_k \leftarrow r_h) \; [Gy] \tag{2}$$

or

$$\bar{D}(r_k \leftarrow r_h) = K \frac{\tilde{a}_h}{\rho_k} \sum_i n_i E_i AF_i (r_k \leftarrow r_h) \; [Gy], \tag{3}$$

where $\tilde{a}_h = \frac{\tilde{A}_h}{V_s} \left[\frac{Bq\,s}{cm^3}\right]$ is the volume-specific cumulated activity, and $\rho_k = \frac{m_k}{V_s} \left[\frac{g}{cm^3}\right]$ is the partial density of target region r_k over the whole bone sample. The activity per unit volume of the sample with volume V_s can be normalized by the volume fraction of the source region r_h, i.e.

$\tilde{a}_h = \tilde{a}_h' VF_h \left[\frac{Bq\ s}{cm^3}\right]$, where $VF_h = \frac{V_h}{V_s}$ is the volume fraction of source region r_h in the bone tissue sample. Thus, $\tilde{a}_h'$ is the net volume-specific cumulated activity in source region r_h. The dose to region r_k can then be expressed as

$$\bar{D}(r_k \leftarrow r_h) = \tilde{a}_h' S^*(r_k \leftarrow r_h)\ [Gy], \tag{4}$$

where $S^*(r_k \leftarrow r_h)$ is defined as

$$S^*(r_k \leftarrow r_h) = K \frac{VF_h}{\rho_k} \sum_i n_i E_i AF_i(r_k \leftarrow r_h) \left[\frac{Gy cm^3}{Bq\ s}\right]. \tag{5}$$

Furthermore, the dose to region r_k is then expressed as

$$\bar{D}(r_k \leftarrow r_h) = a_0 \tau_h S^*(r_k \leftarrow r_h)\ [Gy], \tag{6}$$

where τ_h is the mean residence time expressed as

$$\tau_h = \frac{\tilde{a}_h'}{a_0}\ [s], \tag{7}$$

and a_0 is the initial activity concentration in the blood pool. The above dosimetric system is consistent with the MIRD methodology and it further expands its use at the small-scale level taking into consideration morphological structures.

BONE MARROW AND TRABECULAR BONE CHORD LENGTH DISTRIBUTIONS

One method for modeling trabecular bone structure is based on the use of chord-length distributions. The calculation of chord-length distributions is based on morphological information obtained directly from histological bone samples (24, 13). The present work is based on beagle dog bones which were used to assess the feasibility of the dosimetric methods. Figures 1a through c show three digitized images and the corresponding frequency distributions of marrow and trabecular chord lengths illustrating the wide variation of bone structure obtained from a sagittal cross section of a beagle dog femur. Similarly, Figure 2 shows an example of the corresponding cell clustering and chord length distributions for red marrow and fat cells. These images provide relevant information about bone structure and the degree of trabeculation. The mean chord-lengths obtained in this study for the beagle dog are comparable to those calculated by Spiers et al. (25).

Based on digitized images, a computer code was developed to calculate chord-length distributions for trabecular bone and bone marrow cavities and their respective volume fractions. Because the detailed structure of bone varies widely within the skeleton, the specificity of this method allows for the assessment of localized absorbed doses based on local morphological parameters. The mass associated with each specific region is calculated assuming that a two-dimensional cross section of bone is representative of the three-dimensional bone structure (26).

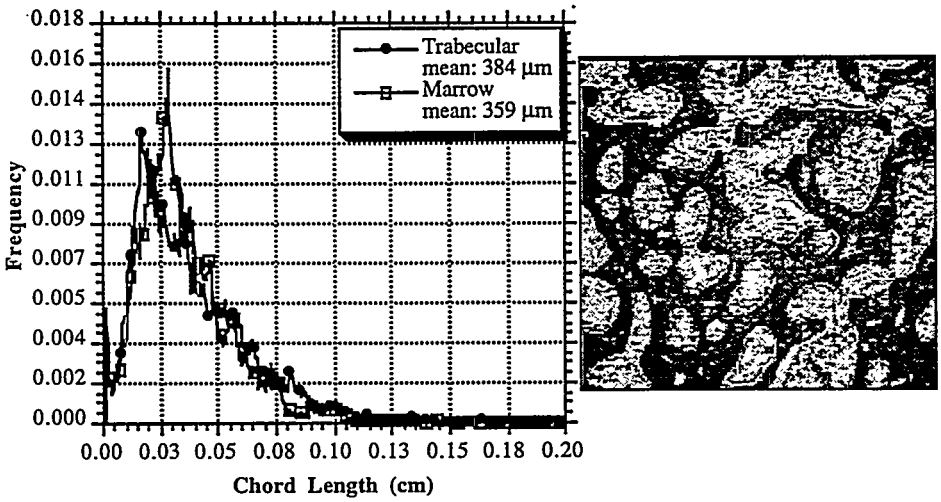

-a-

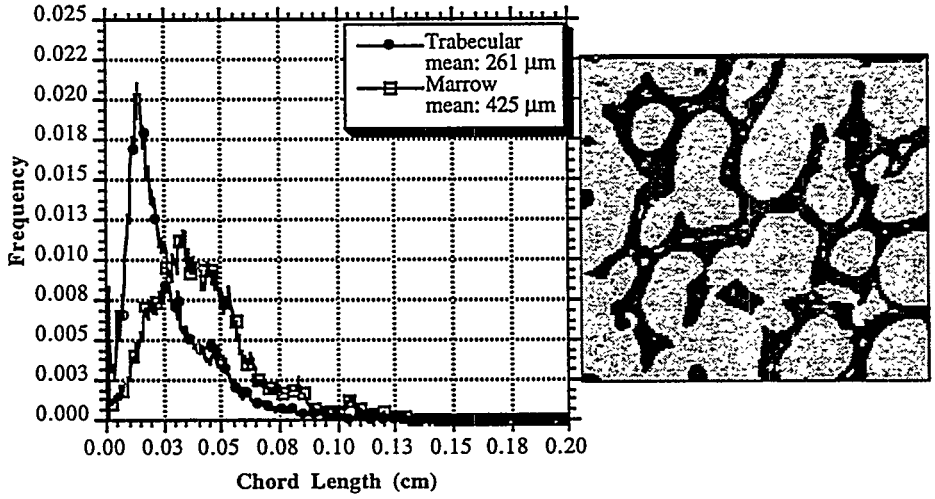

-b-

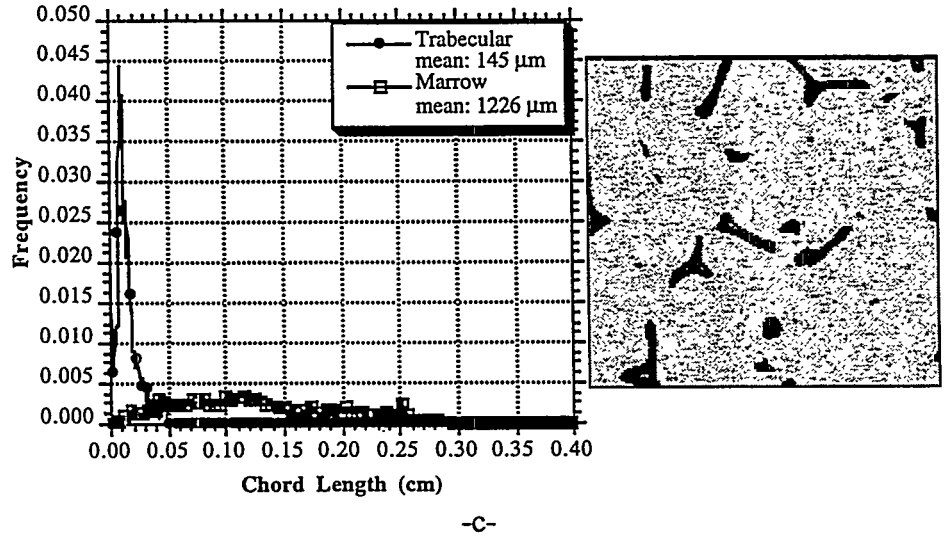

-c-

Figure 1. Chord length distributions for bone marrow and trabecular bone cavities obtained from a sagittal cross section of a beagle femur close to a) cortical bone, b)midcenter, c) center of bone.

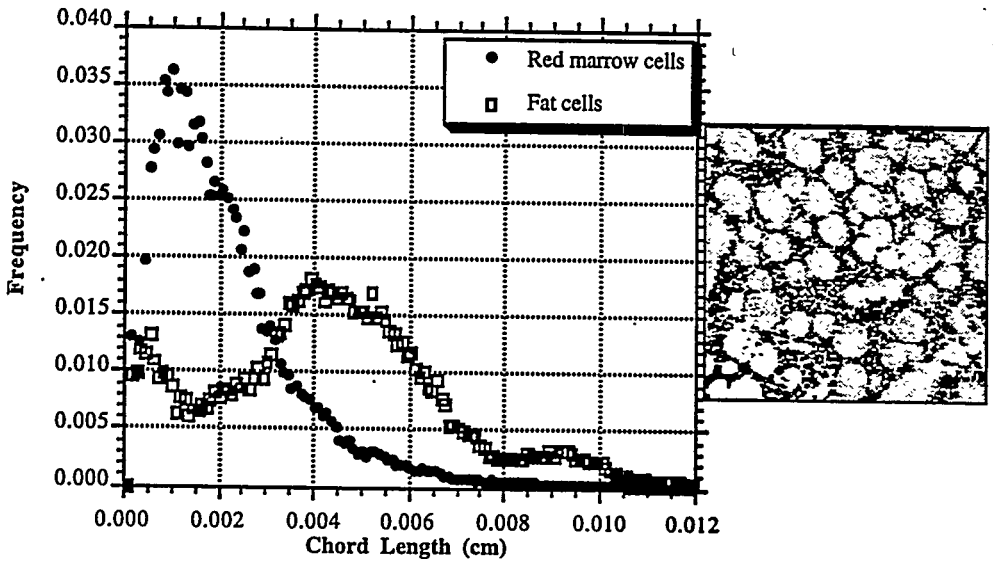

Figure 2. View of marrow and fat cells conglomerations in marrow cavities and their respective chord length distributions. Volume fractions for red and fat cells are 31% and 69%, respectively.

Let VF_{BM} and VF_{TB} be the volume fraction of bone marrow and trabecular bone, respectively, obtained from a specific histological image. Therefore, the mass per unit volume (or partial density) of bone marrow, m_{BM}, and trabecular bone, m_{TB}, can be expressed as

$$m_{BM} = VF_{BM}\rho_{BM} \quad [g/cm^3] \tag{8}$$

and

$$m_{TB} = VF_{TB}\rho_{TB} \quad [g/cm^3], \tag{9}$$

where ρ_{BM} and ρ_{TB} are density of bone marrow and trabecular bone, respectively. The volume fraction associated with the endosteal layer, VF_{EL}, is proportional to the degree of trabeculation. This can be calculated as

$$VF_{EL} = SA_{EL}\,\Delta X, \tag{10}$$

where ΔX is the thickness associated with the bone surfaces assumed to be of 10 μm. The endosteal surface area per unit volume of bone, SA_{EL}, is proportional to the degree of trabeculation and volume of bone marrow, and can be expressed as

$$SA_{EL} = \frac{4VF_{TB}}{\bar{\Omega}_{TB}}\,VF_{BM} \quad [1/cm], \tag{11}$$

where $\bar{\Omega}_{TB}$ is the mean chord length of trabecular cavities and V_{BM} is the volume fraction of bone marrow. Therefore, the mass per unit volume can be expressed as

$$m_{EL} = VF_{EL}\rho_{EL} \ [g/cm^3] . \tag{12}$$

Similarly, the mass of red cells, m_{RC}, and fat cells, m_{FC}, can be expressed as

$$m_{RC} = VF_{RC}\rho_{RC} \ [g/cm^3] \tag{13}$$

and

$$m_{FC} = VF_{FC}\rho_{FC} \ [g/cm^3] , \tag{14}$$

where VF_{RC} and VF_{FC} are the volume fractions for red cells and fat cells, respectively.

LOCALIZED DOSIMETRY OF ^{89}Sr AND ^{90}Y

Slab Dosimetric Model

This model consists of a series of slabs. Figure 3 shows a schematic representation of this model (10). The slab thickness of bone marrow and trabecular bone are given by their respective chord length distributions. The endosteal layer thickness of 10 μm is assumed to be included as part of the trabecular bone region; thus, the bone marrow volume fraction is given by

$$VF_{BM} = \frac{\bar{\Omega}_{BM}}{\bar{\Omega}_{BM} + \bar{\Omega}_{TB}} . \tag{15}$$

The bone marrow region is subdivided into red bone marrow (red cells) and yellow marrow (fat cells) with their respective chord length distributions. This geometry model was implemented into the EGS4 Monte Carlo transport code to assess absorbed doses and absorbed fractions of energy (AF) in the different bone regions. References to the EGS4 code can be found elsewhere (27, 28). The materials used were the red bone marrow, yellow marrow, and trabecular bone with densities of 1.03, 0.98 and 1.92 g/cm^3, respectively (29). A uniform distribution was assumed in the source region and the initial particle direction was perpendicular to the interface plane.

It is relevant to see how the localized absorbed fraction of energy (AF) varies as a function of electron energy based on this bone slab model. For example, the mean chord lengths for bone marrow, trabecular bone, red cells and fat cells from Figure 1a and Figure 2 were used as a geometry input into the slab model to assess the localized AF as a function of electron energy. Figure 4a and 4b show the localized AF where the source region was assumed to be the red bone marrow (red cells) and endosteal layer (bone surfaces), respectively. The target regions were the red cells, fat cells, trabecular bone and bone surfaces. As expected, the localized AF for low energy electrons depends on the initial source region. However, for high energy electrons and under charged particle equilibrium (CPE) conditions, the localized AF tends to be equal to the mass fraction associated with each target region. CPE conditions are assumed for the sake of simplicity; however, if the bone lesion is smaller than the electron particle range, energy deposited beyond this range should not be considered in the assessment of localized AF. Furthermore, Table 1 shows the close agreement between the mass fractions for the different target regions and the results obtained from Monte Carlo calculations for a 2 MeV electron; Bremsstrahlung production was assumed to escape, thus, the sum of all absorbed fractions was less than unity. This example shows that there can be large variability in localized AF from one bone region to another. This variability is dependent on lesion size, particle

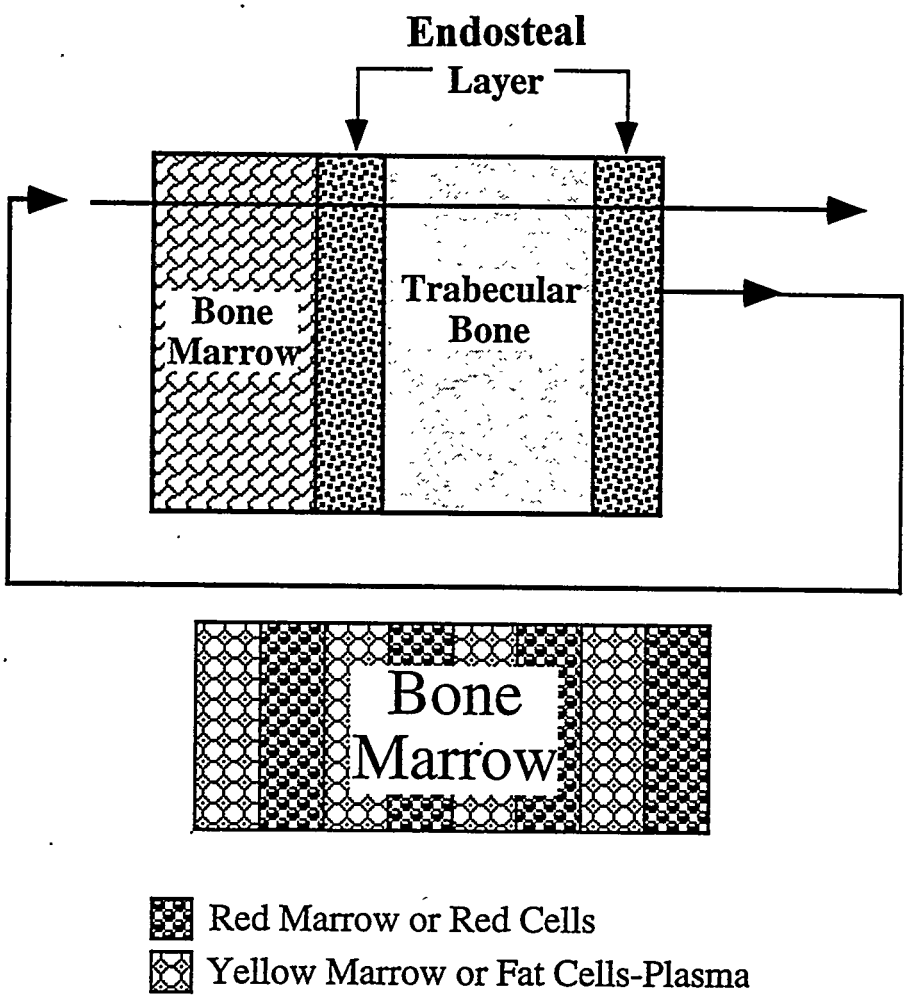

Figure 3. Plane geometry implemented into the Monte Carlo transport code EGS4 for the calculation of absorbed energy into trabecular and marrow cavities where the mean chord length of bone marrow and trabecular cavities are used to assess S* values. Bone marrow is divided into red bone marrow or red cells and yellow marrow or fat cells.

range and mass fractions of the different regions; consequently, large variations in localized absorbed doses can be expected from one bone region to another. However, it is possible to approximate the value of absorbed fractions for high energy electrons by calculating the mass fraction for every bone region.

The slab model was used to assess S* values for bone marrow as a function of bone marrow mean cavity size, $\bar{\Omega}_{BM}$, and bone marrow volume fraction, VF_{BM}, for a uniform distribution of ^{90}Y in bone marrow itself. The bone marrow volume fraction was varied from zero to one and the mean marrow cavity size was varied from 200 to 3000 :m. These ranges of cavity sizes were selected according to those measured in long bones, such as the femur, and bones with small trabecular region, such as the skull. Figure 5 shows the results obtained for ^{90}Y; as the bone marrow volume fraction tends to unity, the dose to bone marrow tends to be that under charged particle equilibrium conditions. However, as the bone marrow volume fraction tends to zero, the S* value tends to a constant proportional to the bone marrow slab thickness.

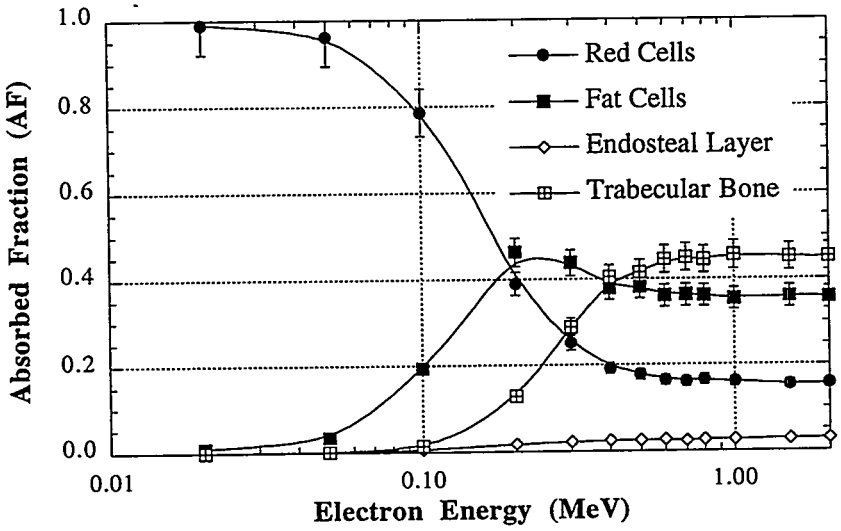

-a-

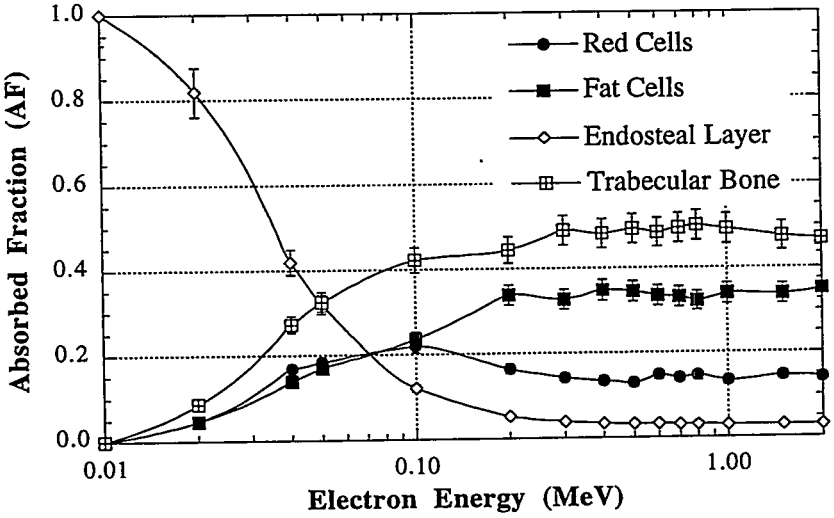

-b-

Figure 4. Absorbed fraction of energy as a function of electron energy for different regions obtained from a specific histological image. The source region were a) red cells and b) the endosteal layer, respectively.

Localized Dosimetry Based on Histological Images

To carry out the dosimetry of bone, a two-dimensional Monte Carlo code based on the EGS4 system code was developed to transport electrons directly on histological images. Bone tissues were recognized in every pixel of an image and electron transport was then carried out according to the pixel material properties. The energy deposited in every pixel was then expunged based on region, and S* values were then calculated. As an example, Figure 5a shows a bone sample image used as a geometry input into the Monte Carlo transport code, and Figure 5b and 5c show the energy deposition patterns for a 10 keV electron and ^{90}Y, respectively, for a uniform distribution in bone marrow cavities. This technique, however tedious, represents a direct method to carry out localized dosimetry of bone marrow, trabecular bone, and bone surfaces.

Table 1
Comparison of Absorbed Fractions (AF) for a 2.0 MeV Electron Based on Monte Carlo Transport, and Mass Fractions Obtained from Histological Images Shown in Figure 1a, 1b and 1c, Respectively

Bone Region	Mass Fractions	Absorbed Fractions Source:	
		endosteal layer	red cells
1a)			
Trabecular bone	0.660	0.633	0.661
Red cells	0.089	0.094	0.086
Fat cells	0.225	0.231	0.226
Endosteal layer	0.026	0.027	0.024
Total	1.000	0.986	0.997
1b)			
Trabecular bone	0.469	0.465	0.450
Red cells	0.146	0.141	0.156
Fat cells	0.358	0.350	0.356
Endosteal layer	0.027	0.029	0.028
Total	1.000	0.987	0.990
1c)			
Trabecular bone	0.133	0.163	0.147
Red cells	0.250	0.240	0.238
Fat cells	0.597	0.555	0.577
Endosteal layer	0.020	0.022	0.019
Total	1.000	0.980	0.981

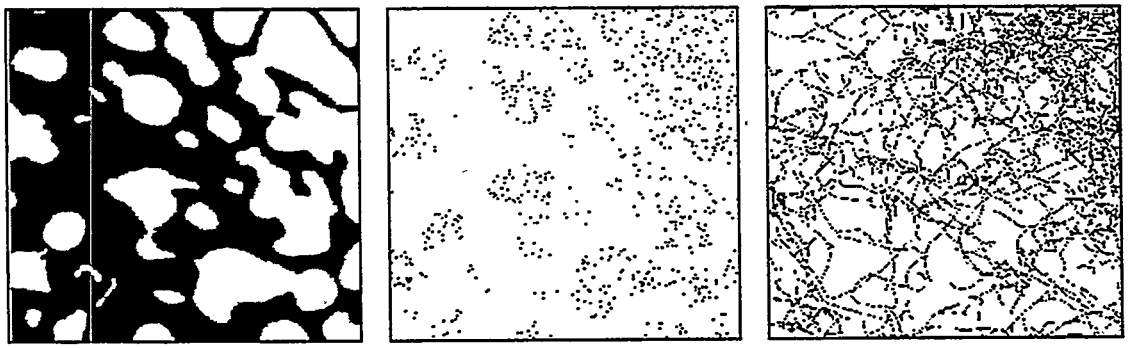

a) b) c)

Figure 5. Two dimensional Monte Carlo transport of electrons in a histological image using the computer code EGS4; a) histological image of trabecular bone; b) 10 keV electron; c) Y-90 energy deposition pattern. The source region is the bone marrow.

Figure 6a and 6b shows a comparison of S*values for ^{90}Y between the slab model and those obtained directly using histological images for sources in bone marrow and bone surfaces, respectively. As can be seen in Figure 7, there is a good agreement between results obtained using the histological images and the results obtained using the slab model. Furthermore, the slab model can be applied to any bone region as long as the mean marrow cavity size, $\bar{\Omega}_{BM}$, and the bone marrow volume fraction, VF_{BM}, are assessed.

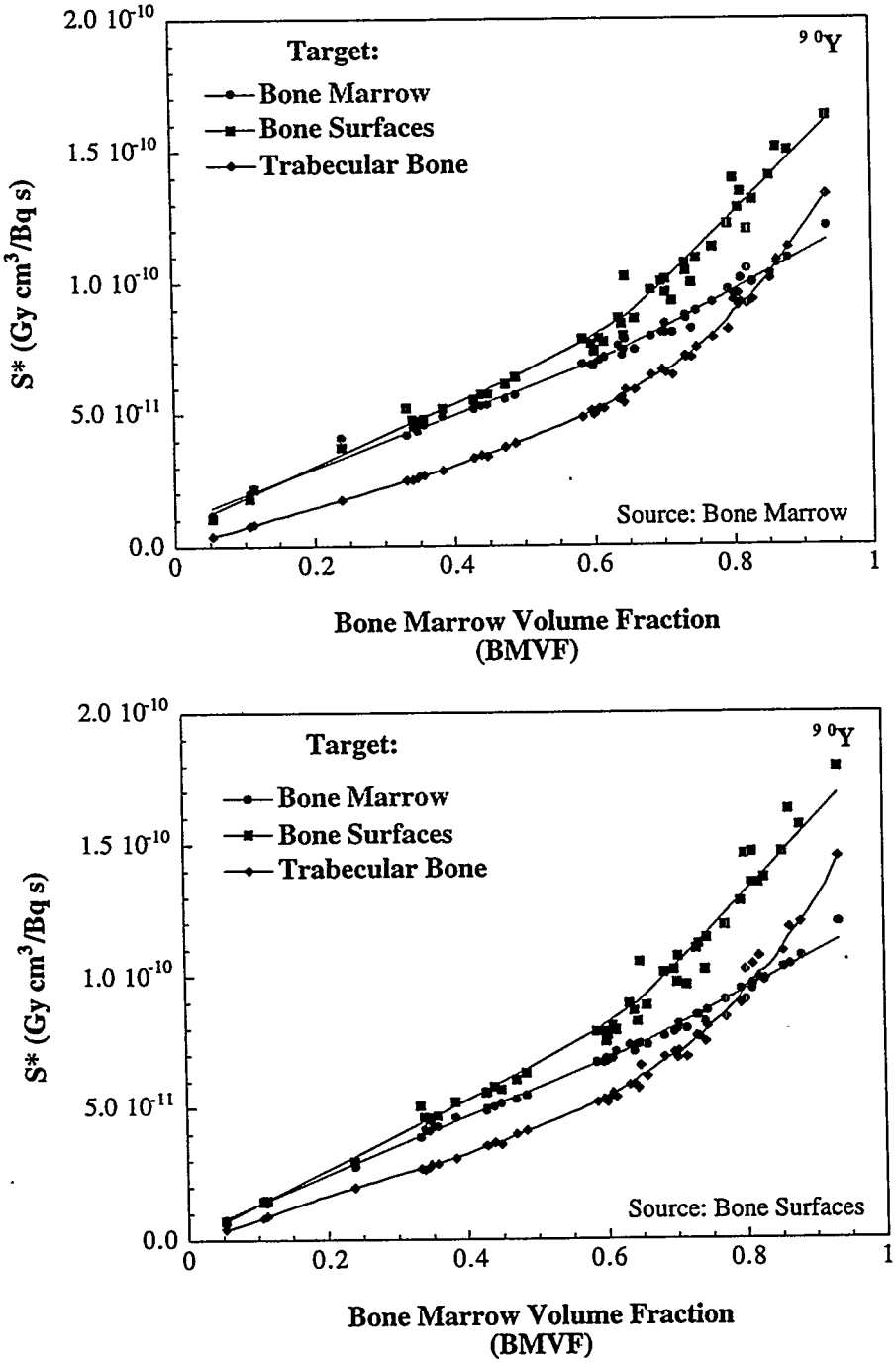

Figure 6. Variability of S* values to target regions as a function of bone marrow volume fraction (BMVF) based on histological images for ^{90}Y. The source regions were the bone marrow and bone surfaces, respectively.

S* values for bone marrow were calculated for a uniform distribution of Y-90 in the bone marrow cavities for 48 histological images. However, it will be impossible to obtain histological samples for every patient and bone region; therefore, the theoretical slab model is required to simplify the dose assessment. S* values for ^{90}Y and ^{89}Sr were carried out using the basic principles on small-scale dosimetry that were outlined previously, and S* values were calculated for bone marrow as a function of cavity size and bone marrow volume fraction. The slab model described above requires corroboration based on the direct assessment of S* values from histological images.

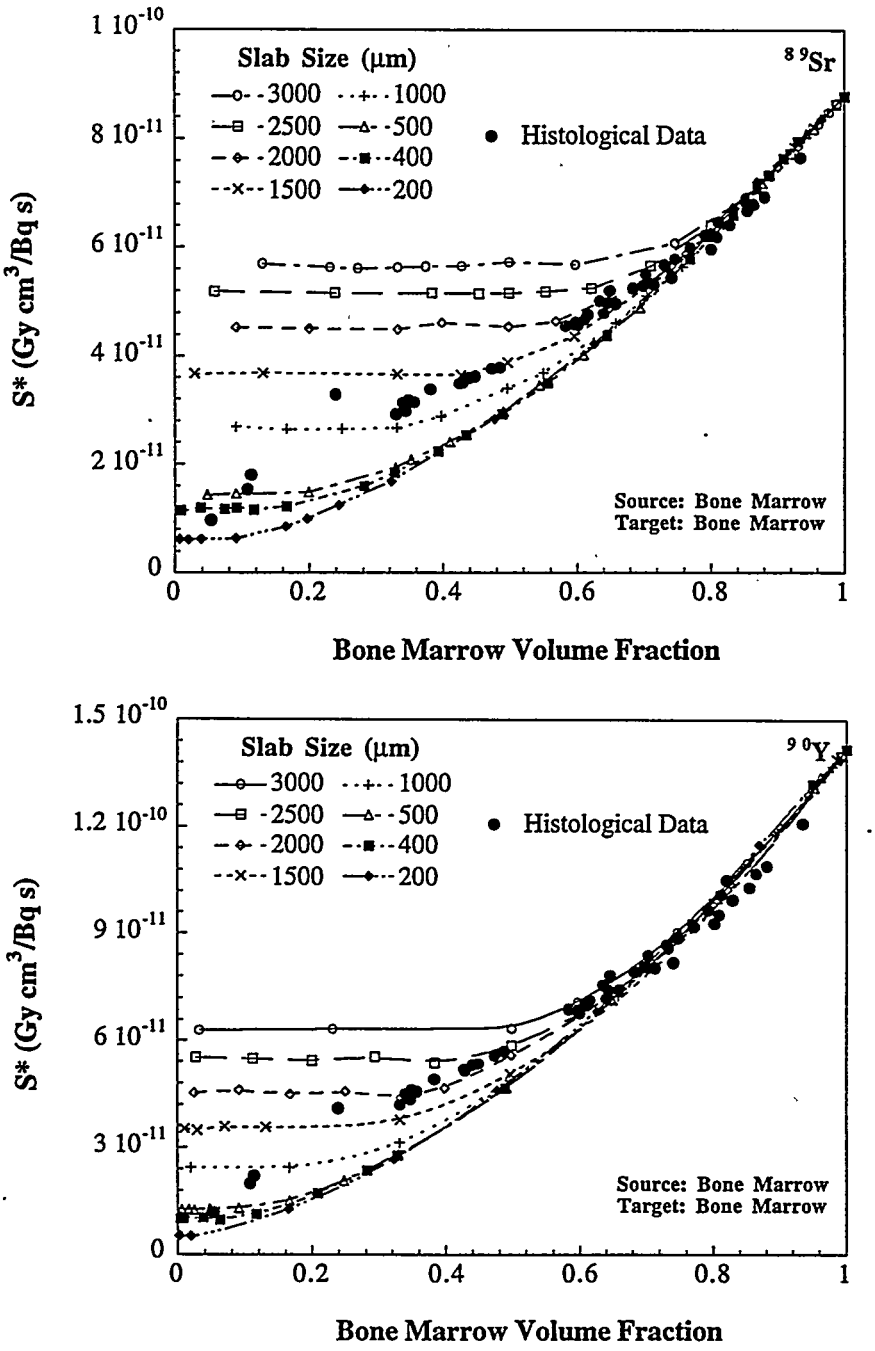

Figure 7. Comparison of calculated S* values as a function marrow volume fraction (BMVF) based on the slab model and histological images for ^{89}Sr and ^{90}Y. The source and target region were the bone marrow.

DISCUSSION

The S* values (Gy cm^3/Bq s) obtained using the slab dosimetric model compare well with those results obtained directly using histological images. Furthermore, some inferences can be made from the results shown in Figure 6. When the source region is the bone marrow or the bone surfaces and the target region is the bone marrow, the S* value tends to a dose equivalent similar to that under charged particle equilibrium conditions (CPE) as the BMVF tends to unity. However, the S* value

for bone and bone surfaces exceed that of bone marrow as the BMVF tends to unity. This dose is due to electron backscattering in bone and, thus, the dose to bone surfaces will be higher than that of bone or bone marrow.

The bone slab model predicts a family of curves based on the mean bone marrow cavity size. However, as the bone marrow volume fraction (BMVF) tends to unity, this family of curves converges. This effect is consistent with the energy of beta particles emitted by ^{90}Y and ^{89}Sr. The higher the energy of the beta particles, the faster the convergence into a single curve where the mean cavity size has no effect on the prediction of S* values. This convergence occurs for a BMVF value of approximately 0.85 and 0.6 for ^{89}Sr and ^{90}Y, respectively. This dosimetric model can be applied to any localized region of any bone of the skeleton. It is only required to assess the morphological properties of the localized bone region in order to assess the corresponding S* value for a given source-target combination.

On the other hand, the results obtained from histological samples show that absorbed doses to the different target regions are not dependent on mean cavity size but rather they have a high correlation only with BMVF. This is due to the fact that mean cavity sizes larger than 2000 :m may not be morphologically feasible for BMVF values of less than 0.5.

As shown in Figure 7, S* values for ^{90}Y for different target regions can be predicted based on a given BMVF value. These S* values can be used to assess the localized absorbed dose to a bone region by calculating the corresponding BMVF. It is important to note that these S* values were obtained from beagle dog bones and further work is required on human bone samples for both normal and neoplastic tissues. Additionally, bone dosimetry should be based on bone type, region and lesion on a patient-specific basis. This dosimetric scheme is consistent with the current MIRD methodology and it expands it applicability into the area of small-scale dosimetry and patient-specific dosimetry.

The morphological characteristics of a bone lesion are considerably different from that of a normal bone and it varies considerably from patient to patient. These morphological changes need to be studied and determined more carefully to assess possible changes in localized absorbed doses. This work has only dealt with the physics of energy deposition in bone and bone marrow; however, radionuclide distribution and concentration at the small-scale and cellular level requires further scrutiny. There are many factors that affect radionuclide distribution and concentration in the skeleton or in any given region of a bone. As an example, Figure 8 shows a ^{99m}Tc-MDP bone scan of a male patient with prostate cancer metastatic to the bone. The high uptake activity regions of

Figure 8. Whole-body bone scan obtained using ^{99m}Tc-MDP of a male patient with disseminated bony metastasis from prostate cancer. Images illustrate bone regions with high uptake activity.

bone demonstrate regions with metastatic involvement. In the clinical arena, the most common tumors that metastasize to the bone are breast, prostate, lung, renal cell, and cervical carcinoma, and other rare metastatic tumors such as those arising from colorectal carcinoma.

Recently, the role of bone scans has been challenged by the use of MRI. However, for the treatment of bony metastases, these techniques are in essence complementary because of the ability of MRI to demonstrate the superb anatomic detail of bone marrow where most of the metastases begin. Furthermore, the comparison of a bone scan with MRI of bone marrow is essentially the comparison of two different organ systems where the supporting bone structure is an organ and the bone marrow is a separate organ. Findings in a bone scan usually become positive in response to osteoblastic changes and findings on MRI become positive when tumor cells infiltrate and replace bone marrow. Nonetheless, there are significant limitations with respect to the evaluation of the bone marrow with MRI techniques. The principal limitation being that total body imaging is not possible, and the expenses preclude its use in all bone scan cases. Thus, the therapeutic treatment planning and tumor staging of bony metastasis can be complemented by using both diagnostic techniques. Once a metastatic site has been evaluated, a biopsy sample can be obtained from which it is possible to assess the radionuclide distribution in bone and bone marrow compartments at the small-scale and cellular level.

This procedure can be carried out during diagnostic studies or therapy treatments with ^{89}Sr or ^{90}Y to assess the localized absorbed doses per unit of injected activity to the tumor and normal bone regions surrounding the tumor. Even though a biopsy procedure is painful and expensive, it conveys morphological and radionuclide distribution data of extreme relevance for treatment planning in cases where abundant dissemination of bony metastasis has taken place. Unfortunately, quantitative radionuclide imaging has not been applied successfully in bone; thus, biopsy samples are still the best source of information regarding radionuclide distribution data at the localized and cellular level. Another method used to define the bone structure of a lesion is based on the use of high resolution CT (HRCT) that is capable of differentiating bone and trabecular bone from soft tissue. Thus, HRCT and MRI image co-registration can be used to assess morphological structures and degree of tumor involvement in bone and bone marrow.

CONCLUSIONS

The results of S* values obtained from histological images and the three-dimensional slab model were in good agreement. The methodology described above established the feasibility to carry out localized dosimetry of bone and bone lesions based on histological images which convey realistic morphological and physiological characteristics of a given bone structure. In principle, this methodology can be applied on a patient-specific basis by assessing the morphological characteristic of the bone lesion via high definition CT for bone-tissue differentiation, MRI for tumor-tissue differentiation, and a biopsy sample to assess activity distributions and concentrations in different bone tissues or compartments. The results from this study emphasizes that bone dosimetry requires to be carried out on a patient-specific basis to gather meaningful dosimetric data for correlation with bone marrow toxicity and tumor control.

REFERENCES

1. Polig E and Jee WS. Bone age and remodeling: a mathematical treatise. Calcif Tissue Int 41:130-6, 1987.
2. Vaughan JM. The Effects of Irradiation on the Skeleton. Claredon Press, Oxford, 1973.

3. Bianco JA, Sandmaier B, Brown PA, Badger C, Bernstein I, Eary J, Durack L, Schuening F, Storb R and Appelbaum F. Specific marrow localization of an ^{131}I-labeled anti-myeloid antibody in normal dogs: effects of a "cold" antibody pretreatment dose on marrow localization. Exp Hematol 17:929-934, 1989.
4. Turner JH and Claringbold PG. A phase II study of treatment of painful multifocal skeletal metastases with single and repeated dose samarium-153 ethylenediamine- tetramethylene phosphonate. Eur J Cancer 27:1084-1086, 1991.
5. Hosain F and Spencer RP. Radiopharmaceuticals for palliation of metastatic osseous lesions: biologic and physical background. Semin Nucl Med 22:11-16, 1992.
6. Buchegger F, Chalandon Y, Pelegrin A, Hardman N and Mach JP.1992. Bone marrow dosimetry in rats using direct tissue counting after injection of radioiodinated intact monoclonal antibodies or F(ab')^2 fragments. J Nucl Med 32:1414-21, 1992.
7. Yorke ED, Huang YC, Schell MC, Wong R and Ling CC. Clinical implications of I-125 dosimetry of bone and bone-soft tissue interfaces. Int J Radiat Oncol Biol Phys 21:1613-619, 1991b.
8. Bayouth JE, Macey D J, Boyer AL and Champlin RE. Implications of heterogeneity doses from Ho-166 administered for bone marrow ablation. Med Phys 20:875-890, 1993.
9. Bayouth JE, Macey DJ, Kasi LP and Fossella FV. Dosimetry and toxicity of samarium-153-EDTMP administered for bone pain due to skeletal metastases. J Nucl Med 35:63-69, 1994.
10. Spiers FW. Beta particle dosimetry in trabecular bone, in: Delayed Effects of Bone-seeking Radionuclides. Ed. Mays CW et al. University of Utah Press, Salt Lake City, 1969.
11. Whitwell JR and Spiers FW. Calculated beta-ray dose factors for trabecular bone. Phys Med Biol 21:16-38, 1976.
12. Makrrigiorgos GM, Adelstein SJ and Kasis AI. Limitations of conventional internal dosimetry at the cellular level. J Nucl Med 30:1856-1864, 1989.
13. Polig E and Jee WS. Bone structural parameters, dosimetry, and relative radiation risk in the beagle skeleton. Radiat Res 120:83-101, 1989.
14. Polig E and Jee WS. Cell-specific radiation dosimetry in the skeleton. Calcif Tissue Int 39:119-122, 1986.
15. Polig E. Radiation dose factors for a-emitters in osteons and some considerations on non-uniformity ratios and relative distribution factors. Phys Med Biol 34:353-367, 1989.
16. Chen H and Poston JW. Estimates of absorbed energy in trabecular bone due to β-particles or electrons. Health Physics 43:647-653, 1982.
17. Shearer TA, Akabani G, Bolch WE and Poston JW, Sr. A model for electron and beta energy deposition within trabecular bone, in: Proceedings of the Fifth International Radiopharmaceutical Dosimetry Symposium, (ed. Watson E.E. and Schlafke-Stelson A. T., May 1991). U.S. Department of Energy, Oak Ridge, Conference CONF-910529, 1992.
18. Akabani G. Absorbed dose calculations in haversian canals for several beta-emitting radionuclides, J Nucl Med 34:1361-1366, 1993.
19. Sgouros G. Bone marrow dosimetry for radioimmunotherapy: Theoretical considerations. J Nucl Med 34:689-694, 1993.
20. Desrosiers MF, Avila MJ, Schauer DA, Coursey BM and Parks NJ. Experimental validation of radiopharmaceutical absorbed dose to mineralized bone tissue. Appl Radiat Isot 44:459-464, 1993.
21. Spiers FW. Radioisotopes in the Human body: Physical and Biological Aspects. Academic Press Inc., New York, 1968.
22. ICRP. International Commission of Radiological Protection. Alkaline Earth Metabolism in Adult

Man, ICRP Publication 20; Pergamon Press, Oxford, 1972.
23. Ghiron J, Volkert WA, Garlich J and Holmes RA. Determination of lesion to normal bone uptake ratios of skeletal radiopharmaceuticals by QARG (quantitative autoradiography). Int J Rad Appl Instrum `B 18:235-240, 1991.
24. Darley PJ. Measurement of linear path length distributions in bone and bone marrow using a scanning technique, in: Proceedings of the Symposium on Microdosimetry, ISPRA, Ed. Ebert HG. Report EUR-3747. 509-526, 1968.
25. Spiers FW, Zanelli GD, Darley PJ and Withwell JR. Beta particle dose rates in human and animal bone, in: Biomedical Implications of Radiostrontium Exposure (ed. Goldman M, and Bustad LK). U.S. Atomic Energy Commission, Oak Ridge, Conference CONF-710201, 1972.
26. Chung H, Wehrli FW and Williams JL. Quantitative assessment of trabecular architecture with MR microscopy. Radiological Society of North-America [Abstract] pp:198, 1994.
27. Nelson WR, Hirayama H and Rogers DWO. 1991. The EGS4 Code System, Stanford Linear Accelerator Center. Report 265, 1991.
28. Bielajew A F and Rogers DWO. PRESTA, The Parameter Reduced Electron-step Size Transport Algorithm for Electron Monte Carlo Transport. National Research Council of Canada, pub. PIRS-0042, 1991.
29. International Commission on Radiation Units and Measurements, ICRU Report 44. Tissue Substitutes in Radiation Dosimetry and Measurement, (ICRU Press, MD 1989).

QUESTIONS

Mattsson: How do you, in the clinical application, determine the radionuclide uptake in bone for the pure β emitters? Do you combine the bone biopsies with ^{99m}Tc-MDP scintigraphy?

Akabani: In a clinical setting it is required that you use ^{99m}Tc-MDP to visualize the lesion and for therapeutic purposes bone biopsy samples are required to assess the biodistribution in the lesion. As long as the ^{90}Y or ^{89}Sr biokinetics are known for a given specific patient, dose estimates will be well determined.

Bolch: In the latter portion of your talk, you alluded to performing in-vivo MRI/CT for patients treated with bone palliation agents. Would clinical MRI/CT images give you the necessary resolution to fully characterize the trabecular bone/marrow cavity microstructure needed for your site-specific dose calculations?

Akabani: MRI will not give the necessary resolution for bone; however, MRI is used to differentiate between tumor tissue and normal tissue with very good resolution (0.5 mm pixels). High definition CT is used to differentiate between bone and tissue structures. The resolution is not good for bone structures less than 1mm in size. However, the ratio between tissue/bone is close to what you find in biopsy samples.

VOXEL S VALUES FOR THE RAPID ASSESSMENT OF SUBORGAN DOSIMETRY FOR NONUNIFORM ACTIVITY DISTRIBUTIONS

Bolch WE[1], Costes SV[1], Bouchet LG[1], Wessels BW[2], Siegel JA[3], Robertson JS[4] and Erdi AK[5]
[1]University of Florida, Gainesville, FL 32611
[2]George Washington University Medical Center, Washington, DC 20037
[3]Cooper Hospital University Medical Center, Camden, NJ 08103
[4]Gaithersburg, MD 20879
[5]Precision Mathematics, Inc., Columbia, MD 21045

ABSTRACT

A traditional assumption made in nuclear medicine dosimetry is that the activity in the source organ is uniformly distributed. Localization techniques such as quantitative SPECT and PET imaging allow one to dispense with this assumption and look at realistic nonuniform activity distributions in selected organs or organ regions. Therapy applications further emphasize the need for direct treatment of nonuniformities. Many researchers have relied upon computational techniques such as dose kernels to assess dose distributions in these regions. In this work, a more simplified approach is proposed which allows direct use of the MIRD schema in conjunction with imaging data to rapidly assess organ dose distributions with minimal computational effort. The EGS4 radiation transport code has been used with a cubical array of tissue voxel elements for a centrally located source cube of P-32, I-131, Sr-89, Y-90, and Tc-99m. Three sets of voxel dimensions are considered: 6 mm for SPECT images, 3 mm for PET images, and 50 x 50 μm by 1 mm for autoradiography. Radionuclide S values are subsequently tabulated as a single function of the source-to-target voxel separation distance. Isodose contours can be subsequently generated through a simple matrix summation. Example are given for (1) a mouse renal cell carcinoma with I-131-labeled antibody, (2) a human colon adenocarcinoma with I-131-labeled antibody, and (3) various tumors directly injected with P-32.

INTRODUCTION

Radiation dosimetry is an essential component to any nuclear medicine protocol. In diagnostic nuclear medicine, estimates of absorbed dose are necessary to assess the relative risks of radiopharmaceutical options which yield equivalent diagnostic information. In therapeutic nuclear medicine, estimates of absorbed dose are necessary to predict the efficacy of a given treatment regime. The MIRD schema provides the fundamental framework for making estimates of the average absorbed dose from internalized radioactivity for any user-defined source-target geometry (1, 2). In diagnostic nuclear medicine, source regions are traditionally defined as whole organs in which the radiopharmaceutical is assumed to be uniformly distributed. Likewise, the target regions are also

defined at the whole-organ level for diagnostic dosimetry. In its simplest form, the MIRD schema defines the average dose to the target region as the product of the cumulative activity in the source region and the S value that source-target combination. With the emphasis on whole-organ dosimetry, the primary source of radionuclide S values used in diagnostic nuclear medicine have come from MIRD Pamphlet No. 11 based on the heterogeneous Fisher-Synder phantom, or the MIRDOSE computer program which, in versions 2 and 3, utilize the Cristy and Eckerman series of phantoms (3, 4).

In the field of internal-emitter therapy, explicit treatment of source organ nonuniformities must be considered. Furthermore, applications of radiolabelled antibodies and intracellular agents require information on the suborgan distribution of absorbed dose within both the treated tumor and the surrounding normal tissues. Consequently, traditional sources of radionuclide S values which consider only whole organs as source/target regions are not applicable to the problem at hand. Two alternative dosimetry methods have thus be utilized: 1) convolution of electron and photon dose point kernels with source/target geometry factors and 2) direct simulation of particle transport utilizing Monte Carlo methods.

From the standpoint of computation speed, point kernel convolution is currently preferred over Monte Carlo simulations. Nevertheless, point kernels are subject to two limitations. First, they are biased to the spherical geometries, whereas most quantitative data on activity distributions is acquired in a cubical or parallelepiped geometries; as a result, they are not in a form which facilitates the direct application of the MIRD schema. Second, their use is not valid near media interfaces such as soft tissue/bone or soft tissue/air. With the proper implementation of the source-target geometry (via CT and/or MR imaging of the patient), Monte Carlo simulations can readily accommodate variations in absorbed dose near media interfaces. In many internal emitter situations, however, interface effects are not significant, and simplified alternatives to the point kernel approach may be sought.

VOXEL S VALUE APPROACH TO NONUNIFORM ACTIVITY DISTRIBUTIONS

In this work, a calculational scheme was devised which allows for the rapid application of the MIRD formalism with quantitative techniques for determining nonuniform activity distributions within target organs and suborgan regions. In the clinical setting, quantitative data on nonuniform distributions of source activity can now be extracted from SPECT and PET scans. SPECT scans are routinely acquired within a 64 x 64 grid resulting in a pixel size of 0.6 cm and a corresponding voxel size of 0.216 cm^3 (0.6 cm slice thickness). Similarly, PET scans are routinely acquired within a 128 x 128 grid resulting in a pixel size of 0.3 cm and a voxel size of 0.027 cm^3 (0.3 cm slice thickness). Through the use of sequential scans during the washin, redistribution, and washout phases of radiopharmaceutical uptake within a source organ or region, cumulative activities per image voxel can be determined. One approach, therefore, is to provide S values which correspond to the voxel geometry of the imaging data. With these two pieces of information, the MIRD schema can be applied in a simple 3-D array summation to rapidly asses the dose distributions throughout the source organ or other body region in which interface effects are considered negligible.

MATERIALS AND METHODS

SPECT and PET S-Value Calculations

The Monte Carlo code EGS4 was used to perform all simulations of radiation transport and energy deposition (5). EGS4 follows the coupled transport of both photons and electrons through any user-defined media. To ensure minimal dependence on the energy-loss step-size in the calculations, the PRESTA algorithms were utilized for each simulation.

Two sets of calculations were performed: one corresponding to the dimensions of typical SPECT image voxels and one for typical PET image voxels. For each data set, a cubical array of target voxel regions was established in which a centrally located source voxel was placed. For the SPECT simulations, each target region was scaled to 0.6 cm on a side; the PET voxels were scaled to 0.3 cm on a side. A total of 81 x 81 x 81 voxel regions were considered. These dimensions correspond to an array size of (81 x 0.6 cm) or 48.6 cm on edge for the SPECT voxel array and (81 x 0.3 cm) or 24.3 cm on edge for the PET voxel array.

Calculations were made for four radionuclides: ^{131}I, ^{99m}Tc, ^{32}P, and ^{90}Y. In each case, the full radionuclide decay spectrum was sampled directly in the simulations. Beta-particle transport included 1) explicit treatment of their energy spectrum and 2) the production and transport of the bremsstrahlung photons. Transport cross sections were based upon the soft tissue composition of the Cristy and Eckerman phantoms (3). Upon completion of the simulations, S values were averaged among all voxels which were equidistant from the source voxel. Final values of voxel S values were then indexed to the source-to-target center-to-center distance for later use in assessing dose distributions within SPECT or PET images.

Autoradiography S-Value Calculations

The voxel S value approach to nonuniform activity distributions may also be applied to perform dosimetry estimates for autoradiographic assays of activity distributions. Additional simulations were thus performed for ^{131}I in a voxel array set with each voxel having dimensions of 50 μm x 50 μm x 1 mm corresponding to activity datasets with an in-plane resolution of 50 μm and a slice thickness of 1 mm. The computational demands of both smaller voxel dimensions and the loss of cubical symmetry required a modified transport geometry. For this S-value dataset, the source voxel was located within the corner of a target voxel array 219 x 219 voxels in the XY plane (corresponding to the 50 μm x 50 μm dimensions) and 9 voxels in the X plane (corresponding to the 1 mm dimensions).

VOXEL S VALUES FOR SPECT AND PET

EGS4-generated voxel S values for the electron/photon emitters ^{131}I and ^{99m}Tc are given in Figures 1 and 2, respectively. In each figure, voxel S values are plotted as a solid curve (upper) and the one-sigma errors at each corresponding voxel separation distance are plotted as a dashed curve (lower). Whereas the cubical array of target voxels allowed estimates of S values up to ~40 cm, the plots are given only up to 30 cm for clarity. For ^{131}I, the S values begin at a value of 0.134 ± 0.00188 mGy MBq^{-1} s^{-1} within the source voxel (as read from both curves at zero distance). The S value then falls to values of $6.32 \times 10^{-6} \pm 5.31 \times 10^{-8}$ and $5.35 \times 10^{-8} \pm 2.00 \times 10^{-9}$ at voxel center-to-center distances of 5.02 and 30.0 cm, respectively. The coefficients of variation at these distances are thus small (1.4% at 0 cm, 0.84%, at 5.02 cm, and 3.74% at 30.0 cm), even though the magnitude of the S-value standard deviation can fluctuate by a factor of 10 at distances exceeding 10 cm.

For ^{99m}Tc, the S values begin at a value of 0.0121 mGy MBq^{-1} s^{-1} within the source voxel and fall to values of 2.31×10^{-6} and 1.39×10^{-8} at distances of 5.02 and 30.0 cm, respectively. The coefficient

of variation for the S values at these distances are 0.015%, 0.58%, and 4.12%, respectively. Within the first 2 cm from the source cube, we see that the S values decrease by a factor 3200 for ^{131}I and by a factor of 880 for ^{99m}Tc. Due to the smaller electron component of the emission spectrum of ^{99m}Tc, the variation in S value with distance within the first 5 cm is shown to be more gradual than that for ^{131}I with its greater electron yield.

Voxel S values are shown in Figures 3 and 4 for the pure beta-particle emitter ^{32}P and the beta-particle emitter ^{90}Y, respectively. While the photon emitters show a gradual variation in S-value magnitude with increasing distance, S values for beta-emitters show a clear discontinuity at a voxel center-to-center distance approaching the CSDA range of the more energetic particles of the spectrum. Beyond this distance, the S value is comprised primarily of energy deposition by bremsstrahlung photons. For ^{32}P, the S values begin at a value of 0.343 mGy MBq^{-1} s^{-1} within the source voxel and fall to values of 5.95×10^{-8} at 5.02 cm and 4.42×10^{-10} at 30.0 cm. A decrease in the S value by a factor of 7.7×10^{5} is seen in the first 2 cm from the source voxel. For ^{90}Y, the S values begin at a value of 0.373 mGy MBq^{-1} s^{-1} within the source voxel and fall by a factor of 4.5×10^{5} within the first 2 cm from the source. Coefficients of variation on the S values vary from 0.03% and 0.026% for the ^{32}P and ^{90}Y source voxels, and increase with increasing distance to 13% and 26%, respectively at 30 cm distance.

To better understand the partial contributions to the total S value from the various radiation components of the radionuclide decay scheme, as well as to visualize these contributions, additional simulations for ^{131}I and ^{32}P were performed within a cubical voxels of dimensions $(0.1 \text{ cm})^3$. These results are shown in Figures 5 and 6. For ^{131}I, the beta particles and conversion electrons (electrons) are shown to dominate the S values at voxel distances of less than 0.1 cm and equal the photon contribution at just under 0.2 cm. Bremsstrahlung contributions are minimal at all distances. For ^{32}P, beta particle and bremsstrahlung contributions equal one another at a voxel center-to-center distance of between 0.7 and 0.8 cm. Thereafter, the bremmstrahlung contribution dominates the contributions to target voxel dose.

To support applications of small-scale dosimetry for PET imaging, similar Monte Carlo simulations were performed with cubical voxel dimensions of $(0.3 \text{ cm})^3$. These results are shown in Figures 7-10 for ^{131}I, ^{99m}Tc, ^{32}P, and ^{90}Y, respectively, out to a distance of 20 cm.

Figure 1. S values for ^{131}I within SPECT voxel dimensions of $(0.6\ cm)^3$.

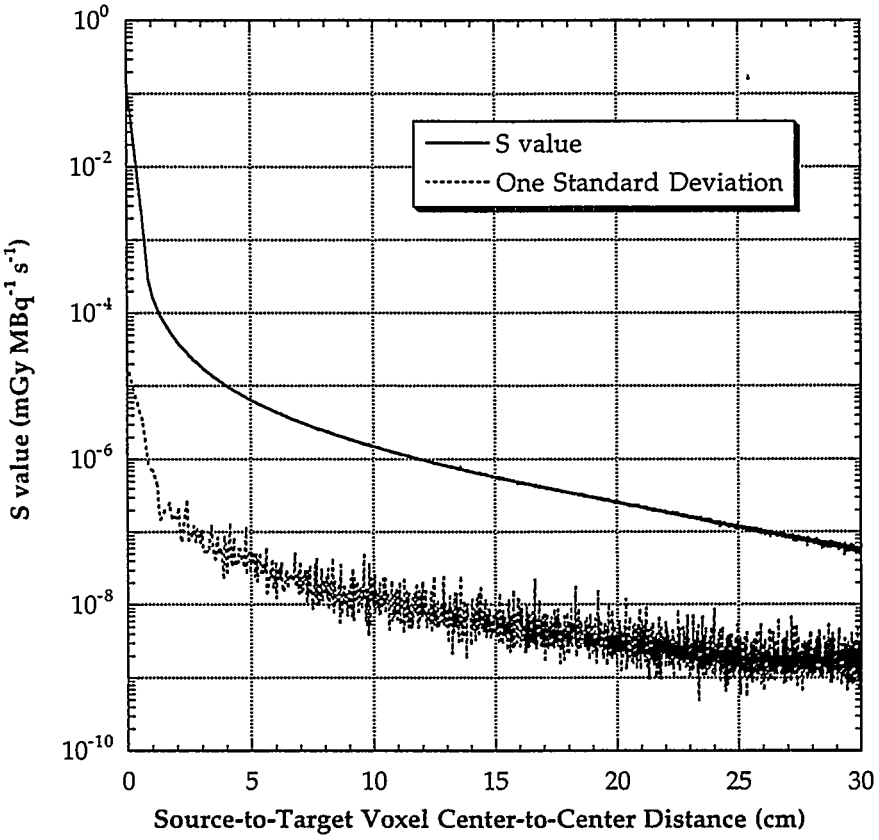

Figure 2. S values for ^{99m}Tc within SPECT voxel dimensions of $(0.6\ cm)^3$.

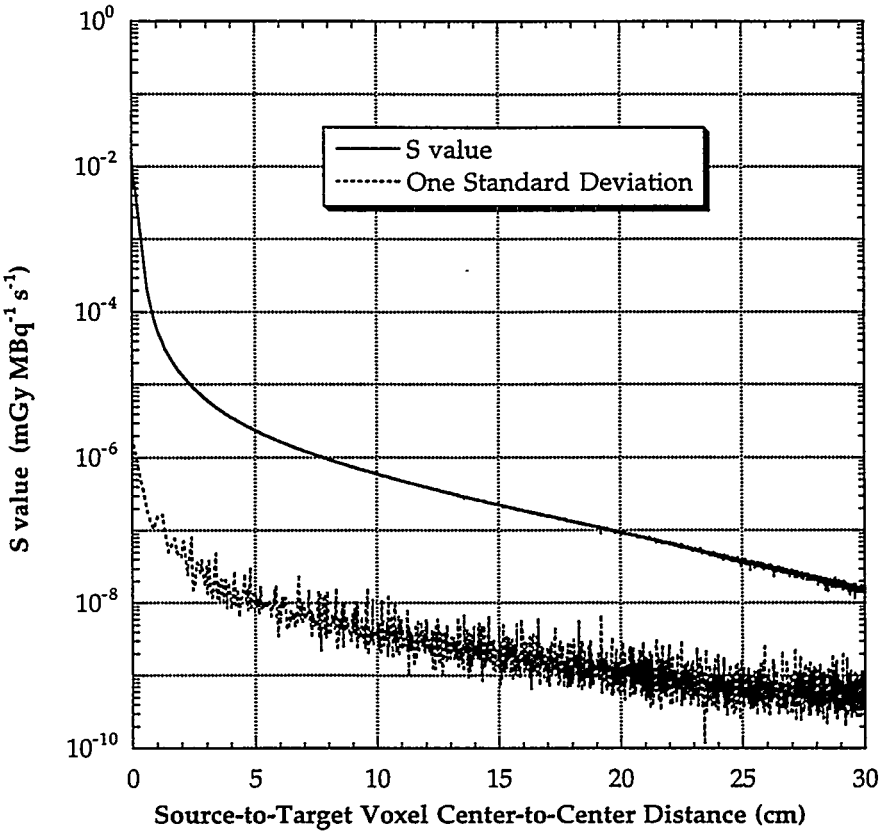

Figure 3. S values for ^{32}P within SPECT voxel dimensions of $(0.6\ cm)^3$.

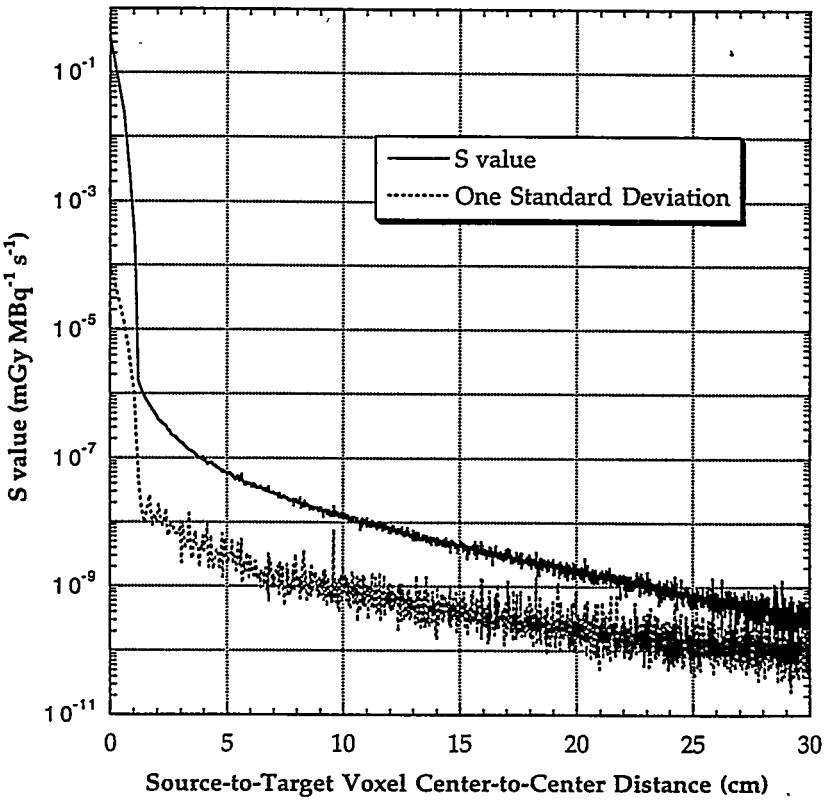

Figure 4. S values for ^{90}Y within SPECT voxel dimensions of $(0.6\ cm)^3$.

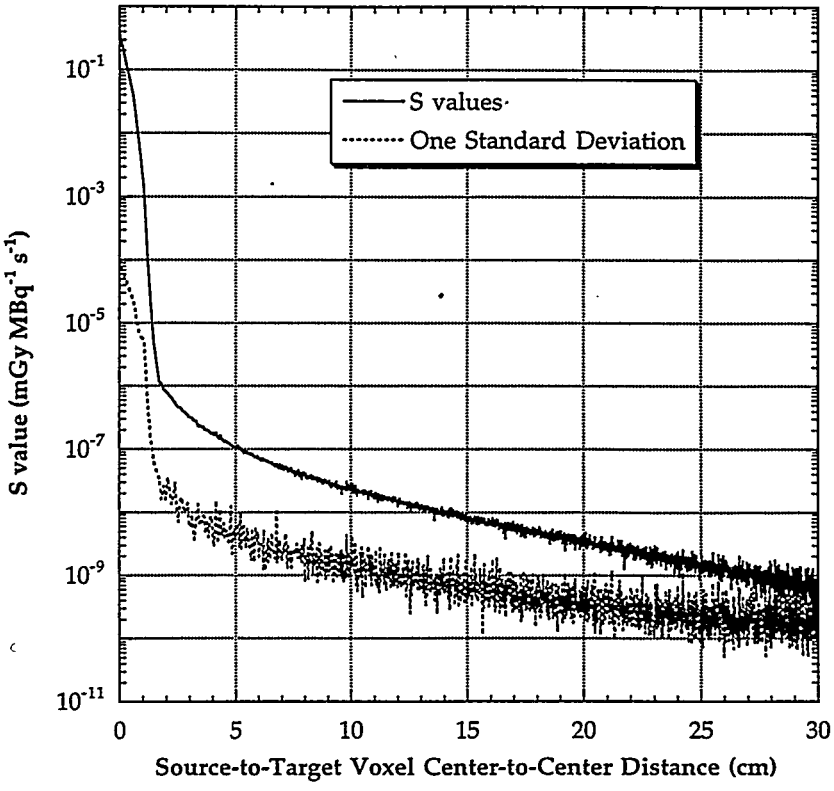

Figure 5. Contributions to the total S value for ^{131}I within SPECT voxel of $(0.1\ cm)^3$.

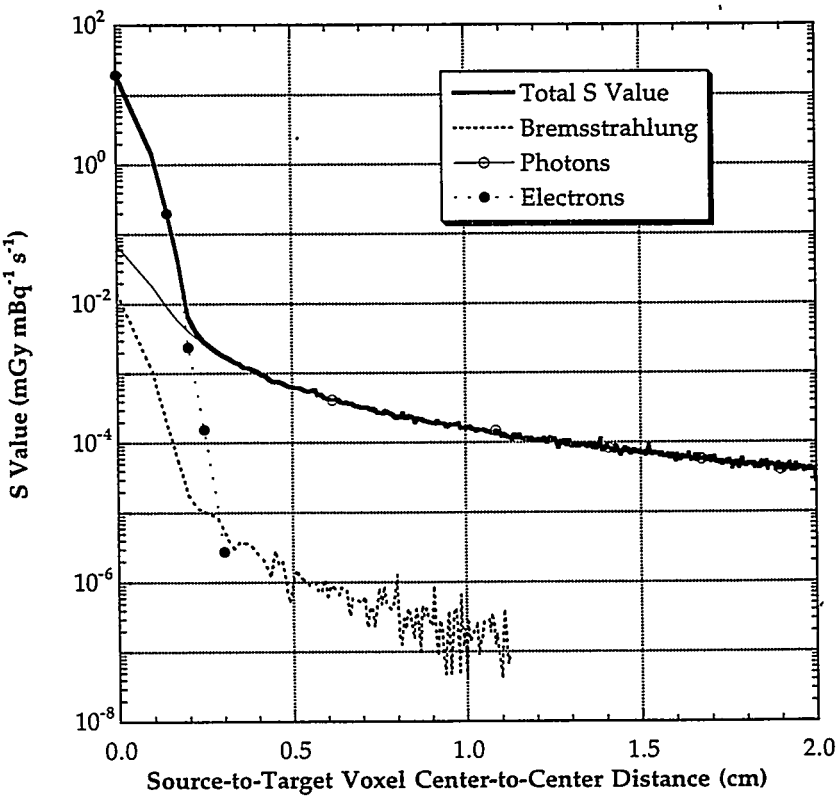

Figure 6. Contributions to the total S value for ^{32}P within SPECT voxels of $(0.1\ cm)^3$.

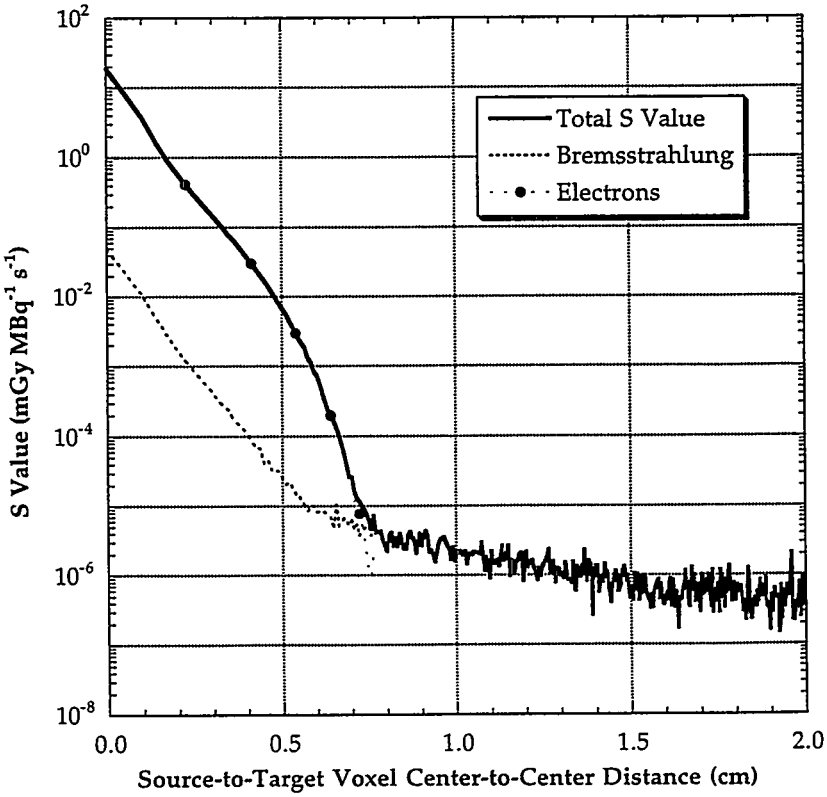

Figure 7. S values for ^{131}I within PET voxel dimensions of $(0.3\ cm)^3$.

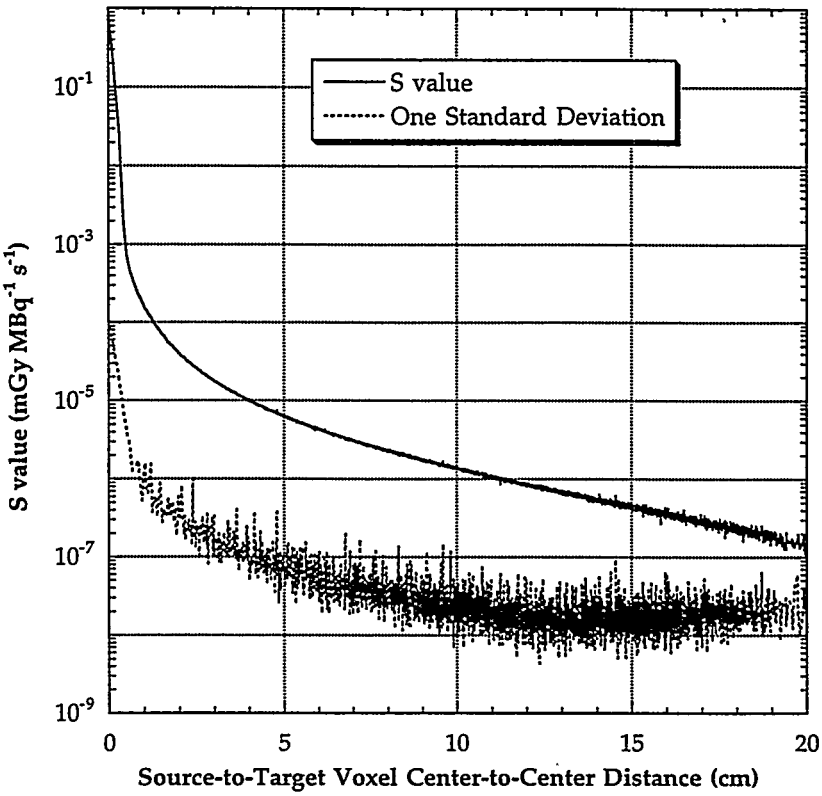

Figure 8. S values for ^{99m}Tc within PET voxel dimensions of $(0.3\ cm)^3$.

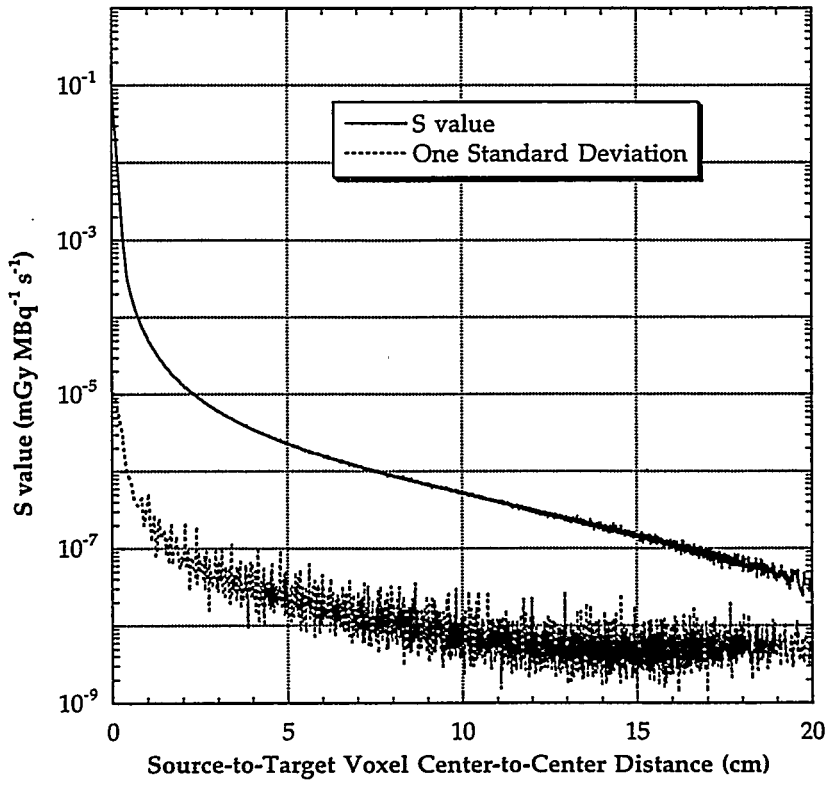

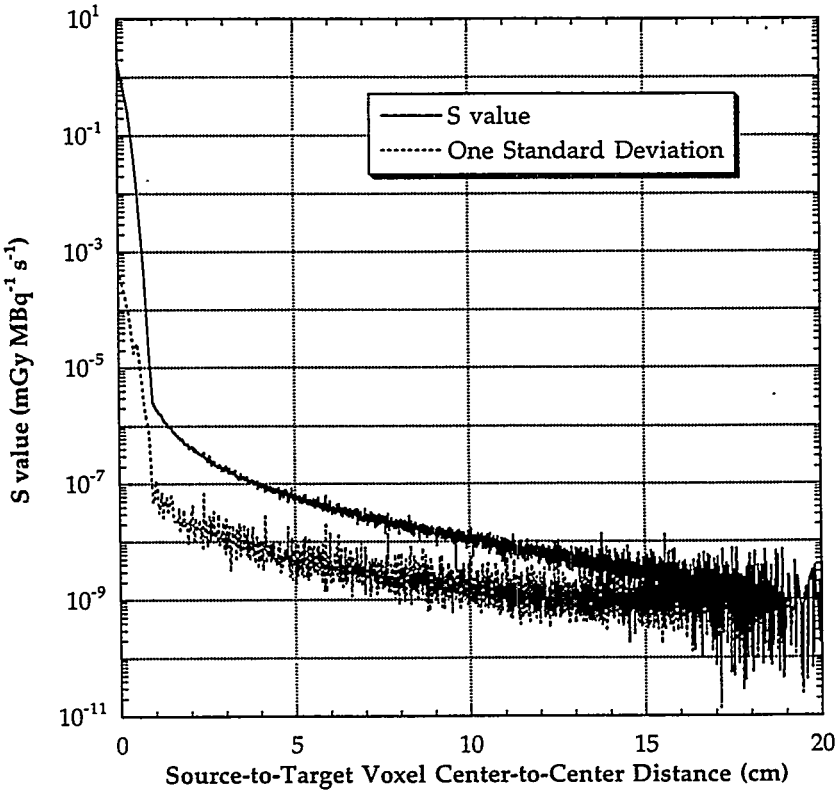

Figure 9. S values for ^{32}P within PET voxel dimensions of $(0.3\ cm)^3$.

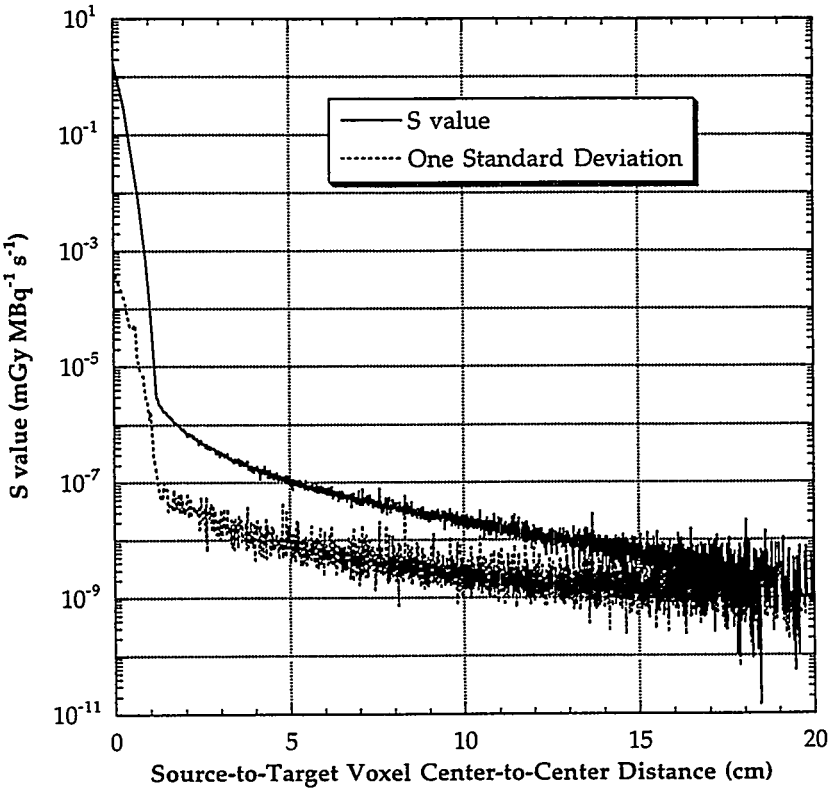

Figure 10. S values for ^{90}Y within PET voxel dimensions of $(0.3\ cm)^3$.

APPLICATIONS TO SPECT IMAGING

Example 1 - ^{131}I SPECT Imaging

To demonstrate the use of the voxel S values for ^{131}I as given in Figure 1, we have utilized the data of Erdi et al. (6). In this study, activity quantification techniques derived from external imaging were correlated to surgical tumor specimens in patients who received radiolabeled monoclonal antibody. Patients were given ^{131}I labeled 16.88 human antibody and scanned 3-5 times by planar and/or SPECT imaging methods to acquire time-dependent activity data in the tumor and normal tissues. The data selected was from SPECT images of a transverse colon adenocarcinoma in the hepatic flexure of Patient No. 3 of this study. Fifteen slices were obtained: 3 from direct measurement (End A, End B, and Middle) and 12 from interpolations between measured slices. Initial activity data was thus provided for 0.63 x 0.63 x 0.63 cm voxels in units of μCi. The effective half-life of the antibody was measured to be 27.7 hr.

Utilizing the voxel S values for ^{131}I given in Figure 1, the tumor activity dataset was scanned in three dimensions, tabulating the voxel-to-voxel dose contribution in a simple matrix summation. Values of the average, maximum, and minimum voxel dose per image slice are shown in Table 1. The corresponding dose-volume histogram for the entire image set is shown in Table 2. Of the 1470 voxels within the tumor image, 52% are found to have doses between 200 and 400 cGy. Three "hot spots" are found to have doses in the ranges 3600-4000, 4200-4600, and 5200-5600 cGy, respectively. With the use of the voxel S-value dataset, the nonuniform dose distribution was assessed within 2 s on a Sun SparcStation 20.

Table 1
Dosimetry Data per Image Slice

Slice Number	Maximum Voxel Dose (cGy)	Minimum Voxel Dose (cGy)	Average Voxel Dose (cGy)
1	3220	203	606
2	3070	162	641
3	3120	180	647
4	6760	195	718
5	5260	208	700
6	3290	203	668
7	3800	309	691
8	3550	245	607
9	3240	310	663
10	3000	309	689
11	4250	308	714
12	5500	306	735
13	6630	304	753
14	3910	268	685
15	4430	146	627

Table 2
Dose Volume Histogram

Voxel Dose Range (cGy)	Number of Voxels	Voxel Dose Range (cGy)	Number of Voxels
0 - 200	4	3400 - 3600	2
200 - 400	766	3600 - 3800	1
400 - 600	182	3800 - 4000	1
600 - 800	153	4000 - 4200	0
800 - 1000	114	4200 - 4400	1
1000 - 1200	90	4400 - 4600	1
1200 - 1400	43	4800 - 4800	0
1400 - 1600	25	4800 - 5000	0
1600 - 1800	19	5000 - 5200	0
1800 - 2000	13	5200 - 5400	1
2000 - 2200	10	5400 - 5600	1
2200 - 2400	9	5600 - 5800	0
2400 - 2600	6	5800 - 6000	0
2600 - 2800	4	6000 - 6200	0
2800 - 3000	9	6200 - 6400	0
3000 - 3200	5	6400 - 6600	0
3200 - 3400	8	6600 - 6800	2

Example 2 - ^{32}P SPECT Imaging of Bremsstrahlung

In this example, we utilize SPECT images provided by J. A. Siegel. These images were obtained from a patient following direct interstitial injection of colloidal ^{32}P chromic phosphate into tumor-bearing regions under CT guidance. Bremsstrahlung photons generated in the slowing down of ^{32}P beta particles within both the tumor and surrounding normal tissue thus serve as the means for SPECT imaging of the activity distributions (7).

Shown in the lower portion of Figure 11 (slice 3) is the original gray-scale SPECT image of a patient following direct injection of ^{32}P chromic phosphate into a liver tumor. Subsequent images outline activity transfer to the spleen as well. Shown in the upper portion of the figure is the corresponding relative isodose distributions outlining the location of the tumor within the liver. The spillover of activity to the spleen can be seen within Figure 12 (slice 10). Analysis of this data set (15 slices of 64 x 64 voxels each) were completed in 76 s on a Sun SparcStation 20.

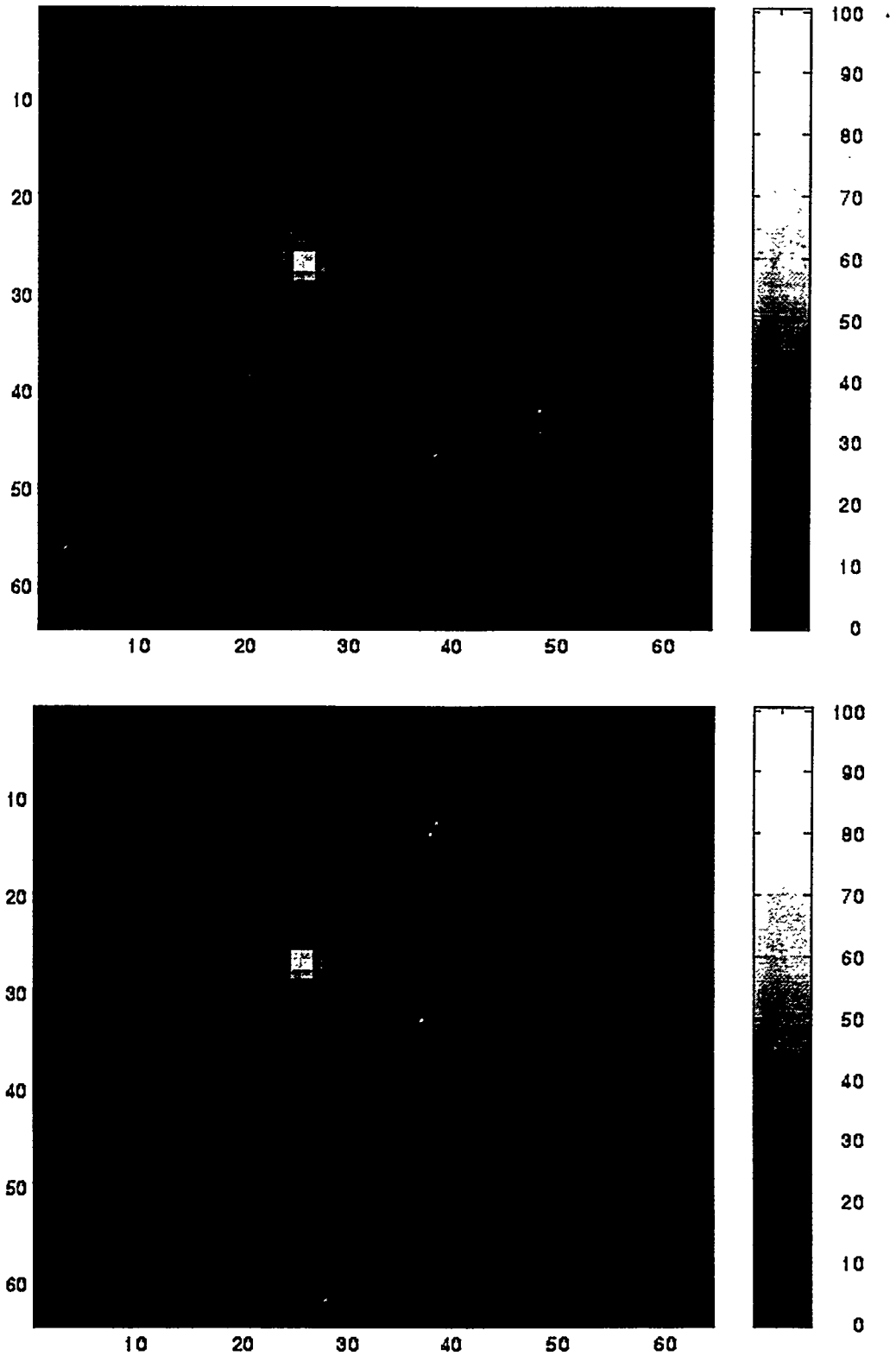

Figure 11. Relative dose distribution for Slice 3 (above) along with the original SPECT image (below).

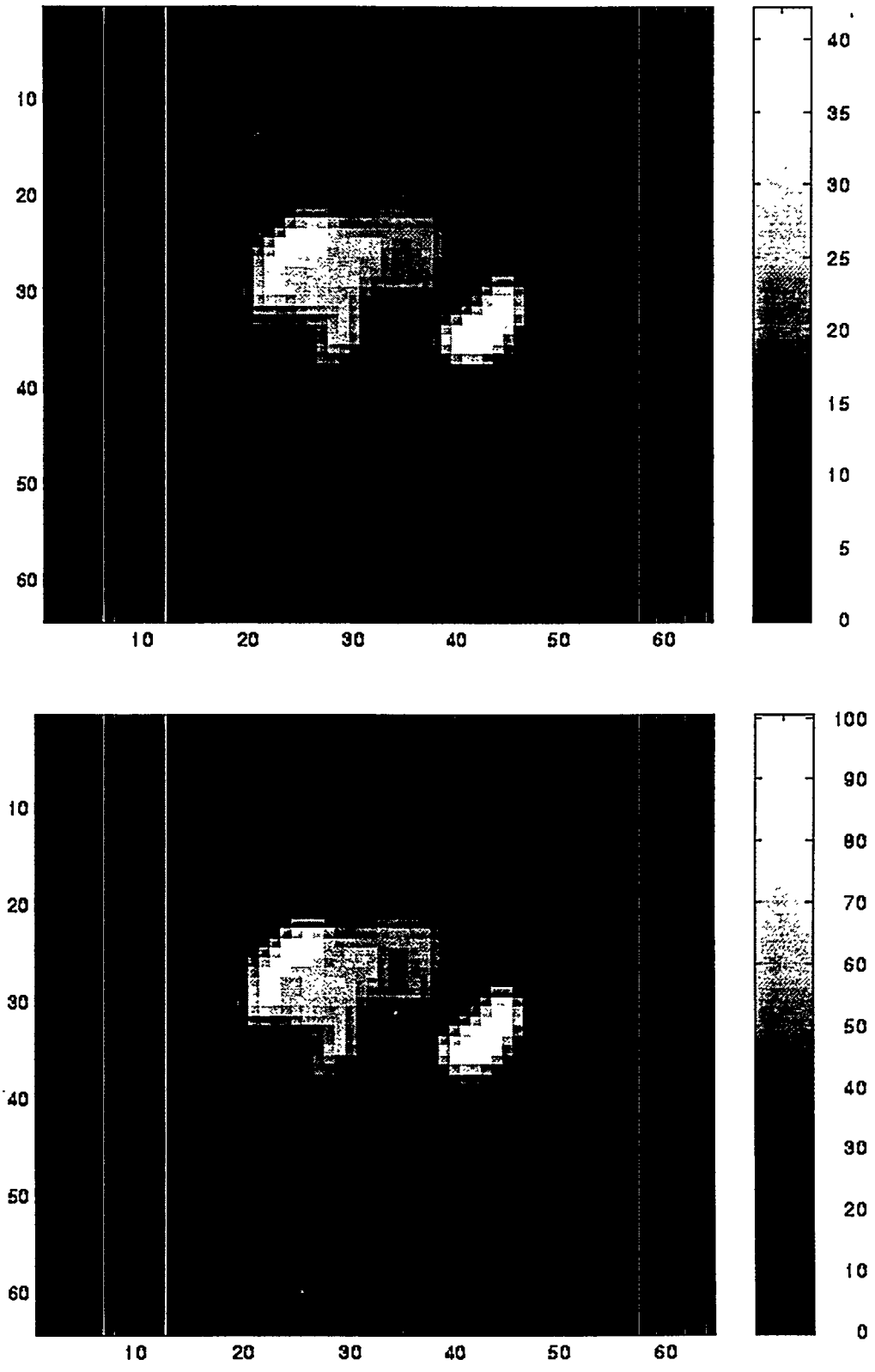

Figure 12. Relative dose distribution for Slice 10 (above) along with the original SPECT image (below).

VOXEL S VALUES AND THEIR APPLICATIONS TO AUTORADIOGRAPHY

The computation of S values for noncubical geometries results in a loss of symmetry (except within the plane of the source voxel), and thus S-value averaging at equidistant center-to-center distances is not performed. In these cases, the set of voxel S values are maintained as a distinct three-dimensional array. Figure 13 displays voxel S values for ^{131}I within the xy plane corresponding to the 50-μm in-plane resolution of the autoradiographs. In this orientation, the S values begin at a value of 1120 mGy MBq^{-1} s^{-1} within the source voxel and fall to values of 0.355 and 0.00325 mGy MBq^{-1} s^{-1} at voxel center-to-center distances of 0.1 and 0.2 cm, respectively. The corresponding coefficients of variation for the S values were 0.0450%, 1.43%, and 16.1%. The variation in voxel S value along the z axis for voxels situated directly above the source voxel and located in different 1-mm slice planes is shown in Figure 14. Here only six S values are plotted, each at 1 mm separations from one another.

In comparing the curves within Figures 13 and 14 at a fixed center-to-center distance of 0.1 cm, the effect of nonsymmetry is readily apparent. Figure 13 shows that, in the xy plane, the S value is 0.355 mGy MBq^{-1} s^{-1} at 0.1 cm. In contrast, the S value for a target voxel located in the same xy position of the array, but one plane above the source voxel, is given as 1.01 mGy MBq^{-1} s^{-1} in Figure 14. While the center-to-center distances are the same, the voxels are in physical contact in the latter case (they share a common 50 μm x 50 μm border) resulting in a higher cross-dose contribution from electrons and low-energy x-rays.

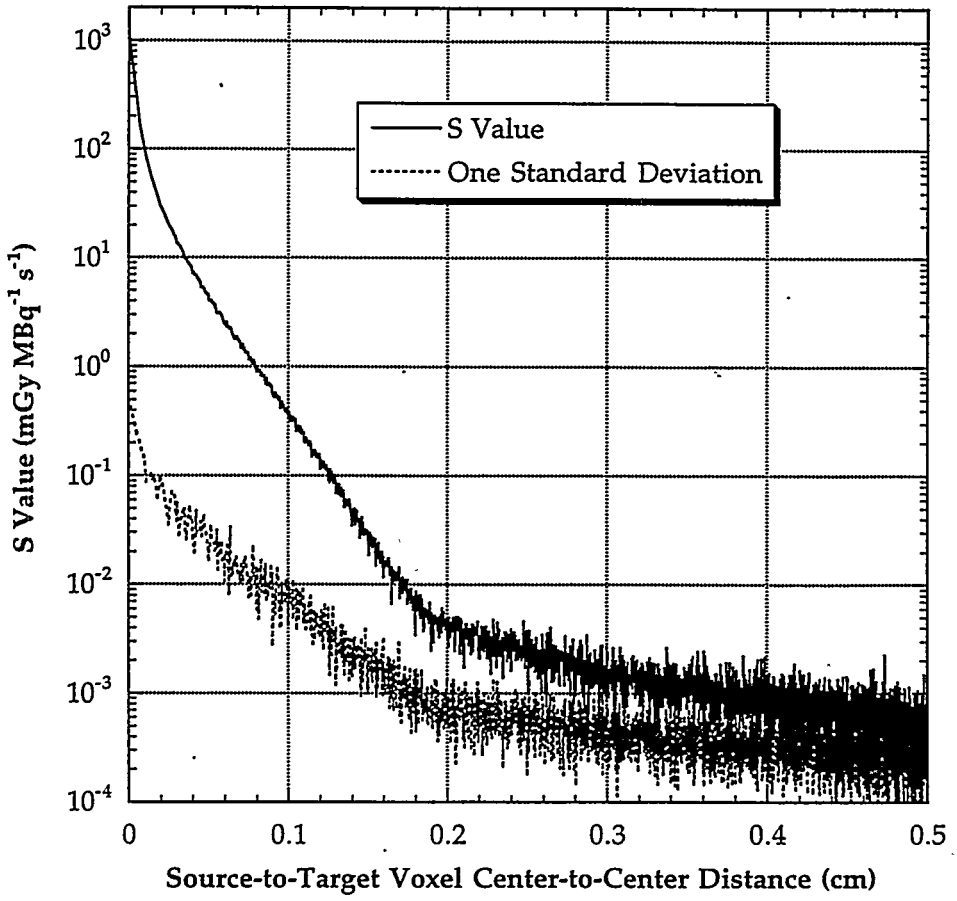

Figure 13. S values for ^{131}I with voxels of dimensions of (50 μm x 50 μm x 1 mm) as indexed by the voxel center-to-center distance in the xy plane (slice in-plane resolution of 50 μm x 50 μm).

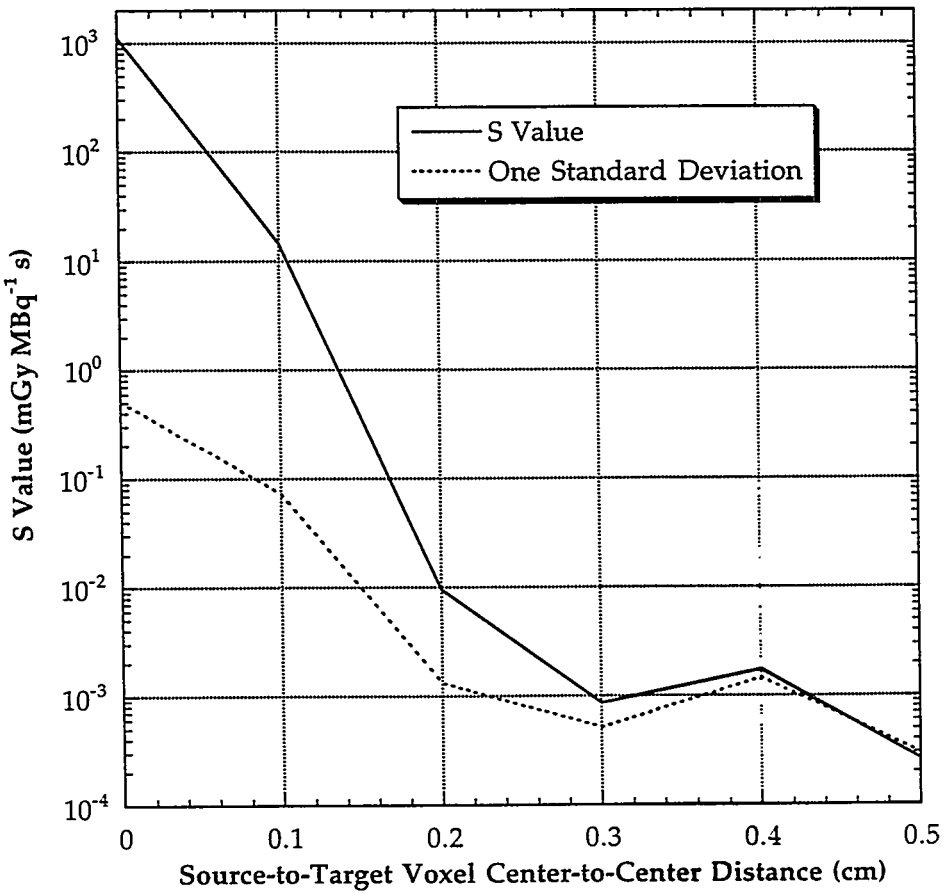

Figure 14. S values for ^{131}I with voxels of dimensions of (50 μm x 50 μm x 1mm) as indexed by the voxel center-to-center distance along the z axis (slice thickness of 1 mm).

Example 3 - Autoradiograph of a Mouse Renal Cell Carcinoma Treated with ^{131}I labeled Antibody

In this final example, we utilize unpublished data from Barry Wessels from autoradiographs from a A6H tumor xenograft (mouse renal cell carcinoma) treated with an ^{131}I-labeled monoclonal antibody. Two-dimensional activity arrays of three separate autoradiographs were provided with two additional arrays generated via interpolation. Correspondingly, a total of five contiguous sections were available for dosimetry calculations each spaced by 1 mm. Cumulated activity values per voxel were derived by direct absorbed dose measurements via micro-TLD implantation and a calibration curve for gray scale versus absorbed dose. The in-plane resolution was 50 μm x 50 μm for an array size of 256 x 256 voxels per slice. Dose distributions were subsequently generated using the three-dimensional array of voxel S values for ^{131}I shown in Figures 13 and 14.

In Figure 15, three images are shown for Section 2 of the image set. Figure 15C shows the original gray-level activity profile for Section 2. Figures 15A and 15B give the corresponding relative dose distributions for two different S-values cutoffs. In Figure 15A, voxel-to-voxel dose contributions were considered only if the corresponding S value was greater than or equal to 1% of the source voxel S value. As shown in Figures 13 and 14, a 1% S-value cutoff corresponds to a physical voxel-to-voxel distance of 0.4 mm in the xy plane and a distance of slightly greater than 1 mm along the z axis. Consequently, in calculating the dose distribution of Figure 15A, only neighboring slices are assumed to contribute dose to voxels in a given slice.

With a 0.01% S-value cutoff, voxel-to-voxel dose contributions are considered out to ~1.3 mm in the xy plane and 2 mm along the z axis. With these two values of S-value cutoff, we see a qualitative difference in the dose profiles shown in Figures 15A and 15B. The image of Figure 15A more closely resembles that of the original activity distribution as the voxel-to-voxel dose contribution is restricted to primarily to electron and beta particles from neighboring voxels. With the lower cutoff assumed in Figure 15B, voxel-to-voxel dose contributions now include a greater component of photon dose giving a general blurring of the dose profile image. By investigating variations in average voxel dose with decreasing values of S-value cutoff, one may optimize the computation speed of the matrix summation without loss of accuracy in the resulting dose distribution. Similar attributes are shown in Figures 16A-C.

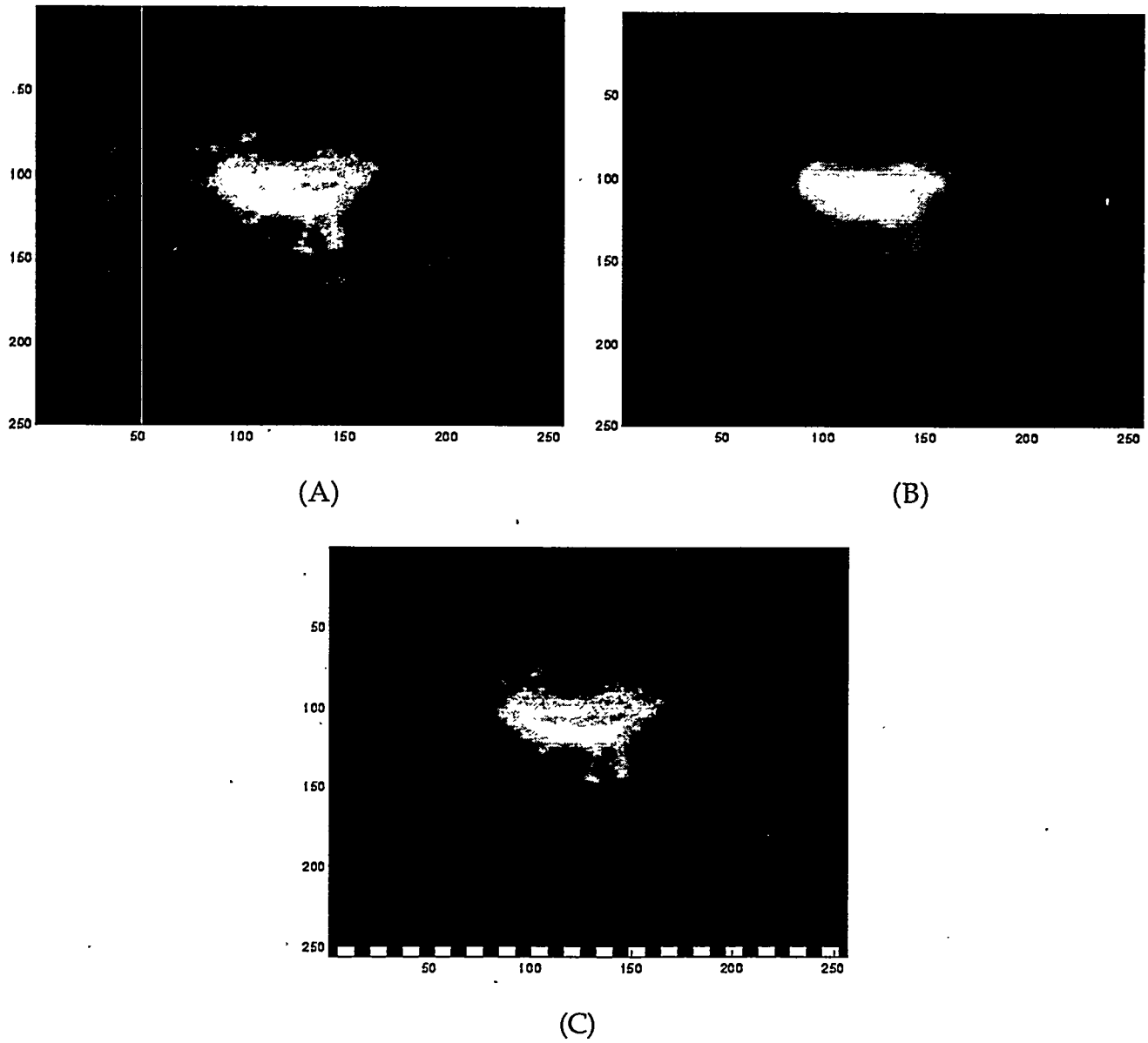

Figure 15. SPECT images and calculated dose distributions for slice 5076KV in a mouse renal cell carcinoma treated with ^{131}I-labeled antibody. Figure 15A gives the dose distribution using an S-value cutoff of 1% of the maximum, while Figure 15B gives the same dose distribution to an accuracy of 0.01% of the maximum. Figure 15C shows the original image of activity distribution.

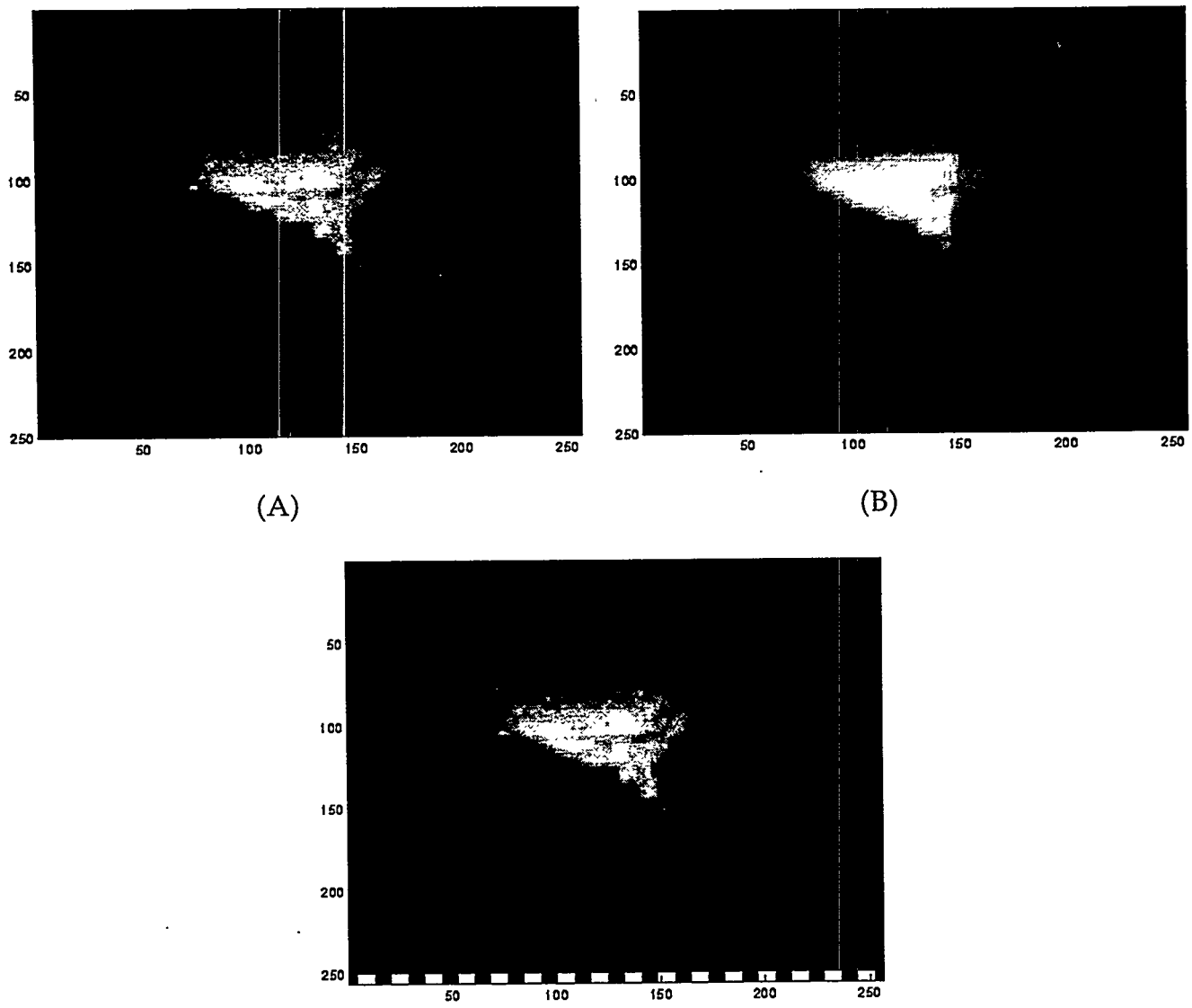

Figure 16. SPECT images and calculated dose distributions for slice 5076VW in a mouse renal cell carcinoma treated with ^{131}I-labeled antibody. Figure 16A gives the dose distribution using an S-value cutoff of 1% of the maximum, while Figure 16B gives the same dose distribution to an accuracy of 0.01% of the maximum. Figure 16C shows the image of activity distribution.

SUMMARY

This study explores an alternative computational scheme for generating three-dimensional dose distributions within tissue regions of nonuniform activity deposition. The use of S values for voxel dimensions which correspond to those for which nonuniform distributions of activity are quantified via SPECT or PET imaging allows one to perform rapid assessment of isodose profiles via the MIRD schema. These calculations are traditionally made via convolution of radionuclide dose point kernels in which the activity per voxel is assumed to be collapsed at the voxel center and the voxel-to-voxel contributions are treated as point-to-point contributions. A more precise method is to assume that the

activity within the source voxel is uniformly distributed and the voxel-to-voxel dose contribution is obtained via a convolution integral over both the source voxel and target voxel volumes. This latter approach would necessarily require the determination of a geometry factor (or reduction factor) in cubical or parallelepiped geometries for each geometric orientation of source and target voxel. The voxel S values presented here avoid the need to separately assess geometry factors and therefore they allow the direct application of the MIRD schema to generate three-dimensional distributions of absorbed dose.

We anticipate that the broader application of this approach will be confined to quantitative SPECT and PET in which activity in cubical voxels is assessed. Current efforts to extend this method include generating voxel S values over a range of monoenergetic photon and electron energies and for a range of voxel dimensions (from 1 to 10 cm on edge). Spectral weighting of these results will allow the generation of voxel S values for any radionuclide of interest for a given voxel size. Interpolation schemes may then be employed between discrete voxel sizes in the dataset. The result is thus a customized set of S values allowing the direct application of the MIRD schema to the problem of nonuniform distributions of activity.

REFERENCES

1. Loevinger R and Berman M. A revised schema for calculating the absorbed dose from biologically distributed radionuclides. MIRD Pamphlet No. 1 Revised, The Society of Nuclear Medicine, March 1976.
2. Loevinger R, Budinger TF and Watson EE. MIRD primer for absorbed dose calculations, revised edition, The Society of Nuclear Medicine, New York, 1991.
3. Cristy M and Eckerman, KF. Specific absorbed fractions of energy at various ages from internal photon sources. I. Methods. Oak Ridge National Laboratory, ORNL/NUREG/TM-8381, Vol. I, 1987.
4. Stabin MG. MIRDOSE: Personal computer software for internal dose assessment in nuclear medicine. J Nucl Med 37(3):538-546, 1996.
5. Nelson WR, Hirayama H and Rogers DWO. The EGS4 code system, SLAC-265, Stanford Linear Accelerator Laboratory, December 1985.
6. Erdi AK, Wessels BW, DeJager R, Erdi YE, Atkins FB, Yorke ED, Smith L, Huang E, Smiddy M, Murray J, Varma VM, McCabe R, McNellis R, John C, Ney A, Nochomovitz L and Hanna MG. Tumor activity confirmation and isodose curve display for patients receiving iodine-131-labeled 16.88 human monoclonal antibody. Cancer 73(3):932-944, 1994.
7. Siegel JA, Zeiger LS, Order SE and Wallner PE. Quantitative bremsstrahlung single photon emission computed tomographic imaging: use for volume, activity, and absorbed dose calculations. Int J Radiation Oncology Biol Phys 31(4):953-958, 1995.

QUESTIONS

Muller: If the S values are available for 3 and 6mm^3 cubes would it be simple for the user to find the S values for 5 or 7 mm^3 cubes?

Bolch: The MIRD Committee proposes to generate a database covering a range of voxel sizes from say several cm on a side down to 1 cm. As always, the committee is interested in hearing from the user community as to what form the data should take to maximize their clinical utility.

Sgouros: The S factor tables accounted for differences in tissue composition and density which would influence attenuation and backscatter. Since the S factors that you have described are based on a homogeneous, uniform medium assumption, wouldn't it be better to give them a different name?

Bolch: You are correct to point out that our technique of small-scale dosimetry would not be appropriate at heterogeneous tissue interfaces such as bone/tissue, tissue/lung, or body edges. Nevertheless, I would disagree with your more restricted definition of the S value. Within the MIRD schema, the S value is defined as the average absorbed dose per unit cumulative activity for any user-defined source-target region combination. As with any dosimetry method, one is obligated to inform the user of all assumptions made in the calculations. The restrictions you have mentioned here are certainly appropriate.

HIGH RESOLUTION, MRI-BASED, SEGMENTED, COMPUTERIZED HEAD PHANTOM

Zubal IG, Harrell CR, Smith EO, Smith AL, Krischlunas P
Image Processing Group, Dept. of Diagnostic Radiology,
Yale University, New Haven, CT, 06510 USA

ABSTRACT

Purpose: We have created a high-resolution software phantom of the human brain which is applicable to voxel-based radiation transport calculations yielding nuclear medicine simulated images and/or internal dose estimates.
Results: A software head phantom was created from 124 transverse MRI images of a healthy normal individual. The transverse T2 slices, recorded in a 256x256 matrix from a GE Signa 2 scanner, have isotropic voxel dimensions of 1.5 mm and were manually segmented by our clinical staff. Each voxel of the phantom contains one of 62 index numbers designating anatomical, neurological, and taxonomical structures. The result is stored as a 256x256x128 byte array. Internal volumes compare favorably to those described in the ICRP Reference Man.
Conclusion: The computerized array represents a high resolution model of a typical human brain and serves as a voxel-based anthropomorphic head phantom suitable for computer-based modeling and simulation calculations. It offers an improved realism over previous mathematically described software brain phantoms, and creates a reference standard for comparing results of newly emerging voxel-based computations. Such voxel-based computations lead the way to developing diagnostic and dosimetry calculations which can utilize patient-specific diagnostic images. However, such individualized approaches lack fast, automatic segmentation schemes for routine use; therefore, our high resolution, typical head geometry gives the most realistic patient model currently available.

INTRODUCTION

Computerized software phantoms serve an important role in simulating radiation transport geometries representing either therapeutic or diagnostic conditions. Much can be learned about the instrument characteristics, expected absorbed radiation dose to human subjects, and anticipated image quality by computing such models on modern day computers. Several computer-based phantoms have been developed over the last two decades to approximate the volume and orientation of internal organs of the human body (1-4). These have been, and are being used, to estimate the dose distribution in humans from external and internal radiation sources, or to evaluate imaging characteristics of radiological instruments. Broadly, these phantoms describe the surfaces or volumes of internal organs by two different methods: analytical equations describing the internal surfaces, or three dimensional arrays in which each voxel contains an index number assigning it to an organ.

The advantage of analytical descriptions is that they can very compactly store the surface information and allow one to very quickly compute the intersection of direction vectors with these surfaces. A disadvantage lies in their inability to easily describe complicated, nonsmooth realistic structures within the human body. Voxel-based phantoms can easily describe complicated, convoluted surfaces by increasing the resolution of the array and appropriately assigning index numbers to the voxels. Two disadvantages of voxel models are: 1) as the resolution of the arrays becomes higher, storage considerations become substantial; and 2) computing intersections of direction vectors with surfaces requires a voxel by voxel search.

Due in part to the recent interest in brain imaging, software phantoms which realistically model the human head are being developed and improved. We have developed a voxel-based head phantom by manually drawing contours on 124 transverse MRI images of a healthy male volunteer. This manual segmentation has resulted in a 256x256x128 byte array describing 62 anatomical, neurological, and taxonomical structures.

METHODS

We selected a volumetric MRI imaging sequence of a 35 year old male weighing 170 lbs and measuring 5' 10" in height, who was considered to be clinical normal and had no head abnormalities. The images were acquired on a GE Signa 1.5 Tesla scanner using SPGR mode ("spoiled grass"). These acquisitions are generally faster than spin echo sequences and demonstrate better gray to white ratios in the brain. Flow compensation was additionally implemented in order to eliminate any artifacts due to moving blood. The acquisition data were stored in a 256x192 matrix size which then was interpolated to 256x256, for carrying out the Fourier transform for image formation. With a field of view equal to 28 centimeters, the pixel size in the x, y, plane equals 1.1 mm. The resolution in the z axis results in a slice thickness of 1.4 mm. The single experiment (nex) acquisition time was 16 minutes.

The data access and processing programs were created on a VAX 3500 workstation running VMS version 5.0-2 using the available User Interface Services (UIS routines) for program control of the resident color display screen. The color display monitor is a 1024x1024 pixel raster display equipped with 8 bit planes. One bit plane is used for overlay graphics while the remaining 7 bits are used for mapping 128 color levels to the displayed transverse images. A serial line high resolution Summagraphics bitpad provided high resolution cursor control. An in-house program was developed to read the transverse slices from disk, display them on the color workstation monitor, and permit outlining of organs under bitpad cursor control. The x and y integer positions of all of the organ outlines are stored on disk with a resolution of 256x256 pixels. Members of the medical staff outlined separate internal organs and known structures contained in the transverse slices. A region of interest coloring routine was used to fill the inside of each organ outline with a unique index value. The MRI original slices were retained so that the original image matrix values can retrieved.

The segmented image information is stored in two independent files. A variable size file is created for each transverse slice and contains the x,y coordinates of each of the contours drawn on that slice. The slice number is retained in the name of the file. These contours serve as the input to the filling routine, which creates a fixed size organ index image. The organ index image is a 256x256 byte matrix filled with integer values which delineate the internal structures (organs) of the body. The organ index image is therefore, in effect, the original MRI T2 values, replaced by integers corresponding to the organ index value. The assignment of integers to the organs are shown in Table 1.

Table 1
Index Numbers and their Associated Structures in the MRI Images

0 outside phantom	77 cerebellum	105 putamen
1 skin	78 tongue	106 optic nerve
2 cerebral fluid	81 horn of mandible	107 internal capsule
3 spinal cord	82 nasal septum	108 septum pellucidium
4 skull	83 white matter	109 thalamus
5 spine	84 superior sagittal sinus	110 eyeball
9 skeletal muscle	85 medulla oblongata	111 corpus collosum
15 pharynx	88 artificial lesion	112 special frontal lobes
16 esophagus	89 frontal lobes	113 cerebral falx
22 fat	91 pons	114 temporal lobes
23 blood pool	92 third ventricle	115 fourth ventricle
26 bone marrow	95 occipital lobes	116 frontal portion eyes
29 trachea	96 hippocampus	117 parietal lobes
30 cartilage	97 pituitary gland	118 amygdala
63 lesion	98 fat	119 eye
70 dens of axis	99 uncus(ear bones)	120 globus pallidus
71 jaw bone	100 turbinates	121 lens
72 parotid gland	101 caudate nucleus	122 cerebral aquaduct
74 lacrimal glands	102 zygoma	123 lateral ventricles
75 spinal canal	103 insula cortex	124 prefrontal lobes
76 hard palate	104 sinuses/mouth cavity	125 teeth

RESULTS

In order to appreciate the internal detail of the voxel based head phantom, we present three arbitrarily selected transverse slices from the segmented volume array in Figure 1.

Figure 1. Three arbitrarily selected transverse slices from the segmented phantom volume. The gray level used to display each structure is directly related to the index number in Table 1.

Another way to appreciate the volumetric structures in our phantom is to fill selected structures with positive integer values and leave other structures filled with zero. Then the three-dimensional volume can be collapsed along each of the three axes in order to obtain a two dimensional

representation of the original three dimensional volume. Since the volume is collapsed by adding the integers filled into the voxels, each of the three views corresponds to a projection of the volume onto a plane. Several internal structures were selected and filled with integer values in order to highlight the skull, white matter, caudate nucleus, putamen, thalamus, globus pallidus, and eye. These are shown in Figures 2 and 3.

Figure 2. A vertex, lateral, and anterior view of the phantom with opacity filled into all voxels corresponding to white matter and skull.

Figure 3. A vertex, lateral and anterior view of the phantom with opacity filled into all voxels corresponding to skull, caudate nucleus, putamen thalamus, globus pallidus, and eye (excluding the lens).

Since the volume (or weight) of each structure is important for both therapeutic and diagnostic applications, we determined the number of voxels contained in each structure and by knowing the voxel dimensions, calculated the structure sizes (Table 2).

Four of the structures found in Table 2 were listed in the ICRP Reference Man Report (5): cerebellum = 143 grams, thalamus = 6.5 grams, eye ball = 13.5 grams, lens of the eye = .4 grams. Except for the thalamus the volume determinations for this one individual are virtually identical to those documented in the Reference Man Report. It is not clear to us why the thalamus in this individual is approximately twice that sited in the literature.

Three data sets have been stored in data archives:

1. The raw MRI data files are stored in a 256x256 two-byte signed integer array. Depending upon hardware, the bytes of these words may need to be swapped before displaying.
2. Segmented image data in a 256x256 one-byte array. Each byte represents a pixel continuing an index number to an associated internal structure. Slice 1 starts at the roof of mouth and slice 124 ends at the top of the head.

Table 2
List of the Segmented Internal Structures and their Associated Volume in Cubic Centimenters

skin	236.7	cerebellum	139.4	putamen	10.3
cerebral fluid	220.6	tongue	17.6	optic nerve	1.5
spinal cord	2.9	horn of mandible	14.9	internal capsule	9.2
skull	459.9	nasal septum	5.7	septum pellucidium	0.9
spine	26.8	white matter	510.7	thalamus	12.3
skeletal muscle	361.3	super.sagittal sinus	4.1	eyeball	12.9
pharynx	4.5	medulla oblongata	3.9	corpus collosum	10.9
esophagus	-	artificial lesion	4.7	sp. reg. fr. lobes	6.56
fat	52.6	frontal lobes	112.8	cerebral falx	4.50
blood pool	24.3	pons	22.4	temporal lobes	231.1
bone marrow	0.9	third ventricle	8.9	fourth ventricle	1.9
trachea	-	occipital lobes	70.1	fr. portion eyes	5.2
cartilage	51.1	hippocampus	7.1	parietal lobes	120.1
lesion	-	pituitary gland	0.086	amygdala	3.9
dens of axis	1.3	fat	501.1	eye	13.4
jaw bone	5.54	uncus(ear bones)	0.8	globus pallidus	4.1
parotid gland	31.3	turbinates	6.4	lens	0.48
lacrimal glands	2.5	caudate nucleus	10.5	cerebral aquaduct	0.5
spinal canal	7.7	zygoma	9.4	lateral ventricles	9.5
hard palate	30.3	insula cortex	13.1	prefrontal lobes	53.2
		sinuses/mouth	172.6		

3. The x,y contours which were manually drawn to segment the internal structures are saved as a list of x,y pairs.

The total storage capacity of the files are: original MRI images = 36 Megabytes, organ index matrices = 28 Megabytes , x,y contours = 3 Megabytes, and are available for public access through our Imaging Processing and Analysis Laboratory. To gain access to the data, send a request to Dr. George Zubal e-mail: George.Zubal@Yale.Edu.

ACKNOWLEDGMENTS

Work performed under contract #DE FG02-88ER60724 with the US Department of Energy and under contract #NS32879 with the US National Institutes of Health. We are thankful to Vivian Ventura for her text processing skills.

REFERENCES

1. Snyder W, Ford MR and Warner, G. Estimates of Specific Absorbed Fractions for Photon Sources Uniformly Distributed in Various Organs of a Heterogeneous Phantom. NM/MIRD Pamphlet No. 5, Society of Nuclear Medicine Publication., New York, 1978.
2. Williams G, Zankl M, Abmayr W, Veit R and Drexler G. The calculation of dose from external photon exposures using reference and realistic human phantoms and Monte Carlo methods. Phys Med Bio 31:449-452, 1986.

3. Wang H, Jaszczak RJ and Coleman RE. Solid geometry-based object model for Monte Carlo simulated emission and transmission tomographic imaging systems. IEEE Transactions on Medical Imaging 11:361-372, 1992.
4. Zubal IG, Harrell CR, Smith EO, Rattner Z, Gindi G and Hoffer PB. Computerized 3-dimensional segmented human anatomy. Med Phys 21(2):299-302, 1994.
5. Snyder WS, Cook MJ, Masset ES, Kaehausen LR, Howells GP and Tipton IH. ICRP Publication No. 23 Report of the Task Group on Reference Man, Pergamon Press 1984.

QUESTIONS

Akabani: A very nice presentation. Have you been asked if your phantom could be used for developing radiosurgery studies?

Zubal: I haven't been asked to specifically supply the phantom for radiosurgery, but many people have downloaded both the torso and head phantom from our anonymous FTP area. I would be happy to e-mail (Zubal@biomed.med.yale.edu) the password to retrieve the data to anyone interested.

S VALUES FOR SUBREGIONS IN THE BRAIN

Tagesson M[1], I. Zubal IG[2], Ljungberg M[1] and Strand S-K[1]

[1]Department of Radiation Physics, Lund University
S-221 85 Lund, SWEDEN
[2]Department of Diagnostic Radiology
Yale University, New Haven, CT

ABSTRACT

An anthropomorphic voxel phantom has been used to simulate activity concentrations in different structures of the brain. S values for the regions in the brain were computed using the SIMDOS Monte Carlo code, which allows the voxel size to be adjusted to scale for different brain sizes. Examples of source and target regions investigated are gray and white matter, the caudate nucleus, thalamus, cerebellum and whole brain. Calculated S values for $^{99}Tc^{m}$, ^{123}I and ^{18}F are presented for different combinations of source and target regions, and a comparison with other dosimetry models is shown. The SIMDOS code calculates absorbed fractions and S values for arbitrary geometries for source and target organs. Applying the SIMDOS to the brain structure, assuming different activity distributions, has generated a new set of accurate S values that are applicable for radiopharmaceutical dosimetry.

INTRODUCTION

Dosimetry of the subregions within the brain is subjected to an increasing interest in the synthesis of new SPECT and PET radiopharmaceuticals, e.g. for blood perfusion and neuroreceptor imaging/studies. Relatively high uptakes of activity may occur in small structures, such as the corpus striatum and the lacrimal glands, which may result in locally high absorbed doses. A realistic model of the brain for dose calculations is therefore essential.

The earliest proposed brain model defines the brain as an ellipsoid. This model has been included in the MIRD phantom (1) and in the Cristy/Eckerman phantoms (2). Eckerman et al. (3) improved this model by adding a gray matter shell around the white matter. In 1984, Poston proposed a brain model with 14 different regions (4), which recently has served as a base for the newly proposed MIRD brain model (5).

In this work, we propose the use of a very realistic brain model, based on segmented MRI head images, for calculation of new S values. This voxel phantom, developed by Zubal et al. (6), allows derivation of S values for large, complex structures as well as smaller regions, and can be used for calculation of S values in regions not represented in earlier brain models.

THE HEAD PHANTOM

The anthropomorphic MRI head phantom is described in more detail elsewhere in these proceedings. The shape of the subregions in the voxel phantom can be adjusted, which is an important feature for dosimetric applications. Also, the voxel size of the three-dimensional data set is easily changed, allowing calculations of S value sets for different brain shapes and sizes. Since the original phantom consists of coded structures, special software has been developed to define the activity distribution and the density distribution. Examples of these distributions are shown in Figure 1.

The mass of a structure or suborgan is very important for absorbed dose calculations. Table 1 shows a comparison of the volume of some regions investigated in this study, with corresponding volumes of the proposed analytical MIRD model.

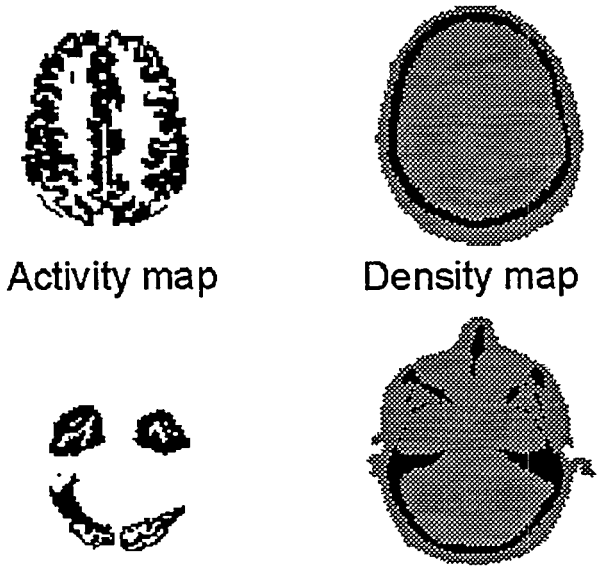

Figure 1. To the left, two axial slices of the phantom where activity has been assigned to the cerebral cortex. To the right, showing the corresponding density maps, the skull and facial skeleton are clearly seen.

Table 1
Volumes (cm^3) in the Proposed MIRD Model and in this Study

Region	Bouchet et al. (5)	This study	Difference %
Whole brain *	1467.7	1468.4	0.1
White matter	648.4	532.7	-21.7
Gray matter	622.4	647.6	3.9
Cerebellum	139.1	149.7	7.1
Thalamus	6.4	13.0	50.7
Caudate Nucleus	10.5	10.9	3.9

* For comparison, the whole brain volume in MIRD Pamphlet No. 5 (1) and the adult ORNL phantom (2) are 1470 and 1370, respectively.

The volume of the white matter is lower in this model than that of Bouchet et al. (5), but most other values are similar. In this study, a few regions, such as the internal capsule (which is a part of the corpus striatum), are not included in the definition of the white matter. This makes the total volume of the white matter in our model slightly smaller. Furthermore, the thalamus mass does not agree well with other models. However, some indications show that a realistic value of the thalamus mass should indeed be in the range of 12 to 16 g.

THE MONTE CARLO CODE

Dosimetric calculations were made using the SIMDOS software (7) that also is described in more detail elsewhere in these proceedings. The different steps in the calculation scheme are shown in Figure 2. For the present study, no explicit electron simulation was done. Instead, all electrons were considered locally absorbed, either in the voxel where the decay was simulated, or in the voxel where a particular photon interaction occurred. This assumption will, however, influence the results, especially for studies of radionuclides emitting higher energy electrons (such as ^{123}I) where the assumption of self absorption in smaller regions (such as the caudate nucleus, the pituitary gland and the lacrimal glands) does not hold.

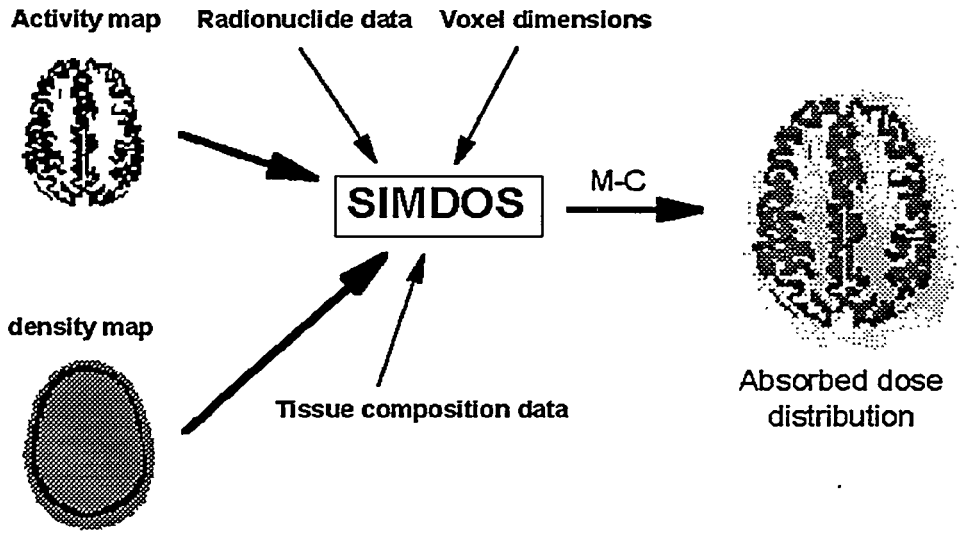

Figure 2. The input data needed for a Monte Carlo calculation of the absorbed dose distribution.

RESULTS AND DISCUSSION

Table 2 shows a comparison between our data and the data obtained from the MIRDOSE 3.1 software (8). Originally, our data was based on a whole brain volume of 1468.4 cm^3, but was rescaled with a factor of 1470/1370 in order to be comparable with results from the ORNL phantom, included in MIRDOSE 3.1. Good agreement is achieved, although values for ^{123}I and ^{18}F are somewhat lower in our results. This difference can probably be explained by the more elongated and curved geometry of the brain in our model.

Table 2
Comparison of Calculated S Values (Whole Brain–Whole Brain)
(Data are Expressed in Units of mGy/MBq-s)

Radionuclide	MIRDDOSE 3.1	This study	Difference, %
$^{99}Tc^{m}$	4.33×10^{-6}	4.41×10^{-6}	-1.8
^{123}I	7.63×10^{-6}	7.42×10^{-6}	2.8
^{18}F	4.77×10^{-5}	4.58×10^{-5}	4.2

Table 3
Comparison of Calculated S Values, Based on our Model and the Proposed New MIRD Brain Model. Data are Expressed as mGy/MBq-s for ^{123}I and the Source and Target Region is the Same

Region, X (source and target)	Bouchet et al.	This study	Difference, %
Thalamus	9.02×10^{-4}	4.66×10^{-4}	-94
Cerebral cortex	1.16×10^{-5}	1.13×10^{-5}	-2.7
Cerebellum	5.22×10^{-5}	4.94×10^{-5}	-5.7
Caudate nucleus	5.10×10^{-4}	5.21×10^{-4}	2.1

Table 4
Comparison of Calculated S Values for ^{99m}Tc Based on our Model and the Proposed New MIRD Brain Model Source Organ is the Cerebral Cortex and the Target has been Varied. Data are Expressed as mGy/MBq-s for $^{99}Tc^{m}$.

Target region, X	Bouchet et al.	This study	Difference, %
Caudate nucleus	1.44×10^{-6}	1.65×10^{-6}	-12.7
Cerebellum	1.43×10^{-6}	9.80×10^{-7}	46
Cerebral cortex	6.39×10^{-6}	6.64×10^{-6}	-3.8
Thalamus	1.46×10^{-6}	1.58×10^{-6}	-7.6
White matter	1.78×10^{-6}	1.95×10^{-6}	-8.7

Table 3 shows S values (due to self absorption) with discrepancies of less than 6%, except for the thalamus. This difference is mostly due to the large difference in the thalamus mass (Table 1). Table 4 shows different S values, calculated for the cerebral cortex defined as the source organ. Good agreements have been achieved, with the exception of a large discrepancy in the S value for cerebellum. Our higher S value can be explained by differences in the distance between the cortex and the cerebellum.

It has been found that discrepancies are mainly explained by differences in target mass, variation

in distances between source and differences in target and source/target region shapes. Another factor may be that no explicit electron transport was made in this study, and that the program codes, used for the calculation of S values in the different models, use different cross-section data for photon interactions. Some statistical uncertainties may also be present.

In this work, we propose a realistic, anatomically correct and detailed model that might give more accurate S values than the proposed MIRD model. Individuals are geometrically more similar inside the skull than inside the trunk. Therefore, using a model based on a high-resolution MRI measurement of a human may produce more accurate results compared to assuming more general analytical shapes, such as, ellipsoids and cylinders. Thus, since the phantom is rescalable (the voxel size, tissue composition, etc.), our model might become useful for radiation protection purposes. On the other hand, the model could be seen as an example of ONE patient only and the results, shown above, can be interpreted as reflecting the discrepancies between the proposed MIRD model and one individual patient. Despite this, we believe that our model can be very useful to derive S-value tables for radiation protection risk estimations and to evaluate the errors introduced when using an average phantom (such as the MIRD phantom) for dose calculation in individuals.

Future work will include derivation of extensive S-value tables for relevant target/source regions and radionuclides of interest for both diagnostic imaging and for therapy. Improvement of the voxel phantom, such as including typical tumor locations, will also be made. Explicit simulation of electron emission needs to be included, which is particularly important in the case of high-energy electron emitting radionuclides in small subregions.

In conclusion, we have proposed a new realistic voxel-based brain model with a large number of subregions, segmentated from a high-resolution MRI study of a male. It is our belief that this phantom is one of the most accurate brain models for dosimetric calculations available today.

ACKNOWLEDGMENTS

This work has been supported by grants from Mrs. Berta Kamprad's Foundation, The Royal Physiographic Society in Lund, John and Augusta Persson's Foundation, The Lund University Medical Faculty Founds and The Swedish Cancer Foundation grant no. 2353-B94-08XAB and3559-B95-02XBB, and the Swedish Radiation Protection Institute #893.95.

REFERENCES

1. Snyder WS, Ford MR and Warner GG. Estimates of Specific Absorbed Fractions for Photon Sources Uniformly Distributed in Various Organs of a Heterogeneous Phantom: MIRD Pamphlet No. 5, Revised, The Society of Nuclear Medicine, New York, 1978.
2. Cristy M and Eckerman KF. Specific Absorbed Fractions of Energy at Various Ages from Internal Photon Sources I-VII, TM/8381/V1-V7, Oak Ridge National Laboratory, Oak Ridge, TN, USA, 1987.
3. Eckerman KF, Cristy M and Warner GG. Dosimetric Evaluation of Brain Scanning Agents, Proceedings of the Third International Radiopharmaceutical Dosimetry Symposium, pp 527-540 Oak Ridge, HHS Publication FDA 81-8166 1980.
4. Poston JW. Research on the Experimental Verification of Dosimetry Calculations. Research Proposal. DOE Report DE-AS05-790EV 10248, 1984.

5. Bouchet LG, Bolch WE and Weber DA, Atkins HL and Poston JW. A revised dosimetric model of the adult head and brain. J Nucl Med 37(7):1226-1236, 1996.
6. Zubal IG, Harrell CR, Smith EO, Rattner Z, Gindi G and Hoffer PB. Computerized 3-dimensional segmented human anatomy. Med Phys 21:299-302, 1994.
7. Tagesson M, Ljungberg M and Strand S-E. A Monte Carlo program converting activity distributions to absorbed dose distributions in a radionuclide treatment planning system. Acta Oncol 35:367-372, 1996.
8. Stabin M. MIRDOSE - the personal computer software for use in internal dose assessment in nuclear medicine. J Nucl Med 37:538-546, 1996.

QUESTIONS

Bolch: Comment. Thank you very much for this most interesting presentation. Nevertheless, I do not feel that the dosimetry community is as yet ready to abandon stylized mathematical models as you suggest. The volume discrepancy in the thalamus between the Zubal brain model and that in the new MIRD head and brain model is interesting and should be investigated further. I would suggest that several additional MRI measurements be performed before a final reference volume is established.

A CONTRIBUTION TO THE STUDY OF THE RADIOPHARMACEUTICAL BINDINGS ON BLOOD ELEMENTS

Freitas RS[1], Gutfilen B[2], Bernardo-Filho M[1,2].
[1]Instituto Nacional de Câncer
Centro de Pesquisa Básica
[2]Universidade do Estado do Rio de Janeiro
I. Biologia, Rio de Janeiro
RJ, 20551-030, Brasil

ABSTRACT

Many factors can affect the biodistribution of radiopharmaceuticals. If unknown, such factors may lead to poor organ visualization and require repeating the examination (increasing the radiation dose to the patient). Understanding the binding characteristics of radiopharmaceuticals on blood is important. Theoretical and practical aspects of radiopharmaceutical binding with plasma (P) have been studied, but have not been adequately evaluated with blood cells (BC). Uptake of radiopharmaceuticals in organs may depend on their biochemical characteristics as well as the binding to blood elements. Free vs. protein-bound radiopharmaceuticals have been studied using plasma protein precipitation methods. However, the results of different studies can not be easily compared because the precipitation methods have not been standardized. We decided to standardize the concentration of trichloroacetic acid (TCA) for each radiopharmaceutical in order to determine the radioactivity present in precipitating P and BC. We compared the results obtained with ^{99m}Tc-radiopharmaceuticals sodium pertechnetate ($Na^{99m}TcO_4$) and phytic acid (^{99m}Tc-PHY). Blood with heparin (3 ml) was withdrawn from Wistar rats, incubated (60 min) with 1 ml of ^{99m}Tc-PHY or $Na^{99m}TcO_4$ (3.7 MBq), centrifuged, and P and BC separated. Samples of P and BC were also precipitated with TCA concentrations (20.0, 10.0, 5.0, 1.0, 0.5 and 0.1%) and soluble (SF) and insoluble fractions (IF) were isolated and counted. The percent of radioactivity (% activity) in P was 29.6 (^{99m}Tc-PHY) and 65.0 ($Na^{99m}TcO_4$) and in BC, 70.4 (^{99m}Tc-PHY) and 35.0 ($Na^{99m}TcO_4$). The % activity in IF-P depends on TCA solutions and it is modified from 36.4 to 65.0 (^{99m}Tc-PHY) and the best precipitation to $Na^{99m}TcO_4$ was 25.4. The analysis of the results to IF-BC showed that % activity is altered from 54.1 to 80.1 (^{99m}Tc-PHY) and the best precipitation to $Na^{99m}TcO_4$ was 71.9. In conclusion, the radiopharmaceutical protein-binding complexity could be explained by the variety of proteins present in P and BC as well as to the mechanisms involved in the labeling method and the type of radiopharmaceutical. Understanding the binding characteristics of radiopharmaceuticals to blood elements can help to reduce the radiation dose to patients.

INTRODUCTION

Many factors can affect the biodistribution of radiopharmaceuticals (1). If unknown, such factors may lead to poor organ visualization and require repeating the examination (increasing the radiation dose to the patient). There is considerable evidence that the biodistribution or pharmacokinetics of radiopharmaceuticals may be altered by a variety of drugs(1-2). One reason for this fact is that the drug can interfere with the binding of the radiopharmaceuticals on plasma proteins and/or blood cell constituents. There are different methods to quantitate the binding of radioactivity to blood elements (3-8). However, it is known that the determination of protein binding is very complex and the results normally are not clear. The precipitation methods are generally reliable, but the dialysis method, which is widely used, was found to be dependent on the association-dissociation equilibrium between the ^{99m}Tc radiopharmaceutical and the protein that complexes with it. With application of dialysis or gel chromatography, only the technetium that is irreversibly bound to proteins is observed (5,7) . Understanding the binding characteristics of radiopharmaceuticals to blood is important. The theoretical and practical aspects of this binding with plasma (P) have been studied. However, the theoretical and practical aspects of this binding with blood cells (BC) have not been adequately evaluated. Free vs. protein-bound radiopharmaceuticals have been studied using plasma protein precipitation methods. However, the results of different studies can not be easily compared because the precipitation methods have not been standardized. Thus, we decided to standardize the concentration of trichloroacetic acid (TCA) for each radiopharmaceutical in order to determine the radioactivity present in precipitating P and BC. We compared the results obtained with ^{99m}Tc-sodium pertechnetate ($Na^{99m}TcO_4$) and ^{99m}Tc-phytic acid (^{99m}Tc-PHY).

MATERIAL AND METHODS

The experiments were carried out with heparinized whole blood withdrawn from Wistar rats. ^{99m}Tc-PHY was obtained from the Radiopharmacy Department, Instituto Nacional de Cancer, Rio de Janeiro, Brazil. ^{99m}Tc, as sodium pertechnetate was obtained from a ^{99}Mo/^{99m}Tc generator purchased from Instituto de Pesquisas Energéticas e Nucleares, Comissão Nacional de Energia Nuclear, Brazil.

Fresh whole blood (3 ml) was incubated with samples of the ^{99m}Tc-radiopharmaceuticals (1 ml containing 3.7 MBq) for 60 min at room temperature. After incubation, the blood preparations were centrifuged and the plasma (P) and blood cells (BC) were isolated. Aliquots (20 µl) of P and BC were precipitated with 1 ml solutions of trichloraocetic acid (Reagen, Brazil) in various concentrations (20.0, 10.0, 5.0, 1.0, 0.5, 0.1%) and the soluble (SF) and insoluble (IF) fractions from plasma and blood cells were separated. The samples (P, BC, IF-P, SF-P, IF-BC and SF-BC) were counted in a well counter with a NaI(Tl) crystal (1272 Clinigamma Gamma Counter, LKB Wallac, Finland).

The percentage of radioactivity in P was determined by dividing the counts in P by the sum of counts in P plus BC and multiplying by 100. The percentage of activity in BC was determined by dividing the counts in BC by the sum of the counts in BC plus P and multiplying by 100. Using the same procedure, the percentage of activity in the IF and the SF in both P and BC were determined.

RESULTS

At 60 min, the percent of activity in plasma was 65.0 ± 5.1% and 29.6 ± 5.5% for $Na^{99m}TcO_4$ and ^{99m}Tc-Phy, respectively. Activity in the blood cells was 35.0 ± 5.1% and 70.4 ± 5.5%, respectively. These values indicate that for $NA^{99m}TcO_4$, the radioactivity is predominantly in plasma

and for ^{99m}Tc-Phy the activity is higher in blood cells. The affinity of the blood cells for ^{99m}Tc-Phy is higher than for $Na^{99m}TcO_4$

Table 1 shows the % activity in insoluble and soluble fractions obtained from plasma samples precipitated with different trichloroacetic concentrations. These plasma samples were obtained from whole blood that was incubated for 60 min with the radiopharmaceuticals. The % activity in IF-P depends on TCA concentration and ranges from 36.4 to 65.0% (^{99m}Tc-PHY). The best precipitation to $Na^{99m}TcO_4$ was 25.4% with 0.5% TCA. The results for the fixation of ^{99m}Tc-PHY in the IF-P showed that there was no difference when the TCA concentrations of 0.1 to 1.0 were used for precipitation. However, for $Na^{99m}TcO_4$ the radioactivity in the insoluble fraction of P increases in the range of 0.1% and 0.5% TCA concentration and then decreases for higher TCA concentrations..

Table 1

Distribution of the % of Radioactivity in Plasma Insoluble Fractions and Soluble Fractions Obtained with the Precipitation of Plasma Samples with Different Trichloroacetic Acid (TCA) Concentrations

TCA Concentrations (%)	Insoluble Fraction (%)		Soluble Fraction (%)	
	$Na^{99m}TcO_4$	^{99m}Tc-PHY	$Na^{99m}TcO_4$	^{99m}Tc-PHY
0.1	8.5 ± 4.6	64.3 ± 1.6	91.5 ± 4.6	35.7 ± 4.6
0.5	25.4 ± 7.5	62.4 ± 9.4	74.6 ± 7.5	37.6 ± 9.4
1.0	13.8 ± 4.2	65.0 ± 6.4	86.2 ± 4.2	35.0 ± 6.4
5.0	9.7 ± 2.2	51.5 ± 0.7	90.3 ± 2.2	48.5 ± 0.7
10.0	10.5 ± 2.5	38.1 ± 9.9	89.5 ± 2.5	62.9 ± 9.9
20.0	9.4 ± 2.1	36.4 ± 4.9	90.6 ± 2.1	63.6 ± 4.9
The values are averages ± standard deviations for 5 experiments.				

Table 2 shows the % activity in blood cells for the insoluble and soluble fractions obtained from precipitations with different trichloroacetic concentrations. These aliquots of blood cells were obtained from whole blood that was incubated for 60 min with the radiopharmaceuticals. The analysis of the results of IF-BC shows that % activity is altered from 54.1% to 80.1% for ^{99m}Tc-PHY with TCA concentrations from 20.0% to 0.1%, respectively. The best % activity for $Na^{99m}TcO_4$ was 71.9% with a TCA concentration of 1.0%. With Tc-PHY, the uptake in BC is larger and the binding is stronger compared to the BC uptake and binding of $NA^{99m}TcO_4$.

Table 2

Distribution of the % of Radioactivity in Insoluble and Soluble Fractions from Blood Cells Obtained with the Precipitation of Blood Cell Samples with Various TCA Concentrations

TCA Concentrations (%)	Insoluble Fraction%		Soluble Fraction%	
	$Na^{99m}TcO_4$	^{99m}Tc-PHY	$Na^{99m}TcO_4$	^{99m}Tc-PHY
0.1	17.7 ± 6.9	80.1 ± 1.3	82.3 ± 6.9	19.9 ± 1.3
0.5	23.0 ± 8.4	80.0 ± 10.1	77.0 ± 8.4	20.0 ± 10.1
1.0	71.9 ± 7.6	76.0 ± 2.1	28.1 ± 7.6	24.0 ± 2.1
5.0	48.0 ± 4.8	80.1 ± 13.7	52.0 ± 4.8	9.9 ± 13.7
10.0	22.0 ± 5.2	70.5 ± 13.4	78.0 ± 5.2	29.5 ± 13.4
20.0	32.1 ± 6.5	54.1 ± 18.1	67.9 ± 6.5	45.9 ± 18.1

The values are averages ± standard deviations for 5 experiments.

DISCUSSION

The correct determination of the binding of radioactivity on blood elements is worthwhile for several reasons: (I) to better understand how a drug is capable of modifying the biodistribution of radiopharmaceuticals, (ii) to evaluate the specific characteristics of the binding of each radiopharmaceutical to its targets in the blood, (iii) to avoid misdiagnosis, (iv) to avoid the repetition of examinations, (v) to avoid poor organ visualization and (vi) to reduce the radiation dose to patients (1).

The radiopharmaceutical uptake in organs may depend on its biochemical characteristics as well as the binding to blood elements. There are conflicting results described in the literature about the binding of radipharmaceuticals to blood elements (4-8). We agree with De Ligny et al. (5) that the value for the protein binding of ^{99m}Tc-radiopharmaceuticals appears to depend on the method used in addition to the experimental conditions. De Lingny et al. (5) also stated that protein binding to ^{99m}Tc-MDP does not occur at all, but Vanlic-Razumenic et al. (7) disagreed with this conclusion and considered that dissociation of the ^{99m}Tc-MDP complex was a consequence of excess dilution in their experiments.

With regard to Tc-PHY, Vanlic-Razumenic et al (7) reported a value of 35.1% in the IF-P using 10% TCA. The corresponding value in our study was 38.15 but this value varied from 36.4% to 65.0% depending on the TCA concentration.

Savelkouk et al. (6) have shown that precipitation with TCA sometimes yields high values, presumably from decomposition of the ^{99m}Tc-diphosphonate complexes in a strong acidic solution, and subsequent binding of the ^{99m}Tc to the denatured proteins. Decomposition can also occur in gel chromatography and dialysis.

The general comparison of the obtained results shows that the fixation of the ^{99m}Tc-PHY to the insoluble fraction of P and BC is higher and stronger than that of $Na^{99m}TcO_4$. Possibly this fact can be explained by the presence of stannous chloride in the ^{99m}Tc-PHY. However, if we compare the radiopharmaceuticals, they present different characteristics when binding to blood cells. When we choose the concentration of 1.0% TCA, the bindings are the same. If we choose other TCA concentrations these bindings will be different.

We can speculate that the binding of the radiopharmaceutical to blood elements and the precipitation effect may depend on the characteristics of each radiopharmaceutical. We suggest that the direct comparison among the various radiopharmaceuticals and the differences in their capability to bind to protein complexes in the blood, should be studied carefully. The comparison of the bindings of ^{99m}Tc-radiopharmaceuticals using only one TCA concentration should be avoided. Specific characteristics of

each radiopharmaceutical should be considered. Studies with other radiopharmaceutials are now in progress.

In conclusion, the radiopharmaceutical-protein binding complexity could be explained by the variety of proteins present in P and BC, in addition to the mechanisms involved in the labeling uptake and the type of each radiopharmaceutical. The understanding of the binding of radiopharmaceuticals to blood elements may help to reduce the radiation dose to patients.

REFERENCES

1. Hladik WB III, Saha GB and Study KT, Editors. Essentials of Nuclear Medicine Sciences. pp: 155-219, Williams and Wilkins, Baltimore, 1987.
2. Hesslewood S and Leung E. Drug interactions with radiopharmaceuticals. Eur J Nucl Med 21:348-356, 1994.
3. Bernardo-Filho M, Gutfilen B and Maciel OS. ^{99m}Tc binding on plasma and red blood cells: Role of various precipitating agents. Biom Letters 50:17-24, 1994.
4. Gano L, Patricio L and Castanheira I. Radiopharmaceuticals for renal studies: Evaluation of protein binding. J Radioanal Nucl Chem 132:171-178, 1989.
5. De Ligny CL, Gelsema WJ, Tji TG, Huigen YM and Vink HA. Bone seeking radiopharmaceuticals. Nucl Med Biol 17:161-179, 1990.
6. Savelkoul TJF, Van Ginkel JJ, Grouls RJE, Oldenburg SJ and Duursma SA. Protein binding and urinary excretion of ^{99m}Tc(Sn)-MDP and ^{99m}Tc-MDP. Int J Nucl Med Biol 12:125-131, 1985.
7. Vanlic-Razumenic N, Joksimovic J, Ristic B, Tomic M, Beatovc S and Adjdinovic B. Interaction of ^{99m}Tc-radiopharmaceuticals with transport protein in human blood. Nucl Biol Med 20:363-365, 1993.
8. Domenech RG, Mendez OA, Alvarez RG and Marti AF. Physico-chemical study of the radiopharmaceuticals ^{99m}Tc-DMSA, ^{99m}Tc-EDTA and ^{99m}Tc-DTPA interaction with plasmatic proteins. Appl Radiat Isot 40(6):536-538, 1989.

A MICRODOSIMETRIC STUDY OF $^{10}B(n,\alpha)^{7}Li$ AND $^{157}Gd(n,\gamma)$ REACTIONS FOR NEUTRON CAPTURE THERAPY

Wang C-KC[1], Sutton M[1], Evans TM[1] and Laster BH[2]
[1]Nuclear Engineering & Health Physics Program
Georgia Institute of Technology, Atlanta, Georgia 30332-0225
[2]Medical Department, Brookhaven National Laboratory, Upton, New York 11973

ABSTRACT

This paper presents the microdosimetric analysis for the most interesting cell survival experiment recently performed at the Brookhaven National Laboratory (BNL). In this experiment, the cells were first treated with a gadolinium (Gd) labeled tumor-seeking boronated porphyrin (Gd-BOPP) or with BOPP alone, and then irradiated with thermal neutrons. The resulting cell-survival curves indicate that the $^{157}Gd(n,\gamma)$ reactions is very effective in cell killing. The death of a cell treated with Gd-BOPP were attributed to either the $^{10}B(n,\alpha)^{7}Li$ reactions or the $^{157}Gd(n,\gamma)$ reactions (or both). However, the quantitative relationship between the two types of reaction and the cell-survival fraction was not clear. This paper presents the microdosimetric analysis for the BNL experiment based on the measured experimental parameters, and the results clearly suggest a quantitative relationship between the two types of reaction and the cell survival fraction. The results also suggest new research in gadolinium neutron capture therapy (GdNCT) which may lead to a more practical modality than the boron neutron capture therapy (BNCT) for treating cancers.

INTRODUCTION

Gadolinium neutron capture therapy (GdNCT) based on the $^{157}Gd(n,\gamma)$ reaction has been studied as an alternative to boron neutron capture therapy (BNCT) for treating cancers (1-4). It was recognized that, although gamma rays from the $^{157}Gd(n,\gamma)$ reactions are not absorbed locally, some of the associated internal conversion (IC) electrons and Auger (and Coster-Kronig) electrons are absorbed locally and may somewhat enhance the cell-killing effect. These studies were not pursued very rigorously, because the enhancement of cell killing requires gadolinium atoms be incorporated into the vicinity of DNA molecules, and such a technique did not exist.

Very recently, Laster et. al. at Brookhaven National Laboratory demonstrated, in an in-vitro experiment, that there is a dramatic enhancement of cell killing upon thermal-neutron irradiation for the cells treated with a Gd labeled tumor-seeking boronated porphyrin (Gd-BOPP) in comparison with the cells treated with BOPP alone (5). The dramatic enhancement of cell killing was speculated to be caused by the high-LET Auger electrons emitted in the vicinity of DNA molecules. This speculation is an indirect evidence of the claim that, for the first time, gadolinium atoms were successfully (at least in the in-vitro study) incorporated into the vicinity of DNA molecules. Because

of the much enhanced cell-killing effect, the results of the BNL experiment also imply that GdNCT has a potential of reducing the required neutron fluence (and thus the beam intensity) by more than a factor of five. This, in turn, makes a small accelerator-based neutron source (as oppose to a multi-MW nuclear reactor currently being used) applicable to NCT. The small accelerator-based neutron source is inexpensive and deployable in hospitals, and therefore may turn NCT into a widely used cancer treatment modality. However, before the potential of GdNCT can be fully explored one must perform a thorough dosimetry study to understand the details about how cells are affected by $^{157}Gd(n,\gamma)$ reactions. The dosimetry calculation previously performed for the BNL experiment was either incorrect or inadequate to support the claim of localization of gadolinium atoms around DNA molecules (5). This paper presents a more rigorous microdosimetric calculation for the BNL experiment, and argues in favor of the claim.

METHOD

Dose Contributors

Because the BNL experiment was done with the cells suspended in a medium at a diluted density of $3.0x10^5$ cells/ml while being irradiated with thermal neutrons, the absorbed dose in the cells may have resulted from the following contributors: 1) the unwanted fast neutrons in the beam; 2) the $^1H(n,\gamma)^2H$ reactions; 3) the $^{10}B(n,\alpha)^7Li$ reactions; and 4) the $Gd(n,\gamma)$ reactions. The first two contributors are mainly responsible for the biological effect observed for the control, which consists of untreated cells. The third and fourth contributors are responsible for the enhanced cell-killing effect observed among the cells treated with BOPP and Gd-BOPP. The purpose of this dosimetry study is to elaborate the possible scenarios which are responsible for the difference in cell survival between the cells treated with BOPP and those treated with Gd-BOPP. Therefore, this study only focuses on the dose contributed from the $^{10}B(n,\alpha)^7Li$ and $Gd(n,\gamma)$ reactions.

Since most of the gamma-rays and x-rays escape the sample vial (holding the solution with cells in suspension) without interactions, their dose contribution to the cells is negligible. That is, for the purpose of dose calculation in this study, one only needs to consider the energy deposition resulting from charged-particle emissions. Three charge-particle emissions are considered as the major dose contributors to the cells: 1) the ^4He and ^7Li ions from the $^{10}B(n,\alpha)^7Li$ reactions; 2) the IC electrons following the $Gd(n,\gamma)$ reaction; and 3) the Auger electrons following the emission of the IC electrons. Because the BNL experiment used natural gadolinium, the $Gd(n,\gamma)$ reactions include both the $^{155}Gd(n,\gamma)$ reactions and the $^{157}Gd(n,\gamma)$ reactions. In this study, we assumed that the yields and spectrum of the IC and Auger electrons are the same for both reactions. This assumption is justified according to the data provided by Groshev (6).

Calculation of Spectrum and Yields

To calculate the absorbed dose resulting from each contributor, one first needs to obtain the energy spectra and yields of the dose contributors. The Q value for the $^{10}B(n,\alpha)^7Li$ reaction (i.e., the sum of the kinetic energies associated with the ^4He and ^7Li ions) is 2.34 MeV, and the cross section for the reaction is 3840 barns (7). The energy spectra and yields of the IC electrons associated with the $^{157}Gd(n,\gamma)$ reaction are available from Greenwood et. al (7). Table 1 shows the energy spectrum and total yield of the IC electrons. The energy spectrum and yield of the Auger electrons associated with the $^{157}Gd(n,\gamma)$ reaction are not available, and they must be calculated.

We have developed a Monte Carlo program to calculate the energy spectrum and yield of the Auger electrons and fluorescent x-rays associated with the $^{157}Gd(n,\gamma)$ reaction. The program is based on the atomic subshell and relaxation data of ^{158}Gd obtained from the Evaluated Atomic Data Library

Table 1
The Energy Spectrum of the IC Electrons Associated with the $^{157}Gd(n, \gamma)$ Reaction

Energy (keV)	Frequency (electrons/capture)
180.0	0.004
173.6	0.015
131.5	0.041
77.7	0.088
72.3	0.179
71.6	0.163
71.2	0.018
29.2	0.217
Total	0.725

(EADL) developed at Lawrence Livermore National Laboratory (8). Figure 1 shows the flow diagram of the program. The program starts with an isolated ^{158}Gd atom which has undergone an IC event. The program randomly selects which shell the conversion electron originates from based on the internal conversion probabilities given by Greenwood (9). The program then randomly selects a transition based on the initial vacancy. The transition may be radiative or nonradiative. If the transition is radiative, then the photon energy is written to a file and the vacancy left by the "filler" electron becomes the basis for the next transition. If the transition is nonradiative, then the Auger electron energy is written to a file and the vacancy left by the "filler" electron becomes the basis for the next transition while the vacancy left by the Auger electron is stored to become the vacancy of interest later. Each time an electron fills a vacancy or is emitted, the number of electrons in the corresponding shell is decreased. The program determines if a transition is allowed by checking the number of electrons left in the filling shell and the emitted shell. If no electron exist in either one of these shells, then the transition is forbidden and the atomic data are adjusted to exclude it. The program will keep filling vacancies and storing the new ones until no more transitions are allowed. Any energy left over is assumed to be local and is written to a file. Once one event is finished, the input data is initialized and the process begins again. The program terminates when the required number of events is reached. The output consists of three files, one each for electron energy, photon energy, and local energy deposition. A second program then reads the energy data, bins it and calculates the yield.

Dose Calculation

Because the charged particles of the three major dose contributors have ranges comparable to cellular dimensions and because ^{10}B and Gd atoms are not uniformly distributed in a cell, the spatial distribution of energy deposition in the cell is nonuniform. To make biologically meaningful calculations, one must choose a biological target. We chose the cell nucleus as the target in this study. Because energy deposition at subcellular level is stochastic by nature, one must first calculate the specific-energy distribution - f(z), and then obtain the absorbed dose (D) by

$$D = \int z\, f(z) dz. \qquad (1)$$

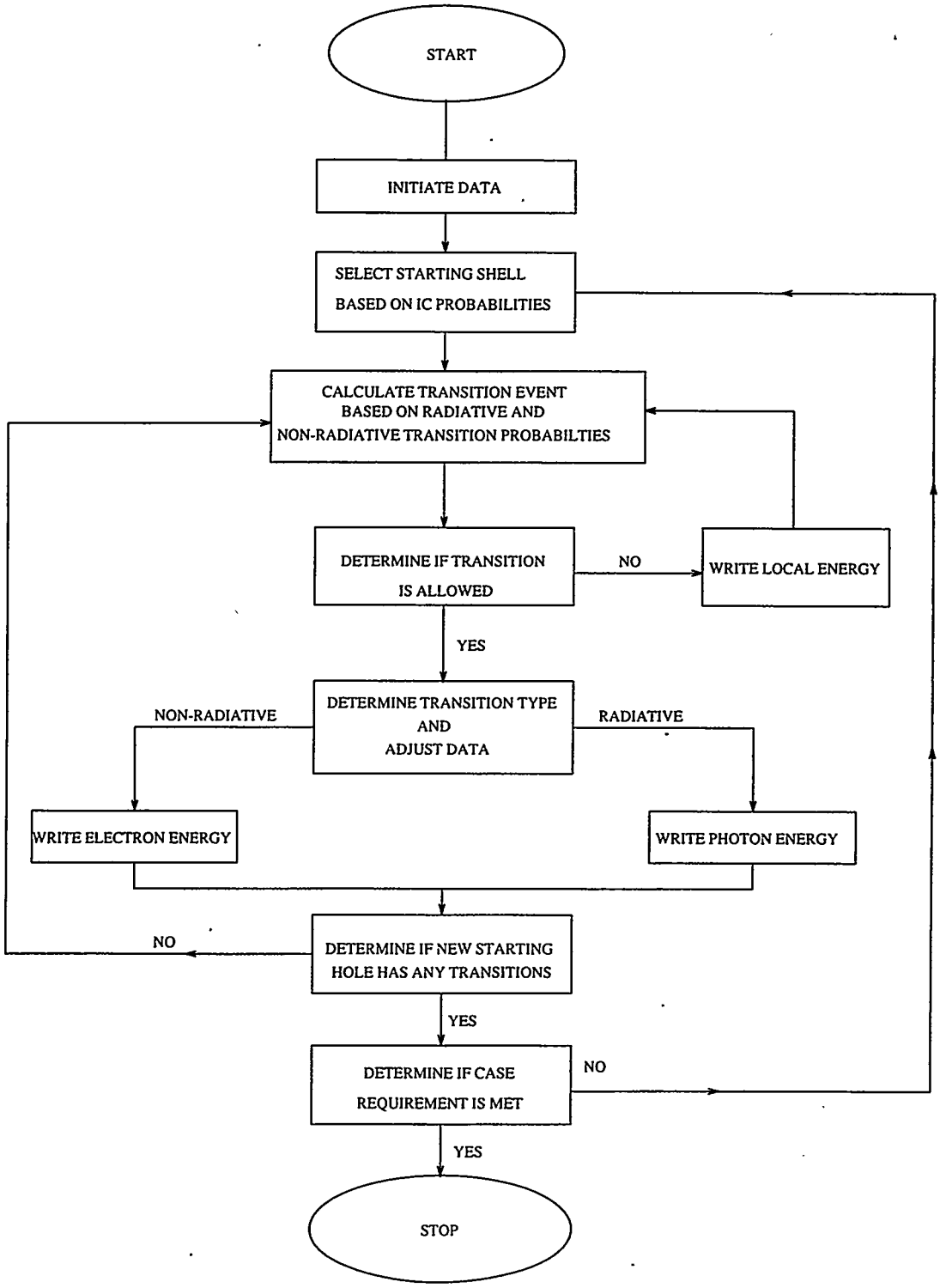

Figure 1. The flowchart of Monte Carlo calculations for Auger emissions associated with the $^{157}Gd(n, \gamma)$ reaction.

We have written a Monte Carlo program to calculate f(z) among the cell nuclei resulting from the three major dose contributors. The following assumptions were made in the program: 1) a biological cell and its nucleus are concentric spheres with diameters of 13.0 mm and 7.6 mm, respectively; 2) the

^{10}B atoms are uniformly distributed in cell cytoplasm, and no ^{10}B atom exists in cell nuclei; 3) the energy deposited by the ^{4}He and ^{7}Li ions from a $^{10}B(n,\alpha)^{7}Li$ reaction can be calculated by the continuous-slowing-down approximation (CSDA); 4) the gadolinium atoms are uniformly distributed inside cell nuclei, and no gadolinium exists in cell cytoplasm; and 5) the energy deposited by the IC and Auger electrons from a $^{157}Gd(n,\gamma)$ reaction can also be calculated by the CSDA.

Assumption 1) was made to be consistent with a similar calculation performed by Gabel (10), and it is valid especially for cells suspended in solution. Assumptions 2) and 4) were based on the measured results obtained by Laster of BNL (5). Assumption 3) is valid because the ranges of delta rays along the heavy ion tracks are significantly smaller than the target volume. Assumption 5) is not totally valid for Auger electrons with ranges comparable to the target volume. These electrons, however, contribute only a very small fraction to the total dose received by a target nucleus, and this assumption therefore should introduce little error to the result.

Figure 2 is a qualitative description of how energies are deposited in a cell nucleus. As shown, the tracks of ^{4}He and ^{7}Li ions from a $^{10}B(n,\alpha)^{7}Li$ reaction often miss the nucleus entirely. But when they do hit the nucleus, the energy deposition in the nucleus is usually quite large. Since the IC and Auger electrons from the $^{157}Gd(n,\gamma)$ reaction are all originated in the cell nucleus, they will always deposit some of their energies in the nucleus. Because the IC electrons are more energetic and they usually deposit a small fraction of their energies in the nucleus. The Auger electrons are less energetic, and they usually deposit most of their energies in the nucleus.

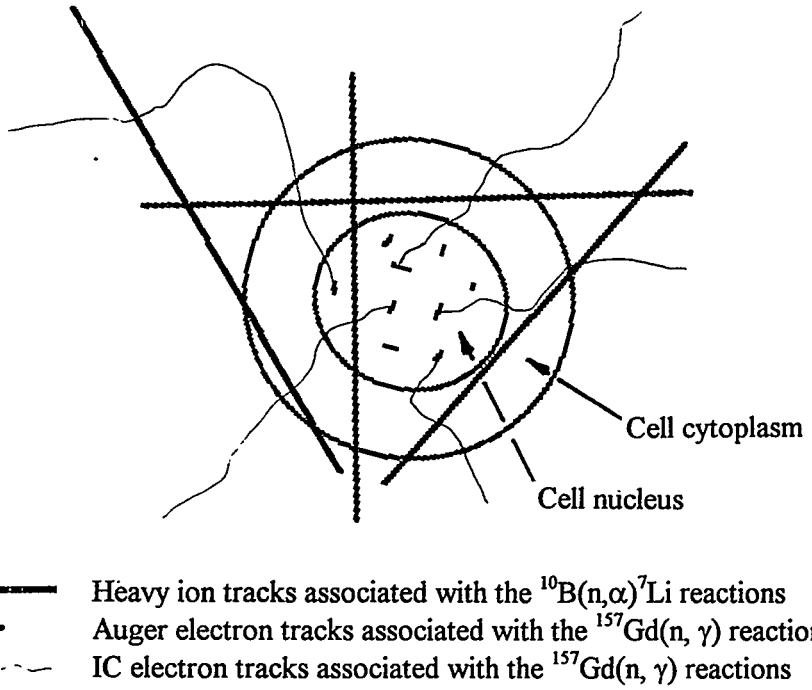

Figure 2. Description of how energies are deposited at subcellular level by the $^{10}B(n,\alpha)^{7}Li$ and $^{157}Gd(n, \gamma)$ reactions.

The frequency distributions of f(z) for the three major dose contributors were calculated based on a specified thermal neutron fluence. The neutron fluence was then converted to the mean number of neutron capture reactions in a cell based on the measured ^{10}B and gadolinium concentrations, which respectively are $3.6x10^{18}$ and $3.3x10^{18}$ atoms/gm of cells. For example, for the thermal neutron fluence of $1.0x10^{12}$ neutrons/cm^2 the corresponding mean number of reactions per cell are 15.9 for the $^{10}B(n,\alpha)^{7}Li$ reaction and 175.5 for the $^{157}Gd(n,\gamma)$ reaction. To obtain f(z), the Monte Carlo procedure

first obtains the number of reactions (N_i) of cell I according to the Poisson distribution. It then picks a direction of the charged particles and calculates the energy imparted (ϵ_{ij}) for reaction j in cell I using the CSDA previously discussed. The z_i is then obtained by

$$z_i = \frac{1}{m} \sum_{j=0}^{N_i} \epsilon_{ij}. \quad (2)$$

After a large number of cells have been processed, the data for z_i are then binned to obtain f(z).

RESULTS and DISCUSSION

Figure 3a shows the calculated Auger spectrum for the ^{157}Gd(n, γ) reaction. The total yield and energy of the Auger electrons per ^{157}Gd(n, γ) reaction are 6.7 electrons and 4.8 keV, respectively. Figure 3b shows the expanded Auger spectrum for electron energies between 0 and 1 keV. These low-energy electrons are high-LET, and if localized in the vicinity of the DNA molecule, may be responsible for the dramatic enhancement of cell killing in the BNL experiment. According to Fig. 3b, the total energy associated with the high-LET Auger electrons per ^{157}Gd(n, γ) reaction only amounts to ~1.4 keV.

Figure 4a shows the distribution of f(z)dz of the cell nucleus resulted from the ^{10}B(n,α)^{7}Li reactions uniformly occurred in the cell cytoplasm. Figures 4b and 4c show the distributions of f(z)dz of the cell nucleus resulted from the IC and Auger electrons, respectively. The IC and Auger electrons are associated with the ^{157}Gd(n, γ) reactions occurred uniformly inside the cell nucleus. All three figures correspond to the thermal neutron fluence of 1.0×10^{12} neutrons/cm^2. As indicated, the mean specific energy (or the average dose) in cell nucleus due to the ^{10}B(n,α)^{7}Li reactions is the largest. However, there is a noticeable probability that the specific energy (z) is very small (or even zero). On the other hand, the mean specific energy in cell nucleus due to the Auger electrons associated with the ^{157}Gd(n, γ) reactions is significantly smaller. But the f(z)dz is much more narrowly distributed among cell nuclei, and therefore all cell nuclei have almost the same specific energy. The distribution of f(z)dz in cell nucleus due to the IC electrons are similar to that due to Auger electrons, but the mean specific energy is a factor of five smaller. According to these results, one may then express the cell survival fraction by

$$S = \int_0^\infty s(z)\, f(z)dz, \quad (3)$$

where s(z) is the survival probability of a cell receiving a specific energy z (11), and its form was suggested to be

$$s(z) = e^{-kz^2}, \quad (4)$$

k is a constant. That is, s(z) is near 1.0 for small values of z and approaches 0.0 for large values of z. Equations 3 and 4 together indicate that the ^{10}B(n,α)^{7}Li reactions alone may overkill many cells, and at the same time allow many cells to survive. The IC and Auger electrons from the ^{157}Gd(n, γ) reactions, however, are received by all cells much more equally. On this basis, the survival curve of cells irradiated by the ^{157}Gd(n, γ) reactions alone should display a drastic change in slope as thermal neutron fluence increases. The slope should be quite flat at low neutron fluences, but then drastically sharpens as neutron fluence exceeds a certain threshold. The change of slope in the survival curve

may be experimentally verified by using cells treated with Gd-^{11}BOPP, in which the ^{157}Gd(n, γ) reactions are solely responsible for the cell death. It will be of paramount interest to find out the threshold thermal neutron fluence. If this threshold neutron fluence is found to be less than that nominally used for BNCT (~5.0×10^{12} neutrons/cm^2), then one may claim that GdNCT itself could be more effective than BNCT and that there is no need to involve ^{10}B-enriched compound in a GdNCT. The ^{10}B(n,α)^{7}Li reactions will do nothing but overkilling those cells which will be killed by the ^{157}Gd(n, γ) reactions alone.

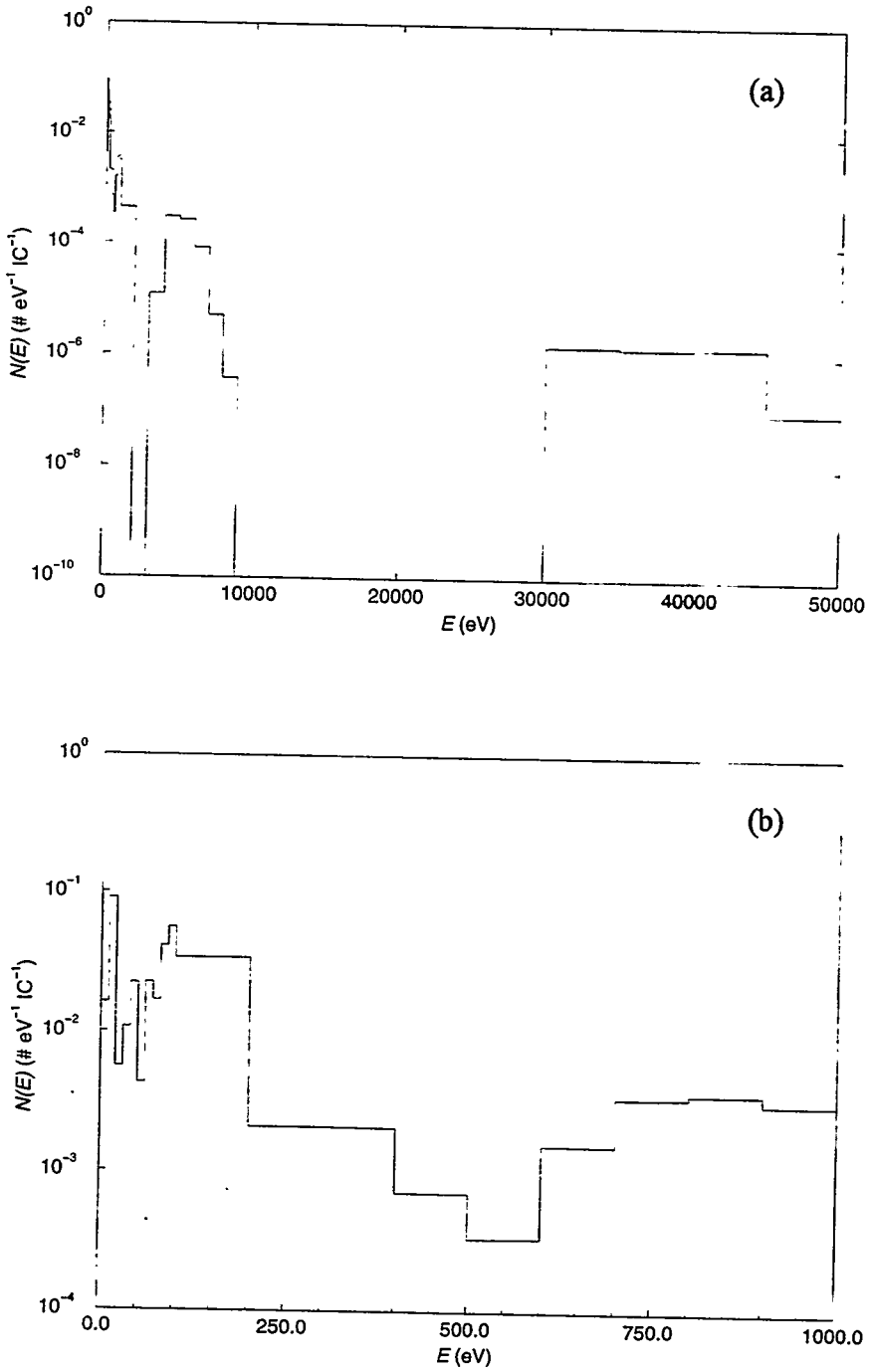

Figure 3. (a) The calculated spectrum of Auger electrons associated with the ^{157}Gd (n, γ) reaction. (b) The expanded spectrum of (a) in the energy range of 0-1 keV.

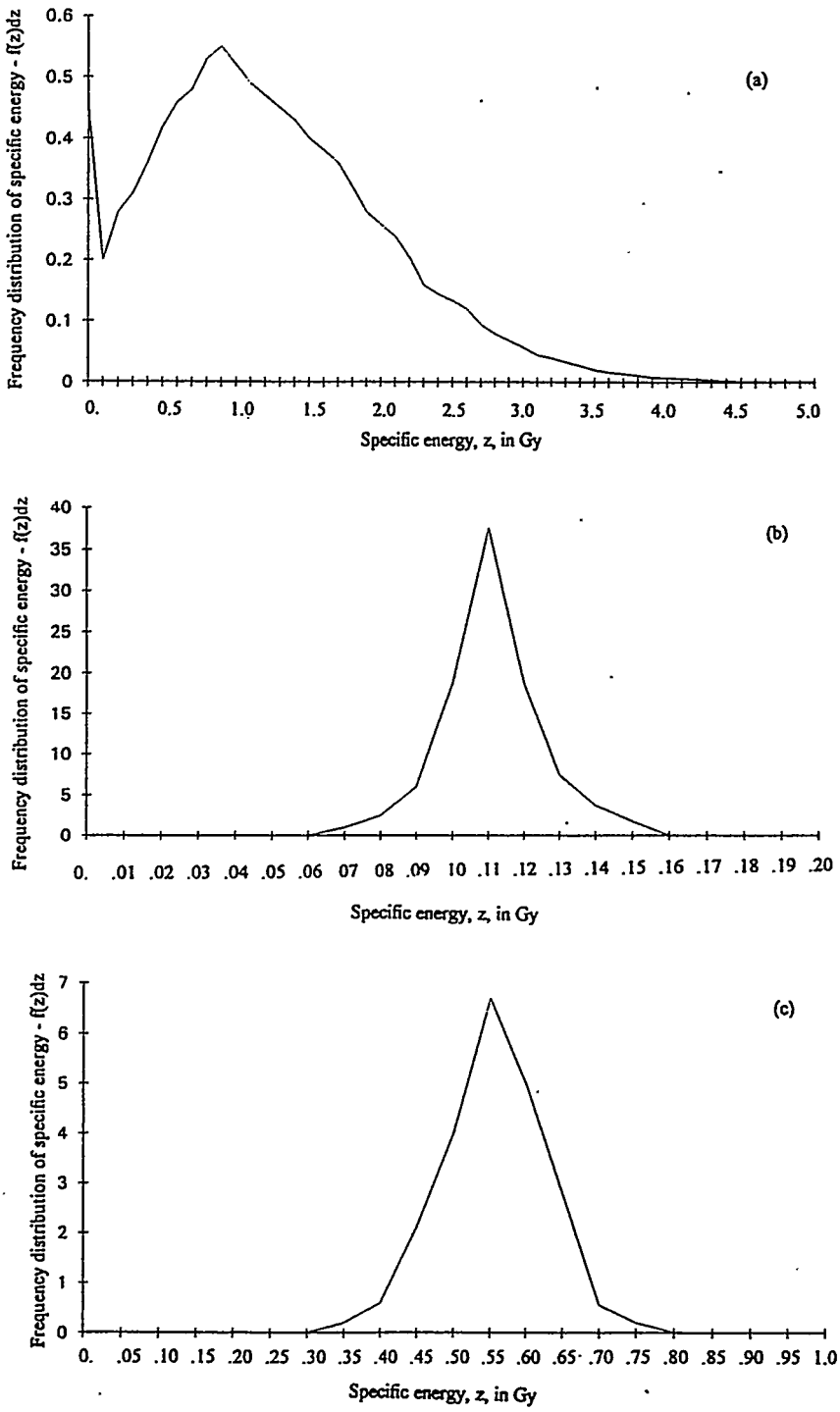

Figure 4. The frequency distribution of specific energy - f(z)dz of the cell nucleus resulted from: (a) the $^{10}B(n,\alpha)^{7}Li$ reactions uniformly occurred in the cell cytoplasm, (b) the IC electrons associated with the $^{157}Gd(n, \gamma)$ reactions occurred uniformly inside the cell nucleus, and c) the Auger electrons associated with the $^{157}Gd(n, \gamma)$ reactions occurred uniformly inside the cell nucleus.

REFERENCES

1. Martin RF, d'Cunha G, Pardee M and Allen BJ. Induction of double-strand breaks following neutron capture by DNA-bond Gd-157. Int J Radiat Biol 54:205-208, 1988.
2. Shih JA and Brugger RM. Gadolinium as a neutron capture therapy agent. Med Phys 19(3):733-744, 1992.
3. Masiakowski JT, Horton JL and Peters LJ. Gadolinium neutron capture therapy for brain tumors: A computer study. Med Phys 19(5):1277-1284, 1992.
4. Miller GA, Hertel NE, Wehring BW and Horton JL. Gadolinium neutron capture therapy. Nucl Technol 103: 320-331, 1993.
5. Laster BH, Shani G, Kahl SB and Warkentien L. The biological effects of Auger electrons compared to α-particles and Li ions. Abstract of an oral presentation at the 1995 International Symposium on Auger Electrons.
6. Groshev LV et. al. Compendium of thermal neutron capture gamma ray measurements. Nucl Data Tables A5:155-180, 1968.
7. Knoll GF. Radiation Detection and Measurement, 2nd edition, p 483, John Wiley & Sons, Inc., 1989.
8. Perkins ST, Cullen DE, Chen MH, Hubbell JH, Rathkopf J and Scofield J. Tables and Graphs of Atomic Subshell and Relaxation Data Derived from the LLNL Evaluated Atomic Data Library (EADL), Z=1-100. Lawrence Livermore National Laboratory Report UCRL-50400 Vol 30, 1991.
9. Greenwood RC et. al. Collective and Two-Quasiparticle States in ^{158}Gd Observed Through Study of Radiative Neutron Capture in ^{157}Gd. Nucl Phys A304: 327-428, 1978.
10. Gabel D, Foster S and Fairchild RG. The Monte Carlo simulation of the biological effect of the $^{10}B(n,\alpha)^{7}Li$ reaction in cells and tissue and its implication for boron neutron capture therapy. Radiat Res 111:14-25, 1987.
11. Zaider M and Rossi HH. Microdosimetry and its application to biological processes, in Radiation Dosimetry: Physical and Biological Aspects, edited by Orton, pp 220-222, CG. Plenum Press, New York, 1986.

EFFECT OF LABELING ISOTOPE ON MONOCLONAL ANTIBODY DOSIMETRY IN NUDE MICE CARRYING HUMAN TUMOR XENOGRAFTS

Kwok CS[1], Li J[2], Maharajh R[2], Gyorffy S[2], Alexandrakis G[2], Lee S[2], Tinkl M[3], Snieckus V[3], Somayaji VV[4], Noujaim AA[4] and Skyes T[4]
[1]Dept. Of Optometry and Radiography
The Hong Kong Polytechnic University
Hung Hom, Kowloon, Hong Kong
[2]Hamilton Regional Cancer Centre
699 Concession St., Hamilton, Ontario, Canada L8V 5C2
[3]Dept. of Chemistry, University of Waterloo
Waterloo, Ontario, Canada N2L 3G1
[4]AltaRex Inc.
1134 Dentistry-Pharmacy Bldg., University of Alberta
Edmonton, Alberta, Canada T6G 2N8

ABSTRACT

Three different methods of radiolabeling the murine monoclonal antibody B43 for targeting human ovarian tumors in nude mice have been carried out. The methods included iodination with ^{131}I in the presence of Iodogen, direct labeling with ^{188}Re, and macrocyclic conjugation with ^{57}Co. The distribution of the three forms of radiolabeled B43 in the same animal model has been compared directly. Differences in the uptake of the three B43 radiolabelings in bone, bone marrow, liver, thyroid, and tumor have been observed. Assuming that the biodistribution of the radiolabeled B43 in mice applies to humans, the MIRD method was used to calculate radiation doses to several organs/tissues and one-gram size tumors in humans not only for ^{131}I, ^{188}Re, and ^{57}Co, but also for ^{186}Re, ^{64}Cu, ^{67}Cu and ^{90}Y. The macrocycle used for ^{57}Co also binds the last 3 isotopes very strongly. The ratio of radiation dose to the tumor and to the bone marrow was lowest for ^{188}Re and highest for ^{186}Re. This illustrates the importance of considering both the physical properties of the labeling isotope and the biological properties of the radiolabeled antibody in successful radioimmunotherapy.

INTRODUCTION

Since the reporting of encouraging data on radioimmunodetection of tumors in animals and humans in the early 1980s, there has been intense interest in the possibility of treating neoplasms with radiolabeled monoclonal antibodies (MAbs). A broad spectrum of problems associated with this new treatment modality was identified shortly after a few initial clinical trials. Limitations posed by physical, chemical, biological and immunological factors must be overcome before radioimmunotherapy (RIT) can be accepted into full clinical practice (1). Physical factors include

physical properties of the labeling nuclides and transport of the labeled MAbs through the vasculature and interstitium of normal tissues and tumors. Combining the physical properties of selected radionuclides and biodistribution data for antibody uptake and clearance in humans available before 1984, Wessels and Rogus (2) performed absorbed dose calculations for tumor associated antibodies labeled with nine radionuclides. They concluded that ^{186}Re and ^{90}Y are among the best therapy radiolabels provided they form stable compounds with an antibody system. Subsequent advances in the development of bifunctional chelating agents and linker chemistry for coupling these agents to antibodies have facilitated direct comparison of radioiodinated MAbs and MAbs labeled with such metallic ions as ^{67}Cu, ^{90}Y and ^{111}In (3-6). Longer retention of the metallic ions than radioiodine by tumor cells was usually observed and was not only due to deiodination of the radioiodinated MAbs, but also due to intracellular retention of catabolic products containing the metallic ions. This paper reports on the direct comparison of a murine MAb B43 labeled with three currently available methods in targeting human ovarian tumors in nude mice. The methods included radioiodination, direct labeling with ^{188}Re, and macrocyclic conjugation with a metallic ion. The importance of considering both the physical properties of the labeling isotope and the biological properties of the radiolabeled MAb in successful RIT will be illustrated.

MATERIALS AND METHODS

Preparation of B43-2IT-BAT-^{57}Co

B43 is a murine IgG_1 type MAb raised against the CA125 antigen, expressed in about 80% of human ovarian cancers. Macrocycle 6-p-aminobenzyl-1,4,8,11-tetraazacyclotetradecane-N,N',N'',N''' tetraacetate (TETA) was synthesized according to the procedure of Moreau and coworkers (7), which was an improved method of that used by Moi et al. (8). p-Bromoacetamidobenzyl-TETA (BAT) was prepared from TETA according to the method of McCall et al. (9) with the following exceptions: a) TETA concentrations were lowered to 0.5 mM; b) bromoacetylation was conveniently carried out in a 60-mL separatory funnel to accommodate the larger volumes, with intimate mixing of the phases ensured through vigorous, intermittent shaking and; c) extracted aqueous layers and HPLC purified fractions were titrated to pH 1.5-2.0 with 1.0% trifluoroacetic acid prior to concentration. Chelator concentrations were determined using the ^{57}Co thin-layer chromatography (TLC) radioassay of Meares and coworkers (10).

We have successfully optimized the reaction conditions developed from over seven human IgG conjugation trials to prepare a B43-BAT conjugate using 2-iminothiolane (2-IT) as a linker arm. In a typical, optimized experiment, solutions of purified BAT and 2-IT were immediately mixed with B43 to afford final concentrations of 2.0, 0.5 and 0.05 mM, respectively in 0.1 M sodium phosphate at pH 8.3. After 30 minutes at 37 °C, the reaction was fractionated according to molecular weight by size-exclusion (SEC) HPLC. The monomeric IgG fraction was collected and concentrated using a passivated Centricon-30 (30 KD cut-off) ultrafiltration concentrator. Retentate characterization via ^{57}Co radiolabeling and calibration curve-based quantitation of protein concentrations using SEC-HPLC revealed a conjugation efficiency of 1.7 BAT chelators/IgG and a high chemical yield. SEC-HPLC and SDS-PAGE analyses of the reaction mixture showed that >95.7% of the conjugate was IgG monomer with <4.3% being due to higher molecular-weight aggregates. The immunoreactivity of the conjugate was about 87% of that of the native B43.

Six radiolabeling experiments were conducted from pH 7.3 to 8.3 to determine the conditions for optimal radiolabeling and radioconjugate yields. Using a 1:1 ratio of total cobalt (cold and hot) to total chelators available for metal-binding, radiolabeling efficiencies in excess of 90% were routinely achieved, provided that the BAT chelator concentration was greater that 10 μM. Increasing the pH

over this range did not significantly increase the labeling efficiency. Moreover, varying the incubation times of the labeling reactions from the typical 30 minutes to 120 minutes at room temperature also yielded a negligible effect. Under equivalent, carrier-free conditions, however, ^{57}Co labeling yields of only 18% could be attained. This markedly lower yield noted for carrier-free labeling was rationalized in terms of the significant amount of metallic impurities (namely Ni^{2+}) in the $^{57}Co^{2+}$ stock (supplied by Nordion International). We have found that labeling yields can be increased to >94% provided that the molar ratio of conjugate to carrier-free ^{57}Co is at least six.

Preparation of ^{131}I-B43

Radioiodination was performed by the Iodogen method (11). ^{131}I labeling efficiency was measured by the TLC assay method and found to exceed 95%. Protein recovery was determined to be greater than 94% based on radioactivity measurements.

Preparation of ^{188}Re-B43

Photoactivated B43 was labeled with generator produced ^{188}Re according to a direct labeling procedure similar to that developed by Sykes et al. (12). A 72% radiolabeling efficiency and a 59% protein yield were obtained with the TLC method using saline as the developing solvent and calibration curve analysis of protein concentrations.

Biodistribution of B43-2IT-BAT-^{57}Co and ^{131}I-B43 in Nude Mice

Human ovarian carcinoma cells OVCAR were implanted subcutaneously into the thighs of adult nude mice until a size of about 5 mm diameter was reached. Approximately 0.74 MBq of ^{57}Co-B43-2IT-BAT (10 μg in mass and 50 μl in volume), 1.48 MBq of ^{131}I-B43 (10 μg in mass and 50 μl in volume) were coinjected into a tail vein of 24 nude mice. Groups of 3 mice were killed by cervical dislocation 1h, 4h, 8h, 12h, 1 day, 2 days, 4 days and 6 days post radiolabeled B43 injection. Blood, long bones, kidneys, livers, lungs, muscle, spleen, thyroid, tumors, and urine were collected from each animal. The ends of the long bones were clipped away and the marrow chased out using a 31 gauge needle. All the tissue samples were weighed and counted in a gamma well together with standards of the injected radioactivity. Percent uptake of the injected activity of the two radiolabeled B43 MAbs per gram of organ/tissue was calculated for each of the sampling times.

Biodistribution of ^{188}Re B43 in Nude Mice

The protocol for this experiment was similar to that for ^{131}I-B43 except for (a) ^{51}Cr-chromate was used to label mouse red blood cells in vitro and about 0.15 MBq was injected into each mouse; (b) 5.9 MBq ^{188}Re-B43 in 80 μg was injected into each mouse; © cohorts of mice were killed 1h, 4h, 8h, 1 day, 2 days and 3 days postinjection of the radioactivity.

Calculation of Radiation Doses

MIRDOSE (V 3.0) was used to calculate the radiation doses to different organs/tissues in an adult human bearing one-gram size tumors, assuming similar biodistribution of radiolabeled B43 as for mice. For the dose to the red marrow, two methods for calculating the residence time of the radiolabeled B43 were used. The first method involved the direct integration with time of the activity curve for the marrow. The second method assumed an uptake ratio of the antibody in red marrow to whole blood to be 0.38 and therefore the residence time of the radiolabeled B43 in red marrow was 38 % of that for whole blood.

RESULTS

Table 1 gives the mean and standard deviation values of the % injected dose of ^{57}Co-labeled B43 per gram of red blood cells (RBC), plasma, bone devoid of marrow, bone marrow, kidney, liver, lung, muscle, spleen, thyroid, tumor, and urine of nude mice bearing human OVCAR tumors at various times post i.v. injection of the radiolabeled B43. Uptake curves derived from the data in the table, as illustrated by Figures 1-6, could be fitted well by either single exponential functions or biexponential functions of time. The only exception is the tumor uptake curve, which is practically sigmoidal in shape. The biodistribution results for ^{131}I-labeled B43 and ^{188}Re-labeled B43 are given in Tables 2 and 3, respectively. The uptake curves of ^{131}I-, ^{188}Re- and Co-57-labeled B43 in plasma, bone and bone marrow of nude mice are shown in Figures 1-3. The uptake curves of ^{131}I-labeled B43 and ^{188}Re-labeled B43 in spleen, thyroid and tumor are shown in Figures 4-6.

Treating ^{131}I-labeled B43 as a comparison "standard", ^{57}Co-labeled B43 showed significantly greater uptake in plasma during the period 8 to 24 hours post injection ($P<0.05$). ^{57}Co-labeled B43 also had significantly greater uptakes in liver and tumors than ^{131}I-labeled B43 at most of the sampling time points. On the other hand, ^{188}Re-labeled B43 had significantly lower uptakes in spleen, thyroid and tumors than ^{131}I-labeled B43 in the early time points. Despite these differences, all three forms of radiolabeled B43 had uptakes in the bone marrow approximately 38% of those in whole blood for all the sampling time points. Uptakes of the three forms of radiolabeled B43 in tumors exceeded those in plasma after 24 hours.

Assuming that the biodistributions of the three forms of radiolabeled B43 in mice apply to humans who bear only one-gram size tumors, MIRDOSE (V 3.0) was used to calculate radiation doses to blood, kidneys, liver, lungs, red marrow, spleen, thyroid, tumors, ovaries and testes delivered by 1 MBq of the radiolabeled B43 (Table 4). The last two organs were assumed to have negligible uptakes of the antibody. Since the macrocyclic approach of chelating cobalt to antibodies also applies to ^{64}Cu, ^{67}Cu, and ^{90}Y (8, 10), and ^{186}Re has the same chemistry as ^{188}Re, radiation doses delivered by 1 MBq of these labeling radionuclides were also calculated and presented in Table 4. Of special interest to RIT is the tumor to red marrow radiation dose ratio. Its value is highest for ^{186}Re-labeled B43 and lowest for ^{188}Re-labeled B43. ^{186}Re-labeled B43 has a dose ratio almost three times as large as that for ^{131}I-labeled B43. It is also worth mentioning that the dose to the red marrow calculated by assuming its uptake of the radiolabeled antibody relative to whole blood was equal to 0.38 was within 50% of the radiation dose calculated using the residence time of the antibody in the red marrow.

CONCLUSIONS

The objective of the present study was to illustrate the importance of considering both the physical properties of the labeling nuclide and the biological properties of radiolabeled antibodies in successful RIT. Only one-gram size tumors in a nude mouse model and three different groups of radionuclides dictated by their respective methods of labeling were considered. The labeling methods included iodination with ^{131}I in the presence of Iodogen, direct labeling with ^{188}Re, and macrocyclic conjugation with ^{57}Co. ^{57}Co-labeled B43 via a macrocyclic chelator TETA had the highest percent injected dose uptake per gram of tumor among the three forms of radiolabeled B43. The same form of labeled B43 also had the highest uptake in the liver. ^{131}I-labeled B43 had the highest uptake in the thyroid at early time points. Combined with the physical properties of the radiolabeling isotope, ^{186}Re-labeled B43 would give the highest tumor to red marrow radiation dose ratio D_R, whereas ^{188}Re-labeled B43 would give the lowest ratio. This conclusion only holds if the specific radioactivity of the ^{186}Re-labeled antibody is sufficiently high so that its pharmacokinetics are not significantly different

Table 1

Biodistribution of ^{57}Co-labeled B43 in Nude Mice Bearing Human OVCAR Ovarian Tumor

Co-57 Labeled B43 Uptake (% injected dose/gram) in Mice																								
Time Post Injection(hours)	1			4			8			12			24			48			96			144		
ORGANS	MEAN	S.D.	n	MEAN	S.D.	n	MEAN	S.D.	n	MEAN	S.D.	n	MEAN	S.D.	n	MEAN	S.D.	n	MEAN	S.D.	n	MEAN	S.D.	n
RBC	10.38	13.75	2	5.23	6.32	2	1.67	1.81	2	2.73	0.87	3	1.35	0.34	3	0.89	0.14	3	0.42	0.18	3	0.28	0.29	3
PLASMA	15.54	3.67	3	15.59	5.07	3	#14.02	0.75	3	#10.90	0.80	3	#6.84	0.30	3	4.06	1.62	3	1.76	0.81	3	1.02	0.69	3
BONE	#0.72	0.16	3	#0.55	0.19	3	#0.89	0.27	3	1.05	0.36	3	1.18	0.60	3	0.65	0.12	3	0.46	0.07	3	0.34	0.10	3
BONE MARROW	1.09	0.89	3	0.47	0.67	2	1.37	0.86	3	1.55	0.62	3	2.67	0.35	3	1.31	0.58	3	1.09	0.42	3	0.73	0.48	3
KIDNEY	13.60	2.11	3	6.10	2.46	3	5.78	1.57	3	3.74	0.96	3	3.20	0.61	3	1.62	0.23	3	1.47	0.41	3	1.17	0.65	3
LIVER	#9.03	1.40	3	10.69	4.05	3	#11.41	3.32	3	7.83	4.24	3	#6.17	1.06	3	#2.45	0.66	3	#2.64	0.51	3	#1.85	0.40	3
LUNG	11.65	6.73	3	4.36	1.10	3	4.08	0.45	2	6.56	1.42	3	3.96	1.26	3	2.33	0.23	3	1.72	0.94	3	1.24	0.56	3
MUSCLE	0.29	0.11	3	0.24	0.22	3	0.63	0.14	3	0.59	0.08	3	1.18	0.52	3	0.38	0.03	3	0.32	0.20	3	0.20	0.15	3
SPLEEN	3.06	2.65	3	2.43	3.81	3	2.84	1.17	3	2.22	0.58	3	1.83	0.35	3	1.33	0.22	3	0.89	0.26	3	0.68	0.47	3
THYROID	2.30	1.40	3	#1.83	0.45	3	2.90	1.06	3	3.16	0.55	3	2.63	0.78	3	1.28	0.24	3	1.69	1.07	3	0.84	0.61	3
TUMORS	#1.21	0.73	6	2.43	1.33	6	4.83	1.52	6	#5.25	0.97	6	#7.36	2.69	6	#6.64	1.89	6	5.83	2.80	6	4.06	1.49	6
URINE	N.A.	N.A.	N.A.	4.90	4.69	3	4.76	6.73	2	8.81	6.03	3	3.94	1.73	2	6.66	0.79	3	5.13	1.32	3	2.27	0.89	3

N.A. = Not Available

Values significantly different from uptakes of I-131 labeled B43 at $p < 0.05$

Table 2

Biodistribution of ^{131}I-labeled B43 in Nude Mice Bearing Human OVCAR Ovarian Tumor

I-131 Labeled B43 Uptake (% injected dose/gram) in Mice																							
Time Post Injection(hours)	1			4			8			12			24			48			96			144		
ORGANS	MEAN	S.D.	n	MEAN	S.D.	n	MEAN	S.D.	n	MEAN	S.D.	n	MEAN	S.D.	n	MEAN	S.D.	n	MEAN	S.D.	n	MEAN	S.D.	n
RBC	1.87	0.69	3	1.98	0.80	3	1.03	0.08	3	2.01	0.95	3	1.44	0.23	3	0.65	0.04	3	0.45	0.10	3	0.36	0.21	3
PLASMA	13.15	1.25	3	13.08	3.52	3	10.78	1.12	3	7.57	0.91	3	5.59	0.59	3	2.78	0.99	3	1.84	0.04	3	1.27	0.22	3
BONE	2.20	0.66	3	2.12	0.37	3	1.70	0.26	3	1.15	0.27	3	1.26	0.43	3	0.54	0.04	3	0.38	0.02	3	0.30	0.10	3
BONE MARROW	4.67	4.04	3	4.38	2.01	2	3.99	0.26	3	2.10	1.00	3	3.19	0.47	3	1.34	0.57	3	1.26	0.35	3	0.80	0.39	3
KIDNEY	7.05	0.73	3	5.43	0.86	3	5.34	0.99	3	3.45	0.46	3	2.89	0.84	3	1.27	0.18	3	1.04	0.29	3	0.86	0.37	3
LIVER	5.05	0.80	3	5.24	0.43	3	5.19	1.25	3	3.77	1.18	3	3.09	0.77	3	1.23	0.19	3	0.92	0.24	3	0.69	0.22	3
LUNG	13.33	6.12	3	7.49	1.97	3	5.56	0.94	2	5.54	1.45	3	4.30	1.18	3	1.92	0.15	3	1.36	0.33	3	1.16	0.56	3
MUSCLE	1.09	0.84	3	1.28	0.90	3	0.81	0.14	3	0.54	0.06	3	1.26	0.53	3	0.34	0.01	3	0.29	0.08	3	0.22	0.09	3
SPLEEN	6.96	4.48	3	4.90	0.90	3	5.22	1.48	3	3.45	0.83	3	3.20	0.73	3	1.41	0.14	3	0.73	0.20	3	0.75	0.33	3
THYROID	8.13	5.18	3	10.14	4.19	3	5.49	1.27	3	3.06	0.71	3	3.30	1.04	3	1.28	0.20	3	1.31	0.49	3	0.70	0.45	3
TUMORS	2.49	0.86	6	3.79	0.80	6	4.37	1.24	6	3.73	0.39	6	4.55	1.35	6	3.69	0.86	6	3.32	1.07	6	2.27	0.39	6
URINE	N.A.	N.A.	N.A.	79.66	40.49	3	74.67	9.83	3	26.75	13.63	3	3.82	0.93	2	5.41	0.95	3	2.47	0.70	3	1.99	1.06	3

N.A. = Not Available

Table 3

Biodistribution of ^{188}Re-labeled B43 in Nude Mice Bearing Human OVCAR Ovarian Tumor

Re-188 Labeled B43 Uptake (% injected dose/gram) in Mice																		
Time Post Injection(hours)	1			4			8			24			48			72		
ORGANS	MEAN	S.D.	n	MEAN	S.D.	n	MEAN	S.D.	n	MEAN	S.D.	n	MEAN	S.D.	n	MEAN	S.D.	n
RBC	1.20	0.61	3	1.52	0.64	3	1.03	0.66	3	0.42	0.13	3	0.22	0.16	3	0.24	0.09	3
PLASMA	8.34	0.46	3	10.10	1.95	3	6.62	0.90	3	3.83	1.02	3	2.27	1.57	3	1.41	0.43	3
BONE	1.16	0.47	3	0.81	0.33	3	0.88	0.09	3	0.63	0.10	3	0.35	0.18	3	0.31	0.12	3
BONE MARROW	4.15	2.75	3	3.56	0.89	3	3.96	2.22	3	2.12	0.59	3	0.83	0.40	3	0.70	0.25	3
KIDNEY	4.55	1.51	3	5.26	1.02	3	5.49	0.66	3	3.78	0.45	3	1.90	0.85	3	1.54	0.34	3
LIVER	4.47	1.67	3	4.16	1.43	3	3.14	0.23	3	2.49	0.55	3	1.33	0.61	3	0.91	0.27	3
LUNG	5.16	1.44	3	4.16	1.17	3	3.49	0.15	3	2.58	0.58	3	1.30	0.83	3	1.13	0.58	3
MUSCLE	0.44	0.29	3	0.44	0.17	3	0.52	0.23	3	0.53	0.05	3	0.29	0.16	3	0.18	0.09	3
SPLEEN	3.24	1.86	3	#2.36	1.17	3	#2.14	0.35	3	#1.70	0.30	3	#0.88	0.07	3	0.74	0.25	3
THYROID	4.26	2.18	3	#2.51	0.65	3	#2.01	0.57	3	1.62	0.26	3	0.93	0.64	3	0.60	0.17	3
TUMORS	#1.12	0.52	6	#2.50	0.89	6	4.04	1.19	6	4.82	0.34	6	4.08	2.78	6	3.81	1.44	6
URINE	15.07	13.81	3	27.21	3.53	3	37.71	12.25	3	19.83	7.03	3	8.59	7.36	3	3.50	2.71	3

#Values significantly different from uptakes of I-131 labeled B43 at $p < 0.05$

Table 4
Radiation Doses to Different Human Organs and Tissues Delivered by MAb B43
Labeled with 1 MBq of Several Radionuclides of Potential Use in Radioimmunotherapy

Dose(mGy) Delivered by 1 MBq of Radiolabeled Intact B43							
Target Organs	57-Co-27	64-Cu-29	67-Cu-29	90-Y-39	131-I-53	186-Re-75	188-Re-75
Blood	7.50e+01	1.51e+02	3.76e+02	2.26e+03	5.49e+02	4.92e+02	5.82e+02
Kidneys	3.54e+01	7.26e+01	2.09e+02	1.27e+03	4.08e+02	4.40e+02	4.55e+02
Liver	6.92e+01	8.72e+01	3.00e+02	1.81e+03	3.40e+02	2.69e+02	2.83e+02
Lungs	3.80e+01	5.17e+01	1.72e+02	1.04e+03	5.32e+02	2.91e+02	3.10e+02
Ovaries	4.43e-03	1.19e-03	2.20e-03	3.26e-09	1.31e-02	3.14e-04	4.13e-04
Red Marrow	2.95e+01	3.87e+01	1.31e+02	7.90e+02	3.09e+02	2.29e+02	2.70e+02
	#2.85e+01	#5.72e+01	#1.43e+02	#8.60e+02	#2.09e+02	#1.87e+02	#2.21e+02
Spleen	2.40e+01	2.77e+01	9.88e+01	5.98e+02	3.31e+02	1.75e+02	1.92e+02
Testes	7.36e-04	2.23e-04	3.55e-04	1.71e-09	2.44e-03	4.80e-05	7.49e-05
Thyroid	2.69e+01	2.98e+01	1.07e+02	6.47e+02	4.40e+02	1.93e+02	2.07e+02
1 gm Tumor	8.47e+01	5.20e+01	3.91e+02	1.77e+03	5.85e+02	1.18e+03	3.23e+02

#Dose to red marrow by assuming its uptake of B43 relative to blood equal to 0.38

Tumor to Marrow Dose Ratio	2.87	1.35	2.99	2.24	1.89	5.5	1.20

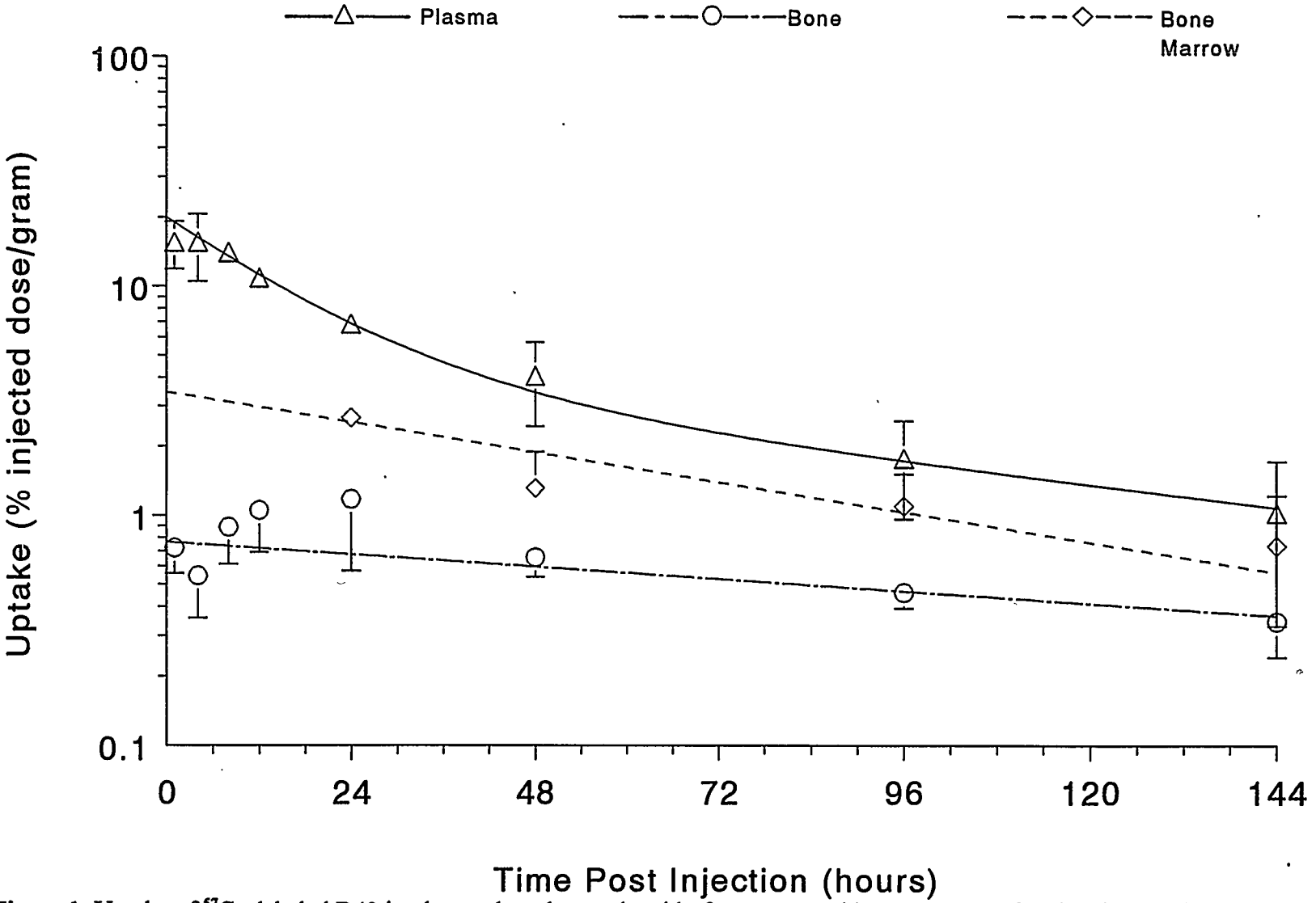

Figure 1. Uptake of ^{57}Co-labeled B43 in plasma, long bones devoid of marrow, and bone marrow of nude mice bearing human ovarian OVCAR tumors post i.v. injection of the radiolabeled antibodies. The curves are least-squares fit to the experimental data.

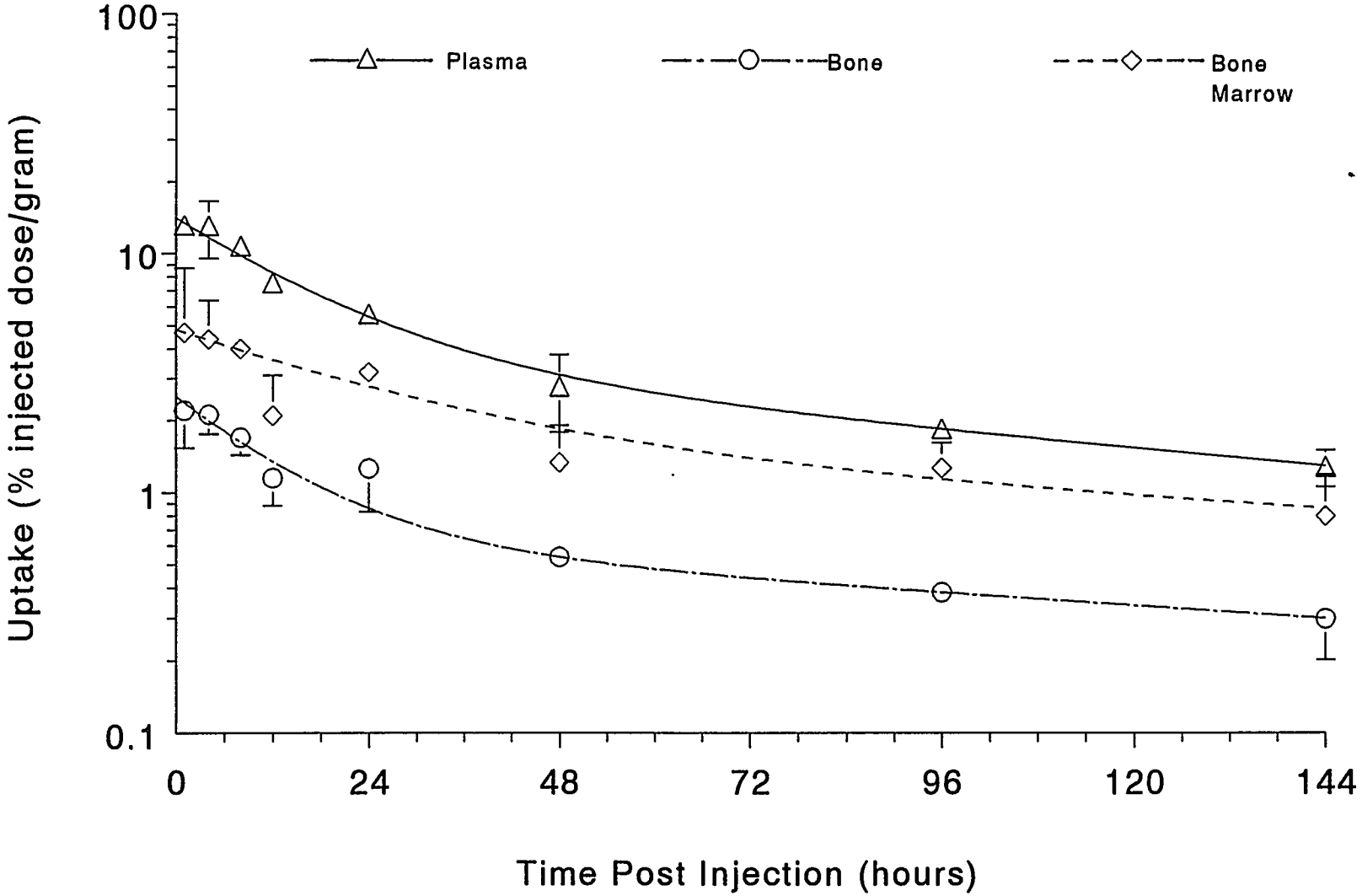

Figure 2. Uptake of ^{131}I-labeled B43 in plasma, long bones devoid of marrow, and bone marrow of nude mice bearing human ovarian OVCAR tumors post i.v. injection of the radiolabeled antibodies. The curves are least-squares fit to the experimental data.

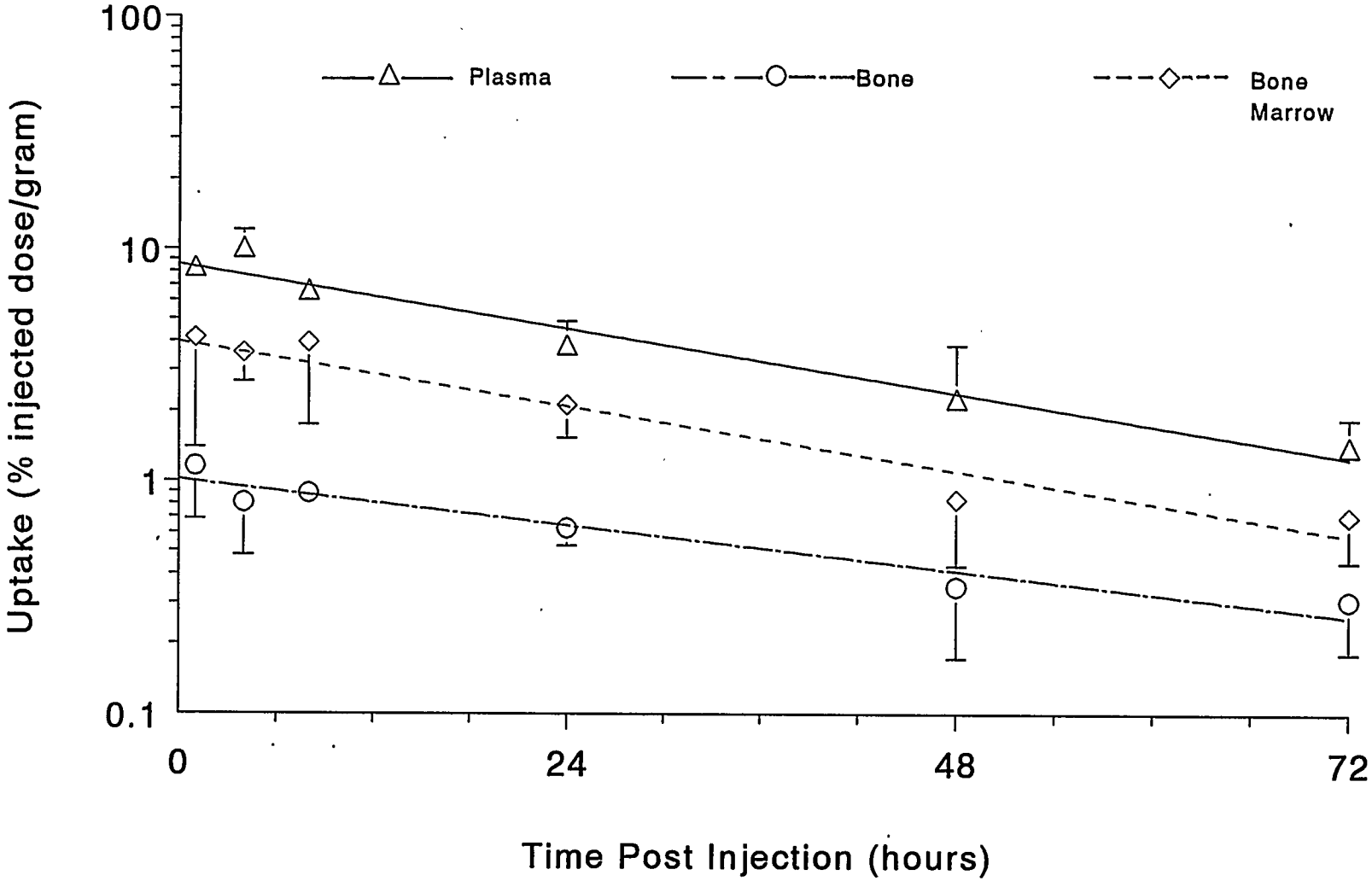

Figure 3. Uptake of ^{188}Re-labeled B43 in plasma, long bones devoid of marrow, and bone marrow of nude mice bearing human ovarian OVCAR tumors post i.v. injection of the radiolabeled antibodies. The curves are least-squares fit to the experimental data.

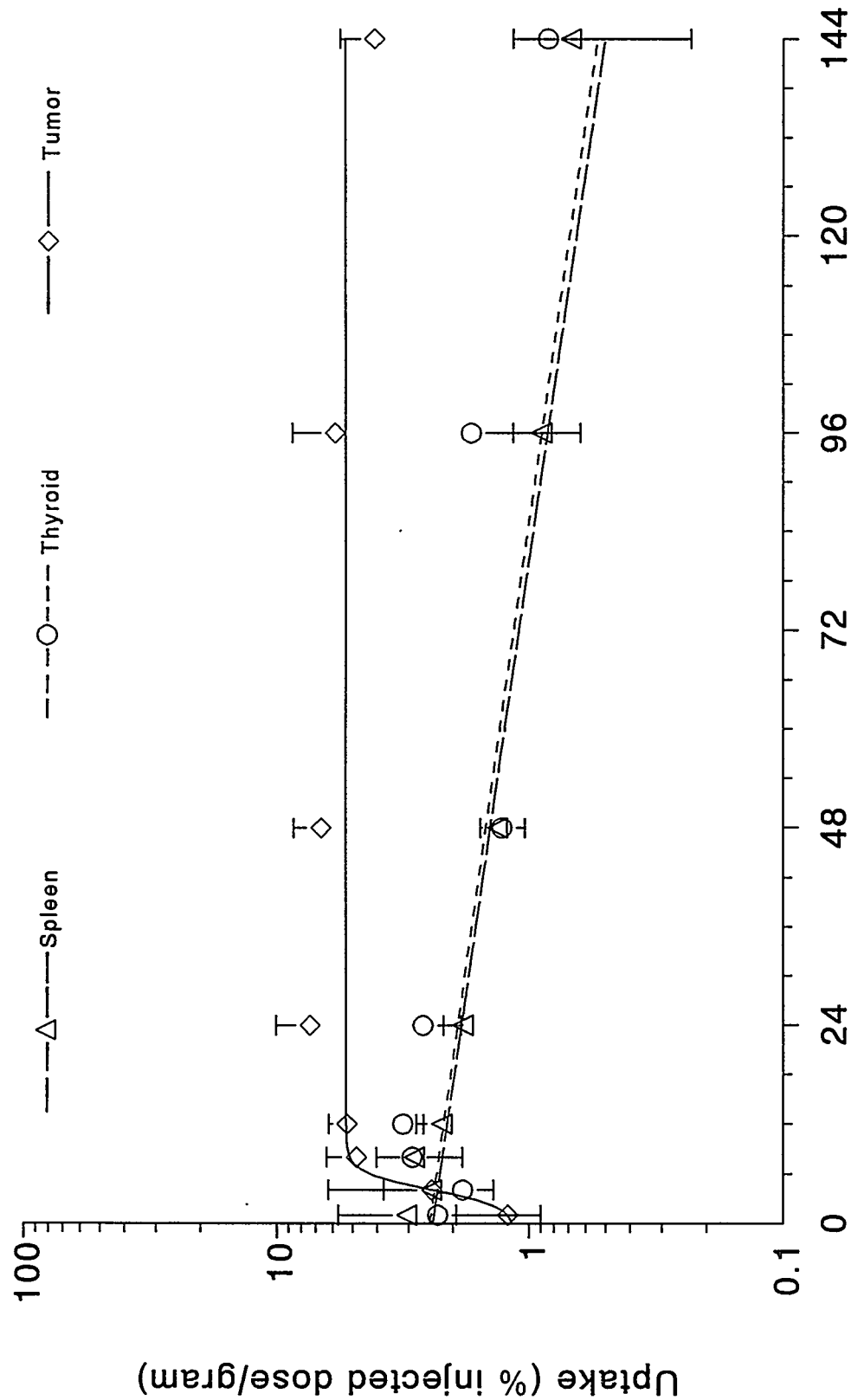

Figure 4. Uptake of ^{57}Co-labeled B43 in spleen, thyroid and tumor of the same animal model as in Figures 1-3 postinjection (i.v.) of radiolabeled antibodies. The curves are least-squares fit to the experimental data.

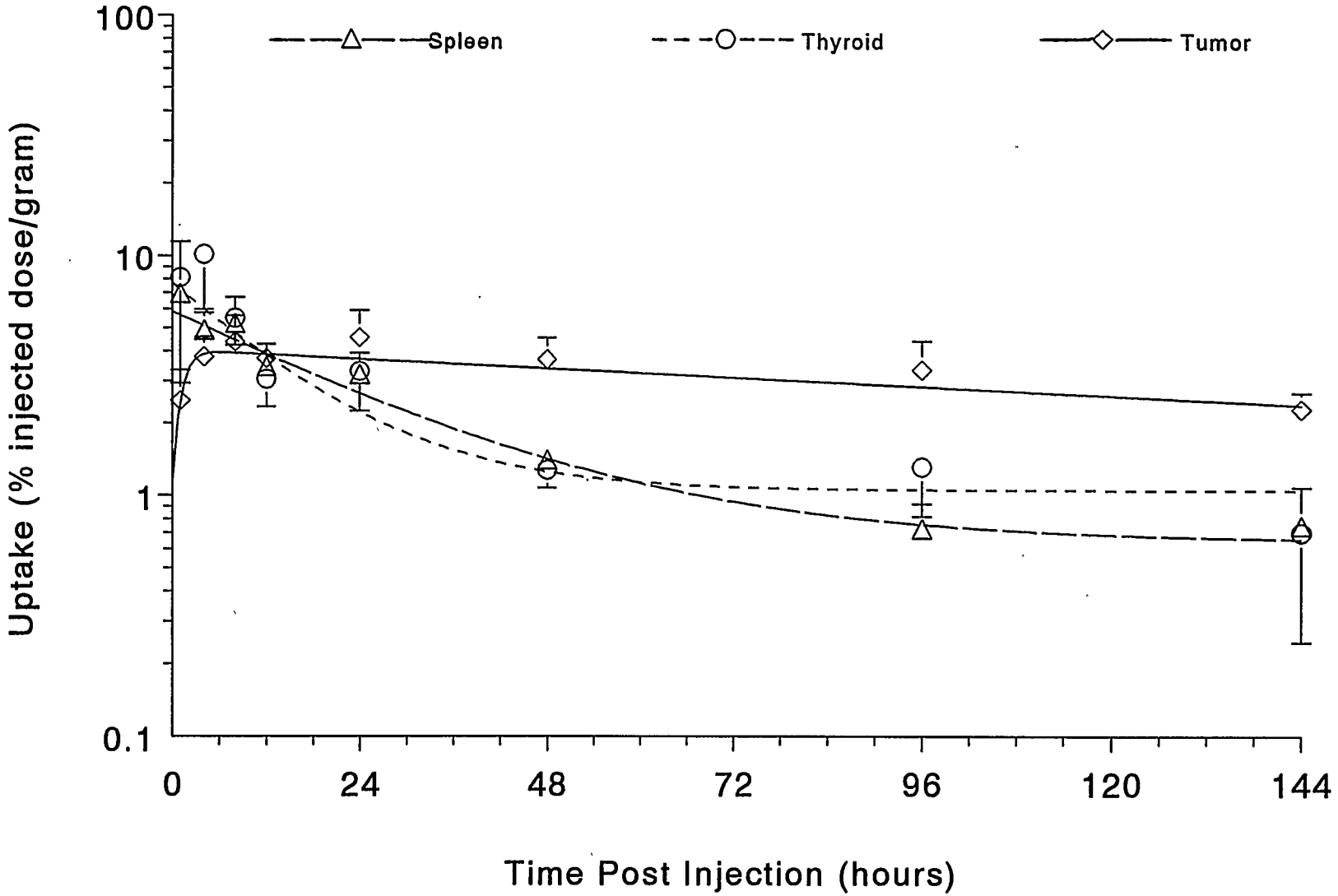

Figure 5. Uptake of ^{131}I-labeled B43 in spleen, thyroid and tumor of the same animal model as in Figures 1-3 postinjection (i.v.) of radiolabeled antibodies. The curves are least-squares fit to the experimental data.

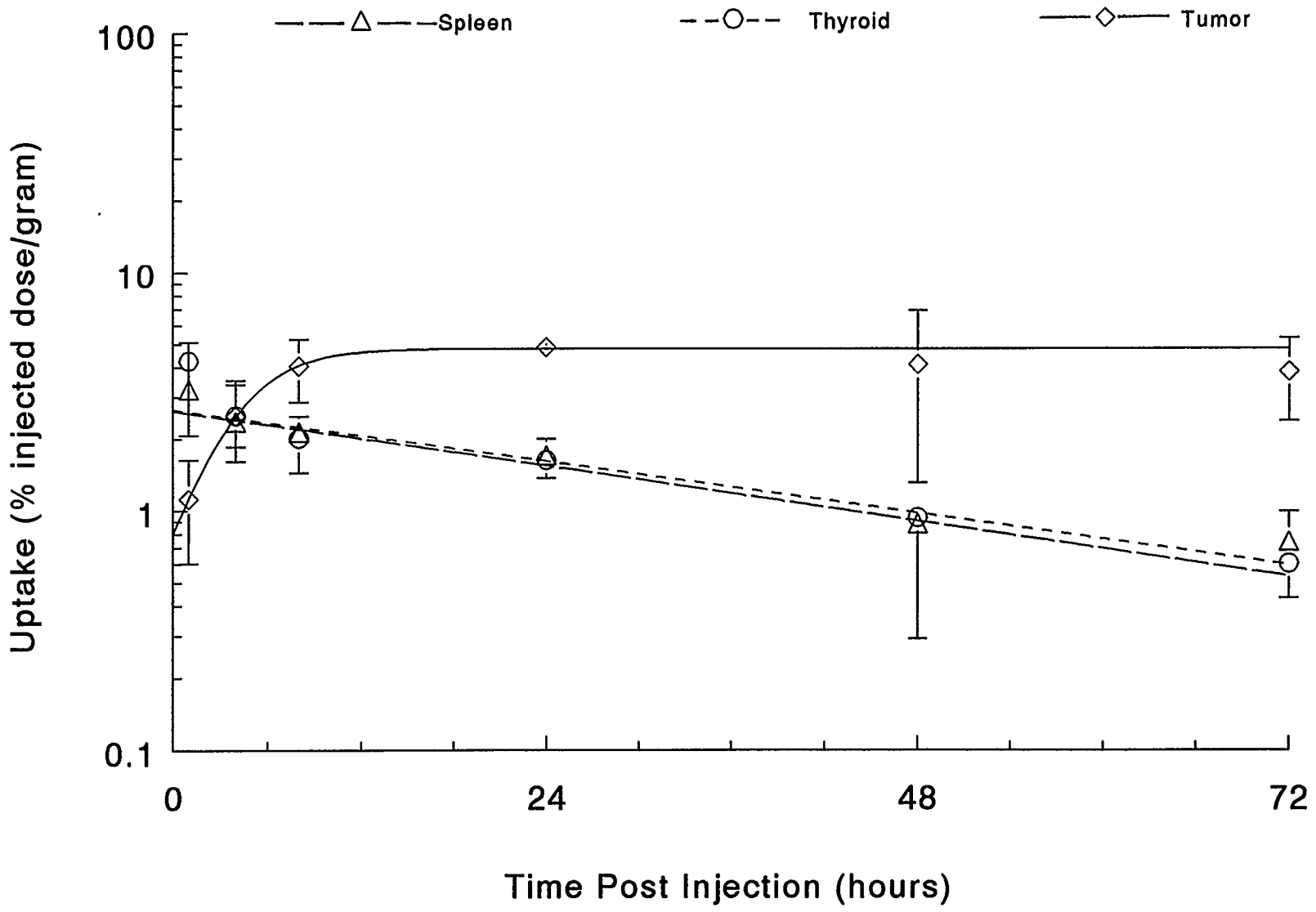

Figure 6. Uptake of ^{188}Re-labeled B43 in spleen, thyroid and tumor of the same animal model as in Figures 1-3 postinjection (i.v.) of radiolabeled antibodies. The curves are least-squares fit to the experimental data.

from carrier-free ^{188}Re-labeled antibody. As illustrated in Table 4, when the physical properties of the labeling isotopes are taken into account with the biological properties of the antibody, ^{186}Re-labeled B43 would give the highest tumor to red marrow radiation dose ratio, whereas ^{188}Re-labeled B43 would give the lowest. Unfortunately at the present time, large quantities of carrier-free ^{186}Re cannot be produced economically. This may limit the use of this isotope for labeling antibodies for RIT where a minimum radiation dose rate has to be exceeded to cause tumor shrinkage. To achieve this minimum dose rate, extremely high doses of noncarrier-free ^{186}Re-labeled antibodies will be required.

ACKNOWLEDGMENTS

We thank Mrs. Donna Laking for typing this manuscript. Research work supported by Natural Sciences and Engineering Research Council of Canada, Strategic Grant No. STR0149306.

REFERENCES

1. Jurcic JG and Scheinberg DA. Recent developments in the radioimmunotherapy of cancer [review]. Curr Opin Immunol 6:715-721, 1994.
2. Wessels BW and Rogers RD. Radionuclides selection and model absorbed dose calculations for radiolabeled tumor associated antibodies. Med Phys 11:638-645, 1984.
3. Shih LB, Thorpe SR, Griffiths GL, Diril H, Ong GL, Hansen HJ, Goldenberg DM and Mattes MJ. The processing and fate of antibodies and their radiolabels bound to the surface of tumor cells in vitro - a comparison of nine radiolabels. J Nucl Med 35:899-908, 1994.
4. Washburn LC, Sun TTH, Lee Y-CC, Byrd BL, Holloway EC, Crook JE, Stubbs, JB, Stabin MG, Brechbiel MW, Gansow OA and Steplewski Z. Comparison of five bifunctional chelate techniques for Y-90-labeled monoclonal antibody CO17-1A. Nucl Med Biol 18:313-321, 1991.
5. Deshpande SV, DeNardo SJ, Meares CF, McCall MJ, Adams GP, Moi MK and DeNardo GL. Copper-67-labeled monoclonal antibody lym-1, a potential radiopharmaceutical for cancer therapy: Labeling and biodistribution in RAJI tumored mice. J Nucl Med 29:217-225, 1988.
6. Moi MK and Meares CF. The peptide way to macrocyclic bifunctional chelating agents: Synthesis of 2-(p-nitorbenzyl)-1,4,7,10-tetraazacyclododecane-N,N',N",N"' -tetraacetic acid and study of its yttrium(III) complex. J Am Chem Soc (USA) 110:6266-6267, 1988.
7. Moreau P, Tinkl M, Tsukazaki M, Bury PS, Griffen EJ, Snieckus V, Maharajh RB, Kwok CS, Somayaji VV, Peng Z, Sykes TR and Noujaim AA. Synthesis of the bifunctional chelating agent 6-(4-aminobenzyl)-1,4,8,11-tetraazacyclotetradecane-*N,N',N",N"'*-tetraacetic acid(H_2NBn-TETA). Submitted to Synthesis.
8. Moi MK, Meares CF, McCall MJ, Cole WC and DeNardo SJ. Copper chelates as probes of biological systems: Stable copper complexes with a macrocyclic bifunctional chelating agent. Anal Biochem 148:249-53, 1985.
9. McCall JM, Diril H, Meares CF. Simplified method for conjugating macrocyclic chelating agents to antibodies via 2-iminothiolane. Bioconjugate Chem 1:222-226, 1990.
10. Meares CF, McCall JM, Reardan DT, Goodwin DA, Diamanti CI, McTigue M. Conjugation of antibodies with bifunctional chelating agents: isothiocyantes and bromoacetamide reagents, methods of analysis, and subsequent addition of metal ions. Anal Biochem 142:68-78, 1984.
11. Salacinski PRP, McLean C, Sykes JEC, Clement-Jones VV, Lowry PJ. Iodination of proteins, glycoproteins and peptides using a solid-phase oxidizing agent, 1,3,4,6-tetrachloro-3α,6α-diphenylglycouril (iodogen). Anal Biochem 117:136-146, 1981.
12. Sykes TR, Woo TK, Baum RP, Qi P, Noujaim AA. Direct labeling of monoclonal antibodies with Tc-99 using a photoactivation process. Submitted to J Nucl Med.

FETAL RADIATION DOSE ESTIMATES FOR I-131 SODIUM IODIDE IN CASES WHERE CONCEPTION OCCURS AFTER ADMINISTRATION.

Sparks RB and Stabin MG
Oak Ridge Institute for Science and Education

ABSTRACT

After administration of I-131 to the female patient, the possibility of radiation exposure of the embryo/fetus exists if the patient becomes pregnant while radioiodine remains in the body. Fetal radiation dose estimates for such cases were calculated. Doses were calculated for various maternal thyroid uptakes and time intervals between administration and conception, including euthyroid and hyperthyroid cases. The maximum fetal dose calculated was about 9.8E-03 mGy/MBq, which occurred with 100% maternal thyroid uptake and a 1 week interval between administration and conception. Placental crossover of the small amount of radioiodine remaining 90 days after conception was also considered. Such crossover could result in an additional fetal dose of 9.8E-05 mGy/MBq and a maximum fetal thyroid self dose of 3.5E-04 mGy/MBq.

INTRODUCTION

The radiation dose to the fetus after administration of I-131 NaI to the mother is always of concern. Physicians typically recommend that patients who are treated for hyperthyroidism wait 6 months before becoming pregnant. Occasionally, conception occurs within a few weeks after administration when some radioiodine still remains in the maternal system. In these situations, the usual fetal dose estimates, which give the cumulative dose starting from the time of administration, do not apply. In this paper, estimates of the radiation dose to the fetus are given for various maternal thyroid uptakes, assuming that conception occurs at various times after administration of I-131 NaI. The euthyroid model of MIRD Dose Estimate Report No. 5 [1] and the model for the hyperthyroid patient given by Stabin et al. [2] are employed. Possible transfer of the small amounts of radioiodide remaining 90 days after conception in the maternal body to the fetus and the fetal thyroid are also considered.

METHODS

Absorbed Dose Calculation for the Fetus

Dose to the fetus was estimated assuming that the absorbed dose in the nongravid uterus of the adult female is a good estimate of fetal dose in early pregnancy. The dose contributions from the nonpenetrating component in the uterus due to activity in the remainder of body were included in this calculation. A simple three compartment model consisting of maternal thyroid, remainder tissues, and urinary bladder was used to estimate the maternal residence times.

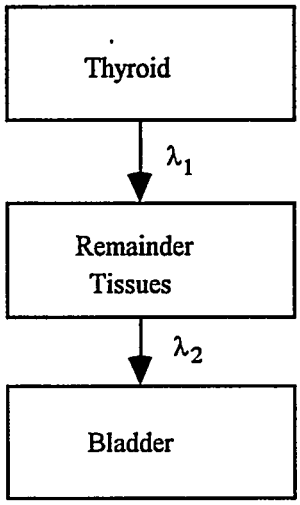

Figure 1. Compartmental model for maternal iodine kinetics.

At 1 week, the earliest time of conception after administration considered by this study, all activity not taken up by the thyroid is assumed to have been lost from the tissues in the remainder of the maternal body. For the euthyroid cases, the biological coefficients for removal from the thyroid were taken from MIRD Dose Estimate Report Number 5 [1]. For hyperthyroid cases, the biological removal rate from the thyroid was assumed to a linear function of maximum thyroid uptake [2]. The biological half-time for removal from the remainder of the body was assumed to be 6.1 hours in all cases [1]. The system of coupled first order differential equations which are represented by this compartmental model was solved analytically for thyroid and remainder tissues, and integrated to yield expressions for the residence times for the various uptakes and times after administration that conception was assumed to have occurred. The residence time in the urinary bladder was determined by applying the dynamic bladder model [3], using a bladder voiding interval of 4.8 hours. These residence times were used as input into the MIRDOSE 3.1 [4] software in order to calculate the maternal contributions to the fetal dose.

Fetal Self Dose

A conservative estimate of the fetal self dose from fetal uptake of activity was calculated for the various maximum maternal thyroid uptakes. It was assumed that conception occurred 1 week after administration of the iodide, since this assumption will yield the highest fetal self dose of all the conception times that were considered in this study. It was also assumed that all of the activity that reaches the maternal remainder tissues from what remains in the thyroid at 3 months (when the placenta was assumed to begin functioning), crosses the placenta and is retained indefinitely in the fetus.

Fetal Thyroid Self Dose

The self dose to the fetal thyroid was calculated for the fourth and fifth months of pregnancy, for the various uptakes assuming conception occurred 1 week after administration of the iodide. The 1 week interval was once again chosen because it will yield the most conservative estimate. The amount of activity remaining in the maternal thyroid at 3 and 4 months was calculated, and the fraction reaching the maternal remaining tissues, f_{Rem}, was calculated as follows [5]:

$$f_{\text{Rem}} = \frac{\lambda_b}{\lambda_b + \lambda_R} f_u, \qquad (1)$$

where: λ_b = the biological removal rate from the thyroid,

λ_R = the removal rate from physical decay, and

f_u = the thyroid uptake fraction.

The compartmental model for iodine metabolism in the fetus and the pregnant woman of Watson [6] was then used to determine the residence times in the fetal thyroid. Conservative modifications to the model were made in this calculation, including allowing no biological removal of the iodine from the fetal thyroid and, removing the maternal thyroid compartments for recycling (Figure 2). Fetal thyroid S values were also taken from Watson [6].

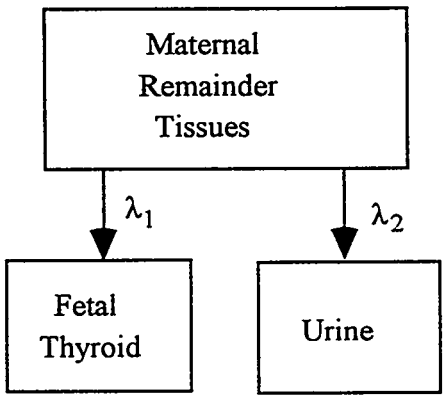

Figure 2. Compartmental model for maternal/fetal iodine kinetics.

RESULTS

Table 1 gives the fetal doses at different times of postadministration conception for the three levels of thyroid uptake in the euthyroid patient considered in MIRD Dose Estimate Report No. 5 (1). Table 2 shows the same information, for the various assumed maximum thyroid uptakes in hyperthyroid individuals.

The maximum absorbed dose to the fetus due to uptake of activity after the placenta begins to function, which was assumed to occur at 3 months gestation, was estimated to be 9.8×10^{-5} mGy/MBq (0.36 mrad/mCi). It should be noted that this is a conservative estimate, as all of the activity that leaves the maternal thyroid to enter the systemic circulation will probably not be taken up by the fetus. The maximum fetal thyroid self dose was determined to be about 3.5×10^{-4} mGy/MBq (1.3 mrad/mCi), which occurred at a maximum thyroid uptake level of approximately 35%.

Table 1

Absorbed Dose to the Embryo/Fetus in Euthyroid Cases (mGy/MBq)

% Max Uptake	Time in Weeks After Administration That Conception Occurs							
	1	2	3	4	5	6	7	8
5%	3.1E-04	1.5E-04	7.7E-05	3.8E-05	1.9E-05	9.5E-06	4.7E-06	2.4E-06
15%	8.8E-04	4.4E-04	2.2E-04	1.1E-04	5.6E-05	2.8E-05	1.4E-05	7.2E-06
25%	1.4E-03	7.1E-04	3.6E-04	1.8E-04	9.2E-05	4.7E-05	2.4E-05	1.2E-05

Table 2

Absorbed Dose to the Embryo/Fetus in Cases of Hyperthyroidism (mGy/MBq)

% Max Uptake	Time in Weeks After Administration That Conception Occurs							
	1	2	3	4	5	6	7	8
5%	4.1E-04	1.9E-04	8.7E-05	4.0E-05	1.9E-05	8.7E-06	4.0E-06	1.9E-06
10%	8.3E-04	3.8E-04	1.7E-04	8.0E-05	3.7E-05	1.7E-05	7.8E-06	3.6E-06
15%	1.3E-03	5.8E-04	2.6E-04	1.2E-04	5.5E-05	2.5E-05	1.1E-05	5.2E-06
20%	1.7E-03	7.8E-04	3.5E-04	1.6E-04	7.2E-05	3.3E-05	1.5E-05	6.7E-06
25%	2.2E-03	9.8E-04	4.4E-04	2.0E-04	8.8E-05	4.0E-05	1.8E-05	8.0E-06
30%	2.7E-03	1.2E-03	5.3E-04	2.3E-04	1.0E-04	4.6E-05	2.0E-05	9.1E-06
35%	3.2E-03	1.4E-03	6.1E-04	2.7E-04	1.2E-04	5.2E-05	2.3E-05	1.0E-05
40%	3.7E-03	1.6E-03	7.0E-04	3.0E-04	1.3E-04	5.7E-05	2.4E-05	1.1E-05
45%	4.3E-03	1.8E-03	7.8E-04	3.3E-04	1.4E-04	6.0E-05	2.6E-05	1.1E-05
50%	4.8E-03	2.0E-03	8.5E-04	3.6E-04	1.5E-04	6.3E-05	2.6E-05	1.1E-05
55%	5.4E-03	2.2E-03	9.2E-04	3.8E-04	1.6E-04	6.4E-05	2.7E-05	1.1E-05
60%	6.0E-03	2.4E-03	9.8E-04	4.0E-04	1.6E-04	6.4E-05	2.6E-05	1.0E-05
65%	6.7E-03	2.6E-03	1.0E-03	4.0E-04	1.6E-04	6.2E-05	2.5E-05	9.7E-06
70%	7.3E-03	2.8E-03	1.1E-03	4.1E-04	1.5E-04	5.9E-05	2.2E-05	8.6E-06
75%	7.9E-03	2.9E-03	1.1E-03	4.0E-04	1.5E-04	5.4E-05	2.0E-05	7.2E-06
80%	8.5E-03	3.0E-03	1.1E-03	3.7E-04	1.3E-04	4.6E-05	1.6E-05	5.7E-06
85%	9.1E-03	3.0E-03	1.0E-03	3.4E-04	1.1E-04	3.8E-05	1.3E-05	4.2E-06
90%	9.6E-03	3.0E-03	9.2E-04	2.9E-04	8.9E-05	2.8E-05	8.6E-06	2.7E-06
95%	9.8E-03	2.8E-03	7.9E-04	2.2E-04	6.3E-05	1.8E-05	5.1E-06	1.4E-06
100%	9.8E-03	2.4E-03	6.1E-04	1.5E-04	3.8E-05	9.3E-06	2.3E-06	5.8E-07

DISCUSSION

The bladder contents and remainder tissues are the primary contributors to the fetal dose, even though many more transitions occur in the maternal thyroid than in these regions. This is due to their much closer proximity to the uterus. The earliest time of conception considered in the model was one week after administration; at this time the only significant radioiodine remaining in the mother's system is located in the thyroid. The cumulated activities in the remainder tissues and urinary bladder result from the biological removal of this radioiodine from the thyroid to the systemic circulation, and its ultimate excretion in the urine.

For a given time of conception postadministration, fetal doses increase with maximum thyroid uptake to a maximum level and then decrease. The increase is due to the larger amounts of activity being taken up by the thyroid and subsequently being excreted. As the uptake level increases, this effect is counteracted by the decreasing biological half-time of removal from the thyroid. The faster

biological removal rates cause the activity to be removed from the body more quickly, and thus deliver less dose to the fetus. In the fetal doses for 1 week after administration, this effect is not seen because of the large number of transitions that occur during the first week.

The dose estimate tables for the hyperthyroidism cases included very low maximum uptake percentages for the thyroid. While very low uptakes are obviously not a characteristic of Graves' disease, they are occasionally seen when the patients have had large amounts of iodine in their systems, perhaps from other sources. In Graves' disease, administered activities are typically several hundred MBq, so the highest fetal doses expected would be a few mGy (Table 2).

ACKNOWLEDGMENTS

The authors would like to thank Evelyn Watson and Carol Marcus for their assistance in this work.

REFERENCES

1. Berman, M., Braverman, L., Burke, J. et al. MIRD Dose Estimate Report No. 5: Radiation absorbed dose estimates for I-123, I-124, I-125, I-126, I-130, I-131, and I-132 as sodium iodide. J Nucl Med 16:857-860, 1975.
2. Stabin MG, Watson EE, Marcus CS and Salk, RD. Radiation dosimetry for the adult female and fetus from iodine-131 administration in hyperthyroidism. J Nucl Med 32:808-813, 1991.
3. Cloutier RJ, Smith SA and Watson EE et al.. Dose to the fetus from radionuclides in the bladder. Health Physics 25:147-161, 1973.
4. Stabin MG. MIRDOSE: Personal computer software for internal dose assessment in nuclear medicine. J Nucl Med 37:538-546, 1996.
5. Stabin MG and Watson EE. An alternative to convolution integrals for radiation absorbed dose calculations. In the Fifth International Radiopharmaceutical Dosimetry Symposium. Editors: Watson EE, Schlafke-Stelson AT. 1991, pp. 457-464.
6. Watson EE. Radiation absorbed dose to the human fetal thyroid. In the Fifth International Radiopharmaceutical Dosimetry Symposium. Editors: Watson EE, Schlafke-Stelson AT. 1991, pp. 179-187.

RADIOBIOLOGICAL MODELING WITH MARCELL SOFTWARE

Hasan JS and Jones TD
Health Sciences Research Division
Oak Ridge National Laboratory
P.O. Box 2008
Oak Ridge, TN 37831-6101

ABSTRACT

A nonlinear system of differential equations that models the bone marrow cellular kinetics associated with radiation injury, molecular repair, and compensatory cell proliferation has been extensively documented. Recently, that model has been implemented as MarCell, a user-friendly MS-DOS computer program that allows users with little knowledge of the original model to evaluate complex radiation exposure scenarios. The software allows modeling with the following radiations: tritium beta, 100 kVp X, 250 kVp X, 22 MV X, ^{60}Co, ^{137}Cs, 2 MeV electrons, triga neutrons, D-T neutrons, and 3 blends of mixed-field fission radiations. The possible cell lineages are stem, stroma, and leukemia/lymphoma, and the available species include mouse, rat, dog, sheep, swine, burro, and man. An attractive mathematical feature is that any protracted protocol can be expressed as an equivalent prompt dose for either the source used or for a reference, such as 250 kVp X rays or ^{60}Co. Output from MarCell includes: risk of 30-day mortality; risk of cancer and leukemia based either on cytopenia or compensatory cell proliferation; cell survival plots as a function of time or dose; and 4-week recovery kinetics following treatment. In this article, the program's applicability and ease of use are demonstrated by evaluating a medical total body irradiation protocol and a nuclear fallout scenario.

INTRODUCTION

Jones et al. introduced a bone marrow radiation cell kinetics model with great potential for application in the fields of health physics, radiation research, and medicine (1,2,3,4). However, until recently, only the model developers have been able to apply it because of the complex array of biological and physical assignments needed for evaluation of a particular radiation exposure protocol. The purpose of this article is to illustrate the use of MarCell ("MARrow CELL Kinetics") software for MS-DOS, a "user-friendly" computer implementation of that mathematical model that allows almost anyone with an elementary knowledge of radiation physics and/or medical procedures to apply the model. A "hands-on" demonstration of the software will be given by guiding the user through evaluation of a medical total body irradiation protocol and a nuclear fallout scenario. A brief overview of the software is given in the Appendix.

SAMPLE APPLICATION: PLANNING OF TOTAL BODY IRRADIATION FOR MEDICAL THERAPY

Since the late 1950's total body irradiation (TBI) has been used as a preparative regimen for allogenic bone marrow transplantation in order to accomplish the following objectives: (a) host immunosuppression to prevent rejection of donor stem cells; (b) eradication of leukemia cells; and (c) ablation of host bone marrow in order to create space for stem cell grafts (5). While ablating the host marrow, it is important to spare the stromal cells because marked damage to stromal cells may lead to graft failure (6). In addition, the TBI protocol must not be overly toxic to normal tissues. Initial TBI protocols consisted of a single dose of radiation (typically 10 Gy) delivered at relatively high dose rates (0.07-0.10 Gy/min). In the late 1970's, normal tissues were found to be sensitive to dose fractionation, and fractionated dose TBI schedules (e.g. 12 Gy delivered in 6 fractions, 2 fractions per day) were introduced to reduce toxicity to normal tissues. Despite its lower normal tissue toxicity, fractionated TBI has been found, in some cases, to be less effective at eradicating host leukemic cells. The controversy over the optimal TBI regimen for allogenic bone marrow transplantation continues today (7). MarCell software is particularly useful in the design and comparison of various TBI schedules and may be helpful in finding the optimal TBI regimen(s).

For purpose of illustration, consider a fractionated TBI schedule of 12 Gy of Co-60 delivered in 6 fractions, 2 fractions per day (one at 9. a.m. and the other at 2 p.m.) at a dose rate of 7 cGy/min. To start with, option 2 ("cell kinetics calculations with 4 week recovery") was selected from the main menu in Figure 1A. From the menu in Figure 1F, option 1 was selected ("1 or more cell types of your choice"). After entering 3 for the number of cell types to be considered, man was selected from the species menu in Figure 1D. Next, Cobalt 60 (choice 4) was selected from the radiation menu (Figure 1B), and the dose information was entered in the following screen. (Note: underlining indicates numbers that were input by the user, while italics indicates information that was output by the program.)

number of radiation doses (maximum of 500) > 6

marrow dose 1 (in cGy) > 200
marrow dose rate for dose 1 (in cGy/minute) > 7
time needed for dose 1: 28 minute(s), 38 second(s)

time in minutes between dose 1 and dose 2 > 300
marrow dose 2 (in cGy) > 200
marrow dose rate for dose 2 (in cGy/minute) > 7
time needed for dose 2: 28 minutes(s), 38 second(s)

time in minutes between dose 2 and dose 3 > 1140
marrow dose 3 (in cGy) > 200
marrow dose rate for dose 3 (in cGy/minute) > 7
time needed for dose 3 : 28 minute(s), 38 second(s)

time in minutes between dose 3 and dose 4 > 300
marrow dose 4 (in cGy) > 200
marrow dose rate for dose 4 (in cGy/minute) > 7
time needed for dose 4: 28 minute(s), 38 second(s)

(A)

Main Menu

1. cell kinetics calculations.
2. cell kinetics calculations with 4 week recovery.
3. cell kinetics calculations from a dose info. file
4. nuclear fallout calculations.
5. nuclear fallout calculations with 4 week recovery.
6. retrieve a set of calculations from disk.
7. view information about this program.
8. exit.

Choose an Option

(B)

Radiation Types

1. Tritium beta
2. 100 kVp x-rays
3. 250 kVp x-rays
4. Cobalt 60
5. Cesium 137
6. 2 MeV electrons
7. 22 MV x-rays
8. Neutron Fission
9. Neutron Fusion
10. Neutron:Gamma (1:1)
11. Neutron:Gamma (5:1)
12. Neutron:Gamma (30:1)
13. Other (enter rate constants manually)

Choose an Option

(C)

Cell Type: Leukemia/Lymphoma

1. M1 leukemia/lymphoma cells (most radiosensitive)
2. M2 leukemia/lymphoma cells.
3. M3 leukemia/lymphoma cells.
4. M4 leukemia/lymphoma cells. (least radiosensitive)

Choose an Option

(D)

Species

1. Mouse
2. Rat
3. Dog
4. Sheep
5. Swine
6. Burro
7. Man
8. Other (enter constants manually)

Choose an Option

(E)

Cell Type

1. Stromal Cells
2. Hematopoietic Stem Cells
3. Leukemia/Lymphoma Cells
4. Other (use custom rate constants)

Choose an Option

(F)

Number of Cell Types

1. 1 or more cell types of your choice.
2. 2 cell types: stem and stroma.

Choose an Option

Figure 1. MarCell menus.

time in minutes between dose 4 and dose 5 > 1140
marrow dose 5 (in cGy) > 200
marrow dose rate for dose 5 (in cGy/minute) > 7
time needed for dose 5: 28 minute(s), 38 second(s)

time in minutes between dose 5 and dose 6 > 300
marrow dose 6 (in cGy) > 200
marrow dose rate for dose 6 (in cGy/minute) > 7
time needed for dose 6: 28 minute(s), 38 second(s).

From the cell type menu in Figure 1E, stromal cells (choice 1), hematopoietic stem cells (choice 2), and leukemia/lymphoma cells (choice 3) were chosen for the first, second, and third cell types, respectively. From the leukemia/lymphoma cell menu (Figure 1C), choice 3 (M3 leukemia/lymphoma cells) was selected to specify the relative radiosensitivity of the leukemia/lymphoma cells. MarCell can compute the proliferation rate of leukemia/lymphoma cells based on cellular doubling time or doubling time of the cancer. For the M3 leukemia/lymphoma cells, we chose to specify the proliferation rate by entering a cellular doubling time of 2 days. Figure 2 shows the cell survival as a function of time, and Table 1 contains the numerical results.

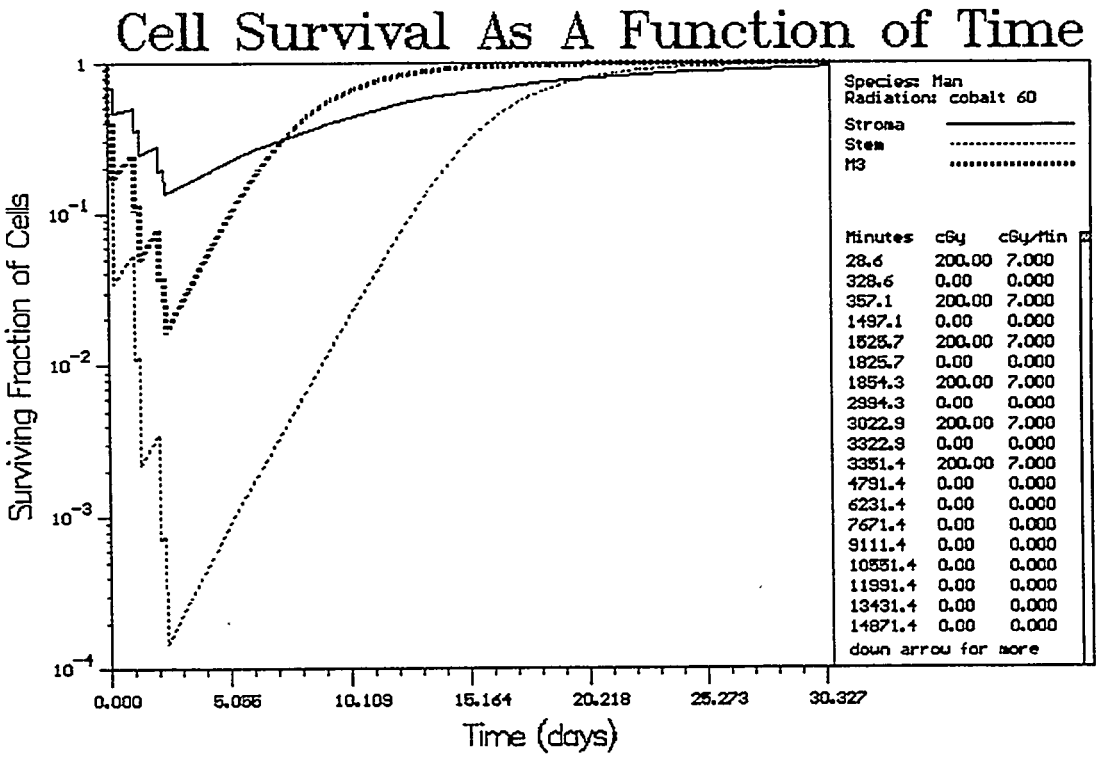

Figure 2. Cell survival for a TBI protocol of 6 fractions of 2 Gy each, 2 fractions per day (9 a.m. and 2 p.m.). For three days, at a dose rate of 7 cGy/min.

Table 1
Calculation Results for a Fractionated TBI Protocol of 6 Fractions of 2 Gy Each, 2 Fractions per Day (9 a.m. and 2 p.m.) for 3 Days, at a Dose Rate of 7 cGy/min

Treatment After Radiation Exposure	**Probability of Death**
no treatment	1.00
antibiotic and blood cell prophylaxis	0.88
marrow transplant (radiation risk)	0.09

Cell Type	**250 kVp x-ray EPD**	**Cobalt 60 EPD**
Stroma	559.922	757.332
Stem	647.490	876.007
M3	478.014	645.355

Note: Stem DREF/RBE factors and risk of cancer could not be computed because the risk coefficients were invalid due to excessive cell killing.

Stromal DREF/RBE's (Co-60 ref.):

based on cytopenia = 0.63111
based on repopulation = 0.92369

SAMPLE APPLICATION: EVALUATION OF RISK FROM EXPOSURE TO NUCLEAR FALLOUT RADIATION

Radiation fallout is characterized by an exponentially decreasing dose rate. For practical purposes, the rate can be described as $T^{-1.2}$ where "T" is the age of the fallout in hours. (8). Thus, the variable dose rate effect and the extremely complex behavior of compensatory marrow cell kinetics serves to demonstrate the great practicality of the MarCell code. For purpose of illustration, consider a hypothetical exposure schedule in which troops are required to work unprotected in a fallout environment for 3 hours per day over 3 days. The variable dose rates and fractionations of exposure leave this problem lacking a modeling algorithm or a parallel practical experience to serve as a basis for decision-making. With MarCell, the evaluation was made as follows. Option 5 ("nuclear fallout calculations with 4 week recovery) was selected from the main menu (Figure 1A). Next, man was selected from the species menu (Figure 1D), stem and stroma cells were selected from the cell types menu (Figure 1F), and Cobalt 60 was selected from the radiation menu. (For nuclear fallout calculations, MarCell limits the radiation choices to Cobalt 60 and Cesium 137.) The fallout dose information was entered in the following screen. (Note: underlining indicates numbers that were input by the user, while italics indicates information that was output by the program.)

Fallout Information:

number of exposure periods > 3

time (hours) after explosion that exposure period 1 begins (minimum = 0.000001 h) > 1

dose rate (cGy/min.) at the beginning of period 1 > 20

exposure time (hours) for period 1 > 3

time (hours) between exposure periods 1 and 2 > 21
exposure time (hours) for period 2 > 3

time (hours) between exposure periods 2 and 3 > 21
exposure time (hours) for period 3 > 3

Figure 3 shows the cell survival as a function of time while Table 2 contains the numerical results.

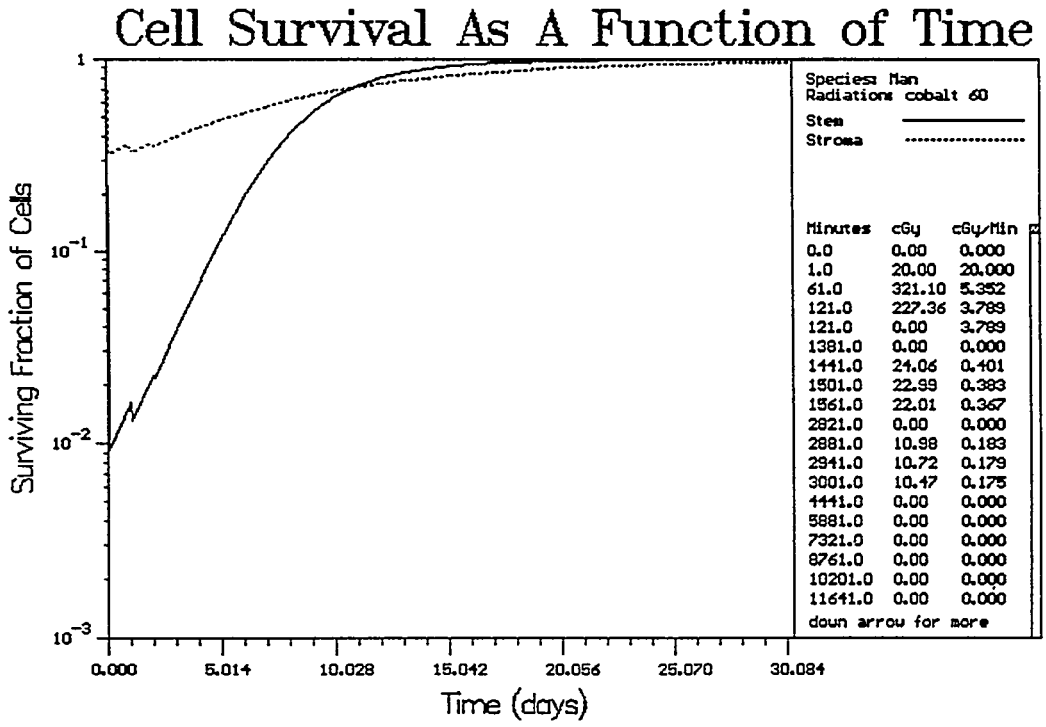

Figure 3. Cell survival for nuclear fallout exposure of 3 hours per day over 3 days

CONCLUSION

MarCell provides an easy way to model bone marrow radiation cell kinetics and has great potential for applicability wherever biological effects of radiation are of concern. We are encouraged by the large amount of interest that has been shown by the medical community, radiation risk personnel, and radiation researchers and hope to extend the software to other computing platforms.

Table 2
Calculation Results for Nuclear Fallout Exposure of 3h per Day over 3 Days.
(Cobalt 60 radiation)

Treatment After Radiation Exposure		**Probability of Death**
no treatment		0.99
antibiotic and blood cell prophylaxis		0.23
marrow transplant (radiation risk)		0.01
Cell Type	**250 kVp x-ray EPD**	**Cobalt 60 EPD**
Stem	345.709	467.716
Stroma	348.473	471.298
Stromal DREF/RBE's (Co-60 ref.):		
based on cytopenia = 0.70377		
based on repopulation = 0.70703		
Cytopenia (stem, Co-60 ref.):		
Lifetime risk of all cancers = 0.36807		
Lifetime risk of leukemia = 0.04677		
Repopulation (stem, Co-60 ref.):		
Lifetime risk of all cancers = 0.36807		
Lifetime risk of leukemia = 0.05184		
DREF/RBE Factors (stem, Co-60 ref.):		
Cytopenia = 0.69843		
Repopulation = 0.77413		
Treatment Dose = 669.672 (cGy)		
Dose based on cytopenia = 467.716 (cGy)		
Effective Dose based on repopulation = 518.411 (cSv)		

APPENDIX: SOFTWARE OVERVIEW

The current version of MarCell runs on IBM-compatible computers with a 80286 chip or higher. The program's main functions are shown in the main menu in Figure 1. For custom dose protocols, the program asks for the number of dose fractions, the dose (cGy) and dose rate (cGy/min.) for each fraction, and the time (h) between each dose fraction. For fallout radiation protocols, dose rate decay is approximated by $T^{-1.2}$ where T is the time in hours after the unit time reference used for fallout dose rate decay (8), and users must enter the number of fallout radiation exposure periods, the arrival time (h), the initial dose rate (cGy/min.) for the first period, the duration (h) of each exposure period, and the time (h) between exposure periods. For both fallout radiation protocols and custom radiation protocols, the user is given the option to extend the cell survival calculations by 4 weeks in order to model post-exposure recovery. When option 3 ("cell kinetics calculations from a dose info. file") is chosen from the main menu (Figure 1), all dose information is taken from an ASCII file, allowing MarCell to be used in conjunction with separate programs, such as radiation transport codes.

Cell kinetics calculations can be performed for the species listed in the species menu (Figure 3). The available radiation types are shown in the radiation menu (Figure 4); however, for nuclear fallout

calculations, the radiation choices are limited to Cobalt 60 and Cesium 137. The cell type choices are stromal cells, hematopoietic stem cells, and leukemia/lymphoma cells. Currently, 4 leukemia/lymphoma cell types are available (M1, M2, M3, M4), where the relative radiosensitivities are: stroma < M4 < M3 < M2 < stem < M1. Based on the choices for species, radiation, and cell type, the appropriate cellular rate constants are used. If "other" is selected for species, radiation, or cell type, custom values for the 5 cellular rate constants can be entered, allowing for modeling of other cells such as lymphocytes or crypt cells of the intestine if rate constants are known.

Output is in the form of automatically-scaling semilog plots of cell survival as a function of time or dose (Gy). When time is used for the x-axis, the most appropriate time units (min., h, days) are automatically selected. In addition to plotting cell survival, the program displays probability of radiation-induced mortality for the following post-exposure treatments: no medical treatment, antibiotic treatment with irradiated blood elements, and marrow transplantation with its attendant core usually including antibiotics and irradiated blood elements. Lifetime risk of all cancers and lifetime risk of leukemia based on either cytopenia (blood cell depletion) or repopulation are also displayed. Additionally, stromal DREF/RBE's (dose rate effectiveness factor/relative biological equivalent) based on cytopenia and repopulation are given, and equivalent prompt doses with respect to Cobalt 60 and 250 kVp x-rays are displayed for each selected cell type. Plots of cell survival as a function of dose or time can be printed out, and all calculation sessions can be saved to disk for later use.

ACKNOWLEDGMENT

This research was sponsored by the U.S. Department of Energy, the U.S. Defense Nuclear Agency IACRO 93-844, and the U.S. Army Nuclear and Chemical Agency MIPR USANCA95RO1014 under contract DE-AC05-84OR21400 with Lockheed Martin Energy Systems, Inc. with the U.S. Department of Energy.

REFERENCES

1. Jones TD, Morris MD and Young RW. A mathematical model for radiation-induced myelopoiesis. Radiation Research 128:258-266, 1991.
2. Jones TD, Morris MD and Young RW. A cell-kinetics model for radiation-induced myelopoiesis. Experimental Hematology 21:816-822, 1993.
3. Morris MD, Jones TD and Young RW. A cell kinetics model of radiation-induced myelopoiesis: rate constant estimates from mouse, rat, sheep, swine, dog, and burro irradiated by photons. Radiation Research 135:320-331, 1993.
4. Morris MD, Jones TD and Young RW. Estimation of coefficients in a model of radiation-induced myelopoiesis from mortality data for mice following x-ray exposure. Radiation Research 128:267-275, 1991.
5. Gale R, Butturini A and Bortin MM. What does total body irradiation do in bone marrow transplants for leukemia? Int. J. Radiat. Oncol. Biol. Phys. 20:631-634, 1991.

6. Cosset JM, Socie G, Dubray B, Girinsky T, Fourquet A and Gluckman E. Single dose vs. fractionated total body irradiation before bone marrow transplantation: radiobiological and clinical considerations. Int. J. Rad. Onc. Biol. Phys. 30(2):477-492, 1994.
7. Cosset JM, Girinsky T and Socie G. The never-ending controversy about TBI schedules. Radiotherapy and Oncology 23(4):268-268, 1992.
8. Glasstone S and Dolan PJ. The Effects of Nuclear Weapons, 3rd Edition. U.S. Department of Defense and U.S. Department of Energy. 1977. p. 394.

EFFECTIVE DOSE ESTIMATES FOR INDIAN ADULT FROM ADMINISTRATION OF $^{3}H_2O$ AND $NA^{131}I$

SC Jain[1], MM Gupta[2], AR Reddy[3] and A Nagaratnam[4]
[1]Institute of Nuclear Medicine & Allied Sciences, Delhi-110054
[2]EMS (ICMR), INMAS, Delhi-110054
[3]Defence Laboratory, Jodhpur-342011
[4]CCE(R&D), Secundrabad-500003, India

ABSTRACT

ICRP 53 gives the radiation dose to various organs and effective dose to patients from administration of various radiopharmaceuticals for ICRP Reference Man. However, an Indian adult differs significantly from his ICRP counterpart as regards to anatomical and physiological characteristics. In this paper, efforts have been made to estimate the radiation dose to an Indian adult from administration of tritiated water and ^{131}I-sodium iodide. For tritiated water, the biological half-time in Indians has been reported to be 4.5 d as compared to 10 d for ICRP adult. For ^{131}I sodium iodide administration, biological half-time for thyroid excretion is reported to be 60 d, which is less than that for ICRP adult. The average thyroid uptake in Indian has been reported to be 30% from multicentre study though the fast component excretion is reported to be 8 h, the same as considered by ICRP. Taking all these parameters into account, the effective dose is found to be 55% lower for Indians for tritiated water. For $Na^{131}I$, considering thyroid uptake of 30% in Indians, the effective dose is found to be 22.3 mSv/MBq as compared to 21.5 mSv/MBq for ICRP adult presuming similar thyroid uptake.